1. Introduction

The Illinois Institute of Technology (IIT) was awarded by the U.S. Department of Energy to lead an extensive effort in forming a world-class wind energy consortium (the Consortium) of multiple universities (domestic and international) and multiple industry participants (all types of wind energy stakeholders) to perform focused research and development on critical wind energy challenges identified in the "20% Wind Energy by 2030" report, including wind technology challenge, grid system integration, and workforce development.

The project started in January 2010 and ended in August 2012. The Principle Investigator of this project is Dr. Mohammad Shahidehpour, Director of the Robert W. Galvin Center for Electricity Innovation at IIT. The Project Team Members (in Alphabetical Order) include Acciona Wind Energy USA, Alstom Grid, Dakota Power, Electric Power Research Institute, EnerNex, Innovative Technology Applications Company, Intellergy, Intelligent Power Solutions, Invenergy, Keyworks, McCoy Energy, S&C Electric, SmartSignal (Now GE Intelligent Platforms), Southern Illinois University, Three Point Square, University of Chicago, Wiedman Power System Consulting.

Project Objectives. The Consortium's research and development objectives are focused on addressing several challenges identified in the "20% Wind Energy by 2030" report, i.e., wind technology, grid system integration, and workforce development. In particular, (1) The consortium members will develop control algorithms for enhancing the reliability of wind turbine components; (2) The consortium members will develop advanced operation and planning tools for accommodating the high penetration of intermittent wind energy in electric power utility systems. (3) The consortium members will educate the stakeholders on critical issues related to the wind energy research and development. (4) The world-class wind energy education and research programs developed by the consortium will outlast the proposed two-year period of the project.

Project Scope. The project will be performed in phases. In Phase 1, the consortium members will procure a utility-scale wind turbine at a wind farm and install a small wind turbine at IIT. In Phase 2, the consortium members will perform research on the wind turbine reliability. In Phase 3, the consortium members will perform wind energy related research and development to facilitate the integration of wind into the electric power grid system. In Phase 4, the consortium members will engage in the workforce development for wind energy research, design, and integration.

Summary of Project Activities. During the two-year project period since January 2010, the consortium members have developed control algorithms for enhancing the reliability of wind turbine components. The consortium members have developed advanced operation and planning tools for accommodating the high penetration of variable wind energy. The consortium members have developed extensive education and research programs for educating the stakeholders on critical issues related to the wind energy research and development. In summary,

- The Consortium procured one utility-grade wind unit and two small wind units. Specifically, the Consortium procured a 1.5MW GE wind unit by working with the world leading wind energy developer, Invenergy, which is headquartered in Chicago, in September 2010. The Consortium

also installed advanced instrumentation on the turbine and performed relevant turbine reliability studies. The site for the wind unit is Invenergy's Grand Ridge wind farmin Illinois. The Consortium, by working with Viryd Technologies, installed an 8kW Viryd wind unit (the Lab Unit) at an engineering lab at IIT in September 2010 and an 8kW Viryd wind unit (the Field Unit) at the Stuart Field on IIT's main campus in July 2011, and performed relevant turbine reliability studies. The operation of the Field Unit is also monitored by the Phasor Measurement Unit (PMU) in the nearby Stuart Building. The Consortium commemorated the installations at the July 20, 2011 ribbon-cutting ceremony.

- The Consortium's researches on turbine reliability included (1) Predictive Analytics to Improve Wind Turbine Reliability; (2) Improve Wind Turbine Power Output and Reduce Dynamic Stress Loading Through Advanced Wind Sensing Technology; (3) Use High Magnetic Density Turbine Generator as Non-rare Earth Power Dense Alternative; (4) Survivable Operation of Three Phase AC Drives in Wind Generator Systems; (5) Localization of Wind Turbine Noise Sources Using a Compact Microphone Array; (6) Wind Turbine Acoustics - Numerical Studies; and (7) Performance of Wind Turbines in Rainy Conditions.
- The Consortium's researches on wind integration included (1) Analysis of 2030 Large-Scale Wind Energy Integration in the Eastern Interconnection; (2) Large-scale Analysis of 2018 Wind Energy Integration in the Eastern U.S. Interconnection; (3) Integration of Non-dispatchable Resources in Electricity Markets; (4) Integration of Wind Unit with Microgrid.
- The Consortium's education and outreach activities on wind energy included (1) Wind Energy Training Facility Development; (2) Wind Energy Course Development; (3) Wind Energy Outreach.

2. Background

Illinois Institute of Technology (IIT), with an ABET accredited engineering program, has led an extensive effort in forming a world-class wind energy consortium (the Consortium) of multiple universities (domestic and international) and multiple industry participants (all types of wind energy stakeholders) to perform focused research and development on critical wind energy challenges identified in the "20% Wind Energy by 2030" report, including wind technology challenge, grid system integration, and workforce development.

The Consortium worked with the world leading wind energy developer, Invenergy, which is headquartered in Chicago, to procure a 1.5MW GE wind unit, and perform relevant turbine reliability studies. The site for the wind unit is the Invenergy's wind farm at the LaSalle County (adjacent to Marseilles), Illinois. The site which is within the 50 mile of IIT is an NREL Class 3 or better wind site as verified by multiple years of onsite data. The Invenergy's extensive experience in the deployment and operation of large numbers of wind turbines in the United States provided guidance to the Consortium for conducting world-class wind energy research and development. The Consortium also worked with the world-leading small wind turbine manufacturer, Viryd Technologies, to procure and install an 8KW Viryd wind unit at the IIT campus. Viryd also provided the second turbine to IIT which is installed in one of the engineering laboratories and used for performing relevant turbine reliability studies. IIT also utilized the two Viryd turbines on its campus to promote the public awareness on wind energy.

The Consortium consists of a world-class leading team and advisory board. The principal investigator (PI) is Dr. Mohammad Shahidehpour, who is the Bodine Distinguished Professor of IIT's ECE Department and the Director of the Robert W. Galvin Center for Electricity Innovation at IIT. He has a 30-year experience in electric power system research. Dr. Shahidehpour was the VP for Publications of the IEEE Power and Energy Society and had facilitated the publication of two new and very prestigious IEEE Transactions on Sustainable Energy and Smart Grid. Dr. Shahidehpour is also leading a DOE-funded Perfect Power project at IIT with a total budget of $13,000,000, a DOE-funded Wind Integration project with a two-year budget of $750,000, a DOE-funded Smart Grid Workforce Development project with a total budget of $12,000,000, and several NSF-funded projects on wind energy research and utilization.

The Consortium is led by IIT, which has a long history of offering one of the finest electrical power programs since 1930's. Other university consortium members include the world-renowned **University of Chicago**, as well as **Southern Illinois University** and four internationally prestigious universities with a strong wind energy program: **University of Castilla-La Mancha (Spain), University of São Paulo (Brazil), Aristotle University of Thessaloniki (Greece), and Polytechnic University of Bucharest (Romania)**. The international faculty and student members participated at the consortium workshops and shared their innovative ideas with American counterparts. The industry consortium members include all types of wind energy stakeholders: **wind turbine companies** (GE Energy, Viryd Technologies, Acciona Wind Energy USA), **wind energy developers** (Invenergy, Pampa Energia Eolica (Brazil), PS Wind Management (Romania)), **power transmission system operators** (ComEd/Exelon, ISO New England, British Columbia Transmission Corporation), **wind energy control device manufacturers and software companies** (Boeing Advanced Global Services & Support, Honeywell, Dakota Power, EnerNex Corporation,

SmartSignal Corporation, Innovation Technology Applications Company) and **energy system consultants** (Electric Power Research Institute, AREVA T&D, Keyworks, Intelligent Power Solutions, McCoy Energy, Wiedman Power System Consulting).

Members of the *World-Class Wind Energy Consortium*

University Members	**Point of Contact (Professor)**
Illinois Institute of Technology (Lead)	Mohammad Shahidehpour, (ms@iit.edu)
University of Chicago	John Birge, (john.birge@chicagobooth.edu)
Southern Illinois University	Morteza Daneshdoost, (daneshdo@siu.edu)
University of Castilla - La Mancha (Spain)	Antonio Conejo, (Antonio.Conejo@uclm.es)
University of São Paulo (Brazil)	Newton Bretas, (ngbretas@sc.usp.br)
Aristotle University of Thessaloniki (Greece)	Anastasio Bakirtzis, (bakiana@eng.auth.gr)
Polytechnic University of Bucharest (Romania)	Mircea Eremia, (eremia1@yahoo.com)
National Labs Members	**Point of Contact**
Argonne National Laboratory	Jianhui Wang, CEEESA (jianhui.wang@anl.gov)
National Renewable Energy Laboratory	Fort Felker, Director of the National Wind Technology Center, (fort.felker@nrel.gov)
Sandia National Laboratory	Matthew Barone, Wind Energy Technology (mbarone@sandia.gov)
Industry Members	**Point of Contact**
Wind Turbine Companies	
GE Energy	Steve Moffitt, Account Executive (steven.moffitt@ge.com)
Viryd Technologies, Inc.	John Langdon, CEO (jlangdon@viryd.com)
Acciona Wind Energy USA	Frank Bristol, Director of Transmission (fbristol@acciona-na.com)
Wind Energy Developers	
Invenergy, LLC	Michael Polsky, President and CEO (MPolsky@invenergyllc.com)
Pampa Energia Eolica (Brazil)	Edgar Pereira, Director (edgar@pampaeolica.com.br)
PS Wind Management (Romania)	Radu Popoiu, Managing Director (rpopoiu@vivalex.ro)

Power Transmission System Operators	
ComEd/Exelon	Terence Donnelly, COO (terence.donnelly@ComEd.com)
ISO New England	Eugene Litvinov, Director of Business Architecture and Technology (elitvinov@iso-ne.com)
British Columbia Transmission Corporation	Ebrahim Vaahedi, CTO (Ebrahim.Vaahedi@bctc.com)
Wind Energy Control Devices and Software Companies	
Honeywell	Tariq Samad, Corporate Fellow (tariq.samad@honeywell.com)
Dakota Power	Richard Gowen, President (dick@dplwed.com)
EnerNex Corporation	Erich Gunther, Chairman and CTO (erich@enernex.com)
SmartSignal Corporation	David R Bell, VP Application Engineering David.Bell@ge.com
Innovation Technology Applications Company	Alan Cain, President (abcain@itacllc.com)
Energy System Consultants	
Keyworks	Kurt Yeager, President and CEO (KYEAGER@epri.com)
Electric Power Research Institute	Don Von Dollen, Program Manager, IntelliGrid (DVONDOLL@epri.com)
AREVA T&D	Jay Giri, Director of Power System Technology and Strategic Initiatives (jay.giri@areva-td.com)
Intelligent Power Solutions	John Kelly, President (jkelly@ippconnect.com)
McCoy Energy	Paul McCoy, President (Pdpdm@aol.com)
Wiedman Power System Consulting	Thomas Wiedman, President (twieds@aol.com)

IIT Faculty Participants

Faculty Name	**Department**	**Area of Expertise Related to Wind Energy Research**
Mohammad Shahidehpour, PI (ms@iit.edu)	Electrical and Computer Engineering	Wind energy unit integration and optimization
Hamid Arastoopour (arastoopour@iit.edu)	Wanger Institute for Sustainability and Energy Research	Turbine design optimization using computational fluid dynamics
Zuyi Li (lizu@iit.edu)	Electrical and Computer Engineering	Wind integration and deployment
Ali Emadi (emadi@iit.edu)	Electrical and Computer Engineering	Wind turbine control and operation
Alireza Khaligh (khaligh@ece.iit.edu)	Electrical and Computer Engineering	Power electronic applications to wind turbine control
Mahesh Krishnamurthy (kmahesh@ece.iit.edu)	Electrical and Computer Engineering	Turbine health monitoring and diagnosis
Ganesh Raman (ramanar@iit.edu)	Mechanical, Materials and Aerospace Engineering	Optimal turbine design and noise reduction
Dietmar Rempfer (rempfer@iit.edu)	Mechanical, Materials and Aerospace Engineering	Wind energy prediction and optimal ramping events
Candace Wark (wark@iit.edu)	Mechanical, Materials and Aerospace Engineering	Turbine design optimization using computational fluid dynamics
Peter Land (land@iit.edu)	College of Architecture	High-rise building retrofitting with wind turbine
Navid Sabbaghi (nsabbagh@stuart.iit.edu)	Stuart School of Business	Economics of wind integration and environment impacts

3. Results and Discussions

3.1 Consortium Wind Unit Installation

3.1.1 Wind Unit Installation at Grand Ridge, Illinois

A. Wind Unit Procurement

We proposed the installation of a 1.5MW GE wind unit at the Grand Ridge wind facility located near Marseilles, Illinois. The facility is owned by Invenergy, a Chicago-based wind energy developer, which has installed 140 similar wind units and is planning to install additional units at the location. It was planned that Invenergy will procure the test wind turbine within 6 months of the date of the award and install the test wind turbine within 12 months of the date of the award.

In April 2010 (three months after the date of the ward), it had become apparent that there would be a significant delay in the installation of a new unit, primarily due to environmental and permitting issues for a new unit. In particular, the Illinois Department of Natural Resources (DNR) had a consulting role in determining Special Use Permits (SUP) in the state of Illinois. For the next phase of the Grand Ridge facility, which had not yet been constructed, DNR had recommended that Invenergy sought a state Incidental Take Permit (ITP) that would allow for Indiana Bat takes. This recommendation was weighed by the County that would issue the SUP. A state ITP had an estimated lead time of at least 6 months and a Federal ITP had a lead time of about 2 years. DNR did not recommend an ITP for previous phases of Grand Ridge facility, which were permitted in 2008 and 2009. This change reflected a rising concern across the country for the Indiana Bat. In addition to being Federally listed as endangered, Indiana Bats (as well as other bat species) were facing further threat from the White Nose Syndrome (http://www.fws.gov/northeast/wnsabout.html).

IIT then decided to acquire an existing unit at Grand Ridge. The proposed existing unit for acquiring was Unit #139. The installation of Unit #139 was completed in December 2009 and the unit was in operation for a few months. The Consortium designated Invenergy as the entity to install test equipment on the turbine in order to perform all proposed research tasks.

The consortium felt that the overall impact of the acquiring an existing unit was much bigger than waiting to get the permit and having the purchase and installation happen in unknown periods, which could be well beyond the two-year project period. Such acquisition allowed all proposed research tasks to be completed according to schedule, and more importantly, allowed the economic and job benefits required by the Recovery Act to occur in a timely fashion. Additional benefits would result from such acquisition. For instance, the interconnection of the wind unit with the real grid would make any research results more practical and meaningful.

Per the approval of the DOE and the mutual agreement between IIT and Invenergy, a Wind Turbine Sale Agreement (Agreement) was signed on September 27, 2010. The Agreement enabled IIT to purchase and own the unit while Invenergy maintained the unit and provided an electrical generation interconnection to the grid.

The purchased GE Wind Turbine Generator (WTG) includes (1) Nacelle: 1.5MW SLE, which includes generator, main shaft, bearings, drive train couplings, rotor hub, gearbox (with oil and cold weather fixtures allowing the unit to withstand design loads at -40C), generator cooling system, hydraulic system, yaw drive system, blade pitch mechanism including drive motors and control system, wind speed and direction sensors, lightning protection system, braking system, instrumentation, and other related components; (2) Tower: 80m MTS 3-section with T-flange, which includes 80m three section steel tower with T-flange base for bolting to concrete foundation. Tower internals include ladders, platforms, power cabling (with all necessary terminations), fall protection, lighting and other items; (3) Blade set: 77 meter rotor diameter, which includes three fiberglass epoxy resin blades; (4) Controller; (5) Hub; (6) Control and data documentation systems: The turbine will report data back to the Central GE SCADA and PI systems for storage. The turbine will also accept commands from the SCADA system and Wind Farm Management System (WFMS) to keep the power and voltage requirements of the site in balance and compliant with NERC, ComEd and PJM. These systems themselves are excluded from the Agreement, however all data related to the WTC being purchased (including the right to access the same) will be owned by IIT.

Figure 1: Screenshots of IIT Wind Turbine at Grand Ridge Wind Farm

B. GE 1.5MW Wind Turbine

The 1.5SLE/XLE 60Hz is a three bladed, upwind, horizontal-axis wind turbine with a rotor diameter of 77/82.5 m, respectively. The turbine rotor and nacelle are mounted on top of a tubular tower. Different hub heights are available. The machine employs active yaw control (designed to steer the machine with respect to the wind direction), active blade pitch control (designed to regulate turbine rotor speed), and a generator/power electronic converter system.

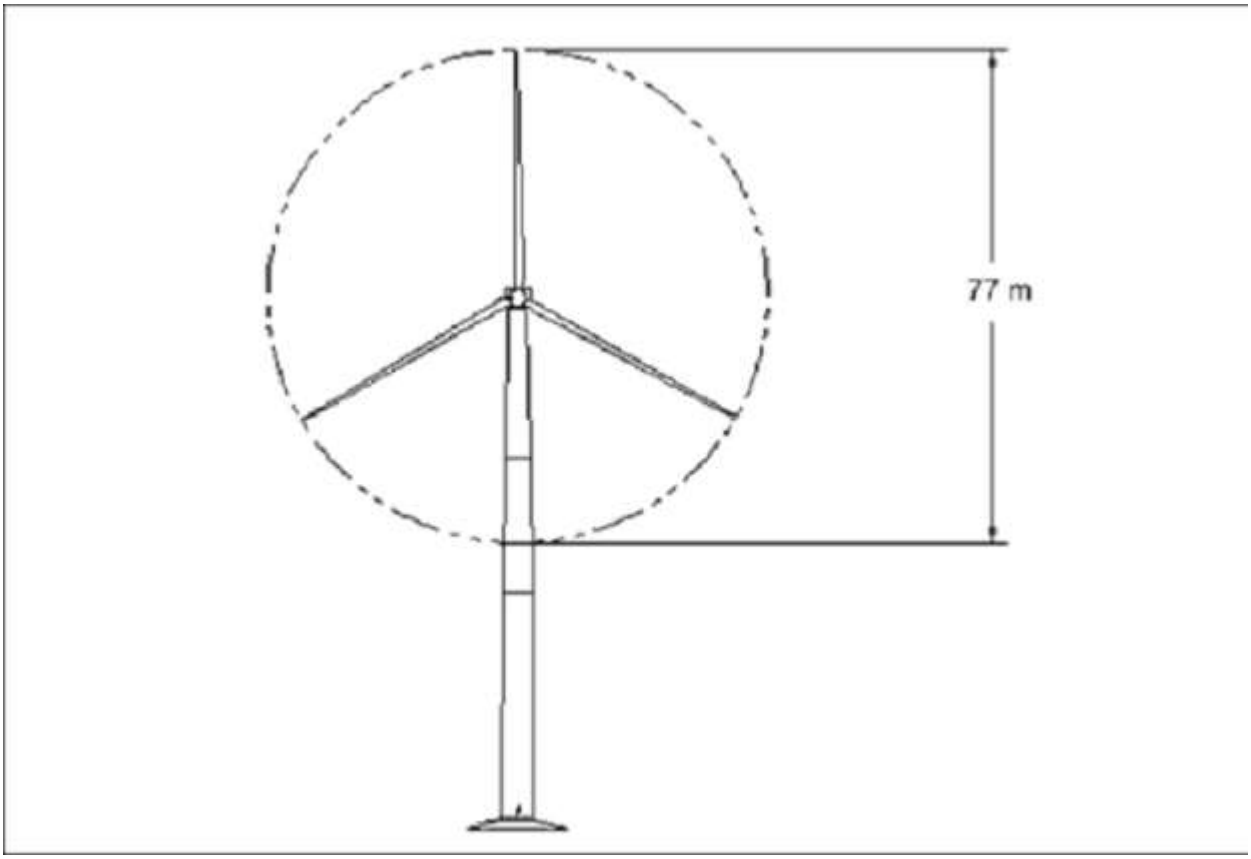

Figure 2: GE Energy 1.5SLE/XLE 60Hz Wind Turbine Generator

The wind turbine features a distributed drive train design wherein the major drive train components including main shaft bearing, gearbox, generator, yaw drives, and control panel are attached to a bedplate.

Rotor

The sle/xle rotor diameter is 77/82.5 m, resulting in a swept area of 4,657/5,346 m2, and is designed to operate between 10 and 20/9 and 18 revolutions per minute (rpm). Rotor speed is regulated by a combination of blade pitch angle adjustment and generator/converter torque control. The rotor spins in a clock-wise direction under normal operating conditions when viewed from an upwind location. Full blade pitch angle range is approximately 90 degrees, with the zero degree position being with the blade flat to the prevailing wind. The blades being pitched to a full feather pitch angle of approximately 90

degrees accomplishes aerodynamic braking of the rotor; whereby the blades “spill” the wind thus limiting rotor speed.

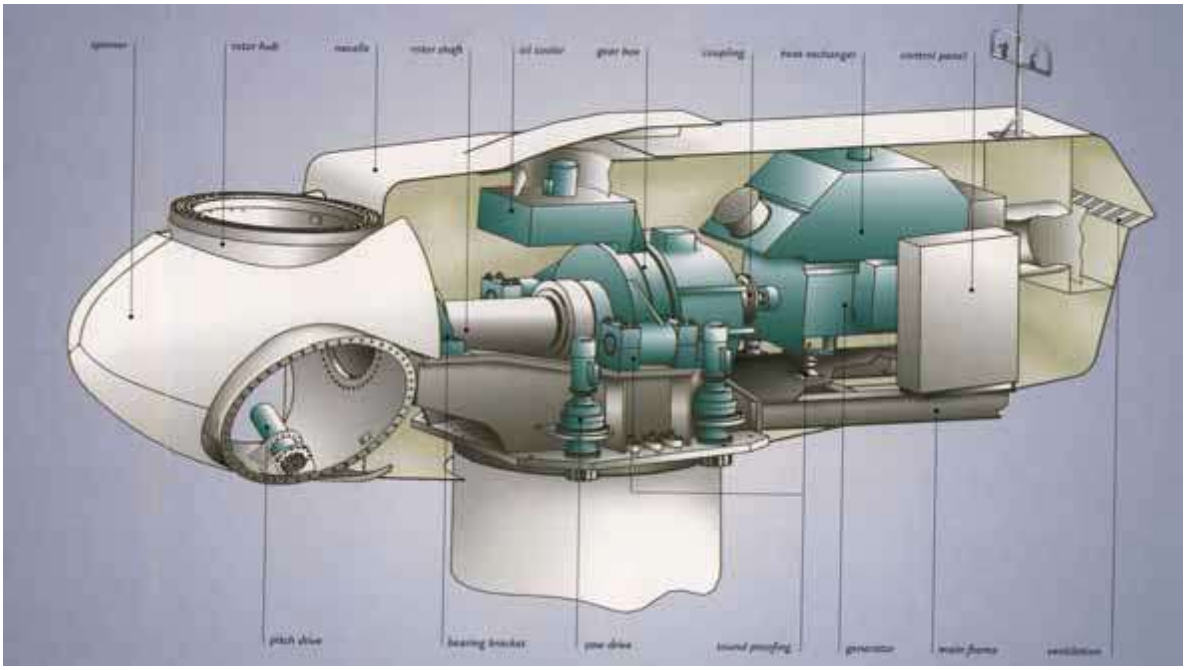

Figure 3: GE Energy 1.5SLE/XLE 60Hz Wind Turbine Nacelle Layout

Blades

There are three rotor blades used on each GE Energy 1.5SLE/XLE 60Hz wind turbine. The airfoils transition along the blade span with the thicker airfoils being located inboard towards the blade root (hub) and gradually tapering to thinner cross sections out towards the blade tip.

Blade Pitch Control System

The rotor utilizes three (one for each blade) independent electric pitch motors and controllers to provide adjustment of the blade pitch angle during operation. Blade pitch angle is adjusted by an electric drive that is mounted inside the rotor hub and is coupled to a ring gear mounted to the inner race of the blade pitch bearing. GE’s active-pitch controller enables the wind turbine rotor to regulate speed, when above rated wind speed, by allowing the blade to “spill” excess aerodynamic lift. Energy from wind gusts below rated wind speed is captured by allowing the rotor to speed up, transforming this gust energy into kinetic energy that may then be extracted from the rotor. Independent back-up units are provided to power each individual blade pitch system to feather the blades and shut down the machine in the event of a grid line outage or other fault. By having all three blades outfitted with independent pitch systems, redundancy of individual blade aerodynamic braking capability is provided.

Hub

The hub is used to connect the three rotor blades to the turbine main shaft. The hub also houses the three electric blade pitch systems and is mounted directly to the main shaft. Access to the inside of the hub is provided through a hatch

Gearbox

The gearbox in the wind turbine is designed to transmit power between the low-rpm turbine rotor and high-rpm electric generator. The gearbox is a multi-stage planetary/helical design. The gearbox is mounted to the machine bedplate. The gearbox mounting is designed such that it minimizes the vibration and noise transfer to the bedplate. A parking brake is mounted on the high-speed shaft of the gearbox. The gearbox is lubricated by a forced lubrication system and a filter maintains oil cleanliness.

Bearings

The blade pitch bearing is designed to allow the blade to pitch about a span-wise pitch axis. The inner race of the blade pitch bearing is outfitted with a blade drive gear that enables the blade to be driven in pitch by an electric gear-driven motor/controller. The main shaft bearing is a roller bearing mounted in an arrangement designed to provide bearing and alignment of the internal gearing shafts and accommodate radial and axial loads.

Brake System

The electrically actuated individual blade pitch systems act as the main braking system for the wind turbine. Braking under normal operating conditions is accomplished by feathering the blades out of the wind. Any single feathered rotor blade is designed to slow the rotor, and each rotor blade has its own back up to provide power to the electric drive in the event of a grid line loss. The turbine is also equipped with a mechanical brake located at the output (high speed) shaft of the gearbox. This brake is only applied as an auxiliary brake to the main aerodynamic brake and to prevent rotation of the machinery as required by certain service activities.

Generator

The generator is a doubly fed induction type. The generator is mounted to the bedplate and the mounting is designed so as to reduce vibration and noise transfer to the bedplate.

Gearbox/generator Coupling

Designed to protect the drive train from excessive torque loads, a special coupling is provided between the generator and gearbox output shaft, which is equipped with a torque-limiting device sized to keep the maximum allowable torque below the maximum design limit of the drive train torque.

Yaw System

The bearing attached between the nacelle and tower facilitates yaw motion. Yaw drives (with brakes that engage when the drive is disabled) mesh with the gear of the yaw bearing and steer the machine to track the wind in yaw. The automatic yaw brakes engage in order to prevent the yaw drives from seeing peak loads from any turbulent wind. The controller activates the yaw drives to align the nacelle to the wind direction based on the wind vane sensor mounted on the top of the nacelle. A sensor provides a record of nacelle yaw position and cable twisting. After the sensor detects excessive rotation in one direction, the controller automatically brings the rotor to a complete stop, untwists the cable by counter-yawing of the nacelle, and restarts the wind turbine.

Tower

The wind turbine is mounted on top of a tubular tower, which is manufactured in sections from steel plates. Access to the turbine is through a steel door at the base of the tower. Service platforms are provided. A ladder provides access to the nacelle and also supports a fall arrest safety system. Interior lights are installed at critical points from the base of the tower to the tower top.

Nacelle

The nacelle houses the main components of the wind turbine generator. Access from the tower into the nacelle is through the bottom of the nacelle. The nacelle is ventilated, and illuminated with electric light. A hatch provides access to the blades and hub.

Anemometer, Wind Vane, and Lightning Rod

An anemometer, wind vane, and lightning rod are mounted on top of the nacelle housing. Access to these devices is accomplished through the hatch in the nacelle.

Lightning Protection

The rotor blades are equipped with lightning receptors mounted in the blade. The turbine is grounded and shielded to protect against lightning, however, lightning is an unpredictable force of nature and it is possible that a lightning strike could damage various components notwithstanding the lightning protection employed in the machine.

Wind Turbine Control System

The wind turbine machine can be controlled locally either automatically or manually. Control signals can also be sent from a remote computer via a Supervisory Control and Data Acquisition System (SCADA) (purchased separately), with local lockout capability provided at the turbine controller. Service switches at the tower top prevent service personnel at the bottom of the tower from operating certain systems of the turbine while service personnel are in the nacelle. To override any machine operation, emergency-stop buttons located in the tower base and in the nacelle can be activated to stop the turbine in the event of an emergency.

Power Converter

The wind turbine uses a power converter system that consists of a converter on the rotor side, a DC intermediate circuit, and a power inverter on the grid side. This allows for variable rotor speed while keeping in synchronization with the grid frequency. The converter system consists of a power module and associated electrical equipment. Variable output frequency of the converter allows variable speed operation of the generator. The technical data for rotor, pitch system, and operational limits are shown in the following tables. The yaw rate is 0.5 degree / s.

Table 1: Technical Data for the 1.5MW GE Wind Turbine: Rotor

Diameter	77/82.5 m
Number of blades	3
Swept area	4,657/5,346 m2
Rotor speed range	10 – 20/9 – 18 rpm
Rotational direction	Clockwise looking downwind
Maximum tip speed	73.8 m/s
Orientation	Upwind
Speed regulation	Pitch control
Aerodynamic brakes	Full feathering

Table 2: Technical Data for the 1.5MW GE Wind Turbine: Pitch System

Principle	Independent blade pitch control
Actuation	Individual electric drive

Table 3: Operational Limits of the 1.5MW GE Wind Turbine

Height above sea level	Maximum 2500 m. See notes in section “Maximum standard ambient temperature” below.
Minimum standard ambient temperature (operational/survival)	Standard Weather Package: -15°C / -20°C Cold Weather Package: -30°C / -40°C (Switching on takes place with a hysteresis of 5°C after a cold temperature trip)
Maximum standard ambient temperature (operational/survival)	+40°C / +50°C The turbine has a feature by which the maximum output is reduced if the component temperatures approach specified thresholds, such that turbine trips are minimized. This feature is especially beneficial for higher altitudes, since the heat transfer properties of air are diminished with decreased density. Note that the units are not “derated” per any specific site conditions; the unit’s reaction related to this feature is based solely on sensor temperatures.
Wind conditions according to IEC 61400 for the standard temperature range	Standard Weather Package: 8.5 m/s @ 18 % turbulence @ 15 m/s Cold Weather Package: 8.5 m/s @ 16% turbulence @ 15 m/s
Maximum extreme gust (10 min) according to IEC 61400	Standard Weather Package: 39.3 m/s Cold Weather Package 37.2 m/s
Maximum extreme gust (3 s) according to IEC 61400	Standard Weather Package: 55 m/s Cold Weather Package: 52 m/s

As a leading global provider of energy products and services, GE continues to invest heavily in advancing its 1.5 MW wind turbine product line. With a core focus on reliability, efficiency, and multi- generational product advancements, GE's 1.5 MW wind turbine is the most widely used turbine in its class. GE's WindBOOST control system upgrade is a unique offering in the wind industry and the latest addition to the 1.5 MW platform, which helps increase the annual energy production (AEP) of a wind plant by allowing increased power output (kW) under certain conditions. This advancement helps increase the return on wind plant investments for our customers. The WindBOOST control system is offered as an option available on new and existing 1.5 MW SLE 60 Hz wind turbine generators with 80 m towers. The WindBOOST control system uses smart control algorithms to assess ambient conditions and calculates an increase in rotational speed of the turbine to maximize AEP. This additional speed increases output power by 100 kW from 1500 kW to 1600 kW. The WindBOOST control system also provides grid stability by allowing the turbine to maintain –0.9 to 0.9 Power Factor during operation. The maximum reactive power of the turbine is maintained by reducing additional output of the WindBOOST control system when grid conditions demand reactive power.

This transition is handled by the control system and returns the turbine to full additional power when grid Volt-Amp-Reactive (VAR) demand is satisfied. GE's WindBOOST control system is designed to minimize changes to turbine hardware components. This can reduce downtime during installation of this product. The WindBOOST control system is operator friendly, SCADA controlled, and can be remotely accessed to turn the feature on or off. Major features and benefits include

- Up to 4% increased annual energy output, resulting in higher return on investment
- Flexibility to increase power production when rates are highest
- Patent-pending control technology for optimum rotational speed, resulting in increased energy production
- Remote capability to turn feature on and off at the turbine level
- Increased power output while maintaining grid stability
- During Noise Reduction Operation WindBOOST control system is not active.

GE has developed controls to improve stall mitigation of the turbines during blade icing. Improved power output is achieved with optimized pitch controls, and minimizing the effects of icing on blade stall reduces potential blade vibrations. Snow and ice accretion on wind turbine blades is common for units located in winter climates. Winter blade ice-fouling can produce aerodynamic stall resulting in reduced power output (See Figure 4). Turbine operation with blade stall can also lead to increased blade vibration levels. In rare cases, blade vibrations at a resonant frequency can lead to blade damage. Anti-stall operation is accomplished with a blade tip speed ratio (TSR) algorithm executed by the PLC. The TSR pitch control algorithm intends to maximize power capture (CP) for the rotor while minimizing the risk of blade stall (See Figure 5). The tip speed ratio is calculated from turbine rotor speed and anemometer wind speed inputs. The modified pitch control scheme applies primarily for operation of the turbine during rated winds or higher. Annualized increase of energy production of approximately 1 to 3% can be achieved for sites with 4 to 6 months winter weather opportunity.

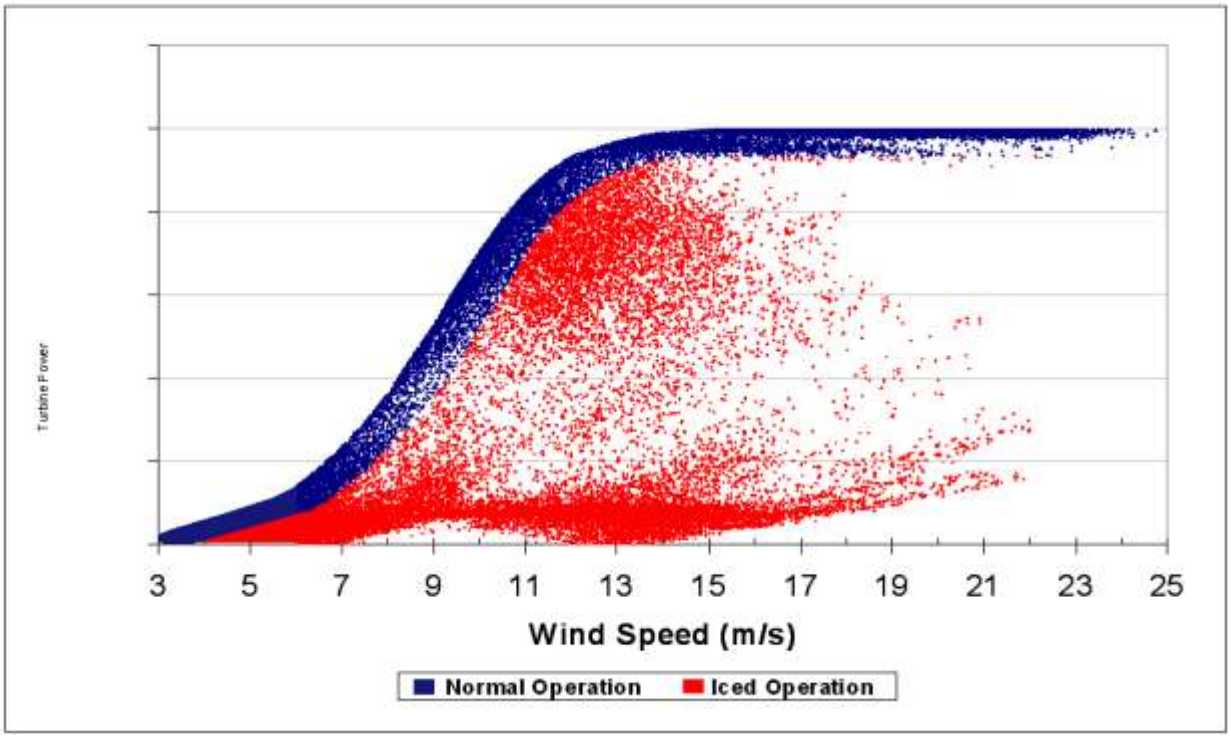

Figure 4: Power performance for winter operation

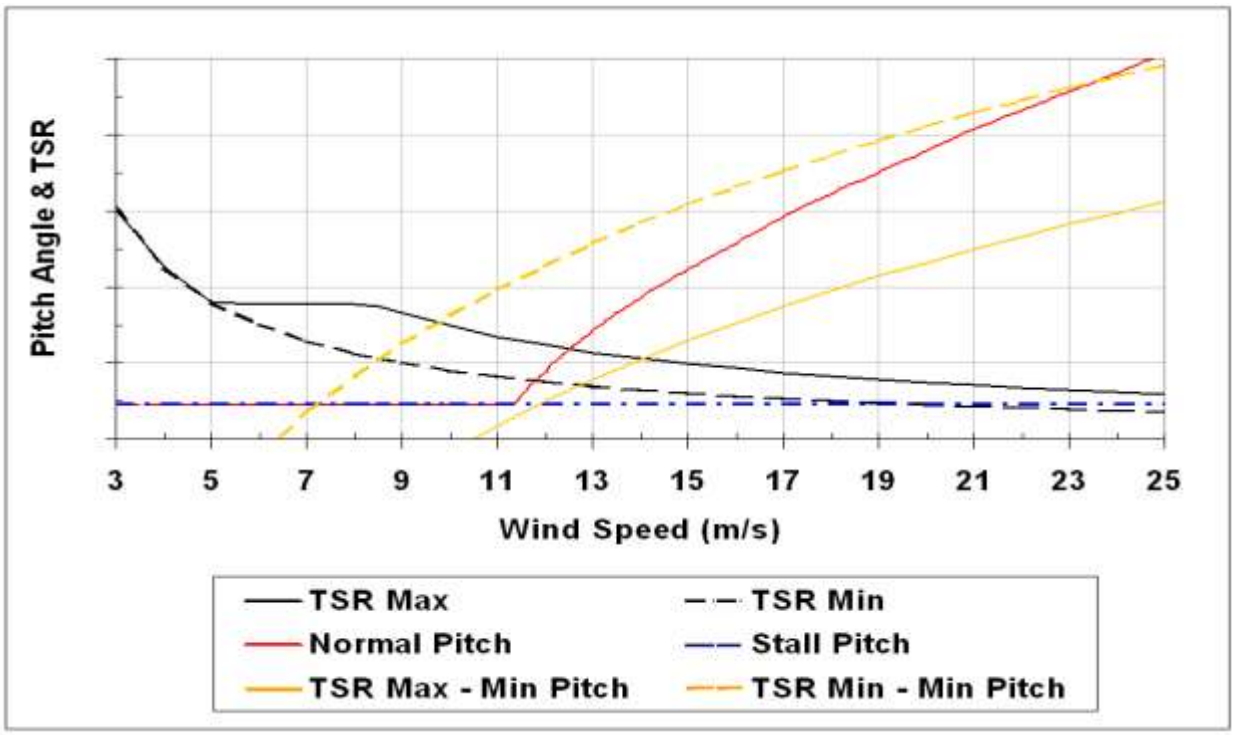

Figure 5: TSR pitch control schedule

3.1.2 Wind Unit Installation at IIT

IIT installed two 8kW Viryd Wind Turbine on campus which are used extensively for research and education. In the following we discuss the specifications of the Viryd unit and elaborate on the specifics of the two installations at IIT.

A. Viryd 8kW Wind Turbine

The Viryd Wind Turbine features a Continuously Variable Transmission (CVT) technology which is defined by its inventors as the next major advancement in the production of practical, clean energy from wind. A variable wind turbine is recognized as the best way of wind energy practical by maximizing efficiency and minimizing production cost. The Viryd Wind Turbine is also known, in general, as Wind Energy Conversion Systems (WECS).

At the heart of Viryd wind turbine technology is the NuVinci® Continuously Variable Planetary (CVP) transmission. This class of CVT technology and innovative energy management system now provides a solution that can make wind energy a more viable alternative by dramatically increasing power production at all wind speeds, greatly reducing system and maintenance costs, and significantly lowering the cost of energy Viryd utilizes NuVinci® continuously variable planetary (CVP) technology to provide benefits that reduce the cost of energy (COE) for wind turbines. Developed by Fallbrook Technologies Inc., NuVinci CVP technology is suitable for use in a wide variety of applications from automobiles to bicycles to wind turbines of all sizes. Viryd has an exclusive license from Fallbrook for the use of NuVinci technology in wind energy applications.

NuVinci technology for wind improves energy capture and can reduce both capital costs, and ongoing operations and maintenance. By increasing energy capture, reducing cost, and providing greater reliability, the Viryd system has the lowest cost of energy (COE) of any competitive system.

The *NuVinci* CVP provides automatic and continuously variable ratio change that changes rotor speed as wind speed changes. This enables the rotor to maintain high efficiency at all wind speeds. If a rotor spins too fast or slow its efficiency drops. Traditional small wind turbines suffer from varying rotor speeds at each wind speed, and all of these rotor speeds except for one produces losses in efficiency. A few small wind turbines, called constant speed wind turbines, have only one rotor speed no matter what the wind speed. These turbines suffer losses in efficiency at all wind speeds except for one (design speed or design condition).

TURBINE	
System	3 blade, horizontal axis, upwind
Rated Power	8 kW at 10 m/s (23 mph)*
Control	Wireless internet accessible
Cut-in wind speed	4.5 m/s (10 mph)
Cut-out wind speed	25 m/s (56 mph)
Survival wind speed	59 m/s (132 mph)
ROTOR	
Size	8 m (26') diameter
Swept Area	50 m² (541 ft²)
Material	Fiberglass with foam core
Yaw	Passive yaw, furling not required
Power Regulation	Stall control aerodynamic braking
Speed	Variable speed – 50 to 150 RPM
GENERATOR	
Type	Grid connected, induction generator
Output	60 Hz, 240 Volts, Single Phase
Inverter	None
TOWER	
Standard	24m (80') guyed, tilt-up, tubular
Optional Styles	Guyed or free-standing lattice or tubular
Optional Heights	18m (60'), 30m (100'), 36m (120')
SAFETY	
Brake	Fail-safe, mechanical
Certifications	UL 1741/IEEE 1547
Automatic Shut-Down	High wind, grid failure, overspeed
QUALITY	
Design Life	20 year minimum design life
Warranty	5 years

*NOTE: V8000 actually achieves rated power at less than 11 m/s

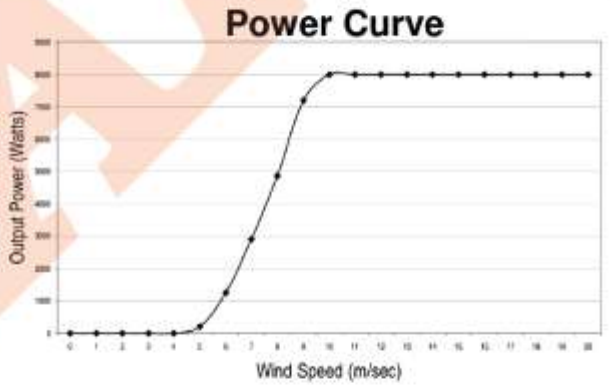

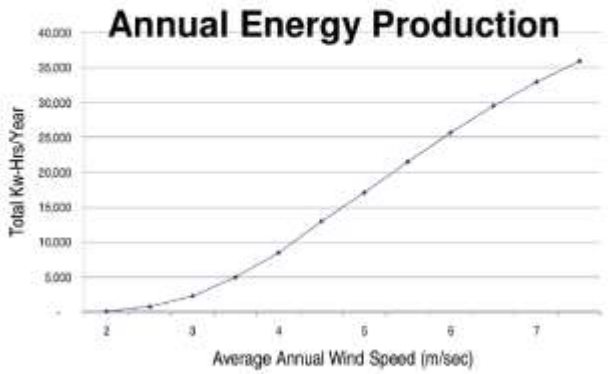

NOTE: Wind speed measured on standard Met tower at 10m, Power is at standard hub height of 24m

Figure 6: Viryd 8KW Wind Turbine Technical Specification

Table 4: Viryd 8000 Technical Datasheet

Turbine	
System	3 blades, horizontal axis, upwind
Rated power	8 kW at 10 m/s (23 mph)
Control	
Cut-in wind speed	4.5 m/s (10 mph)
Cut-out wind speed	25 m/s (56 mph)
Survival wind speed	59 m/s (132 mph)
Rotor	
Size	8 m (26') diameter
Swept area	50 m2 (541 ft2)
Material	Fiberglass with foam core
Yaw	Passive yaw, furling not required
Power regulation	Stall control aerodynamic braking
Speed	Variable speed - 50 to 150 rpm
Generator	
Type	Grid connected, induction generator
Output	60 Hz, 240 volts, single phase
Inverter	None
Tower	
Standard	24 m (80') guyed, tilt-up tubular
Optional styles	Guyed or free-standing lattice or tubular
Optional heights	18 m (60'), 30 m (100'), 36 m (120')
Safety	
Brake	Fail-safe, mechanical
Certifications	UL 1741/IEEE 1547
Automatic shut-down	High wind, grid failure, overspeed
Quality	
Design life	20 year minimum
Warranty	5 years

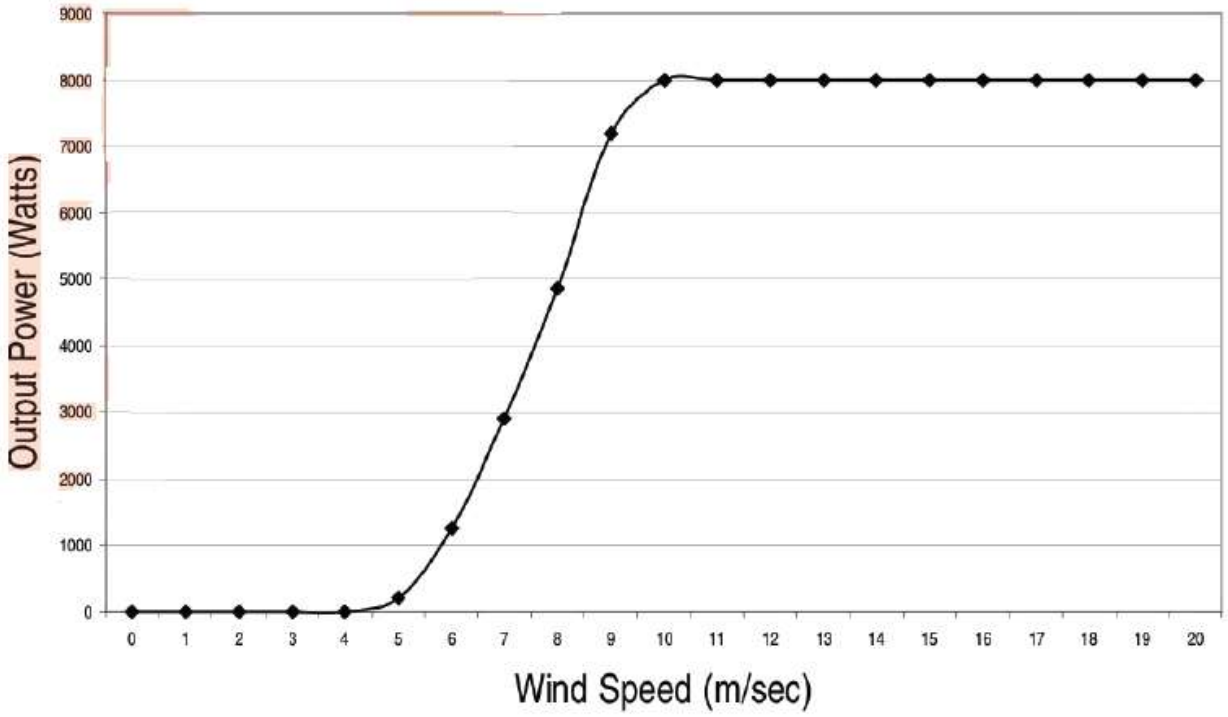

Figure 7: Viryd 8KW Wind Turbine Power Curve

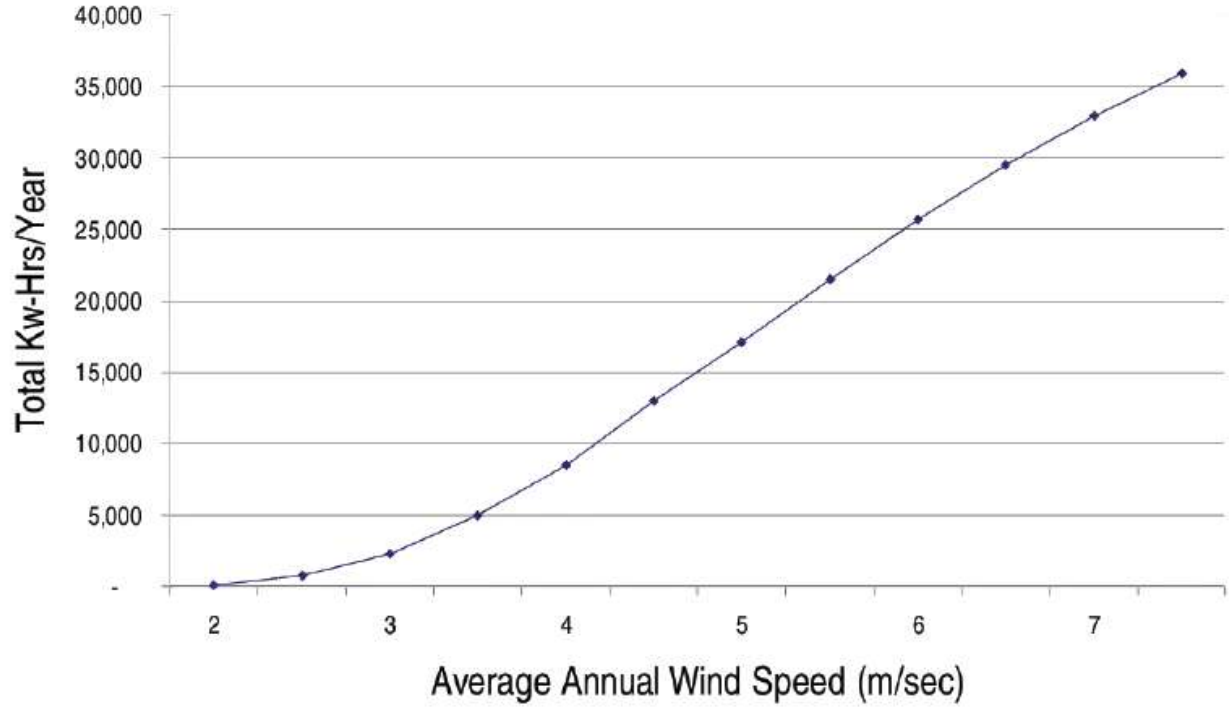

Figure 8: Viryd 8KW Wind Turbine Annual Energy Production

Figure 9: Cross-Section and Components of the Viryd Wind Turbine

The *NuVinci* CVP is the only technology that can produce and maintain the ideal rotor speed for every wind speed. The result is that wind turbines equipped with the NuVinci CVP capture more energy than traditional systems.

High winds produce too much power and can damage wind turbine drive trains. All wind turbines face the problem of how to handle excess power destroying the generator and other components in high winds.

Most small wind turbines employ a crude method called passive furling, which turns the rotor out of the wind when wind speeds are too high. Passive furl is unreliable because wind direction can suddenly change, hitting the rotor straight on during high winds. Small wind turbines compensate for this problem and inherently inaccurate furling by including a safety margin in their passive furl systems. The result is that small wind turbines that use passive furl actually see power production decrease in high winds.

Another method used to control excess power in high winds is called passive stall. With this method, the rotor blades transition to stall in high winds and become inefficient. The result is that wind turbines employing passive stall also produce less power in high winds.

The *NuVinci* CVP can precisely slow the rotor in high winds, shedding the exact amount of power necessary to maintain peak energy production, and capture more energy from the wind.

The unique ability of the *NuVinci* CVP to control rotor speed allows the use of a larger rotor than competing systems. Larger rotors exacerbate the problem of too much power entering the drive train from gusts and high winds. Because the *NuVinci* CVP can precisely control rotor speed, it can use a rotor with approximately 20% more area, resulting in nearly 20% more energy capture.

Variable speed small wind turbines use an inefficient device called an inverter to produce grid acceptable electricity. Good inverters, which advertise efficiencies up to 96%, are actually about 86% efficient when the time spent shut down or not producing power is considered. A gust in high winds can cause an inverter to shut down to prevent damage, and typically the inverter will remain off for a

programmed period of time (~ 5 minutes). A gust at low winds will cause an inverter to turn on, when the low wind speed can't produce power. An inverter will draw power during this standby time.

The *NuVinc*i CVP doesn't need an inverter because it can shift with wind speed changes, allowing it to eliminate the ~ 14% losses from the inverter and capture more energy from the wind than competing systems.

Viryd systems eliminate the inverter which is prone to failure from the variable and harsh conditions produced by the wind. Downtime from inverter failures is expensive, and troubleshooting the source can be difficult. Often a professional must be hired or the entire inverter needs to be replaced. If the source of failure is found, replacement parts can often have long lead times.

Gusts produce torque spikes which can damage wind turbine drive trains. The NuVinci CVP is a compliant device that spreads the torque spike over time. It can also accelerate the rotor to reduce the torque spike. This ability to absorb torque spikes smoothens the variable effects of the wind and helps keep the Viryd system operating longer and without interruption.

B. Viryd Lab Unit Installation at IIT

Viryd Technologies designed, built, tried out and debugged, shipped, installed and trained IIT personnel on a bench top Viryd wind turbine drivetrain system (Figure 10). The system provided by Viryd included all components that are in the Viryd 8000 wind turbine along with additional instrumentation required to run the tests detailed below. This bench top system was designed for use in experimentation and configured to allow several tests to be conducted and for additional tests to be added in the future.

Test Stand includes:

- Test Stand Base
- Mounting System for the Viryd 8000 drivetrain
- Drive motor and Variable frequency drive
- Gear Box (sized to allow system to mimic rotor)
- Coupling to connect drive system to drivetrain
- Inertia (wheel or gearbox)
- Labview DAQ System for operating the drive motor and variable speed drive as well as any instrumentation to e collected and analyzed in the DAQ
- Personal Computer
- Labview software license to be discussed if IIT has current license
- Labview application software configured to conduct several pre-determined tests

Drivetrain includes:

- Viryd 8000W drivetrain including speed increaser- Brake- NuVinci CVP- Generator
- All Viryd 8000 Electrical components, controls and software installed in a NEMA 4 enclosure including a Zigbee wireless communications card.
- All Heat Exchanger and fluid transport
- All pressure and temperature measurements will use a thermistor por pressure transducer as opposed to the normal pressure switch and thermistor

- 1 torque transducer at the input to the drivetrain
- 1 torque transducer at the output of the NuVinci CVP
- Voltage and current probes
- Wattmeter
- Electrical connections will be made at the electrical panel as NO Slip rings will be supplied with this system

Software is provided to perform the following tests: The software will be configured with a graphical user interface to operate the tests below. This interface will be configurable for future testing.

- Static power sweeps – Input static power levels and vary NuVinci CVP ratio manually. Maximize output power for each input power condition
- Component level efficiency testing versus speed, torque or power
- Static power sweeps to measure system level efficiency at varying Nuvinci CVP ratio
- Static power sweeps to measure NuVinci CVP lubrication temperate and generator temperature
- Dynamic wind simulations with capability to modify wind speed, turbulence intensity and wind cycle duration
- Power quality including power factor, THD versus output power
- Cumulative output power for various duty cycles and set-ups
- Error log file (continuous)
- Software to remotely monitor system via wireless network

Additional testing or instrumentation that has been added in addition to the baseline proposal:

- Speed Increaser oil temperature. Solution will be a pipe plug thermocouple capable of 0-250C temperature range. Adapter from speed increaser to NPT fitting will also be supplied.
- Accelerometers mounted in various areas to measure vibration in multiple axis. Solution will be tri-axial accelerometers mounted in 2 locations as well as required cable and signal conditioners.
- Pressure measurements if NuVinci CVP. Solution will utilize a Honeywell Sensotech pressure transducer for measuring the pressure at the input side of the NuVinci CVP.
- Obtain bearing “signature” analysis which could be used as a baseline and compared to as time and testing accumulate. Solution initially will be to have a discrete analysis completed on the system to establish the baseline signatures of all rotating components. These baselines will be documented with the machine for future analysis and if automated data collection and analysis system shall be added
- Ability to simulate very high ambient temperature conditions. Solution is to build an insulated containment system to capture the waste heat being rejected by the components. It can be calculated that the waste heat will allow for the system to reach temperature of 125F or higher similar to that inside a nacelle in an extreme warm environment.

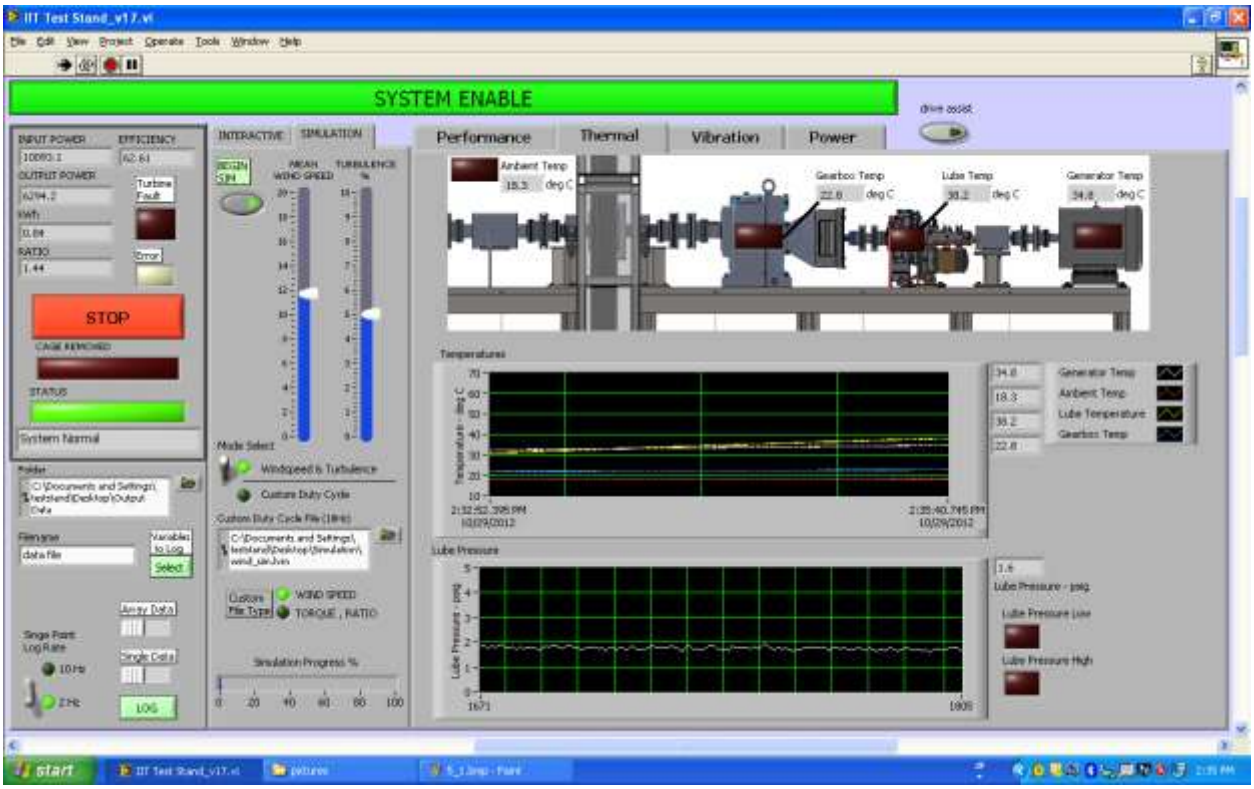

Figure 11Figure 11 and Figure 12 show screenshots of the software monitoring the Lab Field Unit regarding Performance, Thermal, Vibration, and Power.

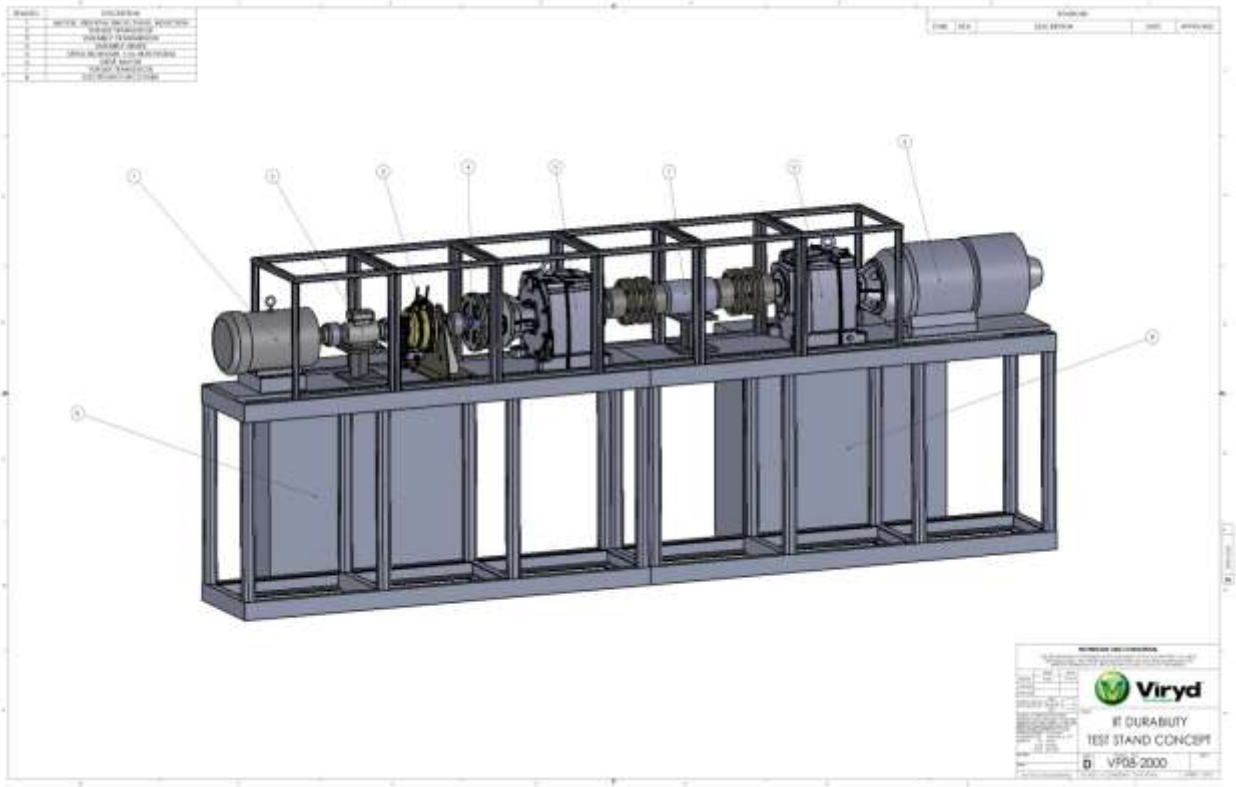

Figure 10: Viryd 8kW Unit Fully Instrumented and Designed for the IIT Lab

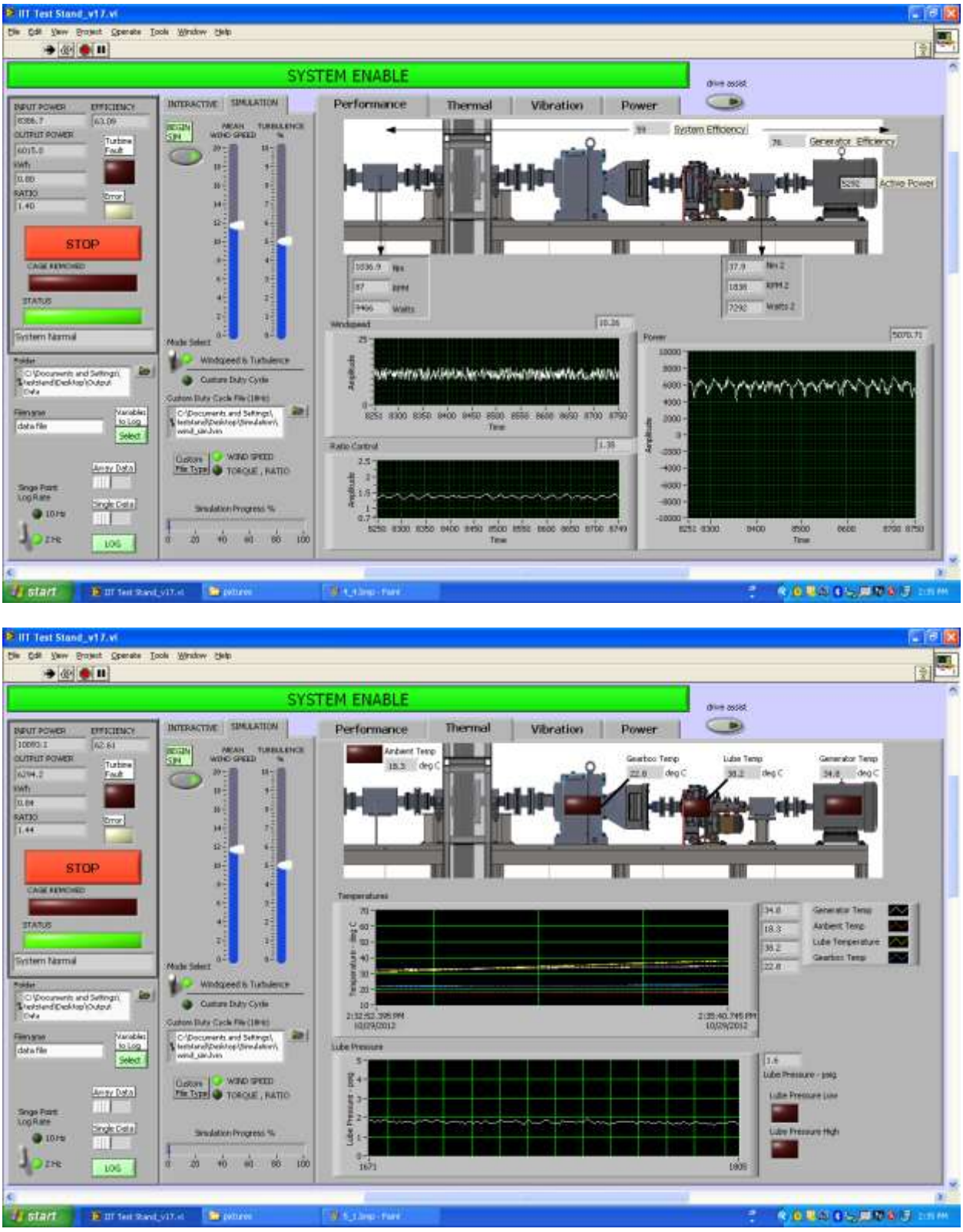

Figure 11: Screenshot of the Lab Unit

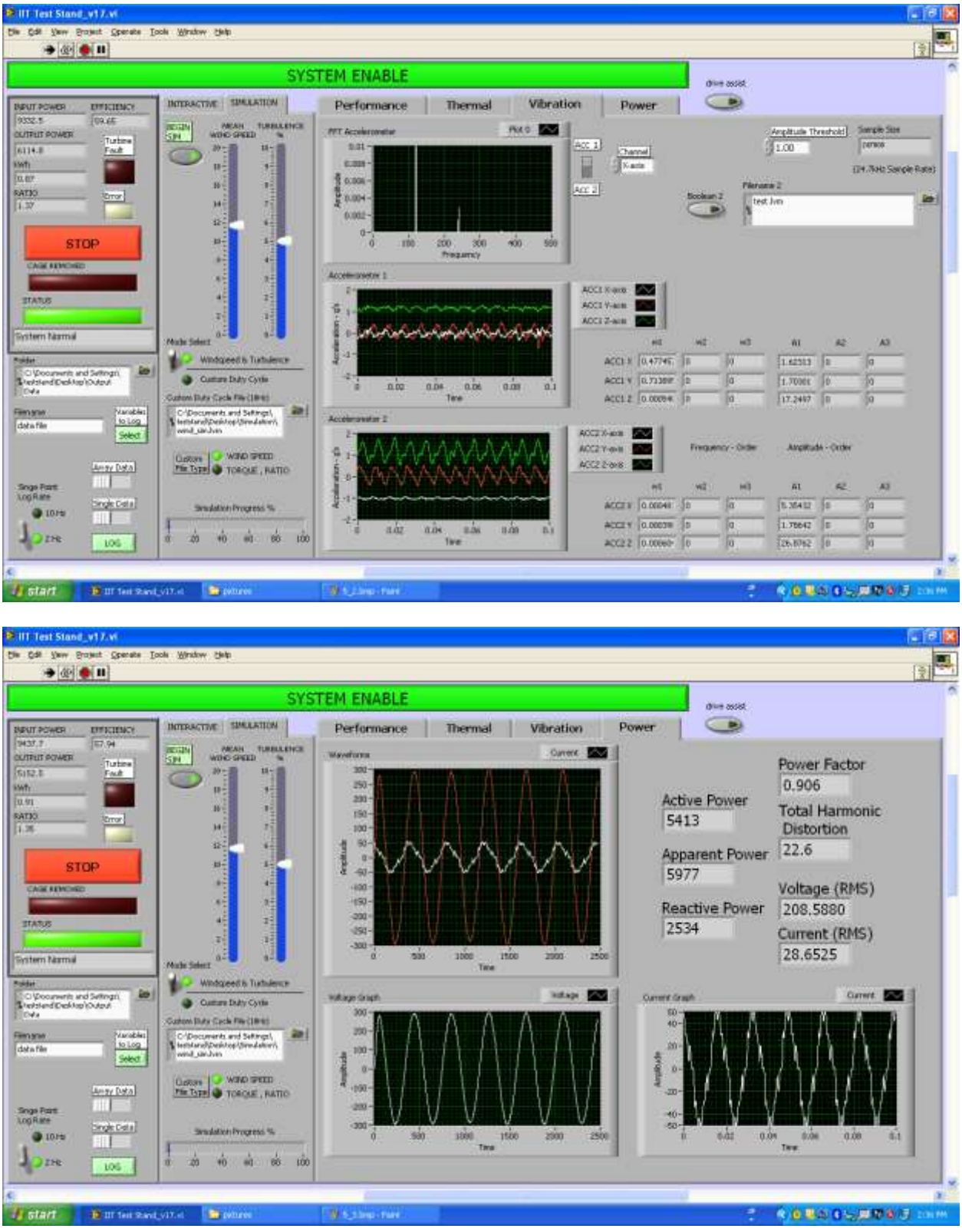

Figure 12: Screenshot of the Lab Unit

C. *Viryd Field Unit Installation at IIT*

IIT installed a wind turbine in the field, which is very similar to the lab unit. This installation enables us to run experiments on the lab unit and then try to validate and correlate data on the actual turbine running in the field. There are also "real world" circumstances in the field that are hard to model in the lab, and the researches can take these into account.

The turbine was installed in mid-2011 at the IIT soccer filed (Figure 13) which would provide easy access to the machine, as well as help promote the University's effort surrounding wind and alternative energy. The unit is an 8kW Single Phase Wind Turbine – Upwind with Induction Generation and Custom Designed 4m Stall-Regulated Blades. The tower is 80' Hydraulic Monopole Tower, which can be brought down for maintenance without a crane.

Figure 13: Viryd 8kW Unit Installed at the IIT Soccer Field

Project Timeline: The building permit was initiated in November, 2010 and granted on June 9, 2011. The installation was delayed by two weeks due to rain. The entire system is completed and signed off on July 19, 2011. Note that the city permit process took about 8 months vs. wind turbine on-site installation 3 weeks.

Figure 14: Installation Chronology for the Viryd 8kW Unit at the IIT Soccer Field

Figure 16 shows a screenshot of the software monitoring the Field Unit and Figure 15 shows the recent wind speed and wind power output as well as some statistics for the Field Unit.

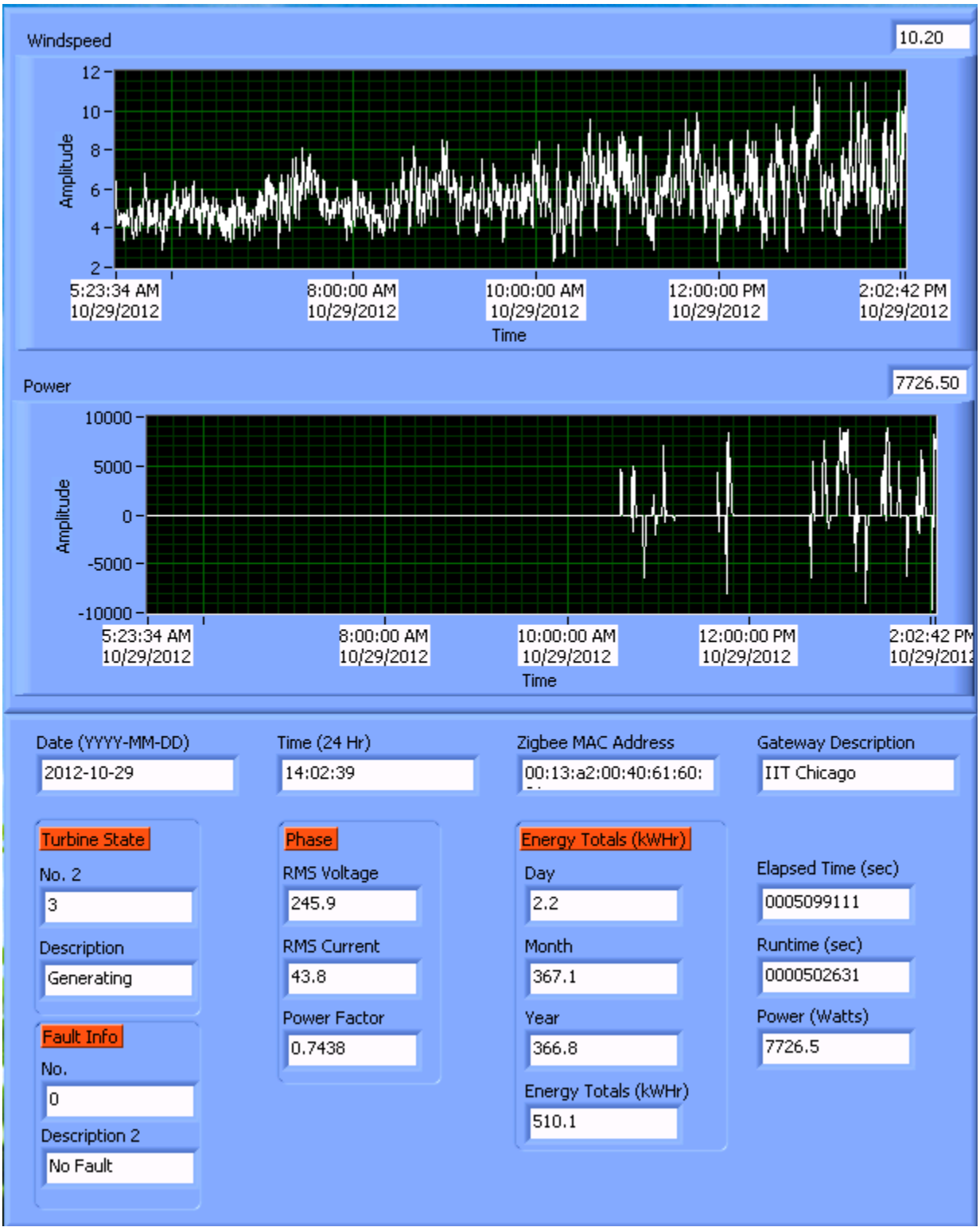

Figure 15: Display of the Wind Speed and Power Output for the Field Unit

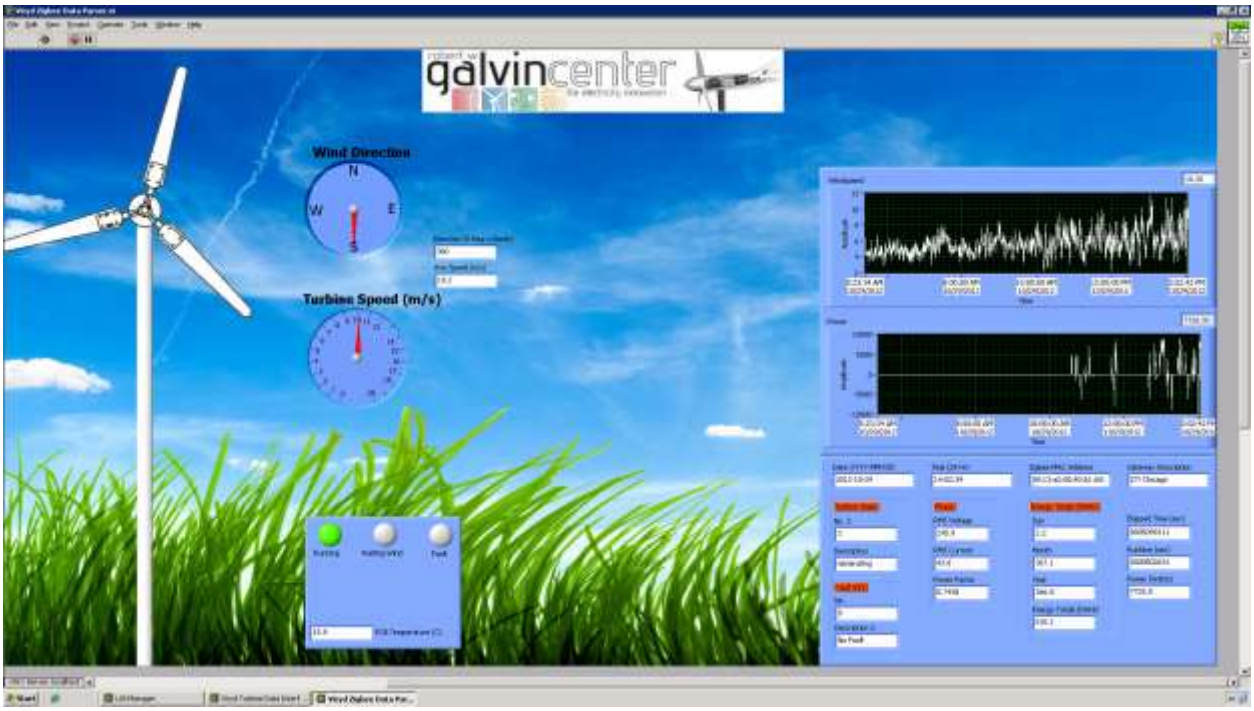

Figure 16: Screenshot of the Software Monitoring the Field Unit

3.2 Wind Energy Research and Development

3.2.1 Wind Turbine Research

A. Predictive Analytics to Improve Wind Turbine Reliability

IIT entered into an agreement with SmartSignal Corporation in early 2010. This agreement brought SmartSignal into a consortium arrangement with IIT and Invenergy. Under these terms, SmartSignal provided overall project management as well as specific system designs, software licenses, and staging hardware in support of SmartSignal's Epi-center Predictive Analytic software. SmartSignal was subsequently purchased by General Electric Company in January 2011.

The scope of the project was to implement SmartSignal Epi-center Predictive Analytic software on the IIT's Grand Ridge Wind Turbine #139 and design, specify, procure and install additional sensors which provide supplemental information to enhance the predictive analytic capabilities in support of Wind Turbine Reliability Research.

The purpose of this project was to determine an optimal set of add-on instrumentation and analytical techniques that can improve the existing state of the art emerging problem detection and be cost effective for broad deployment across large fleets of WTG's. A specific focus on gearbox issues was identified. The goals of this project were to evaluate a range of advanced instrumentation for early detection of gearbox problems including:

- Installation costs
- WTG interface and integration issues

- Determine sensor reliability in WTG environment
- Determine suitability for detection of WTG gearbox problems in real-time
- Develop a least-cost deployment approach for existing WTG assets
- Suitability of sensor data into real-time predictive analytic approaches

The overall project approach is as follows:

- Identify a range of possible instrumentation technologies
- Install multiple technologies on test WTG
- Collect real-time data
- Build SmartSignal Predictive Analytic models with data and assess correlation and ability of models to detect changes in sensed parameters using simulated faults injected into the data stream.
- Perform cost analysis for fleet deployment
- Make recommendation of instrumentation for broader sample fleet deployment

A key concept to also be evaluated during the project is the presumption that precise diagnostics from the analysis of the real-time data will not be required, as long as most failure modes can be detected in some fashion. The assumption is once it is determined there is a possible emerging problem, additional on-machine analysis methods can be used (e.g. oil sampling, boroscoping, supplemental vibration analysis, etc.) to isolate the problem and assess further operational risk.

A monitoring center was established on the IIT campus utilizing the SmartSignal Epi-center Predictive Analytic software and a video camera for visual condition monitoring of wind turbine #139. This monitoring center was linked via a Hardware VPN to the Proficy historian in the data acquisition and storage system at the Grand Ridge Energy Center. A link to the Proficy historian from the existing plant historian enables the existing sensor data to be forwarded to the monitoring center for analysis. Analytical models of this wind turbine utilizing the Similarity Based Modeling technique with the existing sensor data are installed in the monitoring center. The existing sensors will be supplemented with additional sensors measuring gear box oil temperatures, pressures, and contamination levels. The blade pitch motor currents and temperatures will be added to the data transferred from the plant historian to the Proficy historian. This additional information will be incorporated into the models in various combinations to develop the best model configuration.

Designated IIT personnel will be trained in the creation, modification and interpretation of the models. Asset Intelligence will assist in the advanced theoretical aspects of the research as requested. The initial planning phase of the project included network development and identification of hardware and software necessary to support the IT needs of the project. Key milestones were identified. After discussion with Invenergy and relying on SmartSignal's experience in monitoring wind farms across North America and Europe, a strategic set of additional sensors was identified, an overall IT network was agreed upon.

The next step was to execute the project according to plan. Component specifications were developed, work was assigned according to the work breakdown structure to various entities according to their capabilities, including identifying external resources necessary to supplement the consortium members'

own resources. The required purchases were separated into two phases; first to establish the IT infrastructure and activate the SmartSignal Predictive Analytic software and second, to incorporate the additional sensors into the analytic models.

Once component compatibility was established, purchase orders were placed. A trip to the wind turbine was made with the suppliers to install and activate the network servers and software. The servers supporting the analytic software were installed and commissioned on the IIT campus. After server validation, the SmartSignal predictive analytic software was installed. A data feed was established from the wind farm to the campus. The wind turbine models were activated in September and began processing data from the turbine. We now had the established baseline 'industry standard' predictive analytics.

As the sensor orders were being placed a new component vendor emerged with an offer to provide their product at no cost on a trial basis, including modified mounting hardware customized for this application. This change was accepted in principle and is currently being finalized. Invenergy personnel will be performing the sensor installation with factory specialists consulting as necessary.

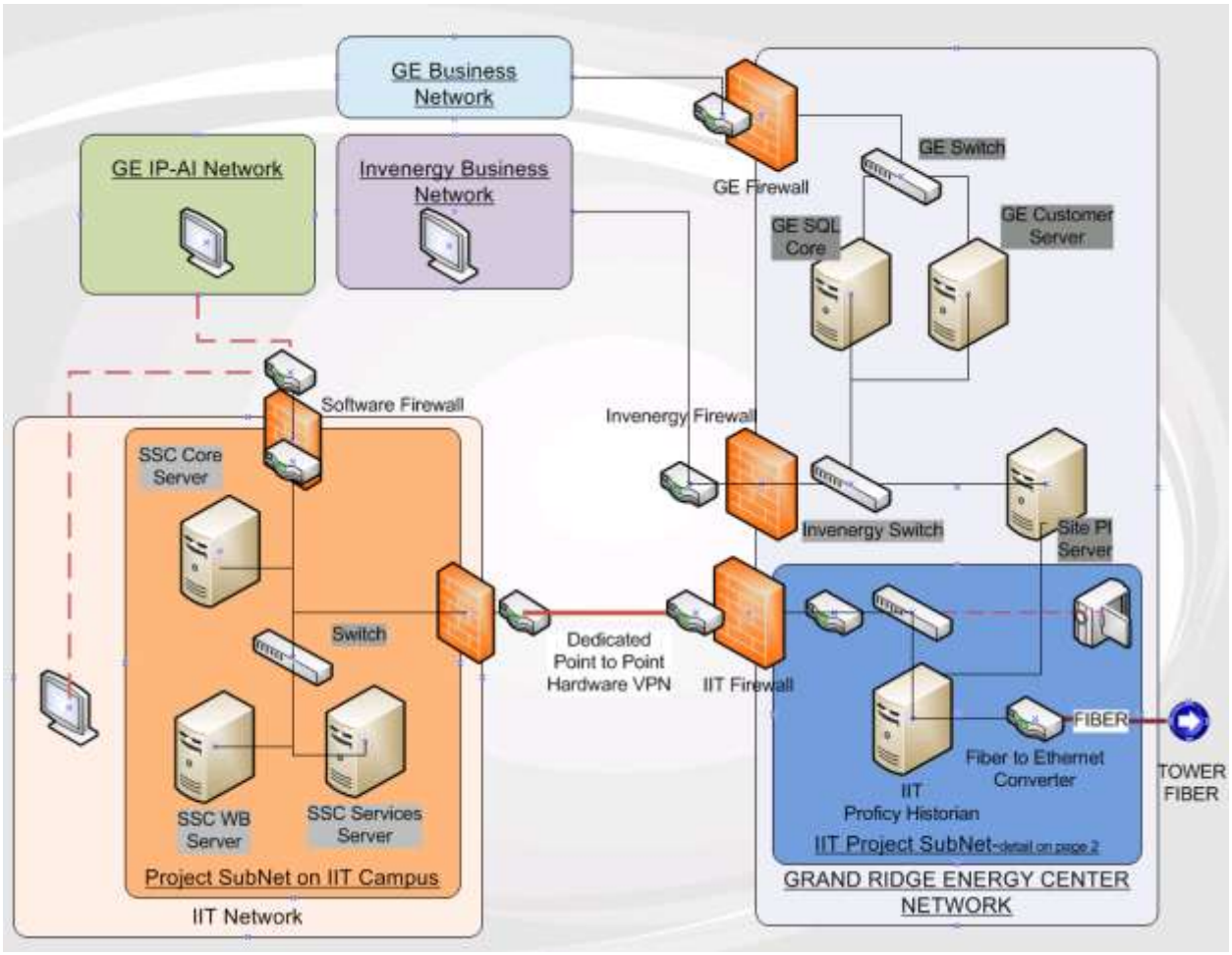

Figure 17: IIT – Invenergy – SmartSignal Wind Project: Overall Network Arrangement

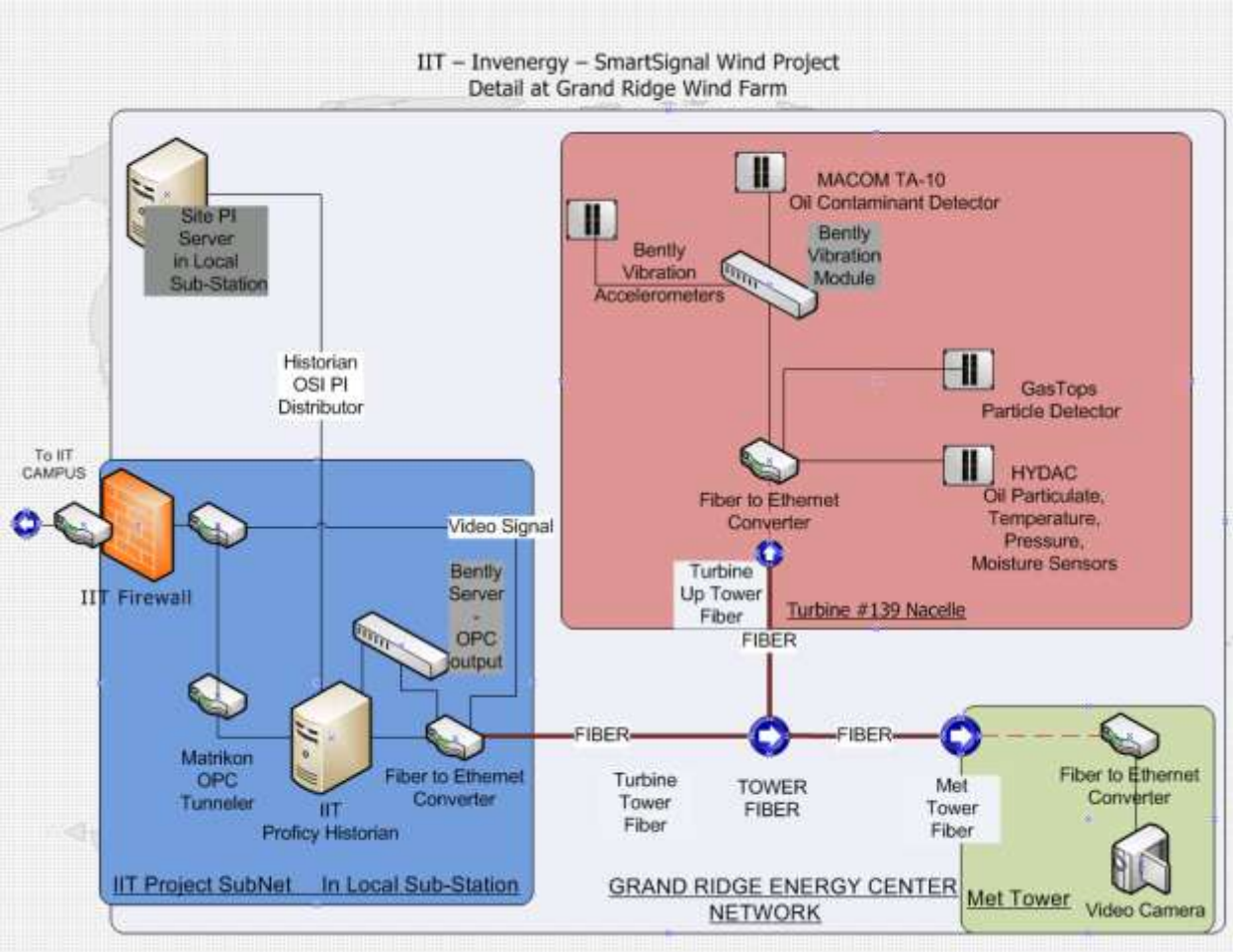

Figure 18: IIT – Invenergy – SmartSignal Wind Project: Detail at Grand Ridge Wind Farm

Once the new sensors are all delivered we will plan and execute a trip uptower to install and activate the sensors. As they are activated their output signals will be routed to the Proficy historian and made available to the SmartSignal predictive analytics software for inclusion into the models and further research.

Upon the completion of the project, the Consortium has (1) installed the GE ADAPT vibrations system; (2) installed the Lube Oil System Monitoring Sensors; (3) installed associated software and hardware to acquire the data and communicate the information to IIT main campus; (4) installed associate software and hardware to receive the data at IIT main campus, capture the data in a historian, and support the Proficy SmartSignal Software; (5) created a SmartSignal Condition Monitoring model using the OEM standard available sensors plus the additional sensors.

The GE ADAPT vibrations system provides vibration indication on the:

- Generator Outboard Bearing
- Generator Inboard Bearing
- High Speed gear Box bearing

- Intermediate Speed Gearbox bearing
- Planetary Stage bearing
- Main Bearing

The Lube Oil System Monitoring Sensors Include

- MaCom Particulate Counter, which provides Ferrous and Non-Ferrous Particulate Count from 101-200 um, from 201-300 um, from 301-400 um, from 401-500 um, from 501-600 um, from 601-700 um, from 701-800 um
- HYDAC Particulate Counter (Sensor and Bracket donated by HYDAC), which provides Ferrous and Non-Ferrous Particulate count for the last 10 minutes. With additional equipment, this unit also has the capability to provide ferrous and non-ferrous totals by particulate size.
- Gastop MetalScan Particulate Sensor, which provides Particulate Count for the last 10 minutes (Both ferrous and non-ferrous together)
- Cooler Inlet temperature (HYDAC)
- Cooler Outlet temperature (HYDAC)
- Filter Differential Pressure

Items that can be identified using the standard OEM Sensors include:

- Yaw control issues
- Blade Pitch Control Issues
- Bearing temperature issues
- Power Related issues such as phase imbalance and shorts
- Nacelle Temperature Issues
- Control Box temperature Issues (Affects the electronics)
- Turbine Efficiency Issues.

Items that can be identified using the Newly Installed Sensors include:

- Better indication of bearing health through direct measurement of vibration. It is expected that the SmartSignal model will identify the early indication of bearing issues such that tower climbs can be limited and more effective. Once identified via SmartSignal, a deeper analysis of the vibrations issues can conducted via the Adapt System.
- Direct Measurement of the count of metal particulate in the oil system. This is an indication of damage to the gears and is traditionally measured by climbing the tower and taking oil samples. Three different particulate counters were installed to allow the comparison between manufacturer capabilities. There particulate counters may differ in their ability to detect particulate, ability to filter unwanted counts (i.e.: entrained air bubbles), and the ability to provide detailed information (i.e.: ferrous verses nonferrous counts, particulate count by size)
- Directly measure filter DP. Filter DP will provide an indication of the condition of the oil filter. Additionally, measuring filter dp may provide an inexpensive alternative to installing a particulate counter (i.e.: If the filter dp increases at a faster rate, it can be assumed that there is more particulate in the oil.)
- Cooler inlet and outlet temperature. Cooler differential temperature can provide an indication of the health of the cooler (plugging) and the effectiveness of the oil cooler.

In summary, the monitoring center has been established on the campus. The video camera is in place and functional. The SmartSignal Epi-center software is installed and active. The data acquisition and storage system has been established and linked to the campus. The models are connected to the data store and active on the campus servers.

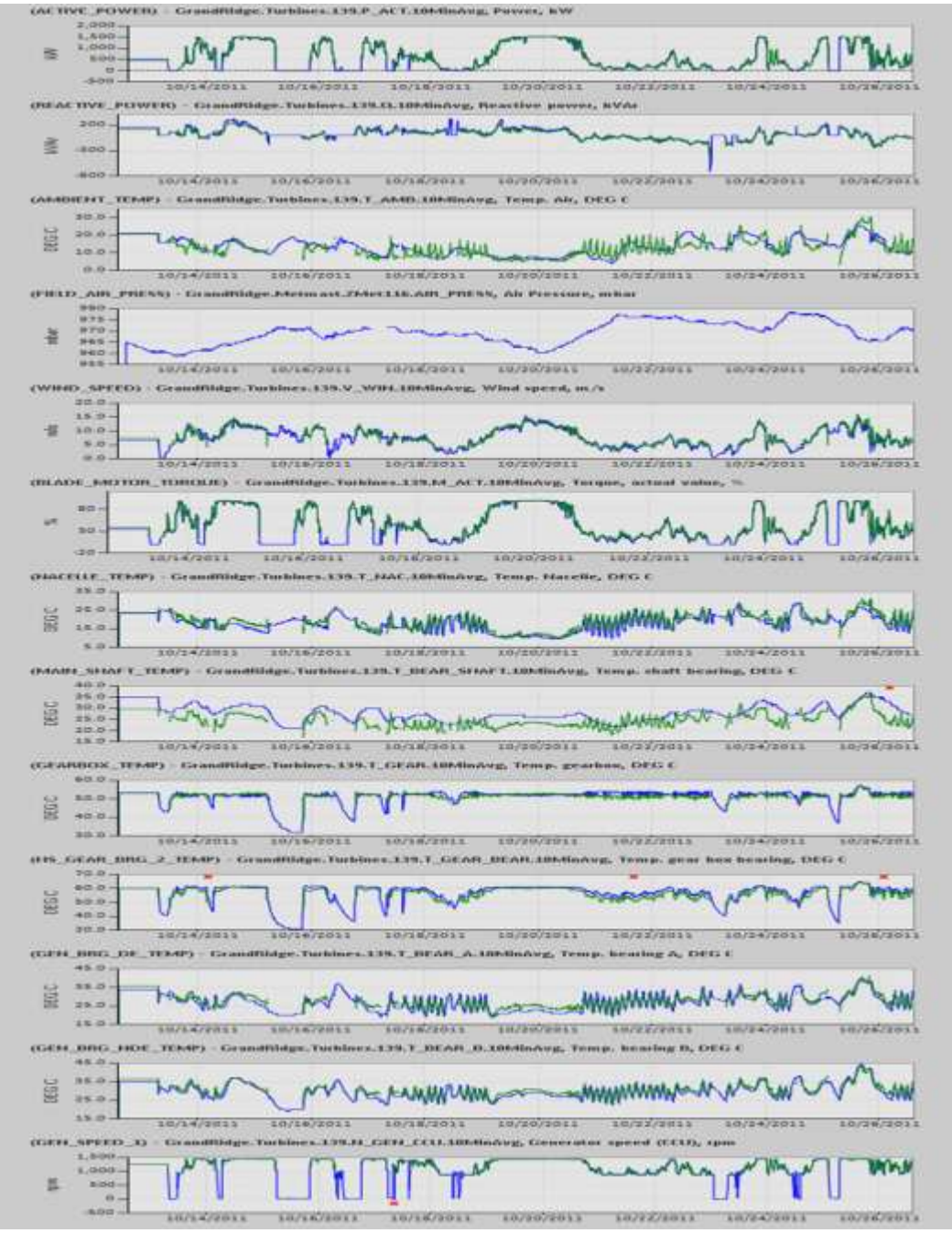

Figure 19: Sample SmartSignal Predictive Analytics Display

Figure 20: Sample SmartSignal Software Display

The Green lines represent the predicted values, the blue lines represent the actual current values, and the red XXX represent significant deviations of actual from estimate, alerting the analyst to further investigate the situation.

B. Improve Wind Turbine Power Output and Reduce Dynamic Stress Loading Through Advanced Wind Sensing Technology

Discussed in this section is a vision for moving from where the industry is today to the progressive improvements now attainable for future wind turbine control. Given that wind turbines have to operate through the dynamics of uncertain and imperfect airflow, sensors and controls can make a major contribution to performance and profitability. The existence of nacelle-mounted look-ahead laser wind sensors, capable of not only high data rates but also of various schemes to map the inflow, leads to the developmental path discussed below and illustrated in the diagram below. Incremental improvements in turbine efficiency and stress control are expected at each stage leading to an optimized control/sensor suite.

Why Is It Needed?

Collecting wind data at the rear of the wind turbine nacelle results in several significant compromises. First, both the effect of the bluff body of the nacelle itself and the blade blockage effects on the airflow have to be corrected using wind speed dependent transfer functions. These empirical correction factors do not account for any flow regimes other than perfect yaw alignment, so in periods of even the slightest misalignment to the wind, the transfer function no longer accurately corrects the measurement. Secondly, the flow encountered at the rear of the nacelle is heavily affected by the wash or wake of the passing blades. Current practice is to use long (up to 10 minute) rolling or binned averages to smooth

out the wake impulses. Not only is this imprecise, it also disguises actual fluctuations in the wind and drastically affects the response time of the control system. Thirdly, the information measured at the rear of the turbine is obtained after the air mass has passed the turbine. There is therefore no possible way to have proactive, anticipatory or feed-forward control using this data.

Installation of strain measurement into the blades, towers, shafting or other components gives an indication of operating conditions. These stresses and strains can be linked to a feedback control loop. While this provides one direct measurement of the turbine's interaction with the wind, it only generates a sensed control trigger after the mechanisms have already experienced excess stress and strain. Stress and vibration data is difficult to use for discerning whether a yaw or blade pitch correction is needed. Using strain feedback, the duration of this undesirable condition can be reduced, but events still use up the finite fatigue life of the components prematurely. This approach also increases the cost of the blades and other instrumented components.

Improving Yaw Control Brings Big Gains

The addition of a forward measuring laser wind sensor provides the control system accurate wind direction information in the undisturbed flow as it approaches the wind turbine. Tests using just this more accurate wind direction information have demonstrated both significant increased power output and reduced stresses from better alignment to the wind. A forward-looking laser not only provides a more accurate flow direction, but the absence of blade wake effects allows this information to be fed to the control system without long averaging periods.

Less averaging informs the control system of the actual flow dynamics as they occur. By virtue of the laser wind sensor measuring wind at various ranges in front of the wind turbine, control actions gain anticipatory data for feedforward controlling. This can be implemented as merely a timing advantage to reduce lag in yaw corrections, as well as the ability to track wind changes and gusts to determine not only their predicted time of arrival at the wind turbine, but also to inform the control logic with information on the "depth" or duration of an approaching gust.

Intelligent Blade Pitch Adds More Benefit

A laser wind sensor looking ahead in the inflow can also provide the blade pitch control logic with wind speed changes and wind speed gusts before they arrive at the blades. This information also can allow estimation of the precise arrival timing to correlate with the reaction times of the pitch control mechanism. The result is a reduction of time spent at a suboptimal blade angle to the flow and experiencing unexpected loads or stress.

Laser wind sensors can be designed to provide multiple measurement points simultaneously at known locations in the inflow to provide spatial flow mapping at multiple ranges. With this spatial wind speed and direction information, the shear and veer of the flow in the inflow can be determined in real time. The pitch control of each blade can then be timed to the sweep angle so that it is optimized based on the spatial wind conditions it is actually passing through. While laser wind direction data can greatly improve the alignment with the wind over time, the relatively slow yaw response of the large nacelle mass compared to the rates of wind direction change results in transients of misalignment which can be

addressed with individual blade pitch adjustments to minimize the vibration caused by the leading/following blade effects. This is similar in concept to the blade pitch adjustments made on helicopters to compensate for the relative airspeed of leading/following blades in forward flight.

What Does The Future Hold?

While current turbine designs are based on unitary blades that account for the span-wise (radially) differences of flow and moment with taper and twist, those designs are based on the assumption of a uniform flow field perfectly normal to the plane of the blade rotation. In fact, as a result of spatial and temporal wind speed and direction variations, the flow field at any point in time is not truly uniform in the radial direction. Even informed individual blade pitch control has to select a best compromise angle of attack for the entire blade length and does not have the ability to handle span-wise flow differences. With real-time spatial wind speed and direction data from a laser sensor, high response rate aerodynamic devices along the blade span could be actuated to correspond to local relative wind. This could be implemented using various flaps, jets, or tabs as developed for aircraft wings or rigid sails. Combined with the other control advances, this stage represents an optimization of active controls.

Ever-increasing sophistication is projected for wind turbine sensors and controls with resultant step-wise increases in efficiency and reductions of undesirable stresses. Wind turbine control practice can begin to catch up to university research and aerospace now that forward-looking laser wind sensors can provide the needed wind accuracy, timeliness, data rates, and spatial mapping. It is time for the wind energy industry to start gaining the power performance and stress reduction advantages.

Forward Looking Laser Technology

The Vindicator® laser wind sensor (LWS) is a ‘next generation’ wind sensor for utility-scale wind turbines. From its position on top of the nacelle, it determines the wind speed and direction in the undisturbed air 250 meters in front of the turbine. As a result, the unit can provide the control system with a predictive, three-dimensional view of actual conditions which allows you to optimize wind turbine performance.

By delivering a more precise and accurate picture of wind speed and direction, the Vindicator® LWS increases wind power output and reduces wear and tear on system components. For example, wind data measured in front of the turbine allows the control system to make proactive decisions about yaw angle and adjustment. Staying in alignment with the wind will significantly increase power output and dramatically reduce turbine stress. It can also adjust blade pitch in anticipation of sudden stress events such as high winds or sudden drops in production due to low wind conditions.

With the accurate predictive data delivered by the Vindicator® LWS, the control system can work smarter to increase efficiency, improve blade alignment, make better pitch decisions and reduce overall system stress, which will extend turbine life and cut maintenance costs.

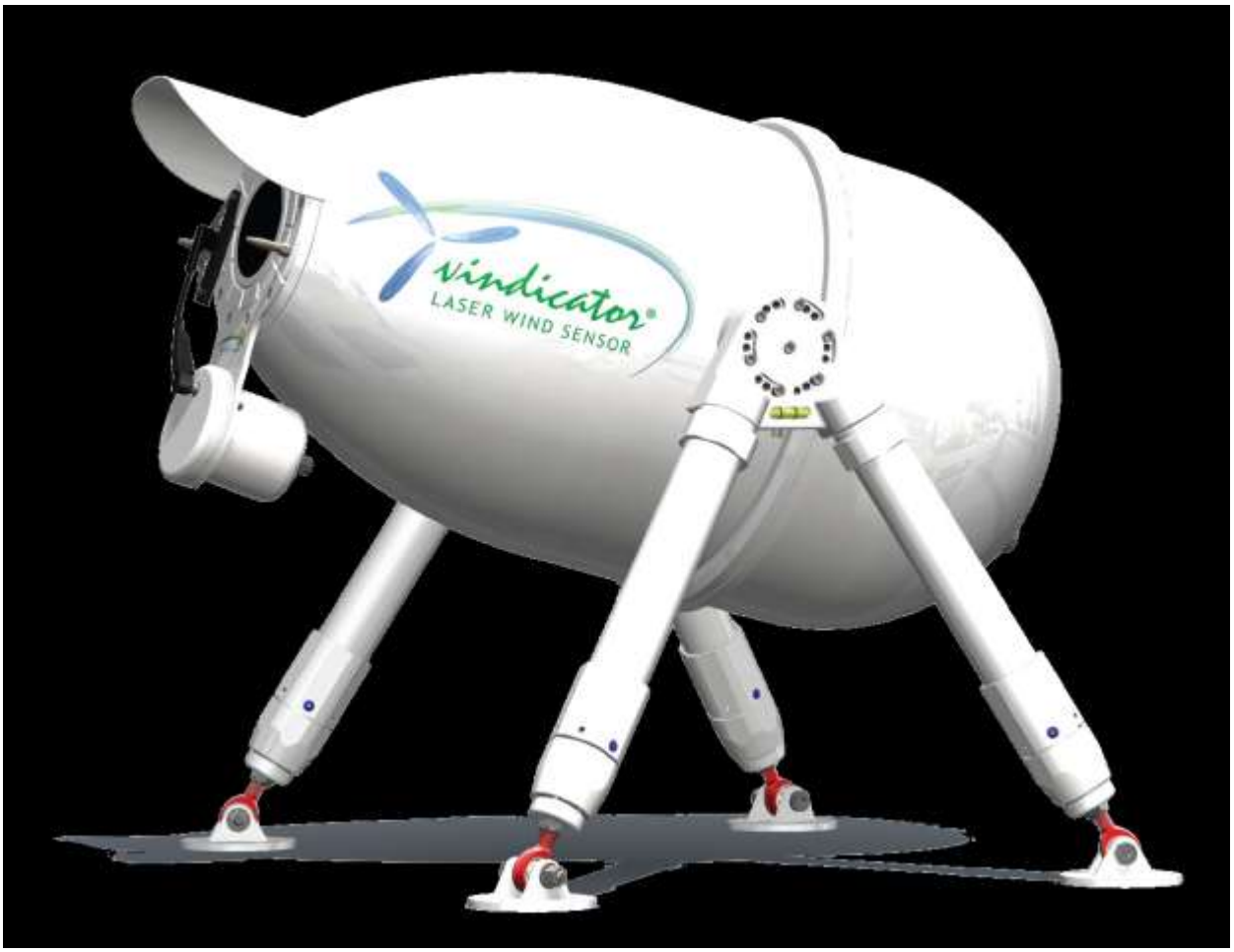

Figure 21: Catch the Wind Vindicator® Laser Wind Sensor

B1. Wind Measurement and Power

The wind is a curious creature, blowing this way and that. Mathematicians would say that wind is a classic example of chaos. If asked about the wind, a surfer would simply shrug and say that waves are crazy, too. This powerful, but also quirky creature, the breeze that makes a child smile- this is what we must capture.

Our world needs us, the wind turbine industry, to produce power, cleanly, efficiently and at low cost. The contribution of this project to the wind industry is to use our understanding of optics to provide a fundamentally deeper understanding of the wind resource - to produce substantial, repeatable increases in the output power of wind turbines.

Synopsis

An Optical Control System (OCS), beta-version, is tested upon an operating utility scale wind turbine. The turbine was operated in four regimes; legacy yaw control (sonic anemometer) and three OCS control regimes. The behavior of the sonic anemometer, measuring both speed and wind angle, is studied. The uptime of the OCS is studied. Power curves in the four regimes are compared.

The data set is large, approximately 500 MB, composed of 335,000 data points taken at 1 second spacing. SAS JMP used as the statistical analytic tool. The dataset includes output from the OCS, two sonic anemometers (giving both wind speed and wind direction), turbine state, ambient temperature, output power, and absolute yaw position.

The Ideal Wind Turbine

Wind has a mind of its own; it is turbulent, has shear, changes direction, and changes velocity.

An ideal wind turbine needs to be pointed in the right direction, with its blades set at the correct angle to the wind. When a gust approaches, an ideal turbine will take actions to avoid damage. Practically, this means that the turbine has sufficient wind data to properly adjust blade pitch and yaw, is equipped with adjustable pitch and yaw, and has a control architecture that is sufficiently sophisticated to translate wind data into the appropriate turbine actions.

To properly adjust the pitch of all of the blades at the same time ("collective" pitch control) requires an accurate understanding of the average wind speed approaching the entire spatial plane of the blades of the turbine.

To properly adjust the pitch of each blade individually ("individual" pitch control) requires both rapid pitch adjustment and an accurate mapping of the variance (either modeled or measured directly) of the wind speed incident upon the turbine. A discussion of 2-D mapping is outside of the scope of this discussion.

Correct yaw adjustment implies that the turbine understands the direction of the wind, as it approaches the blades of the turbine. As an aside, we note that most analysis of a wind turbine, particular work on advanced control algorithms and controller analysis and design tend to begin with an a priori assumption that the there is no yaw misalignment. The data collected in this work, regardless of which control algorithm is used, clearly demonstrated that the assumption of no yaw misalignment is not valid.

Gust avoidance is possible when the turbine knows the wind speed and direction that will hit the wind turbine, with enough warning time to take actions to avoid damage.

Current State of the Art

Speed Measurement

Wind turbines today use anemometers, mounted on the rear of the nacelle, to measure wind speed. Although these are high quality wind measurement devices, they cannot be mounted in front of the turbine and, hence, must operate in the turbulent air that has already passed through the turbine blades, which has little resemblance to the wind condition in front of the blades. Figure 22 shows the raw output of a sonic anemometer in action. The horizontal axis is recorded seconds, with the figure capturing 10 minutes of operation. This particular turbine model has two sonic anemometers; Figure 22 only shows the output of one of the two sonic anemometers. Throughout this Section, the sonic anemometers are referred to as A1 and A2.

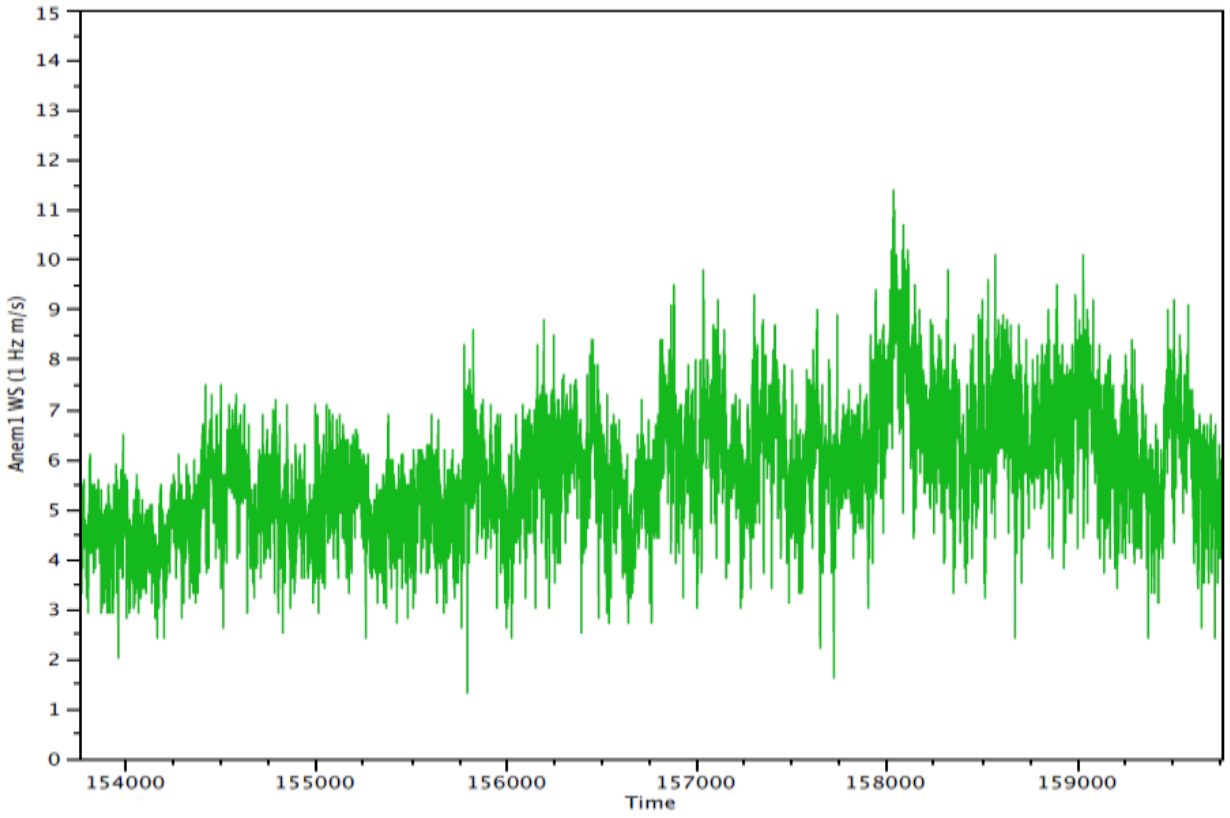

Figure 22: The data of a sonic anemometer, mounted on the rear of the nacelle of an operating wind turbine.

(The data is taken each second of operation. The period shown here covers a 10 minute interval.)

While this data is extremely noisy, much of that noise comes from the turbulence effects of the turbine blades as the wind passes through them. Stated differently, if this sonic anemometer were measuring undisturbed air, the data would be more accurate and much less noisy. This can be seen in Figure 23, where we show the wind speed data measured in front of the turbine, where the wind is free of these turbulence effects. This data, also taken each second of operation, and without any averaging external to the system, is taken using our Vindicator® Optical Control System, or more simply the "OCS". As the OCS utilizes a pulsed laser operating with a pulse repetition rate much higher than 1 Hz, internal averaging is used prior to the 1 Hz output. The industry deals with noisy sonic anemometer data quite pragmatically by averaging the wind data output of the sonic anemometer over time. This is effective in smoothing the data, but requires fairly lengthy averaging times to produce data of sufficient quality to make control decisions. Figure 24 shows a comparison of the OCS output, from Figure 23 above, compared to the outputs of the sonic anemometers, where the sonic anemometer data is averaged over 60 seconds to smooth the data.

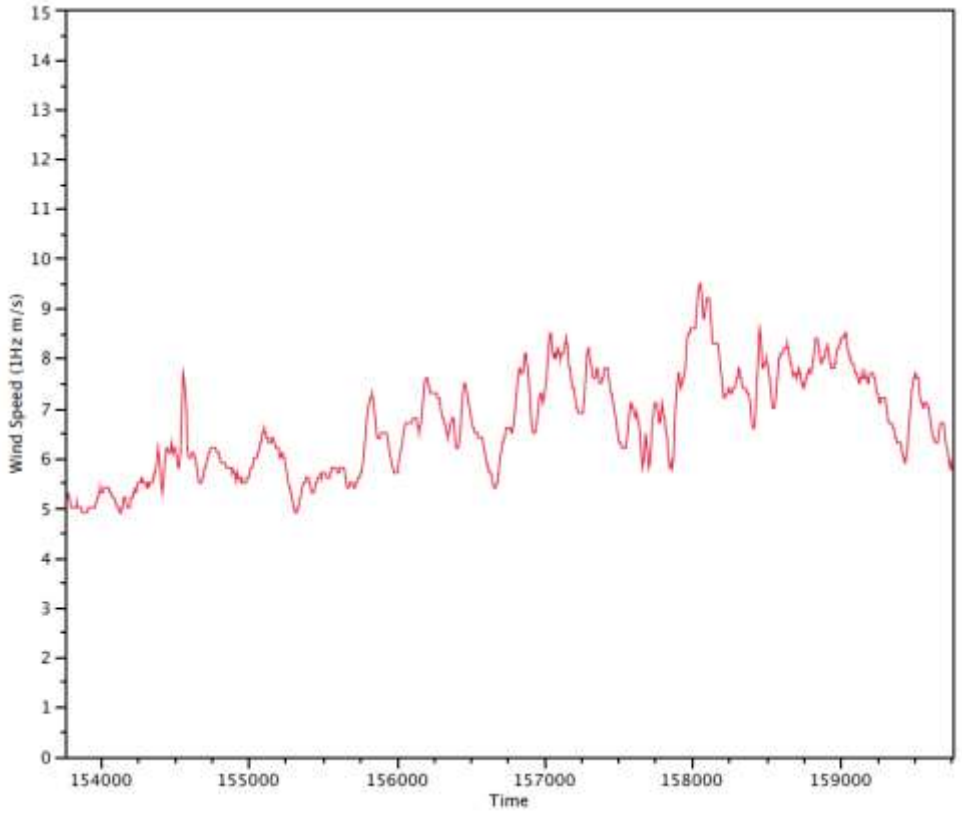

Figure 23: The wind speed in front of the turbine, measured with the OCS.

(This data is also taken each second, un- averaged, with a 10-minute period of operation shown.)

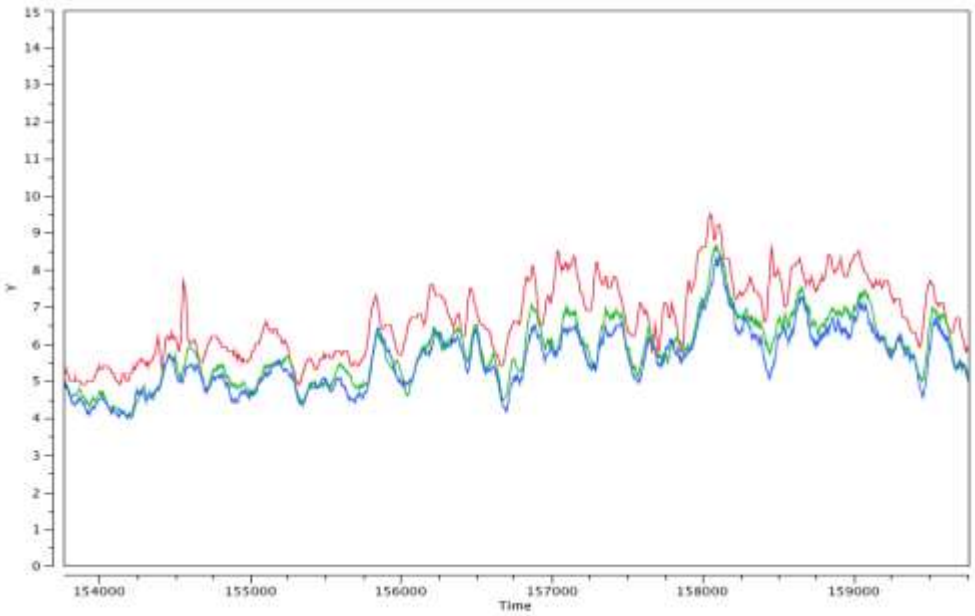

Figure 24: Outputs of the sonic anemometers

(The blue and green lines are the outputs of the sonic anemometers, averaged over a 60 second period, with the vertical axis representing wind speed in meters per second. The correlation between the two sonic anemometers is quite respectable. The sonic anemometers show lower wind velocity than the OCS, as is expected due to the fact that the turbine has extracted power from the wind.)

Figure 24 shows fairly clearly several effects. First, the mean wind speed measured by the sonic anemometers is made much more usable by averaging. Sudden gusts of wind, however, are lost by this averaging as indicated at approximate time 154500 in Figure 24. As expected, since the OCS is measuring the wind in front of the turbine, the OCS captures changes in wind speed slightly ahead of the sonic anemometers.

Second, the wind speed as recorded by the sonic anemometers is significantly lower than the OCS measurement over the same period of time. The OCS is detecting wind behavior well in front of the turbine. As such, the operational state of the turbine has no impact upon the OCS wind speed measurement, or equivalently, the actual wind speed that is being measured.

The fact that wind speed as recorded by the sonic anemometer on the rear of the nacelle is lower than the OCS is actually expected from first principles: as the turbine extracts power from the wind, the velocity of the wind decreases.

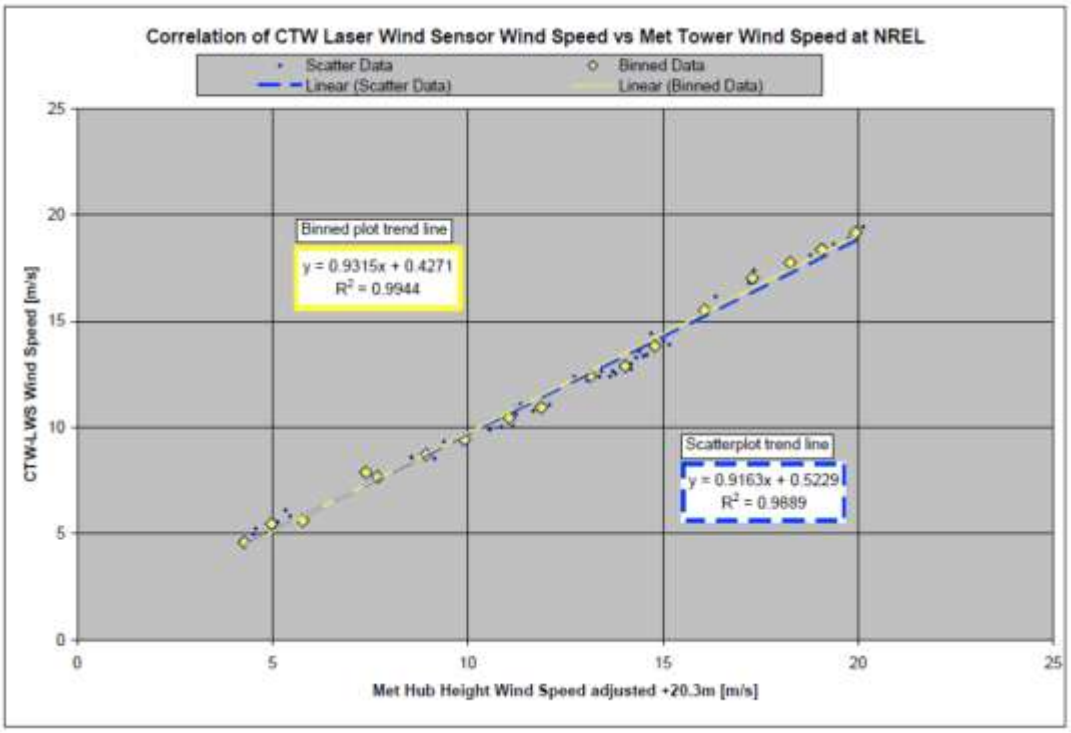

Figure 25: Experimental LIDAR data.

(The comparison is with a calibrated met tower. R^2 is ~0.99. Data in collaboration with NREL.)

Our experience with the OCS is that it shows excellent correlation to calibrated metrological (met) towers whose measurements, like the OCS, are unaffected by the turbulence effect of turbine blades. This has been demonstrated several times now. For reference we show wind speed data taken in collaboration with the U.S. Department of Energy's National Renewable Energy Laboratory (NREL). This level of correlation is consistent with our OCS wind measurement performance in other met tower comparisons. If the reader is interested in a more holistic write-up of experimental LIDAR/met tower correlations, please contact CTW directly.

Following this argument, at wind speeds so low that the turbine blades cease to spin, the well-calibrated sonic anemometer should be accurate. In Region II, where the power extracted rises with wind speed, the sonic anemometer error is expected to increase. In Region III, where the power extracted from the wind is approximately constant since the turbine is operating at its rated power, the velocity error of the sonic anemometer should begin decreasing with increasing wind speed, since the amount of power being extracted from the wind is roughly constant until the cut-off wind speed is reached. Stated differently, the wind speed detected by the sonic anemometers is observed to be, as expected, dependent upon the output power of the turbine.

This effect is borne out in Figure 26. The correlation of sonic anemometer to the free wind speed is not symmetric, and, as expected, is skewed to lower velocity, with this asymmetry particularly apparent in Region II.

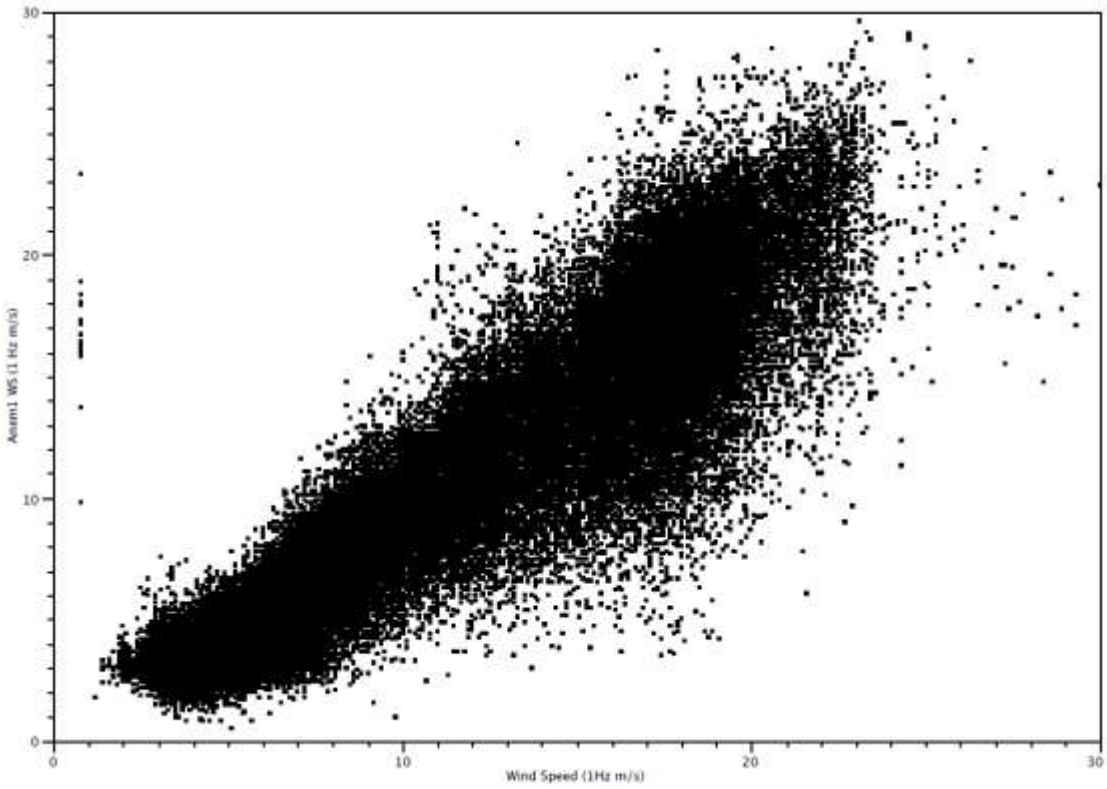

Figure 26: The correlation between the wind speed behind the turbine blades and the free wind

(Wind speed behind the turbine blades measured by the sonic anemometer, and the free wind measured by the OCS)

Next, we examine the wind speed correlations between the free wind measurements (OCS) and the post-rotor wind speed measurements (taken by the two sonic anemometers, noted as A1 and A2) when they are in different control regimes (i.e, we look at the correlations when the turbine is under OCS control versus when the turbine is under legacy control). All correlations between the different wind speed measurement devices improve under OCS control. It is our hypothesis that OCS controls the angular yaw of the turbine such that the actual angle error is reduced, and that the sonic anemometers' measurement is closest to the free wind when they are not additionally perturbed by cross-winds due to angular yaw misalignment. Again, it is noted that rotor blades are generally designed assuming zero yaw angle. Off-axis wind may increase loading on the blades, but this loading would be out of plane such that torque may actually be reduced while lift and drag may increase.

R^2	Turbine Control	
Speed	Legacy	OCS
A1 & A2	0.991	0.995
A1 & OCS	0.947	0.975
A2 & OCS	0.946	0.976

Figure 27: The correlations between the different measurement tools.

(The correlations improve when the turbine is under OCS control.)
In addition to the correlations between the various wind measurement devices improving under OCS control, the difference between wind speed as measured in front of the wind turbine by the OCS, and, in the rear of the turbine by the sonic anemometer as averaged for "smoothing" effects, also decreases under OCS control and, conversely, increases under legacy control. A real-time plot of this is shown below, where, even before the sonic anemometer data is processed, or "smoothed", it is clear that the wind measurement correlation between the OCS and the sonic anemometer is worsened under sonic anemometer control, with the sonic anemometer recording a generally lower wind speed for the post-turbine wind than the free wind speed recorded by the OCS. This effect may be due to the fact that the wind turbine is operating, on average, more out of alignment with the wind when under legacy control, and, therefore, the blades somewhat "shield" off-axis wind (i.e., the sonic anemometer behind the turbine is measuring the projection of the wind along the axis of the wind turbine).

(In general, the sonic anemometers record a lower wind speed behind the turbine blades than the wind speed recorded by the OCS in front of the turbine, as expected from physical arguments. However, this difference increases when the turbine is under legacy control.)

The difference in wind speed measurements can be shown quite simply. Figure 8 shows the linear fits of an average of the two anemometers vs. the wind as measured by the OCS. Under legacy control, the wind speed measured by the anemometers is lower than when under OCS control. We believe that the wind speed measurement of the anemometer, relative to the OCS, drops as the turbine is taken off of alignment with the wind.

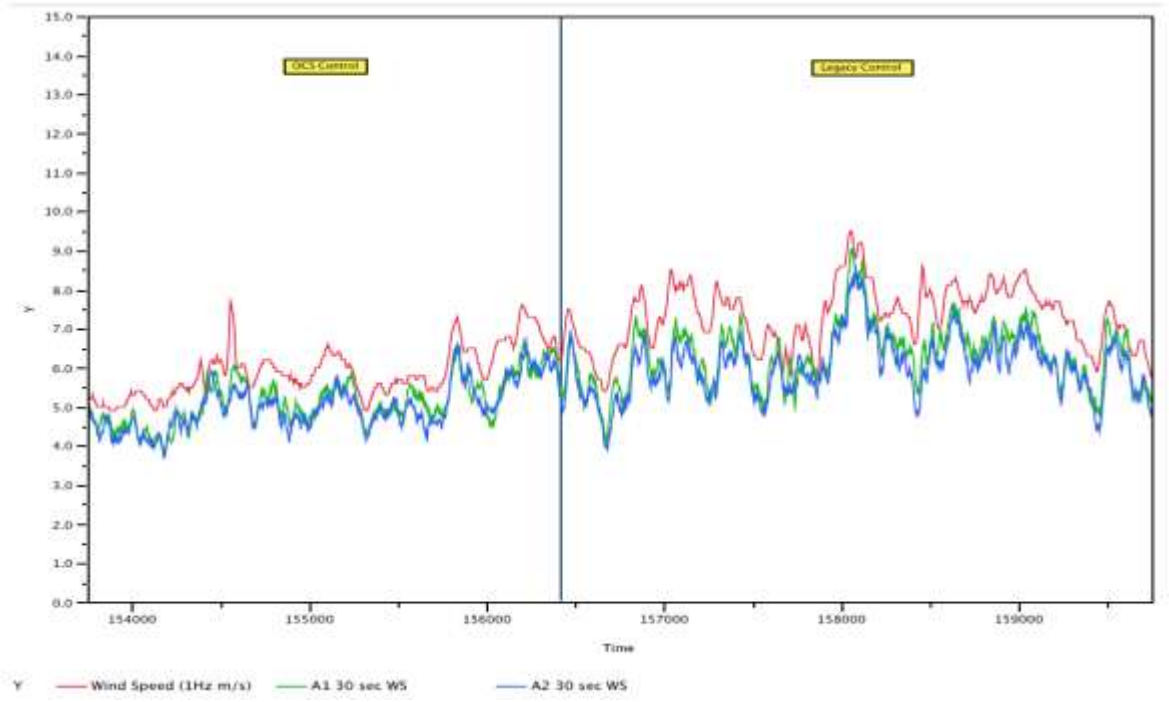

Figure 28: A plot of real-time wind speed measured by the OCS and both sonic anemometers.

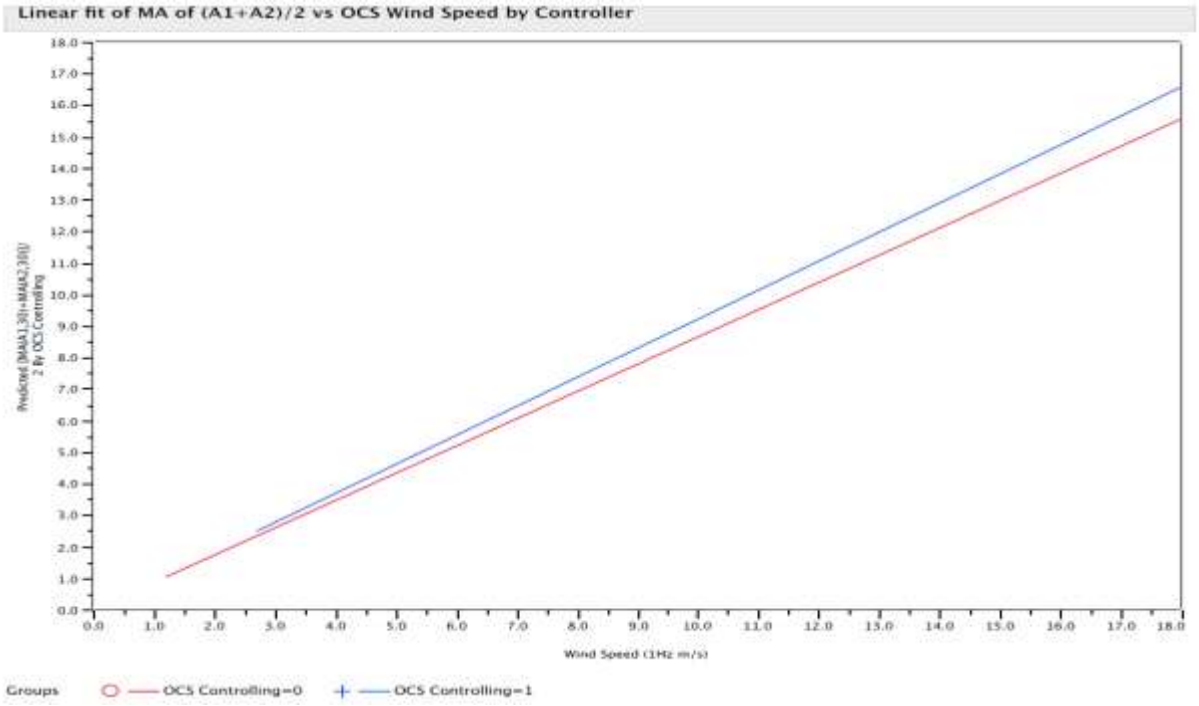

Figure 29: The fitted curves of wind speed as measured by the anemometer and the OCS.

Key Points

- The region at the rear of the nacelle is very turbulent. Wind speed measured within this environment is noisy, and cannot be directly used in controlling the wind turbine. Averaging can be

used to make the outputs of the sonic anemometer(s) useful; however, rapid changes in wind speed are lost.

- Wind speed data from the OCS is real-time, less noisy and does not require further averaging to be usable.
- The operation of the turbine decreases the accuracy and usability of the wind speed measurements that the sonic anemometer records. This effect is most pronounced in Region II.
- The correlation between all wind speed measurement devices improves under OCS control. The wind speed detected by the sonic anemometers is lower, as expected, than the free wind speed. However, the wind speed measured by the legacy system is even lower relative to the OCS when the system is under legacy control.

Measurement of Wind Angle

The wind turbine under study here uses a sonic anemometer to measure the angle of the wind relative to the turbine. For ease of discussion, throughout this document, when we refer to angular measurement, we use the term wind vane. Figure 30 shows the raw output of a sonic wind vane (one of two) in operation.

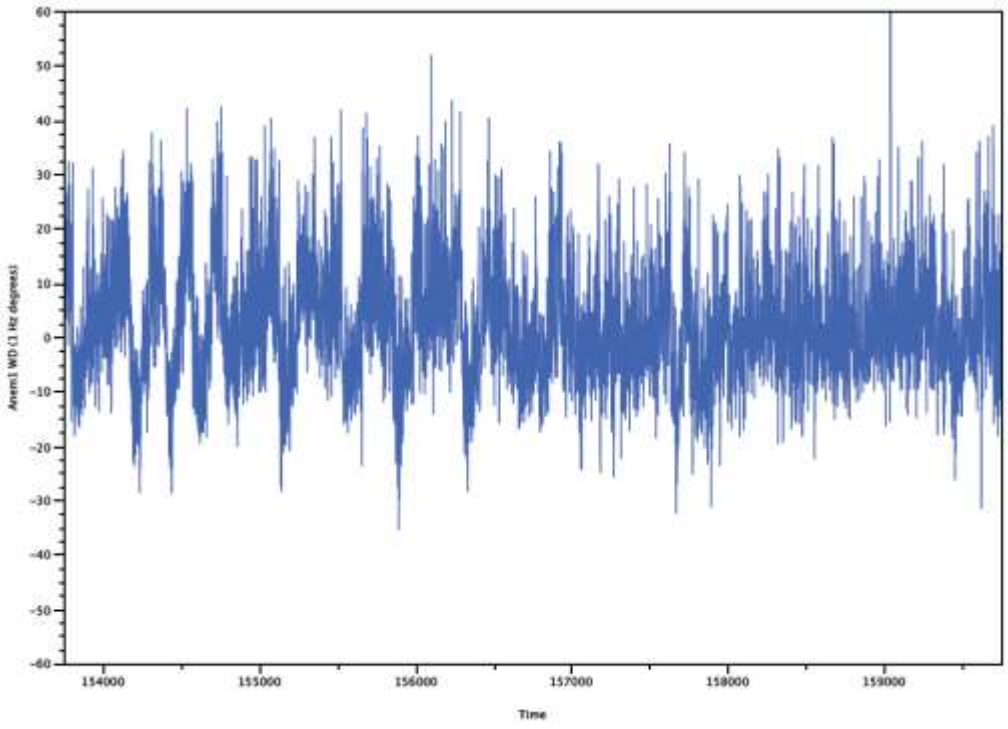

Figure 30: The wind angle, measured each second, of a sonic wind vane mounted at the rear of the nacelle.

We now examine the correlation between the wind angle relative to the turbine, as measured by the two sonic wind vanes and the OCS (which measures the wind direction in front of the turbine). In general, the correlation between the two sonic wind vanes (V1 and V2) is reasonable. However, the correlation between the sonic wind vanes and the measured angle of the free wind is marginal. All

correlations improve under OCS control. These correlations, as measured by the figure of merit R^2, are shown in Figure 31.

R^2	Turbine Control	
Angle	Legacy	OCS
V1 & V2	0.991	0.995
V1 & OCS	0.947	0.975
V2 & OCS	0.946	0.976

Figure 31: The correlations between the sonic wind vanes and the OCS when measuring wind angle.

(The correlations all improve under OCS control.)

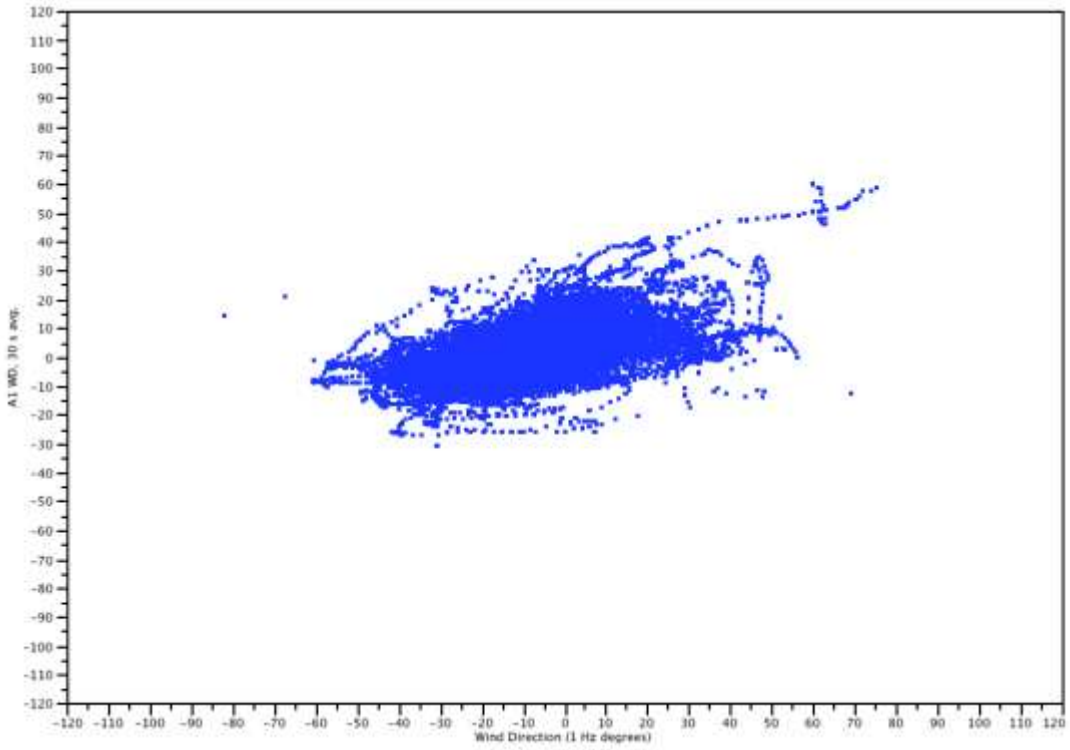

Figure 32: Scatter plot of wind angles relative to the turbine measured by a single sonic wind vane plotted against the wind angle measured by the OCS, while under legacy control.

(R^2 is 0.56. The sonic wind vane measurement is suppressed relative to the measurement of the free wind direction, with the correlation slope)

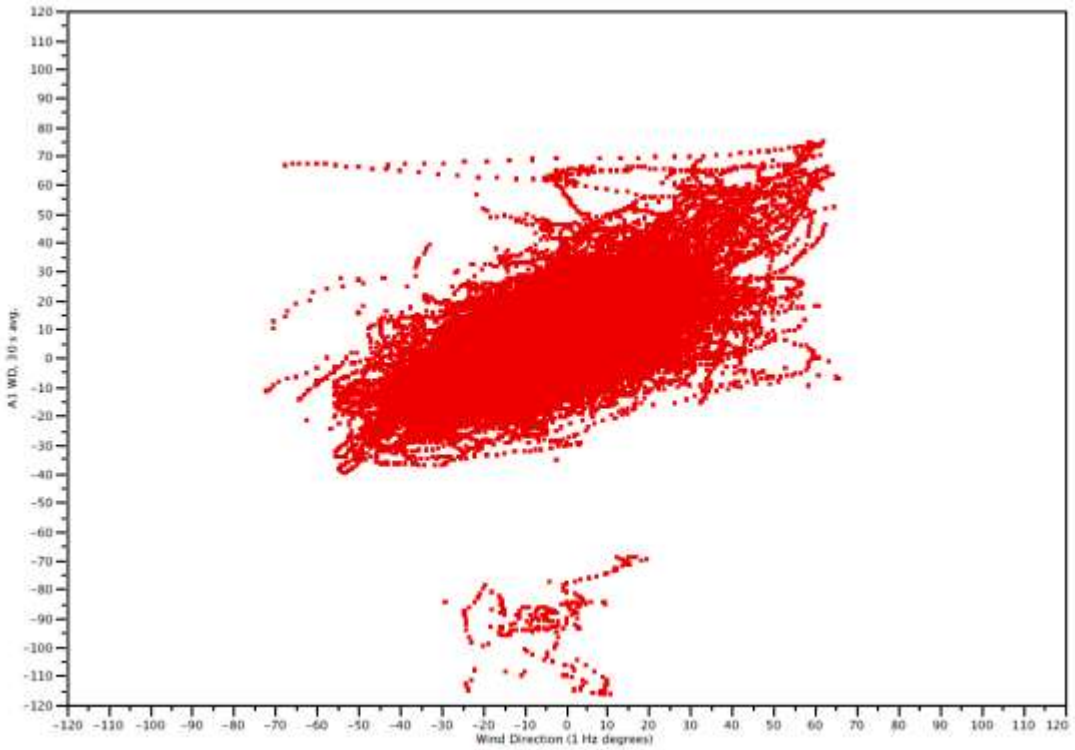

Figure 33: The scatter plot of wind angles of a turbine measured by a single sonic wind vane plotted against the wind angle measured by the OCS, while the turbine is under OCS control.

(R^2 is 0.63. Here, the average yaw angle of the turbine is approximately zero. The sonic wind vane measurement is more tightly correlated to the free flowing wind direction, and the ratio of angle measured by the sonic wind vane to the OCS is closer to unity.)

Two things are now clearly observed. First, the measurements of the angular devices all display superior correlation when the turbine is being controlled by the OCS. Second, the slope of angle measured by the sonic wind vane to the OCS measurement is closer to unity when the turbine is being controlled by the OCS.

There is an aggregation of points, in the lower portion of Figure 12, where the OCS is measuring small angles, while the sonic wind vane is measuring an angle almost orthogonal. This data set is being investigated.

Key Points

- The region at the rear of the nacelle is very turbulent. Wind angles measured within this environment are noisy, and can not be directly used in controlling the wind turbine. Time averaging improves this.
- The correlations, and directionality, of wind angle as measured by the sonic wind vane and OCS are substantially improved while the turbine is under OCS control.

Measurement Asymmetry

To further investigate the disparity between the angles measured by the sonic wind vane and the OCS, we simply generated a scatter plot of power generated vs. measured angle. In this comparison, we are showing all data, whether the system was controlled by the legacy system or the OCS.

If we plot power vs. OCS angle, we see a distribution with a rather flat top, being limited by the rated power of the turbine, roughly centered at angle = 0, with the distributions being rather symmetric around zero. This distribution is what would be intuitively expected.

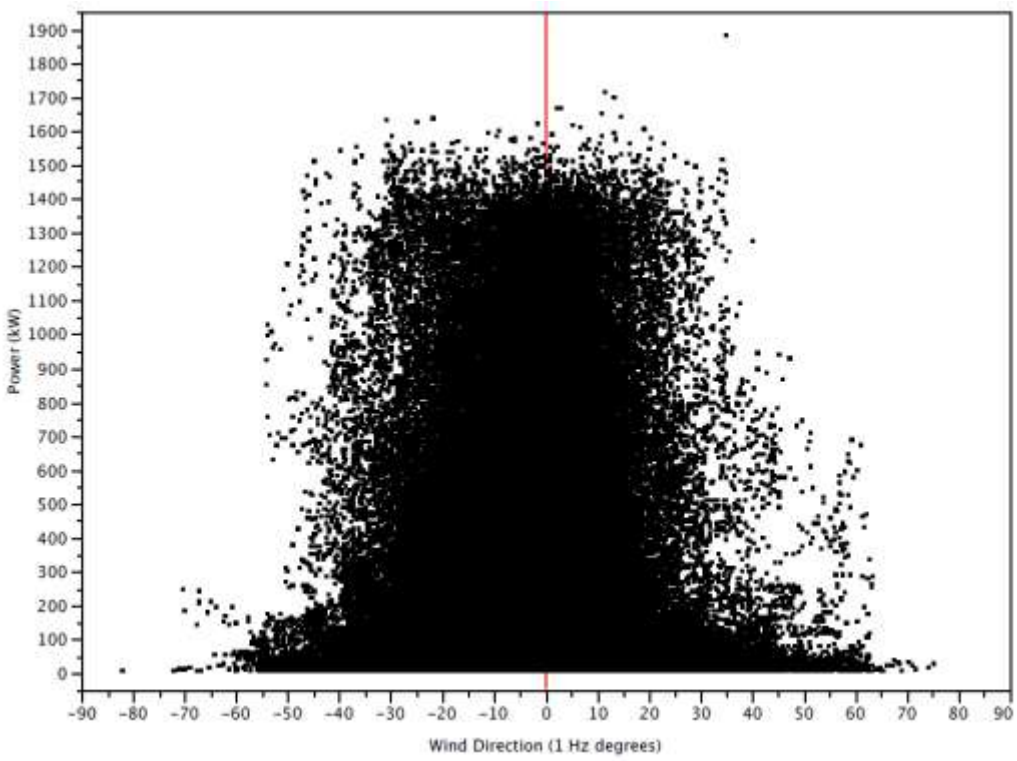

Figure 34: A scatter plot of output power vs. angle as measured by the OCS.

(All operational conditions are shown, including both legacy and OCS control regimes. The distribution is centered at zero and is roughly symmetric.)

Similar data taken with sonic wind vanes measuring wind angle is very different. The distribution is not symmetric, and is in fact skewed strongly in one direction. The amount of "skewedness", including the degree of angular offset, changes with output power, i.e., the angular error of the sonic wind vane is a function of the power, which is related to wind speed. We will discuss later why the apparent angle of the wind, and the wind speed, which should be independent of turbine power, is functionally related to the output power of the wind turbine, making yaw control difficult. However, this is fairly easy to understand intuitively since a gigantic fan (i.e., the blades of the wind turbine) is creating vigorous wind patterns that are a function of blade pitch, angle of attack and actual wind velocity. Stated differently, a large signal error is imposed upon the sonic anemometer, and that error is not constant, but is a function of wind turbine operation, making removal of that systematic error difficult.

Key Points

- The distribution of output powers is centered and symmetric for the OCS. A yaw control algorithm designed to minimize the measured angle of the OCS would maximize turbine power.
- The distribution of output powers is neither centered nor symmetric for the sonic wind vane. The amount of angular offset appears to be a function of output power, and by extension, wind speed.
- Because the yaw angle error of the post-turbine wind, as measured by the sonic wind vanes, is a function of power and wind speed, it is much more complicated to design and test effective control algorithms.

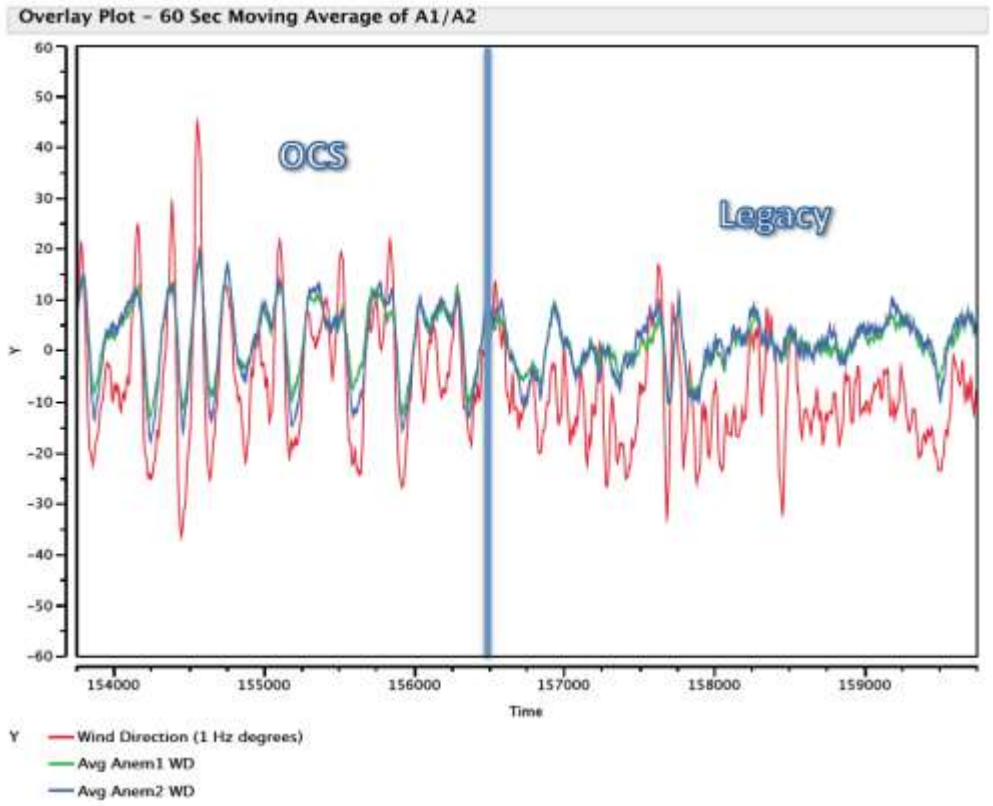

Figure 35: A comparison of measured wind angles.

(In the left portion, with generally good correlation, is data taken with the turbine under OCS control. Conversely, in the right portion, with substantially poorer correlation, is data taken with the legacy control. The red trace is the OCS, the blue and green traces are the sonic anemometer)

Previously we noted that the wind angle correlations for both sonic wind vanes and OCS improved when the turbine was operating under OCS control. The arguments presented above help explain this. However, the difference in these correlations is quite striking to look at in real time. Figure 35 shows a time period of approximately 6000 seconds (1.6 hours) in which the turbine is first under control of the OCS and then under the control of the sonic wind vane. While the sonic wind vane does miss some of the rapid changes in wind angle, the tracking between the OCS and the sonic wind vanes is generally

good while under OCS control. By contrast, when under the control of the legacy sonic wind vanes, substantial differences appear between the OCS, which is measuring undisturbed air, and the sonic wind vanes, which are in air disturbed by the rotating blades.

Uptime

In general, the LIDAR world refrains from discussing device uptime. This is intellectually bankrupt, because if the system is not up and running, it can't control the turbine. If the OCS cannot control the turbine, it obviously generates exactly zero extra power. Within this uptime demonstration, the OCS was in operation a minority of the time as shown in the following figure.

Beta units from CTW did not demonstrate good uptime performance. CTW Generation II, or G2, units, with improvement in both design and manufacturing, have radically improved signal-to-noise (SNR) performance, which directly translates into significantly better uptime. While no measurement will have 100% uptime, we believe that the G2 and subsequent versions of the OCS will have uptime approaching 100%, as demonstrated by recent field results. This study employed a beta OSC unit, which experienced a low system uptime. This is shown below.

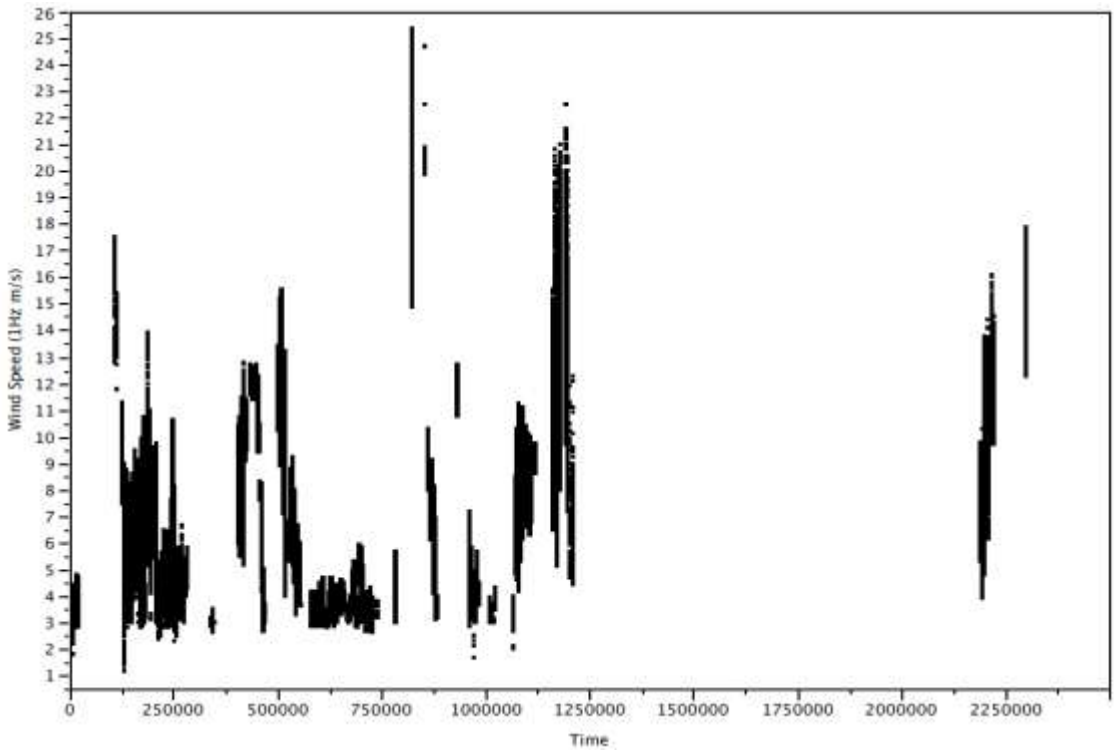

Figure 36: A scatter plot of all wind speed measurements of a turbine from the beta version of the OCS over a period approximately 30 days.

(The OCS exhibited uptime of 33%.)

In order to track the uptime of the OCS, which we believe is a critical figure of merit for any sensing system, we computed an up-time figure, defined as the total amount of time the OCS was operating divided by the total time the turbine was operational. Up-time for this beta unit was 33%.

Key Point:

- The beta version of the OCS used in this study had poor uptime of only 33%.
- The redesigned optical system now used in the G2 version of the OCS has demonstrated uptime in the field approaching 100%.

Turbine Power Production

Instead of just starting the discussion of turbine power production with a comparison of the scatter plots that lead to power curves, we instead begin by looking at what the output power of the wind turbine looks like over time.

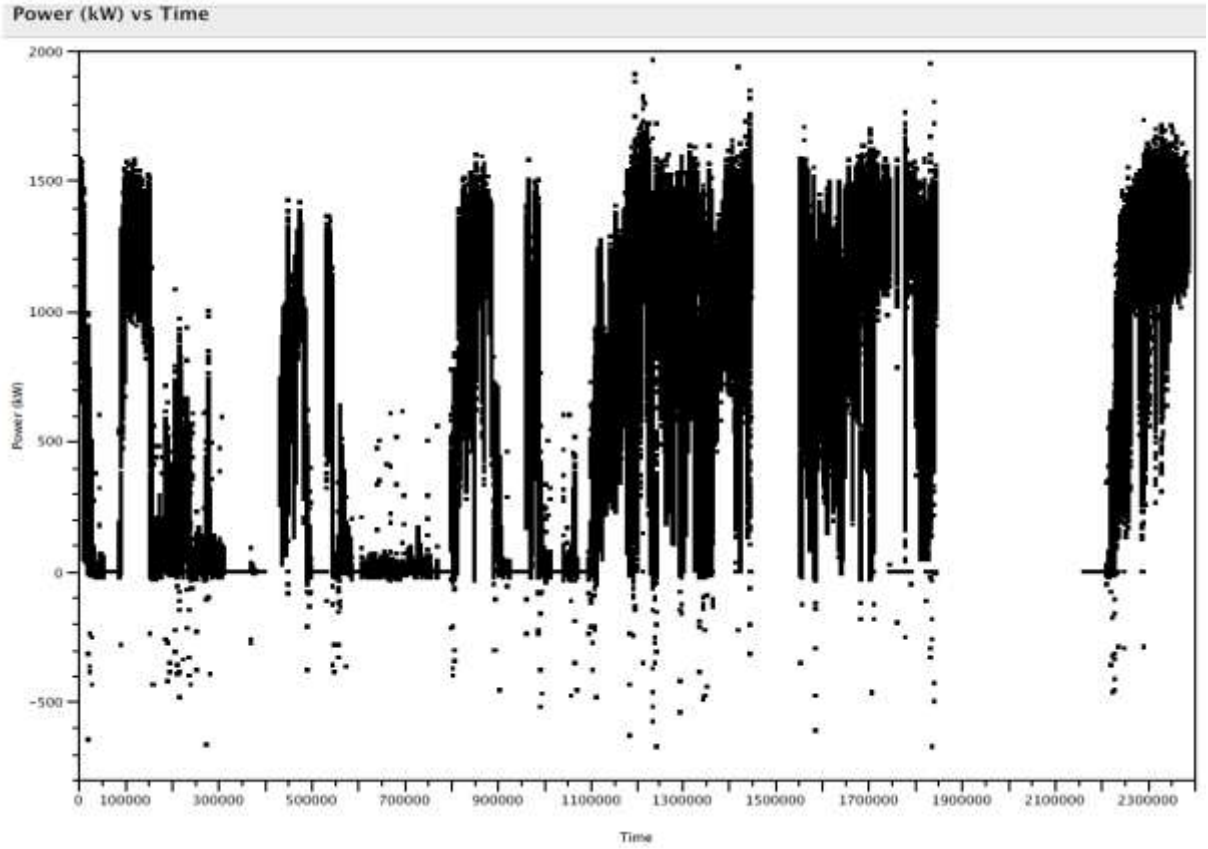

Figure 37: The output power of the turbine during the entire period of study.

In Figure 34, we show all power data for the full period of operation for the turbine, whether the turbine was operating under the control of the legacy sonic anemometer or the OCS. This data shows periods of good output and also periods of minimal or zero output. In addition, there are many data points where the turbine output power is shown to be negative. We don't fully understand negative power production in turbines, but do note this data. In Figure 38, we show 100 seconds of power output data for the same wind turbine. The data was surprising; within that timeframe, the power output of the turbine fluctuated from 400 kW to 160 kW, with +/- 50% changes in power output occurring within seconds. As an aside, we understand that the wind can change very quickly. These changes in wind speed drive substantial torque fluctuation which yield rapid changes in power output. That being said,

the electrical generation properties of wind turbines are outside of our area of expertise, and as such, we now move onto the calculation of the actual power curves.

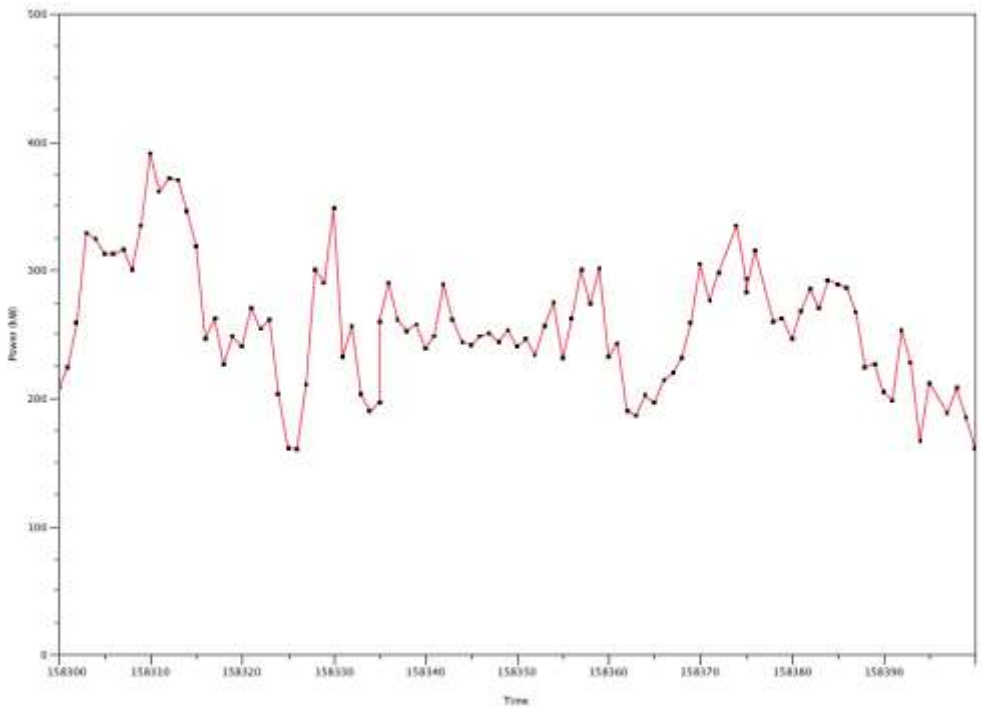

Figure 38: The power output of the turbine, at one-second intervals, over a 100 second period.

Power Curves

Before we begin here, it is important to tackle a simple question: what device should we use as the reference point for wind speed? We start with the philosophy of the IEC standard which uses met towers to measure the undisturbed wind in front of the turbine. Based upon this philosophy, the OCS, which measures air in front of the turbine, is the correct choice.

On the one hand, the industry has experience with the sonic anemometers measuring the disturbed air after the turbine propellers. However, the sonic anemometer measurement is strongly related to power output (i.e., is not an independent variable), leading to all sorts of non-linear effects. The anemometer understates actual wind speed, thereby exaggerating the efficiency of the turbine. The data of this report clearly demonstrates the deficiencies of using a measurement device in the middle of the rotor turbulence as the benchmark for power curve computation.

Thus, to align with IEC standards, the correct benchmark measurement is that of the free- flowing wind in front of the turbine nacelle. In cases where met towers are available, we believe that a met tower is a convenient, non-controversial choice. However, given the excellent correlation that the OCS shown to have with met towers, we chose the OCS wind speed measurement as the power curve benchmark.

We start by showing the power curve of the turbine operating in legacy mode. The curve is fitted to a generalized logistics (Richards' curve) function. The generalized logistic curve or function, also known as

Richards' curve is a widely-used and flexible sigmoid function for growth modeling. Other curves could have been used, but the function matches the general shape of the power curve well and is well known in the statistical world.

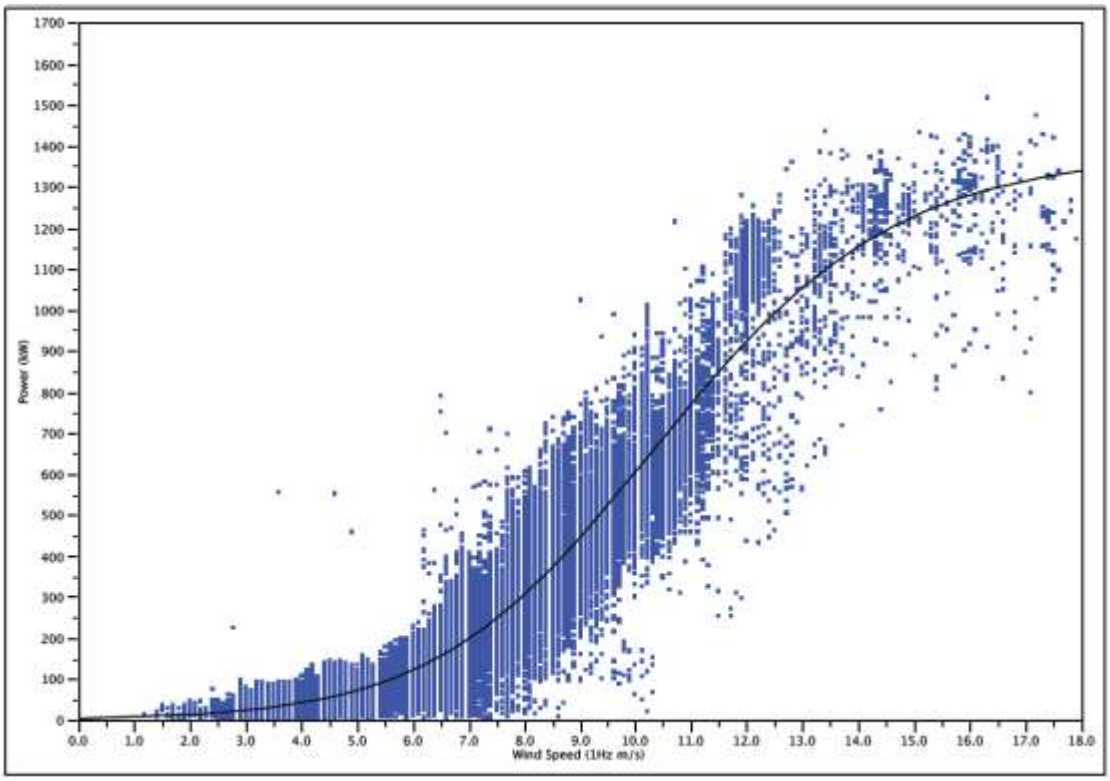

Figure 39: A scatter plot of power output vs. wind speed.

(The turbine is under legacy sonic anemometer control mode, with the free wind speed in front of the turbine, on the horizontal axis, as measured by the OCS. The data is fitted to a Richards' function.)

Next, we show the performance of the same turbine under OCS control. Please note that the OCS has three modes, and the data captures all three OCS modes. These three modes are proprietary to CTW, and the specifics of the differences between these modes of operation will not be discussed within this document.

There is a cut-off of wind data at about 3 m/s in the OCS modes. The system is effectively only recording data in a power-on status, after cut-in.

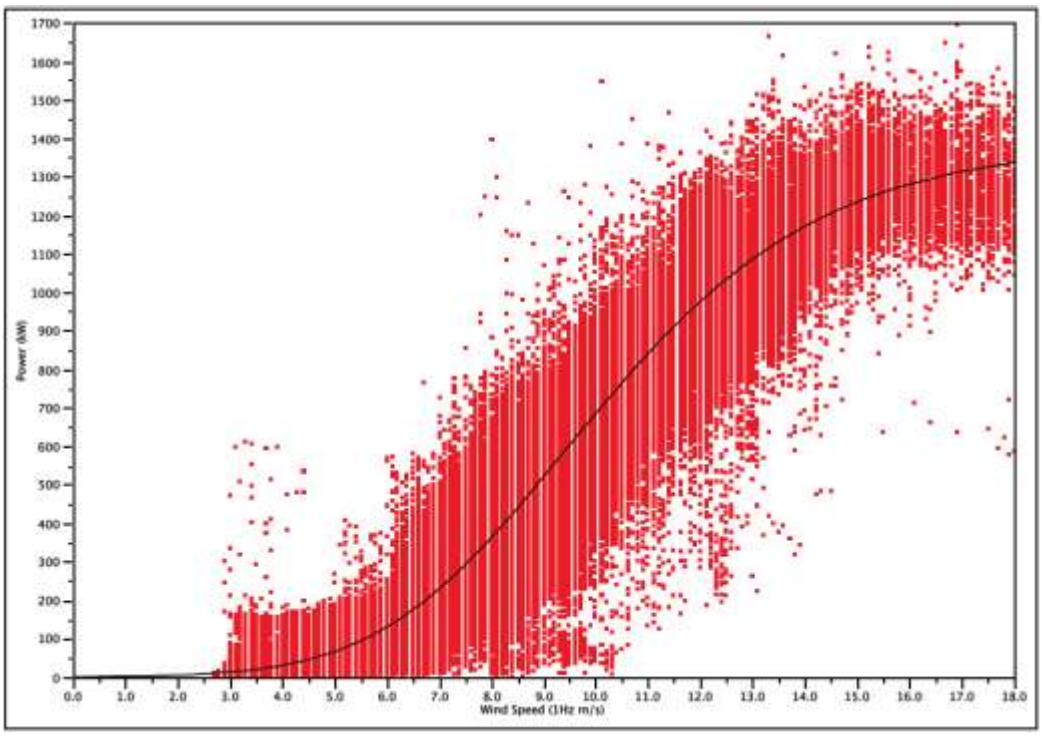

Figure 40: A scatter plot of output power vs. wind speed.

(The free wind speed in front of the turbine, on the horizontal axis, as measured by the OCS. The data is for the turbine under one of three OCS control modes. The data is fitted to a Richards' function.)

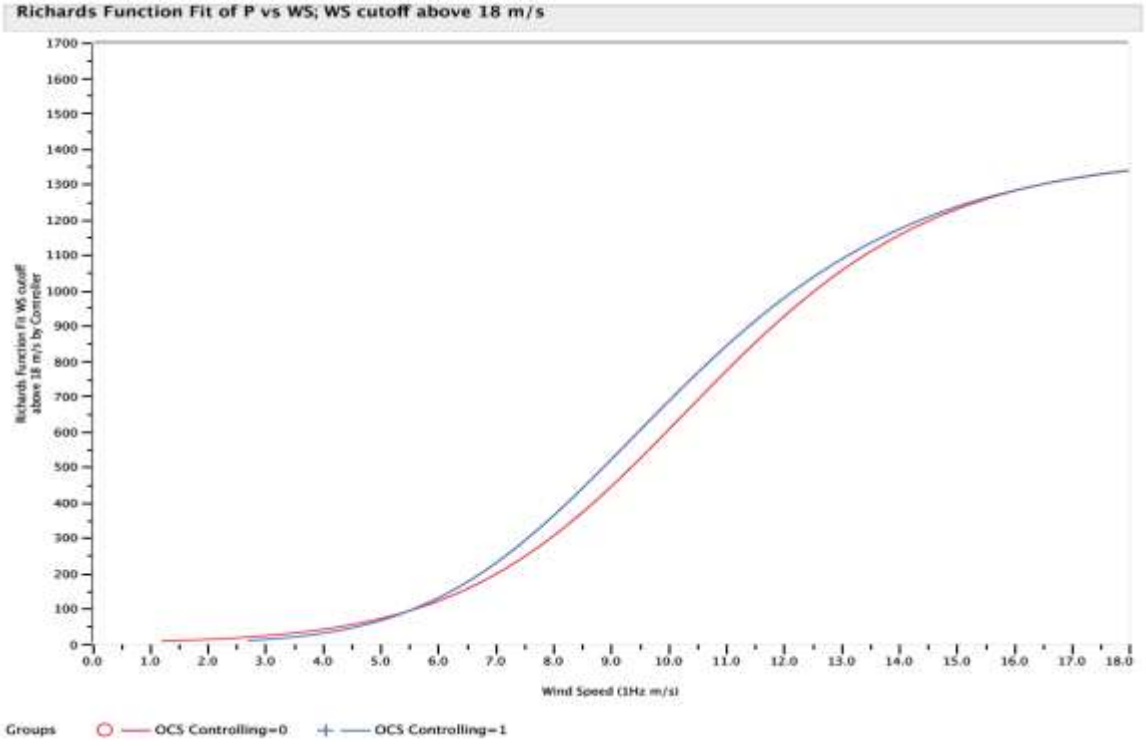

Figure 41: The fitted functions for legacy (red curve) and OCS (all three control modes) (blue curve).

(The OCS generates substantial increases in power throughout Region II.)

We then show the two fitted functions together: with the OCS controlling the turbine and with the sonic anemometer controlling the turbine. The OCS control generates extra power throughout Region II. However, the OCS control situation operated in three proprietary modes. These modes had substantially different performance. The following table lists the results of this experiment in terms of anticipated increases in energy production, and, for a turbine producing $0.5M of revenue a year, the actual increase in annual revenue.

		Control Method		
% AEP Improvement	Legacy	3	2	1
Uptime = 100%	0.00	0.50%	7.60%	15.00%
Uptime = 35%	0.00	0.18%	2.66%	5.25%
Assume Turbine Revenue = $500K/yr		Control Method		
Additional Turbine Revenue/Yr	Legacy	3	2	1
Uptime = 100%	0	$ 2.50	$ 38.00	$ 75.00
Uptime = 35%	0	$ 0.88	$ 13.30	$ 26.25

Figure 42: The tabulated results of the various control methods.

(The OCS increased energy production in all cases. The increases varied from less than a one percent increase, which is in the noise of the experiment, to a substantial 15% increase in energy production)

To illustrate the more dramatic power increases of Mode 1, the fitted curves for Legacy control and OCS Mode 1 control are shown in Figure 40.

Conclusions

The behavior of wind speed and angle measurements for a utility scale turbine, taken in front of the turbine by the OCS, and following the turbine blades by sonic anemometers and sonic wind vanes, respectively, are compared.

The measurements in the perturbed air are very noisy, and, even after averaging, are so heavily affected by the operation of the turbine that they present very substantial control theory problems when considered as inputs to a control algorithm for turbine yaw.

The free wind measurements may be used without secondary processing, such as averaging. By examining the output power of the turbine, we conclude that the alignment of the turbine under OCS control is significantly better than under legacy control.

The OCS operated in three modes. Averaged over all modes, the OCS improved the output power of the turbine by ~10% when it was operating. The highest performance enhancement occurred when the turbine was operated in OCS Mode 1, where a 15% improvement in energy production was shown against the wind distribution of the location when the OCS was operating.

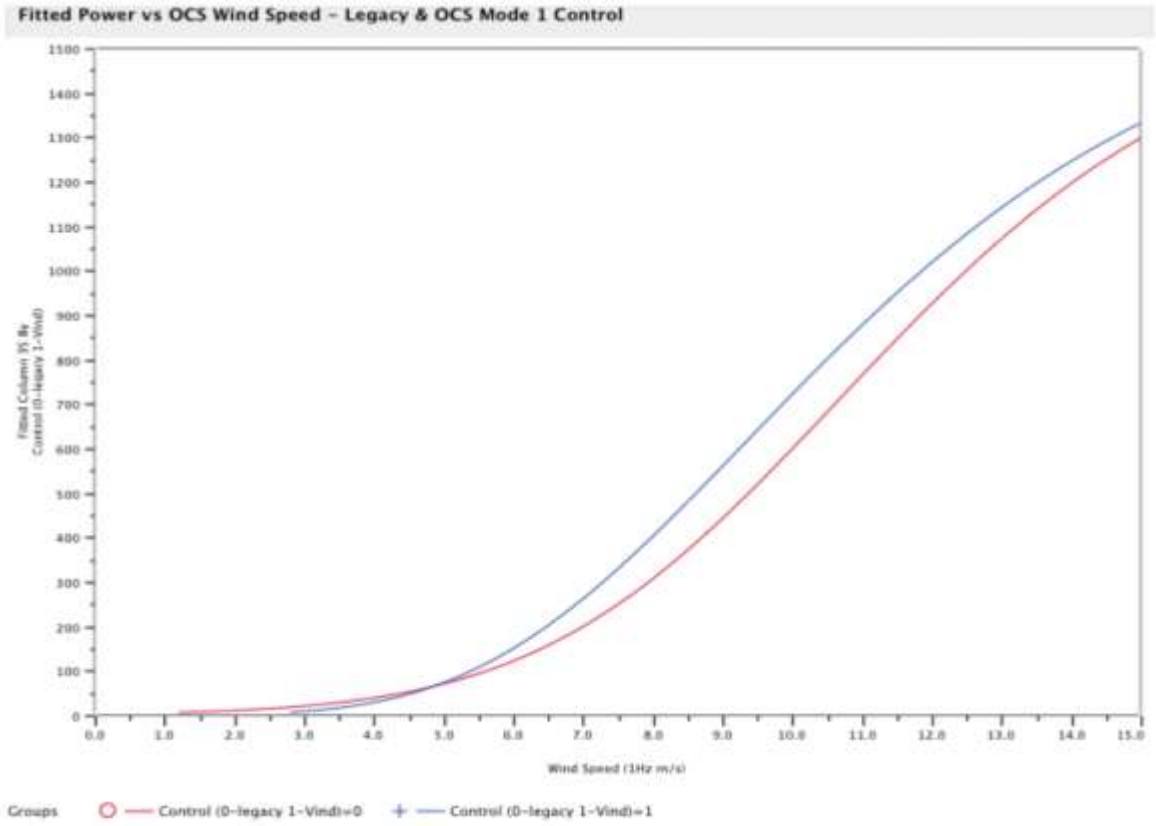

Figure 43: The fitted functions for legacy (red curve) and OCS Mode 1 (blue curve).

(This control mode generated a 15% increase in energy production using the measured wind distribution of this turbine location.)

The beta version OCS had substantial periods of time when it was not collecting good data, and by extension, was not controlling the turbine. This is being improved in the G2 version of the OCS. For the period of time studied here, the uptime of the beta OCS was 33%. In future G2 units, we anticipate that the uptime of the device will be close to 100%.

B2. Analysis of Traditional Yaw Measurements

Limitations of Post-Rotor Yaw Measurements

In a recent analysis we demonstrated two key points. We demonstrated that the wind speed measurement of the post-rotor anemometer had an error related to the wash produced by the rotating blades. As such, free wind measurements are much better to determine wind speed for calculating the output power curves of turbines than the wind speed measurements via nacelle-mounted anemometers.

In general, the industry does accept that the speed measurement of an anemometer located in the post-rotor flow is flawed, and that measurement of the wind in front of the turbine is superior.

The second was that by switching to yaw control based upon free wind characteristics real and substantial power increases can be achieved.

In general, the industry is dubious of the amount of extra power that can be generated by changing yaw control.

A reading of the literature suggests that yaw angle isn't nearly as exciting as pitch control. Perhaps that's because yaw is sort of like yawn? Maybe it's because the industry thinks the vanes behind the turbine are nicely calibrated and believes the simple COS^3 math and doesn't see how it could really matter all that much. Or perhaps the turbine manufacturers just don't like to talk about how silly it is to point a multi-million dollar turbine based upon measuring the wind direction right after a gigantic spinning propeller?

However, when yaw is not set properly, power is lost, but more importantly, stresses are placed onto turbines. Because of the potential magnitude of the economics of these issues, we believe spending some time asking fundamental questions about yaw, and then using actual data from field turbines to try to answer these questions, might be of some benefit to the operators of wind turbines trying to maximize their economic viability.

In this section, we look in greater detail at the yaw angle of the turbine relative to the wind.

Key questions

- Based upon data from the nacelle-mounted measurement system, what are the characteristics of the current yaw measurement system?
- Does the rotating vortex post-rotor have an effect on measurement of yaw angle?
- Can rotor-induced errors in yaw measurements be corrected so that a good control system can be designed?

Our world needs us, the wind turbine industry, to produce power, cleanly, efficiently and at low cost. Here at BlueScout, our contribution to the wind industry is to use our understanding of optics to provide a fundamentally deeper understanding of the wind resource – to produce substantial, repeatable increases in the output power of wind turbines.

An Optical Control System (OCS), Generation I, is mounted upon an operating utility scale wind turbine. The yaw angle of the turbine is studied in a variety of different ways to better understand the physics of basing control decisions upon measurements of the post-rotor flow.

The data set is large, approximately 500 MB, composed of 335,000 data points taken at 1 second spacing. SAS JMP used as the statistical analytic tool. The dataset includes output from the OCS, two sonic anemometers (giving both wind speed and wind direction), turbine state, ambient temperature, output power, and absolute yaw position.

A wind turbine produces the most power when it is pointed directly in the wind. As the turbine moves away from facing the wind, two things happen- it produces less power and endures more mechanical stress.

Let's begin by looking at the distribution of output power against the measured wind angle. We start with the data from the OCS.

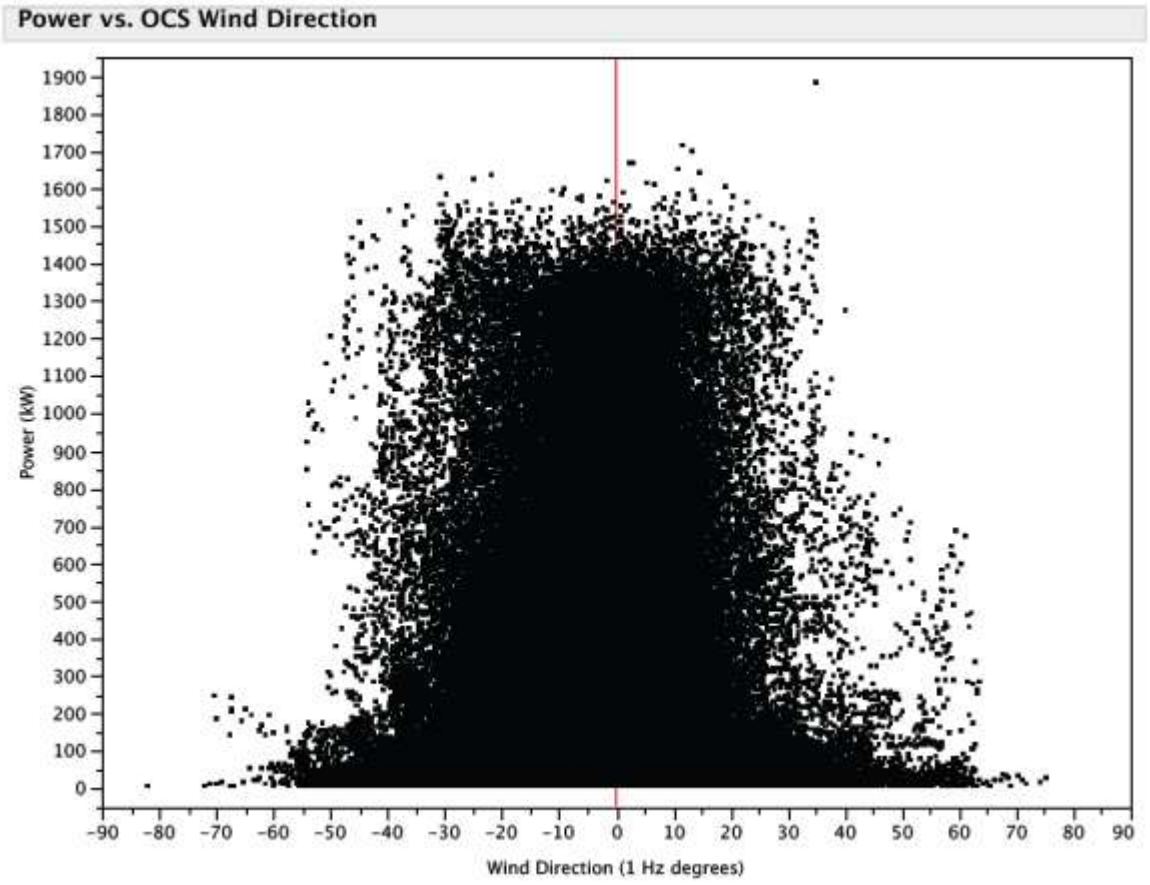

Figure 44: A scatter plot of the output power of the turbine vs. wind angle as measured by the OCS.

In general, the data of Figure 44 fits our intuition. The measured output power is roughly capped at 1.5 MW. The power of the turbine falls off as the angle of the wind relative to the turbine (yaw error) increases. The data is symmetric, and roughly centered at zero.

Now the same data set is used to do a scatter plot with the angle being measured by one of the sonic anemometers. Again, the power peaks at about 1.5 MW. Again, the power falls off as the post-rotor angle increases. The scatter plot is narrower than what is measured in the free stream. The data set is not symmetric, with the center of power distribution now being ~10-15 degrees. Further, the amount of angular offset changes with turbine power. Finally, the measurement of post-rotor angle shows very sparse data for angles less than -30 degrees.

This section focuses upon understanding this behavior in greater detail.

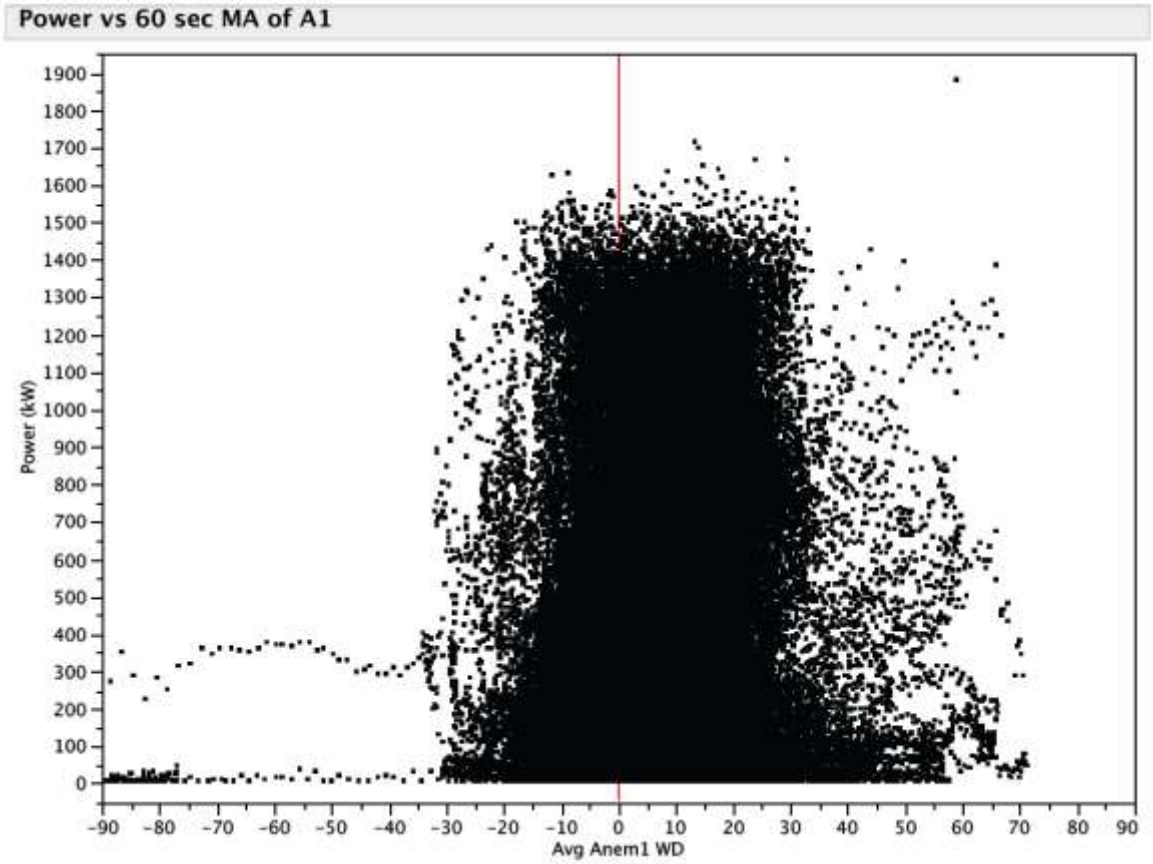

Figure 45: A scatter plot of power vs. post-rotor wind angle measured by the anemometer.

(The data is not symmetric, with the center of the distribution being offset by ~10 degrees.)

Post-Rotor Yaw Measurements

Let's start with basics. The turbine is going to produce the most power when it faces the wind. The fundamental task of yaw control is to aim the turbine into the wind. We look first at the distribution of wind angles, as judged by post-rotor wind as measured by the sonic anemometer, while the legacy yaw control is operating the turbine. In this work, we do not look to the OCS to judge the legacy control system, rather we look closely at the post-rotor measurements and use very simple physical arguments to understand the efficacy of trying to figure out a yaw angle while sitting in the vortex of the rotor.

It should be noted that when we do compare the OCS to the legacy measurement system, that comparison compares two different attributes. The first is the type of measurement device. While the physics of wind measurement with LIDAR are a bit different than measurements based upon a physical wind vane or an acoustic anemometer, we believe that each of these devices can be calibrated and do a fine job of measuring wind characteristics. The second, and we believe much more significant, is the physical position of the wind that is being measured. The sonic anemometer (or wind vane) is behind the rotor. As such, it is situated in place with a constant rotational bias. This effect, where the direction of the airflow is partially due to the wind and partially due to the rotating blades is one of the items that we wish to investigate in this paper.

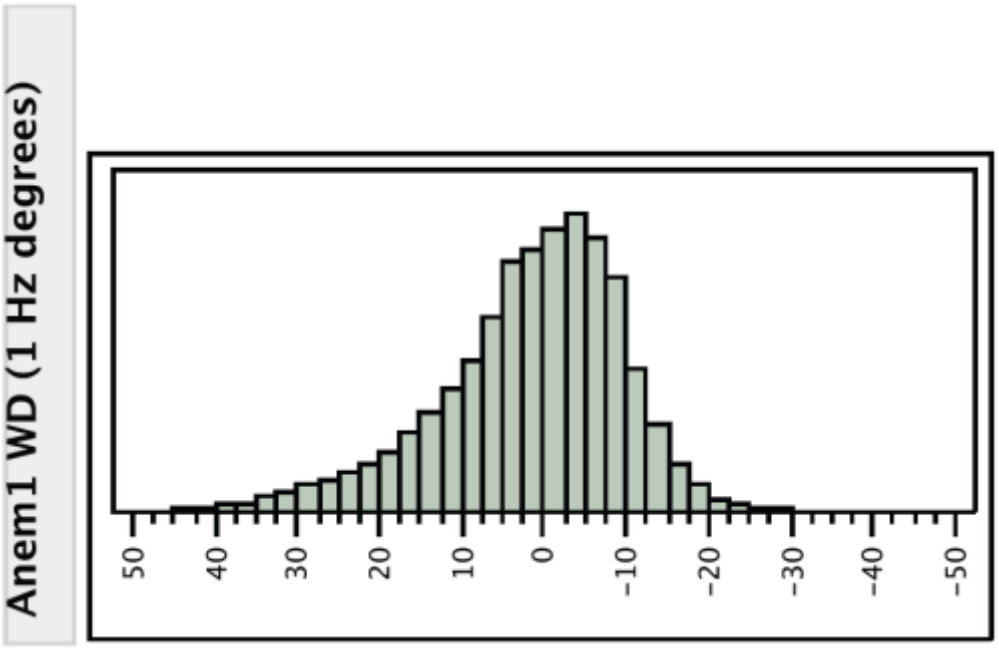

Figure 46: The measured distribution of wind angles, as measured in the post-rotor wind flow.

(The bottom is degrees. The distribution has mean and median of 1.55 and 0 degrees, respectively. The standard deviation is 11.3 degrees.)

Figure 46 shows the distribution of yaw angles, as measured by the acoustic anemometer. In looking at this distribution, we note that the mean and median are very well centered, at 1.55 degrees and 0 degrees, respectively. The standard deviation is 11.3 degrees. The distribution is not symmetric, as one would expect for a device in the rotor wash of the turbine. This implies that the measurement system is non-linear with respect to wind angle.

Figure 47 shows the same distribution, under legacy control, but now measured by the OCS on the free wind in front of the turbine. This distribution is roughly symmetric, but is now centered about 8 degrees off of the zero axis of the OCS.

Key Points

- The legacy control does a good job of centering the yaw angle as judged by post-rotor wind measured by the sonic anemometer. The yaw angle is measured to be asymmetric, with standard deviation of ~11.3 degrees.
- Under legacy control, the OCS measures a free-wind angle distribution that is about as broad as distribution measured by the sonic anemometer, but centered at -7.8 degrees. This distribution is symmetric.

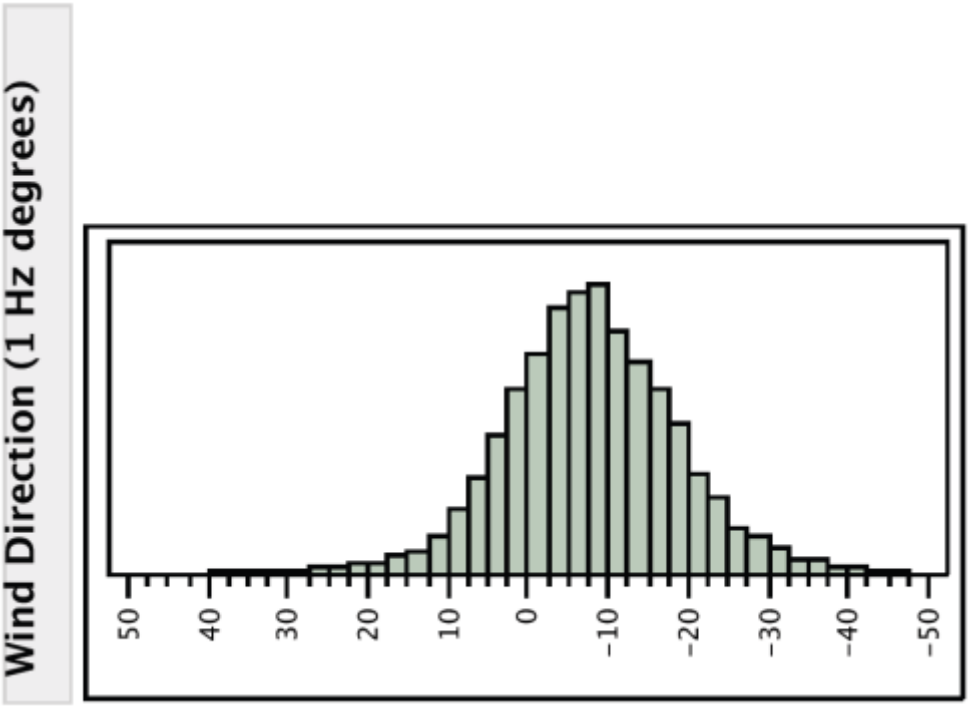

Figure 47: The distribution of yaw angles with respect to the free wind, as measured by the OCS.

(The turbine is under legacy control. The distribution is roughly symmetric. The mean of the distribution is -7.8 degrees, with a standard deviation of 11.8 degrees.)

Now we consider the distributions when the turbine sets yaw based on the free wind angle in front of the turbine as measured by the OCS. We again start with the yaw-angle measured post-rotor by the sonic anemometer.

As the anemometer is measuring wind in the rotating rotor wash, the measurement shows asymmetry. The distribution is shifted away from zero and is substantially broadened. Given that the distribution of yaw angle, as measured by the post rotor flow, is worsened under OCS control, the turbine should produce less power under OCS control if the post rotor yaw measurement is correct. The yaw angle distributions, using the free wind in front of the turbine as measured by the OCS, is shown below. The distribution is still symmetric, but is now much better centered, with a distribution that is substantially narrower than when the turbine is under legacy control. Given that the distribution of yaw angle, as measured by the free wind flow, is improved under OCS control, the turbine should produce more power under OCS control if the OCS measurements are correct.

The curious reader says, “whoa! Those paragraphs can’t both be right!” While we don’t wish this paper to deal with power production under different control regimes, the fact that the yaw angle distributions are very different when controlled differently does imply that the power that will be extracted from the wind, and the mechanical wear and tear upon the turbine, will be different in the different control regimes (i.e., under OCS control or legacy control). *Spoken bluntly, yaw control does matter*.

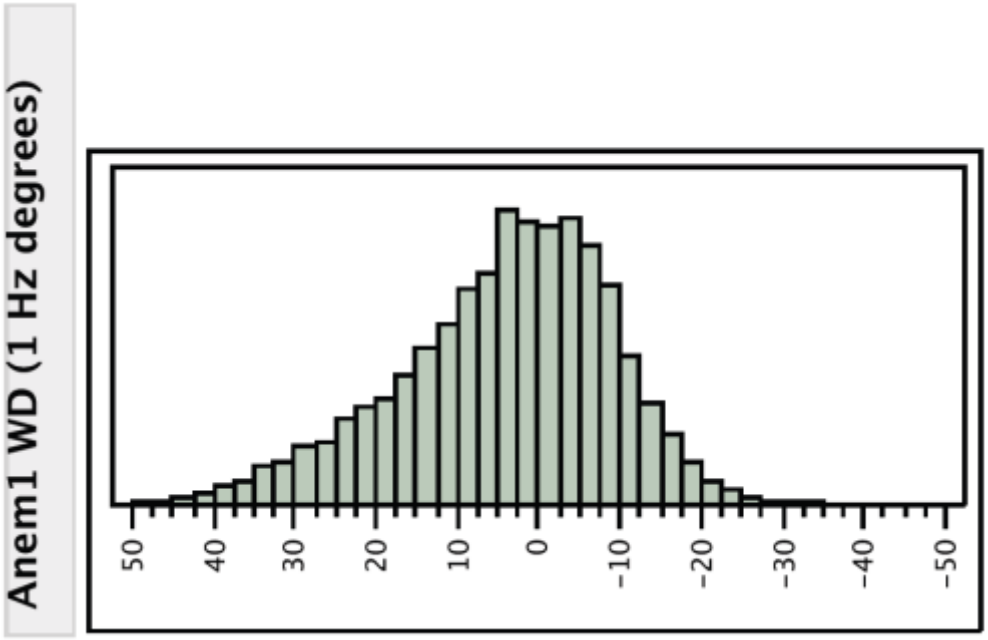

Figure 48: The distribution of yaw angles, measured in the post-rotor flow by the sonic anemometer.

(The distribution is still asymmetry, as before, but the mean of the distribution has been shifted to 4.2 degrees. Under OCS control the distribution measured by the anemometer significantly broadens, with standard deviation increasing to 13.6 degrees.)

Key points

- Under OCS control, the distribution of yaw angle, as measured by the OCS, is center at ~0 degrees and is made substantially narrower.
- Under OCS control, the distribution of yaw angle, as measured post-rotor, is moved away from being centered at zero, and is substantially broadened.
- The yaw distributions, as measured by either the OCS or the legacy post- rotor anemometer, change substantially between the two control schemes. Because yaw angle directly impacts the performance of the wind turbine the performance of the turbine will be different under OCS control than legacy control.

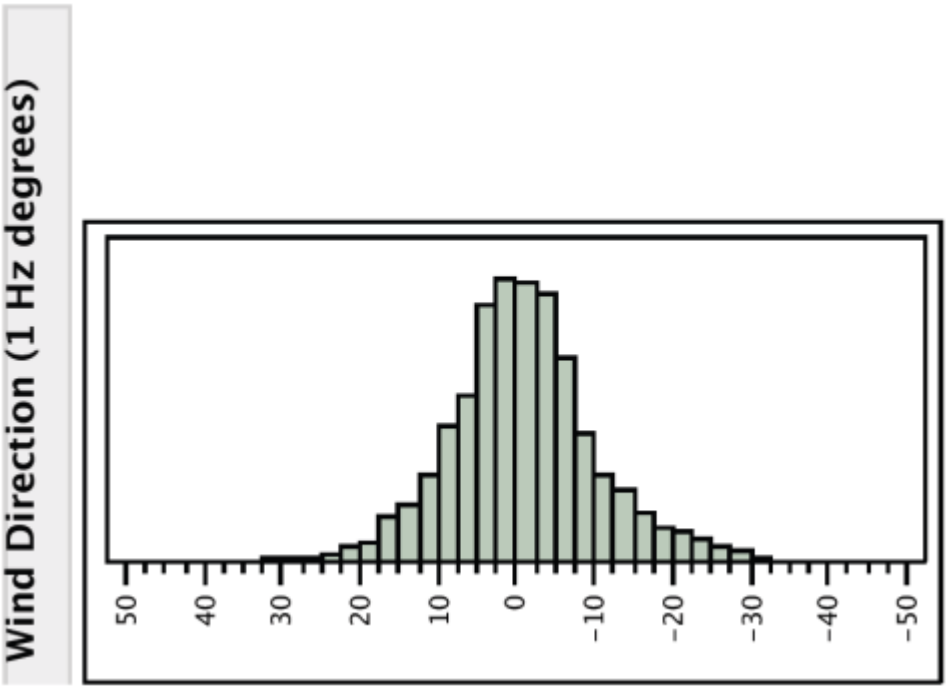

Figure 49: The distribution of yaw angles, based upon the free wind in front of the turbine as measured by the OCS.

(The distribution is shifted, with the mean now at -0.9 degrees. The distribution of yaw angle is substantially narrower, with standard deviation now down to 9.7 degrees.)

Practical Yaw Optimization Using Post-Rotor Yaw Measurements

It is tempting to look at the data just presented and think that a neat controls protocol could fix up the problems associated with a control algorithm based upon post-rotor wind measurements.

To investigate this, we begin by grouping the data into angular buckets, -25 to -15, -15 to -5, -5 to 5, 5 to 15, 15 to 25, and 25 to 35 degrees. Next, we compute power curves for each angular group. For clarity, this is shown by coloring the data points by which angular bucket they fall into as shown below.

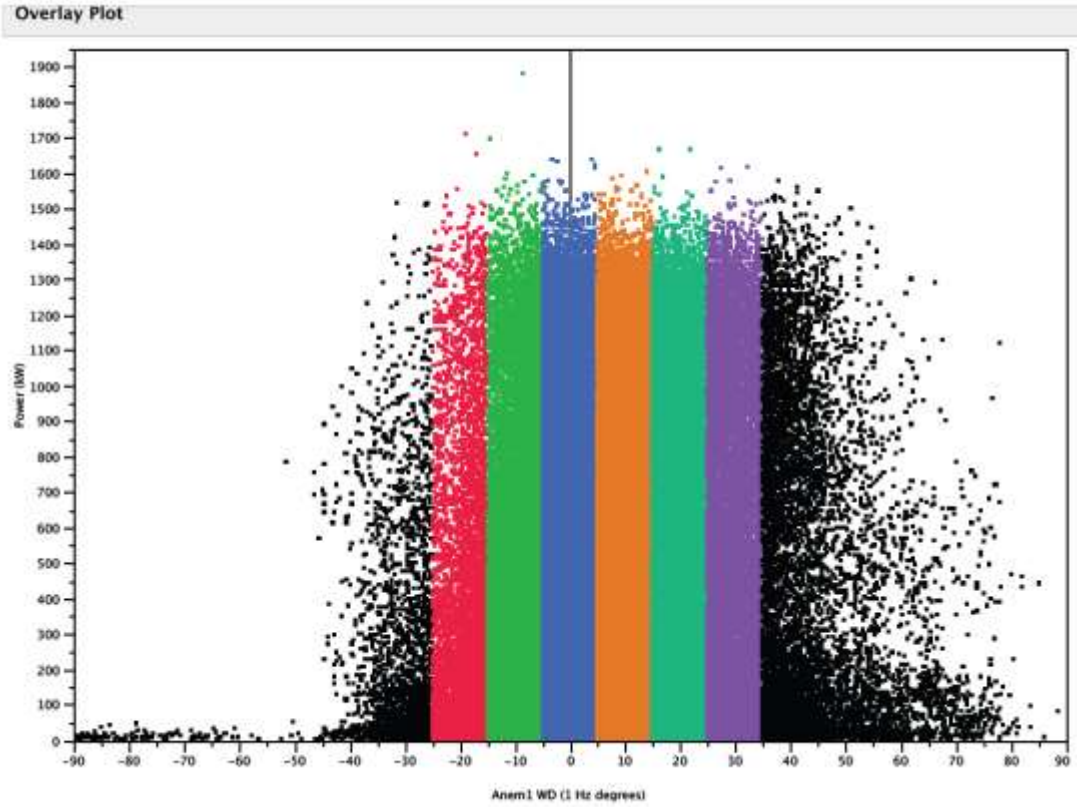

Figure 50: The scatterplot of wind angle as measured by the post-rotor anemometer.

(The color-coding of the data points indicates the angle bins.)

We next cut power curves for each of the angle buckets. As expected, the efficiency of the turbine changes with angle. However, the angle where maximum power occurs changes with output power as shown in the following figure. Given that the turbine always produces maximum power with a zero yaw angle, we conclude that the anemometer has an angular error that is dependent upon wind speed, and that a simple offset is not capable of fixing the post-rotor yaw angle error.

For this turbine, the optimum angle for power extraction, as measured by the sonic anemometer, varies with power. Obviously, the true “optimal” angle, with respect to the free wind in front of the turbine, is zero degrees, implying that a wind measurement device in the post-rotor turbulence has a rotor-induced error, at a true angle of zero degrees to the turbine, which is dependent upon the operational state of the turbine. This angular error has variance of approximately 40 degrees over the operation of this turbine.

Thus, the measurement of yaw angle is non-linear with respect to both yaw angle and wind speed.

For this turbine, the post-rotor error crosses zero at ~10 m/s wind speed. In heavy wind, the legacy turbine control will be misaligned to the wind by ~20 degrees.

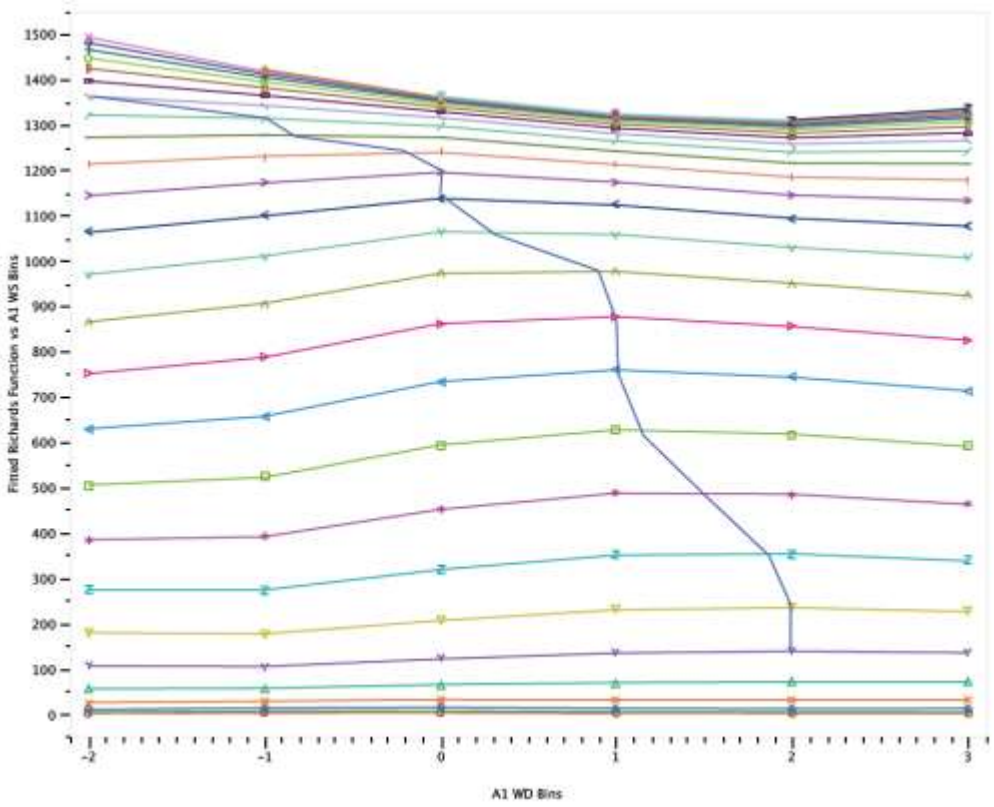

Figure 51: A contour plot showing curves of constant wind speed.

(The blue line indicates the angle of maximum power production. Each integer unit on the X-axis corresponds to 10 degrees, indicating that the angle of maximum power varies substantially.)

Key Points

- The rotation of the blades induces an error into the measurement of yaw angle. This error changes as the wind speed increases. The turbine has no way of sensing this error.
- There is no magic offset angle for the anemometer. A control algorithm that uses a constant offset angle to optimize power based upon post-rotor wind measurements will sub-optimize the power production.
- In moderate to heavy wind, the turbine is misaligned to the wind by ~20 degrees, resulting in increased operational stresses.
- These conclusions are based simply upon the legacy post-rotor sonic anemometer and upon the idea that turbine power is maximized at zero yaw angle.

B3. Yaw Control Optimization

Overview

It is widely believed in the wind industry that improvements in yaw control can only produce a small improvement in output power. This belief simultaneously exists with an acknowledgement that attempting measure wind characteristics in the turbulent post-rotor wind is problematic.

It has been shown, on a variety of turbines, that power increases can be achieved when improved wind angle information is fed into the yaw control systems of turbines. However, this early work typically uses the legacy control strategy of the turbine. In truth, turbine manufacturers have invested considerable time and thought into developing yaw control strategies that compensate for the errors of the post-rotor measurement system. However, those strategies typically include long averaging times and allow considerable variance in yaw before correcting the yaw angle of the turbine.

Accurately measuring the incoming wind properties, with dramatically reduced noise, means that different control strategies can be considered for yaw control. Put most simply, beyond the gains achieved by simply feeding better information into the legacy control system, how much extra power can really be generated by employing control strategies that take advantage of the improvement in wind information?

This work takes real data from an operating turbine under the yaw control of the Optical Control System (OCS). The summary describes the methodology used in the simulation and the results of the parametric study for the two control parameters of wind direction moving average time and yaw direction threshold. Power performance increases and turbine yaw actuation times are presented. For unlimited yaw activity, a power increase of about 6% is demonstrated. If yaw activity is limited to 8%, it was found that an additional 3% power gain may be achieved with settings for the site/turbine installation evaluated in the study at a moving average time for the wind direction of 60 seconds and a yaw direction threshold of 8 degrees.

Methodology

A simulation was developed in order to estimate optimal control parameters for the OCS. The simulation and model were developed in MATLAB and Simulink, the model being presented in Figure 52. The design of this controller model was based on existing turbine yaw algorithms: the system utilizes a moving average of the wind direction as measured by the nacelle anemometry and begins yawing when the moving average exceeds a specific threshold. The turbine continues to yaw until the moving average of the direction error is zero degrees. Both the moving average time and the direction error threshold are parameters in the simulation.

The input to the simulation is the sum of the OCS measured wind direction on an operational wind turbine (wind direction relative to the nacelle) and the turbine nacelle position. This sum is a measure of the wind direction relative to north, and represents the wind field to which the turbine is exposed in time. The data utilized to run these simulations is real data from an installation of an OCS on an

operational turbine. The data set includes OCS variables, such as wind speed and direction, as well as the nacelle orientation and power production.

The simulation models how this actual turbine will react to this changing wind field based on the turbine's yaw rate, and the two parameters of moving average time and yaw error threshold. The output of the simulation is the yaw actuation of the turbine and an estimate of the local wind direction error to which the rotor is exposed. The yaw actuation data allows for calculation of number of yaw events and time yawing. The wind field measurements from the OCS upwind of the turbine are propagated to the turbine assuming a constant convection velocity equal to the mean velocity of the sample data being processed. Utilizing the wind from north data and the current simulated nacelle position, and assuming the time to convect to the rotor from the OCS measurement locations, a local rotor wind direction error can be calculated. This data allows for statistics of the instantaneous yaw error and estimates of power production to be determined. Power production is modeled as the cos3 of the local rotor wind direction error. This relationship comes from the argument that the effective wind speed for power production is the cube of the normal component of the wind to the rotor. The relative power production is proportional to cos3 of the wind direction error, so the cos3 of the convected wind direction error is the metric for performance increase in this study.

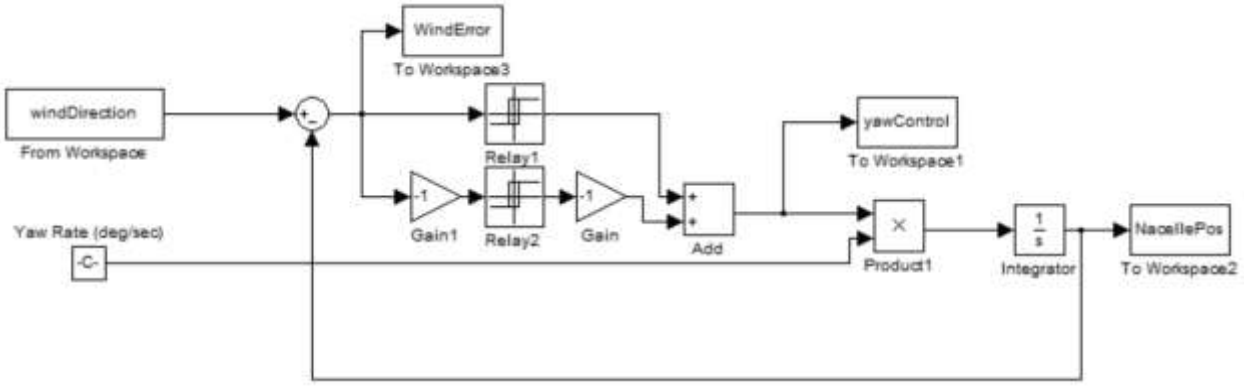

Figure 52: Simulink model of the yaw control system.

Results

A parametric study was conducted using the simulation for a variety of moving average times and yaw threshold values. The simulation assumes that the power produced by the turbine is proportional to the cos3 of the wind direction error at the rotor, so this value is used as the metric for power performance improvement. Results of this study can be seen in Figure 53 and Figure 54. Figure 53 demonstrates how the cos3 of the yaw error varies with the two-parameter settings. Figure 54 demonstrates how the fraction of time yawing changes with the two-parameter settings. In looking at these curves, as the moving average time is decreased and the yaw dead-band is tightened, both the relative power captured and the amount of time yawing increase. This is as expected: the turbine is more accurately tracking the wind, especially smaller turbulent scales, such that the local rotor wind direction error is reduced, but at the cost of much more yaw actuation. Figure 53 also demonstrates that there is an upper limit to this benefit in power capture given the upwind nature of the measurements. Once the

moving average time becomes small enough, the phase lag this introduces is smaller than the convection time from the OCS measurement volume, such that the controller is introducing an error by yawing too soon. This is more evidence that these studies should be more rigorous in being done at specific speed regimes, and that the parameter settings will probably be optimized with a scheduling routine to account for this phase issue.

Given these results, a recommend set of parameters where there is moderate power performance gain, while limiting the increase in yaw actuation, would put the moving average time around 60 seconds, and the yaw direction threshold at 8 degrees. This would be an increase in power performance of roughly 3% while changing the time yawing from about 5% of time yawing to roughly 8%. Again, performing this study while focusing on differing wind regimes would be beneficial, as a representative power curve showing the relative increase with scheduled parameters could also be developed.

Note that this is optimization of the OCS. The OCS has greatly improved performance over legacy control systems with existing nacelle anemometry at any of the parameter settings in the range demonstrated in this study.

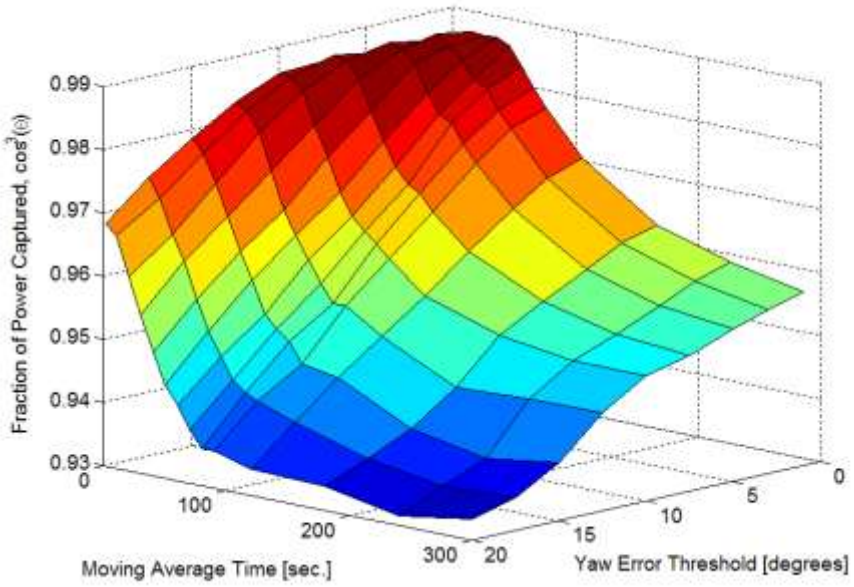

Figure 53: Surface plot of the representative power improvement based on the model of cos3 of wind direction error at the rotor versus the two parameters: yaw threshold and moving average time.

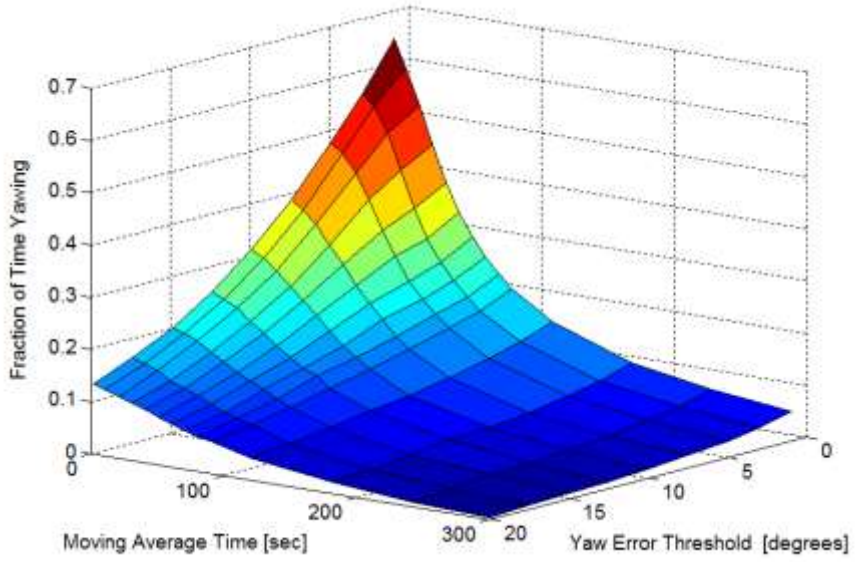

Figure 54: Surface plot of the fraction of time yawing versus the two parameters: yaw threshold and moving average time.

Discussion and Further Work

The results presented here are mean results over all wind speeds. The model for power performance of the cos3 of the wind direction error is only applicable below rated power. The performance increase may vary depending on wind speed. The simulation could be run taking speed regimes in to account, which may lead to scheduling of parameters for different wind speeds.

This simulation is run using local wind data and turbine characteristics. Parameters may vary by time of year (seasonal weather patterns), or by nominal wind direction (local properties – terrain, etc. – which may affect turbulence), as well as for turbine model (unique yaw rates). A schedule of parameters could be developed if optimal parameters were found to vary for these changing conditions (such as scheduling by wind sector). Historical MET data from the original site assessment could be utilized to do this work, but this would ignore the local affects the turbine has on the inflow wind. The data used for this study had the benefit of an OCS installed on an operational wind turbine, so blockage/induced flow effects are present in the real inflow measured data.

This simulation is based on a simple turbine control algorithm. More advanced algorithms could be developed and implemented. The same processes as described in this study could be utilized, where the Simulink model has more capability. More complexity could also be added for scheduling yaw rates (variable yaw rate machines), as well as scheduling the given parameter settings. The overall algorithm could also be modified, where the simple on/off relay model is replaced. Manufacturers could also modify the physical yaw actuation systems to allow for different control strategies, such that the controller is not limited by the amount of time yawing. This research is currently ongoing in order to best utilize the novel optical control system. Implementation of such algorithms is relatively simple, as these are simply software changes in existing control hardware implementations.

B4. Turbine Controller Integration

Turbine Model: GE 1.5 SLE

The Optical Control System (OCS) is designed to improve turbine performance by enhancing alignment of the turbine with approaching wind while maintaining or enhancing the overall safety and reliability of the turbine. The OCS utilizes state of the art laser sensors to detect the approaching wind before it reaches the rotor, and commands yaw actuations of the nacelle in order to reduce yaw error. More timely and accurate alignment with the wind leads to improved power capture. This document describes the integration concept of the OCS, with emphasis on mechanisms that maintain safe control of the turbine.

The OCS is designed to take over the yaw actuation of the turbine utilizing the LIDAR for accurate and look-ahead wind data. In this control configuration the OCS utilizes a Bachmann Programmable Logic Controller (PLC) as the basis of the design. This system has a processor module, Ethernet ports, and digital I/O modules that allow it to easily interface with the legacy GE central controller, the laser sensor unit, and the digital hardware of the turbine.

There are two primary modes of operation of the system: automatic control and bypass mode. In automatic control, the OCS utilizes the laser wind sensor to align the nacelle with the approaching wind. In this mode, the system outputs signals to the legacy controller that mimic a mean zero wind direction error – this results in the turbine operating as normal, but without the legacy system providing any yaw actuation commands to the yaw brakes or motors. The OCS then sends its own yaw commands to the yaw brakes and yaw motors to track the wind. In bypass mode, all of the digital signals are passed directly through the system, such that the OCS acts like it is not present. In bypass, the legacy controls all yaw activity.

Communication

Ethernet: TCP & SMI

The PLC communicates to the laser sensor via Modbus-TCP over a local Ethernet network. The messages the OCS monitors include wind speed, direction, status of the laser system, and validity of the measurements at the various range gates.

The OCS for GE 1.5 SLE integrations makes use of Bachmann PLC components. Bachmann PLC systems are designed for industrial control systems, and the BlueScout solution mirrors the GE 1.5 controller strategy. Utilization of a Bachmann PLC allows for the BlueScout controller to directly communicate with the GE PLC utilizing the Standard Module Interface (SMI) libraries supplied by Bachmann. The BlueScout PLC can directly read internal variables from the turbine so that it has knowledge of the operating conditions of the turbine.

The OCS has a Modbus server running for data capture. Internal values of the OCS are recorded along with performance data such as wind speed, direction, and power.

Digital I/O

The OCS makes use of digital Input and Output lines in order to intercept or monitor the following signals from the turbine controller and turbine hardware:

- Yaw brakes
- Yaw motors
- Wind Vane
- Yaw teeth counters

The yaw teeth counters are only read in by the OCS, but are still physically connected to the turbine controller. The OCS sends these teeth counts to the legacy controller – this ensures the legacy controller always has accurate knowledge of the absolute nacelle position.

The digital signals are connected to the OCS via a set of controlled relays. The normal states of the relays pass the original signals to and from the legacy controller and the turbine hardware. Only when in automatic mode are the relays engaged in order to intercept signals and feed OCS derived values to the legacy controller and turbine hardware. This also ensures that any issues with the OCS PLC (or the powering off of the PLC) result in the turbine returning to legacy control so that OCS does not adversely affect turbine performance or safety.

State Machine

There are four states for the OCS controller: Initialize, Auto, Bypass, and Fault (see Figure 55 and Table 5 for state transitions). The Initialize state acts as a default initialization state and dictates transitions at startup of the OCS, or when the system returns from the Fault state. The Auto state is when the OCS is directly controlling the yaw of the turbine. The Bypass state acts as if the OCS is not present. The Fault state is when there is any fault detected with the BlueScout OCS (not with the turbine controller; a fault of the legacy controller will result in the system switching to Bypass mode). In the three states of Initialize, Bypass, and Fault, the relays for the interception of digital I/O signals are in the default state, and the turbine is wired as if the OCS is not present. The faults that are monitored by the OCS are:

- Untwisting Right
- Untwisting Left
- Yaw drive end position
- Timeout yaw count
- Wrong yaw drive direction
- Yaw end switch activated
- Yaw motors over temperature
- OCS Communications Fault
- SMI Fault
- Wind Direction Limit
- OCS Wind Measurement Status
- UPS alarm
- UPS battery mode

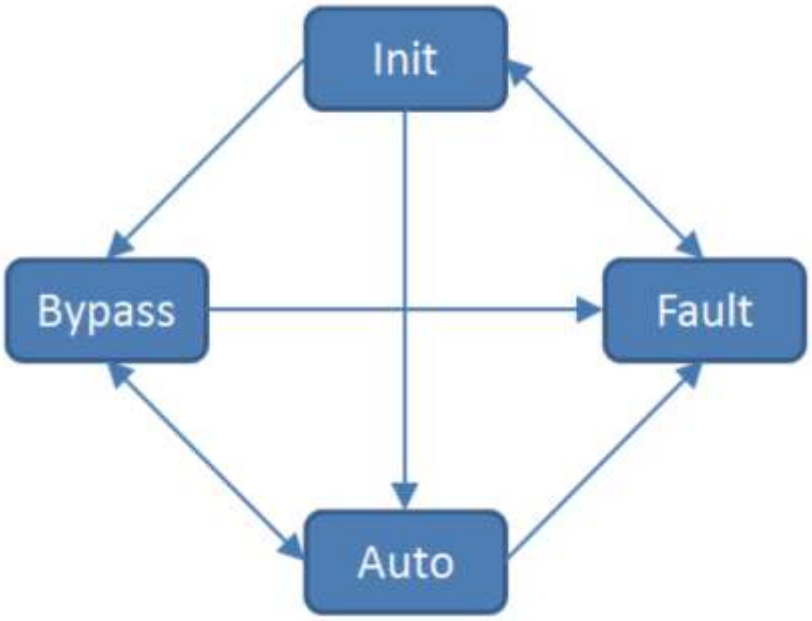

Figure 55: State diagram for the OCS, showing the direction of state transitions.

Table 5: State table for the OCS, demonstrating logic for state transitions.

State Transitions From -> To	Init	Bypass	Auto	Fault
Init		No Entry	No Entry	No Fault
Bypass	NOT bFault AND (Par_bBypass OR (Par_bSwitchBtwControllers AND bSwitchBtwCtrlsBypass)) OR NOT bLoadOperation		NOT bLoadOperation OR IN_bYawToTheLeft_CC OR IN_bYawToTheRight_CC OR IN_bYawBrakes12_CC OR IN_bYawBrakes34_CC OR bFlagAvoidRunaway OR Par_bBypass OR (Par_bSwitchBtwControllers AND bSwitchBtwCtrlsBypass)	No Entry
Auto	Ton_CentralCtrlYaws.Q bLoadOperation AND NOT Par_bBypass AND NOT bFault AND NOT(Par_bSwitchBtwControllers AND bSwitchBtwCtrlsBypass)	NOT bFlagAvoidRunaway AND NOT OUT_bYawToTheLeft AND NOT OUT_bYawToTheRight AND bLoadOperation AND NOT(Par_bSwitchBtwControllers AND bSwitchBtwCtrlsBypass) AND NOT Par_bBypass AND Ton_CentralCtrlYaws.Q		No Entry
Fault	Fault	Fault	Fault	

States Summary

Initialize: The system enters this state upon start up. If the turbine is in load operation (status = 2 and turbine is generating power) and the turbine has yawed to reset its current position since the PLC last went in to Auto mode, then the system will transition to Auto mode. If the bypass parameter is enabled, then the Auto state will be overridden, and the system will stay in Bypass mode. If the switching parameter is enabled and the timer is currently in Bypass mode, the system will not transition to Auto,

but will transition to Bypass. If any faults are detected internally to the OCS, the system transitions to the Fault state. The digital I/O relays are disengaged and the turbine is functioning as normal.

- **Auto**: The system will utilize the laser wind sensor to track the wind and will command the yaw brakes and motors. Zero error vane signals are sent to the legacy controller to prevent the turbine from yawing. If the legacy controller does command a yaw, for any reason, the system will transition to bypass mode and pass through the yaw commands. If the turbine status changes away from a value of 2 or it is not producing power (indicating a potential issue with the turbine), the system will transition to Bypass mode. If the switching parameter is enabled, and the period for the Bypass mode is enabled, the system will transition to Bypass. If the OCS detects that it tries to yaw beyond the parameter 11.13 value, the Avoid Runaway flag will be triggered, and the system will transition to Bypass mode until the turbine resets its current yaw position.
- **Bypass**: The system will disengage the relays and the turbine will perform in its original configuration. If the OCS does not have the Bypass parameter set, the turbine is not currently yawing, the turbine is in load operation (no alarms), the turbine has yawed such that it has reset its current yaw position for the yaw runaway alarm (since the last time in the Auto state), and the system is not switching between controllers with the timer currently set for the Bypass sate, then the system will transition to the Auto state. If a fault is detected, the system will transition to the Fault state.
- **Fault**: This state lets the OCS know that an internal fault has been detected and records the fault in the system's Modbus data. In practice, this state acts like Bypass, in that the relays are disengaged and the turbine is essentially in its original configuration. The Fault state allows for safe handling of the OCS interface and insures the system is only able to control the yaw systems when safely in the Auto state. The system transitions to Initialize when the faults clear.

Summary

The OCS is designed to increase turbine performance while maintaining conservative safety requirements. When in OCS control, the system utilizes an advanced laser measurement device to drive the nacelle yaw motors to more accurately align the nacelle with the approaching wind direction.

The OCS control architecture is designed to only take control when both the turbine and the OCS are operating well and without any indication of issue. In all situations where either the turbine or the OCS exhibits any cautionary signals, turbine control is returned to the legacy system until these system issues are resolved and the OCS has worked through the Initialize state. This control strategy allows the turbine to maintain all of its current functionality regarding safety monitoring.

C. Phasor Measurement Units Installation

Phasor Measurement Units (PMUs) provide GPS time stamped voltage and current samples with one phasor sample per cycle (60 samples per sec). Accordingly, PMUs provide detailed load models for individual buildings and detailed power measurements for renewable and distributed sources. The 8KW field wind unit is connected to IIT's Stuart Building, which is located within the Loop 1 of the IIT microgrid. PMUs are installed in the Stuart Building to enable engineers to develop more accurate load models, which is one of the most significant sources of uncertainty in understanding, predicting and controlling power delivery network behavior. The load characterization application will develop both static and dynamic load models to facilitate reliable and secure operation of the Perfect Power system, which is especially valuable under islanding conditions.

Figure 56: Phasor Measurement Unit (PMU) Installed at IIT's Stuart Building

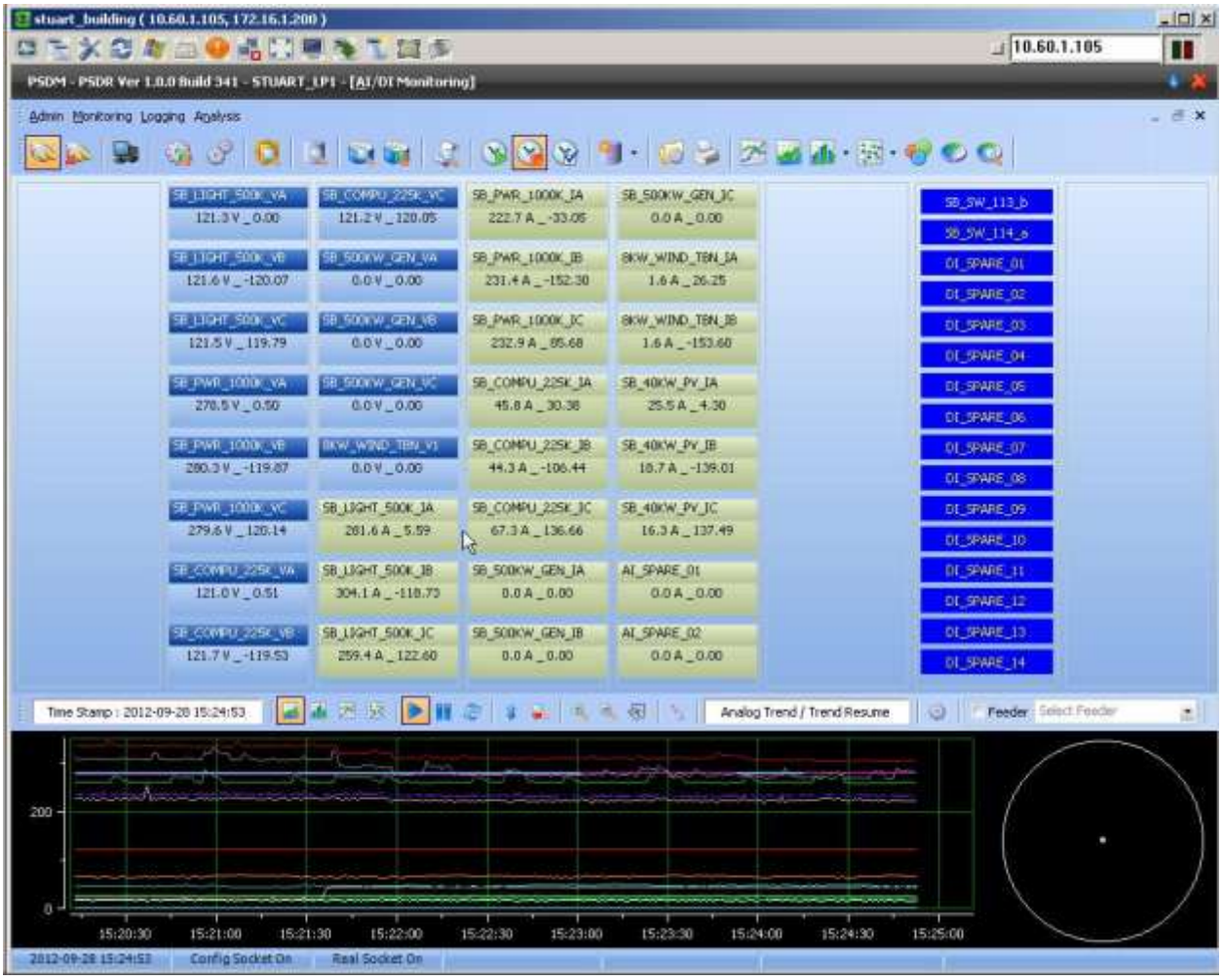

Figure 57: Stuart Building PMU data showing the building transformer loads, wind turbine, and PV system

D. Use High Magnetic Density Turbine Generator as Non-rare Earth Power Dense Alternative

Dakota Power, LLC (DP) is developing unique electric drive and power generation systems. This project provides for the application of DP technology to the generation of electricity from wind power. DP technology provides a non-rare earth power dense alternative for the operation of wind turbines. DP is integrating switched reluctance technologies with other sources of magnetic energy to produce high-performance electrical machines. The DP technology has the potential to provide a lightweight, low-cost wind turbine for residential and light industrial applications.

DP is developing next-generation light weight electric drive systems for military and civilian applications through a Cooperative Agreement with the Army Research Office (ARO). This project provides for the application of DP electrical machine technology to the generation of electricity from wind. This report

provides a comprehensive summary of the development of DP switched reluctance technology and the potential for its application to the generation of electricity from wind.

The process for the development of DP switched reluctance technology includes the transition of a concept for a machine through design and simulation using advanced FEA software. DP provides commercially developed Maxwell FEA simulation software to validate the potential performance of each proposed design. The optimal design, including the specific geometry, stator winding turns and current, is then fabricated to provide a prototype test machine. The performance of each prototype machine is tested and evaluated through the capabilities of the DP Dynamometer Test Facility (DTF). The resulting performance information is analyzed and incorporated into subsequent developments of the DP switched reluctance technology.

DP has evaluated the potential for switched reluctance technology to provide a non-rare earth direct drive wind turbine. This section includes the development of a switched reluctance machine to validate the performance of DP short path switched reluctance technology for application as residential wind turbines.

DP has developed a Quick Machine software program to support the introduction of switched reluctance technology in the development of wind turbines and other machine applications. The QuickMachine software provides an approximate result as compared to the detailed design produced with hours of computation with the Maxwell FEA software. The QuickMachine software facilitates the application of the principles of switched reluctance technology to the development of residential wind turbines.

D1. Generation of Electrical Energy from Wind

Increasing global demand for energy has placed new emphasis on the development of alternative sources of energy. The United States Department of Energy identified the major target of producing 20% of the nation's electrical energy needs from wind by 2030.

There are two main targets that have been identified for wind energy. A report by the National Renewable Energy Laboratory (NREL) estimated the need for more than 300 GW to achieve the 20% wind target by 2030. The NREL report identified the need for the wind industry to produce 16,000 MW per year to achieve the 2030 target. The increasing role of wind in the generation of electrical energy as reported by the Energy Information Administration is shown in Figure 58. While this figure illustrates the results of the significant technological advances that have enabled the development of large wind turbines, wind farms, and expanding electrical distribution grids, there are challenges to the continued growth of wind turbines. The distribution of wind resources in the United States as shown in Figure 59 provides for the potential generation of electrical energy along the coasts and in the middle of the country. This distribution of wind resources highlights the challenge of delivering electrical energy generated by wind to the users who are located outside of the areas of concentration when resources are available. The development of wind generating capacity in the middle of the United States is hampered by the existing transmission grids that have traditionally served the rural farmland region.

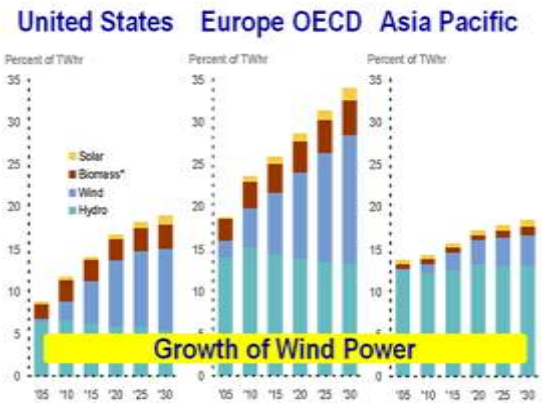

Figure 58: Growth of Wind Power

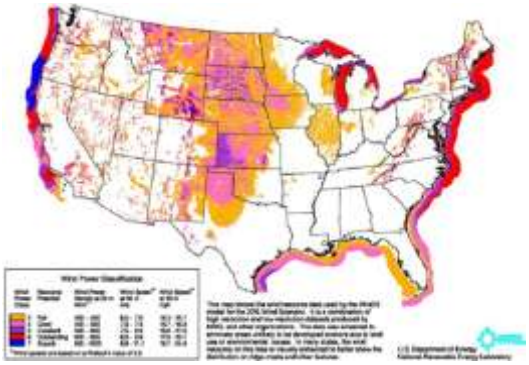

Figure 59: Distribution of Wind Resource

Figure 60: Transmission Grid for 400 GW

The expansion of electrical distribution is a priority to transport electrical energy generated to population centers. The effective development of wind as a source of electrical energy requires the development of a high-capacity country-wide electric power grid such as illustrated in green in Figure 60.

Additionally, there is increasing global interest in the generation of electric energy from large wind turbines located offshore. These turbines would provide electrical power to population centers located on the coast and through the new grid to areas of low population density. As the preparation of wind farms of large wind turbines in areas of high wind resources is being developed, there is also growing interest in the development of residential and small industrial wind turbines.

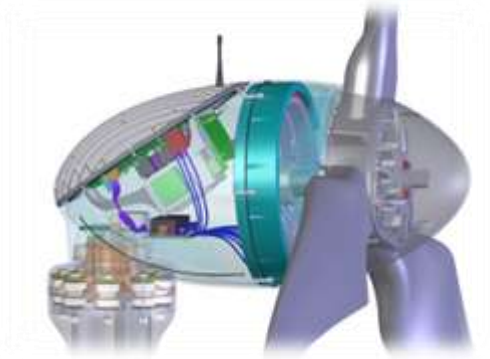

Figure 61: Skystream Residential Wind Turbine

While there are commercially available electrical generators to produce electrical energy for residential and small industrial applications as shown in Figure 61, there is growing interest in the potential of new electrical machine technologies to improve the conversion of wind to electricity. The use of a new switched reluctance technology, being developed by Dakota Power, has the potential to reduce the cost of the production and distribution of electrical energy generated by small-scale wind turbines. With the increased availability of residential and small industrial wind turbines, it is possible to significantly expand access to wind resources without the need for significant increase in the capacity of the local electrical grid.

The need for gearboxes to convert the relatively low rotation rate of wind to the more efficient higher rotation rate of induction generators is both a significant initial investment and an on-going maintenance cost. Technologies, such as permanent magnet generators and switched reluctance generators, that have the capability to provide a direct drive for converting wind energy to electrical energy. There is interest in the application of direct drive technologies to large wind turbines, particularly wind turbines used in off-shore wind farms. The potential use of direct drive switched reluctance technology for residential and small industrial applications has the advantage of lower weight and cost relative to permanent magnet machines.

The non-rare earth Dakota Power switched reluctance technologies provide an option to the growing concerns for the availability of rare earth materials currently supplied through China. The potential of unique new capabilities for residential and small industrial wind turbines through the use of DP switched reluctance technologies offers a significant new approach to expanding the electrical energy available from wind.

D2. Switched Reluctance Technology

DP switched reluctance machine (SRM) technology employs the fundamental principal of reluctance motion will be created to minimize the separation of two pieces of iron or other ferromagnetic material when placed in a magnetic field. SRM technology converts magnetic energy into rotational torque through reluctance alignment of the salient pole of a fixed machine stator with the salient pole of a movable rotor.

Electrical energy is applied to a pole of the stator through current flowing through a coil of wire wound around that pole. The current flowing through the stator coil creates the magnetic field that induces the movement of the rotor. Figure 62 illustrates the salient poles of a stator. Figure 63 illustrates the salient poles of the rotor. Figure 64 illustrates the relationship of the salient poles of the stator with the poles of a rotor in a typical switched reluctance machine.

Since it is intended that the rotor will rotate, there is an air gap between the poles of the stator and the rotor. The magnetic path from the pole of the stator to the pole of the rotor travels through the air gap. Torque is produced by the reluctance action between the magnetically energized stator pole and rotor pole. The rotation torque is transmitted through the shaft at the center of the rotor.

Figure 65 is an end view of a switched reluctance machine with the housing removed showing the coil windings of the stator, the rotor, and the output shaft. The coils of wire placed around each of the stator poles provide magnetic fields essential to the operation of the switched reluctance machine.

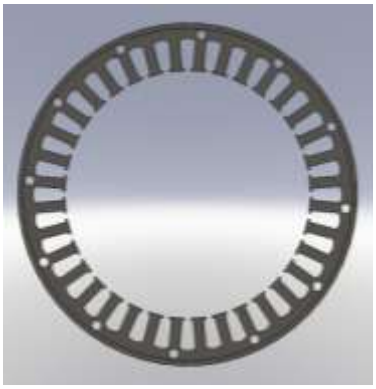

Figure 62: Stator salient poles

Figure 63: Rotor salient poles

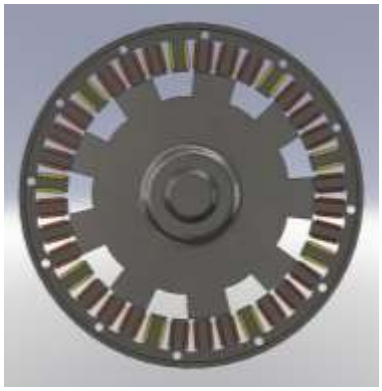

Figure 64: Stator and rotor poles separated by air gap

Figure 65: End of a Switched Reluctance Machine

The principle of magnetic field reluctance was applied to motors and generators over 150 years ago. Early switched reluctance machines controlled the switching of current to the stator windings with a mechanical switch. However, the mechanical switching system was incapable of responding to the need

for higher speed rotation which led to the development of other motor technologies, including brushed DC and AC inductance motors. The development of electronic switches, such as Insulated Gate Bipolar Transistors (IGBT), with capability to control significant electrical current has led to a resurgence of interest in switched reluctance technology. The capability to embed low-cost, high-performance microprocessors to control the switching of stator current is enabling the design and development of unique switched reluctance machines for applications as motors, generators, and electric drive systems, including residential wind turbines.

Figure 66 illustrates the magnetic field created between poles of the stator and rotor. The full flux of the stator is transmitted to the rotor through the increasing alignment between the stator in rotor across the air gap interface. The red areas of Figure 66 depict the high intensity of the flux density of the magnetic field with the initial alignment of the stator and rotor poles. The reluctance principal will cause the rotation of the rotor until there's equal distribution of the magnetic flux across the interface between the rotor and stator. The rotor rotates so that the center line of the rotor equals the center line of the stator, which is termed the fully aligned position. In the fully aligned position, there is no longer an inequality to provide a reluctance force to create motion.

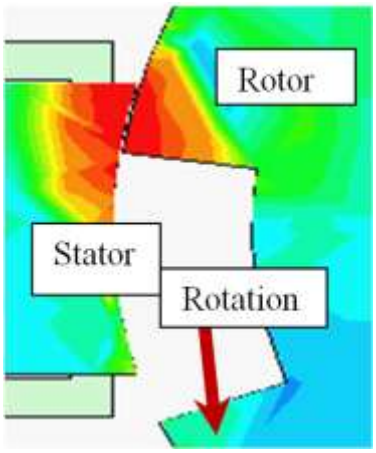

Figure 66: Magnetic Field Produced by Stator Coil

To achieve continuous rotation the magnetic field created by current in the stator coil must be switched to the stator pole in which the rotation of the rotor is approaching alignment. The ability to achieve switched reluctance across the stator and rotor poles requires accurate sensing of the location of the rotor pole relative to the stator pole. The ability to control the switching of current in the stator is essential to operating switched reluctance machine as a motor or as a generator. DP has developed a proprietary sensor system to sense the location of a rotor pole relative to the adjacent stator pole. The DP switched reluctance technology includes the development of embedded microprocessor control systems to switch the stator coil current to maximize the performance of DP switched reluctance machines.

Switched reluctance machines offer several advantages over conventional motor and generator technologies. The low cost of manufacturing the stator and the rotor is an advantage of switched

reluctance machines. The rotor has no windings or permanent magnets, and therefore can operate at high speed. Additionally, switched reluctance machines have the capability to operate as a direct drive machine which eliminates the need for a gearbox. Operation as a direct drive makes switched reluctance technology an attractive option for wind turbine generation of electrical energy. Direct drive operation has the potential to reduce the cost of manufacturing and maintenance of wind turbines, particularly residential wind turbines.

The ability to operate without permanent magnets, particularly rare earth permanent magnets, provides switched reluctance machines both advantages and challenges. The elimination of rare earth materials enables switched reluctance machines to operate at increased levels of temperature without the degradation of magnetic flux at Curie temperatures. However, the lack of the higher levels of magnetic flux of permanent magnets presents the challenge of achieving increased power densities comparable to rare earth permanent magnet machines. DP is developing processes for the integration of additional sources of magnetic fields to increase the specific power performance of switched reluctance machines. DP is evaluating applications of switched reluctance as a direct drive wind turbine, as vehicle traction motors, and as an electrical generator powered by a high-speed light weight combustion turbine

D3. Prototype development

Dakota Power (DP) provides an environment for the enhancement of the performance and application of switched reluctance machine technology. The DP process of design, simulation, fabrication, test, and evaluation has produced prototypes of potential major developments in the application of switched reluctance technology. The DP prototype development process includes the capability for a full FEA simulation of the magnetic fields of a potential design. DP has acquired Maxwell computer software that includes the ability to simulate the both the electrical and magnetic operation of a potential switched reluctance machine.

Once the potential prototype design is optimized to provide the target power density and efficiency, the design is fabricated. The prototype development includes the design of stator, rotor, and the switching control system. DP has facilities to both fabricate a proposed machine design and evaluate the performance of the resulting prototype machine. The DP Dynamometer Test Facility (DTF) has the capability to evaluate prototype machines with output power up to 10 hp and speeds up to 10,000 RPM. The results of the development of each DP prototype machine continue to extend the understanding of switched reluctance and associated technologies.

Table 6 provides a summary of the prototypes developed by DP. The initial prototypes evolved from a patented proof of concept electric drive system prepared by the inventor, Dr. William Hughes. DP has designed 12 prototype switch reluctance machines. The prototypes developed include a range of potential switched reluctance technologies including axial and radial flux paths. The axial flux path prototypes have a path that includes dual stators separated by a DC field coil. The radial flux path prototypes have a single stator and employ a short flux path that does not pass through the shaft of the rotor. These prototypes provided a understanding of switched reluctance operation that led to concepts for unique designs for lightweight switched reluctance motors and generators.

Table 6: Dakota Power Switched Reluctance Technology

Model	Type	Flux Path	Stator Poles	Phases	Rotor	Status
Hughes-1	SRDCM	Axial	12 Pole	3 Phase	6 Lobe	Built by Hughes 2006
Hughes-2	SRDCM	Axial	12 Pole	3 Phase	6 Lobe	Built by Hughes 2006
DP-01	SRDCM	Axial	9 Pole	4 Phase	9 Lobe	Built by DP 02/10
DP-02	SRDCM	Axial	9 Pole	4 Phase	9 Lobe	Built by DP 10/10
DP-03	SRDCM	Axial	12 Pole	3 Phase	6 Lobe	Built by DP 12/10
DP-04	SRDCM	Axial	9 Pole	4 Phase	18 Lobe	Built by DP 01/11
DP-05	SRM	Axial	2 Pole	4 Phase	6 Segment	Built by DP 02/11
DP-06	SRM	Radial (Short)	18 Pole	2 Phase	18 Lobe	Built by DP 02/11
DP-07	SRM	Radial (Short)	12 Pole	3 Phase	12 Lobe	Design completed
DP-08	IPM	Radial	6 Pole	3 Phase	6 Lobe / NdFeB	Built by DP 03/11
DP-09	IPM	Radial	6 Pole	3 Phase	6 Lobe / Ceramic	Built by DP 04/11
DP-10	SRM	Radial	20 Pole	5 Phase	18 Lobe	Pending Testing
DP-11	SRM	Radial	12 Pole	2 Phase	6 Lobe	Pending Testing
DP-12	SRM	Radial	12 Pole	3 Phase	10 Lobe	Pending Testing

The DP-06 prototype is designed to operate as a symmetrical machine with two phases. This symmetrical design demonstrates potential for providing optimal power density and efficiency as a residential wind turbine. DP-10, he a lightweight version of DP-06 has the potential to an ideal residential wind turbine machine.

Prototypes developed by DP are evaluated using the DP Dynamometer Test Facility (DTF). The evaluations both the performance of machines built by DP and the performance of purchased commercially available machines. The DTF has the capability to provide test results in the to document the performance of each Machine Under Test (MUT). The DTF also has the capability to test machines as both motors and generators. DP has developed standardized test and evaluation procedures to measure and record the performance data of each MUT.

Figure 67 shows DP-06 mounted in the DTF. The DP testing and evaluation procedure combines data collected from the MUT with data recorded by the engineers performing the test. The DP standardized test and evaluation procedure includes the ability to display the collected data in graphs that present information about torque, speed, and efficiency of a MUT. The data collected during the evaluation of a MUT enables adjustment of the initiation of switching of current to the stator coil relative to the position of the rotating stator pole which will result in the optimization of power density and efficiency.

Figure 67: Dakota Power machine DP-06 mounted in the Dynamometer Test Facility

Figure 68 is a comparison of the peak specific power of DP-06 with the peak specific power of other commercial switched reluctance motors, arranged from the highest to the lowest value. The DP-06 peak specific power of .67 kW/kg compares favorably with the peak specific power of .69 kW/kg produced by the Danahar switched reluctance motor.

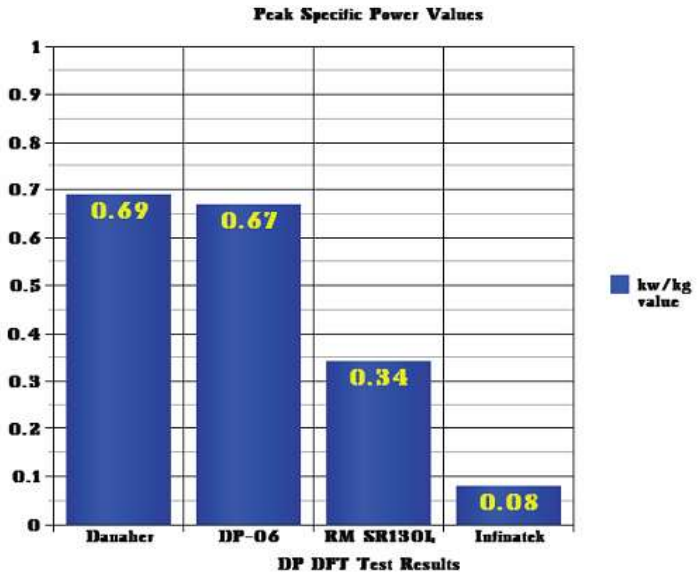

Figure 68: Comparison of peak specific power of DP-06 of .67 kW /kg to peak specific power of commercial machines

The test and evaluation of DP-06 identified the potential for enhancements in the control of the switching of current to stator coils in response to the location of an approaching rotor pole. Additionally, the availability of new high speed compact IGBT modules provides the opportunity to expand the capability to evaluate the performance of the DP switched reluctance technology machines throughout the full range of the capabilities of the DTF. Figure 69 shows the new fabricated IGBT circuit board with capability to provide operation with a stator coil current of 90 A and system bus voltage by up to 600 V. The upgrade of the IGBT stator current drivers also provided the opportunity to expand the

microprocessor memory and to implement additional software code to enhance the feedback operation of DP switched reluctance machines.

Figure 69: IGBT power driver board

Figure 69 shows one of the six IGBT stator drive circuit boards for providing stator coil current for DP switched reluctance machines. The lower two-thirds of the circuit board provides the operation of the power IGBT and stator current. The top one-third of the circuit board provides the interface connections with the microprocessor in software code.

It is anticipated that the DP-06 will be fully evaluated as a switched reluctance machine in October 2011 and the results will be documented at this location in this report. The DTF will be configured with the capability to dissipate generated electric energy for operation as a generator. DP-06 will be tested and evaluated as a generator with the potential to be a prototype of a switched reluctance wind turbine in November 2011.

D4. Switched reluctance generation

The DP switched reluctance machine will operate as a motor or generator depending on the timing of the switching of stator current. Figure 70 is a schematic diagram for the two phase control circuit for DP-06. The high current IGBT power switches are identified as S1, S2, S3, and S4. The stator coils are designated as Phase 1 and Phase 2. Current is provided to the stator coils of Phase 1 when the IGBT S1 and S2 are switched to the “on” state. The IGBT current flowing through the stator coils of Phase 1 will cause the rotation of the rotor. The IGBT S1 is switched between the “on” and “off” states to provide Pulse With Modulation (PWM), which in conjunction with the capability to control the voltage across the stator coils, provides control of the introduction of current to energize the inductance of the stator coils.

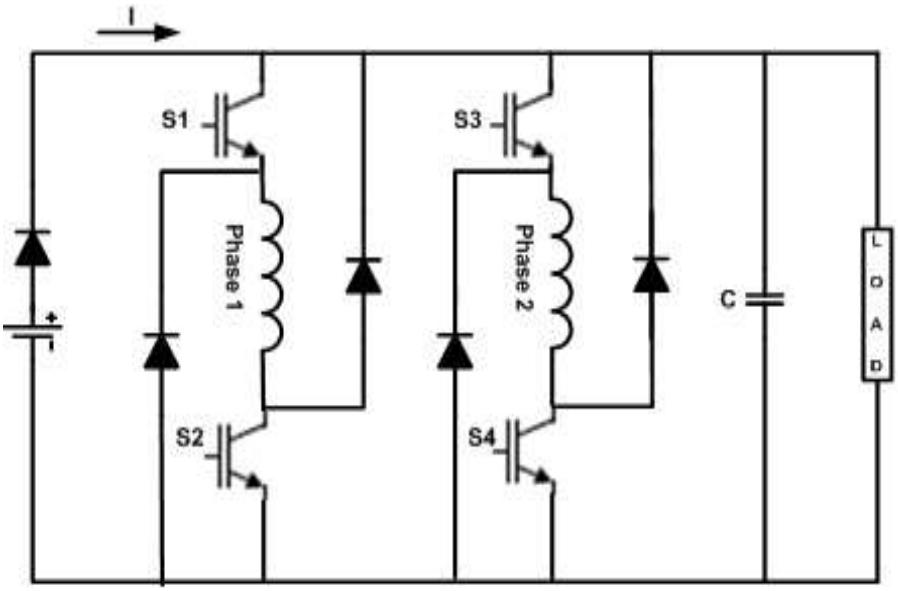

Figure 70: Schematic diagram for DP 06

Figure 71 is a diagram of the current of the stator coil for three electrical cycles of a switched reluctance machine operating as a generator. The middle cycle of Figure 71 illustrates the desired change in stator current as the pole of the rotor rotates through a full electrical cycle. At the beginning electric cycle, the stator current is switched "on" and the stator current transfers energy to create a magnetic field in the stator coil creating a reluctance force to cause the rotor to rotate. As the rotor and stator reach full alignment, the stator coil achieves maximum inductance with maximum stator current. In addition to current flowing to the stator, current also charges the capacitor and provides power to the load. The IGBT S1 and S2 are switched to the "off" state and current continues to flow through the stator coil producing magnetic flux. The continued rotation of the rotor through the magnetic flux generates a current through the stator for the remainder of the electrical cycle. As the rotor moves to alignment with the next pole of the stator, IGBT S3 and S4 are switched "on" and the cycle is repeated.

By changing the timing of the IGBTs, DP switched reluctance machines can be operated as generators. A diagram of the circuit used for operating the two phase DP-06 as a generator is shown in Figure 70.

Figure 71 shows an example of phase current with respect to time for a generating cycle. The IGBTs are switched on while the rotor is aligning with the stator. This is necessary to increase the current through the phase and create magnetic flux. Shortly after alignment, the desired phase current is reached and the IGBTs are switched off. At this point, the current in the phase windings flows back into the upper bus. While the rotor is unaligning, the back emf caused by the rotation of the shaft and the magnetic flux maintains the level of current flowing through the phase windings, thus electricity is generated and approaches zero and the current in the phase windings decreases.

The evaluation of DP-06 to function as a switch reluctance generator is projected to be completed the first half of November 2011. The results of this evaluation will be included in the final version of this report.

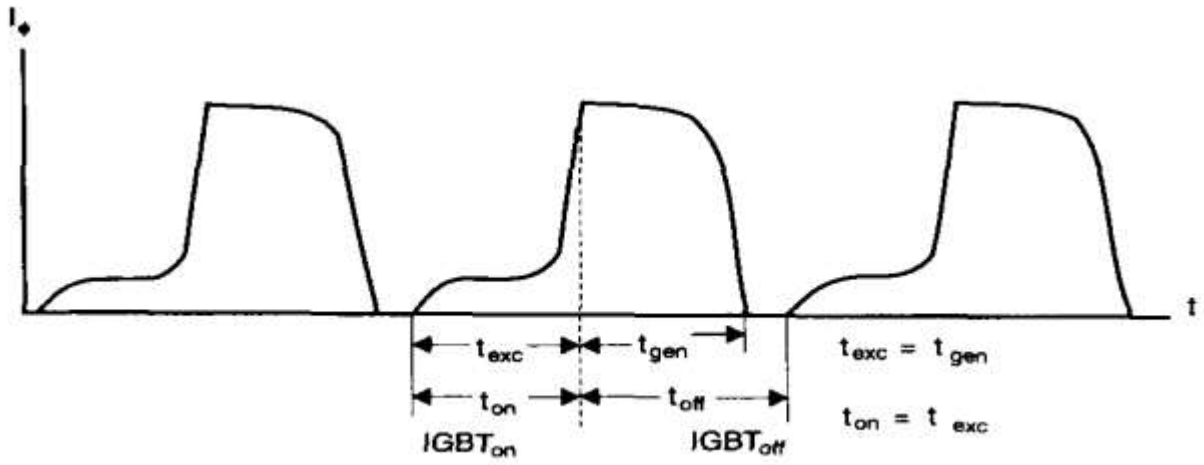

Figure 71: Stator current diagram for generating electricity

D5. Lightweight wind turbine

The development of a light weight electric drive system is a major objective of the DP research and development program. Studies of the Maxwell FEA simulation of the magnetic flux show the variability in the flux density of the magnetic field. In concept, it will be possible to remove the portion of the stator with minimum flux density, thereby reducing the weight of the stator, without significantly impacting the performance of the motor. The reduction in the weight of the stator will produce a lighter weight machine and higher specific power.

Figure 72 is a graphic of a Maxwell simulation showing the variability in the field density on the left for DP-12, a three phase short path reluctance machine. The reduced level of flux in the stator between the energized poles to provide the short path magnetic field led to the removal of this portion the stator in DP-10 as shown in the simulation on the right.

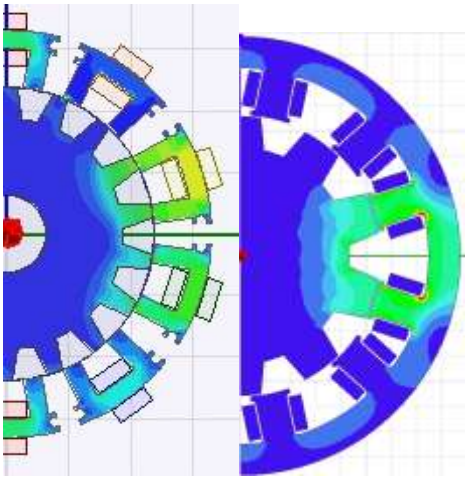

Figure 72: Maxwell plot showing the stator reduced flux density

Figure 73 is a graphic of the stator and rotor of DP-10 with a 20 pole stator and 10 pole rotor. The DP-10 is designed as a lightweight version of DP-06. The stator of DP-10 consists of 10 segmented sections mechanically linked through an aluminum frame. The windings of this stator are distributed on each of the segments of the stator. The 10 pole rotor of DP-10 has the same outside diameter as the rotor of DP-06. The DP-10 is an asynchronous five phase motor. The Maxwell FEA simulation of the DP-10 indicates the performance should be equivalent to DP-06 and the reduction in weight will result in an increase in specific power. In addition to reducing the weight of the motor, the segmented stator has a potential advantage of reducing the cost of winding stator coils.

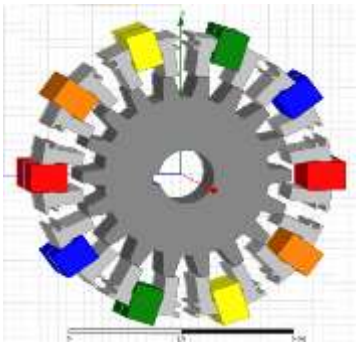

Figure 73: The DP-10 lightweight segmented stator

Figure 74 shows the coil winding of a stator segment of DP-10. While a traditional stator requires the insertion of windings around each stator pole, the stator windings of the DP-10 segmented stator are wound directly on each segment. Each DP-10 stator coil segment is wound with 35 turns of 17 gauge magnet wire. Each of the 10 stator segmented coil windings provide the magnetic flux for the pole pairs of each of the five phases of DP-10.

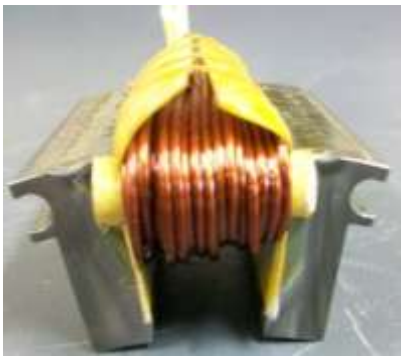

Figure 74: DP-10 stator stack wound with 35 turns of 17gauge magnet wire

Figure 75 is a Solid Works drawing of the assembled DP-10 motor. The wound stator segments are shown as salient poles on the circumference of the motor. The DP-10 will be evaluated in November 2011.

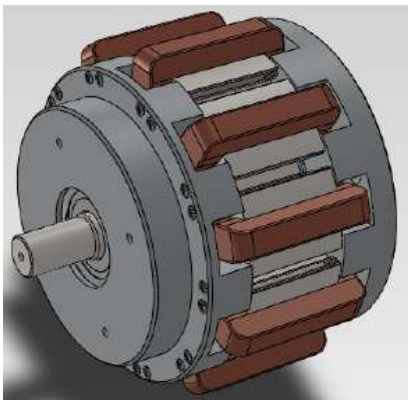

Figure 75: Model of an assembled DP-10 showing the segmented windings

D6. Scalability of switched reluctance

The development of DP technology includes demonstration of the capability to scale switched reluctance technology to produce prototype machines of various diameters, length, torque, and efficiency. In order to provide a baseline for comparing potential changes in performance with changes in the size of new prototype machines, DP-06 has been designated as the baseline machine.

Two of the test prototype machines have been designed with an outside diameter of 3.5 inches, length of 4.25 inches and weight of 7 pounds. DP-11 is designed as a radial short path synchronous two phase switched reluctance machine equivalent to DP-06. DP-12 is designed as a radial short path asynchronous switched reluctance machine with identical size and weight of DP-11.

DP-11 has 12 stator poles and 6 rotor poles to provide a synchronous two phase motor. DP-06 is also a synchronous two phase motor, but it has 36 stator poles and 18 rotor poles. The one third fewer stator and rotor poles of the DP-11 and DP-12 machines is the result of the need for sufficient space between the adjacent stator poles for the insertion of the stator windings.

As a comparison, the DP-06 has a stator winding of 16 turns of parallel 19 gauge wires. DP-06 has an outside diameter of 7.5 inches, length of 6 inches, and weight of 25 pounds. DP-11, with reduced volume for stator winding, has a stator winding of 56 turns of 23 gauge wire. The Maxwell FEA simulations of DP-11 and DP-12 project specific power and efficiency equivalent to DP-06.

DP-12 has the same physical dimensions as DP-11 but is configured as a three-phase switched reluctance machine. Figure 76 shows the results of the Maxwell simulation of DP-12, and illustrates the unique asymmetrical stator geometry designed to provide high specific power and efficiency in the performance of this machine. Figure 77 is a graph of the phase current of DP-12 and illustrates the switching sequence of the three phases of this machine to function as a switched reluctance generator.

It is anticipated that the scalability test and evaluation of DP-11. DP-12 will be completed in November of 2011 and the results will be included in the final report.

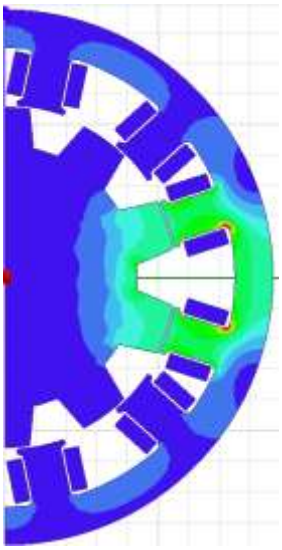

Figure 76: Maxwell plot of DP-12 illustrating the unique geometry of the poles of the stator

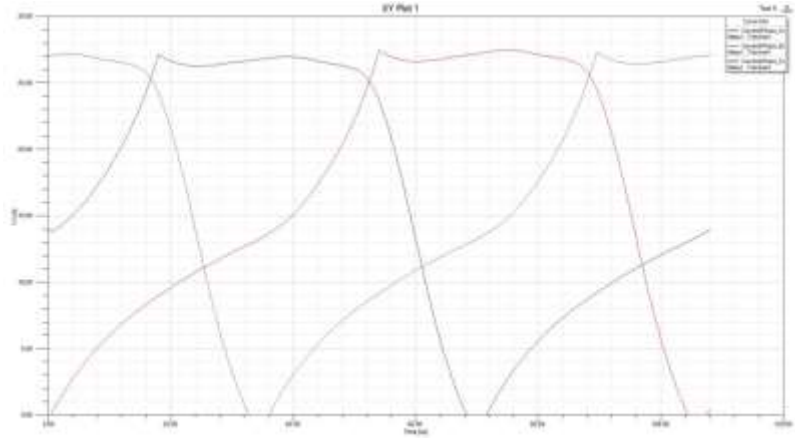

Figure 77: Plot of the Maxwell simulation of the stator current of the three phases of DP-12 with operation as a switched reluctance generator

D7. Quick machine

In support of this project, DP has developed a software program for the design of switched reluctance machines. The software is intended to assist users to apply the principles a switch reluctance machines and produce a prototype design. The goal of the Quick Machine software is to provide “quick” design results in comparison to the longer time required to produce a more detailed design using Maxwell or other FEA software. The Quick Machine software will be made available free for open source use through the DP website in the final report of this contract.

The Quick Machine software has the capability to design the geometry of the stator and rotor of a switched reluctance machine and to provide a simulation of the operation of the machine. The following section provides an introduction to the operation of the Quick Machine. The manual describing the full

details of the operation of the Quick Machine software is provided in Appendix B. The Quick Machine program will be available to download at the website for Dakota Power at the www.dplwed.com.

Quick Machines operation begins with the provision of three sets of parameters:

- Geometric Parameters – the physical dimensions of the machine
- Electric Parameters – the electrical components of the machine (phase windings and switching circuit)
- Material Parameters – the materials used in the machine

Once the geometric parameters are loaded, an interactive figure of the machine will appear. Figure 78 shows the DP-06 modeled inside Quick Machine. The rotor of the interactive figure can be rotated by clicking and dragging any rotor lobe – this allows the user to visualize the design, and helps in defining the switching circuit.

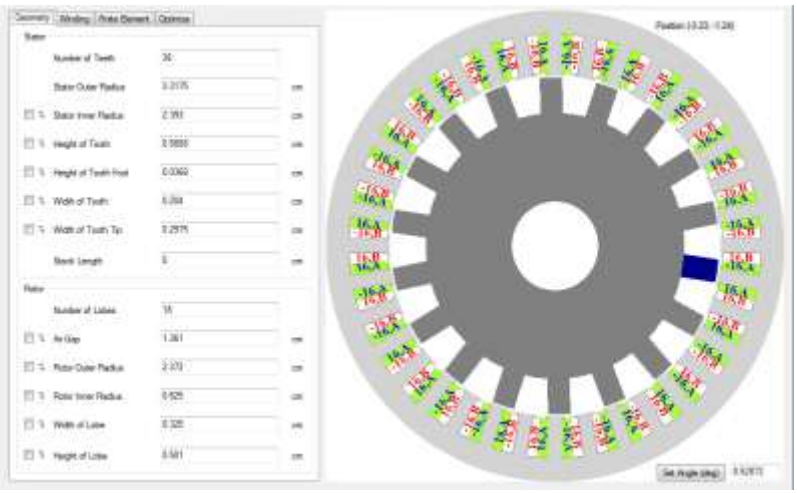

Figure 78: Quick Machine model of DP-06.

(The figure on the right is interactive – clicking and dragging a rotor lobe will cause the rotor to rotate)

Quick Machine uses an auto phasing algorithm that automatically sets the electrical components. The algorithm creates the phases based on the symmetry of the motor, then designs the switching circuit to produce maximum torque – given a rotor position, the switching circuit will fire all phases that produce a clockwise torque. With the auto phase algorithm the user can create a model in a matter of seconds. If the design requires a more customized phase set up and switching circuit, there is an option to design the phases manually – this option allows the user to explicitly set their phases, winding configurations, and firing angles.

Once the model is created, it is exported to an open source FEA program called Finite Element Magnetics Method (FEMM). FEMM is a widely used FEA simulator, and is the primary FEA tool in a number of research papers. Once the model is exported to FEMM, it performs a static finite element

analysis. This analysis provides the user with a graph of the flux densities and flux path, as well as calculations of torque, inductance, flux linkage, etc. Figure 79 shows an FEMM analysis of DP-06.

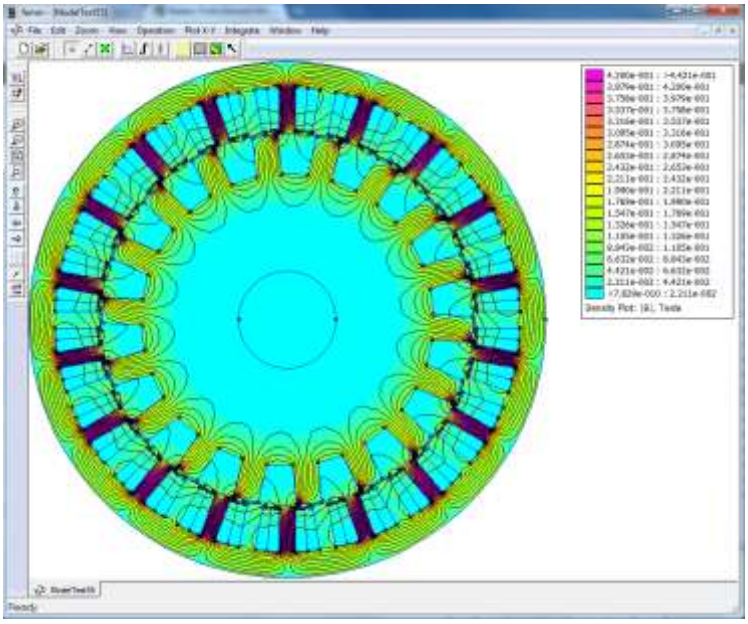

Figure 79: FEMM simulation of DP – 06.

(The solid lines show the flux path, while the colors indicate the flux densities)

The most powerful feature of Quick Machine is its ability to optimize a geometry by iterating the value of any number of parameters. This parametric sweep is performed given a list of parameters, each containing a start, end, and increment value. To execute the sweep, Quick Machine creates a model for each permutation in the sweep and sends it to FEMM for analysis. FEMM has a scripting interface that provides a list of commands; these commands can be used to specify the output of an FEMM simulation (i.e. torque, inductance, flux linkage, etc.). Quick Machine uses user input to generate a script of the above commands, and controls the output of FEMM with this script. This allows the user to customize the FEMM analysis for each parametric sweep. Once each permutation is analyzed, a single data file is created. Excel or MATLAB (or a similar program) can be used for further analysis.

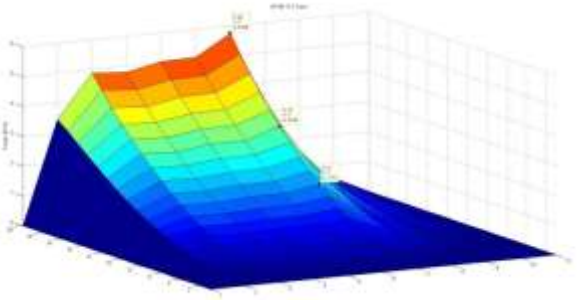

Figure 80: MATLAB plot of a parametric sweep of the current and rotor angle – Z Axis torque

Quick Machine allows the user to optimize any of the input parameters – including the electrical parameters. Figure 80 shows an example MATLAB plot of data created by Quick Machine iterating the phase current and rotor angle of DP-06. The analysis shown on Figure 80 is a combination of 200 simulations with a combined computation time of approximately one hour on a quad core 2GHz processor. The same analysis was performed using Maxwell – the Maxwell simulations gave similar results; however the 200 Maxwell simulations took a combined computation time of 13.3 hours.

E. Survivable Operation of Three Phase AC Drives in Wind Generator Systems

E1. Introduction: Advantages and Challenges of Wind Energy

Wind energy has gained increasing popularity over recent years due to the depletion of natural resources and the increasing concern about our environment. According to the data from Department of Energy (DOE) and American Wind Energy Association of the United States, as shown in Figure 81, the installed wind power generation capacity of the US has increased from 2,500 MW in 2000 to more than 35,000 MW in 2009. As of 2009, 26 states have more than 100 MW installed and more states will join the 100 MW club in the near future. In addition, as shown in Figure 82, wind energy takes 50% of all renewable electricity and reaches 1.8% of all the electricity generated in the US in 2009. Also, in report [**1**] of DOE, wind energy is targeted to reach 20% of all electricity generated in the US by 2030. In this scenario, enough energy can be extracted from wind to replace 11% natural gas consumption and 18% coal consumption, which could reduce 25% of the CO2 emissions and 17% water consumption in electric sectors in 2030. From these data, it can be easily noticed that there is global trend to replace conventional unhealthy energy generation modes with wind energy generation. Though the initial investment for the installation of wind farm might be large, this kind of energy generation mode is profitable and environment-friendly in the long run.

Although wind energy has a promising future, several challenges exist that hinder the wide-spread acceptance of this technology. These challenges including materials, manufacturing, transportation, initial investment and wind turbine stability etc. Wind turbine stability is one of the main concerns in the development of wind energy. Wind turbine faults happen frequently after installation. As shown in Figure 83 [1], the designed life-span for a wind turbine is 20 years. During this time period, the most frequent failure in the wind generator is in its sensor and control unit failure which begin to occur around 2.5 years right after the warranty. Though the repair cost is relatively cheap compared to other failures, frequent stops can significantly reduce the effectiveness of the generator and cause large loss of revenue. The gearbox might only last for 6 years without any problem, but after that, it begins to have faults and the risk of failure is increasing as time goes on. Unfortunately, the gearbox is one of the most expensive components in wind plant and its failure will cause the longest downtime of the wind plant [**2**], [**3**]. Besides, motors and switchgear can last for 6 years. The generator bearings begin to have faults around 11 years. Yaw drive and pitch drive can be used for 10 years etc. Based on the above data and analysis, it can be noticed that the low reliability of wind turbine components greatly hinder the development of wind energy.

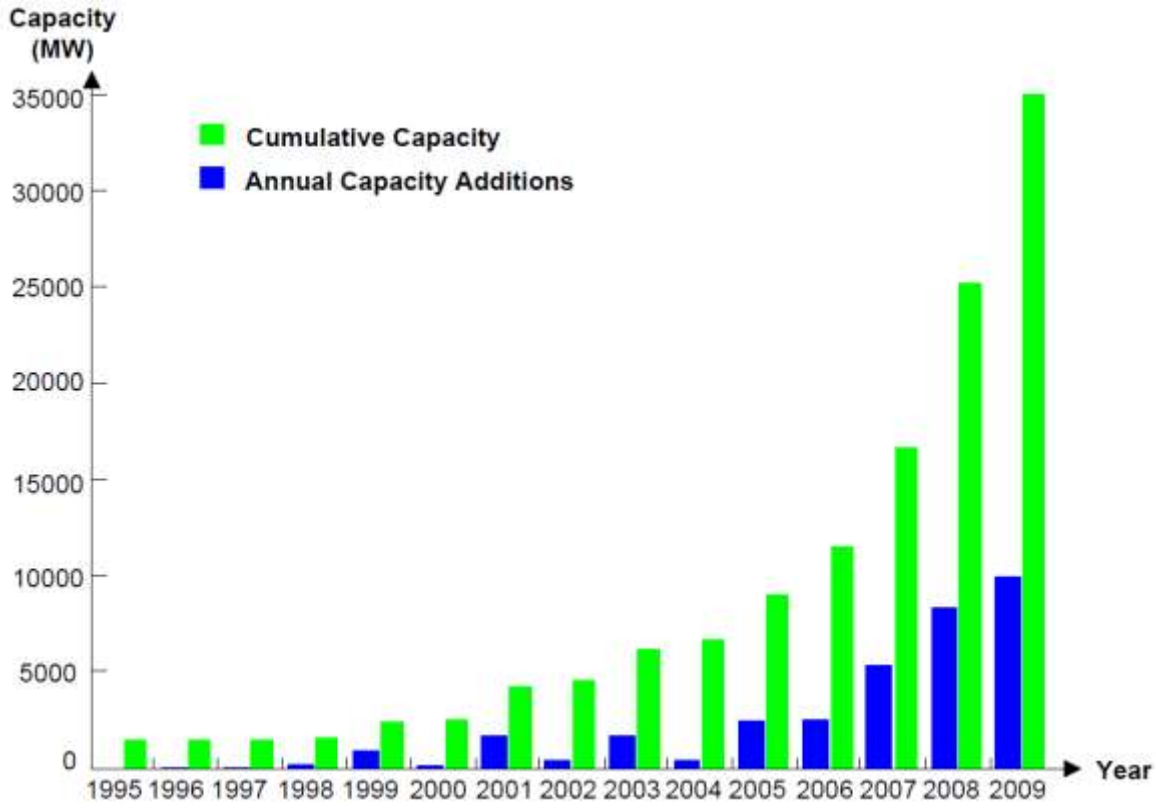

Figure 81: US annual and cumulative wind power capacity growth [1]

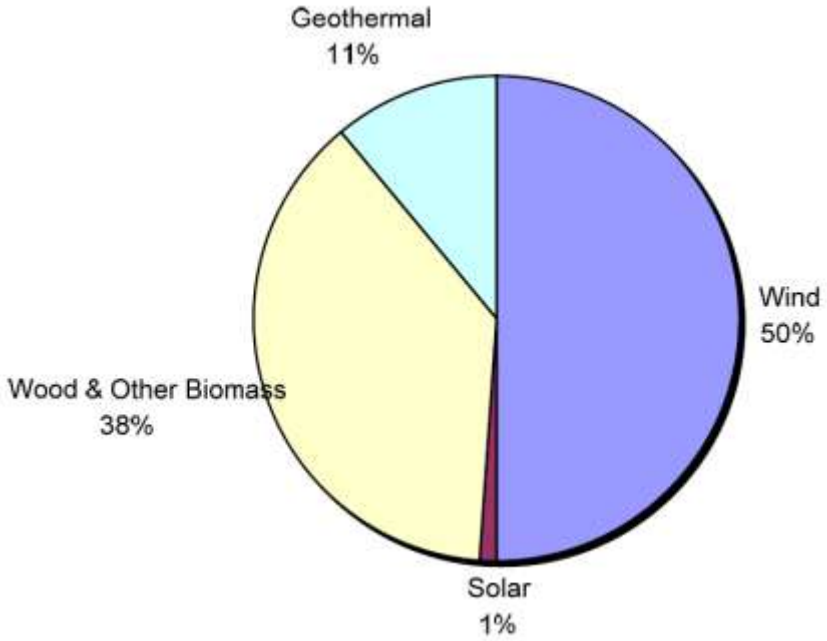

Figure 82: Percentage of renewable electricity [1]

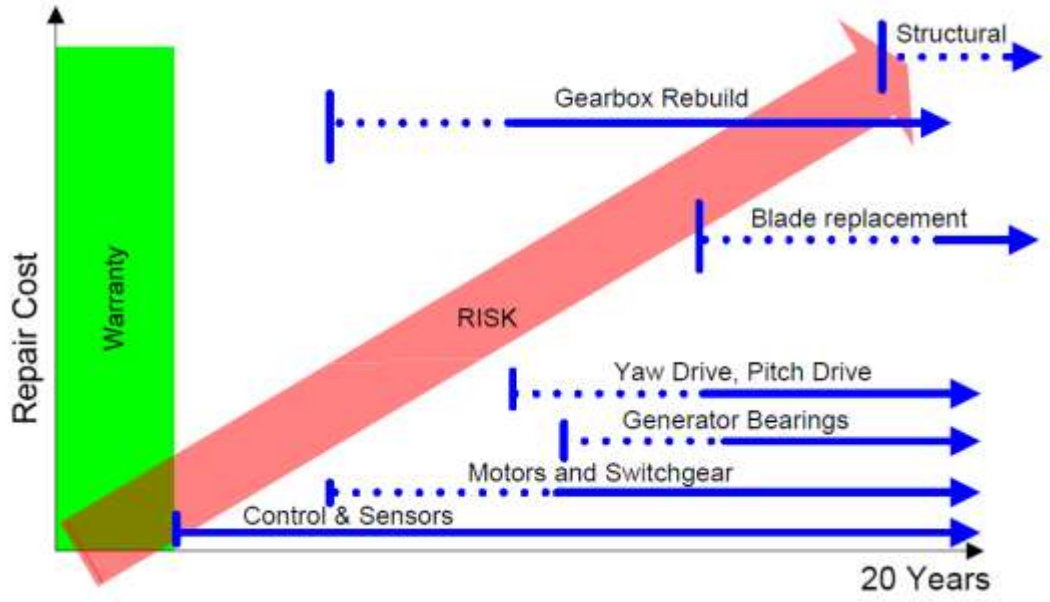

Figure 83: Unplanned repair cost and risk of failure with wind plant age [1]

Induction machine is one of the most popular machines in industry due to its robustness and low maintenance. Similarly, this machine is also widely used in all power levels of wind power applications. However, the control of induction motor (IM) and induction generator (IG) is complicated. In order to maximize the performance of induction machine, vector control is often utilized to decouple the flux and torque and control them individually. This control method usually requires complex control routines, fast processing unit and multiple system feedbacks including three phase current sensors. However, as shown in Figure 83, the most unreliable part of the wind plant is the control and sensors. Frequent sensor failures or even the drift of system parameters can result in unscheduled maintenance issues that require the unit to be frequently stopped, leading to a reduced power yield. In addition, unscheduled maintenance often results in longer downtime and causes reduction of availability of the wind generator especially for those wind turbines located offshore or in remote areas.

In order to enhance the reliability of the wind generator system, a novel simplified control strategy, state switching control, has been proposed and implemented for the induction machine in both motoring mode and generating mode, which have never been done before. This control method requires low signal processing need, low memory capacity and no current sensor. Therefore, it is a simple, cost-effective and very reliable control strategy. By utilizing this control method, system is only allowed to operate at two different duty cycles of PWMs which are given to the PWM rectifier and produces phase voltages with different magnitudes. Meanwhile, the frequency of the phase voltages is derived from the reference speed. By switching between these two states, different torque can be generated at the generator side, which leads to precise speed regulation and output power control.

Based on the simplified control strategy, a survivable control algorithm for wind generators is further proposed in order to deal with the failure of sensors (mainly for current sensors). The concept of survivable drive is that when system is healthy, the induction generator is often controlled by

sophisticated control algorithms such as vector control. When sensor fault happens, the wind plant can survive and the generator can be controlled by state switching control strategy and still be operated with relative lower but acceptable performance. Survivable drive is very useful for wind turbines when sensor fault happens. This ability ensures the power production and greatly reduce the lost of revenue.

Besides, the idea of survivable drive can be extended to Brushless Permanent Magnet Machine. Brushless PMSM is also one of the popular machines for wind power application due to its high power density. However, the potential failure possibility of current sensor will also cause stability problems to Brushless PMSM generator system. By utilizing the survivable algorithm and state switching control, the failure of current sensor can be tolerated, which greatly improves the reliability of the PMSM generator systems.

This section consists of six parts. Section E1 introduces the advantages of wind energy and the benefit in increasing wind plant installations in the US in recent years. This chapter then discusses current challenges in the reliability of wind generators and introduces the concept of a survivable generator drives in the event of failure of current sensors. Section E2 offers an overview of the common faults of different components of a wind generator setup. It identifies faults that are most frequent and ones that are most fatal causing the longest downtime with expensive repair costs. Section E3 presents a fundamental description of an induction machine model. In addition, converter topologies and generator control methods which are often used in wind plants are explained. Section E4 describes the principle and performance of a state switching control strategy for induction machine. As a backup control strategy, a novel state switching control method is proposed and implemented on hardware to control the induction machine without relying on current feedback. Simulation and hardware results are included to verify the feasibility of this method. Section E5 proposes a survivable drive algorithm for induction machine in wind power application when there is a failure of in current sensor(s). First, the principle and implementation of a sensor failure detection method is introduced. Then, implementation of vector control as a main control strategy for induction machine is introduced. After that, a change in control algorithm is proposed when sensor failure occurs. In addition, a controller smooth transition method is designed to ensure the seamless controller transition without stopping the system and causing speed vibration. Detailed simulation and hardware results are included to validate these methods. Section E6 concludes achievements in this research and identifies future work.

E2. Current Existing Faults for Wind Power Generator Systems and Corresponding Solutions

Wind energy has a promising future. However, wind turbine has many challenges in its reliability. Different components of a wind plant have different failure rates. As shown in Figure 84 [**1**], the electrical faults take more than 50% in fault rates and sensor faults take 9%. Such a high failure rate greatly hinders the development of wind energy. Detailed information regarding certain failures and their corresponding fault tolerant solutions is presented in the following sections.

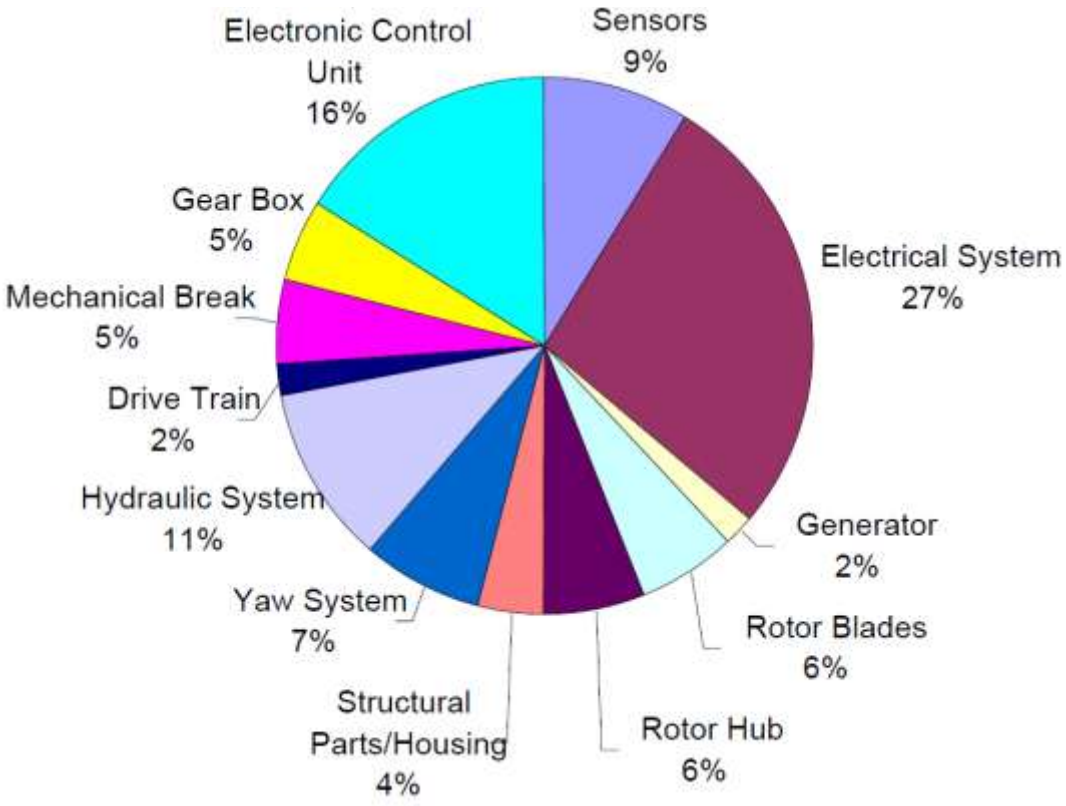

Figure 84: Failure rate of different component in wind turbine [1]

In wind turbine applications, converter failure happens much more frequently than any other wind turbine faults. In paper [**4**], it pointed out that the MTBF (Mean Time between Failures) of a conventional converter (or inverter) is 20,800 hours (about 2.4 years) which is too short for wind power applications. The topology of a conventional converter can be displayed in Figure 85. The right side is connected to the three-phase generator and the left side is connected to the DC link. In between them, six IGBT switches with six parallel diodes forms three converter legs which are connected to different machine phases independently. Converter fault can be single switch failure (open circuit or short circuit) or two-switch failure—usually one leg is open circuit or short circuit. All of these faults are fatal and will cause the wind turbine system to be shut down. Since unscheduled maintenances experience relatively longer period. It leads to the decrease of power production and availability of healthy wind turbines.

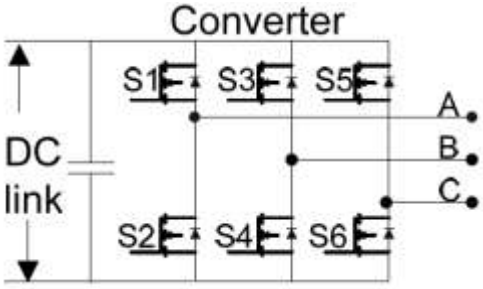

Figure 85: Typical topology of converter

Fault-tolerant strategy for inverter failure is introduced in paper [**5**], which is also applicable to converter failure. In [**5**], the inverter fault is tolerated by introducing the forth leg to conventional inverter. As shown in Figure 86, the forth leg (Switch S7 & S8) is added to the conventional inverter with its middle point connected to the neutral of the three phase AC machine. When inverter failure happens, the faulty leg is isolated while the forth leg is activated. As a result, one phase of the AC machine connected to the faulty leg is also isolated and the machine is operating with the rest two phases. The advantage of this inverter topology is that it can handle single switch open-circuit or short-circuit fault and one leg open-circuit fault. If additional isolating devices are added to inverter legs, one leg short-circuit fault can also be tolerated. The torque performance under fault condition is claimed to be the same as a healthy machine by proper compensating the phase current of the machine. However, this method has some disadvantages in practical applications. Inverter fault must be detected quickly and isolated immediately. Otherwise, it will cause severe damage to the machine and other electrical components. The challenge is how to detect and isolate the inverter leg failure fast enough before causing undesirable troubles. In addition, in order to maintain same torque performance after failure happens, the current flowing through the rest two phases and inverter legs increased especially for the fourth leg (the maximum current flowing through the forth leg is near three times greater than conventional inverter). As a result, high power rating switches are required compared with conventional inverter, which will increase the cost of hardware.

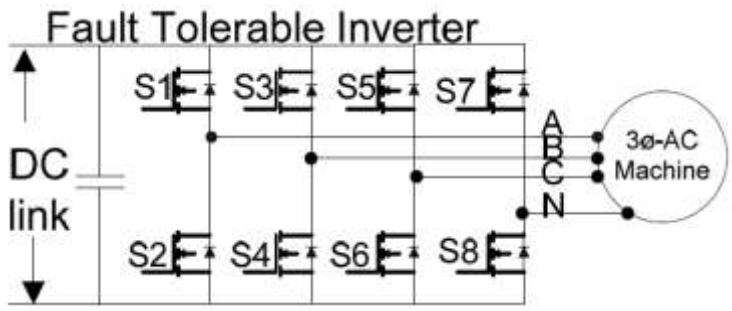

Figure 86: Four-leg fault tolerant inverter

In paper [**4**], several voltage source redundant inverter topologies are presented and their reliabilities are discussed and compared with the conventional inverter. Two redundant inverter topologies are shown in Figure 87. Instead of using two switches, multiple switches are used to form one leg of the inverter.

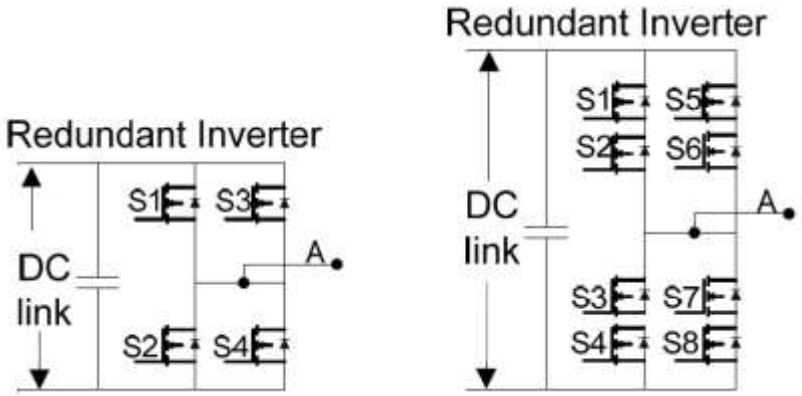

Figure 87: Redundant inverter topology

By using redundant inverter topologies, the reliability will increase obviously for short term operation (around several hundreds of hours) compared with conventional inverter. However, for long term operation (longer than 80,000 hours), the reliability tend to become the same. Since the reliability of the redundant converter doesn't change very much for long term operation, this method is not recommended for wind turbine application to improve the converter reliability.

In wind power generation, a bunch of sensors work together to provide feedbacks regarding the conditions of a wind turbine. These feedbacks can be used to control the efficiency of the wind turbine system and ensure its safety. The control of generator and power electronics requires current sensors and voltage sensors. The control of electric drive also need speed or position sensors. Besides, temperature sensors monitor the temperature of different part of the wind turbine such as the generator and the gearbox. Vibration sensors sense the vibration of the transmission as well as the wind turbine tower to avoid possible damages caused by large vibration. Therefore, sensors are necessary for the operation of a wind turbine. A sudden sensor failure will decrease the system performance and even lead to system malfunction, which is harmful to the availability of the wind turbines. Among these sensors, voltage sensors, current sensors and speed sensor (or position sensor) plays more fundamental roles in a wind turbine system. They provide basic information about the generated voltage, current and their frequency. The failure of these sensors might lead to uncontrolled power which is harmful to the system and the grid. In addition, these sensor outputs are often used in close-loop control strategies such as Field Oriented Control and constant V/f Control. If one of these sensors is in fault condition, these control strategies cannot perform correctly since basic feedbacks are missing. Therefore, in order to improve the reliability of the system and prevent unscheduled shutdown, sensor fault detection and compensation method are often adopted. 1) Current sensor and voltage sensor failure

In literature [**6**], current sensor failure is detected and isolated using three-phase current balancing test. Under normal operation, the sum of the measured three-phase currents is very small (near zero). If one of the current sensors is in fault condition, this value will change dramatically. Therefore, by comparing the sum of measured currents with a small threshold value, the current fault can be detected. Then, the faulty current is identified and compensated by fuzzy logic state observer. The observer basically estimates the stator flux and phase current which is then used to replace the faulty current and

reconfigure the control loops. Similar method can be found in literature [**7**] and [**8**]. This technique for tolerating the current sensor failure also applies to three-phase voltage sensor because these voltage signals have the same characteristics.

In paper [**9**], the failure of sensor is tolerated by reducing the performance of the control using control strategies that requires fewer sensors. As a result, one can toggle between different control strategies based on the availability of the sensors. For example, if all voltage sensors, current sensors and position sensor are available, sophisticated control strategies can be employed to enhance the performance of the system such as Field Oriented Control and Direct Torque Control. If only voltage sensor is good, constant V/f method can be used to control the induction machine.

In paper [**10**], the failure of phase current sensor is tolerated by eliminating the phase that the faulty current sensor belongs to. As shown in Figure 86. The PMSM machine can be operated with the rest two phases and with the natural point connected to the forth leg of the inverter. The torque performance is claimed to be the same with the three-phase machine using this method. 2) Speed or position sensor failure

In wind power generation, position information is typically required to calculate the shaft speed of the machine in order to control it properly and employ Maximum Power Point Tracking (MPPT) schemes. As a result, the failure of the speed or position sensor often leads to system malfunction and unscheduled shutdown. Sensorless techniques are often used to handle the position sensor failure. Large amount of literatures are dealing with different kind of sensorless techniques including Motional-EMF based prediction [**11**], [**12**], Inductance variation based prediction [**13**] and FluxLinkage variation based prediction [**14**] etc. These sensorless methods can be employed to handle the position sensor failure. However, the performance of sensorless method is poor in low speed conditions.

The gearbox is a mechanical device which connects the low-speed shaft and thegenerator. Gearbox is indispensable for indirect drive wind turbines due to the high rotating speed requirement of generators. Usually, it can speed up to 1500rpm (50Hz) to 1800rpm (60Hz). The lifetime expectation of a wind turbine is around 20 years. However, according to literature [**15**], [**2**], the current existing gearboxes can only last for 7 years on average, which is far less than the designed lifetime objective. Worse still, gearbox is the most expensive part of the wind turbine system and the most responsive component for the wind turbine down time. Replacing a gearbox and lubrication will cost 38% of the total budget of the entire wind turbine and make the wind turbine stop for a long time [**2**]. This down time data can be displayed in Figure 88.

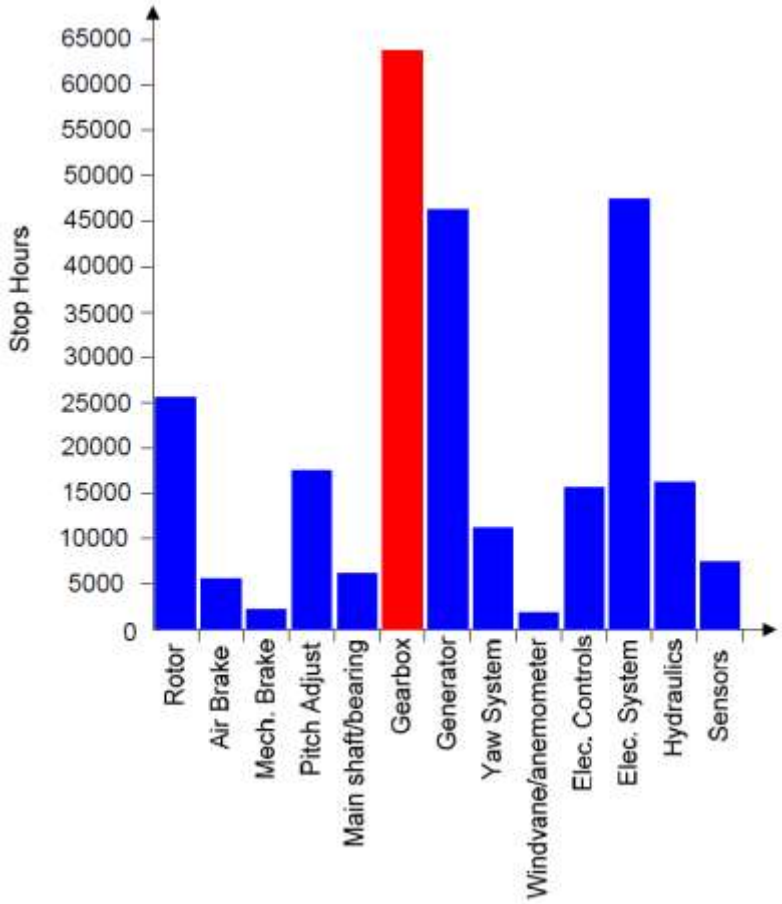

Figure 88: Wind turbine down time caused by component failure [2]

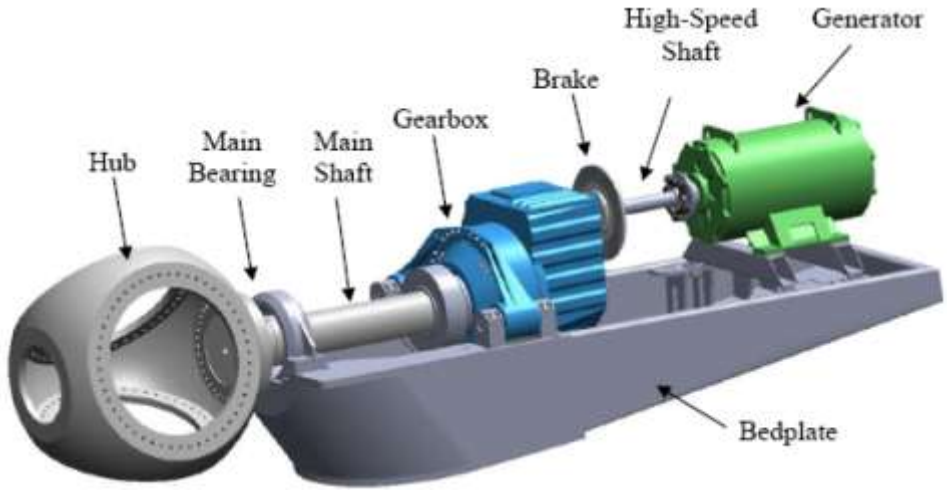

Figure 89: Conventional drive train of wind turbine [2]

The fundamental reasons for the failure of gearboxes are still not clear. But certain reasons can be estimated from observations and software simulation [**3**].

1) Improper design of wind turbine gearboxes without considering the complicate load conditions. This is primary due to the lack of communication between gearbox manufactures and wind turbine designers.

2) Non-torsional load is transferred between different components of the drive train including the gearbox. Non-torsional of the drive train load is introduced by the conventional rotor support structure. As shown in Figure 89, the gearbox not only performs mechanical acceleration, but also works as a rotor support of heavy wind blades. This kind of rotor support structure hastens the wearing of the gearbox.

3) The quality of bearings is essential for the health of the gearbox. If the bearing is broken or even worn due to strain, there will be a misalignment in the drive train which will cause damage to the gearbox.

4) Improper installation and lubrication problems will also cause damage to the gearbox.

Gearbox failure is fatal. But there are no fault tolerant strategies till now. Certain methods can be used to increase the reliability of the gearbox according to the above mentioned causes.

1) Redesign the gearbox according to the practical load conditions of the wind turbines. National Renewable Energy Laboratory (NREL) of the US has lunched several projects aim to improve the reliability of the gearbox of wind turbine.

2) Redesign the rotor support structure and eliminate the non-torsional load in the drive train. Actually, wind turbine designers begin to try new structures. As shown in Figure 90 [**15**], the rotor which connected to the hub and heavy blades is supported by the wind turbine tower instead of the gearbox. As a result, non-torsional load can be eliminated from the drivetrain.

3) Ensure the quality of the bearing and enhance the communication between wind turbine designers and bearing suppliers.

4) Direct drive is also an option to fundamentally solve the gearbox problem since this kind of wind turbine structure eliminates the gearbox and the generator is directly connected to the wind turbine shaft, as shown in Figure 91. However, this method requires a generator with large diameter and increased number of poles due to the low speed of the shaft, which will not only significantly increase the cost of the generator but also make the control strategy complicate if the generator working in variable speed generating mode. Moreover, the failure rate of the converter in the direct drive wind turbines is much higher than in the indirect drive wind turbines [**16**]. Therefore, direct drive wind turbines still have a long way to go before replacing the indirect drive wind turbines.

Other failures including generator failure, yaw drive failure, pitch failure, rotor blade failure and structural failure etc. Failure rates of most of these failures are smaller then those introduced in the previous part of this chapter. In addition, most of these failures cannot be tolerated. As a result, detailed information regarding these faults will not be introduced.

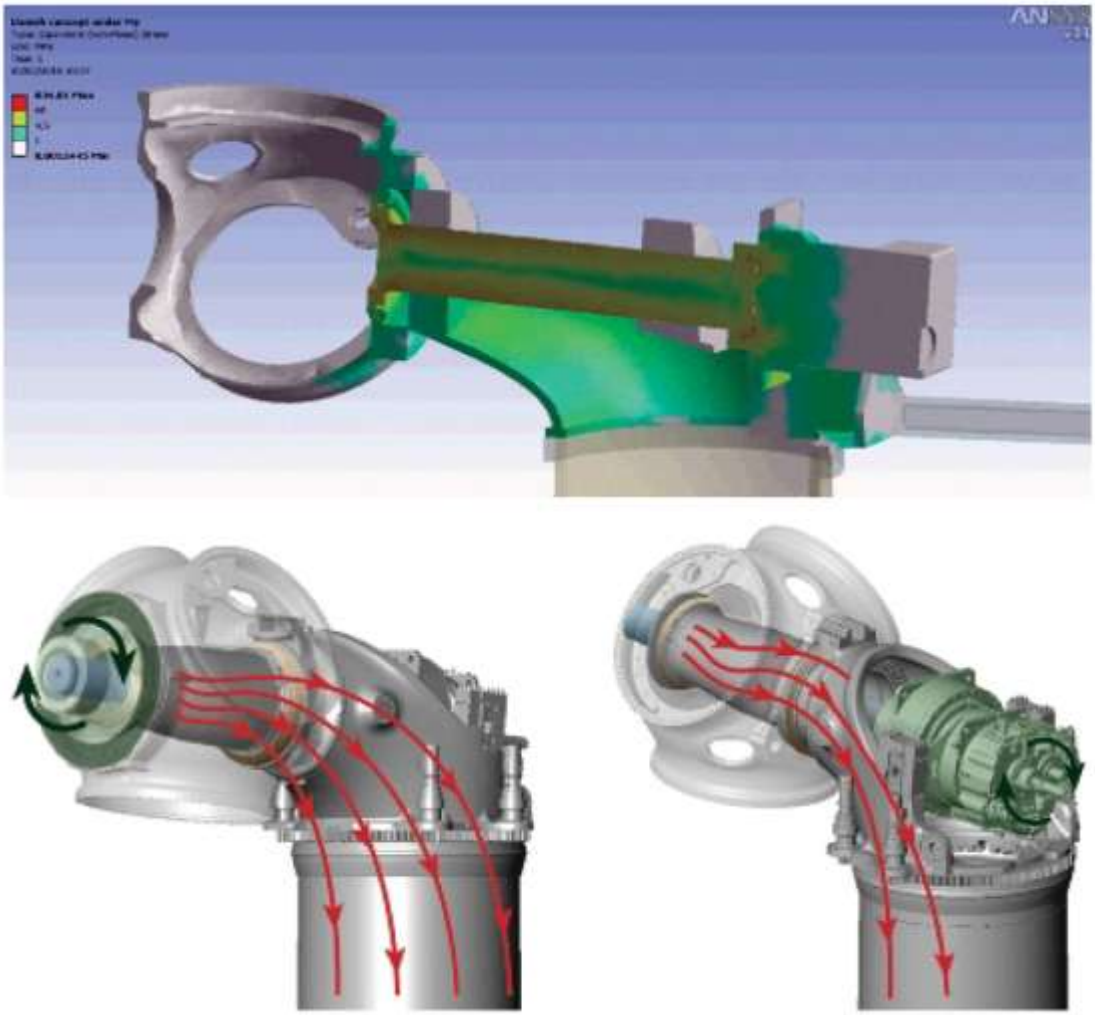

Figure 90: Tower supported rotor configuration [15]

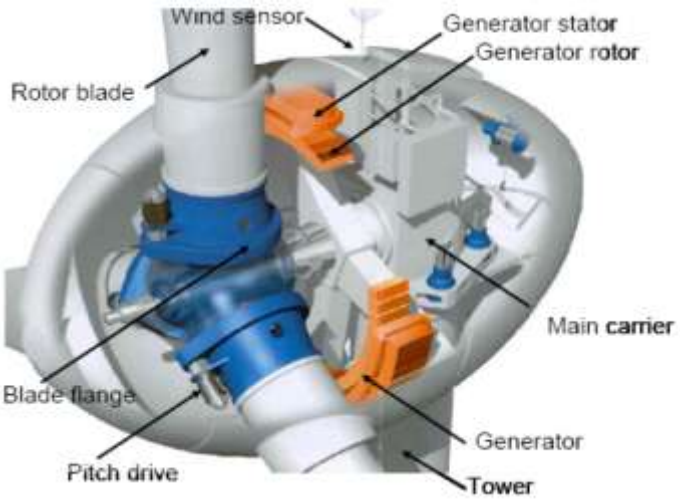

Figure 91: Direct drive wind turbine configuration [2]

In this section, several types of component failures are introduced and their corresponding fault tolerant solutions are discussed. Electrical faults take the highest percentage of failure rate. While mechanical faults often causes longest downtime and cannot be tolerated.

E3. Fundamentals of Induction Machine Drive

Induction machines are popular due to their robustness, cheap price and low maintenance. They can be found in wind turbines at almost all power levels. For small power level, squirrel cage induction machines are often utilized. For medium and high power level, wound rotor induction machines (Double Fed Induction Machine) are often employed.

One of the commonly used induction machine model is the synchronous rotating reference frames model. The equivalent circuit of this induction machine model can be displayed in Figure 92. According to equivalent circuit, the mathematical model of the induction machine can be derived and expressed in equations (1) to (5). Mechanical system of the induction machine can be expressed in equation (6) and (7).

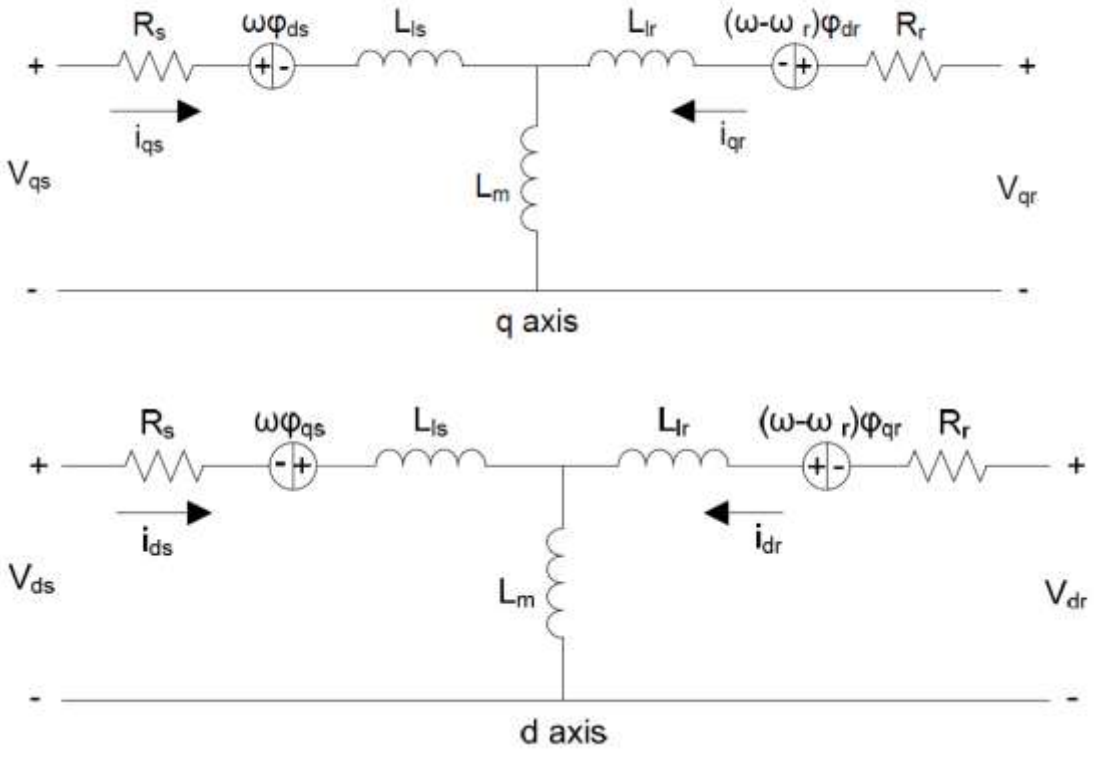

Figure 92: Equivalent circuit of induction machine in d-q axis

$$V_{qs} = R_s i_{qs} + \frac{d}{dt}\varphi_{qs} + \omega\varphi_{ds} \quad \textbf{(1)}$$

$$V_{ds} = R_s i_{ds} + \frac{d}{dt}\varphi_{ds} - \omega\varphi_{qs} \quad (2)$$

$$V_{qr} = R_r i_{qr} + \frac{d}{dt}\varphi_{qr} + (\omega - \omega_r)\varphi_{dr} \quad (3)$$

$$V_{dr} = R_r i_{dr} + \frac{d}{dt}\varphi_{dr} - (\omega - \omega_r)\varphi_{qr} \quad (4)$$

$$T_e = 1.5p(\varphi_{ds} i_{qs} - \varphi_{qs} i_{ds}) \quad (5)$$

$$\frac{d}{dt}\omega_m = \frac{1}{2H}(T_e - F\omega_m - T_m) \quad (6)$$

$$\frac{d}{dt}\theta_m = \omega_m \quad (7)$$

where

$$\varphi_{qs} = L_s i_{qs} + L_m i_{qr}$$

$$\varphi_{ds} = L_s i_{ds} + L_m i_{dr}$$

$$\varphi_{qr} = L_r i_{qr} + L_m i_{qs}$$

$$\varphi_{dr} = L_r i_{dr} + L_m i_{ds}$$

$$L_s = L_{ls} + L_m$$

$$L_r = L_{lr} + L_m$$

The converter topologies for induction machine drives can be grouped into two major categories. One is passive converter and the other is active converter.

The topology of a commonly used passive converter is shown in Figure 93. This topology is often used when the generator is operating at constant speed. For example, an induction generator is often required to operate at 1500rpm synchronous speed when its output is directly connected to the grid with 50Hz frequency. In such a circumstance, shaft speed of the generator is maintained by the

mechanical part of the wind turbine instead of the converter. This topology can also be found in some direct drive wind turbine. In this case, the shaft speed of the generator is not constant, which results in the change of the DC link voltage. As a result, an active inverter is often required after the passive converter stage to convert DC power into three phase power for sending to the grid.

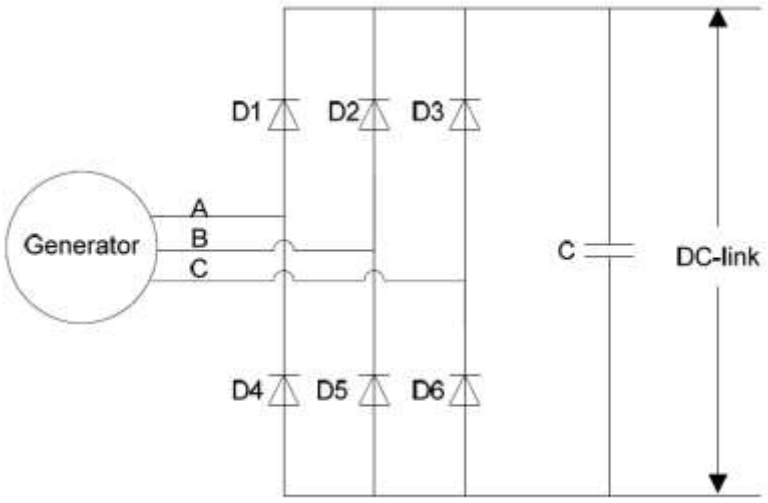

Figure 93: Passive converter topology

The topology of a typical active converter is illustrated in Figure 94, in which active components (IGBT or MOSFET) are used instead of diodes. In this topology, power flow can be bidirectional. Power can flow from generator side to the source and vise versa. As a result, this topology is extremely popular in Hybrid Vehicle applications. Active converters are also popular in wind power application, since the use of an active converter allows the generator torque to be properly controlled. By manipulating the generator torque, shaft speed of the generator can be controlled. This ability is very useful in direct drive wind turbines since the maximum power point is related to specific shaft speeds.

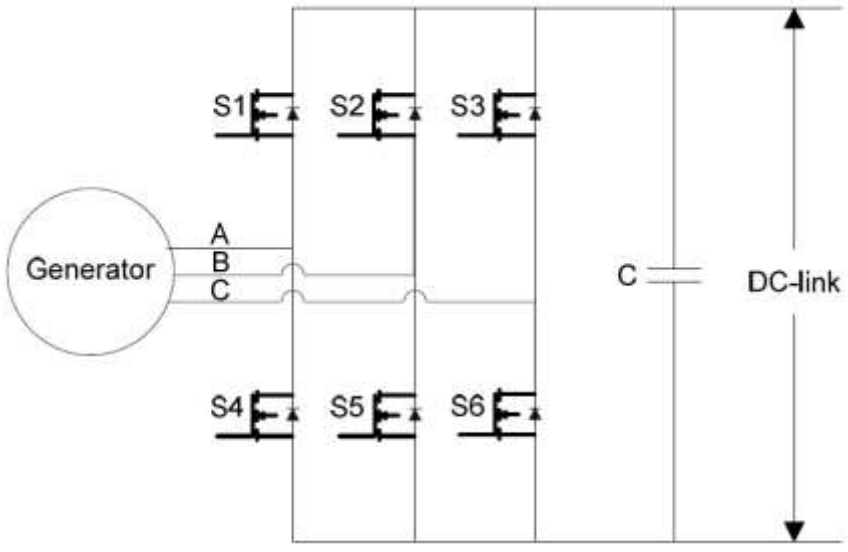

Figure 94: Active converter topology

In order to control induction machine properly and efficiently, different kinds of control strategies emerged in the past. Among these control strategies, most commonly used control strategies are constant V/f control and vector control.

Constant V/f control [**17**], [**18**] is popular for induction machine mainly because of its simplicity. In general purpose applications, most constant V/f controls are open-looped and control the voltage and frequency proportionally. By applying a specific phase voltage and frequency to induction machine, it can work at a desired speed. However, the speed control of conventional constant V/f controls lacks accuracy due to the existence of the rotor slip. When load increases or frequency decreases, rotor slip increases. This results in the increase of error between reference speed and actual speed. In order to deal with these problems, stator voltage boost [**19**], [**20**], [**21**] and slip compensation methods [**20**], [**21**] are often used. However, these methods increase the complexity of the system and require additional voltage or current sensors.

Vector control [**22**], [**23**], [**24**] has gained popularity over the last three decades due to its high efficiency and better transient performance. This method controls the flux and torque of induction machine separately and makes it work as a DC machine. Vector control turns out to be the most efficient and promising control strategy for induction machine. However, the implementation of vector control is complicated and expensive. It not only requires fast computation speed devices such as DSP and FPGA, but also additional sensors including current sensors and position sensor.

In this section, the basic model and the equivalent circuit of induction machine and permanent magnet machine is introduced individually. In addition, two typical converter topologies are explained including passive converter and active converter.

E4. State Switching Control as a Back Up Control Strategy for Three Phase AC Machine

Current sensor failure is one of the most frequent faults in wind plants. A back up control strategy is required to continue operating the system. Otherwise, wind plant has to be shut down. State switching control is one of the simplest control methods which only need speed feedback. In other words, if current sensors are in faulty condition, system can still be operated with state switching control. State switching control is a variation of digital control method which is first designed to control BLDC, Switch Reluctance Machines (SR) and DC-DC converters. In this report, a state switching control method is proposed and applied on induction machine. The performance of this control method is highly acceptable.

In recent years, digital control has been proposed in [**25**], [**26**], [**27**], and [**28**]. This control method is extremely simple and very effective for many applications, such as BLDC, SR control and DC-DC converter control. In this method, two different states (state “High” and state “Low”) are predefined, these states can be voltage, current and PWM duty cycle. Then, state is switching between these two states by comparing the actual output value with the reference value. As a result, the system output can be well regulated. Therefore, there is no need for any massive computation controllers or even PI controllers. Only a comparator is required for the implementation.

Digital control has been found effective in several applications. This section presents the realization and implementation of state switching control technique for induction machine. The proposed state switching control method is based on six-step drive method [**17**] which is a basic drive technique for induction machine. By integrating PWM signals to gate signals of traditional six-step drive, a PWM based six-step drive method is derived. Then, by defining two different duty cycle for those PWMs, two phase voltages with different magnitudes (VH or VL) can be obtained. At the same time, by defining the frequency of the phase voltage according to given reference speed, the state switching control method for induction machine can be realized. By using this method, the induction machine system is only allowed to operate at a high duty cycle (DH) or low duty cycle (DL) which corresponds to VH and VL respectively. Speed regulation is achieved by defining the frequency of the phase voltage according the given reference speed and then switching between these two different duty cycles. Therefore, this controller is extremely simple. This technique also reduces the cost and complexity of hardware implementation. Simulation and experiment results regarding the speed response, change of duty cycle and phase current are included in this chapter to prove the effectiveness of the proposed approach.

For a three phase induction machine, the most frequently used driver topology is the three phase inverter which can be illustrated in Figure 95. This inverter includes six switches (MOSFETs or IGBTs) and six freewheeling diodes. By applying specific signals to these switches, induction machine can be operated properly.

Six-step drive method [**17**] is one of the simplest methods to drive the induction machine. Gate signals from the inverter are shown in Figure 96. In every electrical circle, each switch is turned on for 180 electrical degrees. The switching status of the upper and lower switches of each phase is always complementary in order to avoid short circuit. At the same time, for different phases, switching statuses are 120 electrical degrees phase shifted from each other. In other words, only three switches are turned on for every 60 electrical degrees. Two in high side and one in low side, or one in high side and two in low side. Therefore, for a wye-connected three phase induction machine, three six-stepped and quasi-sine phase voltages can be formed in the stator winding of the induction machine. These phase voltages are illustrated in Figure 96.

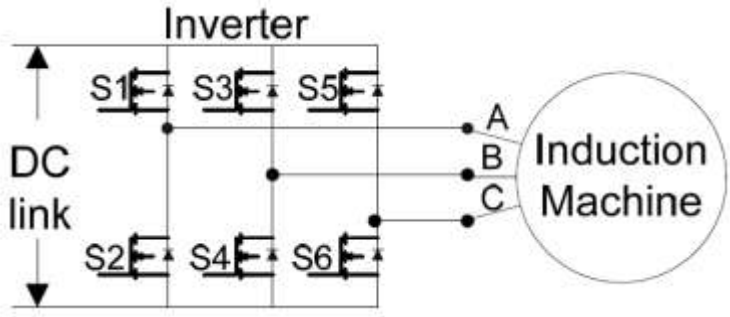

Figure 95: Inverter for induction machine

The implementation of the six-step drive method is also very simple. The electrical cycle is first divided into six equivalent regions with 60 degrees each. Then, each region corresponds to a specific

combination of switching status. These combinations can be described in Table 7. Finally, by generating these gate signals and applying them to the inverter with proper frequency, the induction machine can be operated.

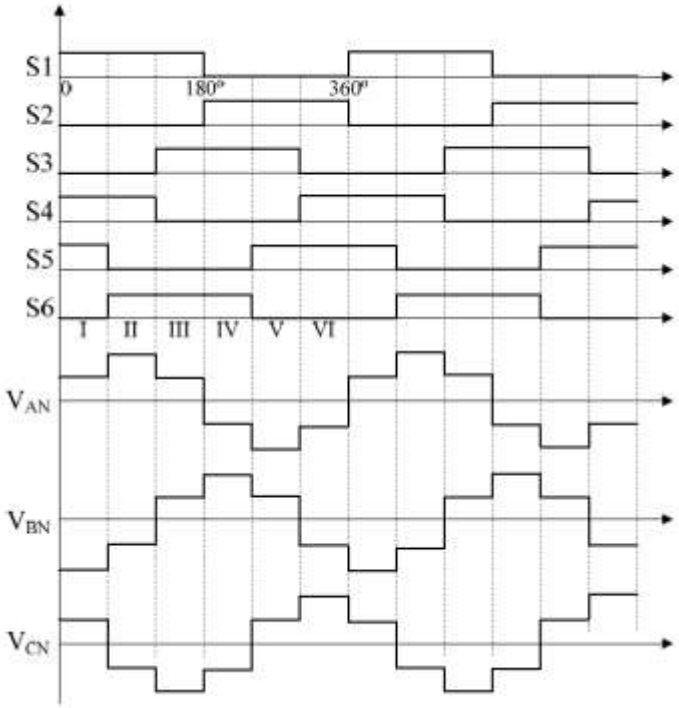

Figure 96: Six-Step waveform

Table 7: Switching Status for Different Regions of Six-step Drive Method

Region No.	Switch Status					
	S1	S2	S3	S4	S5	S6
I	ON	OFF	OFF	ON	ON	OFF
II	ON	OFF	OFF	ON	OFF	ON
III	ON	OFF	ON	OFF	OFF	ON
IV	OFF	ON	ON	OFF	OFF	ON
V	OFF	ON	ON	OFF	ON	OFF
VI	OFF	ON	OFF	ON	ON	OFF

Speed control of induction machine involves two parameters–the magnitude and frequency of the applied voltage across the phase winding. The frequency of the applied phase voltage mainly determines the shaft speed of the induction machine. This relationship can be explained in the following equations.

$$\omega_s = \frac{2\pi f_s}{P} \quad (8)$$

$$\omega_r = \omega_s(1-s) \quad (9)$$

where ωs is the synchronous speed of the induction machine in rad/s, fs is the frequency of the applied phase voltage in Hz, P is the number of pole pairs, ωr is the speed of the shaft in rad/s and s is the slip rate.

By changing the frequency of the phase voltage, the synchronous speed can be changed. At the same time, the variation of the synchronous speed results in the change of the shaft speed since shaft speed is very close to the synchronous speed at steady-state. Therefore, the shaft speed can be determined mainly by the frequency of the phase voltage. On the other hand, if the reference speed of the shaft is defined, we can also obtain the frequency of the applied phase voltage using equation (8) and (9).

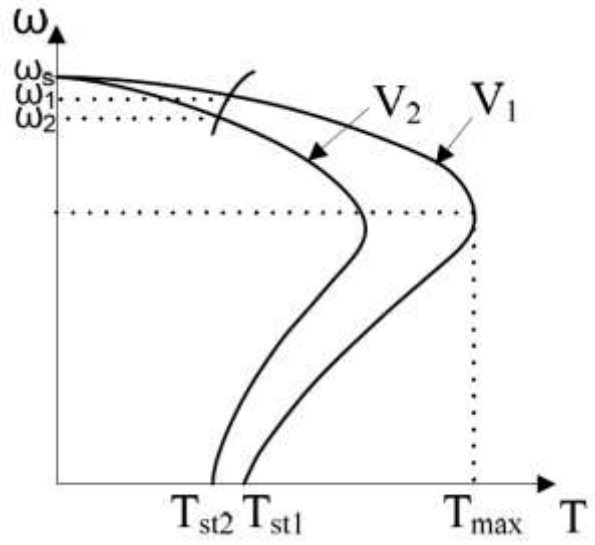

Figure 97: Speed torque characteristics at different voltage level

The magnitude of the applied phase voltage is also a factor which could affect the shaft speed. This relationship is shown in Figure 97 [**29**]. If the magnitude of the applied phase voltages is increased (V1>V2), the torque performance of the induction machine will be changed, as a result, the shaft speed will increase slightly (ω1>ω2), but the synchronous speed will be the same.

Based on the above analysis as well as the six-step drive method, a state transition control technique can be designed and expressed in Figure 98. According to the reference speed (ωref), the applied phase frequency can be defined using equation (8) and (9) if slip is approximated to be constant (roughly 5% in this case). By applying this frequency to the induction machine with proper magnitude of the phase voltage, shaft speed can be obtained, which is close to the reference. Then, by comparing the actual speed to the reference speed, the magnitude of the phase voltage can be switched between high

voltage level (VH) and low voltage level (VL). As a result, the actual speed (ωact) of the induction machine can be regulated accurately.

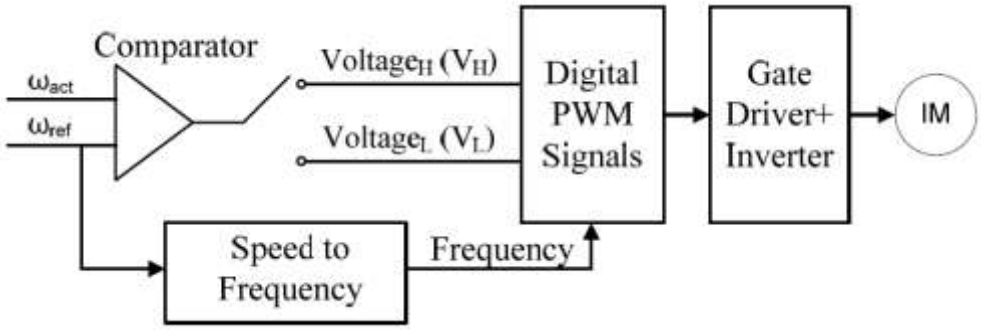

Figure 98: Principle of state transition control of induction machine

The change of the magnitude of the applied phase voltage is done by a new drive method—PWM six-step drive method. As shown in Figure 99, compared to traditional six-step drive method which is shown in Figure 96, switches are given PWM gate signals instead of turning them "ON" all the time for 60 electrical degrees. As a result, in Figure 99, the phase voltages are also PWM shaped if the load is resistive. Therefore, by changing the duty cycle of the PWM, the magnitude of the phase voltage of the induction machine could be changed.

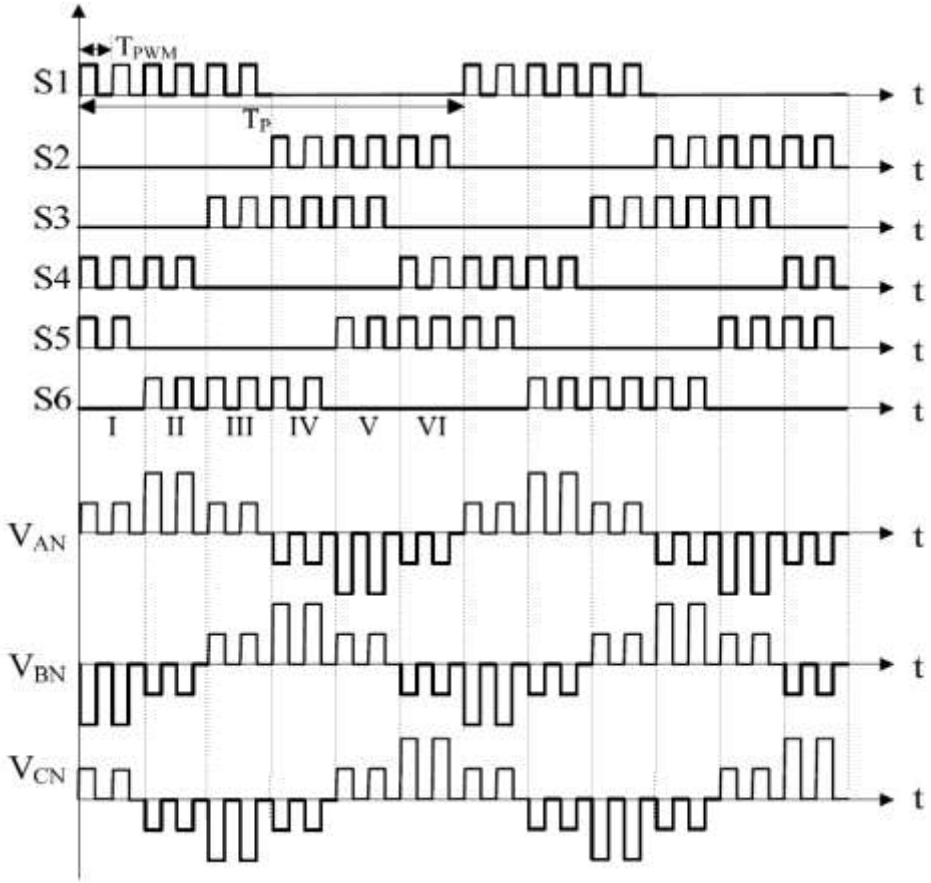

Figure 99: PWM six-step waveform

Therefore, the principle of the state transition control of induction machine can be shown in Figure 100 and concluded as follow:

1) The reference speed determines the frequency of the applied phase voltage. In our case, it determines the frequency of the six-step waveform.

2) The duty cycle (dL or dH) of the PWM is determined by comparing the actual speed (ωact) with the reference speed (ωref). The frequency of the PWM is set to 5 kHz in our case.

Table 8: Switching Status of PWM Six-step Drive Method

Region No.	Switch Status					
	S1	S2	S3	S4	S5	S6
I	PWM	OFF	OFF	PWM	PWM	OFF
II	PWM	OFF	OFF	PWM	OFF	PWM
III	PWM	OFF	PWM	OFF	OFF	PWM
IV	OFF	PWM	PWM	OFF	OFF	PWM
V	OFF	PWM	PWM	OFF	PWM	OFF
VI	OFF	PWM	OFF	PWM	PWM	OFF

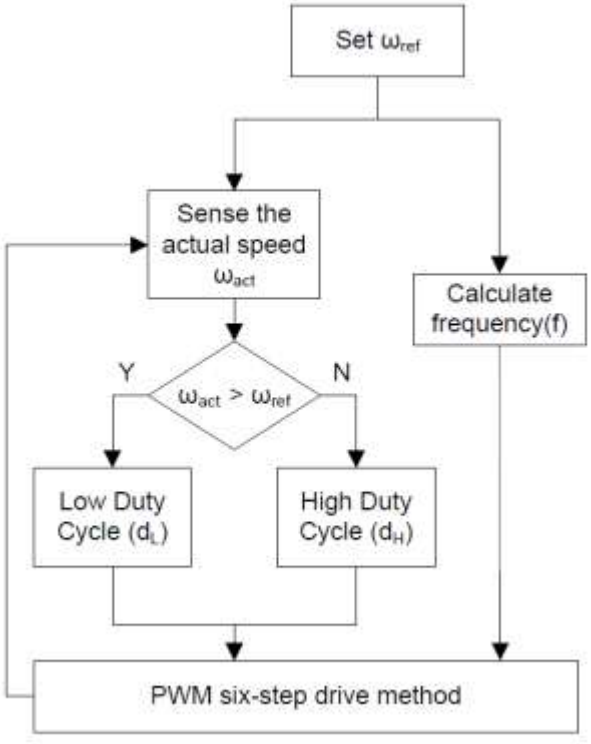

Figure 100: Principle of state transition control of induction machine

In order to design the controller, operating conditions for the induction machine and load conditions must be defined to calculate the frequency (which also defines TP of switch signals in Figure 99 and duty cycle of PWM (dL & dH). However, the first step is to find the relationship between angular velocity and operating parameters under steady-state conditions. From the torque equation, we have

$$T_e = J\frac{d\omega_m}{dt} + b\omega_m + T_L \tag{10}$$

Where Te is the generated electromagnetic torque, ωm is the rotor speed in rad/s, J is the rotor moment of inertia, b is the viscous friction constant and TL is the load torque.

The rotor induced torque of the induction machine is

$$T_e = \frac{3V_s^2 R_2 / s}{\omega_{syn}\left[\left(R_1 + R_2/s\right)^2 + \left(X_1 + X_2\right)^2\right]} \tag{11}$$

Where Vs is the magnitude of the applied phase voltage, ωsyn is the synchronous speed of the induction machine in rad/s, s is the slip, R1 and X1 refers to the stator impedance, R2 and X2 refers to the rotor impedance.

Substituting (11) into (10), we get

$$\frac{3V_s^2 R_2 / s}{\omega_{syn}\left[\left(R_1 + R_2/s\right)^2 + \left(X_1 + X_2\right)^2\right]} = J\frac{d\omega_m}{dt} + b\omega_m + T_L \tag{12}$$

(4.5)

At steady state, the shaft speed ωm and the slip s is constant. Meanwhile, stator and rotor impedances are also constant. As a result, (13) can be simplified as

$$k\frac{V_s^2}{\omega_{syn}} = b\omega_{mss} + T_L \tag{13}$$

Where ωmss is the rotor steady state speed and

$$k = \frac{3R_2 / s}{\left[\left(R_1 + R_2/s\right)^2 + \left(X_1 + X_2\right)^2\right]}$$

Therefore, the relationship between voltage magnitude and rotor speed can be obtained as

$$V_s = \sqrt{\frac{(b\omega_{mss} + T_L)\omega_{syn}}{k}} \quad (14)$$

In six step method, the magnitude of the applied phase voltage Vs is 2/3 of the DC link voltage VDC. If the duty cycle of the PWM is d, we get

$$\frac{2}{3} dV_{DC} = \sqrt{\frac{(b\omega_{mss} + T_L)\omega_{syn}}{k}} \quad (15)$$

Therefore, the relationship between the duty cycle and the rotor speed of the induction machine can be expressed as

$$d = \frac{3\sqrt{\frac{(b\omega_{mss} + T_L)\omega_{syn}}{k}}}{2V_{DC}} \quad (16)$$

From (16), the duty cycle is a function of the desired steady-state rotor speed. It can be used to find the necessary duty cycle to produce ωH and ωL. Let

$$d(\omega_{mss} = \omega_H) = d_H \quad (17)$$

$$d(\omega_{mss} = \omega_L) = d_L \quad (18)$$

Meanwhile, the frequency of the applied voltage can be calculated using (19) which is derived from (8) and (9). Slip is considered as a constant which equals to 5% in our simulation and experiment.

$$f = \frac{\omega_{ref} P}{2\pi(1-s)} \quad (19)$$

To obtain ωH, ωsyn can be calculated since slip is set to a constant value, which also determines the phase voltage frequency using (19). According to (16), the duty cycle of PWM must be equal to dH. Similarly, in order to obtain ωL, the duty cycle of PWM must be equal to dL.

Therefore, the state switching controller for induction machine can be implemented in the following procedure.

1) Find the following parameters of the induction machine from the manufacture's datasheet.

R1 and X1: Stator impedance

R2 and X2: Rotor impedance

b: Friction constant

2) Define the desired operating speed and specify the load torque TL. Specify ωH and ωL to cover the desired speed range.

3) Set slip to constant values for simplicity (5% in our case)

4) Use (16) to determine the values of dH and dL base on ωH and ωL.

5) Use (19) to calculate the frequency of the phase voltage (which also determines TP of switch signals in Figure 99)

At steady state, speed ripple is closely related to the sampling time. In order to minimize the speed ripple, the relationship between sampling time and speed ripple need to be defined. According to the torque equation listed in equation (10), we have the following differential equation:

$$\frac{d\omega_m}{dt} + \frac{b}{J}\omega_m = \frac{T_e - T_L}{J} \tag{20}$$

The speed response can be calculated as (21) by solving the above differential equation.

$$\omega_m(t) = \frac{T_e - T_L}{b} + Ce^{-\frac{b}{J}t} \tag{21}$$

where C is a constant. Suppose the steady state speed response can be shown in Figure 101, the upper side maximum speed ripple (ΔωH) happens after time t1 and the lower side maximum speed ripple (ΔωL) happens after t2.

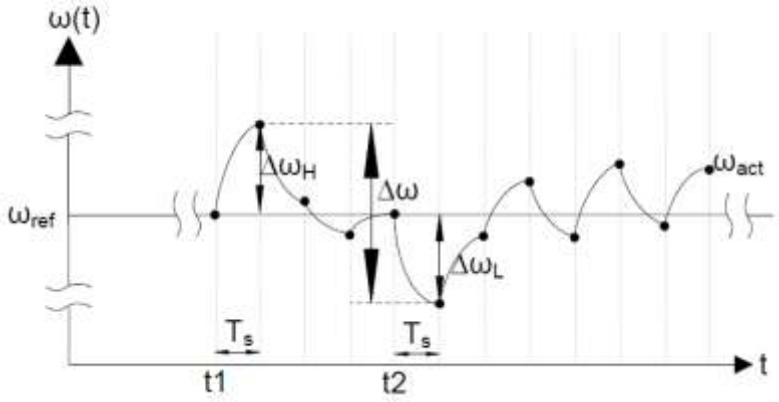

Figure 101: Speed response in steady state

At time t1, we have

$$\omega_m(t1) = \omega_{ref} = \frac{T_{e1} - T_L}{b} + Ce^{-\frac{b}{J}t1} \quad (22)$$

We get,

$$C = (\omega_{ref} - \frac{T_{e1} - T_L}{b})e^{\frac{b}{J}t1} \quad (23)$$

Therefore, at time t1+Ts,

$$\omega_m(t1 + T_s) = \frac{T_{e1} - T_L}{b} + (\omega_{ref} - \frac{T_{e1} - T_L}{b})e^{-\frac{b}{J}T_s} \quad (24)$$

$$\omega_m(t1 + T_s) = \omega_{ref} + \Delta\omega_H \quad (25)$$

During the sampling time period after t1, speed is increasing. We can define

$$T_{e1} - T_L = \Delta T_{em} \ (\Delta T_{em} > 0)$$

to get,

$$\Delta\omega_H = \frac{\Delta T_{em}}{b} + (\omega_{ref} - \frac{\Delta T_{em}}{b})e^{-\frac{b}{J}T_s} - \omega_{ref} \quad (26)$$

Similarly, at time t2,

$$\omega_m(t2) = \omega_{ref} = \frac{T_{e2} - T_L}{b} + Ce^{-\frac{b}{J}t2} \quad (27)$$

We get,

$$C = (\omega_{ref} - \frac{T_{e2} - T_L}{b})e^{\frac{b}{J}t2} \quad (28)$$

Meanwhile, at time t2+Ts,

$$\omega_m(t2 + T_s) = \frac{T_{e2} - T_L}{b} + (\omega_{ref} - \frac{T_{e2} - T_L}{b})e^{-\frac{b}{J}T_s} \quad (29)$$

$$\omega_m(t2+T_s)=\omega_{ref}-\Delta\omega_L \tag{30}$$

During the sampling time period after t2, speed is decreasing. Defining

$$T_{e2}-T_L=-\Delta T_{em}$$

we get,

$$\Delta\omega_L=\frac{\Delta T_{em}}{b}-(\omega_{ref}+\frac{\Delta T_{em}}{b})e^{-\frac{b}{J}T_s}+\omega_{ref} \tag{31}$$

Since

$$\Delta\omega=\Delta\omega_H+\Delta\omega_L$$

we have

$$\Delta\omega=2\frac{\Delta T_{em}}{b}(1-e^{-\frac{b}{J}T_s}) \tag{32}$$

As a result, we get the expression given in (33):

$$T_S=-\tau_m\ln\left(1-\frac{\Delta\omega}{2\omega_{\max}}\right) \tag{33}$$

where

τ_m is the mechanical time constant and ωmax is the maximum speed under no load condition.

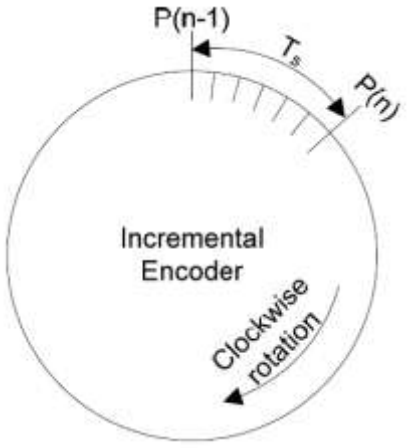

Figure 102: Instantaneous speed read from an incremental encoder

From (33), it can be seen that the smaller the sampling time results in better the speed tracking performance. However, in practical applications, speed tracking results is also limited by the resolution of the speed sensor. Suppose the encoder can generate Ptotal pulse per revolution and the speed of the shaft is ω rpm. The number of pulses generated in one second is ωPtotal/60. Therefore, the minimum sampling time (only one pulse can be detected within this sampling period) at speed ω is,

$$T_{S\_\min} = \frac{60}{\omega P_{total}} \tag{34}$$

This sampling time is often too small, which can cause significant instantaneous speed error. If an incremental encoder is used, instantaneous speed is defined in terms of pulses generated divided by its sampling time Ts and encoder's pulses-per-revolution Ptotal. This can be shown in Figure 102 and equations (35) and (36).

$$\omega(n) = 60\frac{P_{act}}{P_{total}T_s} \tag{35}$$

$$P_{act} = P(n) - P(n-1) \tag{36}$$

Where Pact is the actual pulses generated by the encoder during a sampling time Ts. Then, the speed error between reference speed and actual speed is,

$$e(n) = \omega_{ref}(n) - \omega_{act}(n) \tag{37}$$

$$e(n) = \frac{60}{P_{total}T_s}(P_{ref} - P_{act}) \tag{38}$$

In (38), Pref is reference pulses generated during each sampling time Ts. In order to minimize the instantaneous speed error, pulse error should be kept small (|Pref –Pact|=1) while sampling time Ts should be maintained as large as possible. This can be proved by experimental results shown in Figure 103 and Figure 104. Figure 103 and Figure 104 shows the instantaneous speed tracking error of the proposed state switching control under no load condition when reference speed is 1025rpm. Figure 103 shows that when sampling frequency is 5 kHz, the minimum pulse variation is one pulse which corresponds to 73.2 rpm in speed error (Ptotal =4096 pulses in our case). However, as shown in Figure 104, if the sampling frequency is increased to 10 kHz, the pulse variation stays at the minimum value (one pulse). But instantaneous speed error increases to 146.5 rpm since the sample time is half of the previous case. The detailed speed error versus sampling time under different conditions is plotted in Figure 105 through experiments. A range of sampling time (from 0.2ms to 2.8ms) is defined which ensures the performance of state switching control. In our case, 1ms (1kHz) is chosen as the sampling time, which not only ensures the speed tracking performance of state switching control, but also guarantees the fast response of the control strategy.

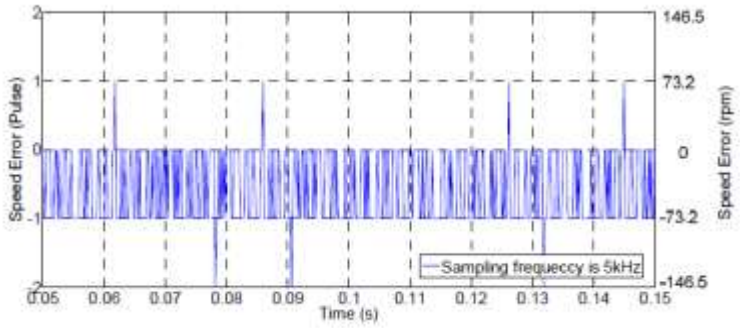

Figure 103: Speed error when sampling frequency is 5kHz

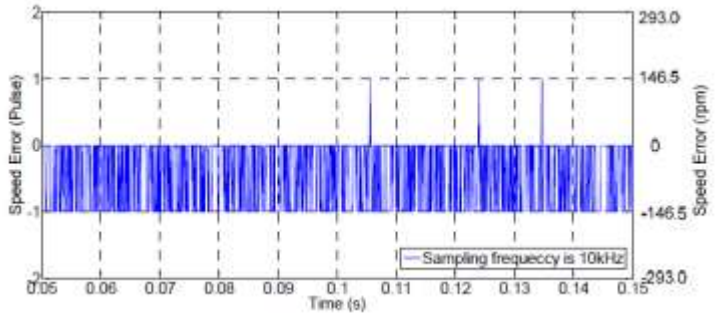

Figure 104: Speed error when sampling frequency is 10kHz

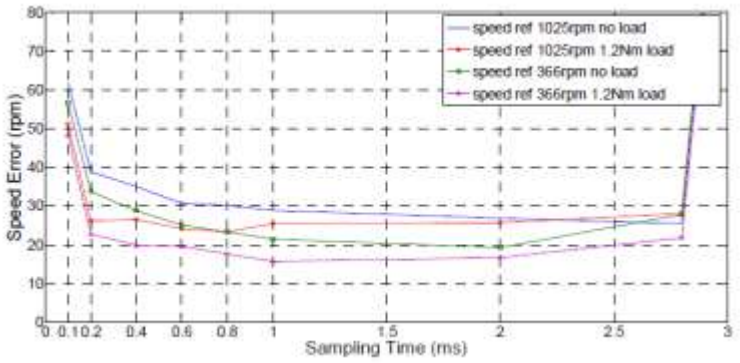

Figure 105: Speed error under different conditions

In practical implementation, deadband must be added to switch signals shown in Figure 99. Otherwise, it might cause short circuit when region changes and damage power components. For example, as shown in Figure 99, when region change from region I to region II, S5 tries to change from PWM to OFF state. At the same time, S6 tries to change from OFF state to PWM state. For safety consideration, S5 must be turned OFF before S6 is turned ON. As a result, deadband is required to be inserted into these signals. The insertion of deadband to switch signals can be easily done by turning OFF all the switches at the instant when transition of region occurs. The modified PWM six step waveforms can be illustrated in Figure 106 with deadband in red circles. However, this results in significant spikes in phase voltages during region transition moment. Figure 107 shows measured phase voltage and phase current in the

induction machine when gate signals in Figure 106 is applied to the switches with duty cycle of PWM equals to 100%. The six-stepped phase voltage can be clearly noticed and large spikes exist during region transition instant. These spikes are induced due to the rapid change of current flowing back to the source when all the switches are turned OFF. In order to eliminate these spikes, further improvement can be done by turning OFF two switches during transition. The improved gate signals are shown in Figure 108 with deadband in red circles. This time only two switches will be turned OFF during each transition. Figure 109 shows the hardware results of phase current and phase voltage with reduced spikes.

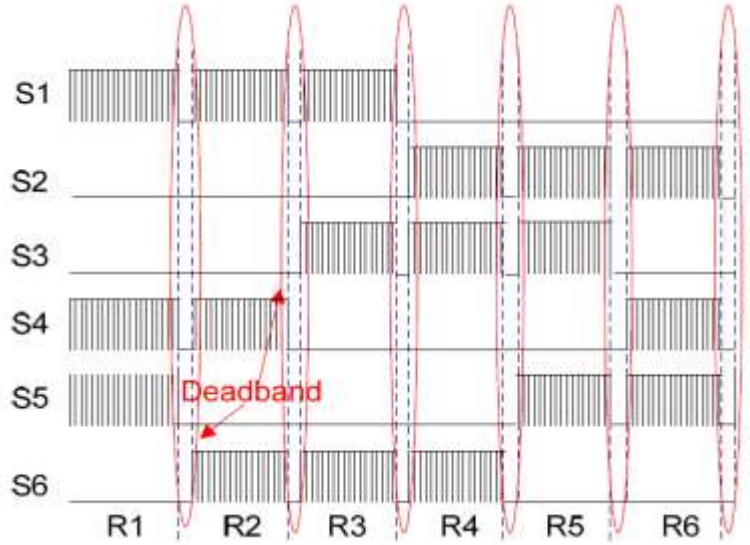

Figure 106: PWM six-step waveform with deadband

In order to verify the feasibility of the proposed state transition control of induction machine, simulation is implemented in Matlab/Simulink. The block diagram of the proposed state transition control of induction machine in simulation is shown in Figure 110, in which a 60Hz, 4 pole induction machine is used with a rated speed of 1725rpm.

Figure 111 shows the speed response of the proposed digitally controlled induction machine. Although the actual speed has a little oscillation during starting period, it quickly settles down and precisely tracks the reference speed.

Figure 112 to Figure 114 is simulation results in steady-state. Figure 112 shows the steady-state speed of the induction machine. The speed error between reference speed and actual speed is very small. Figure 113 shows the change of duty cycle during steady-state. Figure 114 shows the phase current of the induction machine.

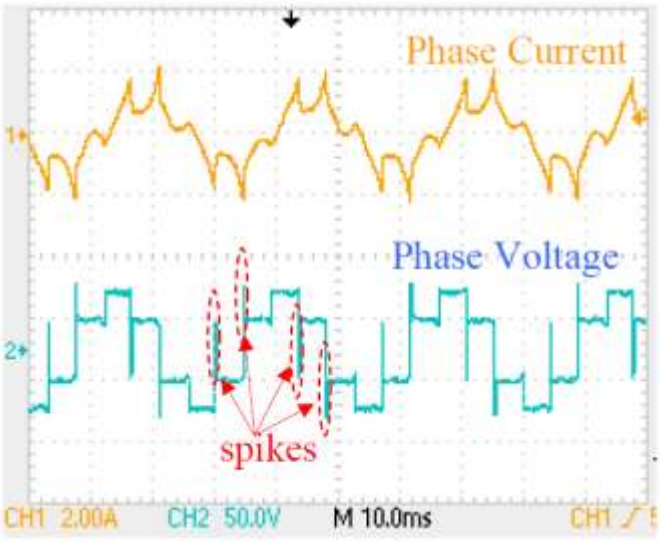

Figure 107: Induction Machine Phase Voltage with spikes

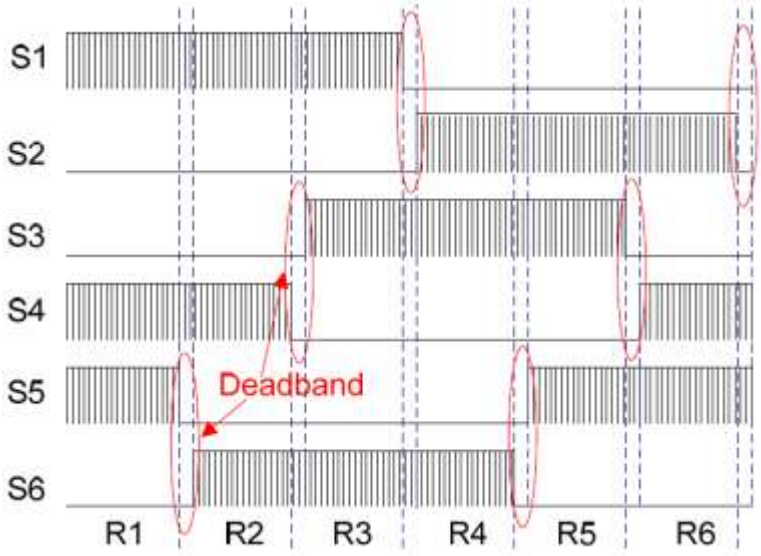

Figure 108: PWM six-step waveform with deadband

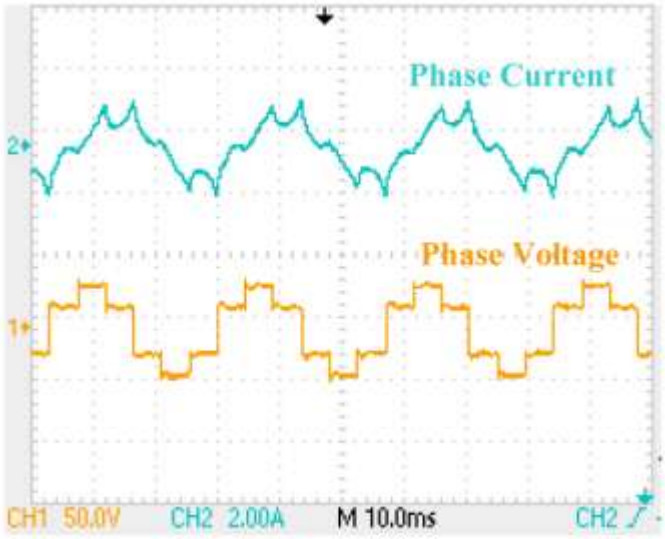

Figure 109: PWM six-step waveform with deadband

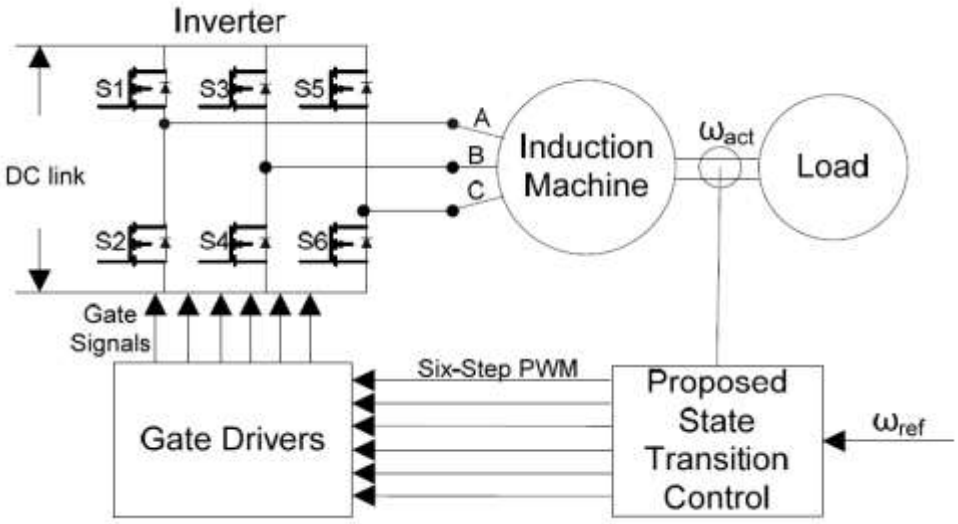

Figure 110: Block diagram of the proposed state transition control of Induction Machine

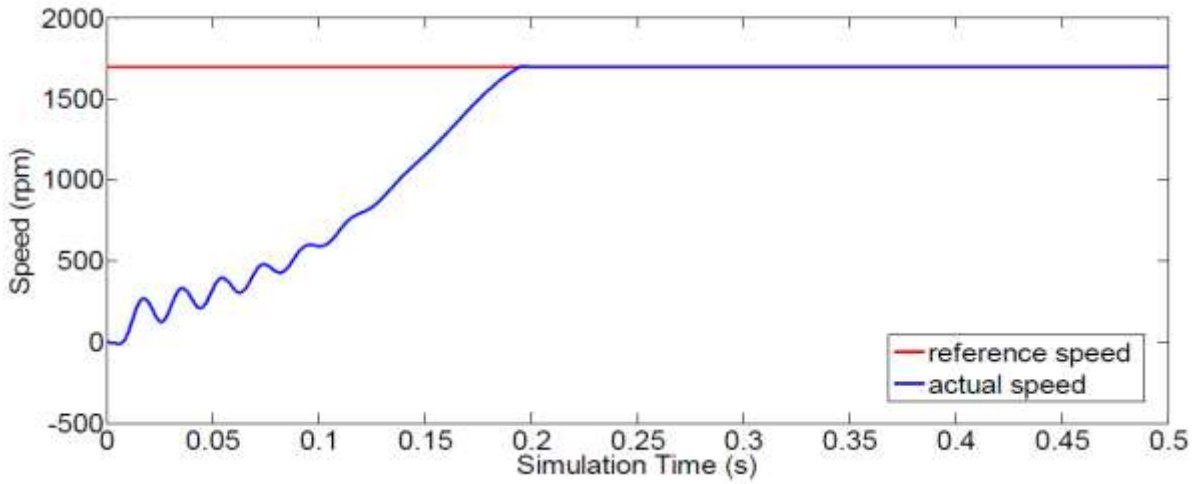

Figure 111: Speed response of the state transition control of induction machine

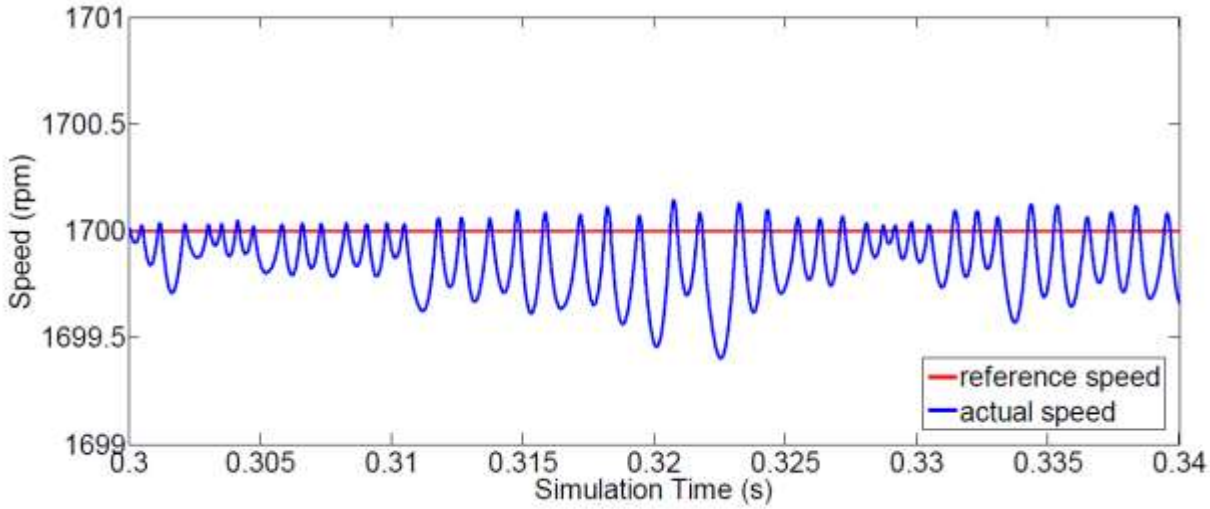

Figure 112: Speed response in steady-state

In order to verify the effectiveness of the proposed state transition control method for induction machine as well as its simulation results, an experimental setup has been developed which is shown in Figure 115. It includes a DC power supply, a TMS320F2812 based DSP controller, three phase inverter and gate drivers, voltage and current sensors, a torque sensor, an induction machine and a PM DC Load. Specifications regarding the induction machine and the PM DC load are listed in Table 9.

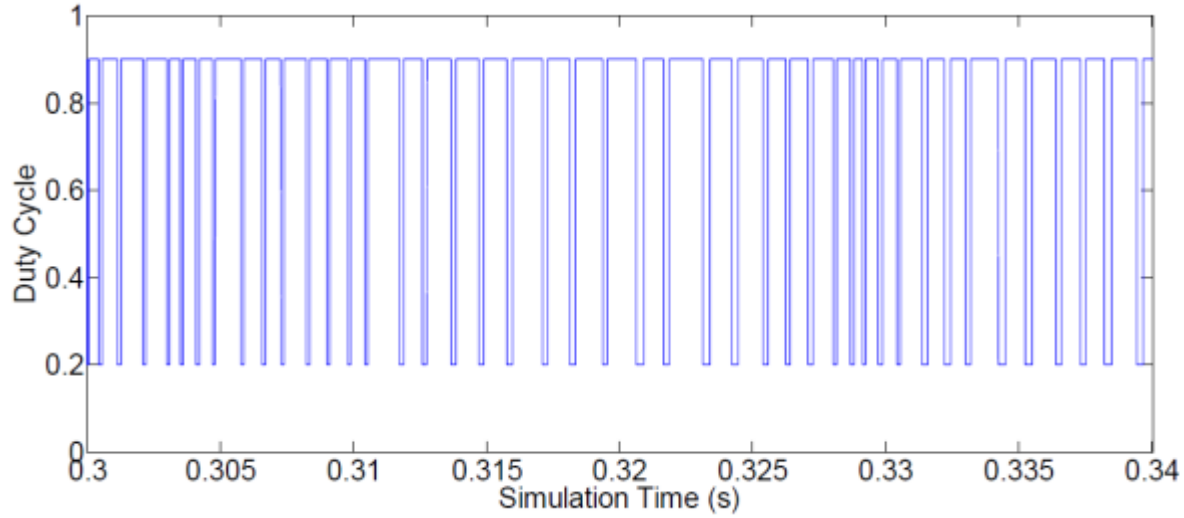

Figure 113: Change of duty cycle in steady-state

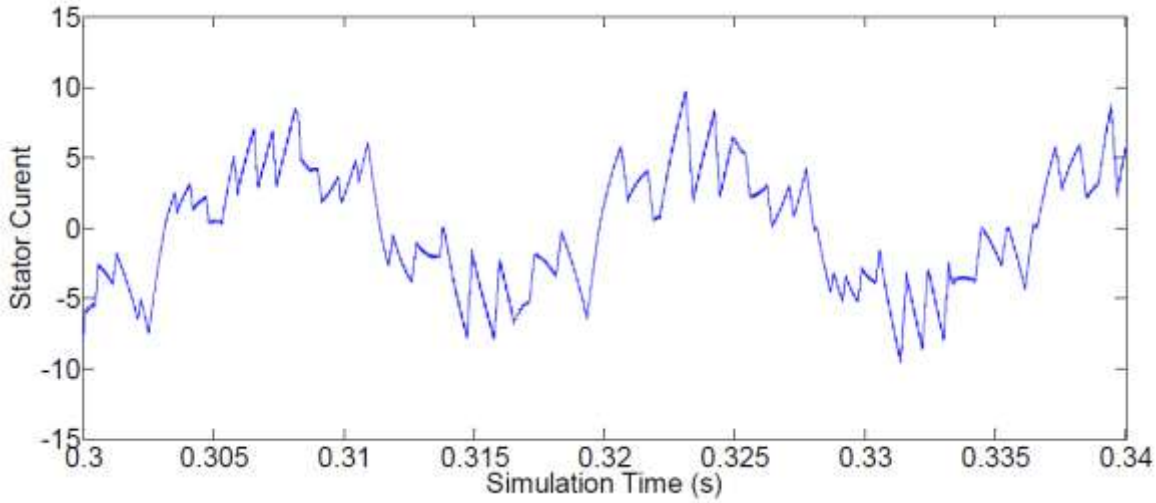

Figure 114: State current in steady-state

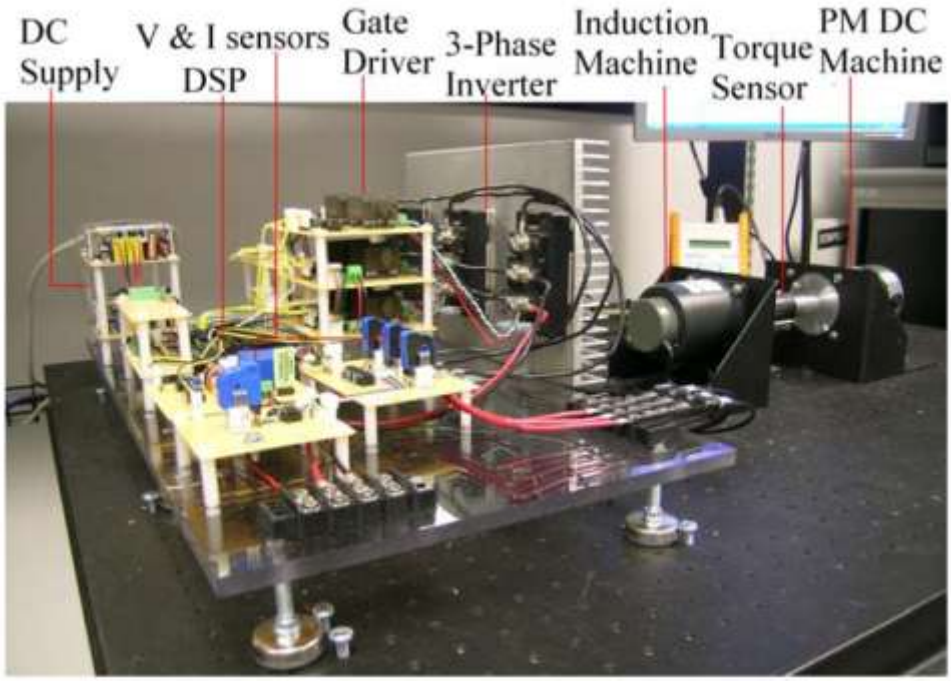

Figure 115: Hardware setup for experimental verification of proposed state transition control strategy of an Induction Machine

Table 9: Parameters of the Induction Machine and DC Brush Load Used

	Induction Machine	PM DC Load
Rated Power	130 watts	250 watts
Rated RPM	3396	4000
Rated Volts	30VAC	42V
Rated Current	3.93 A/phase	8.4 A/phase
No. of poles	4	2
No. of phases	3	N/A

Figure 116 to Figure 123 show experimental results obtained from the setup under different operating conditions. Figure 116 shows the speed response of the induction machine when reference speed is 2850rpm (84% of the rated speed) and load is 0.15Nm. Figure 117 shows the corresponding duty cycle. From these two figures, we find out that the speed response can be divided into two regions: acceleration and steady state (constant speed). During acceleration, a constant high duty cycle PWM is applied to the induction machine since the reference speed is greater than actual speed. During steady state, the duty cycle of PWM begins to switch between high duty cycle and low duty cycle since the actual speed is varying about the reference speed. The current profile during the acceleration is shown in Figure 118 and the current profile during the steady state is shown in Figure 119.

Similarly, Figure 120 and Figure 121 show results when the reference speed is 2250rpm (66% of the rated speed) and 1125rpm (33% of the rated speed) respectively and load is 0.15Nm. From these figures, it can be noticed that the proposed state transition control method has a wide range of speed control capability.

In order to test the performance of the control strategy for sensitivity to change in operating conditions, a step change in reference speed was applied to the machine. Figure 122 and Figure 123 shows the response of the induction machine when reference speed was changed.

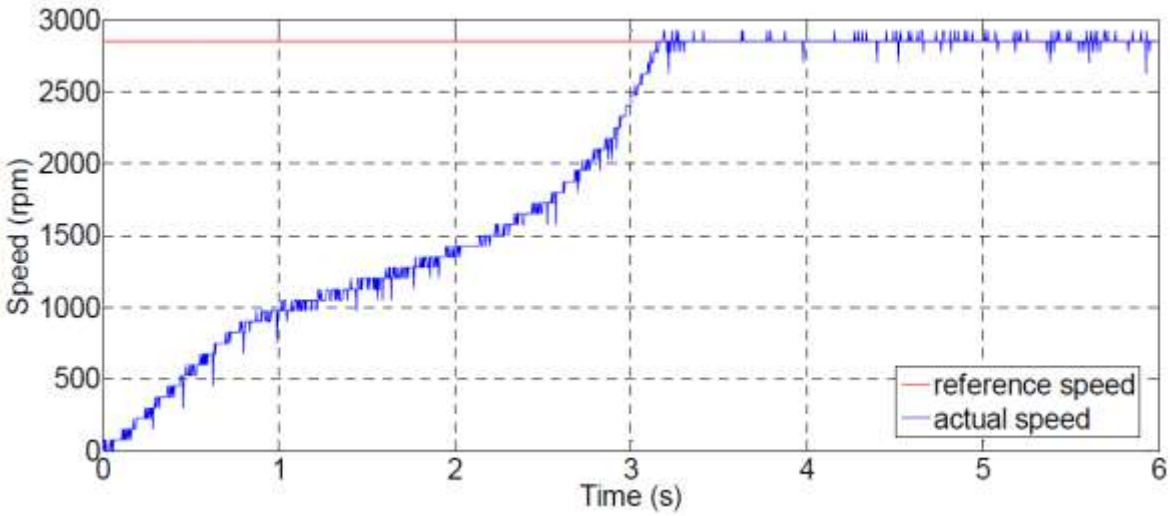

Figure 116: Speed response when reference speed is 2850rpm

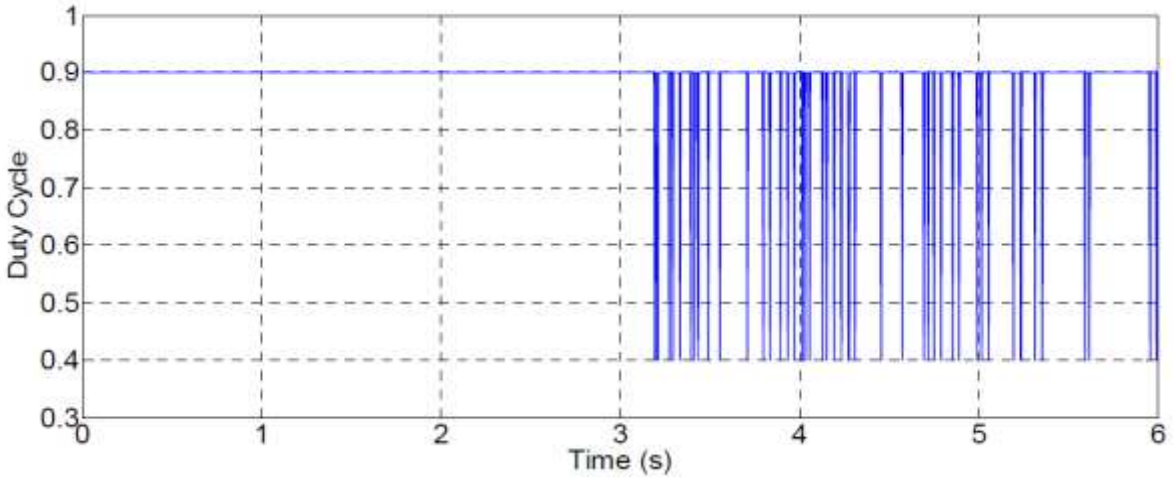

Figure 117: PWM duty cycle profile when reference speed is 2850rpm

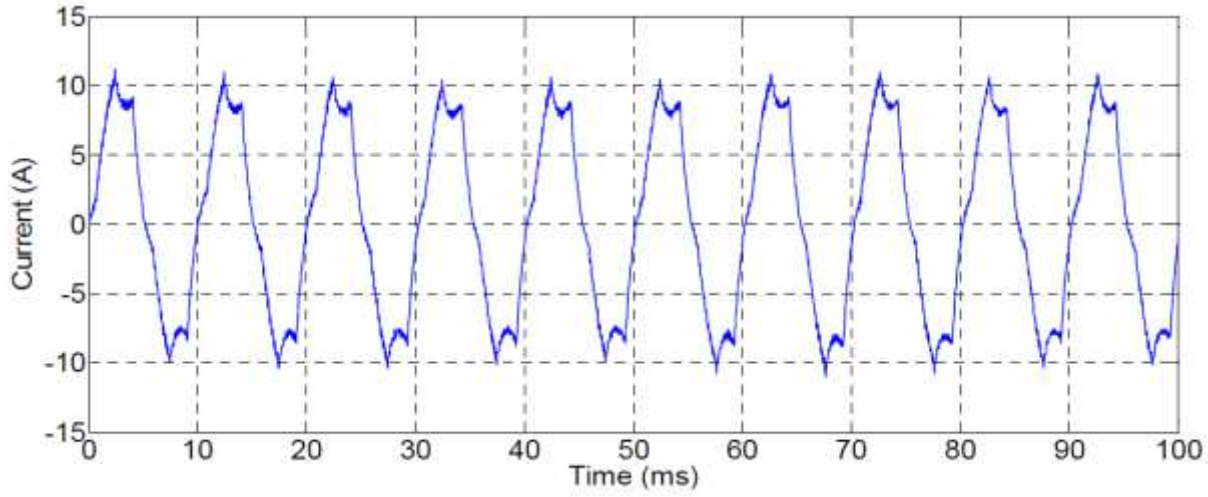

Figure 118: Phase current of Induction machine during start-up when reference speed is 2850rpm

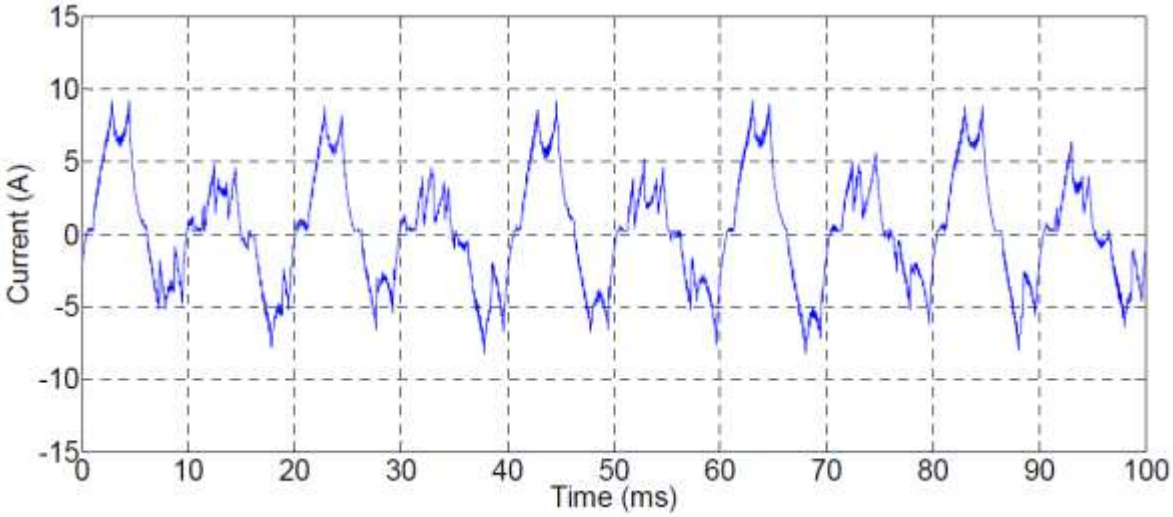

Figure 119: Phase current of Induction Machine during steady-state when reference speed is 2850rpm

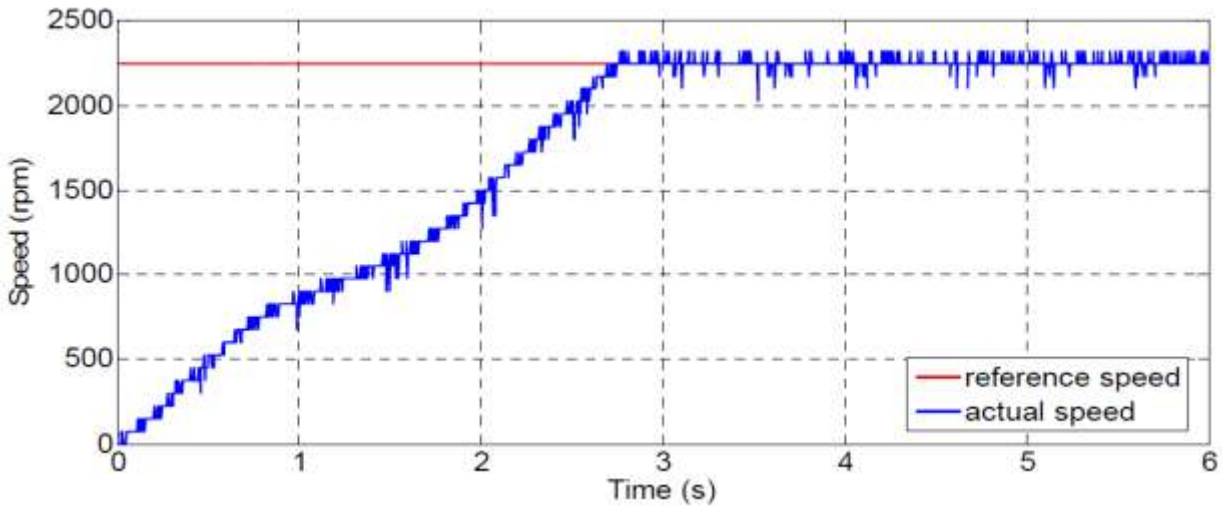

Figure 120: Speed response when reference speed is 2250rpm

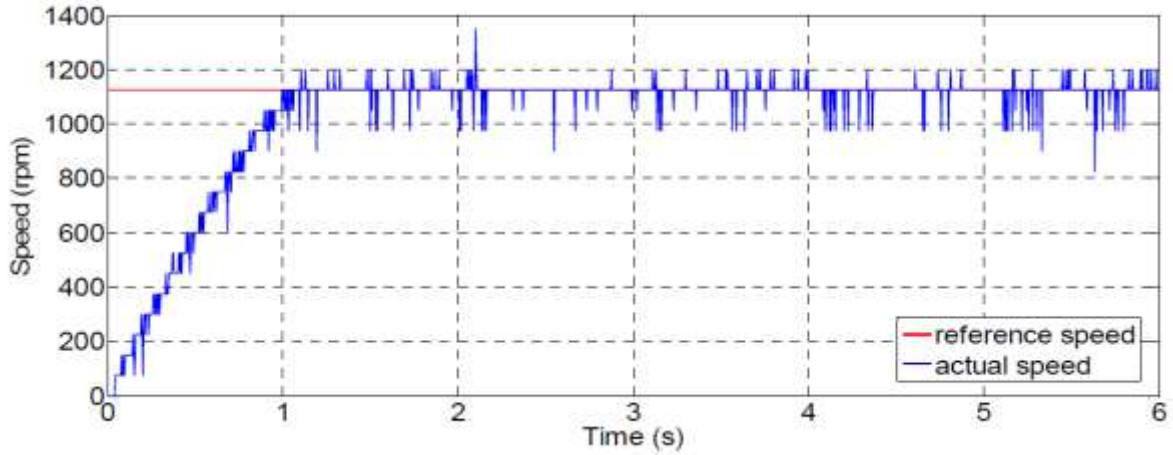

Figure 121: Speed response when reference speed is 1125rpm

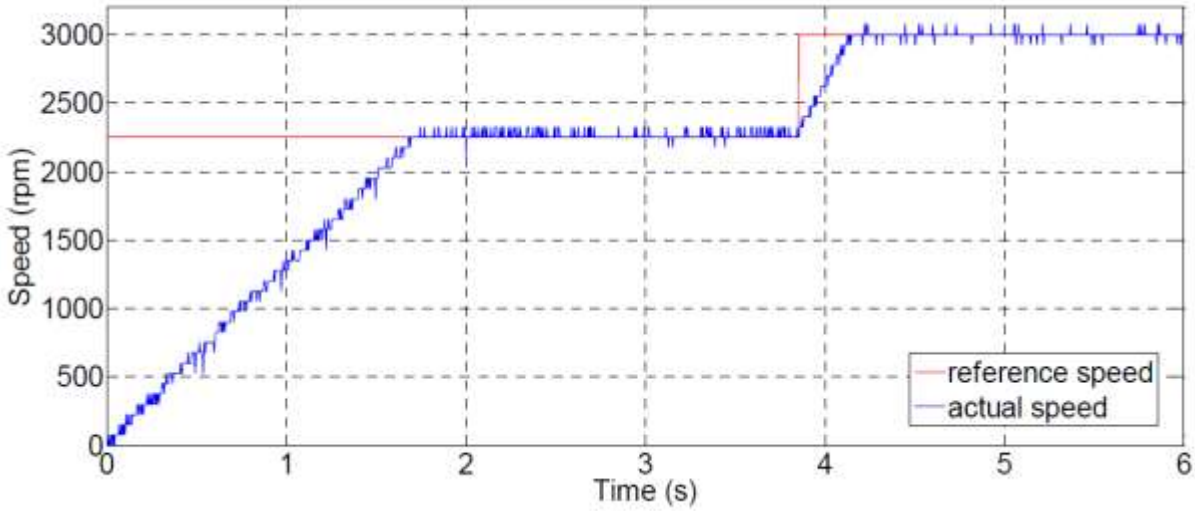

Figure 122: Step change of speed from 2250rpm to 3000rpm

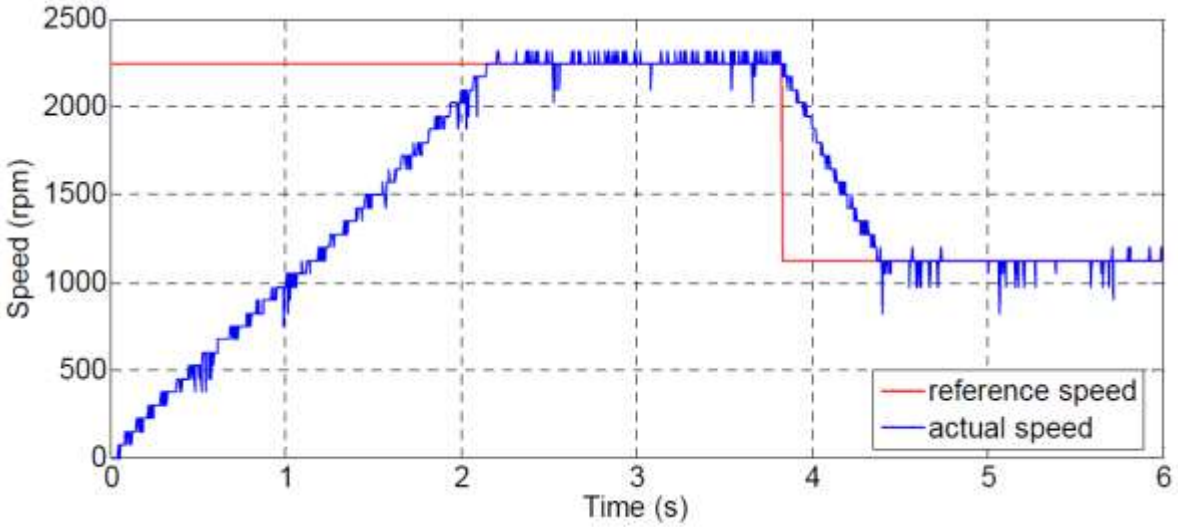

Figure 123: Step change of speed from 2250rpm to 1125rpm

From the results obtained, it can be seen that the speed ripple was found in an acceptable range under different conditions. This shows the effectiveness of the control scheme. In addition, the system responds to any change in speed command within an acceptable time period.

In order to further validate the effectiveness of the proposed state switching control. The experimental setup has been upgraded to PCB boards with kilowatt level induction machine installed which is shown in Figure 124. It includes a 3kW PM DC Load, a 2.2kW induction machine, a speed encoder, a TMS320F2812 based DSP controller, three-phase inverter and gate drivers. Specifications of the induction machine and the PM Dynamometer are listed in Table 10.

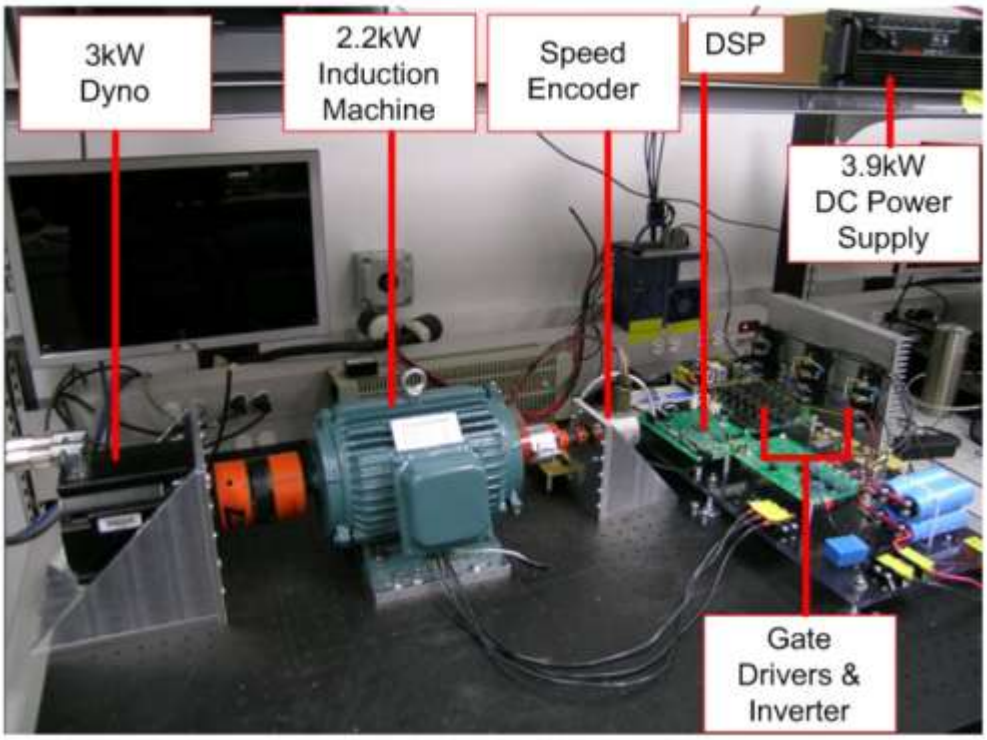

Figure 124: Hardware setup for experimental verification of proposed state switching

Table 10: Parameters of the Induction Machine and DC Brush Load Used

	Induction Machine	PM Dyno
Rated Power	2.2kW	3 kW
Rated RPM	1420	6000
Rated Volts	380/Y Conn.	640DC
Rated Current	5A/phase	12.4A/phase
No. of poles	4	N/A
No. of phases	3	3

Figure 125 to Figure 132 show experimental results obtained from the setup under different operating conditions. Figure 125 shows the speed response of the induction machine when reference speed is 1025rpm under a load torque of 1Nm. It can be seen that the actual speed of the induction machine quickly settles down to the reference and tracks precisely without any overshoots, which verifies fast dynamic response of this control method. Figure 126 shows the phase current profile and the change of PWM duty cycle between DH and DL. As mentioned previously, presence of harmonics in the phase current is the main trade-off in the implementation of this control technique.

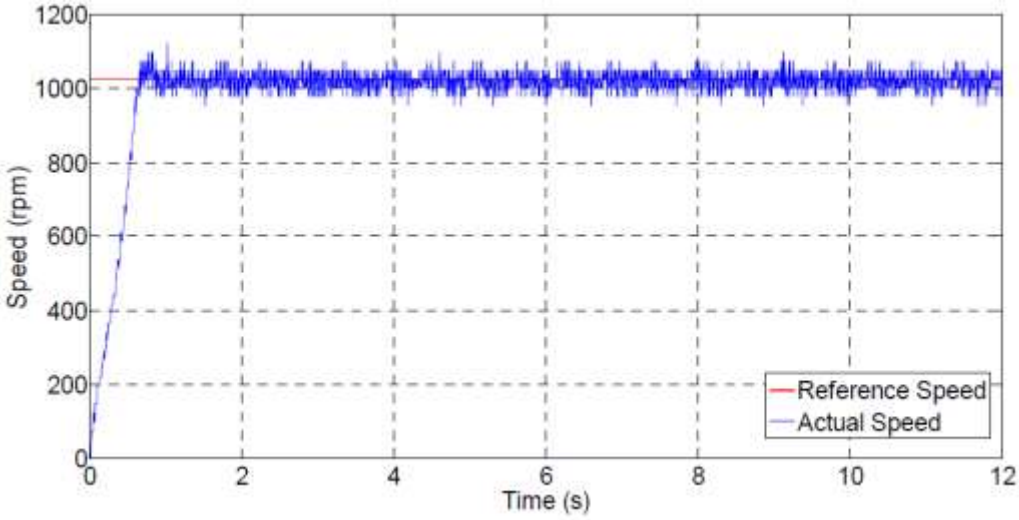

Figure 125: Speed response when reference speed is 1025rpm and load torque is 1Nm

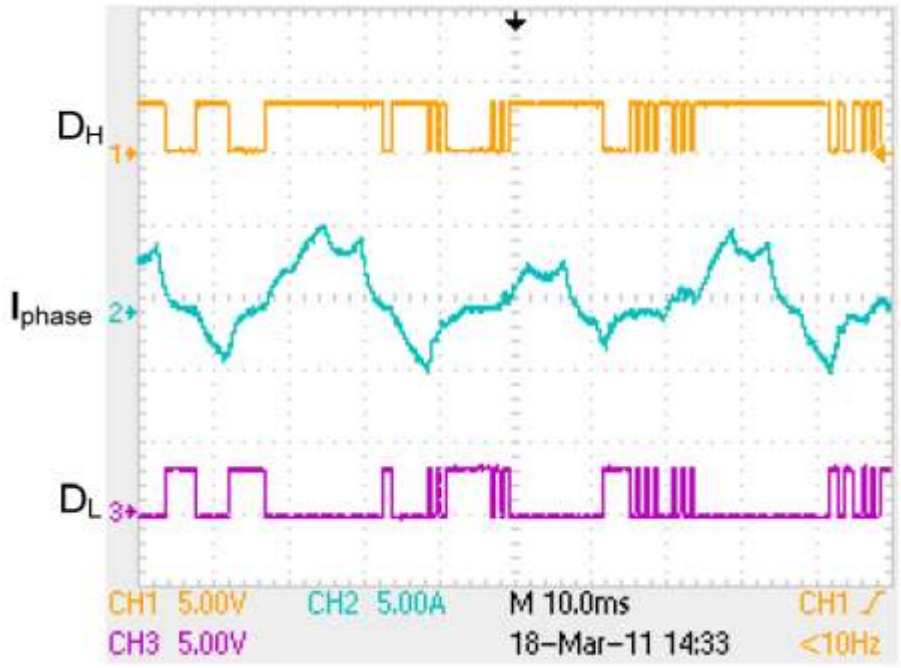

Figure 126: Phase current and change of PWM duty cycle when reference speed is 1025rpm

Similarly, Figure 127 and Figure 128 show results when reference speed is 366rpm and load is 1Nm. From these figures, it can be noticed that the proposed state switching control method also has a wide range of speed regulation capability.

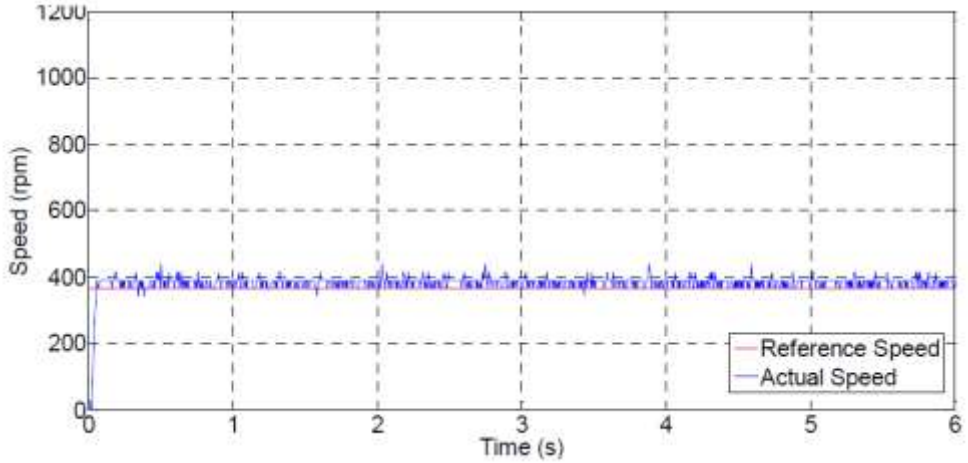

Figure 127: Speed response when reference speed is 366rpm and load torque is 1Nm

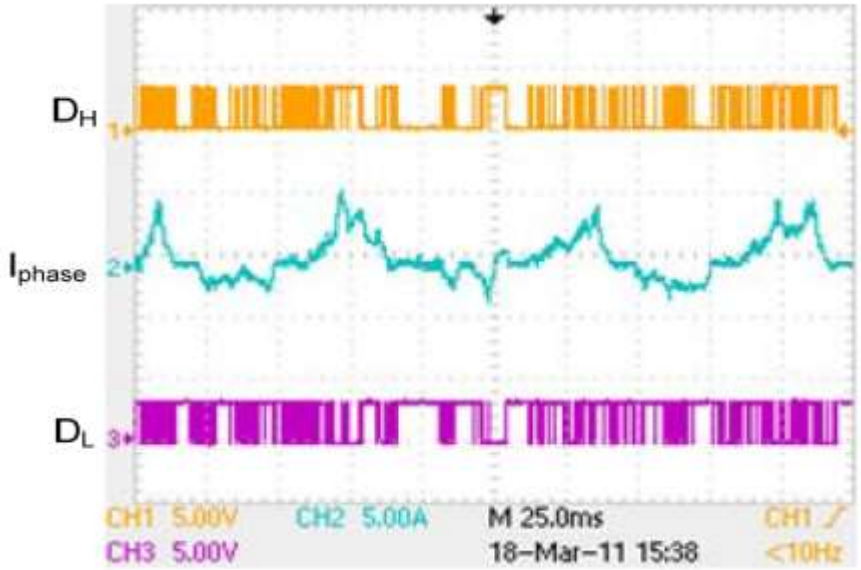

Figure 128: Phase current and change of PWM duty cycle when reference speed is 366rpm

In order to test the performance of the control strategy for sensitivity to change in operating conditions, a step change in load torque and reference speed was applied to the machine. Figure 129 shows the speed response of the induction machine when load torque was changed from 0.5Nm to 1.5Nm. Figure 130 and Figure 131 shows the phase current, change of PWM duty cycle before and after torque change respectively. Figure 132 shows the speed response of the induction machine when reference speed was changed from 1025rpm to 366rpm (load torque is 1Nm). The measured results show that the proposed control strategy allows the system to respond to any change in speed command within an acceptable time period.

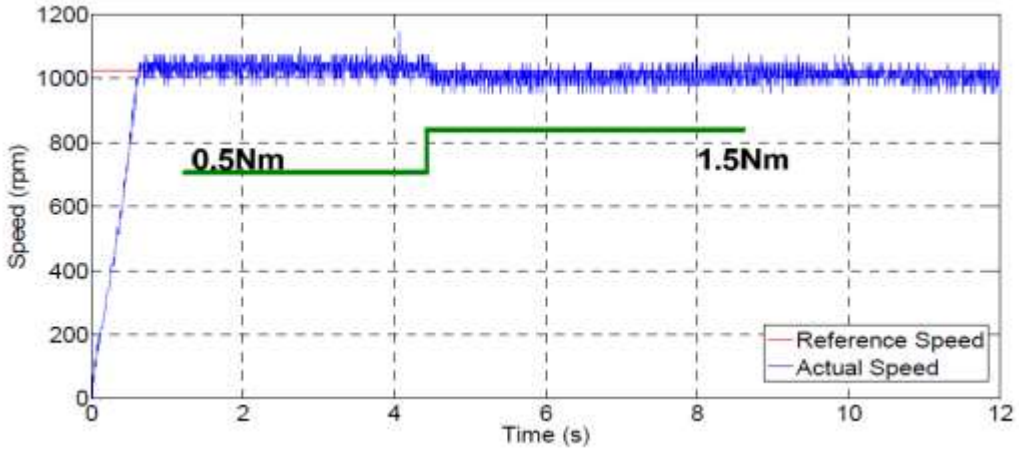

Figure 129: Speed response when reference speed is 1025rpm and load torque changes from 0.5Nm to 1.5Nm

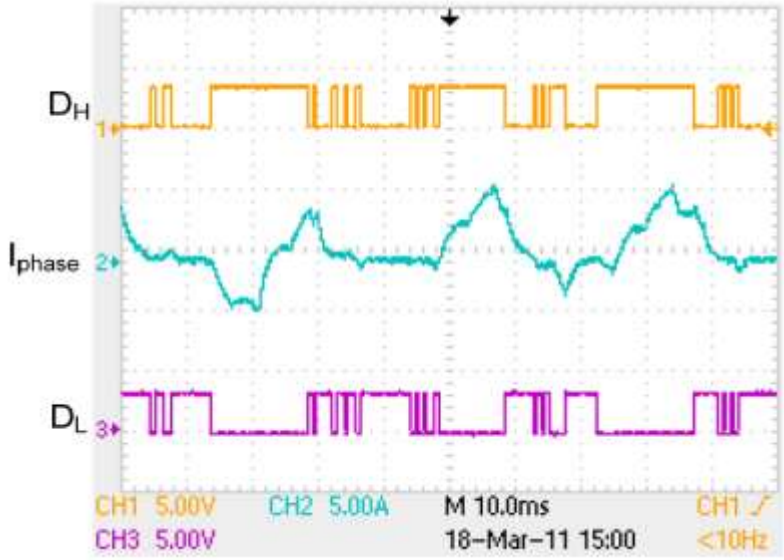

Figure 130: Phase current and change of PWM duty cycle when load torque is 0.5Nm

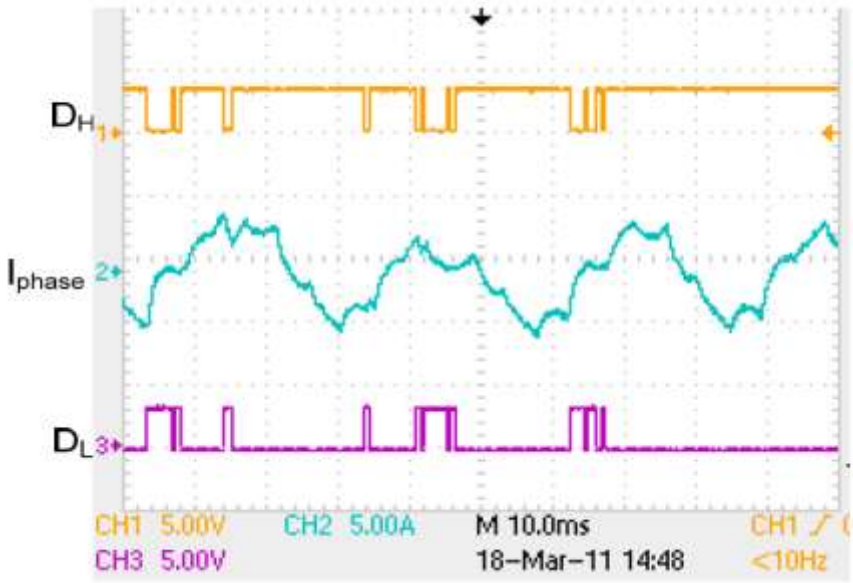

Figure 131: Phase current and change of PWM duty cycle when load torque is 1.5Nm

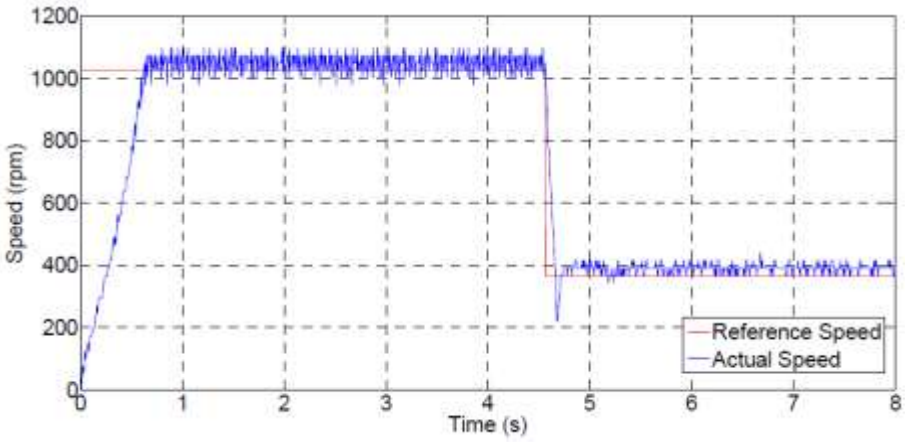

Figure 132: Speed response when reference speed changes from 1025rpm to 366rpm

The block diagram of the proposed state transition control of induction generator in Simulink is shown in Figure 133. A 60Hz, 4 pole induction machine is used with a rated speed of 1725rpm. Two different PWM duty cycles are defined at 30% and 90%. Simulation results are shown in Figure 134 and Figure 135. Figure 134 shows the speed response of the proposed digitally controlled induction machine. The speed quickly settles down and precisely tracks the reference speed. Figure 135 shows the steady-state speed error between reference speed and actual speed and the corresponding duty cycle adjustment.

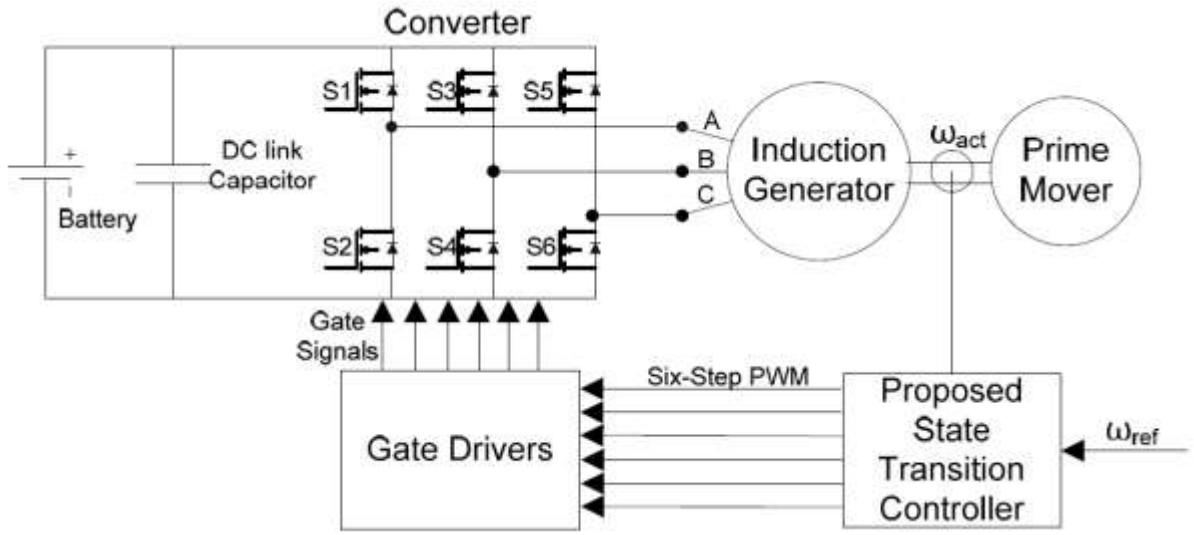

Figure 133: Block diagram of state transition control of Induction Generator

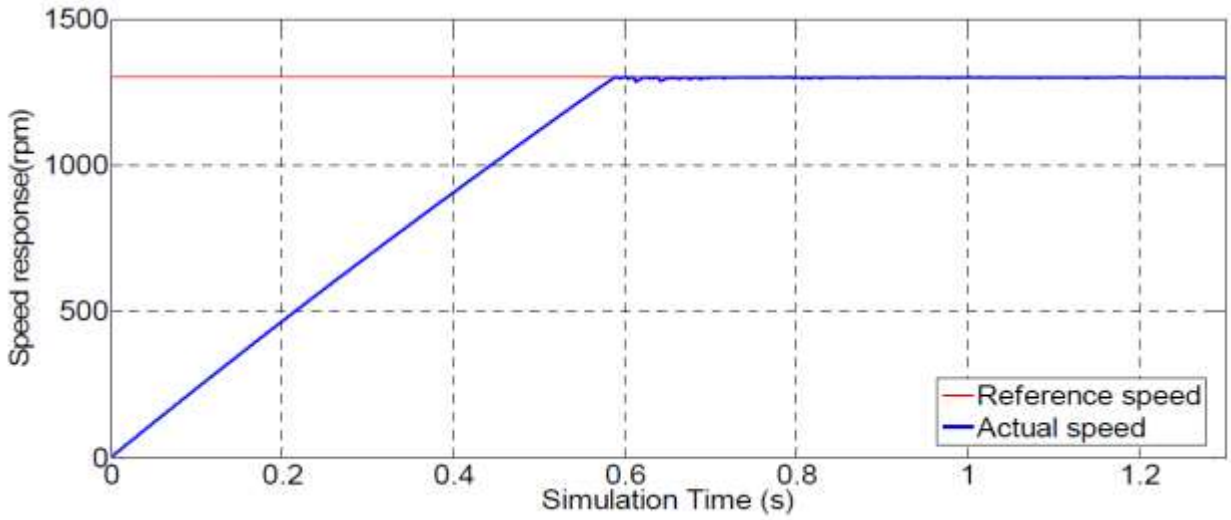

Figure 134: Speed response of the induction generator

The proposed state switching control method for induction generator is verified on the 2.3kW induction machine setup, as shown in Figure 136. Figure 137 to Figure 145 show experimental results obtained from the setup under different operating conditions. Figure 137 shows the speed response of the induction generator when reference speed is set to 1025rpm and the torque of prime mover is 1Nm. Since the prime mover is turned on before starting the induction generator, initial speed at startup increases to 1500rpm. Once the induction generator is started and state switching control is applied, speed quickly settles down to the reference speed with a steady state error lower than 7%. Figure 138 shows the generated DC link voltage and DC link current flowing into the dump resistor and the change of duty cycle between DH and DL. It is clear that the average DC link current is positive which confirms the operation of the IM in generating mode. Figure 139 shows the steady state phase current as well as

the change of duty cycle. It can be observed that the phase current has significant harmonics which is the main trade-off in the implementation of this control technique.

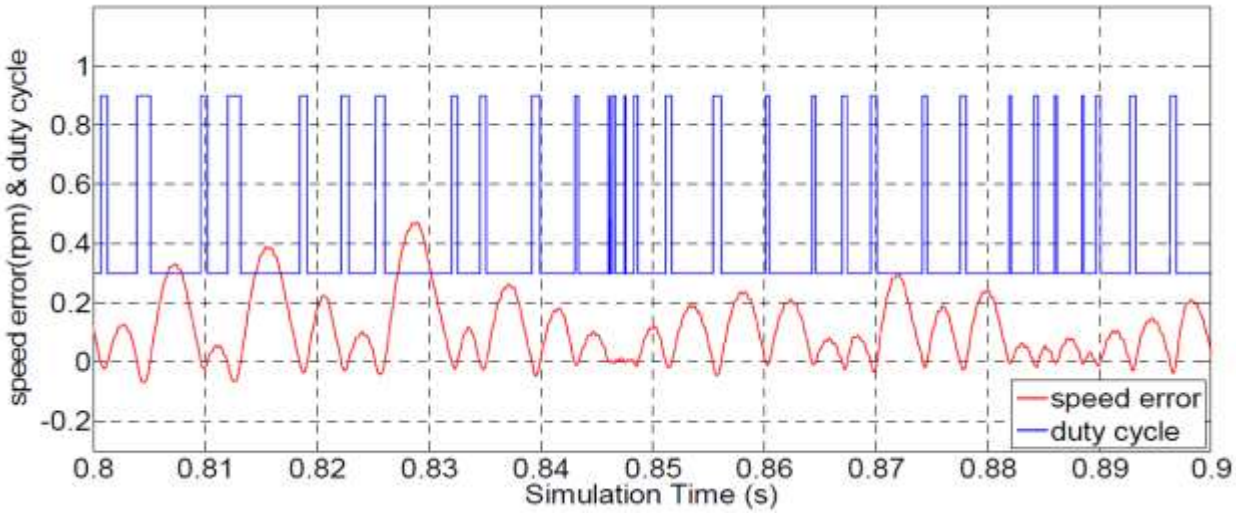

Figure 135: Steady state error and change of duty cycle

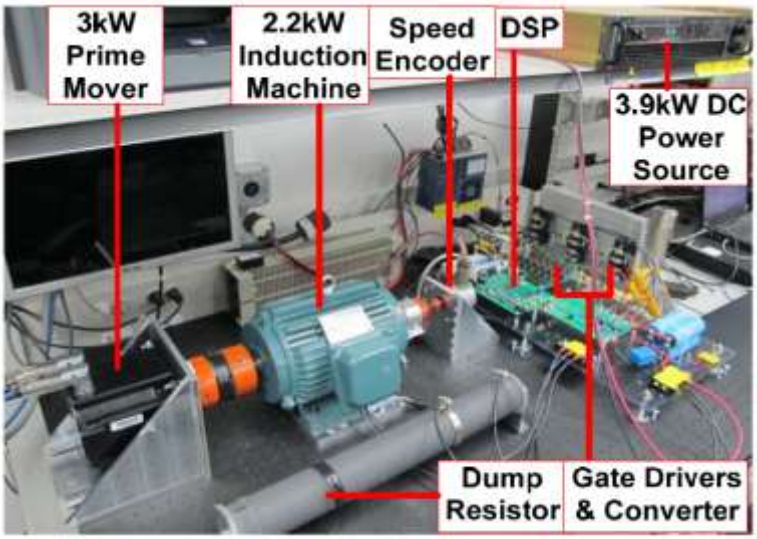

Figure 136: Hardware setup for experimental verification of proposed state switching control strategy of an Induction Generator

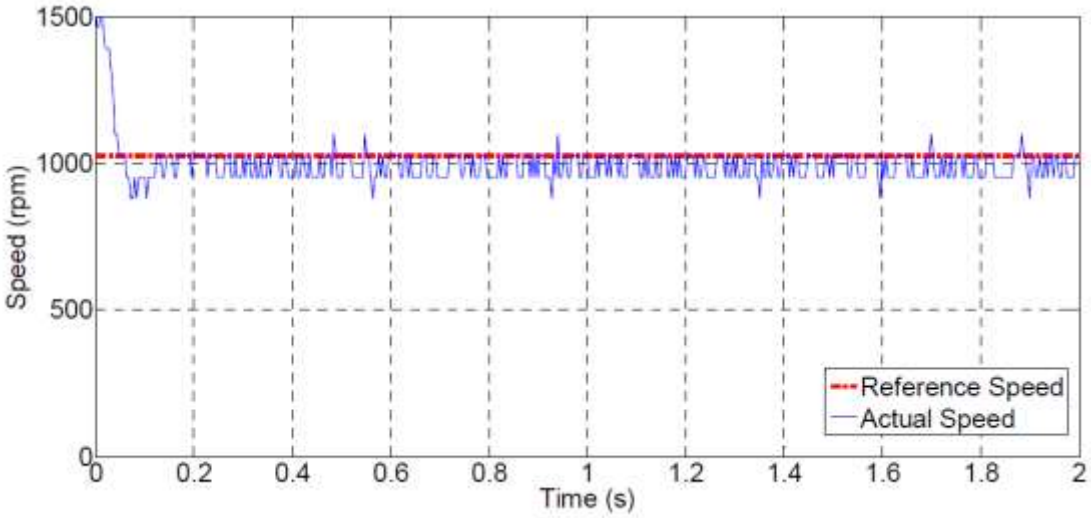

Figure 137: Speed response when reference speed is 1025 rpm

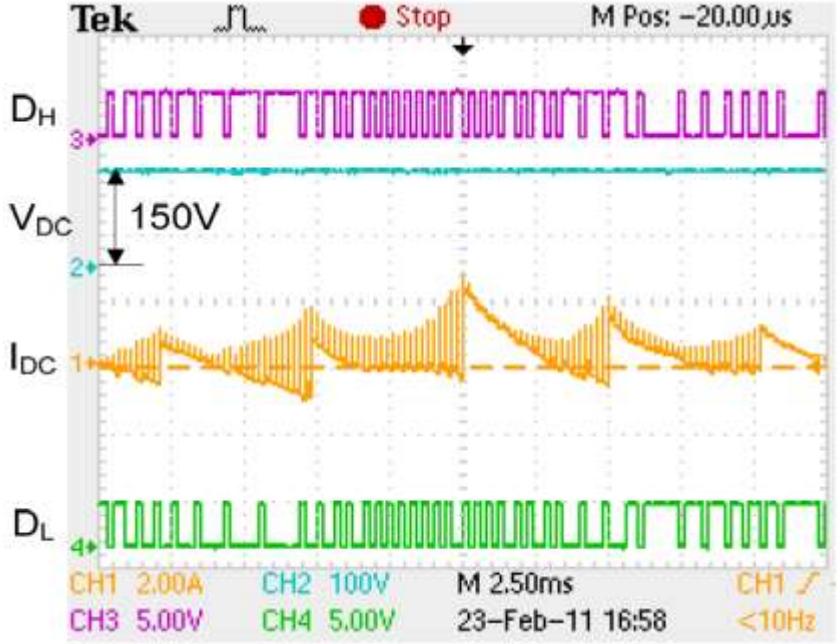

Figure 138: DC link voltage, current and change of duty cycle

Figure 139: Phase current and change of duty cycle

Figure 140 to Figure 142 show results when the reference speed is 586rpm and the prime mover torque is 1Nm. Figure 140 shows the speed response of the induction generator. The initial speed is 1150rpm before exciting the induction generator. After the induction generator is excited, shaft speed quickly goes down and tracks the reference speed. Figure 141 shows the DC link voltage and DC link current flowing into the dump resistor and the change of duty cycle. Figure 142 shows the steady state phase current and the change of duty cycle. From these figures, it can be noticed that the proposed state switching control method also has a good speed tracking performance at relatively low speeds.

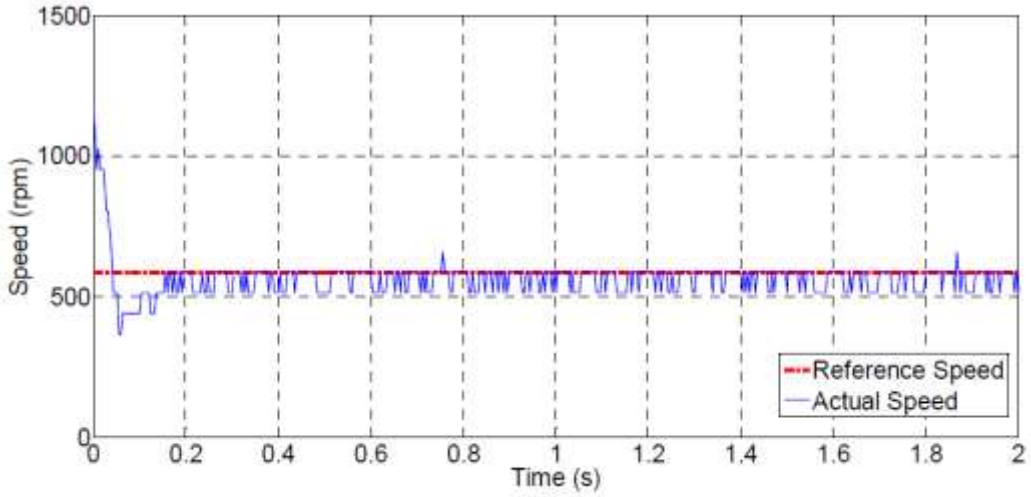

Figure 140: Speed response when reference speed is 586rpm

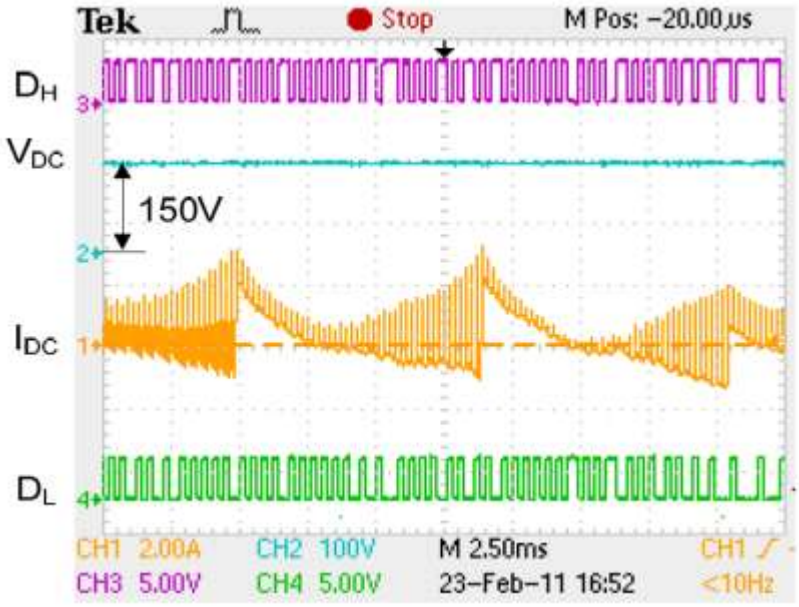

Figure 141: DC link voltage, current and change of duty cycle

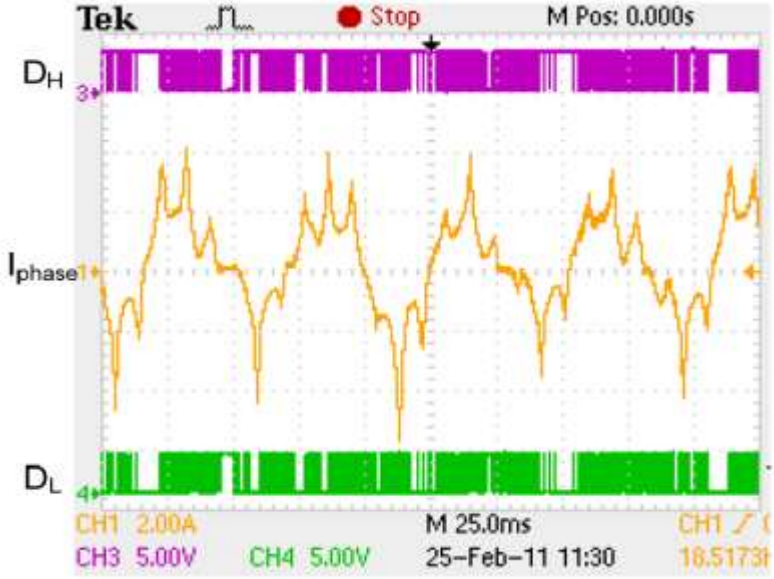

Figure 142: Phase current and change of duty cycle

The speed response and the generated DC link voltage and current for a step change in torque from 1Nm to 2Nm from the prime mover are shown in Figure 143 and Figure 144 respectively. It is clear that when the prime mover torque becomes larger, more power is generated and transmitted to the dump resistor. In addition, a step change of reference speed is also applied to the machine. Figure 145 shows the speed response of the induction generator when reference speed changes from 1025rpm to 586rpm. The actual speed again can track the reference speed precisely.

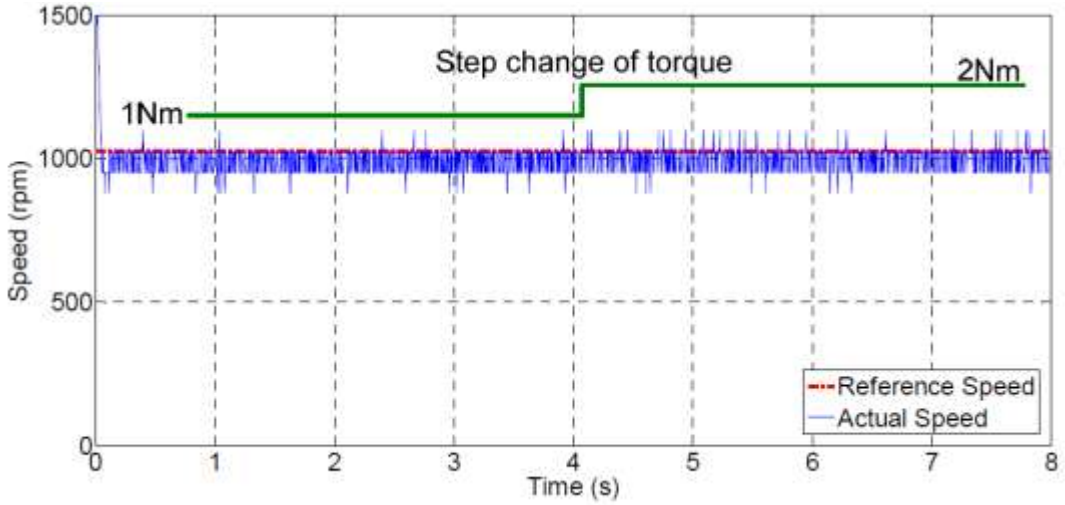

Figure 143: Speed response under step change of prime mover torque

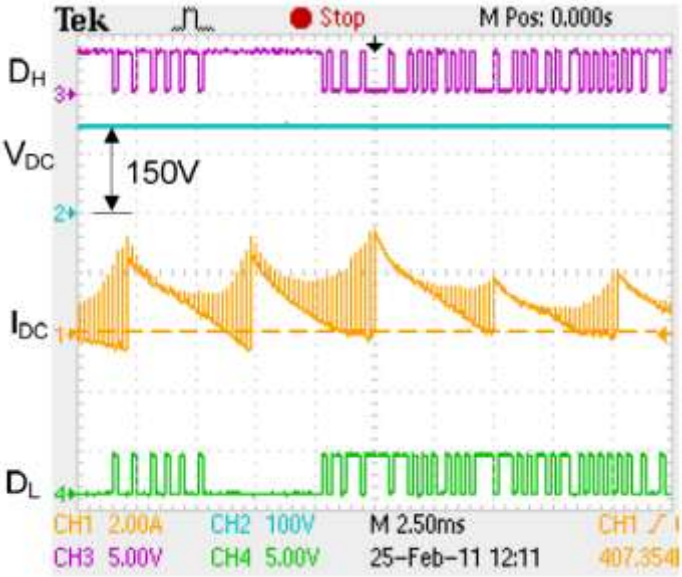

Figure 144: DC link voltage, current and change of duty cycle at 2Nm

In this section, state switching control is designed and implemented for induction machine. From simulation results and some hardware results, it can be found that state switching control can control three-phase AC machine with highly acceptable performance but requires least system information. Therefore, state switching control can be a very good option to work as a back-up control strategy.

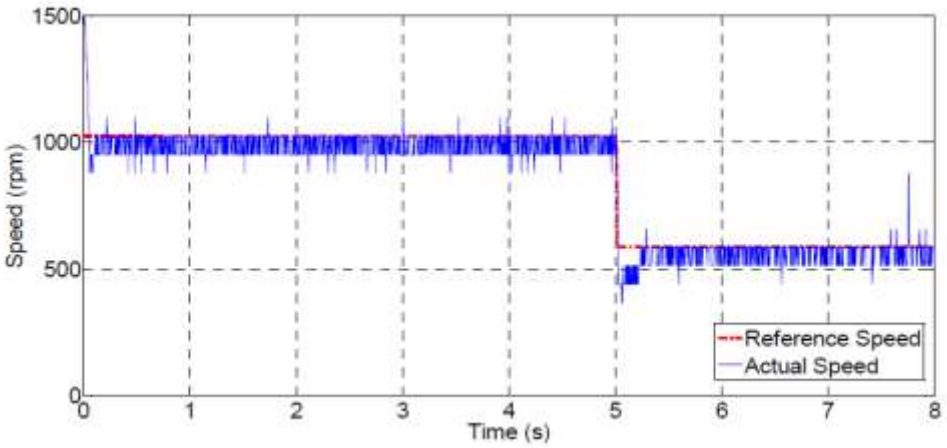

Figure 145: Speed response under step change of reference speed

E5. Survivable Operation of Induction Machine

Survivable operation of electric machines is required in wind power generation especially for those wind turbines located in remote areas. Failure of current sensors could bring the wind generator to a standstill and cause reduction of wind plant availability in the absence of immediate maintenance or redundancies, which in turn, could affect the overall stability of the power system. This section proposes a technique for survivable operation of three-phase Induction Machine drives in the event of current sensor failure by switching from vector control to state switching control with smooth transition strategy. A simple current sensor failure detection method keeps monitoring the conditions of current sensors and can trigger a fault flag if current sensor fails. Simulation and experimental results are included to show the effectiveness of the proposed strategy.

The proposed survivable drive for IM is illustrated in Figure 146. The basic idea is that if system is healthy, vector control is activated to regulate the speed and maximize the performance based on three-phase current feedbacks and one speed feedback. At the same time, a fault detection algorithm continuously monitors the health of vector controlled IM system. If the system shows signs of failure owing to a fault in current sensor(s), the fault detection algorithm can sense it. Vector control is then disabled and state switching control is activated to continue regulating the IM speed only using speed feedback. Therefore, the rules that the survivable drive algorithm follows are extremely simple and are ideally suited for hardware implementation. It can be represented in terms of one “IF ELSE” statement.

IF, Fault Detection = 0

Vector Control = Enable;

State Switching Control = Disable.

Else,

Vector Control = Disable;

State Switching Control = Enable.

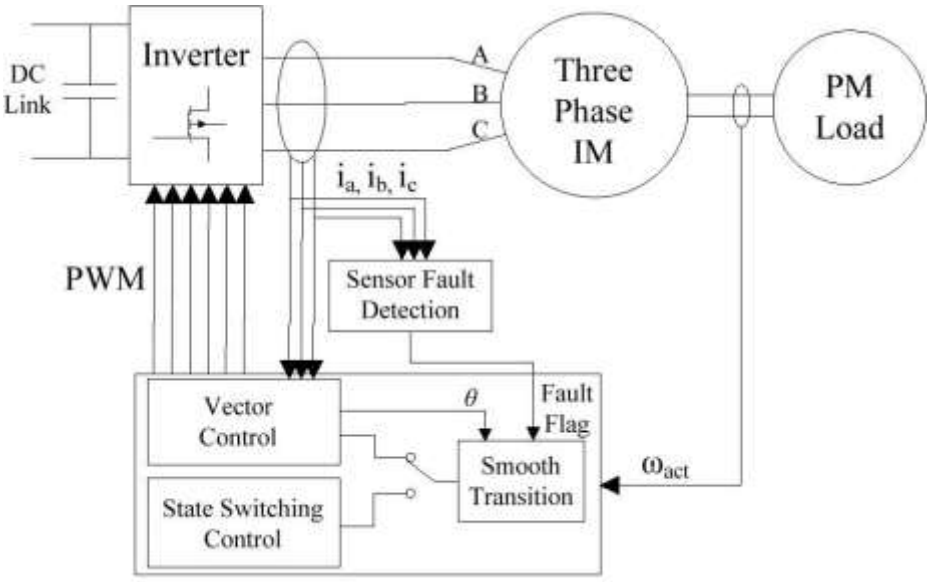

Figure 146: Proposed survivable drive for three-phase IM

The current sensor failure detection method presented in this report is based on the Kirchhoff's law. The sum of all three phase currents (Isum) equals zero. If current sensor fails, this value changes dramatically. Theoretically, sensor failure detection can be achieved by comparing Isum to zero, which is applicable in Simulink. However, in practical applications, Isum usually is a small value which oscillates around zero, as shown in Figure 147. Therefore, a threshold value (Ith) which is larger than |Isum| needs to be defined to monitor the health of current sensors. If |Isum| exceeds the threshold value, a fault flag is generated.

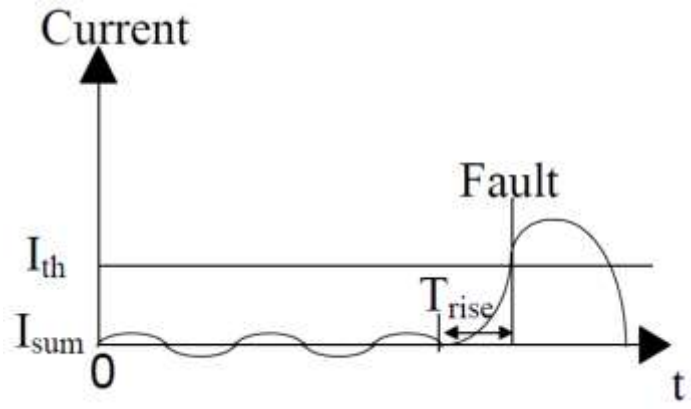

Figure 147: Basic principle of current sensor failure detection

The definition of this threshold value (Ith) is subject to the output voltage type of current sensor—with DC offset or without DC offset.

Current Sensor without DC Offset: the relationship between input current and output voltage signal can be expressed in equation (39), while equation (40) is used to calculate the input current in microprocessor (DSP).

$$V_{out} = \frac{1}{k} I_{in} \quad \textbf{(39)}$$

$$I_{calc} = kV_{out} \quad \textbf{(40)}$$

Where Vout refers to the output voltage signal of the current sensor, Iin is the input current. Icals is the calculated value of input current. With this kind of current sensors, Vout will be zero when current sensor fails. As a result, Isum becomes the sum of the remaining current sensors' outputs, which usually is a sinusoidal waveform with its magnitude significantly larger than the value of Isum in normal condition. As shown in Figure 148, in order to quickly detect the failure of current sensor, the threshold value (Ith) should be defined slightly greater than the maximum possible value of |Isum| for the purpose of minimizing the rise time Trise of |Isum| to generate a fault signal. The maximum possible |Isum| can be found by running the IM under different load conditions. It must be mentioned that this method is not applicable when all current sensors fail simultaneously since Isum remains zero in this case. This fault can be detected by comparing |Ia +Ib| to Ith. The fault detection logic for current sensor without DC offset can be shown in Figure 148.

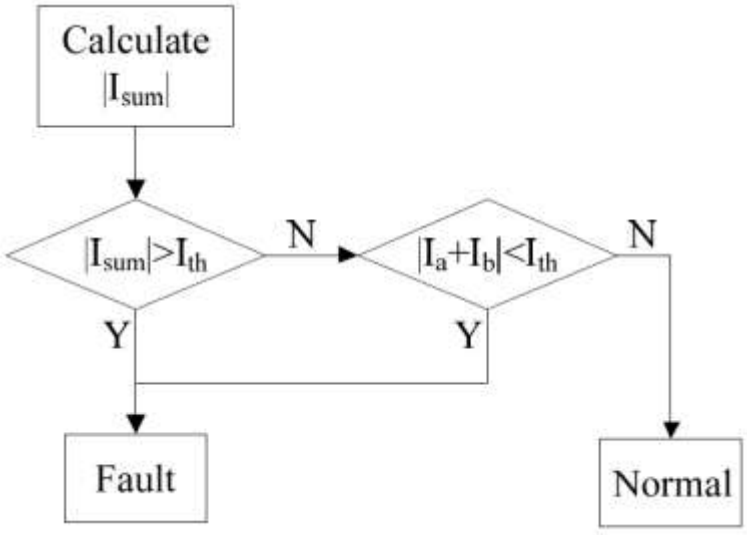

Figure 148: Current sensor failure detection method (without DC offset)

Current Sensor with DC Offset: Similarly, the current sensor with DC offset equals to kDC functions as (41) while equation (42) is implemented in DSP to calculate the input current.

$$V_{out} = \frac{1}{k} I_{in} + k_{DC} \quad (41)$$

$$I_{calc} = k(V_{out} - k_{DC}) \quad (42)$$

With this kind of current sensor, the threshold value (Ith) is much easier to define. This is because when a current sensor fails, Vout becomes zero, which leads to a sudden increase in the DSP-calculated current |Icalc| (|Icalc|= k*kDC). Therefore, Ith can be defined slightly smaller than k*kDC. If the value of Ith is greater than k*kDC, a fault signal is generated. In this paper, current sensors with DC offset are used. Current sensor used in this paper is LTS 25-NP with its DC offset equals to 1.875V. Three current sensors' output is calibrated in the DSP using the flowing equations.

$$I_a = 0.0123(V_{a\_adc} - 2310) \quad (43)$$

$$I_b = 0.01236(V_{b\_adc} - 2180) \quad (44)$$

$$I_c = 0.01244(V_{c\_adc} - 2200) \quad (45)$$

$$|I_{sum}| = |I_a + I_b + I_c| \quad (46)$$

where Vadc is the analog to digital conversion result of Vout and the range of current sensor output in normal conditions is within ±15A. Based on the above equations, current sensor failure, the resultant |Isum| as well as the definition of Ith are presented in Table 11. The threshold value Ith is set to 20A which can be used to detect all possible current sensor failures.

Table 11: Sensor Failure and Parameters

No. of Current Sensor Fails	Failed Phase Current Sensor(s)	Failed Current Sensor(s) Output (A)	|Isum| (A)	Ith (A)
1	a	28.4	≥28.4	
	b	26.9	≥26.9	
	c	27.4	≥27.4	
2	a & b	55.3	≥55.3	20
	a & c	55.8	≥55.8	
	b & c	54.3	≥54.3	
3	a & b & c	82.7	≥82.7	

Experimental results from sensor failure detection are shown in Figure 149, in which (a) stands for single sensor failure, |Isum| exceed the value of Ith at 3s and trigger the fault flag. Similarly, (b) and (c) represents two and three current sensor failure respectively.

The vector control module implemented in this paper is a conventional vector control scheme which relies on three-phase current feedbacks (ia, ib and ic) and one rotor speed feedback (ωact). As shown in Figure 150, three phase currents (ia, ib and ic) are transformed into stator d-q axis currents (isd and isq) using Clarke and Park transformation (equations (47) and (48)) based on rotor flux angle (θ). This rotor flux angle is estimated by the rotor flux estimator based on d-q axis currents (isd and isq) and rotor speed (ωact). A speed control loop calculates the q axis reference current (isq*) by comparing the actual rotor speed (ωact) to the reference rotor speed (ωref). Two stator d-q axis current control loops calculate stator d-q axis voltages (Usd and Usq) which are then be transformed into voltages (Uα and Uβ) in stator stationary reference frame using inverse Park transformation. Uα and Uβ are then sent to the Space Vector PWM module (SVPWM) to generate the desired switching signals.

$$\begin{bmatrix} i_\alpha \\ i_\beta \end{bmatrix} = \sqrt{\frac{2}{3}} \begin{bmatrix} 1 & -\frac{1}{2} & -\frac{1}{2} \\ 0 & \frac{\sqrt{3}}{2} & -\frac{\sqrt{3}}{2} \end{bmatrix} \begin{bmatrix} i_a \\ i_b \\ i_c \end{bmatrix} \quad (47)$$

$$\begin{bmatrix} i_d \\ i_q \end{bmatrix} = \begin{bmatrix} \cos\theta & \sin\theta \\ -\sin\theta & \cos\theta \end{bmatrix} \begin{bmatrix} i_\alpha \\ i_\beta \end{bmatrix} \quad (48)$$

Decoupling of d-q axis current components requires accurate position information of the rotor flux-linkages at every instant. Unlike PMSM, this position cannot be obtained directly from speed or poison sensors due to the existence of slip. Rotor flux estimator therefore is necessary and essential, which is also one of the most challenge parts in implementing vector control. The rotor flux estimator is shown in Figure 151 and expressed mathematically by equations **Error! Reference source not found.** to **Error! Reference source not found.**.

$$\lambda_{rd} = \frac{L_m}{1 + s\tau_r} i_{sd} \quad (49)$$

$$\omega_{da} = \frac{L_m}{\lambda_{rd}\tau_r} i_{sq} \quad (50)$$

$$\omega_d = \omega_{da} + \omega_m \quad (51)$$

$$\theta = 0 + \int_0^t \omega_d(\tau) d\tau \quad (52)$$

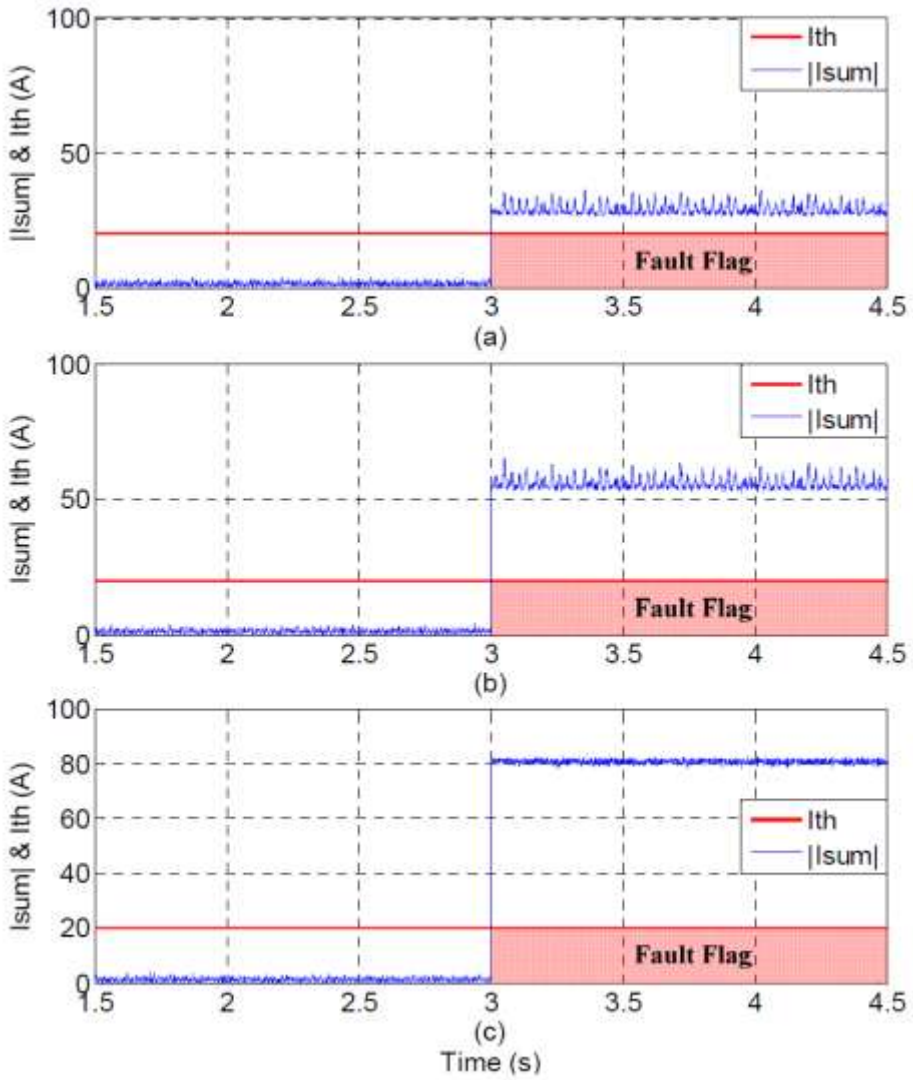

Figure 149: |Isum| of three phase currents under different number of current sensor failure

One current sensor failed at 3s (b) Two current sensors failed simultaneously at 3s (c) Three current sensor failed simultaneously at 3s

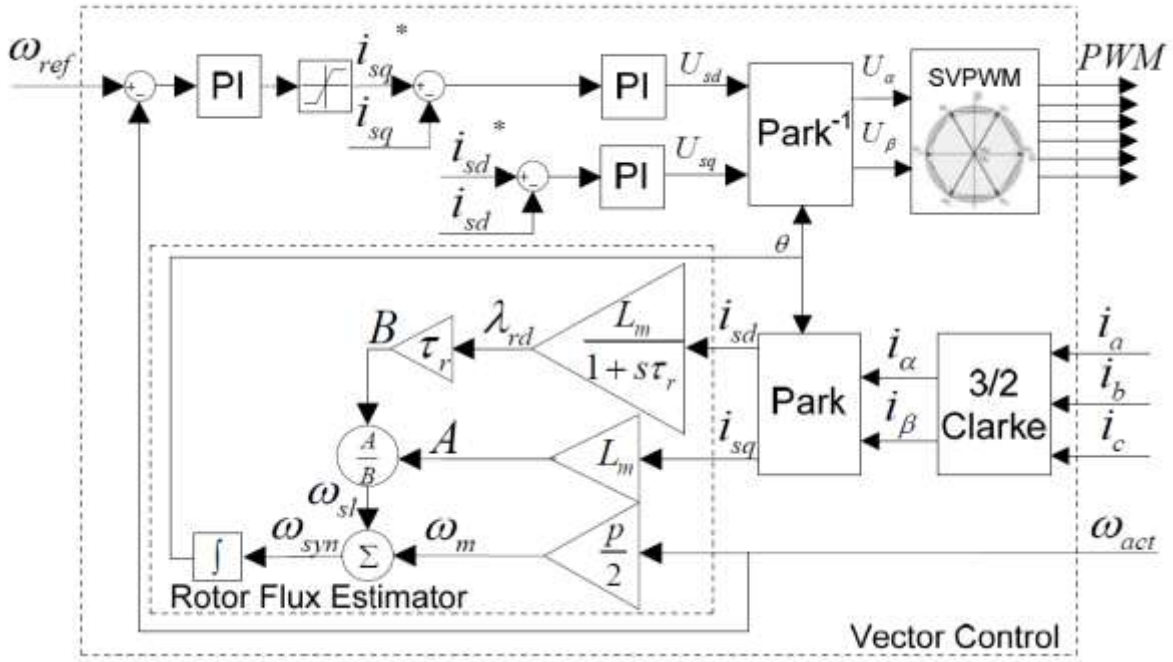

Figure 150: Block diagram of vector control

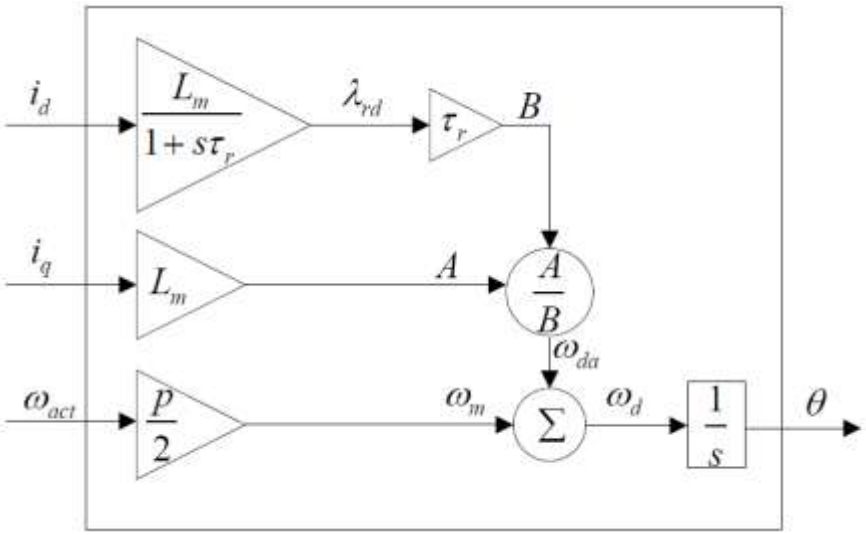

Figure 151: Rotor flux position estimation

In hardware implementation, the above equations need to be discretized. Before that, equation **Error! Reference source not found.** is first transformed into a time-domain equation (53).

$$\frac{d\lambda_{rd}}{dt} = \frac{L_m}{\tau_r} i_d - \frac{1}{\tau_r} \lambda_{rd} \tag{53}$$

Then, (53) can be discretized into (54),

$$\frac{\lambda_{rd}[k] - \lambda_{rd}[k-1]}{T} = \frac{L_m}{\tau_r} i_d[k] - \frac{1}{\tau_r} \lambda_{rd}[k] \tag{54}$$

Where T is the sampling step time, k is the current step and k-1 refers to the previous step. As a result, rotor flux estimation can be expressed in the flowing equations and can be easily transformed into C-code for DSP.

$$\frac{\lambda_{rd}[k] - \lambda_{rd}[k-1]}{T} = \frac{L_m}{\tau_r} i_d[k] - \frac{1}{\tau_r} \lambda_{rd}[k] \tag{55}$$

$$\omega_{da}[k] = \frac{L_m}{\tau_r \lambda_{rd}[k]} i_q[k] \tag{56}$$

$$\theta_{da}[k] = \omega_{da}[k]T + \theta_{da}[k-1] \tag{57}$$

$$\theta_m[k] = \omega_m[k]T + \theta_m[k-1] \tag{58}$$

$$\theta[k] = \theta_{da}[k] + \theta_m[k] \tag{59}$$

Space Vector Pulse Width Modulation (SVPWM) has become a popular PWM technique for voltage source inverter fed three-phase AC machines. SVPWM has two main advantages over conventional SPWM. One advantage is that the voltages and currents created by SVPWM have fewer harmonics. The other one is that the DC link voltage usage of SVPWM is higher than SPWM. The detailed principle will not be explained in this dissertation. But the realization of SVPWM in real application is introduced as follow.

According to the previous section, we know that the inputs of the SVPWM of module are Uα and Uβ, as shown in Figure 150. Based on these two values, the following steps show how to implement SVPWM in real applications.

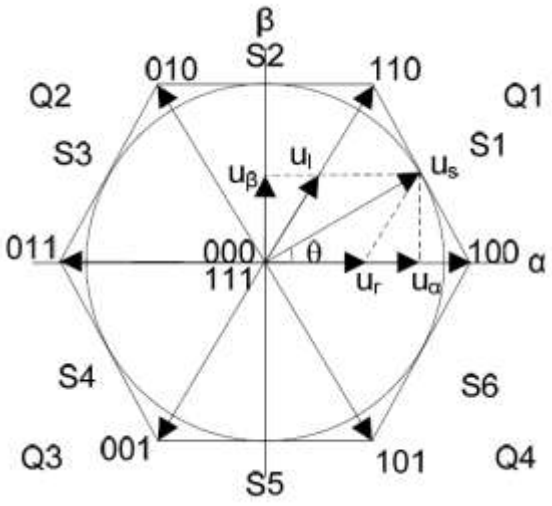

Figure 152: Voltage vector space

Table 12: The relationship between P and sector number

P	1	2	3	4	5	6
Sector	S2	S6	S1	S4	S3	S5

Step 1: Determine which sector the voltage vector belongs to. In order to do so, following equations can be used to get the value of P and the sector number can be obtained according to Table 12.

$$B_0 = U_\beta \tag{60}$$

$$B_1 = U_\alpha \sin\frac{\pi}{3} - U_\beta \sin\frac{\pi}{6} \tag{61}$$

$$B_2 = -U_\alpha \sin\frac{\pi}{3} - U_\beta \sin\frac{\pi}{6} \tag{62}$$

$$P = 4sign(B_2) + 2sign(B_1) + sign(B_0) \tag{63}$$

Step 2: Calculate |ur|, |ul|and |usmax|.

After sector number is calculated, two adjacent switch vectors can be defined for specific voltage vector. Then, based on the value of Uα and Uβ, Ur and Ul can be determined by geometric calculations. Ur and Ul stands for voltage vectors that locate on two adjacent switch vectors, which can be used to determine the switch time for these two switch vectors. Take the case shown in Figure for example, voltage vector Us is located in sector 1, which is formed by Uα and Uβ. Since Ur and Ul forms the same voltage vector Us, their modulus can be calculated using the flowing two equations.

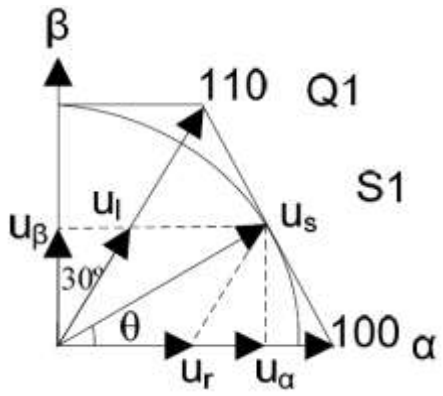

Figure 153: Ur and Ul Calculation

$$|U_r| = |U_\alpha| - |U_\beta| \tan\frac{\pi}{6} \tag{64}$$

$$|U_l| = \frac{|U_\beta|}{\cos\frac{\pi}{6}} \tag{65}$$

Similarly, the value of |Ur |and |Ul | for other sectors can be concluded in Table 13.

Table 13: |Ur| and | Ul| calculation table

		|Ur|	| Ul|
S1	Q1	b	c
S2	Q1	a	-b
	Q2	-b	a
S3	Q2	c	b
S4	Q3	b	c
S5	Q3	a	-b
	Q4	-b	a
S6	Q4	c	b
$a = \|U_\alpha\| + \frac{1}{\sqrt{3}}\|U_\beta\|,\ b = \|U_\alpha\| - \frac{1}{\sqrt{3}}\|U_\beta\|,\ c = \frac{2}{\sqrt{3}}\|U_\beta\|$ S: Sector; Q: Quadrant			

|Ur| and | Ul| can be determined according to Table 7. For S2 and S5, there are two groups of values for |Ur| and |Ul|. In order to determine which group will be assigned to |Ur| and | Ul|. We need to know which quadrant the voltage vector is located. This can be done by examine the value of Uα. For example, for S2, if Uα>0, the voltage vector is located in Q1, otherwise, it is located in Q2.

The maximum modulus (amplitude) of voltage vector is 2UDC/3 (UDC is the amplitude of the DC link voltage). However, in practical applications, in order to reduce harmonics in the output voltage, the hexagon area is not used. Only the area of the inner circle which touches the hexagon is used, as shown in Figure 154. The maximum usable DC link voltage with lowest phase current harmonics is:

$$\left|U_{s\max}\right| = \frac{1}{\sqrt{3}} U_{DC} \tag{66}$$

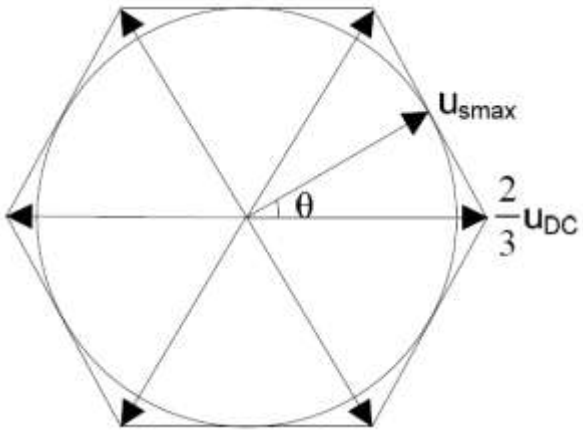

Figure 154: Usable area for the voltage vector us

Step 3: Calculate Tr, Tl and T0.

These values Tr, Tl and T0 determine the turn ON time of corresponding voltage vectors. The relationship between these values can be expressed in equations (67) to (70) and Figure 5.10.

$$T_r = T_p \frac{\left|u_r\right|}{\left|u_{s\max}\right|} \tag{67}$$

$$T_l = T_p \frac{\left|u_l\right|}{\left|u_{s\max}\right|} \tag{68}$$

$$T_0 = \frac{T_p^* - T_r - T_l}{2} \quad (69)$$

$$T_p = \frac{\sqrt{3}}{2} T_p^* \quad (70)$$

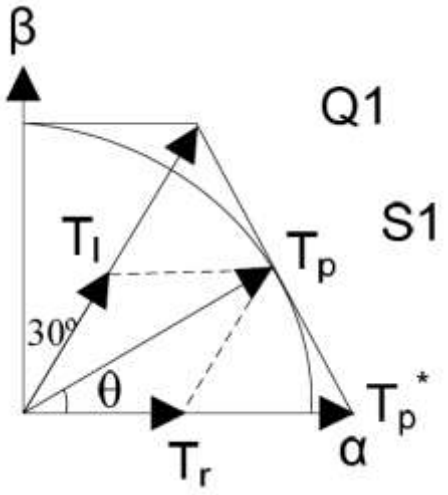

Figure 155: Tr and Tl calculation

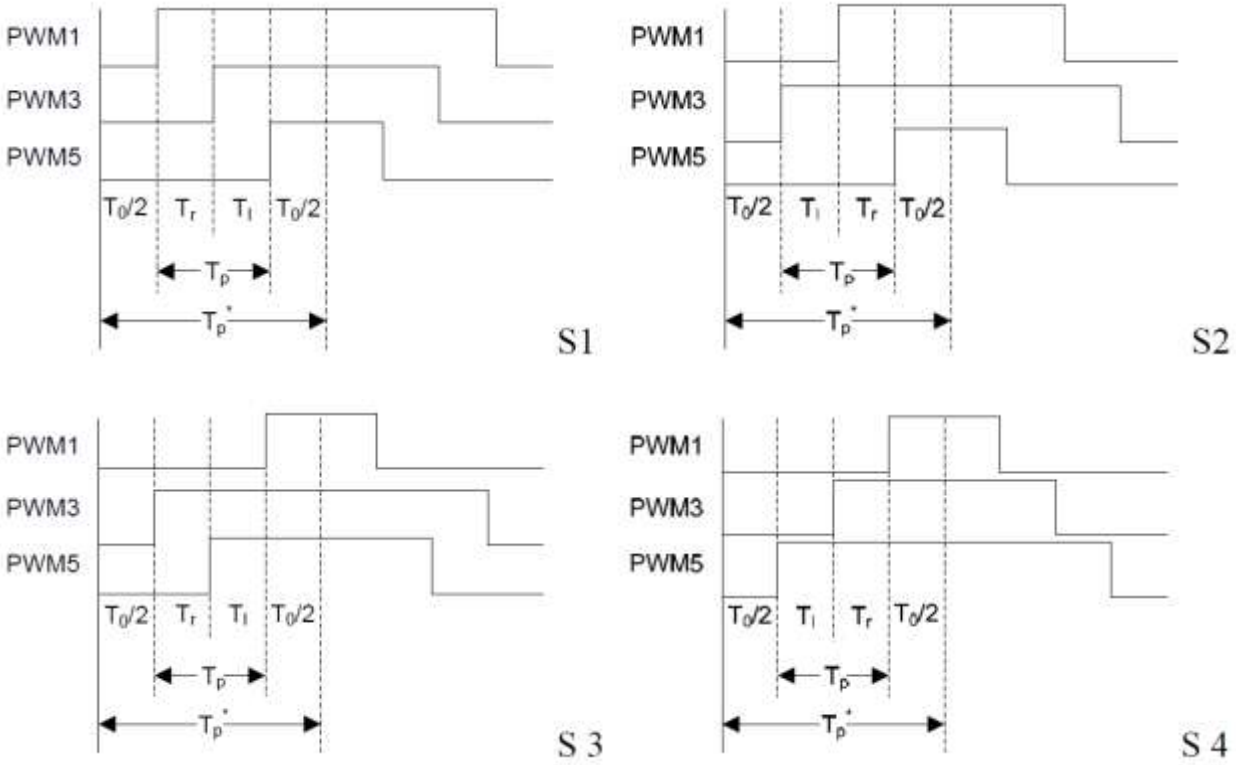

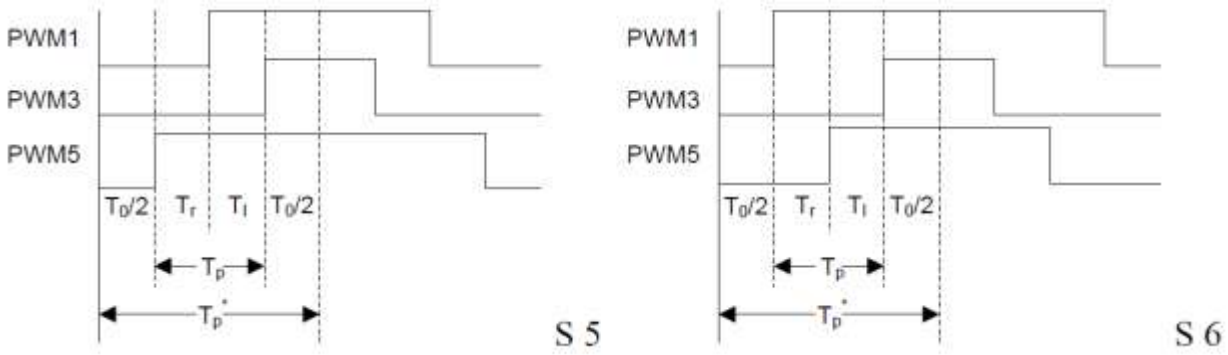

Figure 156: Relationship between switching time variables

Step 4: Limit Uα, Uβ or Tr, Tl proportionally

Two input parameters Uα and Uβ of the SVPM module are calculated from other modules of vector control. During startup or when the load increases, system might generates two large Uα and Uβ which forms a very large voltage vector Us that exceed the range of the hexagon, as shown in Figure 157. The result is that two large turn-on time Tr and Tl (Tr+Tl >Tp^*) is required for switch vector 100 and 110. However, it is not achievable physically. What need to be done is to either limit Uα, Uβ or limit Tr, Tl.

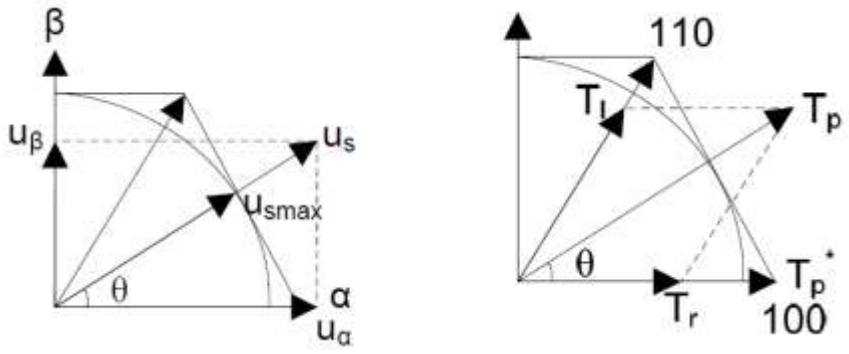

Figure 157: Limit voltage vector

If system is required to have lowest harmonics in its current and lowest vibration in its torque performance even during startup or load increase, input value of Uα, Uβ need to be limited proportionally. By doing so, the voltage vector will stay inside the inscribed circle with its modulus be equal or lesser than Usmax. Flowing two equations need to be implemented when Us is larger than Usmax.

$$U_\alpha^{'} = U_\alpha \frac{U_{s\max}}{U_s} = U_\alpha \frac{\frac{1}{\sqrt{3}} U_{DC}}{\sqrt{U_\alpha^{\,2} + U_\beta^{\,2}}} \quad (71)$$

$$U_\beta^{'} = U_\beta \frac{U_{s\max}}{U_s} = U_\beta \frac{\frac{1}{\sqrt{3}} U_{DC}}{\sqrt{U_\alpha^{\,2} + U_\beta^{\,2}}} \tag{72}$$

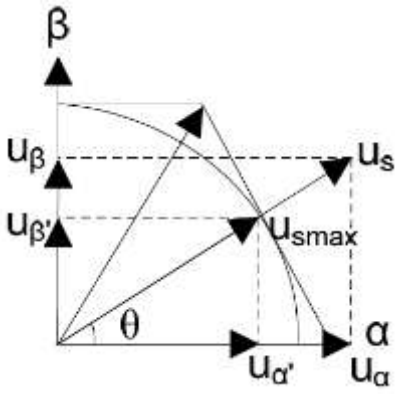

Figure 158: Limit voltage vector within the inscribed circle

If system is required to respond faster during startup or load increase and have better DC link voltage usage, Tr and Tl is limited proportionally instead of Uα, Uβ. When the sum of Tr and Tl is greater than Tp^* (Tr+Tl >Tp), following two equations are need to be implemented. By doing so, the voltage vector will cover the whole hexagon which maximize the usage of the DC link voltage. During startup or when load increases, the voltage vector can goes to the region that exceeds the inscribed circle of the hexagon, which is also called "Over Modulation". Disadvantage of over modulation is that it will create harmonics for phase current and result in torque vibration. Simulation results regarding the vector controlled induction machine in motoring mode can be shown in Figure 160 to Figure 162. Figure 160 shows the speed response of the induction machine under vector control. The speed quickly settles down and precisely tracks the reference speed. The torque performance of the induction machine under vector control is shown in Figure 161. Step change of reference torque can be tracked. In addition, the phase current can be illustrated in Figure 162.

$$T_r^{'} = T_r \frac{T_p^{*}}{T_r + T_l} \tag{73}$$

$$T_l^{'} = T_l \frac{T_p^{*}}{T_r + T_l} \tag{74}$$

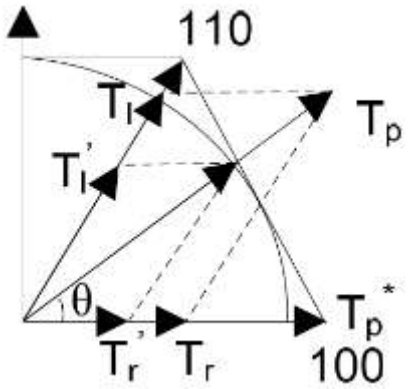

Figure 159: Limit voltage vector within the hexgon

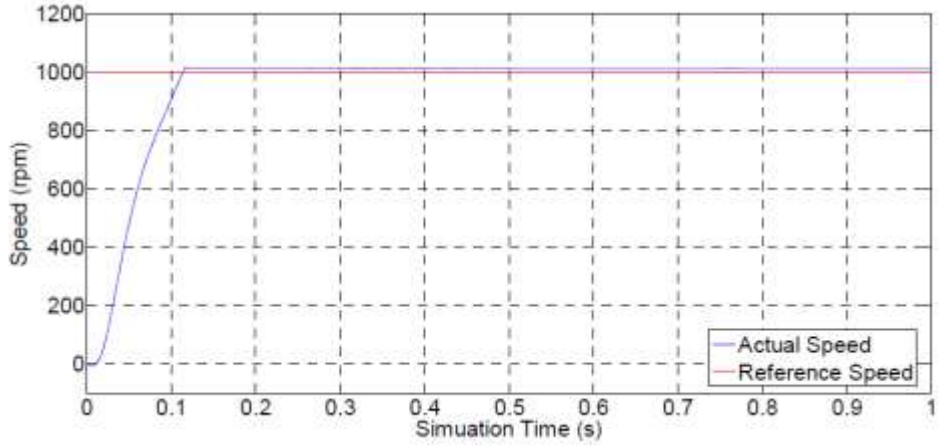

Figure 160: Speed response of vector controlled induction motor

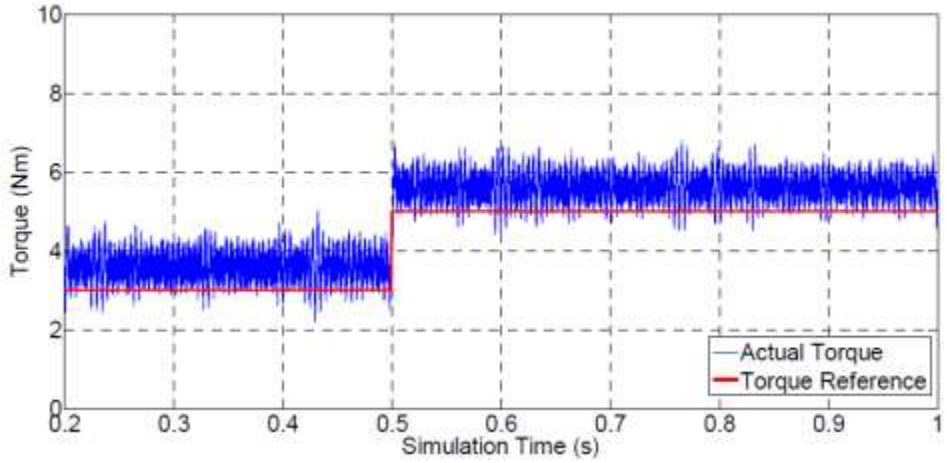

Figure 161: Torque performance of vector controlled induction motor

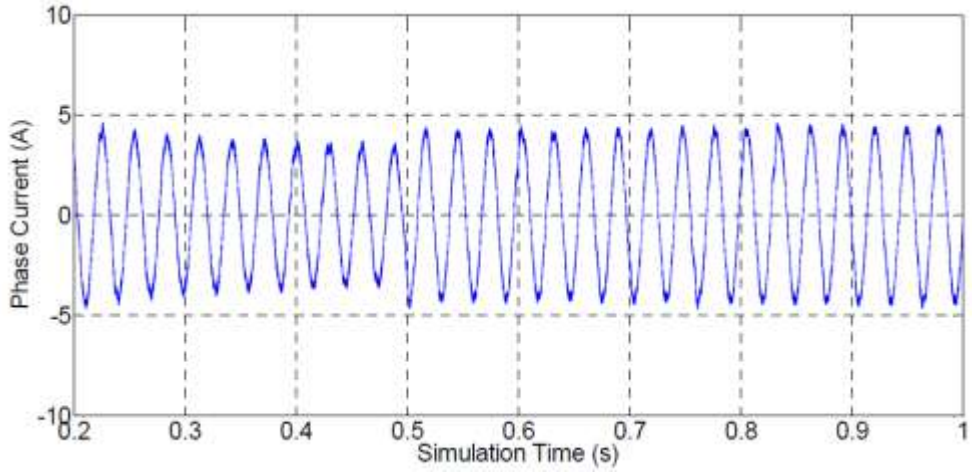

Figure 162: Phase current of vector controlled induction motor

Simulation results regarding the vector controlled induction machine in generating mode can be shown in Figure 163 to Figure 166. Figure 163 to Figure 165 shows speed, torque and current performance in generating mode. Figure 166 shows the generated DC link current flowing to the battery.

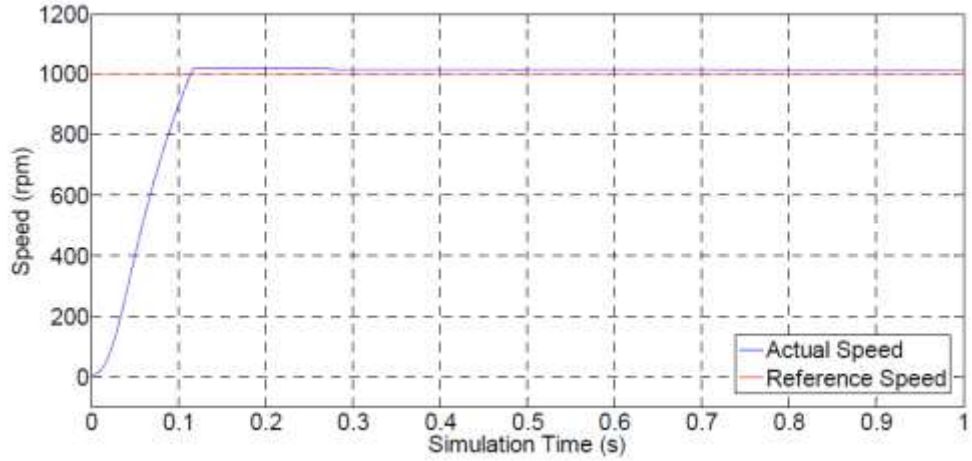

Figure 163: Speed response of vector controlled induction generator

The transition strategy for survivable operation proposed in this paper is described as follows-when current sensor failure occurs, vector control is disabled and state switching control is enabled. The smoothness of the controller transition greatly depends on how state switching control fires its switches at the very beginning. As shown in Figure 167, firing the wrong subsequent switches will cause undesired braking torque which could lead to large speed dip and even cause mechanical damage. In fact, this phenomenon can be explained using voltage space vector. As shown in Figure 168, under vector control, the desired voltage vector Us which rotates around the circle inside the hexagon of voltage space creates a smooth rotating rotor flux λrd (Suppose the rotation is anticlockwise).

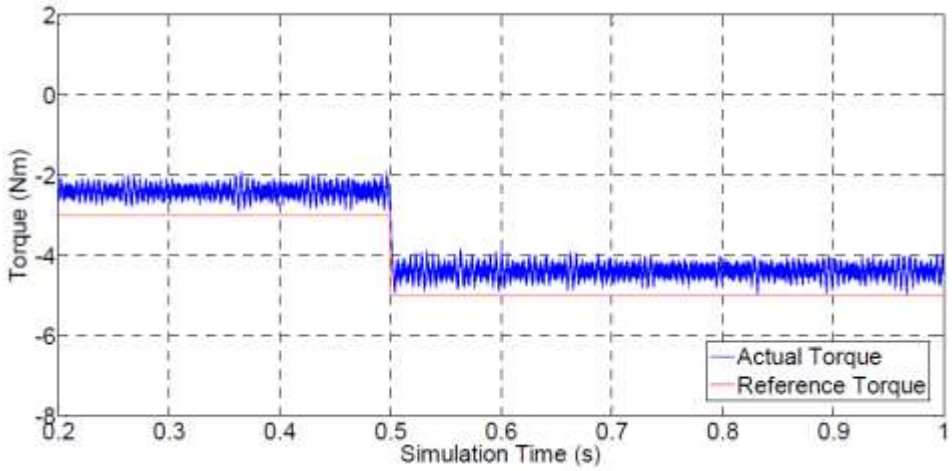

Figure 164: Torque performance of vector controlled induction generator

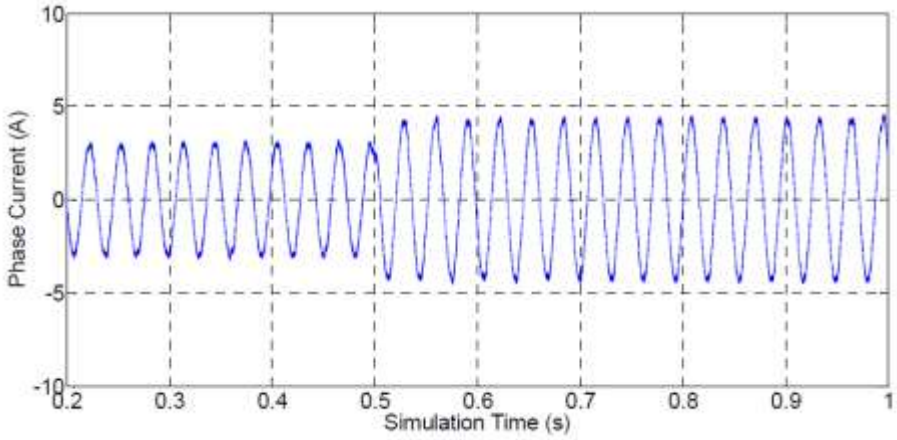

Figure 165: Phase current of vector controlled induction generator

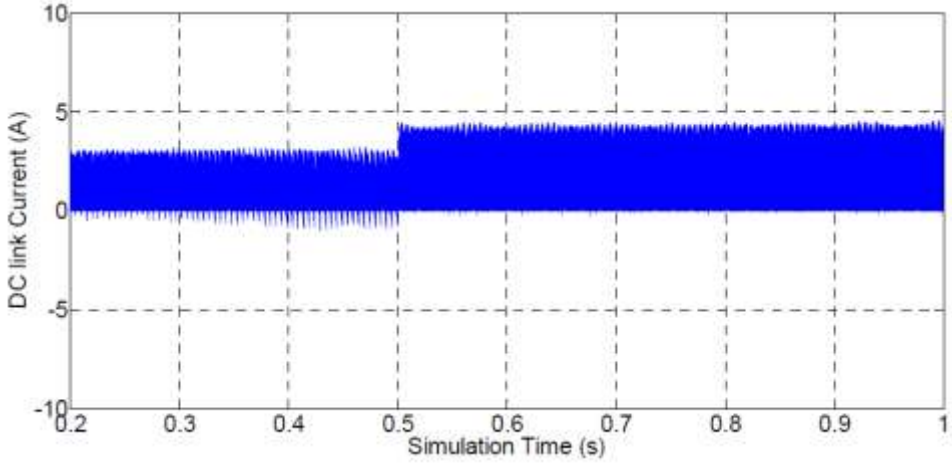

Figure 166: The generated DC link current flowing into the battery

This voltage vector Us should always be perpendicular to the rotor flux λrd. If at the moment of vector control failure, we assume that the rotor flux position is located in sector 6 and has an angle of θ with α-axis, the next desired voltage vector Us should be located in sector 1 and have a angle of 90º-θ with α-axis. However, if the initial position of the voltage vector Us' generated by state switching control is located in the right side of the dotted line along the direction of rotor flux position, a negative braking torque will be generated which will cause phenomenon shown in Figure 167.

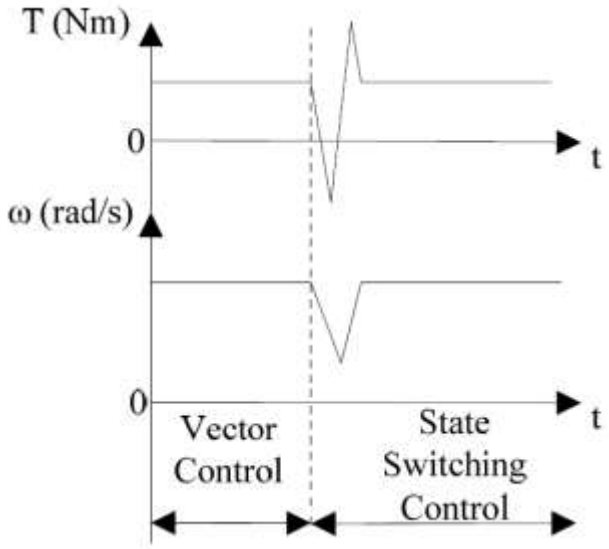

Figure 167: Braking torque and speed dip caused by misfiring of switches

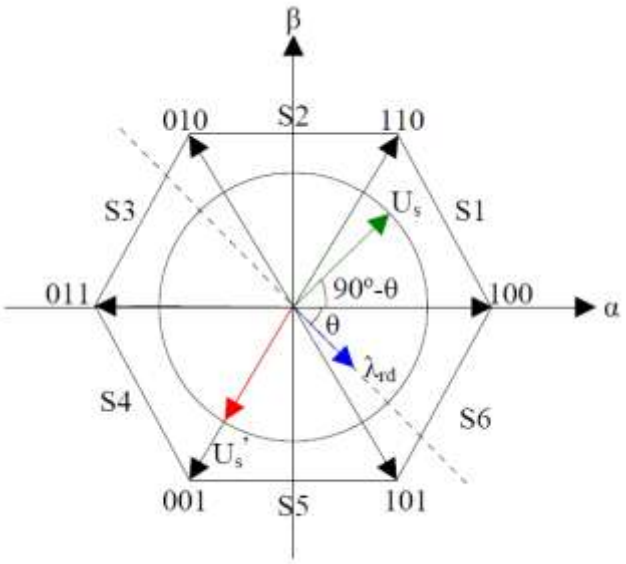

Figure 168: Phasor diagram of rotor flux angle and voltage vector

Therefore, in order to obtain a smooth transition, the initial voltage vector Us' of state switching control should be placed as close as possible to Us in sector 1. Since state switching control uses PWM

integrated six-step drive methods. Only voltage vectors located at 0^{o}(100), 60^{o}(110), 120^{o}(010), 180^{o}(011), 240^{o}(001) and 300^{o}(101) can be used. In this case, the 60^{o}(110) voltage vector is the best option to achieve a smooth transition from vector control to state switching control. Based on the above analysis, the following steps should be implemented in order to achieve a smooth transition from vector control to state switching control.

1) When current sensor failure detection mechanism senses the failure of current sensors and vector control is going to be disabled, the rotor flux angle θ should be saved to determine the initial voltage vector for the subsequent state switching control.

2) Based on the rotor flux angle θ, the initial voltage vector of state switching control can be concluded in the following Table 14.

Table 14: Initial Voltage Vectors for State Switching Control Based on Rotor Flux Angle

Rotor Flux Angle (θ)	Initial Voltage Vector (Us')
0°~60°	120° (010)
60°~120°	180° (011)
120°~180°	240° (001)
180°~240°	300° (101)
240°~300°	0° (100)
300°~360°	60° (110)

In order to verify the feasibility of the proposed survivable operation of IM in the event of current sensor failure, simulation is implemented in Matlab/Simulink. The block diagram of the survivable operation of IM is the same as the one shown in Figure 146, in which a 3kW, 60Hz, 4 pole induction machine is used with a rated speed of 1725rpm.

Figure 169 shows results of the first simulation without smooth transition strategy. Speed regulation of IM is done by vector control and the output of the current sensor is a sinusoidal waveform when system is healthy. The failure of current sensor happens at 0.505s by manually disabling the sensor and the output becomes zero. At the same time, the fault signal is triggered by the current sensor fault detection mechanism and the control strategy is toggled from vector control to state switching control. Due to the lack of smooth transition technique, a significant braking torque is induced at the moment of transition, which causes a large speed dip in speed response. After that, state switching control take over the control and precisely regulate the speed.

Figure 170 shows results of the second simulation with smooth transition strategy employed. Similarly, the failure of the current sensor happens at 0.505s and the control strategy is switched from vector control to state switching control. This time, speed regulation is not influenced by the controller transition and keeps tracking the reference precisely without any dips. The torque has a small drop during transition due to discontinuous voltage vectors of six-step method, but it quickly recovers so it doesn't affect the speed. In order to verify the effectiveness of the proposed survivable operation of

induction machine as well as its simulation results, experiments were carried out on the same hardware setup displayed in Figure 124 without adding additional hardware. Parameters regarding the 2.2kW induction machine are listed in Table 15. Hardware results of survivable operation of induction machine in motoring mode are shown in Figure 171 to Figure 172. Once the fault flag is triggered, the survivable algorithm will be activated to cancel the current sensor dependence, in which the vector control will be disabled and the state switching control will be enabled. At the same time, a smooth transition strategy will take place to ensure the smoothness of the transition process. Experiment results are shown in Figure 171 and Figure 172. Figure 171 shows the results when the reference speed is 1000rpm at 1Nm load condition. Sensor failure happens at 3s and the fault flag is trigger which is shown in Figure 171 (a). Figure 171 (b) shows how smooth transition is achieved.

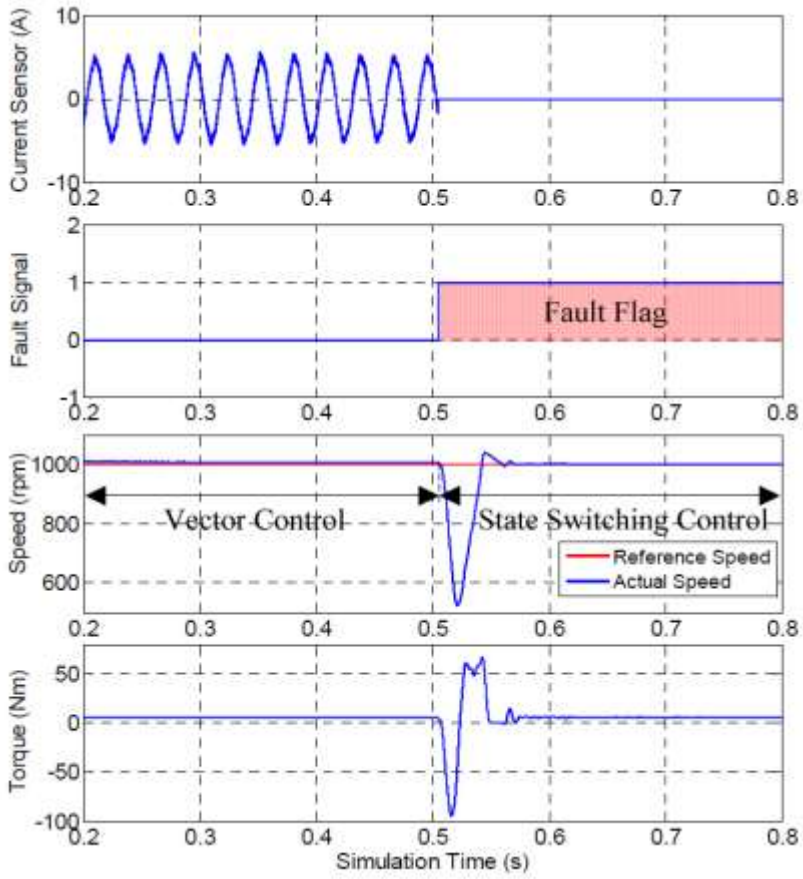

Figure 169: Survivable operation of IM without smooth transition strategy

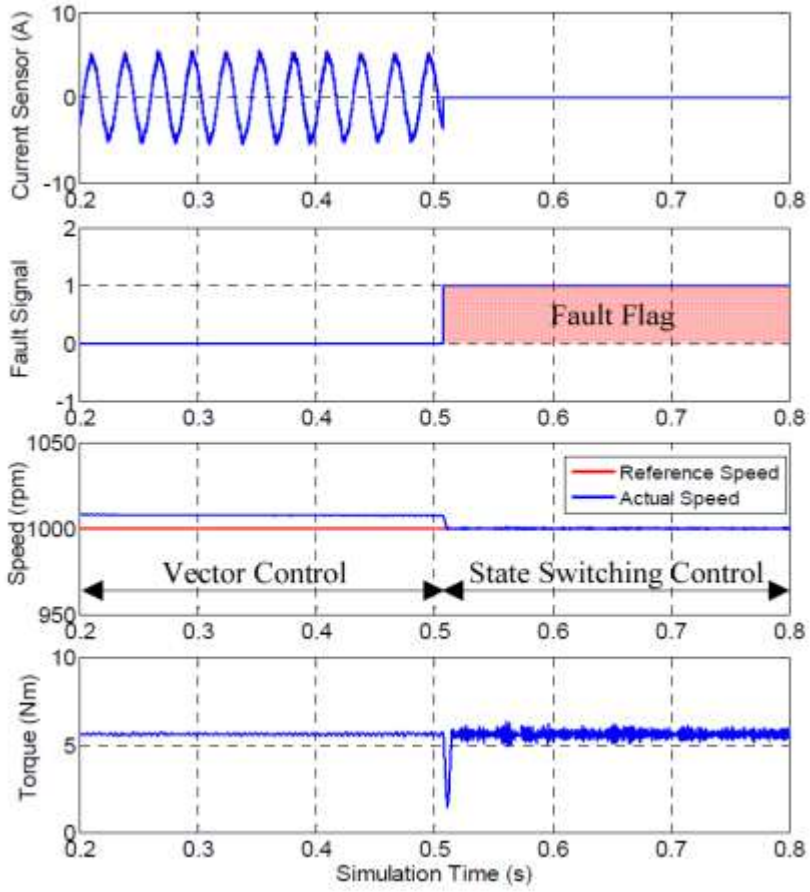

Figure 170: Survivable operation of IM with smooth transition strategy

Table 15: Induction Motor Parameters

Symbol	Parameters	Values
Rs(Ω)	Stator Resistance	2.9
Ls(mH)	Stator Inductance	245.7
Rr(Ω)	Rotor Resistance	2.1
Lr(mH)	Rotor Inductance	253.2
Lm(mH)	Mutual Inductance	238.4

The red dotted line represents the rotor flux angle (0~360º) estimated by vector control. The blue solid line is the voltage vector which always leads 90º under vector control. At the moment of transition, the rotor flux angle (143.7º) is saved as the starting point for state switching control, based on this value and Table 8, the 240º (001) voltage vector is chose as the first step of the consecutive state switching control. After that, voltage vector is moving in the six-step style. Figure 171 (c) illustrates continue operating of IM after sensor failure happens. It can be noticed that speed is precisely regulated without any dips during and after controller transition. Therefore, both smooth transition and survivable operation is achieved. Figure 171 (d) shows the three-phase current waveforms before and after controller transition.

When vector control is active, phase currents are sinusoidal waveforms with high system efficiency and low noise. When state switching control is activated, phase currents are distorted with harmonics due to the lack of current monitoring. As a result, system efficiency is lower than vector control, but the speed regulation is highly acceptable.

Similarly, Figure 172 shows experiment results when reference speed is 500rpm and load torque is 1Nm. Sensor failure happens at 3s. Figure 172 (a) shows the fault flag triggered by the sensor failure detection mechanism. Figure 172 (b) illustrates the smooth transition of voltage vector based on rotor flux angle. Figure 172 (c) displays the capability speed tracking at relative low speed. Figure 172 (d) shows the phase current waveforms before and after transition.

Survivable operation of induction machine in generating mode was carried out on the same setup displayed in Figure 136 without adding additional hardware. Hardware results regarding the survivable operation of induction generator is shown in Figure 173. The reference speed of the induction generator is 1000rpm and the prime mover torque is 1Nm. As shown in Figure 173 (a), fault flag is triggered by the current sensor failure event. Figure 173 (b) shows how state switching control picks up an optimal voltage vector based the previous rotor flux position. Figure 173 (c) shows the entire speed response in which speed is not influence at the moment of controller transition. Figure 173 (d) and € shows phase current waveforms before and after sensor fails. Figure 173 (f) and (g) shows the generated DC link current before and after controller transition respectively.

In this section, the survivable operation technique has been introduced for the continuous operation of induction machine in the event of current sensor failure. A current sensor failure detection mechanism is used to monitor the conditions of current sensors and trigger the fault flag if current sensor fails. Vector control has been implemented as the strategy typically chosen for optimizing performance when the system is healthy. A simplified state switching control has been proposed and implemented to take over the control when the fault flag is triggered. Since this technique does not require any additional hardware and is not computationally intense, it is very suitable for survivable operation and can be embedded in the processor without overloading it. In addition to the state-switching strategy, a strategy has been implemented for smooth transition to avoid braking torque and any significant fluctuations in speed. Simulation and experimental results verify the effectiveness of this method.

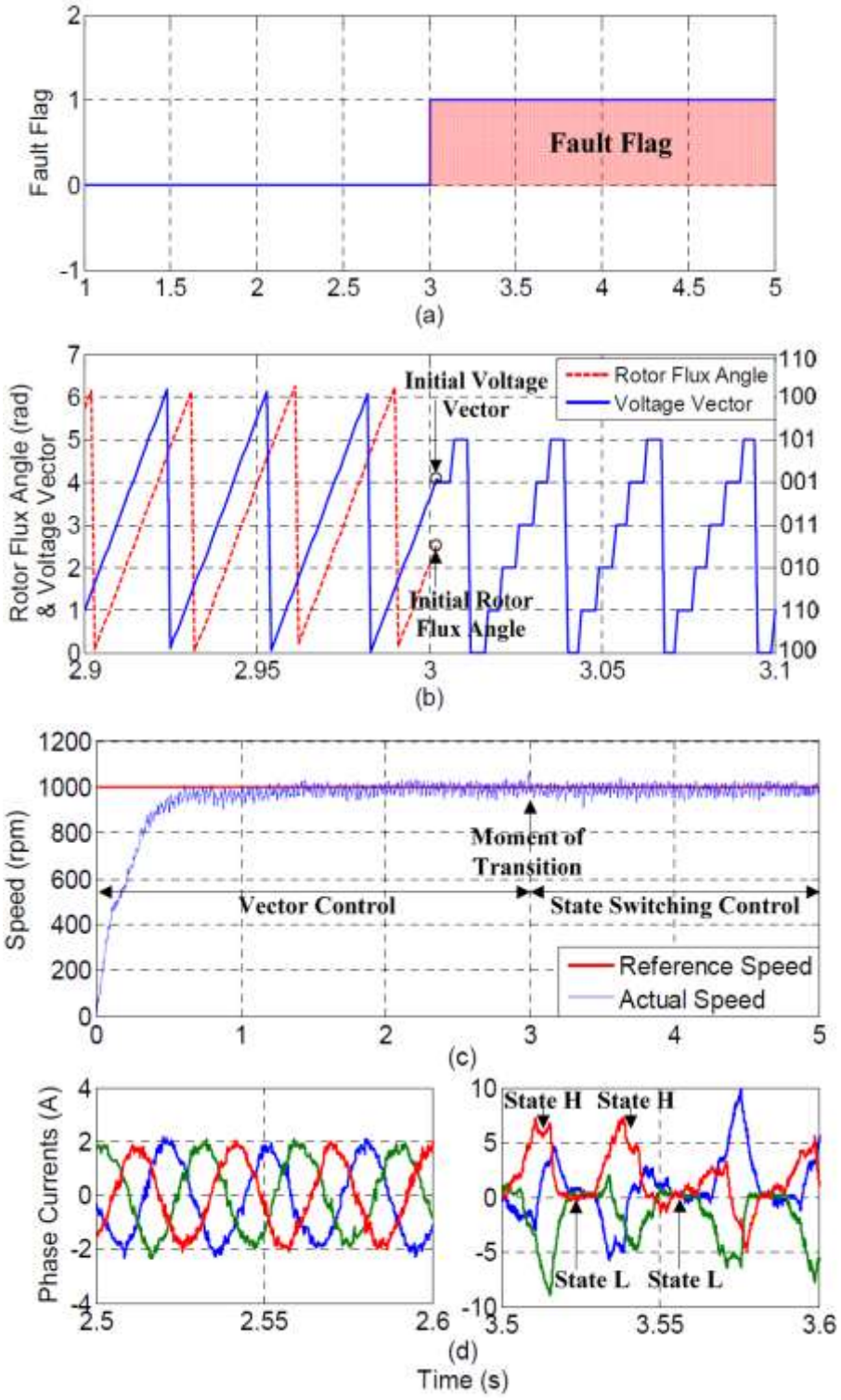

Figure 171: Experimental results of survivable operation of IM in the event of current sensor failure with smooth transition strategy (speed ref 1000rpm, load torque 1Nm)

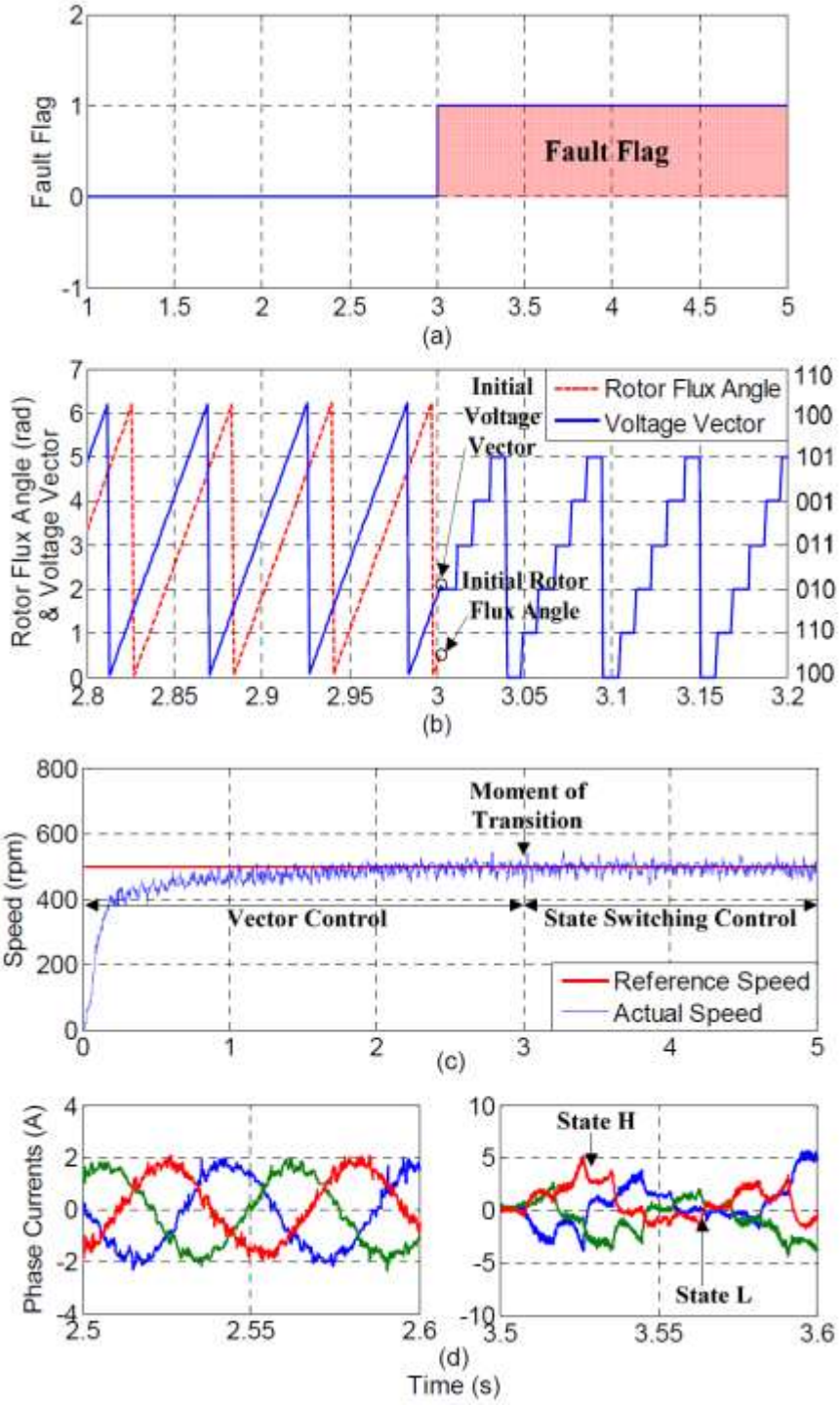

Figure 172: Experimental results of survivable operation of IM in the event of current sensor failure with smooth transition strategy (speed ref 500rpm, load torque 1Nm)

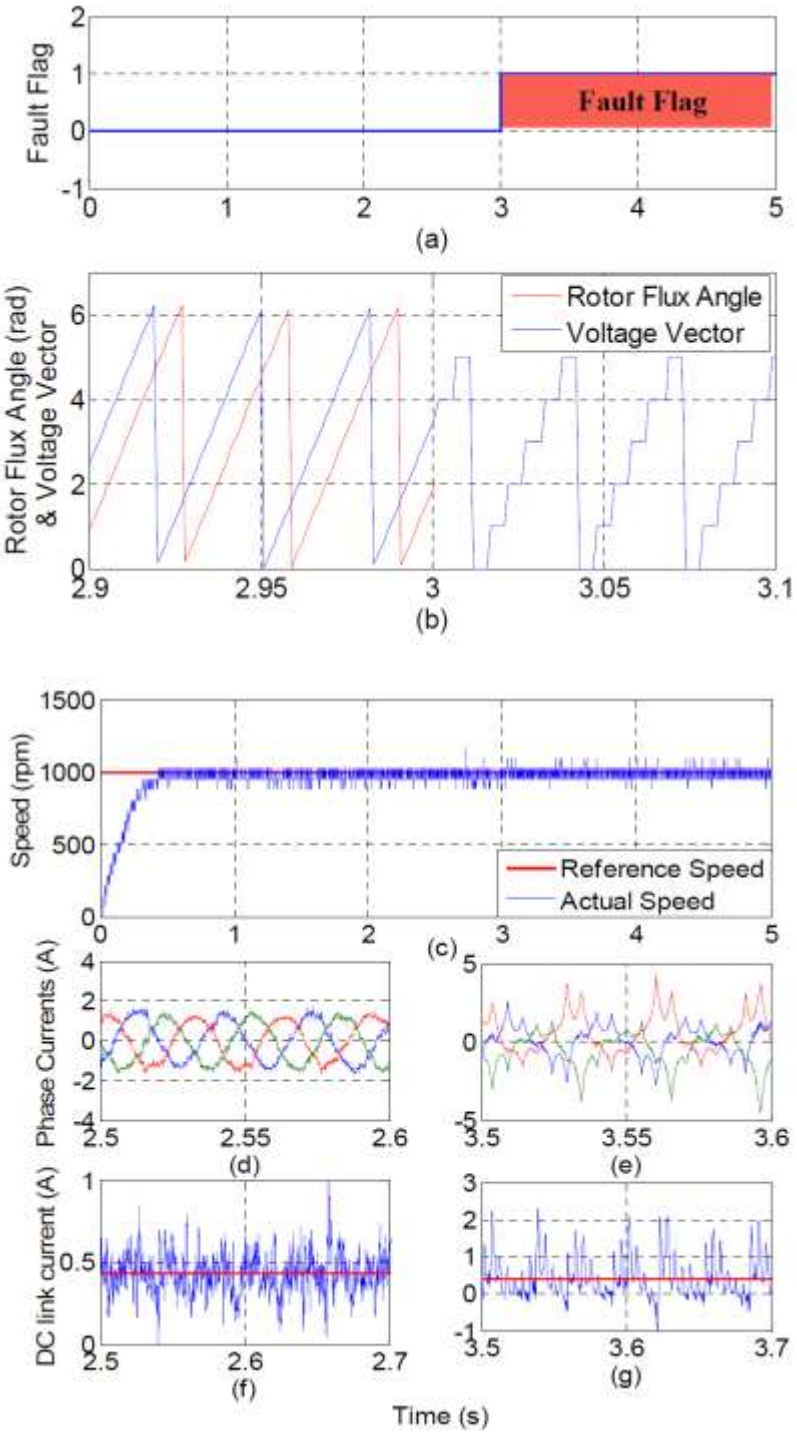

Figure 173: Experimental results of survivable operation of IG in the event of current sensor failure with smooth transition strategy (speed ref 1000rpm, load torque 1Nm)

E6. Conclusions and Future Work

In this section, a survivable drive method is proposed to handle the current sensor failure and continue operating the wind turbine when current fault happens. Vector control is implemented and used control

the three-phase AC machine when system is healthy. When current fault happens, a current sensor failure detection mechanism is used to generator a fault signal which can trigger the transition from vector control to a simplified control method. In this section, a simplified control method—state transition control is proposed for induction machine to work as a backup control strategy. Simulation and experimental results are provided in this section to show the effectiveness of the proposed survivable drive method. More simulations and experiments are undergoing and more results will be provided in future reports. Future work includes

- Extensively test survivable operation of induction machine in generating mode and compare the efficiency before and after controller transition.
- Extend the survivable operation algorithm to PMSM machine in both motoring mode and generating mode.

F. Wind Turbines Acoustics – Localization of Wind Turbine Noise Sources

Localization of wind turbine noise sources on a 1.5 MW production scale wind turbine using a compact microphone array

The primary objective of the current work was to study the behavior of various beamforming algorithms and use that understanding to locate various noise sources on a production scale 1.5 MW wind turbine located in a wind farm using a compact microphone array. The sound sources in the wind turbine include both mechanical and aerodynamic noise. The sources on the wind turbine are mostly broadband and are moving sources. The beamforming algorithms were validated in the laboratory using three speakers which could produce both coherent and incoherent noise. The spacing between the three speakers could be changed on a speaker frame. The microphone array was also tested on a moving source. The microphone array was then used to measure the wind turbine noise to locate aerodynamic and mechanical noise sources. Measurements were also made on a small wind turbine drive train simulator. This report includes a detailed discussion of all these experimental results.

In the United States, officials responsible for energy policy have been exhibiting renewed interest in wind energy as an alternate power source that is clean and renewable. One of the important factors determining the approval of a site permit for wind turbines is the level of wind turbine noise. Many researchers have spent the past decade in trying to understand wind turbine noise and developing various techniques to reduce them. In order to better understand the noise generated from the wind turbines we would need to localize the source of various types of noise. Using a single microphone one can only obtain a quantitative value (sound pressure level, SPL) of the noise. The use of multiple microphone array along with the use of beamforming will help us connect the different types of noise generated by the wind turbine to their respective components of mechanical/aerodynamic parts. Properly utilized, arrays are powerful tools that can often be used to extract noise source radiation information in circumstances where other measurement techniques may fail. Some of the widely used beamforming algorithms are Delay and Sum (DAS) beamformer, Classical Frequency Domain Beamforming (FDBF), deconvolution approach for the mapping of acoustic sources [**30**] (DAMAS), modified DAMAS [**31**], [**32**], (DAMAS2), CLEAN based on spatial source coherence [**33**] (CLEAN-SC) and TIDY. The use of basic beamformers like FDBF and DAS require very large arrays (of the order of 4 m^2) for

localizing the sources on a 1.5 MW production wind turbine. The requirement of large array spread over a large area serves as a major drawback of using this technique. Our idea was to use a compact microphone array along with advanced beamforming algorithms such as CLEAN-SC and TIDY to locate the wind turbine noise sources. This served as the objective for the current work. This report is a documentation of our effort to study the principles behind the advanced algorithms and conduct a thorough validation of these algorithms on a compact microphone array using coherent and incoherent sources. The quantification experiments were done before measurements on full scale unit at the wind farm.

F1. Wind turbine noise

Wind turbines generate both aerodynamic and mechanical noise from its various components (see Figure 174(a)). Aerodynamic noise includes low-frequency sound, in-flow turbulence sound, and airfoil self- noise. The cylindrical tower can produce additional noise due to vortex shedding in various regimes. Mechanical sources include sound from the gearbox, generator, yaw drives, cooling fans, and hydraulics. Even though wind turbines have become much quieter over the years, their sound is still an important siting (installation site selection) criterion. Mechanical sounds originate from the relative motion of mechanical components and dynamic response among them. Examples of mechanical sound sources include the gear box that houses gears that connect the low speed shaft to the high speed shaft. Typically the rotor blade rotations occur at 30-60 rotations per minute (rpm). These rotations are transmitted to the high speed shaft at 1000-1800 rpm and during the process noise is produced by the gears and the high speed shaft. Aerodynamic broadband sound is typically the largest component of wind turbine acoustic emissions. It originates from air flow around the blades. Figure 174(b) shows a number of complex fluid dynamic phenomena occurring, each of which might generate sound. Aerodynamic sound generally increases with rotor speed and the noise producing mechanisms can be divided into three groups: *Low Frequency Sound, Inflow Turbulence and Airfoil Self Noise.* [**34**], [**35**]

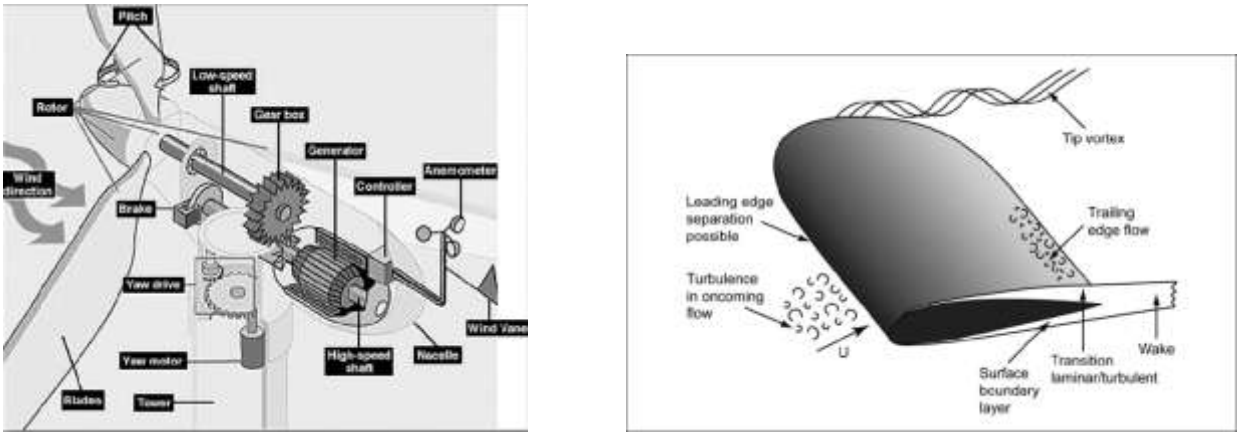

(a) (b)

Figure 174: Schematic of (a) components of a wind turbine and (b) Noise producing mechanisms on a rotor blade.

(a) components of a wind turbine. Source: US Department of Energy (http://www1.eere.energy.gov/windandhydro/images/illust_large_turbine.gif) and (b) Noise producing mechanisms on a rotor blade (as described in [34]).

F2. Beamforming

The use of phased arrays provides very valuable information about the sources of wind turbine noise at various operating conditions. The very first step after acquiring data from the phased array system for every beamforming algorithm considered is the computation of cross spectral matrix (CSM). The pressure time series of each microphone is divided into B blocks and the FFT of each block is computed after applying a suitable spectral window. Then each element of the CSM is calculated via sample averaging. Since the locations of the sources are unknown in practice, a scanning grid that covers a region of interest with a certain resolution is formed and every point of this grid is considered as a potential source whose corresponding sound pressure level at the array center is estimated. This results in a beam forming map representing the acoustic source distribution in the region of interest. DAMAS attempts to estimate the true signal powers from the contaminated DAS results by constructing a linear system of equations that relate the DAS estimates at every scanning point to the signal powers at every scanning point. It utilizes the iterative Gauss-Seidel method. A potential drawback of this is computation time. DAMAS2 solves this problem by calculating the point spread function only once and using the same for all the points in the scanning grid. Another widely used method is the CLEAN-SC which iteratively builds up the beamform maps corresponding to the dominant sources using the previously estimated signal powers. TIDY is philosophically similar to CLEAN-SC, but it works in the time domain using the cross correlation matrix (CCM) instead of the frequency domain with CSM.

F3. Calibration of microphone array

The microphone array had to be tested for its accuracy using four different beamforming algorithms namely FDBF, DMS2, CLSC and TIDY. The array was tested for many possible conditions such as,

- Single and multiple sources
- Stationary and moving sources
- Coherent and incoherent sources
- Broadband and tonal noise

The compact microphone array system with integral preamplifiers and a built-in camera developed by OptiNav was tested and used for the experiments. The signal from the microphone array is acquired by an A/D converter which has 24 I/O audio interfaces. A MAGMA express box handles the task of interfacing the PCI 424 card to the computer. A USB cable connects the camera to a USB port on the computer. The sound sources for this experiment were produced using three 4 ohm dual cone speaker with a maximum power of 60 W connected to a dedicated amplifier which received input from a white/tonal noise generator. The speakers were mounted on a rectangular frame support which had 21 different mounting locations each separated by distance of one inch (see Figure 175(a)). One speaker was mounted at the center most location on the frame, referred to as the 0^{th} position. The other two

speakers were mounted on the frame at a distance of 9 inches, both to the left and right of the 0th position, and the setup was referred to as 9_0_9. The amplitude of the speakers were individually controlled by dedicated amplifiers. Before the experiments were conducted three different amplitude levels were selected, a low amplitude (69-71 dB), one mid amplitude (75-77 dB) and a high amplitude (82-84 dB). For ease of reference these three amplitude cases were assigned a number; low amplitude case- '2', mid amplitude case- '4' and high amplitude case- '6'. The speaker switched off case was assigned a '0'. For example, if the center speaker was fed with high amplitude input and the other two speakers were switched off then the case was referred to as 9.0_0.6_9.0. Similarly if the right and left speaker were fed with high amplitude input and the center one was switched off then it was referred to as 9.6_0.0_9.6. This nomenclature will be used throughout the report. A Coherent source scenario was created by feeding the three amplifiers with input from the same white noise generator whereas three different white noise generators were used to feed the amplifiers in the incoherent case. The data acquired from the microphone array was then processed through four different beamforming algorithms namely the Frequency Domain Beamforming (FDBF), DAMAS (DMS2), CLEAN-SC (CLSC) and TIDY. A single 0.25" B&K 4939 microphone with a flat response from 1 Hz – 100 kHz was used for acquiring acoustic data for comparison with the results obtained from the microphone array. The microphone was positioned such that it was located exactly at the center of the microphone array. The calibration of the microphone was done using a piston phone which emits sound at 250 Hz at an amplitude of 124 dB.

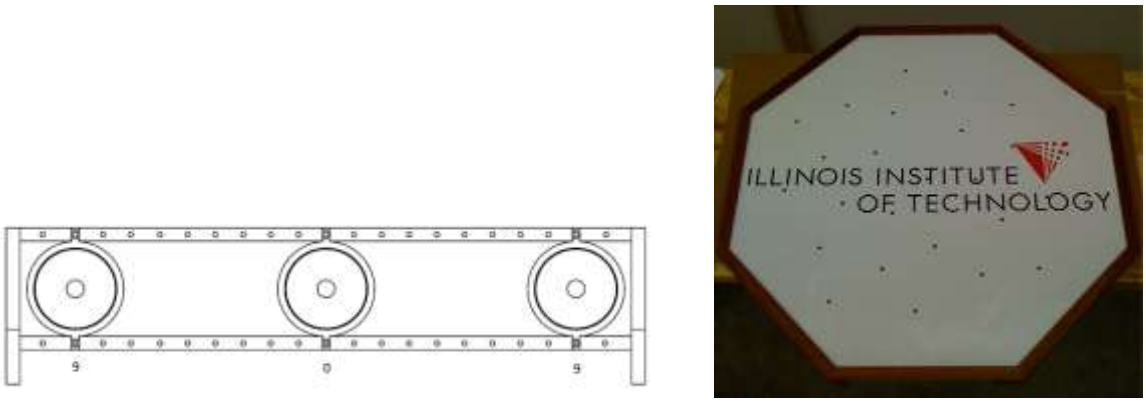

(a) (b)

Figure 175: Schematic of (a) the speaker arranged on the rectangular frame support at the 9_0_9 position and (b) the microphone array.

The microphone array was tested for a single source where only one speaker is switched on. The input signal to the speaker was a broadband noise signal. Three frequency ranges were examined: 972.5-1020.3 Hz, 2174.6-2299.3 Hz and 5777.0-6120.6 Hz. The results for the 9.0_0.6_9.0 case for the above mentioned frequency ranges are shown in Figure 176. It was observed that the FDBF and DMS2 give a very broad map for the source at low frequency (<2000 Hz) whereas the TIDY and CLSC give a clean map compared to the other beamformers. As we increase the frequency of the source the beamformers' performance gets better. It has to be mentioned that the results obtained are for the particular

arrangement of microphones on the array being tested. The spectrum obtained by the beamforming algorithms is compared with that of a calibrated single microphone. The spectra for the cases 9.0_0.2_9.0, 9.0_0.4_9.0 and 9.0_0.6_9.0 are shown in Figure 177. We observed that the spectra from the single microphone matched well with that of the microphone array.

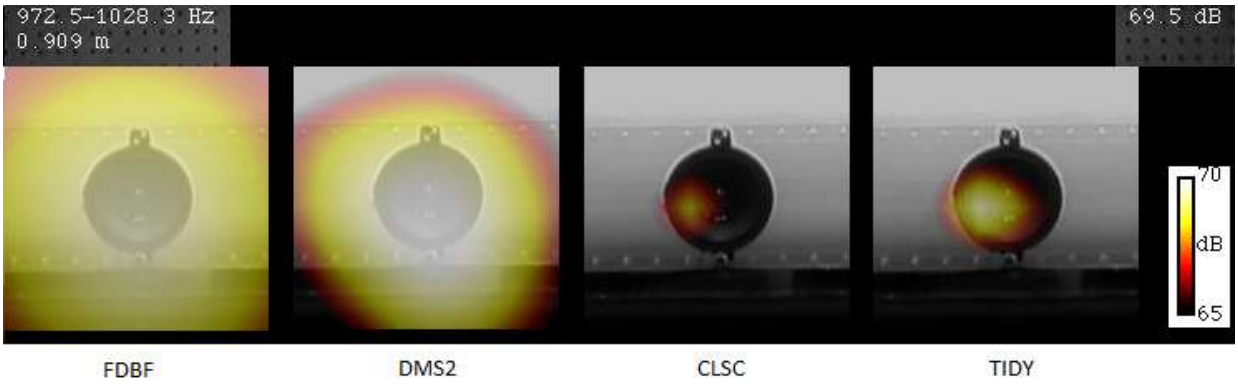

(a)

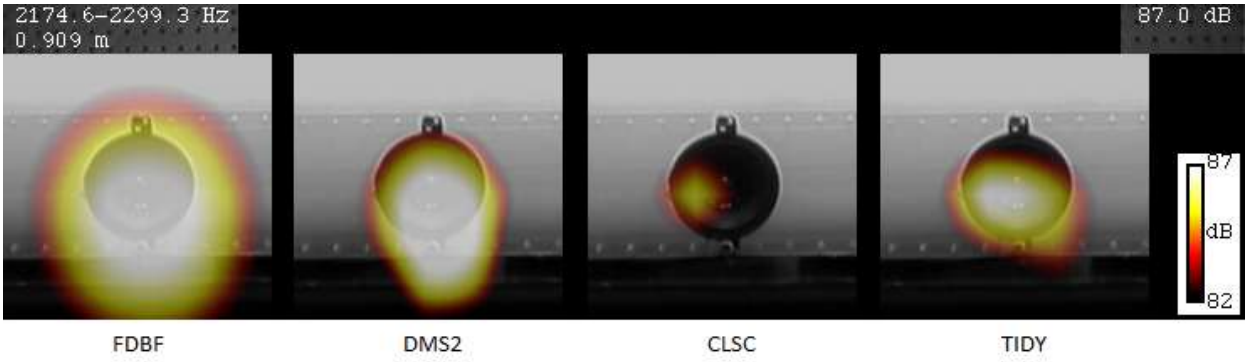

(b)

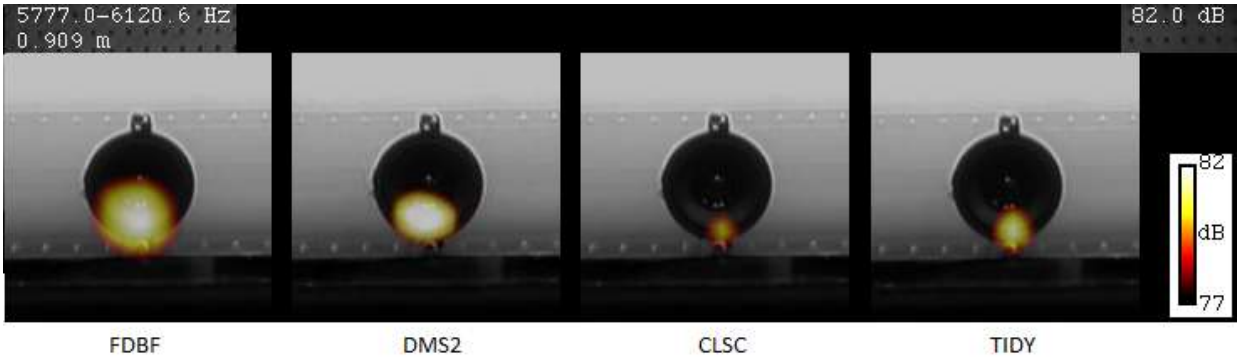

©

Figure 176: Beamform maps of narrowband frequency ranging between

(a) 972.5-1028.3 Hz, (b) 2174.6-2299.3 Hz and (c) 5777-6120.6 Hz.

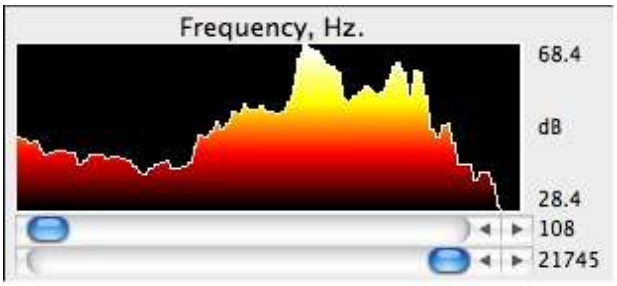

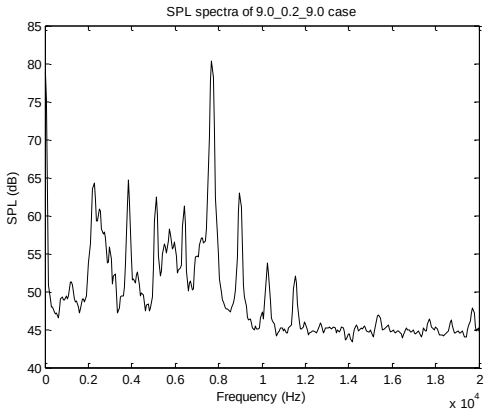

(a)

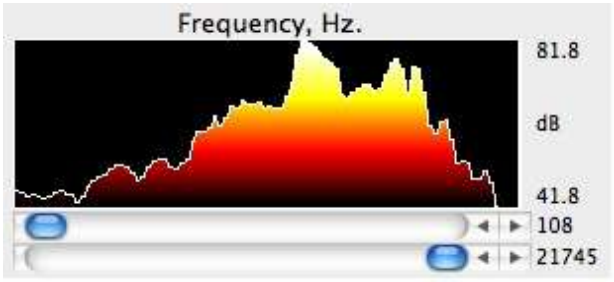

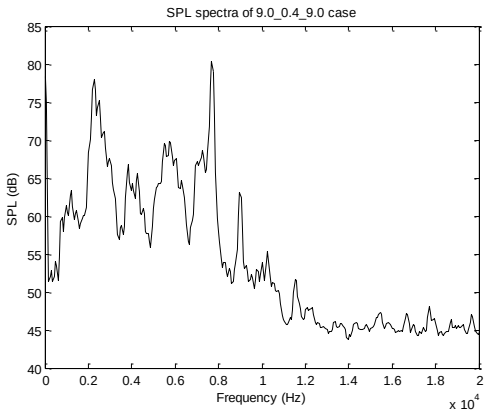

(b)

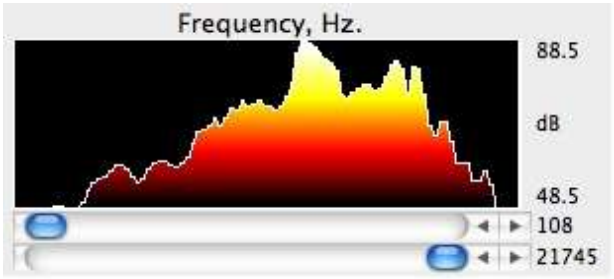

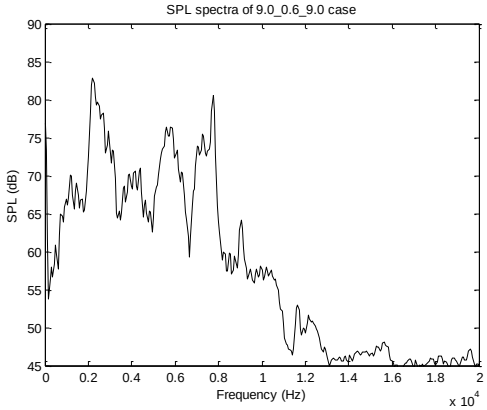

©

Figure 177: Sound pressure level spectra from the microphone array and single microphone respectively of the cases

(a) 9.0_0.2_9.0, (b) 9.0_0.4_9.0 and (c) 9.0_0.6_9.0.

The ability of the microphone array to locate multiple sources was examined in the next set of validation experiments. In this particular case we used two sources both at the same amplitude level 6 separated by a distance of 18 inches (9.6_0.0_9.6). In order to understand the behavior of the beamforming algorithms when exposed to coherent and incoherent sound sources we fed the speakers with both coherent and incoherent signals. The beamform maps for this case are shown in Figure 178. In this particular analysis the frequency band of interest was chosen to be 2292.3-2431.5 Hz and the dynamic range was chosen to be 10 dB. We observed that the FDBF, DMS2 and TIDY algorithms whose formulation was based on incoherent sources was able to pick up both the sources in both incoherent and coherent cases. The CLSC algorithm is formulated to pick out the highest of the coherent sources as evident from our results. Also in the incoherent case the CLSC was able to locate both the sources. The cleanest map was given by the CLSC followed by TIDY then DMS2 and finally FDBF.

In the next set of validation experiments the number of sources and the distance of separation were the same as the latter case whereas the amplitude of the two sources was different. The idea behind this experiment was to check the beamformers' ability to locate sources of different amplitudes. Figure 179 shows the beamform maps of the case 9.6_0.0_9.4 both for coherent and incoherent cases. We observed that all the beamforming algorithms were able to distinguish the two sources. In this case the difference in amplitude was about 8 dB. It was observed that the beamforming algorithms were able to locate the two sources with an amplitude difference of up to 12 dB beyond which they were not able to distinguish the sources clearly.

The number of sources was then increased to three separated by a distance of 9 inches from each other. The amplitude of the sources was the same and both incoherent and coherent cases were tested. The beamform maps of the case 9.6_0.6_9.6 are shown in Figure 180. We observed that for the frequency range of interest the beamforming algorithms were able to locate the three sources. In case of FDBF and DMS2 we observe that when the sources are coherent the algorithms tend to merge sources together. The CLSC algorithm locates only a single maximum amplitude source in the coherent case true to its formulation. The TIDY algorithm was able to locate all the three sources in both the incoherent and coherent case.

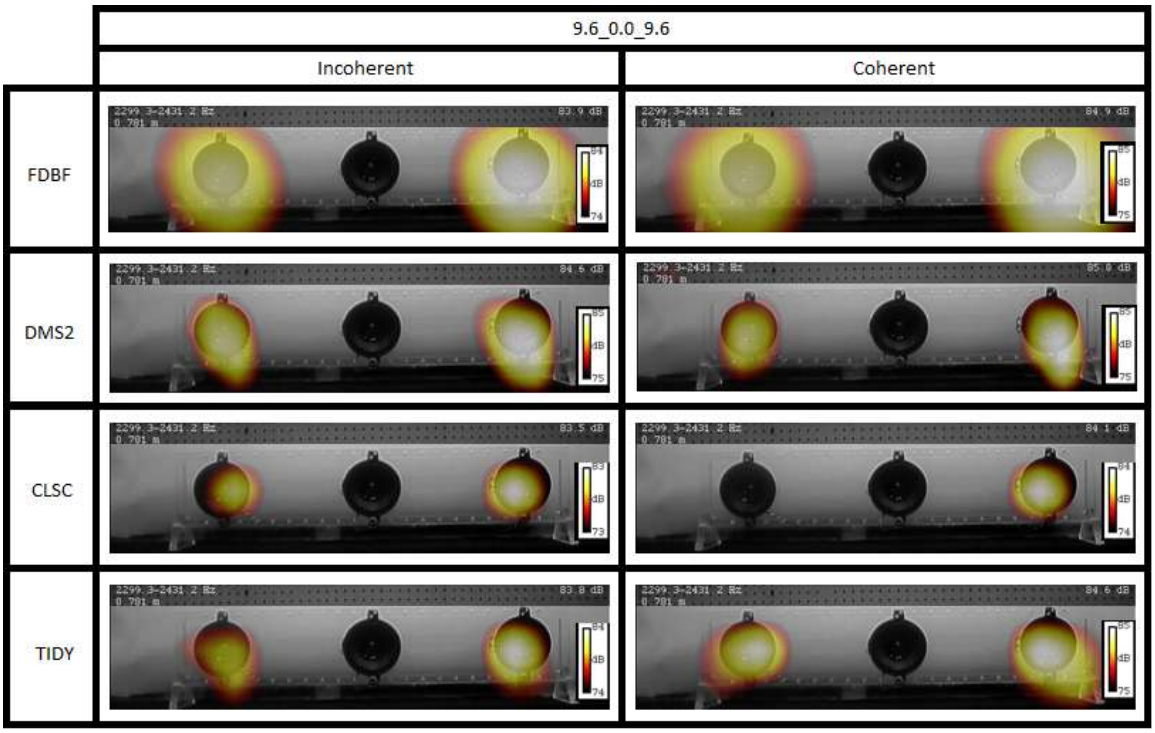

Figure 178: Comparison of beamform maps obtained from FDBF, DMS2, CLSC and TIDY for multiple incoherent and coherent sources of the same amplitude (9.6_0.0_9.6).

As the aerodynamic sources on a wind turbine are moving sources, we used one of the speakers suspended from a rod which could be oscillated to study a moving source. The frequency range of interest here was a broadband range 1371.2-5146.6 Hz (as the primary sources on wind turbine are broadband in nature). In order to measure broadband noise the only advanced algorithm is TIDY. The beamform map for the oscillating source is shown in Figure 181. We observe that TIDY is able to locate the source as it is in its motion. As before with increase in the frequency range the beamform maps gets cleaner and sharper.

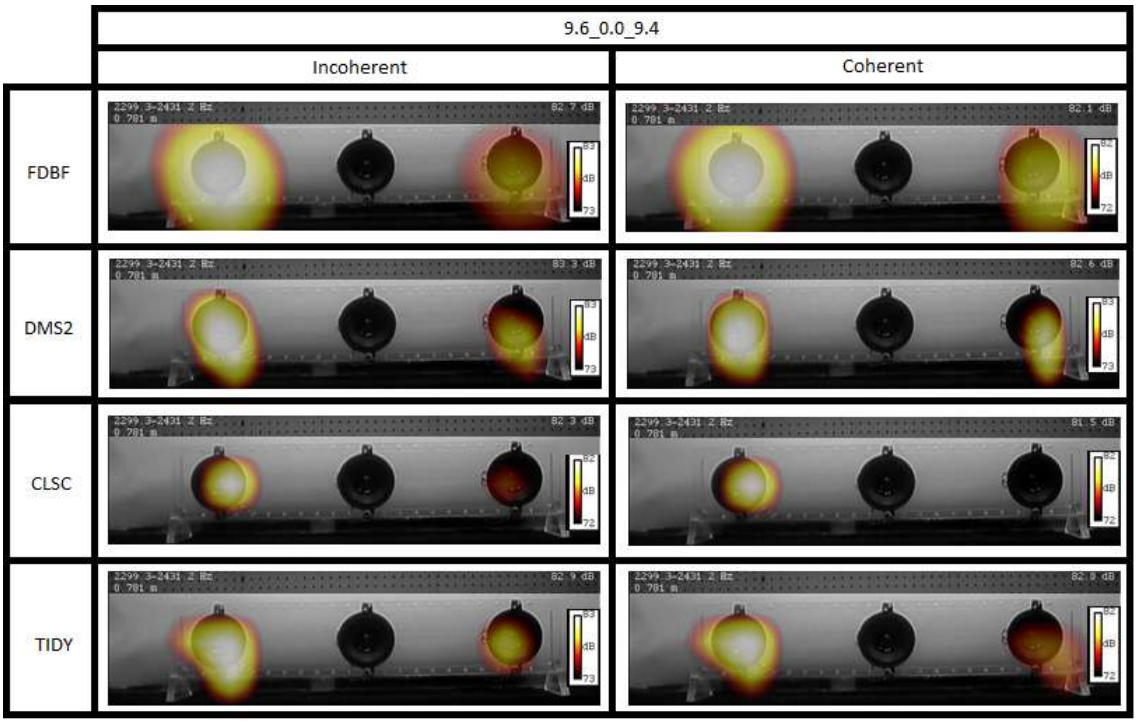

Figure 179: Comparison of beamform maps obtained from FDBF, DMS2, CLSC and TIDY for multiple incoherent and coherent sources of different amplitude (9.6_0.0_9.4).

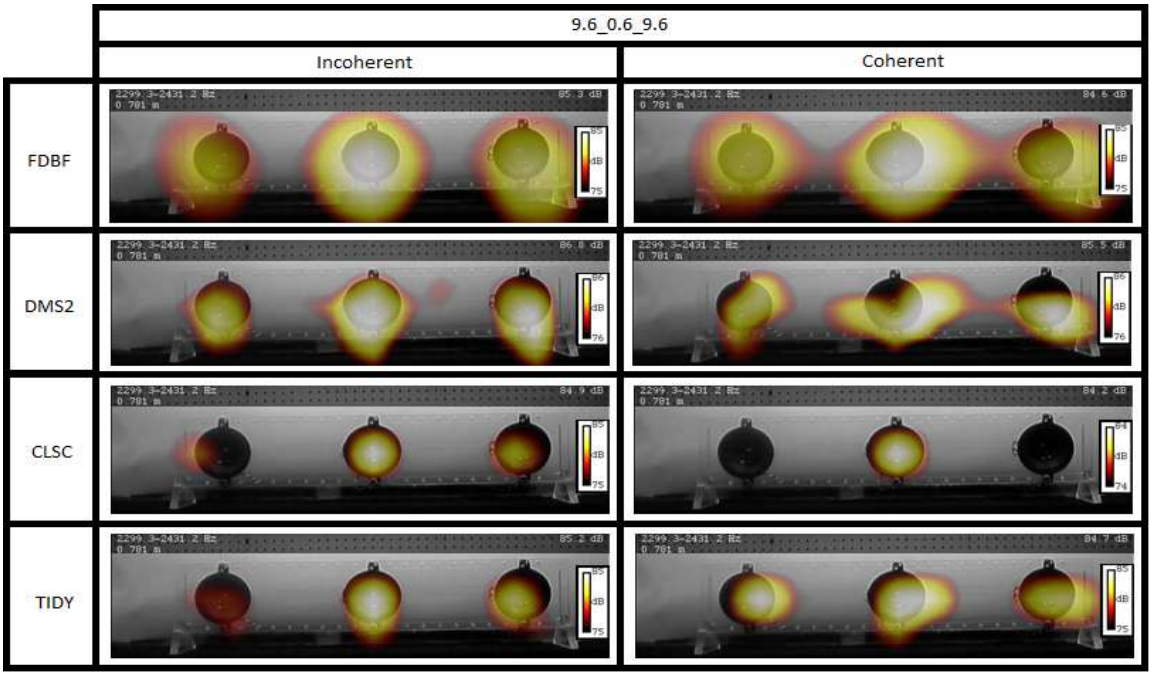

Figure 180: Comparison of beamform maps obtained from FDBF, DMS2, CLSC and TIDY for three incoherent and coherent sources of the same amplitude (9.6_0.6_9.6).

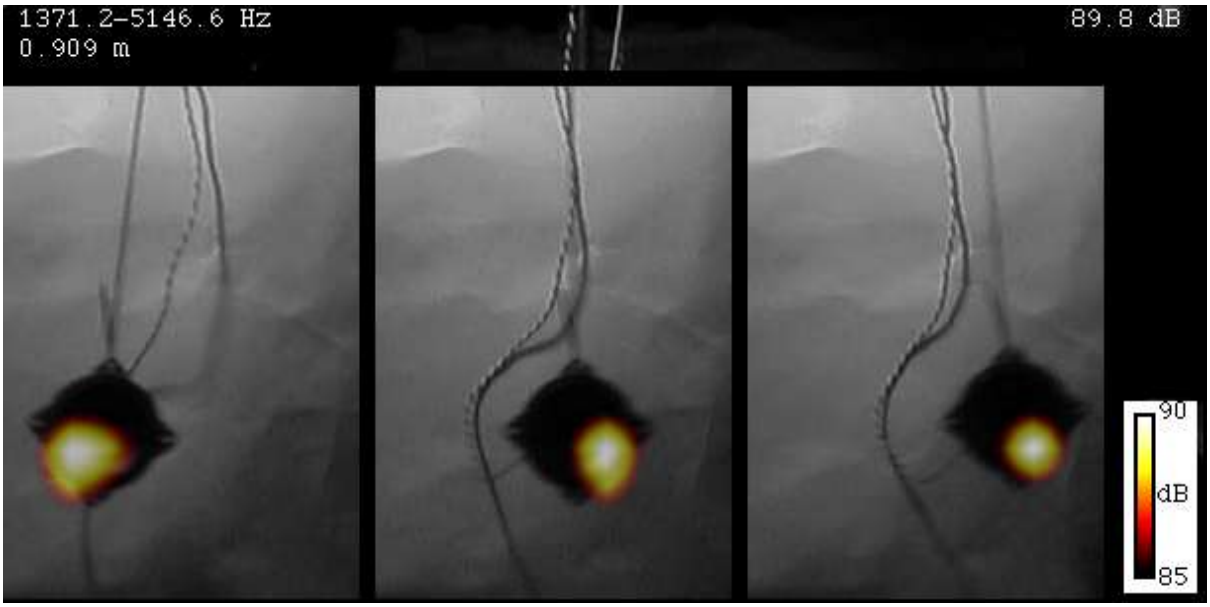

Figure 181: Beamform map of a single oscillating source at three different positions during oscillation obtained using TIDY.

F4. Wind Turbine Noise Measurement

The objective of this part of the study was to use a compact microphone array along with the use of advanced beamforming algorithms to successfully measure and locate sources on a production scale 1.5 MW wind turbine located at a wind farm.

As a part of this project the university (under DOE sponsorship) purchased a GE 1.5 MW wind turbine. The picture of this wind turbine is shown in Figure 182. This wind had a hub height of 85m with the rotor diameter of 77m. The turbine has a variable rotor speed of 10.4 to 10.4 rpm. The rated wind speed of this turbine is 12 m/s. The wind turbine is located at the Invenergy farm at Grand Ridge Illinois. In addition, to study the noise from the mechanical parts in the nacelle, a Viryd 8kW wind turbine drive train simulator which can simulate various wind conditions was used. The drive train consists of four part namely, Gear box, brake, CVP and Generator. This drive train is attached to a fly wheel which is in turn connected to a drive side with gearbox and a motor controlled by a user program. The program allows the user to input various parameters such as the wind speed and turbulence level. Based on which the drive motor will be given the appropriate amount of current to simulate the wind conditions. The picture of the wind turbine drive train is shown in Figure 187. The distance from the base of the wind turbine to the array was measured to be 85 m.

Figure 182: The GE 1.5 MW wind turbine located at the Invenergy wind farm in Grand Ridge, Illinois.

The wind turbine noise was first measured using a conventional beamforming algorithm, the delay and sum (DAS) beamformer. The beamform map for this case is shown in Figure 183. We observed that the DAS beamformer produced a smeared sound pressure level (SPL) map that covered the entire wind turbine. It was not possible to distinguish between the different aerodynamic and mechanical source of noise from the wind turbine. Next, the noise from the same the wind turbine was measured using an advanced algorithm, TIDY. The beamform map for this case is shown in Figure 184. We observed that the TIDY beamformer was able to distinguish the various noise sources on the wind turbine. The noise around the edge of the rotor blades are the blade tip vortex noise. The noise at the nacelle of the wind turbine is mainly produced by mechanical sources. Figure 185 shows the beamform map of wind turbine noise using TIDY at a particular instant in time during its rotation. We can clearly indentify the mechanical noise that arises inside the nacelle and the aerodynamic noise from the blade tip.

The important application of using the microphone array to measure wind turbine noise is that we could detect changes that arise due to various components and various modes of operation of the wind turbine. For instance we measured the noise due to yaw motor when it was operational. The particular wind turbine under interest has a unique technology which is known as the catch the wind. This technology detects the wind speed and direction up to 300 ft in front of the wind turbine and turns the nacelle to the direction of the wind. This is made possible by the yaw motors in the wind turbine. Figure 186(a) shows the time series of the microphone array measuring the noise from the wind turbine. In this particular case we see the yaw motor in action. The frequency of interest in this particular case was 1087-1149 Hz. We see that there is an increased amplitude for a particular period of the time series. This is due to the yaw motor. In Figure 186(b) we observe the amplitude of the noise from the nacelle to be about 7.7 dB. From Figure 186(c) we observe that in the case where the yaw motor is operational the

noise increases to up to 24.3 dB at the particular frequency of interest. This is an increase of about 16 dB in the nacelle.

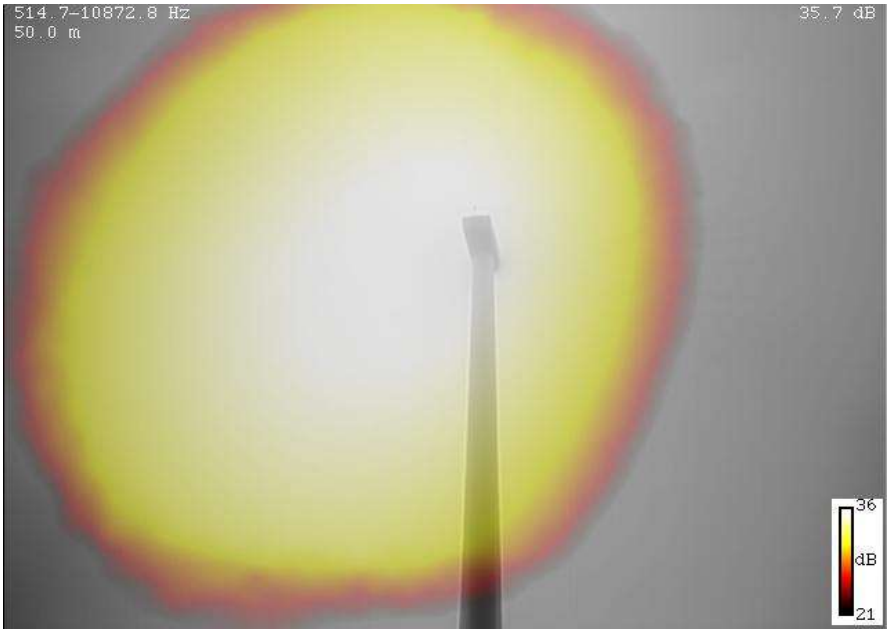

Figure 183: Beamform map of the GE 1.5 MW wind turbine using DAS.

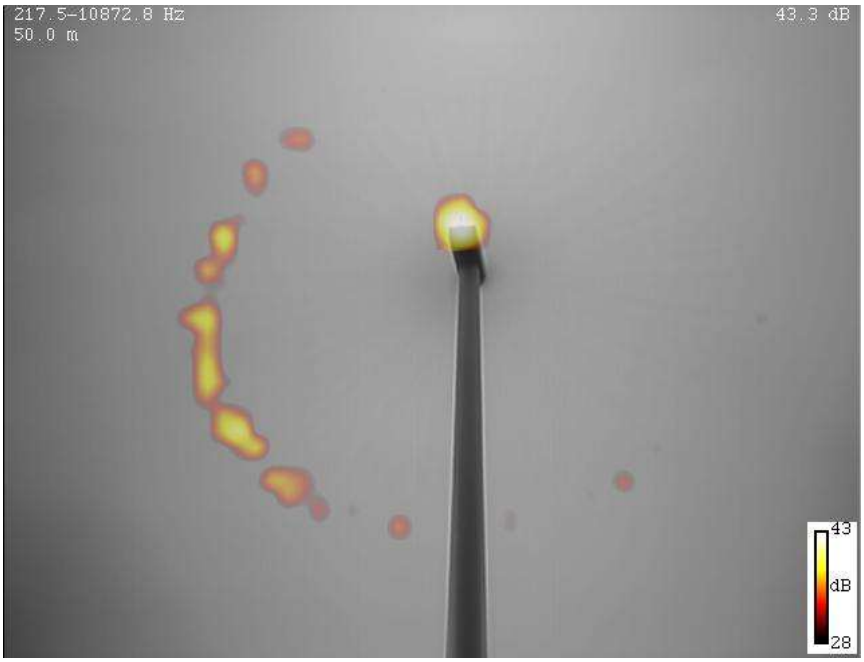

Figure 184: Beamform map of the GE 1.5 MW wind turbine using TIDY.

Figure 185: Beamform map of the GE 1.5 MW wind turbine using TIDY at a particular instant of time during its rotation.

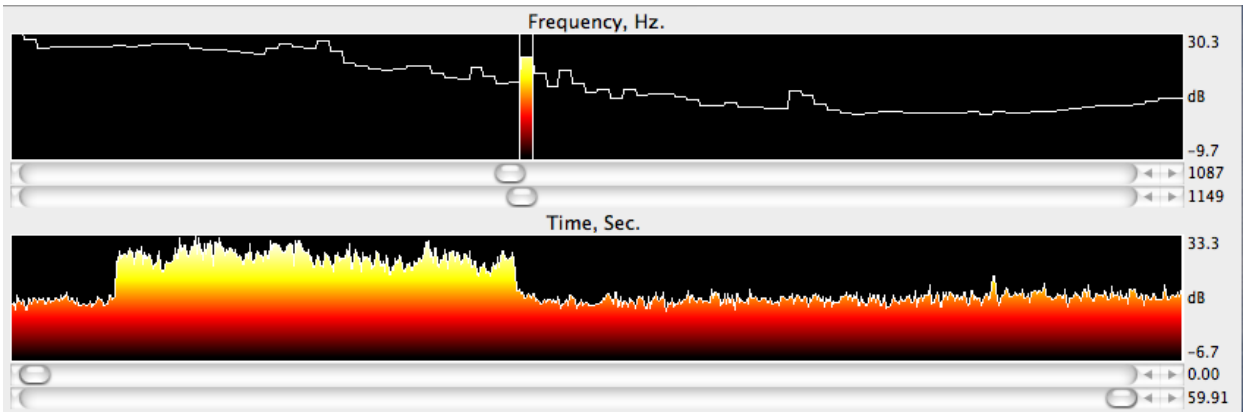

(a)

(a) (c)

Figure 186: Schematic of. (a) time series of the wind turbine noise measured using the microphone array showing the increase in amplitude due to yaw motor, (b) the beamform map (TIDY) showing the nacelle noise at 1087-1149 Hz when the yaw motors are not operational and (c) the beamform map (TIDY) showing the nacelle noise at 1087-1149 Hz when the yaw motors are operational.

In order to study in detail the noise produced inside a nacelle, measurements were conducted on the Viryd 8kW wind turbine drive train simulator. The beamform map of the gearbox at a wind speed of 6 m/s and 0% turbulence level using TIDY is shown in Figure 188. The frequency of interest was chosen to be 164-2056 Hz and the microphone array was placed 0.6 m away from the drive train. We observe that in this particular frequency of interest the noise from the drive train was about 75.7 dB. The gear box and the generator produces considerable amount of noise. The beamfrom map for the generator using TIDY for the same wind conditions are shown in Figure 189. We observe that for the frequency range of interest chosen the noise produced by generator is about 72.5 dB. At frequencies above 3000 Hz we observed that the CVP was producing a considerable amount of noise. The beamform map of the CVP using TIDY with the same wind conditions is shown in Figure 190. We observe that the noise produced by CVP was about 66.6 dB for the frequency of interest considered.

Figure 187: Viryd 8 kW wind turbine drive train simulator.

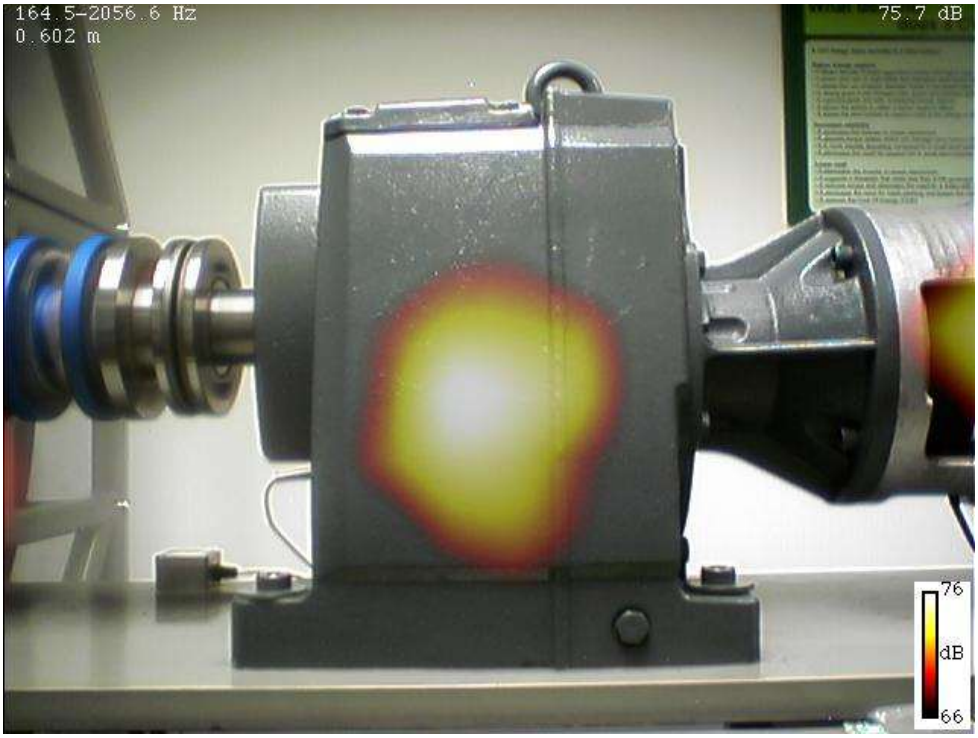

Figure 188: Beamform map of the gearbox at wind speed 6 m/s and turbulence 0% using TIDY.

Figure 189: Beamform map of the gearbox at wind speed 6 m/s and turbulence 0% using TIDY.

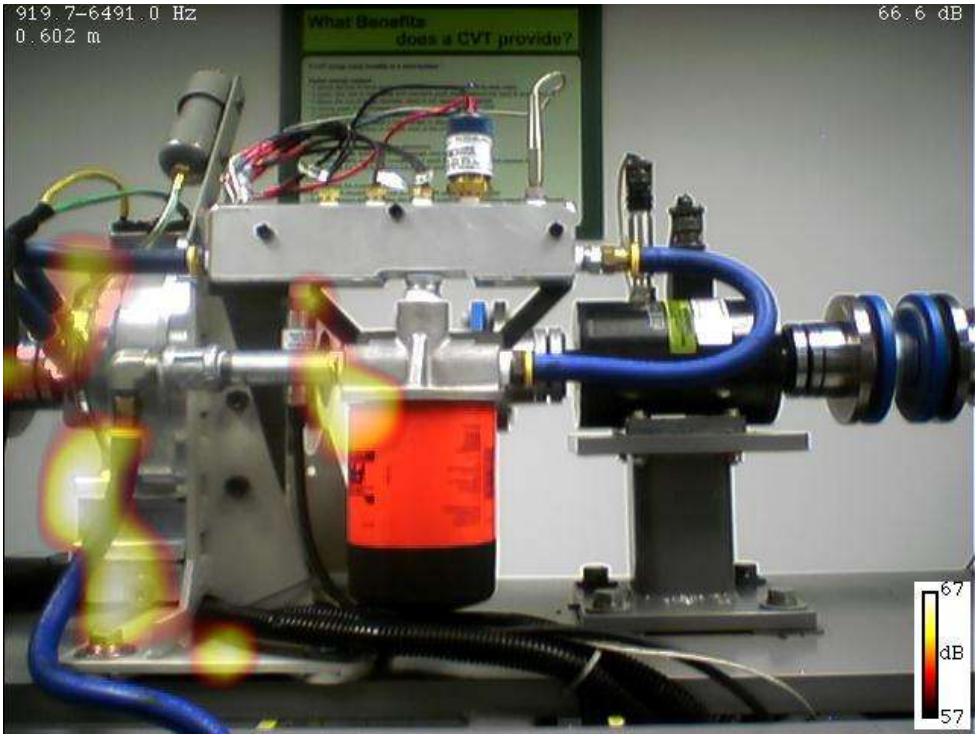

Figure 190: Beamform map of the CVP at wind speed 6 m/s and turbulence 0% using TIDY.

F5. Summary and Future Possibilities

The results of the initial calibration of the array provided us with the knowledge of how various beamforming algorithms behave on exposure to different types on noise sources. The FDBF, DM2 and CLSC were all limited to narrowband analysis whereas DAS and TIDY could be used for broadband analysis. Even though the FDBF, DMS2 and TIDY beamformers were all formulated on the assumption of incoherent sources, they were able to locate coherent sources as well. TIDY, however, produced cleaner spectrum map than FDBF and DMS2. The CLSC beamformer was formulated to pick the maximum of the coherent sources as evident from our experimental results. The CLSC however was able to locate the incoherent sources too. In terms of the frequency of the source, for the particular array and the distance of the source from the array, the microphone array was able to clearly locate the sources above 1000 Hz. The distance of source separation for which the beamformers were able to separate the sources was about 6-8 inches from each other for the frequency range of 1000 – 4000 Hz. From the study it was clear that there was no single algorithm that was perfect for measuring wind turbine noise. In order to study the narrow band sources CLSC was the best algorithm and for broadband analysis TIDY was the best. In view of moving sources TIDY provided the best results again.

From the results of actual wind turbine measurements, it was evident that the compact microphone array was effectively able to separate various noise sources, both mechanical and aerodynamic, produced by the wind turbine. The results from the GE 1.5 MW wind turbine show the potential of the microphone array by effectively separating the blade tip vortex noise and the nacelle mechanical noise. Further we were able to separate out the yaw motor noise which was a narrow band source. The results from the Viryd 8kW wind turbine drive train simulator show that using the microphone array we could further separate the mechanical noise in the nacelle to its particular components such as the gearbox, cooling fan and the generator. In this particular case we were able to separate out the noise components from the gearbox, CVP and generator.

From the detailed study we conducted, we have realized our objective of studying various beamforming algorithms and using them to locate the noise sources on a wind turbine with a compact array. This demonstrates the potential of the microphone arrays in the future of wind turbine noise management. We could use this tool to further investigate the different types of aerodynamic noise that arise on the blade such as the blade tip noise and the trailing edge noise. A lot of interest has been shown in recent years to study these noise sources. This could provide valuable information on modifying the blade configuration to further reduce the aerodynamic noise. Also measurements could be made on a variety of wind turbines such as smaller urban wind turbine and larger wind turbines. One other possible application for the microphone array is to use them as a health monitoring tool for the wind turbine.

G. Wind Turbine Acoustics – Numerical Studies

Modern industrial economies are heavily reliant on electricity. As a result, developing and maintaining a sufficient supply of affordable and reliable power is a priority for every nation. At the same time, a number of factors have combined to stimulate increased interest in more “environmentally friendly” methods of power generation, such as wind or solar. With the currently ongoing political turmoil in the Middle East and the recent Fukushima nuclear accident, this interest is only increasing.

This work involves the numerical simulation of the flow around wind turbines and investigating the acoustic field associated with the unsteady fluid behavior. This section discusses the progress made in this work, the analysis methods used, and the results obtained.

G1. Numerical Methods

The current methodology combines the abilities of three different numerical tools to predict the unsteady flow around a wind turbine, the resulting acoustics, and an analysis of the noise sources. The Navier-Stokes equations are solved using the OVERFLOW solver to obtain an unsteady flow field in the vicinity of the turbine. Data from this solution is then fed into the PSU-WOPWOP Ffowcs-Williams Hawkings solver to predict the farfield acoustics. This prediction is used to record sound levels at virtual microphone locations, and this information is fed into the Beamform Interactive software package which is used to analyze the data using a variety of beamforming methods.

This methodology is referred to as the "synthetic array technique" as it uses numerical methods to perform an analysis identical to that used for experimental data from microphone arrays. A similar technique was successfully used in a previous joint effort for the acoustics of an airfoil with a blunt trailing edge.

The CFD code used for this work was version 2.2 of the OVERFLOW solver, which is the latest release of this widely used code from NASA Langley [**36**], [**37**]. This software is a state-of-the-art Navier-Stokes solver for structured meshes. The original OVERFLOW code has long been used successfully for a wide variety of Reynolds-averaged Navier-Stokes (RANS) simulations [**38**], [**39**], [**40**].

OVERFLOW 2.2 solves the time-dependent Navier-Stokes equations in an implicit manner on overset structured meshes. The compressible form of the equations are solved in conservative form on a curvilinear coordinate system.

Recent additions to the code make it particularly attractive for the work reported here [**41**], [**42**], [**43**].

With version 2, OVERFLOW introduced the OVERFLOW-D mode (originally from the code of the same name by Robert Meakin). Compared to the regular mode of operation, this mode requires some additional input files and NAMELIST input, but what it enables is the use of internal mesh assembly algorithms (called "Domain Connectivity Function"—DCF) for simulations with moving meshes. This obviates the need for an external mesh assembly package (such as PEGSUS or SUGGAR).

OVERFLOW-D mode also allows automatic off-body mesh generation. When used in this fashion, Cartesian outer meshes can be automatically generated prior to mesh assembly using DCF. Only the near-body meshes must be provided to the code.

For the current work, the code was run in "OVERFLOW-D" mode. Thus, OVERFLOW's internal mesh motion, hole cutting, and block coupling algorithms were used. In addition, automatic off-body mesh generation with mesh adaption was used throughout the run.

Similar to OVERFLOW-D mode, OVERFLOW now has a built-in 6-DOF (six degree-of-freedom) mesh motion module called the "Geometry Manipulation Protocol" (GMP). GMP is a protocol for specifying

geometric hierarchies and associated rigid-body motion. OVERFLOW currently implements only a subset of the larger GMP, but this capability is more than sufficient for the current work, and eliminates the need for an external mesh motion package.

With GMP, two files are used to set up mesh motion parameters for a simulation. For a case like this, which has a simple prescribed motion for the rotor meshes, the configuration is quite simple. First, a file named "Config.xml" is used to identify which meshes are associated with each other, assign labels to these groupings (called "components"), and specify an initial orientation for each component. The Config.xml file for the wind turbine case consists of the following:

```
<?xml version='1.0' encoding='utf-8'?>
<Configuration AngleUnit="degree">
  <Component Name="Rotor" Type="struc">
    <Data> Grid List=1-12 </Data>
    <Transform>
      <Rotate Center="0.,0.,0." Axis="0.,0.,1." Angle="-45." />
    </Transform>
  </Component>

  <Component Name="Tower" Type="struc">
    <Data> Grid List=13 </Data>
    <Transform>
      <Rotate Center="0.,0.,0." Axis="0.,0.,1." Angle="0." />
    </Transform>
  </Component>

  <Component Name="Nacelle" Type="struc">
    <Data> Grid List=14-16 </Data>
    <Transform>
      <Rotate Center="0.,0.,0." Axis="0.,0.,1." Angle="0." />
    </Transform>
  </Component>

</Configuration>
```

The above file identifies three different components: "Rotor", "Tower", and "Nacelle". The near-body meshes (blocks 1-16) are each assigned to one of the three components. The rotor is identified as being initially at the negative 45 degree position.

The prescribed motion is then specified using a second XML file: Scenario.xml:

```
<?xml version='1.0' encoding='utf-8'?>
<Scenario AngleUnit="radian">
 <Prescribed Component="Rotor" Start="0" Duration="100000">
```

```
  <Rotate Center="0.,0.,0." Axis="0.,0.,1." Speed="-0.198846689" Frame="parent" />
 </Prescribed>

 <Prescribed Component="Tower" Start="100000" Duration="0">
  <Rotate Center="0.,0.,0." Axis="0.,0.,1." Speed="0." Frame="parent" />
 </Prescribed>

 <Prescribed Component="Nacelle" Start="100000" Duration="0">
  <Rotate Center="0.,0.,0." Axis="0.,0.,1." Speed="0." Frame="parent" />
 </Prescribed>

</Scenario>
```

The above XML specifies that the "Rotor" component (defined in Config.xml) is rotating about the *z*-axis at a constant speed of approximately -0.199 radians per non-dimensional time unit. The motion starts at the beginning of the simulation, and continues, effectively, forever (technically, the motion would stop at non-dimensional time of 100,000). The other two components (the "Tower" and the "Nacelle") are both set as stationary.

Another extremely useful capability of the OVERFLOW solver is Adaptive Mesh Refinement (AMR). This is the ability to adapt the off-body Cartesian meshes (generated using the OVERFLOW-D mode discussed above) to better resolve the propagation of flow features away from the near-body meshes. The initial off-body Cartesian mesh generation algorithm produces a multi-block configuration where the blocks surrounding the near-body meshes closely match the resolution of those near-body meshes. Away from the near-body meshes, however, the resolution coarsens until, near the farfield boundaries, the mesh spacing exceeds one meter in each direction.

The initial configuration is perfectly suitable for starting the simulation, but as the run progresses, the vortices shed from the rotor (as well as from the nacelle and tower) will be dissipated due to the lack of mesh resolution unless the computational mesh is refined in the necessary regions. Likewise, because the rotor is constantly sweeping through space, there may be regions which at one time require refinement, but which later do not need it.

The traditional approach to such a situation is to generate a mesh which is refined everywhere that might ever need such refinement throughout the entire simulation. This typically results in a huge mesh (in terms of number of points). Furthermore, such meshes almost always have one of two significant drawbacks. In the first case, the flow features of interest do not always move exactly as expected, and thus some may move beyond the refined region of the mesh (and thus fail to propagate correctly). In the other case, meshes are often over-refined, or finely spaced in regions which do not need them. This results in a significantly increased run time for the simulation.

OVERFLOW's mesh adaption algorithm allows the off-body mesh to be refined and/or coarsened as the solution progresses. Our initial wind turbine simulations did not employ the adaptive mesh refinement

algorithm, and a consequence of this was that the unsteady features in the flow were largely dissipated once they had propagated more than one radius downstream.

The results reported here did use the AMR algorithm, and because of this, the unsteady flow features were successfully propagated much further downstream. For the current work, vorticity magnitude was used to trigger the adaption sensor. Mesh refinement was performed every 40 time steps for the cases reported here, which corresponds to every five degrees of rotation of the rotor.

One drawback of the AMR algorithm is that, while it is more efficient than refining the mesh everywhere, it still results in a significant increase in mesh size. In this case, the baseline mesh had approximately 17 million points, but with AMR, the runs reported here ultimately used meshes which had between 40 and 55 million points on any given time step.

After our initial results with AMR (which are reported here) were obtained, it was discovered that the settings we used were not ideal. Preliminary tests using the most recent version of OVERFLOW (version 2.2c) and the recommended AMR settings indicate that the mesh size can quickly grow too large for the limited resources on ITAC's in-house compute cluster. When two or three levels of refinement were permitted, the mesh grew so quickly in size that the ITAC cluster was unable to capture even 90 degrees of rotation of the rotor before the run crashed. Even when limiting the number of off-body refinement levels to one, the total number of mesh points climbs to more than 100 million on more than 2000 blocks by the time a complete revolution of the rotor has been modeled.

The solver was run with a second order implicit scheme in time in conjunction with a dual time marching method to obtain a time-accurate solution. Six sub-iterations per time step were used to synchronize the boundaries with the interior flow and better allow for signals to propagate between computational mesh blocks.

A second order central difference method was used for the explicit convective terms on the near-body meshes, with spectral-radius based smoothing to prevent spurious oscillations. Our initial simulations used the same algorithm for the off-body meshes, and did not make use of the adaptive mesh refinement capability. Based on those results, however, the more recent simulations discussed here employed, for the off-body meshes, both AMR and a 4^{th} order central scheme with a higher-order filter to prevent the build-up of spurious oscillations. Since the majority of the flow domain contains very low speed flow (compared to the typical aircraft external flow situations for which OVERFLOW was originally designed), a Low Mach number preconditioning algorithm was used to stabilize the code.

An SST turbulence model was used in the near-body meshes (with Delayed Detached Eddy Simulation), but the off-body meshes were run inviscid. The turbulence model convective terms were solved second order.

The PSU-WOPWOP code is based on the concept of an acoustic analogy. The acoustic analogy was introduced by Lighthill [**44**] in his seminal paper on sound generated aerodynamically. In an acoustic analogy the equations of motion are rearranged into the form of a wave propagator and equivalent

sources. This pioneering work introduced the concept of convective amplification and Doppler frequency shift.

Lilley [**45**] introduced an acoustic analogy in which the wave propagator included the effects of mean shear and density gradients. In the case of a parallel shear flow the equivalent sources are all at least second order in the turbulent fluctuations. Noise prediction methods based on Lilley's equation generally use steady calculations of the flow development, such as provided by a RANS-based Navier-Stokes solver. These are used to set the length and time scales of the turbulence. Examples include methods for jets developed by Khavaran et al. [**46**] and Khavaran [**47**].

In their 1969 paper, Ffowcs Williams and Hawkings [**48**] utilized the powerful technique of generalized function theory to an extension to the Lighthill acoustic analogy that enabled them to consider the noise generated by surfaces in arbitrary motion. The FW–H equation is an exact rearrangement of the continuity equation and the Navier–Stokes equations into the form of an inhomogeneous wave equation with two surface source terms (monopole and dipole) and a volume source term (quadrupole). Although the quadrupole source contribution is insignificant in many subsonic applications with solid surfaces, it is the only noise source term in the original Lighthill acoustic analogy and is particularly relevant for jet noise. Even so, the quadrupole source term in the FW–H equation is a volume source term, therefore it is considerably more expensive to evaluate than the surface source terms.

Although originally pointed out by Ffowcs Williams and Hawkings, the usefulness of the FW–H equation as a Kirchhoff type equation was demonstrated by Brentner and Farassat [**49**]. In this application, the fictitious surface used in the derivation of the FW–H is located not on a solid body, as in the classical implementation, but rather surrounding all the relevant noise sources. Thus the integration surface (or acoustic data surface) is a fictitious surface (like a control volume) located in the fluid; hence, this application of the FW–H is called the permeable (or porous) surface formulation because fluid may flow through the surface. With all the significant acoustic sources contained inside the surface, the volume quadrupole term does not need to be computed – saving substantial computational effort. The permeable surface formulation has become a valuable noise prediction tool primarily because CFD has advanced sufficiently to provide the time-dependent flow field solution on the integration surface with high spatial and temporal fidelity, as required by the permeable surface formulation of the FW–H.

PSU-WOPWOP is a general purpose Ffowcs Williams–Hawkings (FW-H) solver developed at The Pennsylvania State University by Dr. Brentner and his research team [**50**], [**51**], [**52**], [**53**]. The code was originally developed to compute the noise of rotorcraft in maneuvering flight, but was developed using an object-oriented design in the Fortran 95 language in a very general manner. Both the classical and permeable surface formulations of the FW-H equation [**54**], as expressed by Farassat's Formulation 1A [**55**], [**56**], have been implemented in the code and have been thoroughly tested.

The PSU-WOPWOP code has extensive source motion capability—originating from its roots as a maneuver noise prediction tool. The integration surfaces (solid or permeable) may be either rigid or flexible. PSU-WOPWOP predicts the acoustic pressure time history in the near and far fields, for either stationary or arbitrarily moving observers. PSU-WOPWOP also has significant output signal processing

to convert the acoustic pressure time history into acoustic spectra, including narrow band spectra, $1/n^{th}$ octave bands, etc. The code's output processing also includes the ability to filter the data over arbitrary frequency ranges and include various types of windowing functions for the frequency domain processing.

PSU-WOPWOP has recently been upgraded to predict the acoustic pressure gradient at arbitrary observer locations [**57**], [**58**]. The acoustic pressure gradient is an input to either frequency or time domain acoustic scattering codes, which then can predict the scattered field when rigid bodies are in the vicinity of the noise predicted by PSU-WOPWOP. PSU-WOPWOP has been used for rotor noise prediction, landing gear noise prediction, acoustic scattering, prediction of trailing edge noise, and jet noise.

In the current work, the permeable integration surfaces (also referred to as acoustic data surfaces or ADS) will be used for the FW-H noise prediction. PSU-WOPWOP will require the time-dependent location of the surfaces along with the time dependent specification of density, momentum and pressure at each of the surface mesh points.

The computation of the acoustic pressure at a large number of observer positions, as might be used, for example, in an extensive phased array, should be very efficient because PSU-WOPWOP uses an observer parallel implementation, employed via the Message Passing Interfaces (MPI). This parallelism effectively sends the acoustic computation for each observer to single processor on a computer cluster, up to the number of processors available. As the processors become free, a new observer position is sent to the processor, keeping all the processors busy until the entire job is done. PSU-WOPWOP has previously been coupled with OVERFLOW and several other CFD codes using a file-based method, which is relatively easy to implement and should be ideal for this project.

Given that OVERFLOW can accurately compute the wind turbine near-field, and that PSU-WOPWOP can compute the acoustic farfield, it remains to enable the two separate solvers to communicate with each other. There are several possibilities for doing this; three of these have been identified and evaluated for the current wind turbine work.

One option is to try to obtain and use a utility which takes data from surface meshes, as processed by MIXSUR, to create the input needed by PSU-WOPWOP. The drawback to this approach is that the primary acoustic sources for this case are expected to be off-body (associated with separated regions of the flow). As such, a FWH surface on the blade surface will not properly enclose these regions, and their contribution will be lost.

To overcome this limitation, a second possibility is to create a "pringle can" mesh around the spinning blade (avoiding any intersection with the hub or mast) and use OVERFLOW's "Acoustic Data Surface" (ADS) capability to save data on it. This data can then be converted for later processing with PSU-WOPWOP. A utility would have to be created to perform this conversion. Also, when the ADS is inserted into the CFD mesh, the solution file must be somehow modified to add some form of initial conditions or else the solution must be restarted from scratch. Either option requires expenditure of additional time and resources.

A third option, and the one which appears to best fit the requirements of the current work, is to use OVERFLOW's capability to save solution data in specified regions of the flow (the "SPLITM" controls). By selecting an appropriate set of surfaces, a reasonable integration surface can be assembled around the spinning blade. The SPLITM data can then be assembled into the "patch file" (containing the surface mesh data at each time step) and "flow data file" (containing the density, momentum, and pressure on the surface at each time step) needed by PSUWOPWOP.

Using SPLITM means that no additional mesh needs to be generated, and no special manipulation of the restart solution file is required to insert initial conditions for the surfaces. Thus, this is the approach which we have taken.

There are two drawbacks to the SPLITM approach. One is that OVERFLOW saves a separate file for each SPLITM surface specified. Also, a new file is created every time the SPLITM data is output to the disk. Since each SPLITM surface must come from only one block, multiple surfaces (twelve, in fact) were required in order to construct the FWH surface. As a result, a full run of the wind turbine case will result in over 150K files which must be processed.

A new utility was written to semi-automatically assemble all of these SPLITM files into the patch and flow data files which PSU-WOPWOP reads.

Beamfom Interactive is a commercial product of OptiNav, Inc. for processing microphone array data. There are several different modules in Beamform Interactive, which allow the user to apply various beamforming methods to analyze the data. The most basic method is the "Conventional Beamforming" algorithm. This is a high speed, wide band implementation of the classical formula. An "Enhanced Resolution" variant of the classical beamforming technique is also available. This approach weights cross spectral matrix elements to improve resolution. Another algorithm available is DAMAS2. This is a high-speed version of DAMAS which employs an FFT for improved processing speed. It also used a nonuniform mesh to avoid problems with the PSF model. The CLEAN-SC method is an implementation of Sijitsma's algorithm [**33**], which is another deconvolution-based approach to beamforming. Finally, TIDY is an OptiNav method, related to CLEAN-SC, which allows analysis with unlimited bandwidth.

G2. Previous Application of the Synthetic Array Technique

As mentioned above, ITAC has previously worked with Dr. Dougherty and Profs. Brentner and Morris to couple a CFD solver with PSU-WOPWOP and Beamform Interactive to obtain insights into acoustic noise sources. This work was performed in the context of a NASA-sponsored Phase I SBIR. While the full analysis process has not been completed for the current wind turbine work, it was successfully demonstrated on an airfoil with a blunt trailing edge (specifically, a truncated NACA 0012 airfoil). The results of that work are repeated here to illustrate the potential of the approach for current wind turbine work.

Given the solution on the specified FWH integration surface(s) for the truncated airfoil test case), PSU-WOPWOP predicted acoustic data at "observer" locations corresponding to phased array microphone locations. The microphone array used for the proof-of-concept work was based on coordinates

provided by the NASA customer as representative of their MADA arrays. Figure 192 shows the array layout, with two microphones noted in particular.

The spectra predicted at these two locations are shown in Figure 193 and Figure 194. Microphone 1 identifies a peak near 5 kHz, which corresponds to the drag peak for this case. Microphone 23, on the other hand, picks up both the lower frequency peak associated with lift and the drag-related peak.

Three array views of the trailing edge segment (simulated by the CFD) were used. The first view (the "side" view) positioned the array 1.39 meters to the side of the airfoil, looking down the trailing edge, with the center of the array aligned with the trailing edge of the airfoil (see Figure 195). The second view was a "top" view, with the array positioned above the sliver of airfoil section which was simulated and looking down at the trailing edge (as shown in Figure 196). Again, the array was positioned 1.39 meters from the airfoil. The final view was the "back" view, shown in Figure 197, in which the array was positioned 1.39 meters aft of the airfoil trailing edge and faced upstream.

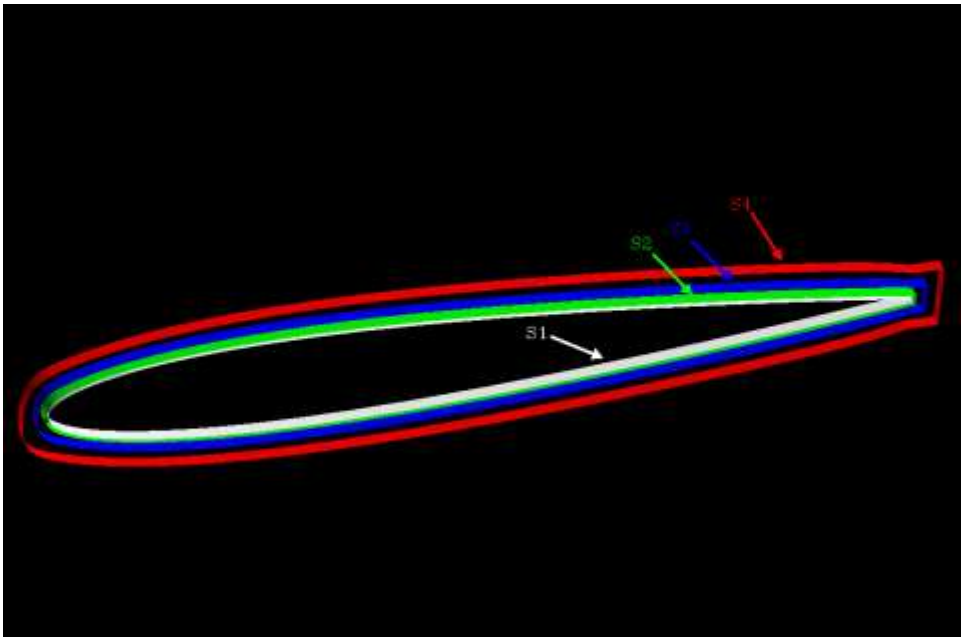

Figure 191: Locations of Ffowcs Williams-Hawkings surfaces at which data was saved in the unsteady 3-D case

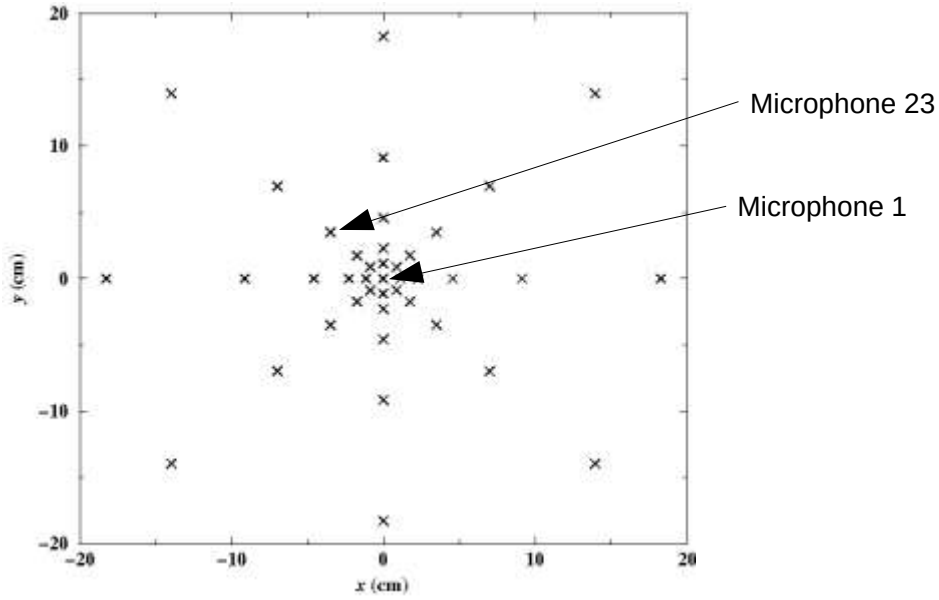

Figure 192: Arrangement of the synthetic microphone array used for the Phase I work

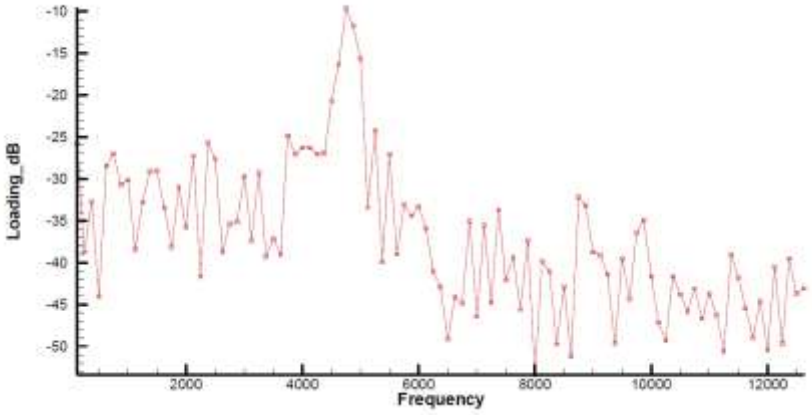

Figure 193: Spectra predicted by PSU-WOPWOP at Microphone 1 location

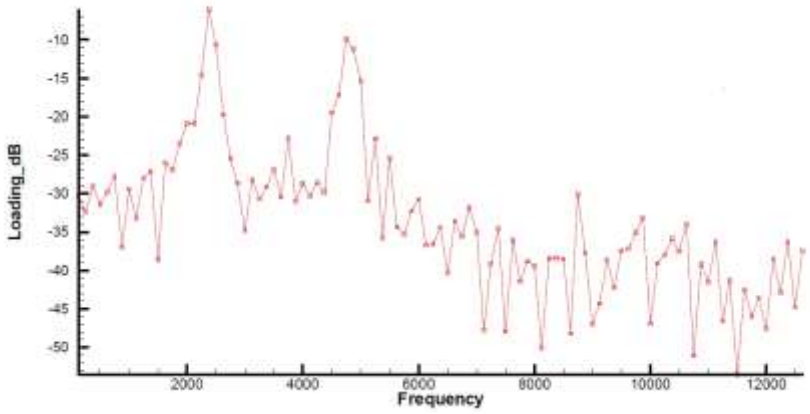

Figure 194: Spectra predicted by PSU-WOPWOP at microphone 23 location

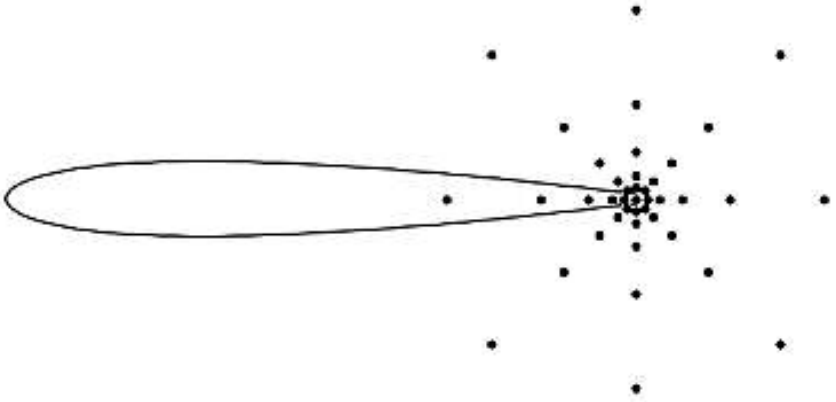

Figure 195: "Side view" orientation of the microphone array

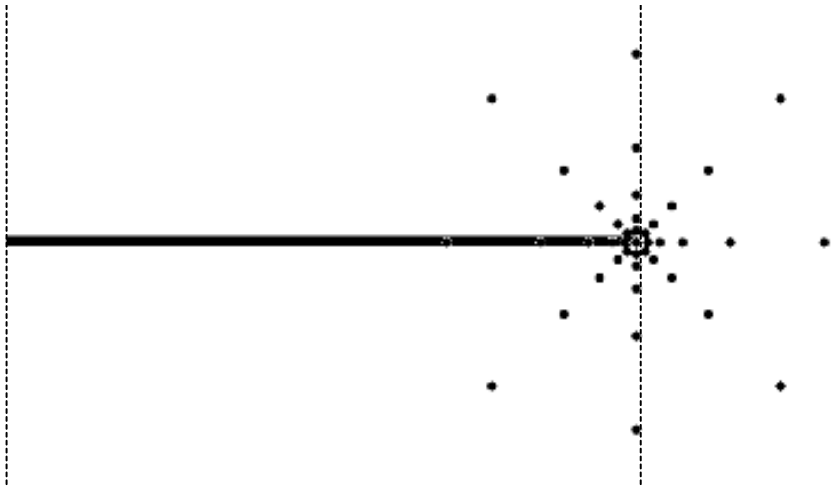

Figure 196: "Top view" orientation of the microphone array

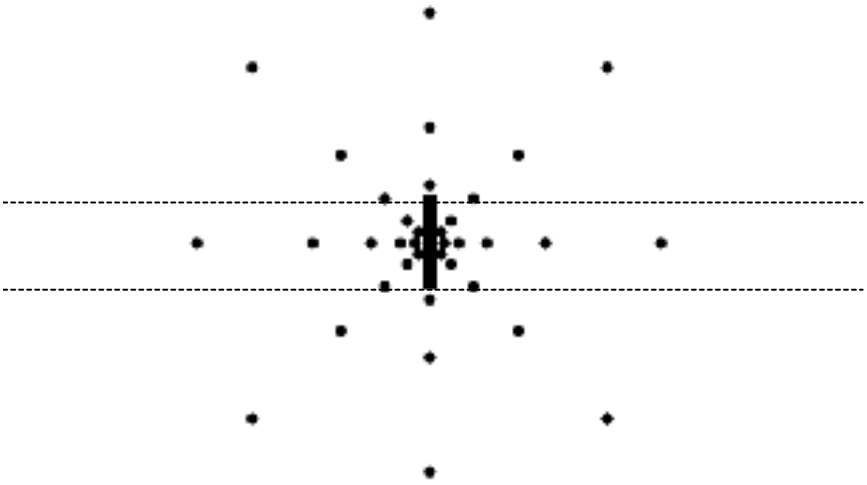

Figure 197: "Back view" orientation of the microphone array

The average array spectra detected from the three different viewpoints are shown in Figure 198. Note that the "back view" detects the peak frequency to be around 5 kHz, while the other two views show the 2.5 kHz peak having the largest amplitude.

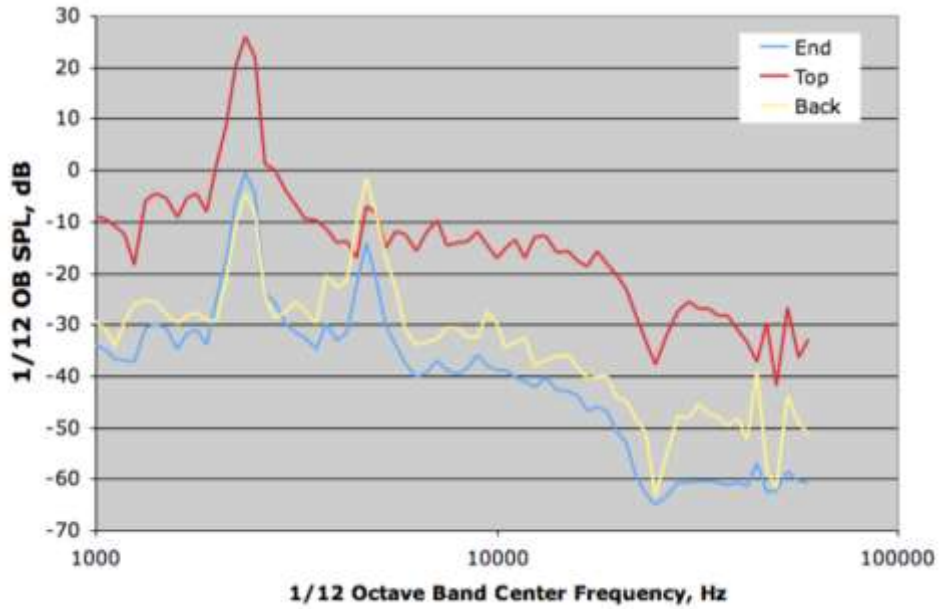

Figure 198: Average array spectra computed at the three different array positions

Several beamforming methods in OptiNav's "Beamform Interactive" product were used to analyze the data from PSU-WOPWOP. The first set of results look at the "side view" data and focus on the frequencies in the vicinity of the 5 kHz peak. The frequency range used for these results is indicated in Figure 199. A monopole-oriented analysis was used for these results.

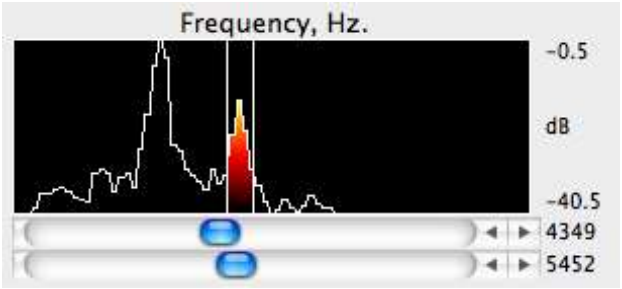

Figure 199: Frequency range used for monopole-oriented analysis of 5kHz peak

Figure 200 to Figure 204 show the predicted noise sources using the various algorithms. Conventional beamforming, shown in Figure 200, shows a large region centered about the trailing edge. When the enhanced resolution conventional beamforming variant is used, the region identified as containing the noise sources is somewhat reduced in size, as shown in Figure 201. This algorithm achieves enhanced resolution by weighting cross spectral matrix elements. When applying the DAMAS2 algorithm, the source region is predicted even smaller (shown in Figure 202). DAMAS2 is a high speed version of DAMAS which uses an FFT algorithm for improved performance and nonuniform meshes to avoid problems with the PSF model. In Figure 203, the CLEAN-SC algorithm (Sijtsma's algorithm [**33**]) predicts a slightly smaller source region. OptiNav's TIDY algorithm result, shown in Figure 204, shows the source extending further downstream than either DAMAS2 or CLEAN-SC. Since the integration surfaces used by PSU-WOPWOP to predict the sound measured by the microphone array was on the airfoil surface, and since the computational mesh only resolved significant unsteadiness in the vicinity of the trailing edge, these figures indicate that, as expected, DAMAS2, CLEAN-SC, and TIDY are better able to predict the source location than conventional beamforming techniques.

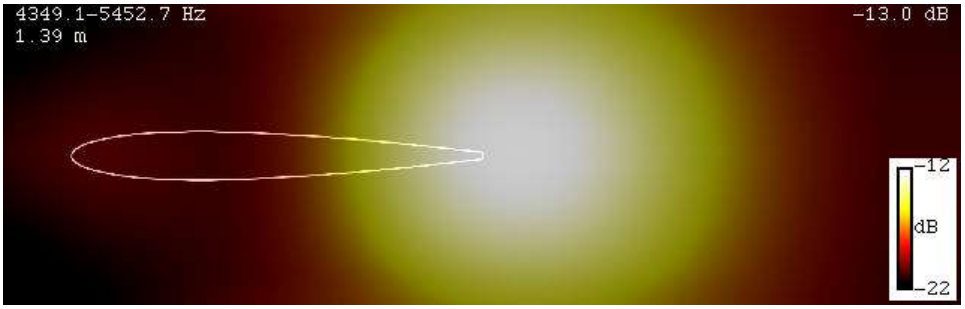

Figure 200: Noise sources identified by conventional beamforming

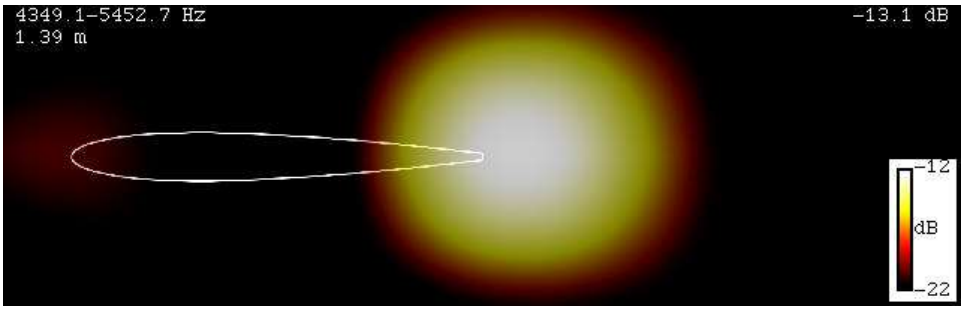

Figure 201: Noise sources identified by conventional beamforming with enhanced resolution

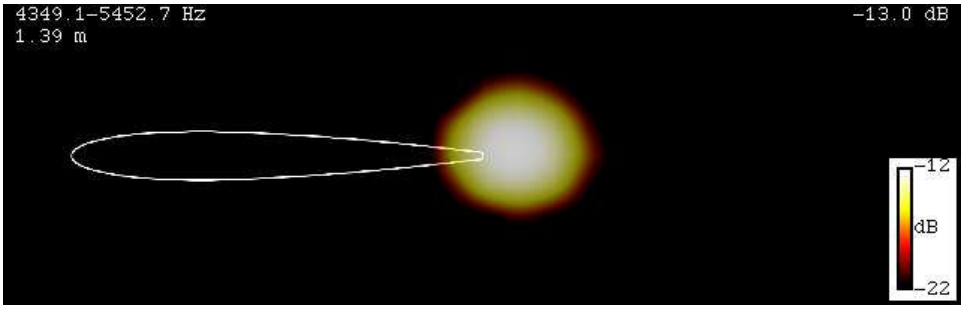

Figure 202: Noise sources identified using the DAMAS2 algorithm

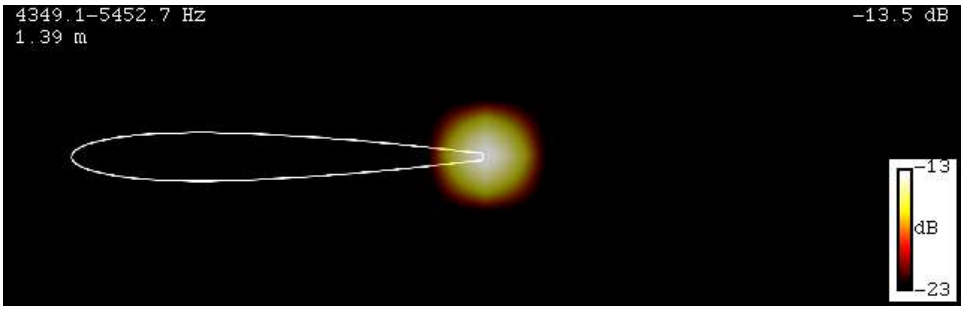

Figure 203: Noise sources identified using the CLEAN-SC method

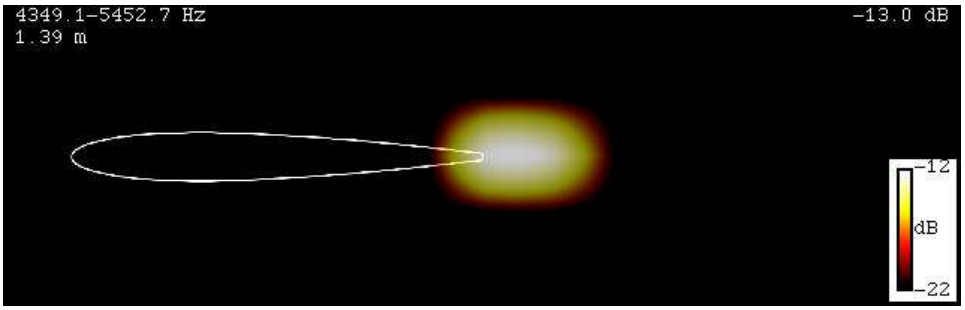

Figure 204: Noise sources identified using OptiNav's TIDY algorithm

In the next set of plots, the results of the low frequency peak analysis are presented. This analysis was performed using dipole-based methods. The frequency range used here is illustrated in Figure 205.

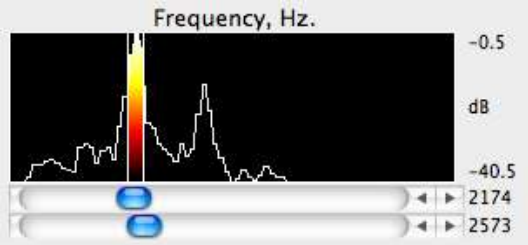

Figure 205: Frequency range used for monopole-oriented analysis of 2.5kHz peak

The predicted low frequency peak noise source regions, as determined by various methodologies, are shown in Figure 206 to Figure 209. Again, the conventional beamforming methods (Figure 206 and Figure 207) indicate a much larger source region, whereas the deconvolution-based methods, DAMAS2 and TIDY, are able to focus more tightly on the trailing edge region, as shown in Figure 208 and Figure 209.

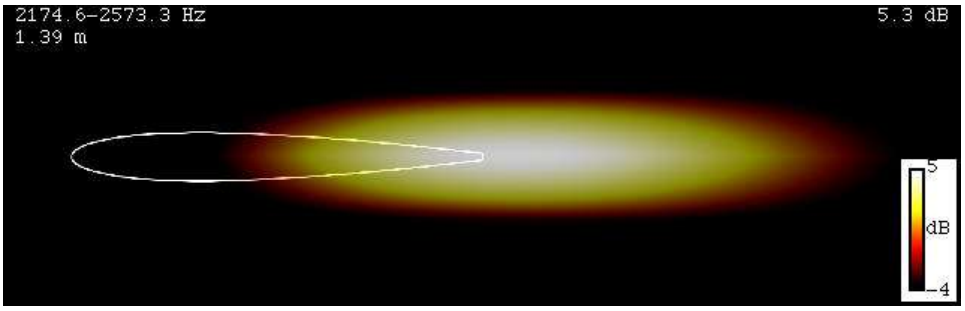

Figure 206: Low frequency peak noise sources identified using conventional beamforming

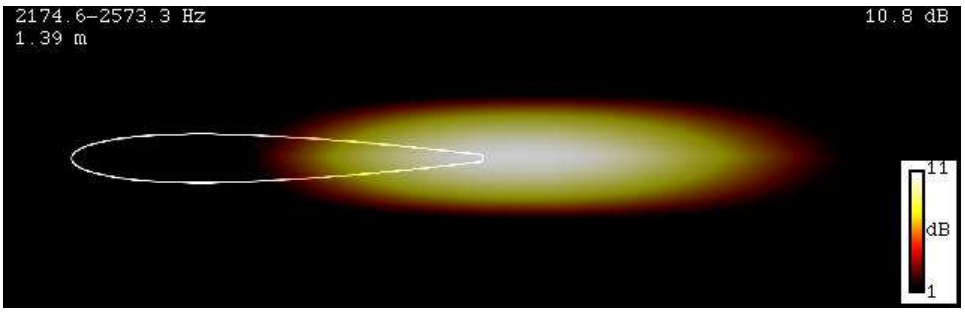

Figure 207: Low frequency peak noise sources identified using conventional beamforming with enhanced resolution

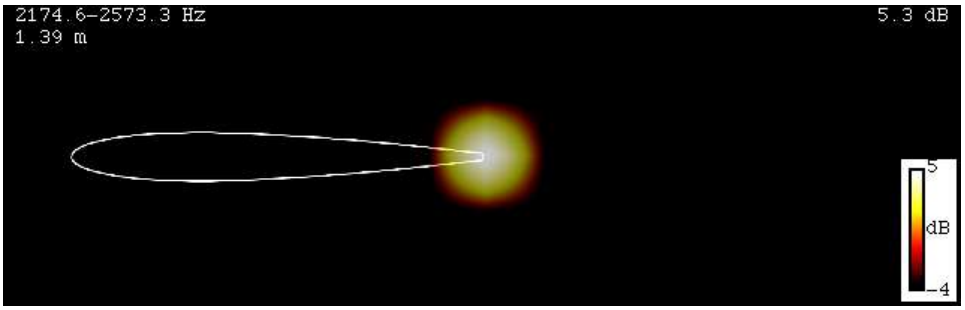

Figure 208: Low frequency peak noise sources identified using DAMAS2

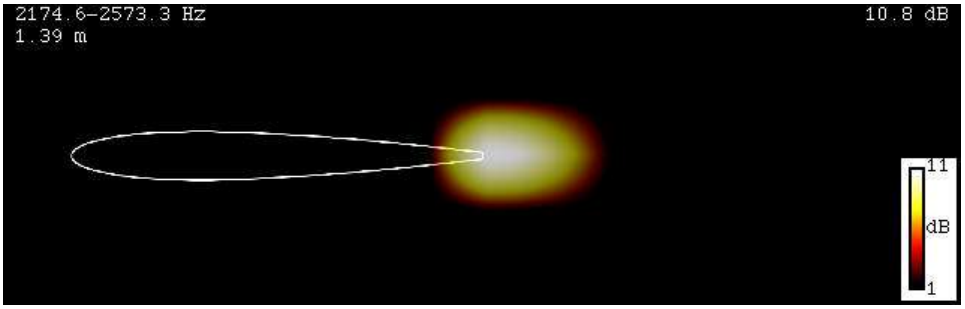

Figure 209: Low frequency peak noise sources identified using TIDY

The next set of results are from the analysis of the data taken by the array in the "top view" position. Figure 210 shows the results from a wide-band analysis using conventional beamforming. One strength of the TIDY algorithm is its ability to process data with unlimited bandwidth. Thus, the results of a wide-band analysis of the same data using the TIDY algorithm are shown in Figure 211. Compared to the conventional beamforming approach, TIDY predicts a much tighter region of noise, which is what one would expect, given the knowledge of the CFD data used to create the synthetic array.

The above analysis was followed up with a series of investigations using TIDY which focused on different frequency bands. Figure 212 looks at the frequencies surrounding a secondary peak in the vicinity of 1.4 kHz. Again, the sound sources are detected just aft of the trailing edge.

Figure 213 shows the noise sources responsible for the primary peak at 2500 Hz. Again, TIDY indicates that these sources are located in the vicinity of the trailing edge and just aft of it. The same is true of the secondary peak at 5 kHz, shown in Figure 214.

In Figure 215, which examines the sources of another secondary peak near 7 kHz, some sources are detected on the surface of the airfoil upstream of the trailing edge. Given the limitations of the computational mesh used in the CFD simulations, it is unlikely that this is an accurate reflection of the simulated physics, nor is the similar prediction shows in Figure 216 for a range of higher frequencies.

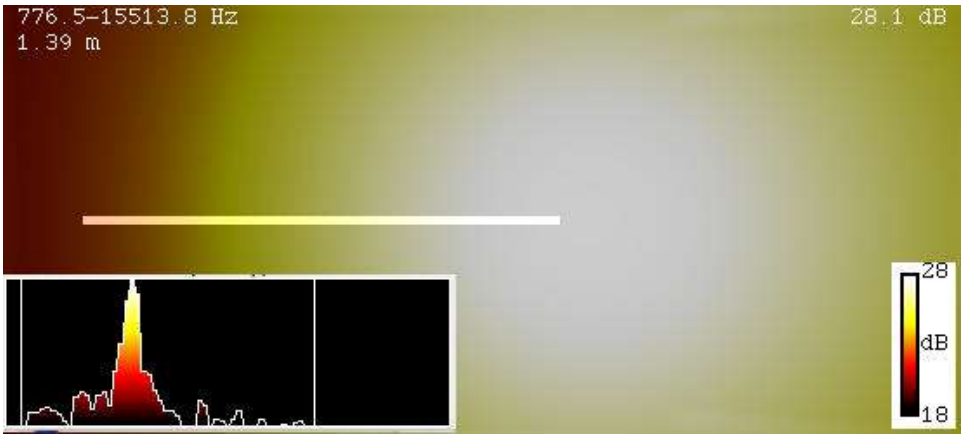

Figure 210: Wide frequency band processing results using conventional beamforming

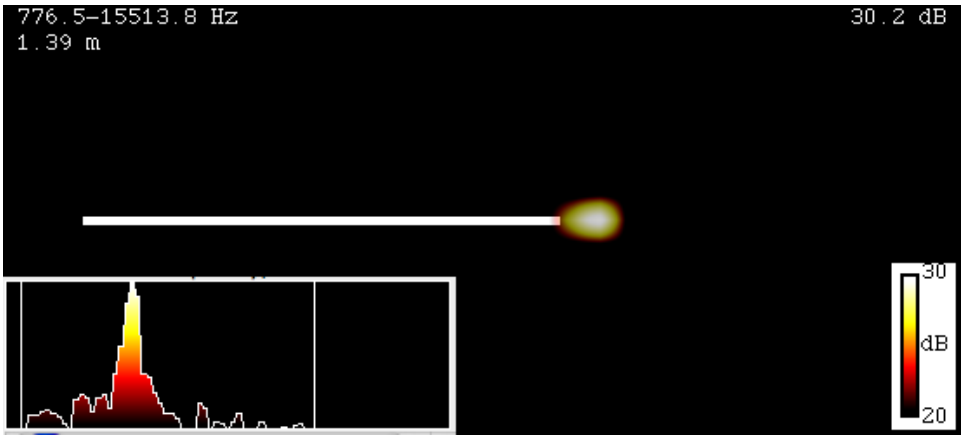

Figure 211: Wide frequency band processing results using TIDY

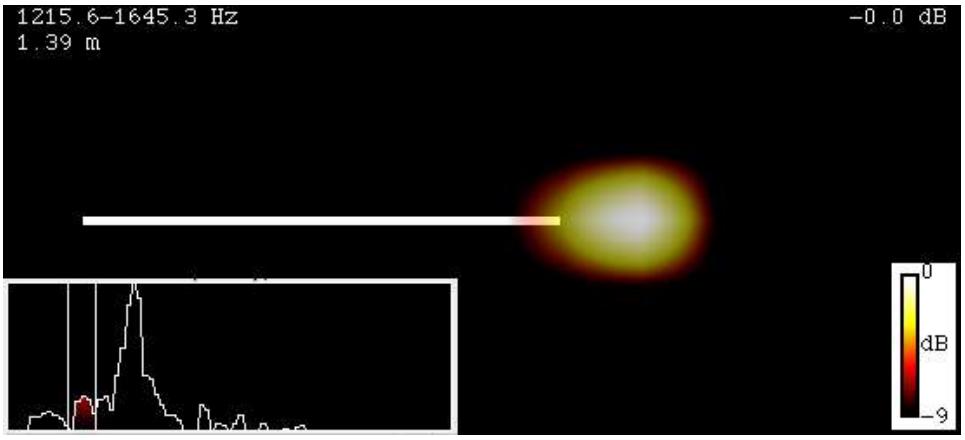

Figure 212: TIDY analysis of top view data in a frequency band centered on secondary peak near 1.4 kHz

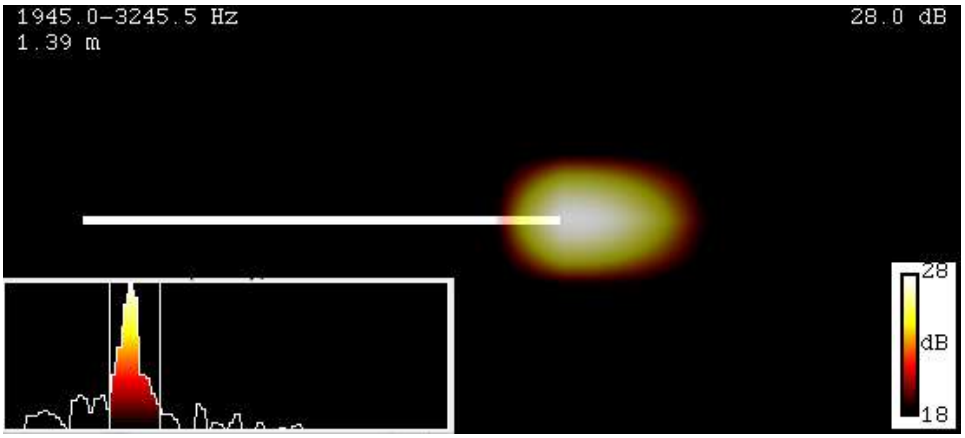

Figure 213: TIDY analysis of top view data in a frequency band centered on primary peak near 2.5 kHz

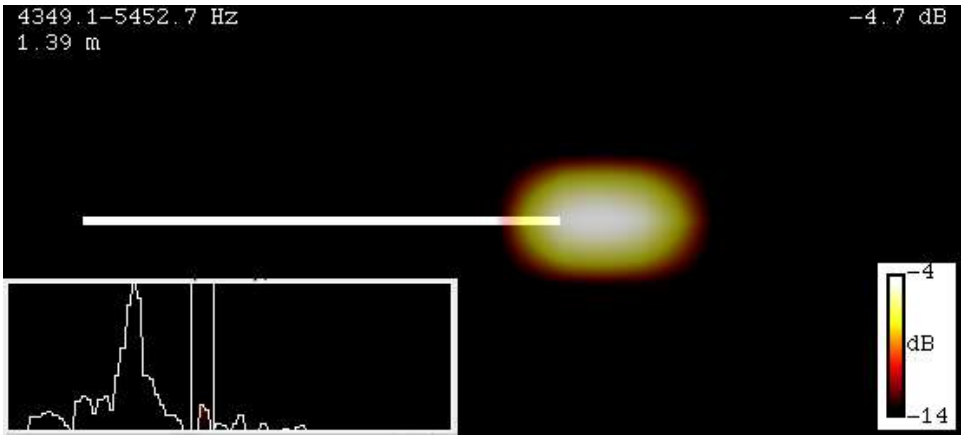

Figure 214: TIDY analysis of top view data in a frequency band centered on secondary peak near 5 kHz

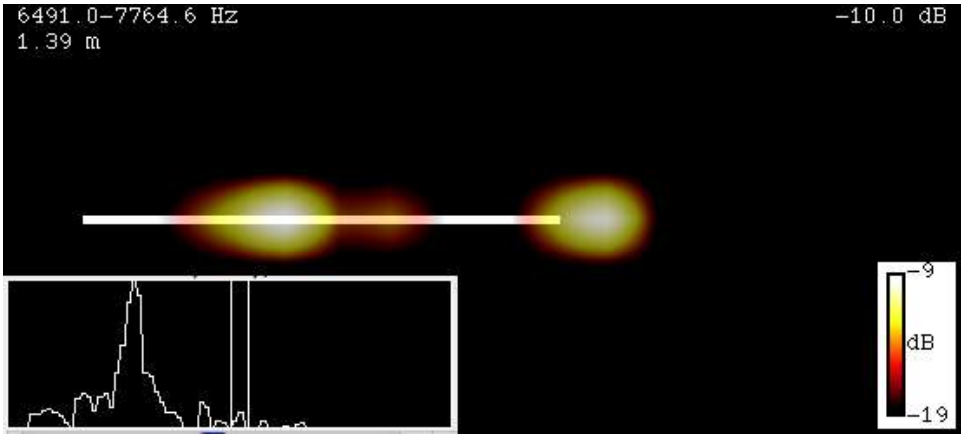

Figure 215: TIDY analysis of top view data in a frequency band centered on secondary peak near 7 kHz

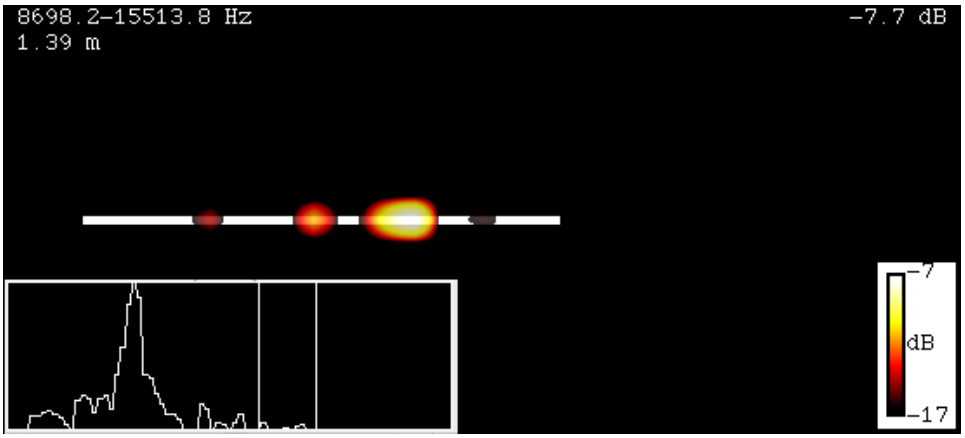

Figure 216: TIDY analysis of top view data in a frequency band between 8 and 15 kHz

The final set of beamforming results comes from positioning the synthetic array downstream of the trailing edge and looking upstream at the trailing edge. The analysis was conducted using 1/3 octave bands. All of these results employed TIDY beamforming algorithm. Except where noted, a monopole-oriented analysis was used. Figure 217 shows the results of the relatively lower frequency bands (up to 2.8 kHz). The off-body noise sources identified in the lower frequency bands are almost certainly non-physical, given the methodology employed to generate the acoustic measurements being analyzed. Note that the two highest frequency bands on this plot are clearly of a dipole nature. Figure 218 continues this analysis and presents results from frequency bands up to 44 kHz. At the highest frequencies, one can again see some non-physical results.

The results of the beamforming analysis are summarized in Figure 219. Much of the data is consistent with the dramatic vortex shedding behind trailing edge which was observed in the CFD. The spectral analysis of the flow quantities was consistent with theories of lift and drag dipoles.

In general, we consider this proof-of-concept application of the synthetic array technique a success. The lower-frequency tone (the lift dipole) was indeed seen by the beamforming analysis to have a dipole spatial structure. The higher frequency (2x) tone, which presumably corresponds to the drag dipole, was observed from the side and the back, but the dipole character was not evident. Sources were also seen forward of the trailing edge at high frequencies.

We expect that applying the synthetic array technique to the wind turbine problem will provide results of similar or better quality. The airfoil case was limited by the thin spanwise dimension which could be modeled on the then-available computational resources. The wind turbine case, on the other hand, includes the full rotor geometry, as well as the nacelle, mast, and ground plane. While the spanwise resolution of the rotor is not perfect, it is sufficient to resolve significant instabilities, including those which we believe to be responsible for the most intense acoustics.

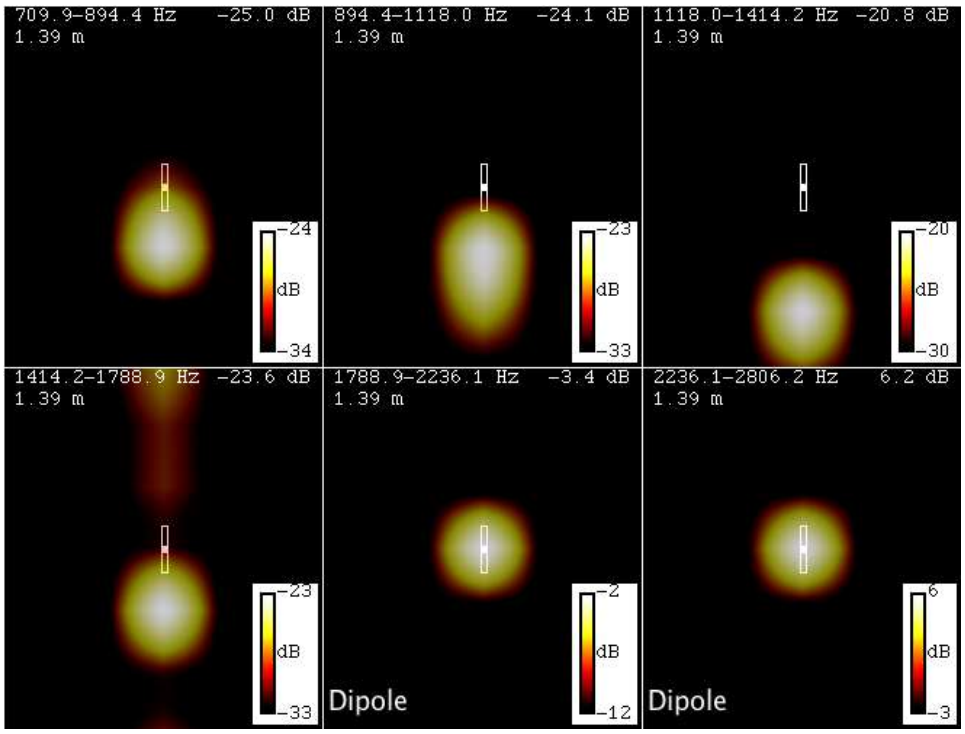

Figure 217: TIDY analysis of 1/3 octave lower frequency bands with the synthetic array in the "back view" position

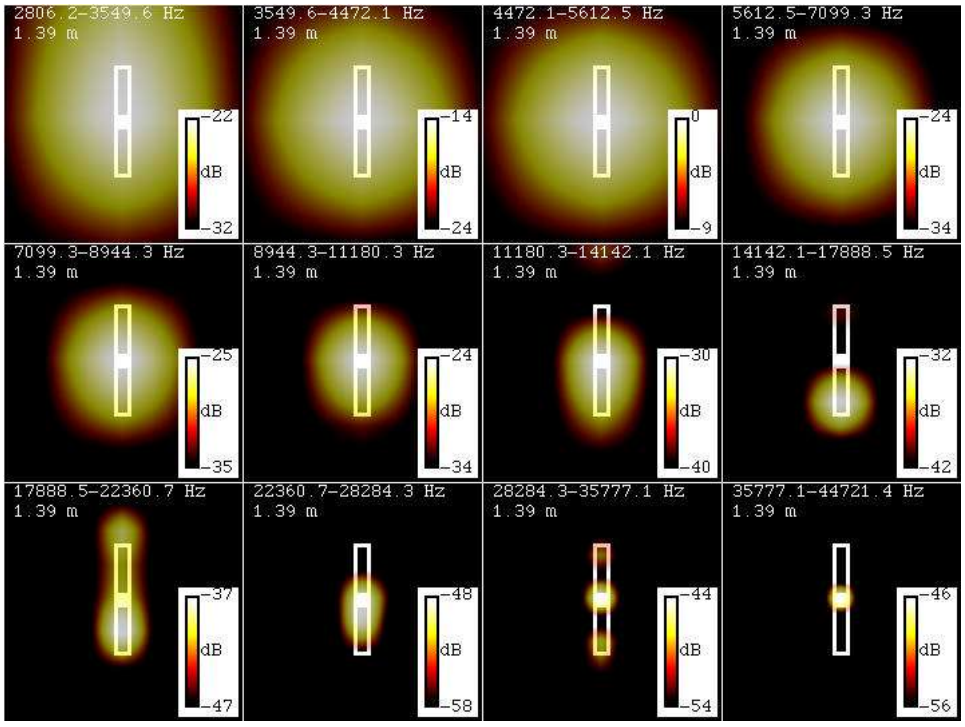

Figure 218: TIDY analysis of 1/3 octave higher frequency bands with the synthetic array in the "back view" position

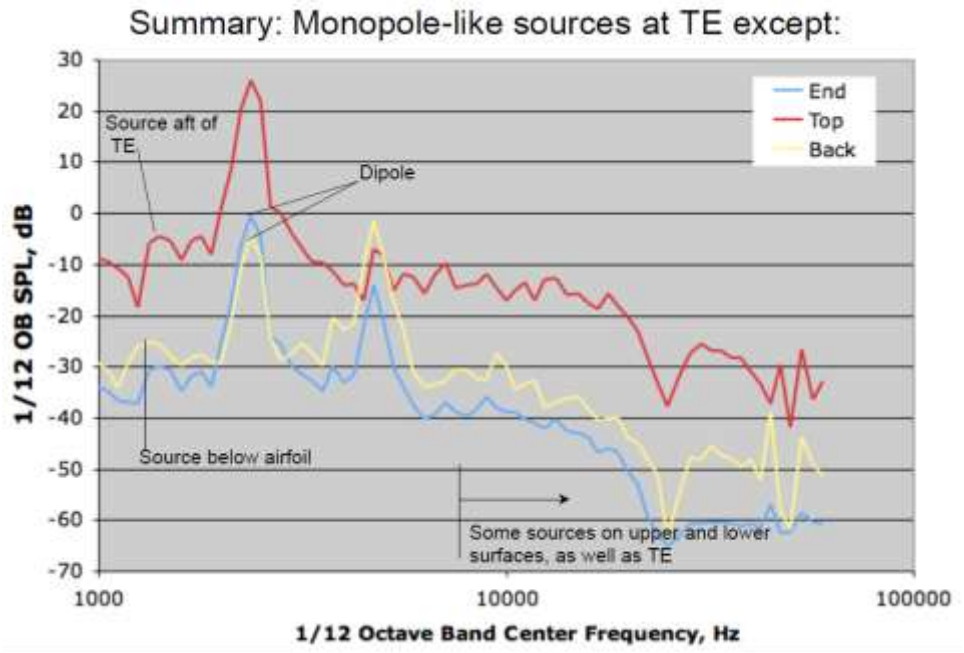

Figure 219: Summary of beamforming analysis results

G3. Problem Identification

The configuration used for the current work is based on the U.S. Department of Energy National Renewable Energy Laboratory (NREL) 10m diameter research wind turbine, shown in Figure 30. This device has been field tested field-tested in various configurations since 1989 at DOE's National Wind Technology Center located near Boulder, Colorado. It has been operated in outdoor atmospheric turbulent wind conditions up to 31 m/s (70 mph), and has been exposed to winds above 65 m/s (145 mph) with the rotor parked. Test data have been made available to the research community through International Energy Agency Annex XIV and Annex XVIII. Reports summarizing results of the atmospheric turbine tests have demonstrated the extremely complex dynamic nature of the typical wind turbine operating environment. Highly turbulent wind and sheared inflow conditions are major factors that contribute to the complexity.

Some of these issues have been addressed by testing the device in NASA's 24.4 by 36.6 meter (80' by 120') wind tunnel. This tunnel is part of the National Full-Scale Aerodynamics Complex (NFAC) which is located at the NASA Ames Research Center in Moffett Field. Testing in a controlled wind tunnel environment eliminates many of the uncertainties of a field test, and the resulting data provide information from which a significant portion of the complex inflow-induced operating environment is removed.

The current work seeks to accomplish a similar reduction in uncertainty, in that, even more than a wind tunnel, a numerical experiment can isolate specific features of interest. For example, in the current work, the turbine geometry is assumed to be rigid. Also, the effects of tunnel walls and/or unsteady inflow conditions are eliminated.

Figure 220: The NREL 10m research wind turbine

Computational Mesh

A near-body computational mesh for the NREL wind turbine geometry was obtained from Drs. Chris Stone and Marilyn Smith, who developed the mesh under contract from the National Science Foundation. The blade tip pitch was four degrees. This original mesh consisted of 2.6 million points in 16 blocks. As mentioned above, the OVERFLOW-D option to automatically generate Cartesian off-body meshes was employed to fill in the remainder of the flow domain.

The basic layout of the geometry is shown in Figure 221. As the figure shows, the mast and the generator housing were included in the simulation, but the other features shown in Figure 220 were not (most notably the shaft and the cone-like structure attached to the front of it).

A close-up of the surface mesh in the rotor tip region is shown in Figure 222. The mesh is clustered toward the leading edge, trailing edge, and the tip, but away from these regions, the spanwise spacing of points becomes fairly large, considering the nature of the acoustics we wish to resolve. If more computational resources were available, this is one aspect of the mesh which would have been modified in order to better resolve the unsteady shedding. The present mesh does capture significant unsteadiness, however, as will be shown below, since a large portion of the flow features of interest are generated at the blade tips or aft of the trailing edges.

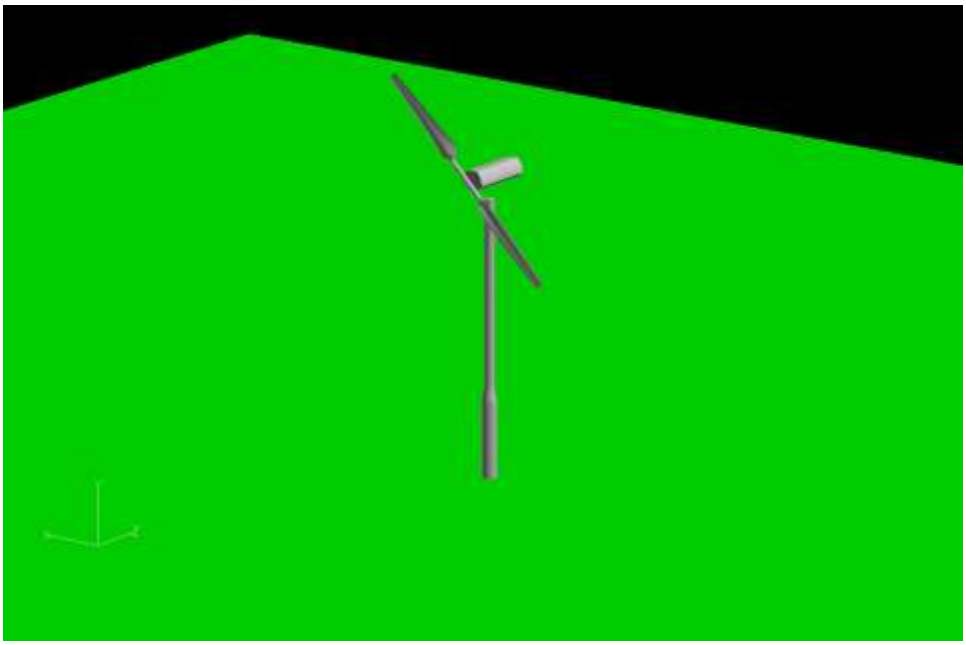

Figure 221: Simulated NREL 10 m research wind turbine geometry (solid surfaces)

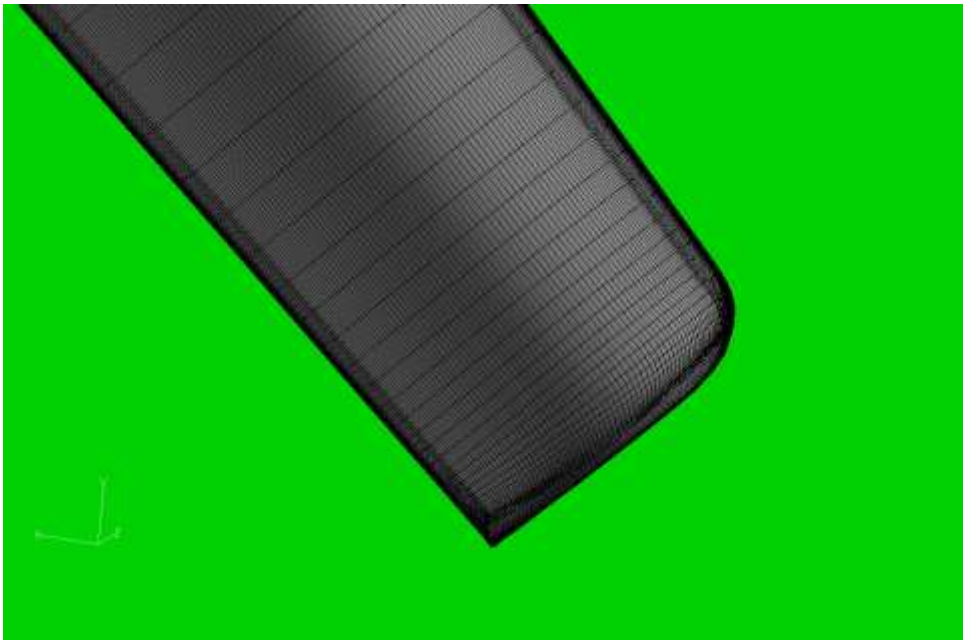

Figure 222: Surface computational mesh in the blade tip region of the NREL 10 m research wind turbine

Figure 223 shows a similar plot to Figure 222, but for the surface mesh near the rotor hub. Again, the spanwise spacing of points is somewhat coarse, but the surface mesh does have good resolution along the chord and also normal to the surface (not shown).

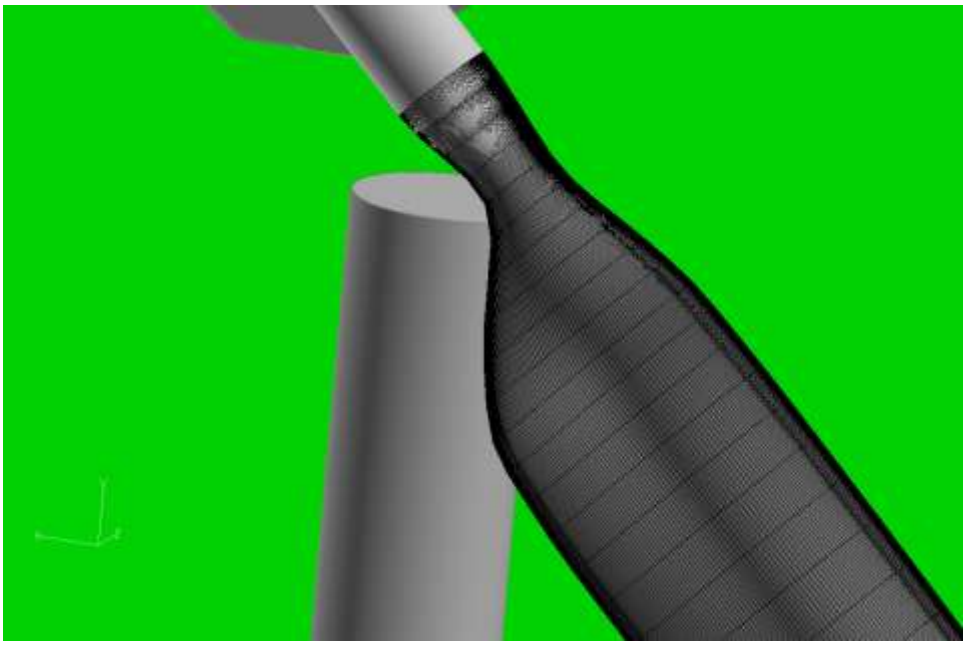

Figure 223: Surface computational mesh in the blade near-hub region of the NREL 10 m research wind turbine

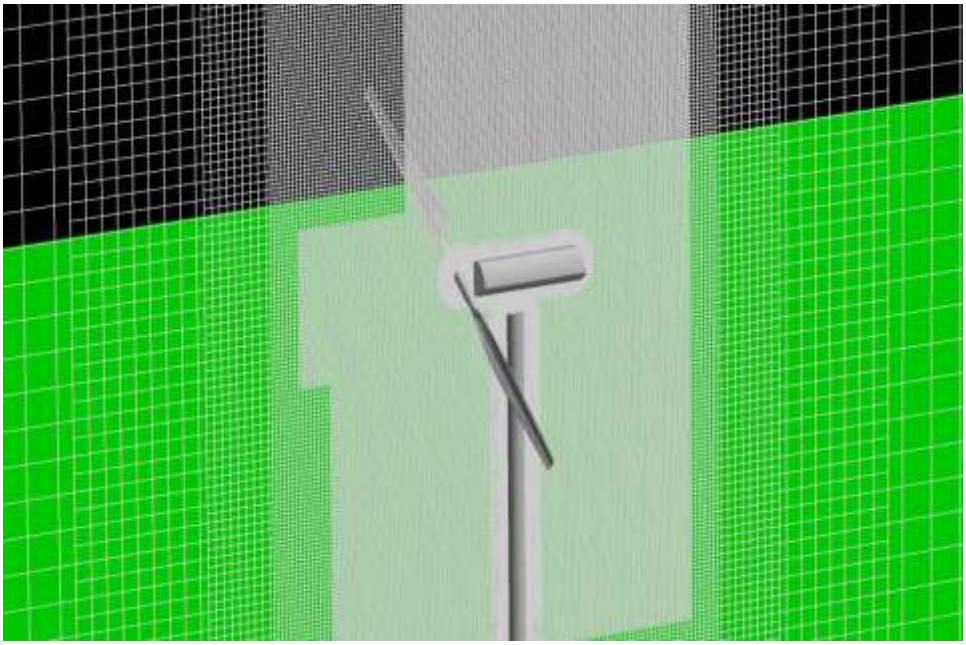

Figure 224: Cross-section through the centerline of the mesh near the start of the simulation (after 8 time steps)

A cross-section of the computational mesh through the centerline of the turbine is shown in Figure 224. In this view, the automatically generated off-body Cartesian meshes are readily seen. As the flow has only advanced for eight time steps at this point (one degree of blade rotation), the automatic mesh refinement algorithm has not modified the initial Cartesian meshes. Recall that AMR is used only every forty time steps (five degrees of blade rotation).

The need for the automatic mesh refinement is clearly seen in Figure 34, where, beyond about three meters aft of the nacelle, the mesh becomes too coarse to resolve any significant unsteadiness.

G4. Results

The simulated case corresponds to a 7 meters per second constant inflow velocity. The reference Mach number, based on tip speed, was 0.11158. The Reynolds number was 2.67 million.

The flowfield solution has been advanced for a total of 5,488 time steps (over multiple runs), with a solution saved every 16 steps. For the fixed time step which was used, this corresponds to solutions saved at every two degrees of rotation, and a total rotation for the blades of 686 degrees. The following plots were made using the final state (at step 5,488).

Note that, because of the automatic mesh refinement, the original 30.5 million point mesh (in 68 blocks) became a 1028 block mesh with more than 46 million points. Further, had the simulation continued, the point count would have increased still more, because the unsteady flowfield still had not propagated to the edges of the domain.

Figure 225 shows a centerline cross-section of the mesh at the final step run thus far (step 5488). For clarity, the plot shows only every other point in each direction. The region where the adaptive mesh refinement has been active is clearly visible and corresponds closely to the extent that the solver has propagated the 210ertical structures shed from the turbine.

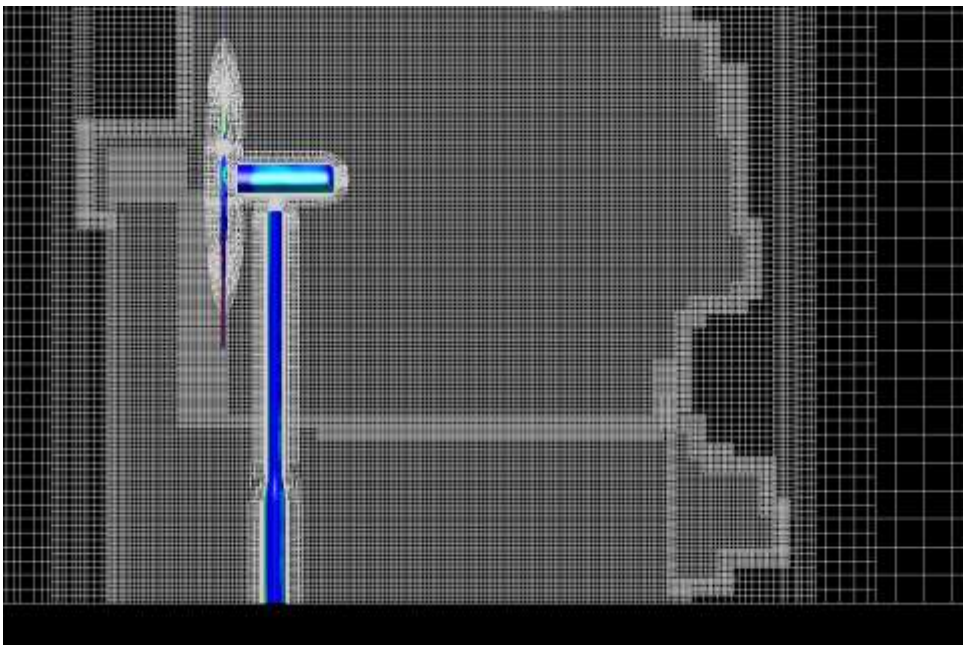

Figure 225: Mesh cross-section along centerline after 5488 steps (every other point plotted)

Figure 226 shows the surface pressure on the wind turbine and the ground plane. While faint, the traces of a Karman vortex street can be seen on the ground plane downstream of the mast.

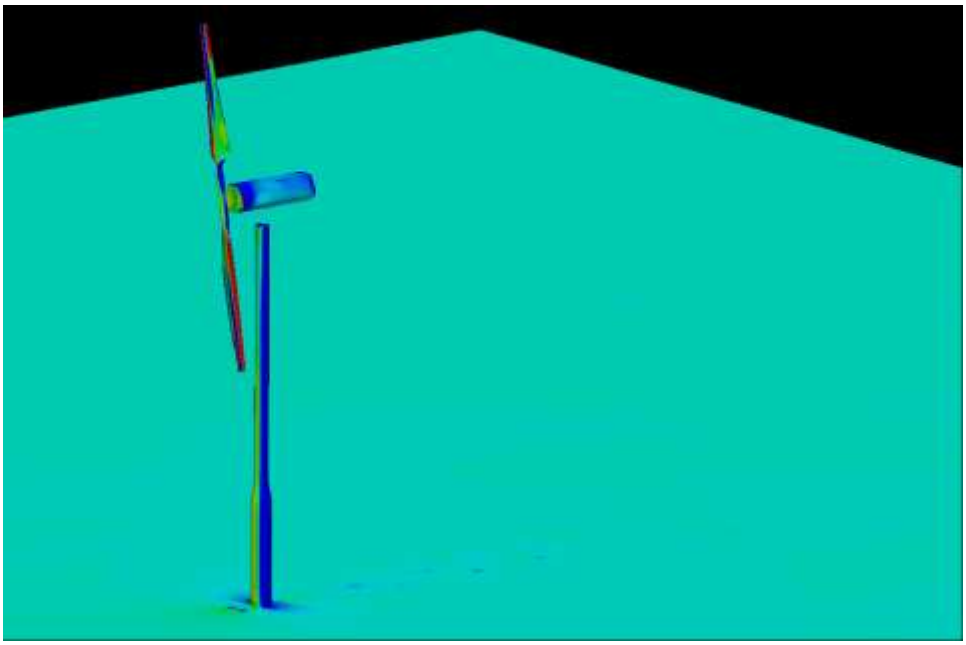

Figure 226: Computed surface pressures on the 10 meter wind turbine

The nature of the unsteady flowfield downstream of the rotor is somewhat more apparent in Figure 227, which shows streamlines of flow around turbine. The effect of the moving rotors is apparent in the coiling of the streamlines downstream of the turbine housing.

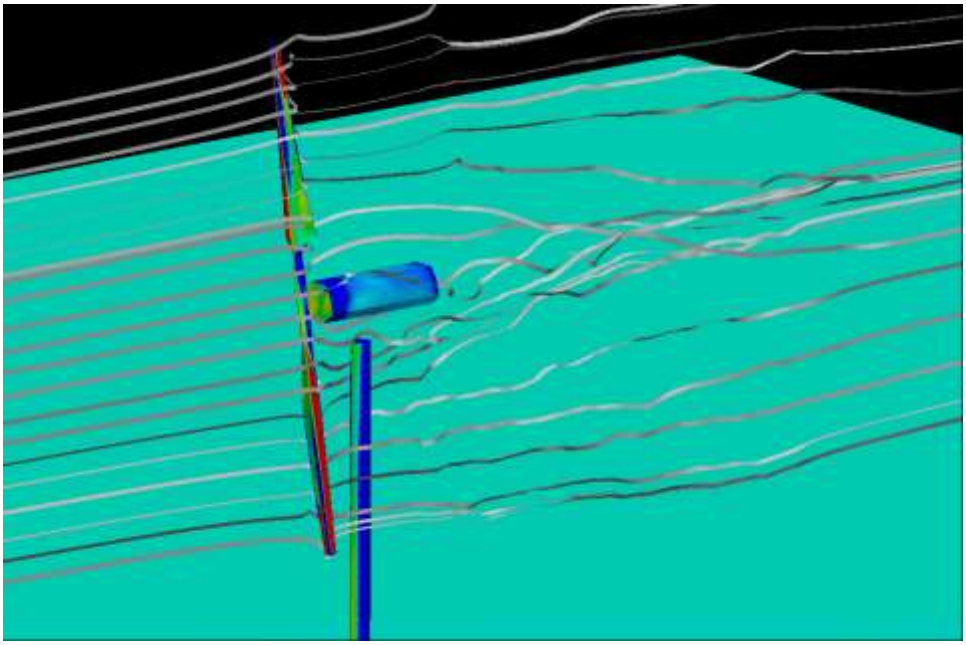

Figure 227: Streamlines of flow around the wind turbine rotor

Figure 228 shows an iso-surface of vorticity magnitude. Here, the tip vortices shed as the rotor spins are clearly visible, as are the 211ertical structures shed off the mast. Numerous smaller structures are also seen throughout the downstream region.

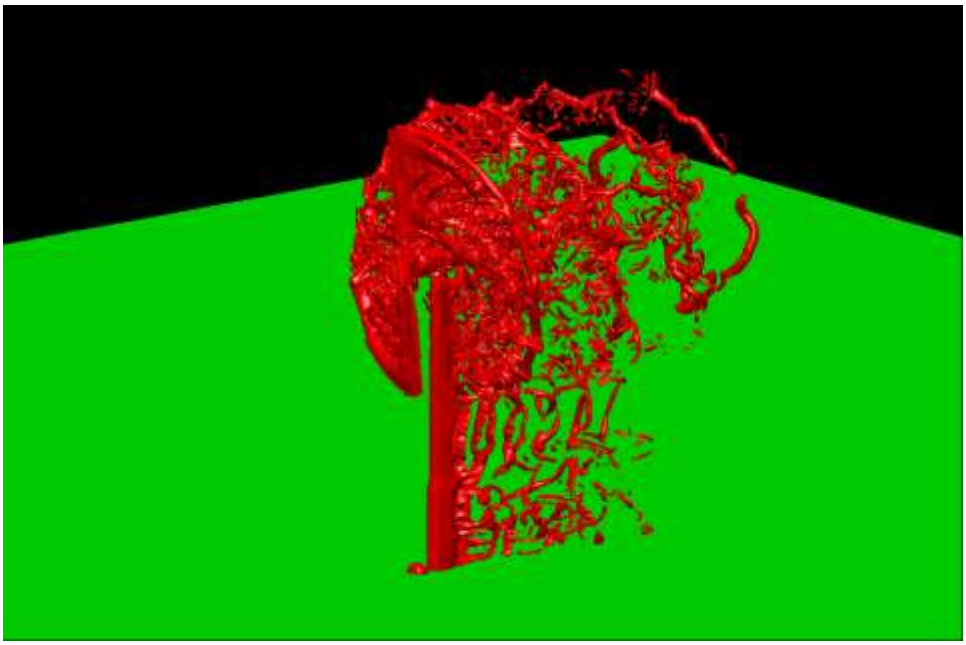

Figure 228: Iso-surface of vorticity magnitude in the flow around the wind turbine

Note that, without automatic mesh refinement, these flow features would not be so well resolved. The initial attempts to run this problem, which did not use AMR, were only able to resolve unsteady features for about half the downstream distance shown here. Further note that this does not represent the limit of OVERFLOW's capabilities, since the vorticity observed here includes the initial transients, which have not yet propagated out of the domain. It thus appears that, to the extent the near-body meshes are able to generate the 212ertical structures, the off-body Cartesian meshes with AMR are able to propagate them. Also note that the above results were obtained using sub-optimal settings for the AMR algorithm.

An integration of the forces and moments over the entire wind turbine structure, including the mast and nacelle was performed. The technique used was not exact, in that the overlapping meshes used by the OVERFLOW simulation were not precisely accounted for. The results, however, are expected to be proportional to the actual loads, and can thus be used to determine whether or not a time-dependent loading is being predicted.

The coordinate system for this simulation had the oncoming wind blowing in the positive *z* direction. The *y*-axis points in the vertical direction, and the *x*-axis points to the left when facing the front of the turbine. The force (in arbitrary units) in the *z*-direction is shown in Figure 229 as a function of solution time steps. Recall that the timestep is such that the rotor sweeps out one degree every eight steps. Thus, 2880 steps are required for a full 360 degree sweep. The history plotted in Figure 39 therefore represents only about two full rotations of the rotor. Clearly, the load is trending to some sort of asymptotic value, but it is not clear whether or not any ongoing periodicity will be resolved in this component of the force.

The vertical and side-force components as a function of time are shown in Figure 230, along with their combined magnitudes. All of these quantities show a clear unsteadiness, and there are also hints that some sort of periodicity may be setting up. At this point, however, the simulation has not run far enough to detect the presence of harmonics with any certainty.

The moments on the wind turbine about the base of the mast, have been plotted as a function of time step count in Figure 231. As with the previous plots, a clear time dependence is observed, and there are hints of some sort of periodicity setting up, but until the solution is run farther, it is not possible to draw too many conclusions.

Hints of this vortex street can still be seen in the wake higher above the ground plane, such as that shown in Figure 233. In regions behind where the rotor sweeps, the helical structures created by the vortices shed from the blade tips and trailing edges become more dominant. Note the region of strong vorticity which has just been shed from the rotor as one of the blades reached its lowest point the sweep.

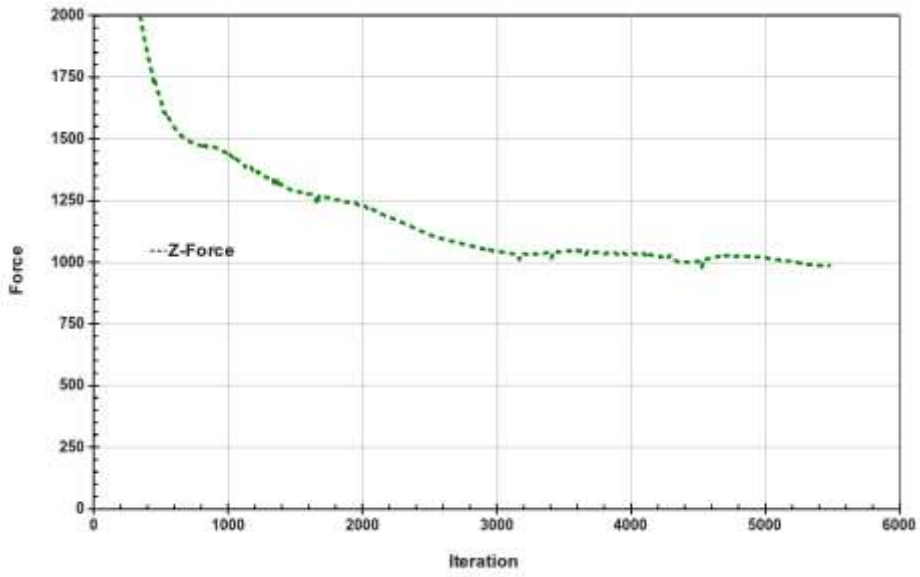

Figure 229: Streamwise force on wind turbine as a function of time step

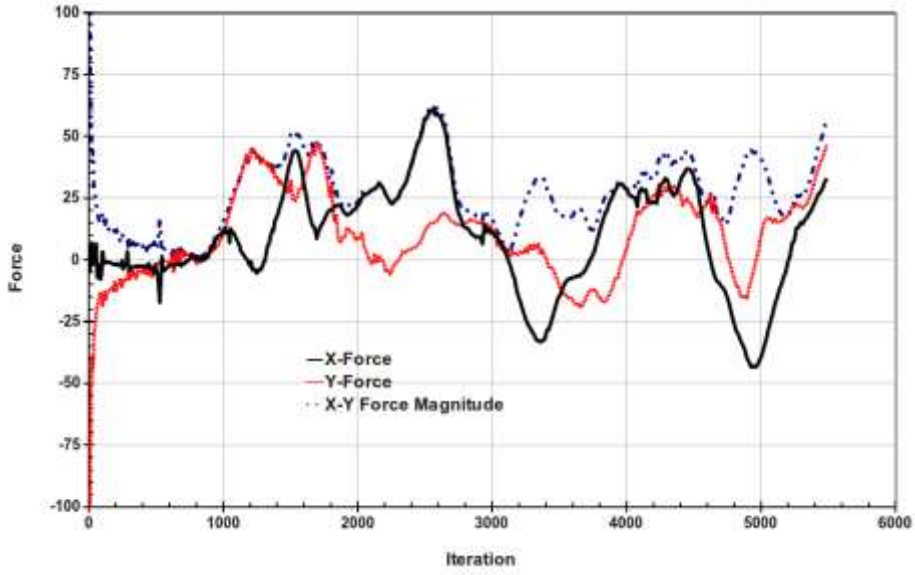

Figure 230: History of forces normal to the streamwise direction on the wind turbine simulation

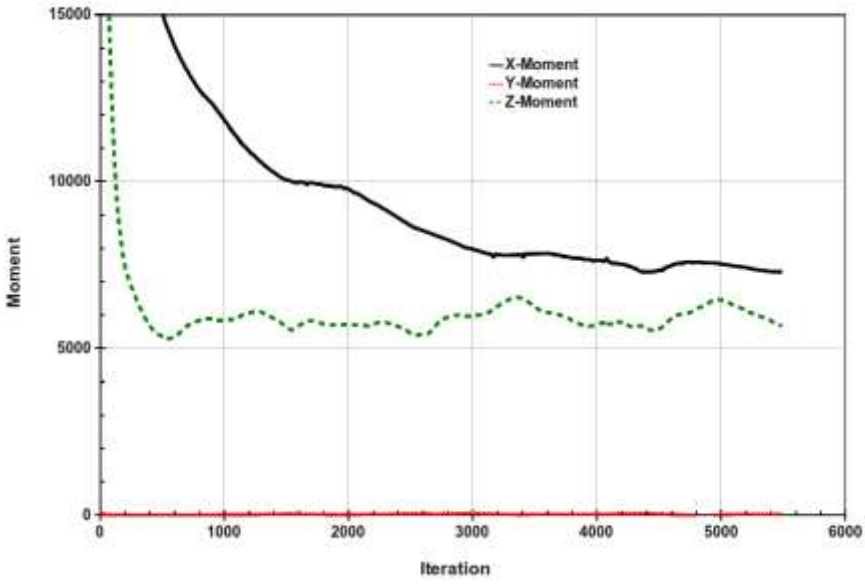

Figure 231: Moments about the base of the wind turbine mast as a function of time

Another way to look at the unsteadiness in the flow is to examine the vorticity in the wake at various points. The plot of vorticity magnitude in Figure 232 shows that, below the level swept by the rotor, the wake behind the mast takes on a Karman vortex street structure.

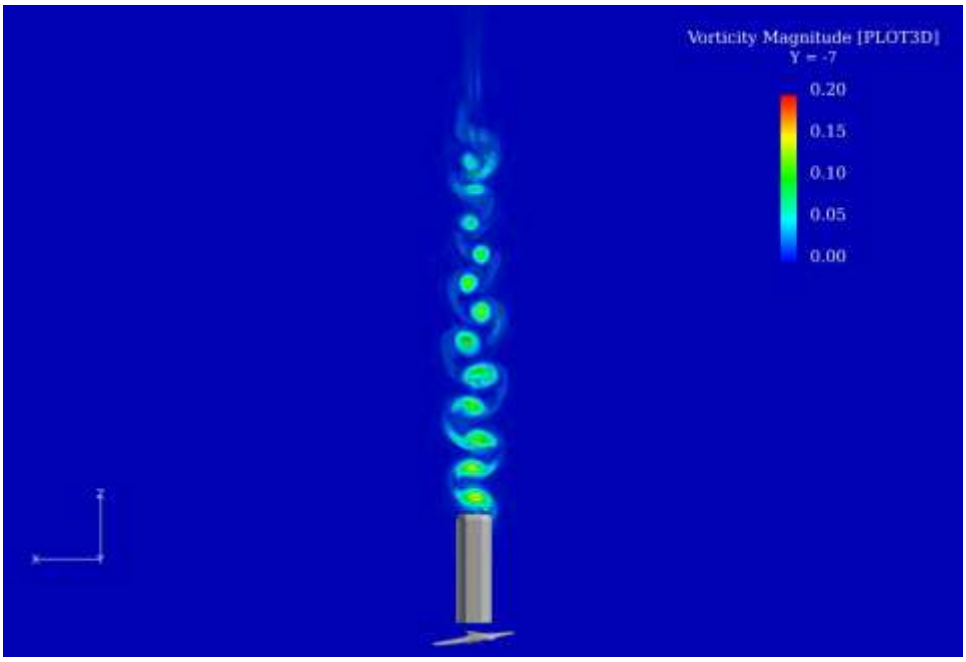

Figure 232: Vorticity magnitude behind the wind turbine mast five meters above the ground plane

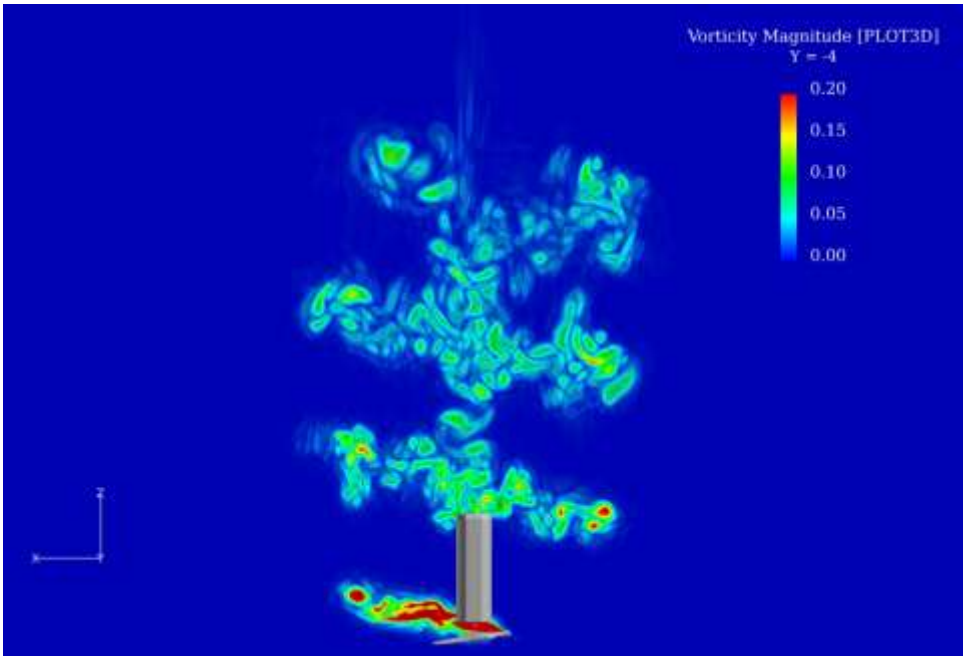

Figure 233: Vorticity magnitude on a constant-y plane one meter above the lower limit of the rotor sweep

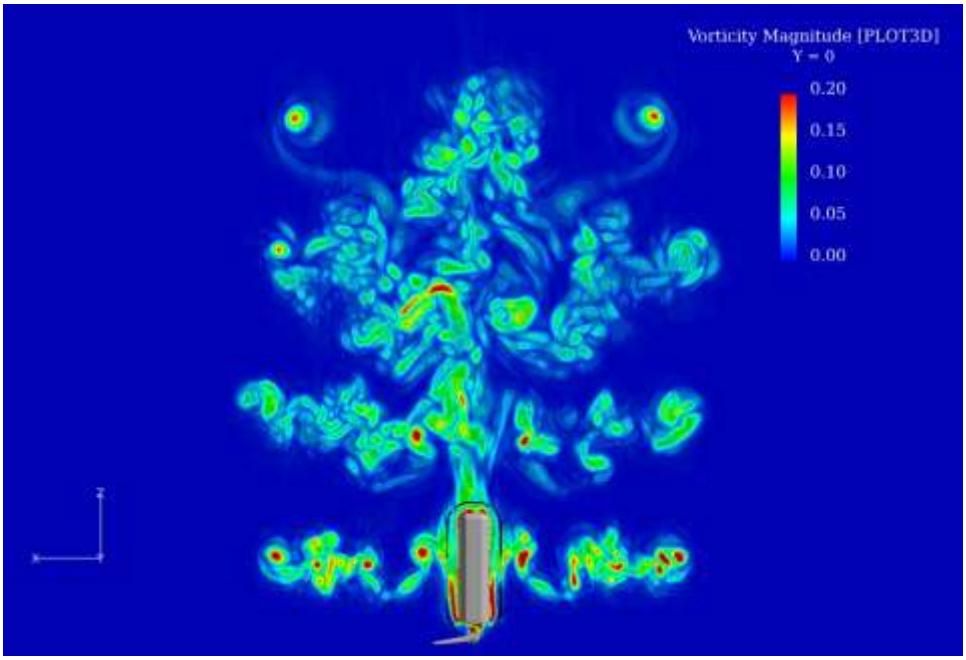

Figure 234: Vorticity magnitude on a constant-y plane through the nacelle centerline

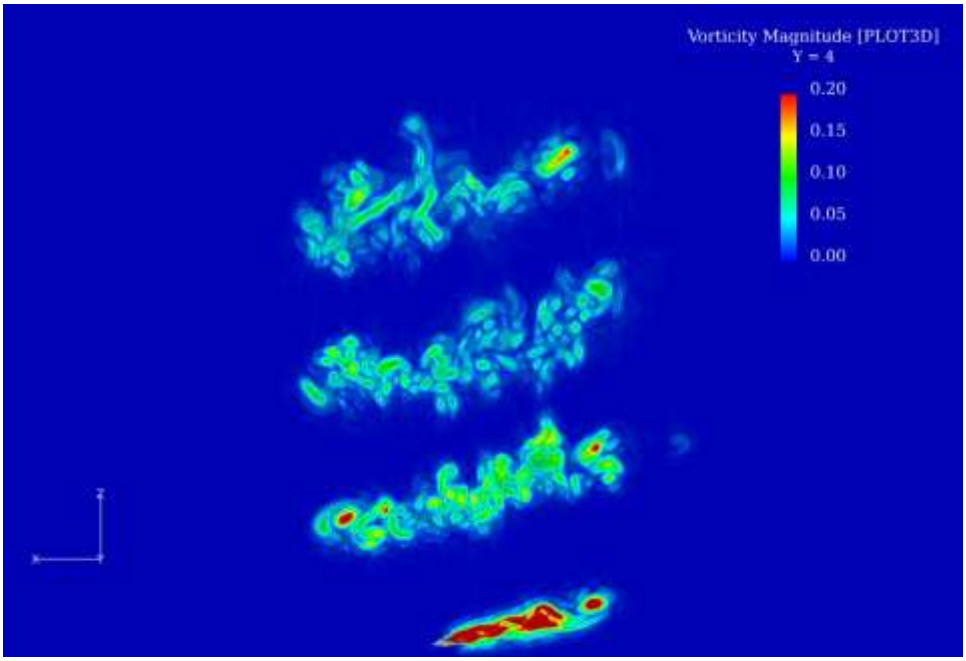

Figure 235: Vorticity magnitude on a constant-y plane one meter below the upper limit of the rotor sweep

The vorticity magnitude contours shown in Figure 234 are plotted on a horizontal cut through the nacelle centerline (and the rotor hub). The starting vortices are clearly visible at the top of the plot (not having had enough time to propagate beyond the domain. The complex wake vortex interactions are clearly visible. The "gap" visible surrounding the nacelle region in this plot is due to the decision to only

plot at interior points, and not plot contours at fringe points, in order to minimize the plotting of overlapping contours due to the overlapping computational meshes used by the OVERFLOW solver. As such, the gap is a numerical artifact, and does not represent any discontinuity in the solution.

The final plane of vorticity magnitude contours is shown in Figure 235. This plane is positioned four meters above the rotor hub (one meter below the maximum height swept by the rotor). This plot is very similar to Figure 233, but lacks the wake from the mast. Again, the simulation predicts a complex interaction of the wake and tip vortices shed from the rotor.

Vortical structures such as those visualized in the preceding Figures are associated with noise emission, but the acoustic field itself consists, of course, of pressure fluctuations. The pressure field is shown in Figure 236 on the same horizontal plane where vorticity magnitude was plotted in Figure 233. The pressure footprints of the 217ertical structures are clearly evident, but in addition, there are traces of what appear to be acoustical waves radiating away from the turbine and the wake.

Note that, because of the low speed of the flow, the pressure variations in the flow are close to the limits of what can be resolved due to the numerical precision of the calculation. This is a known phenomenon of low speed flows, and is the reason why low Mach number preconditioning was used for these simulations. The fine-grained oscillations observed in the pressure contours are believed to be largely due to the precision limitations, along with the effects of the changing resolution of the overlapping computational meshes, possibly incomplete convergence of the subiteration process, and the lack of dissipation in the fourth order scheme used away from the near-body computational mesh blocks.

To highlight the acoustical field, the pressure gradient magnitude has been plotted in Figure 237 on the $y = -4$ plane. This plot clearly shows the radiating pressure waves centered on the rotor. The noise which was present in the pressure field contours is magnified when the gradient is computed. In addition, slight differences in the predicted gradient in overlapping regions results in a noisier appearance to the contours than the flowfield actually warrants.

Also, it should be noted, both for this plot and the vorticity magnitude contours, that the gradients for these quantities are being computed by the flow visualization package using a different algorithm (and boundary conditions) than that used by the OVERFLOW solver for the actual solution. Despite this limitation, the values shown in the plots should be reasonably close to the “actual” values seen by the CFD solver.

A view of the pressure gradient magnitude on a plane upstream of the rotor is shown in Figure 238. Here, the radiating waves are again clearly visible. In addition, pressure waves can be seen reflecting from the ground plane. The regions of elevated pressure gradient magnitude appear to be related to the rotor position (which is almost vertical at this point in the simulation). We believe that these also correspond to regions of increased noise production.

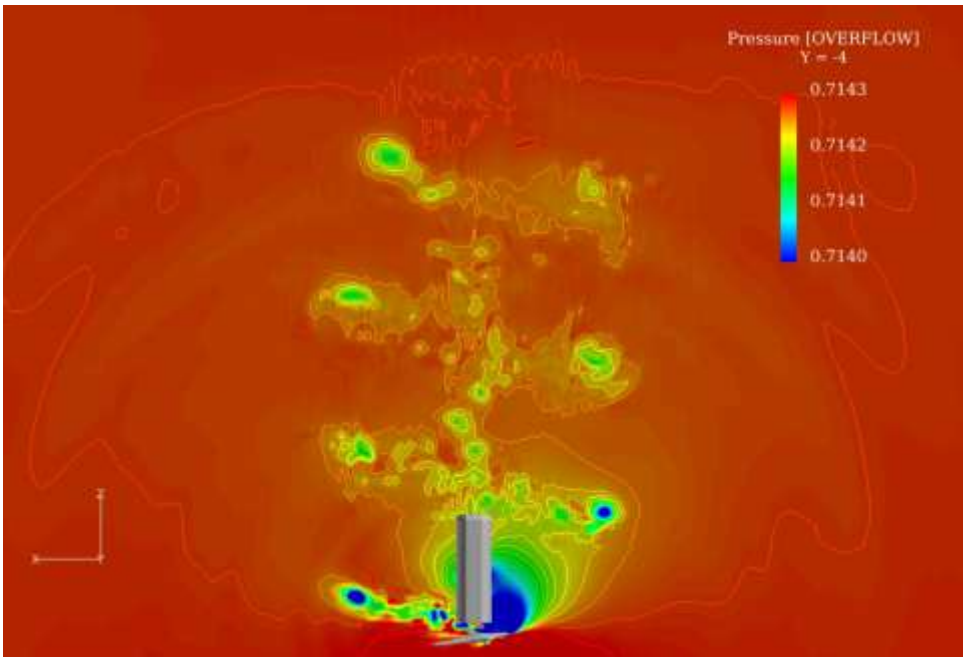

Figure 236: Pressure on a constant-y plane one meter above the lower limit of the rotor sweep

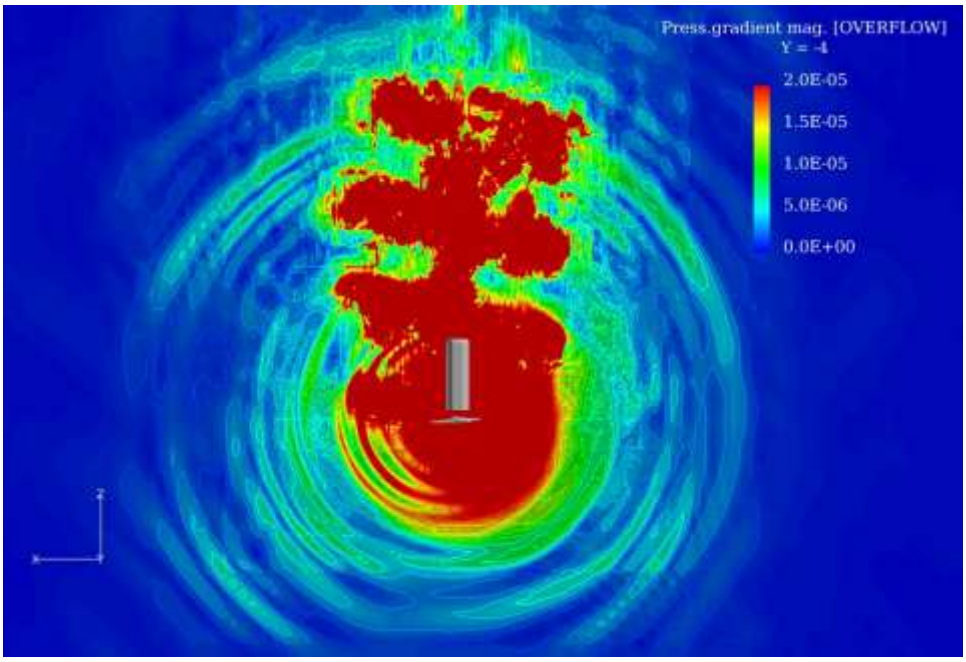

Figure 237: Magnitude of pressure gradient on a constant-y plane

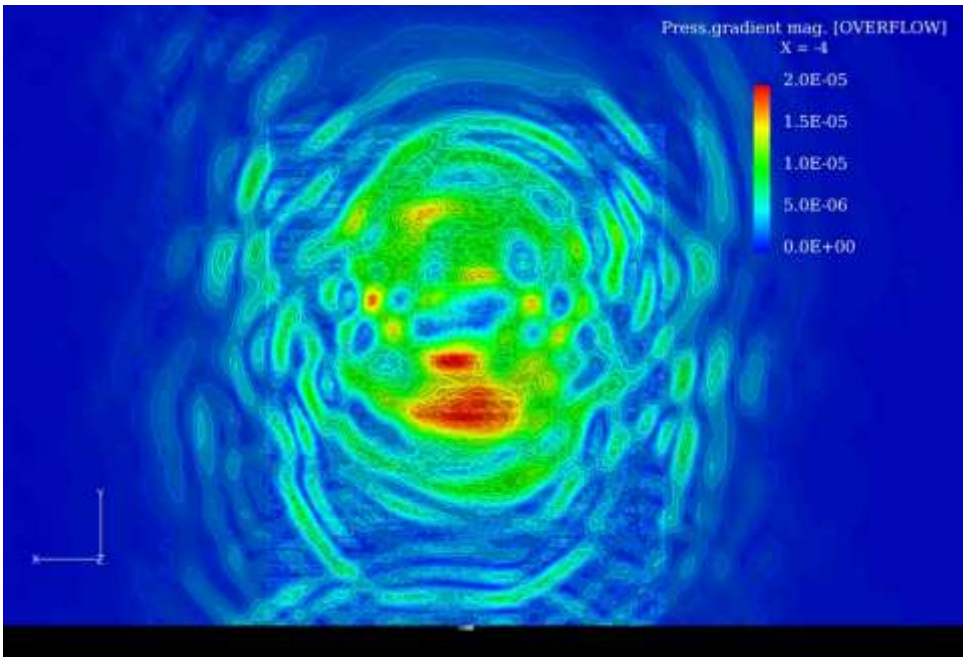

Figure 238: Magnitude of pressure gradient on a constant-x plane upstream of the rotor

G5. Conclusions

All of the pieces have been assembled to enable a full acoustic analysis of the flow around an operational wind turbine. The OVERFLOW code solves the unsteady Navier-Stokes equations to predict the acoustic near-field. The near-field data is used by the PSU-WOPWOP Ffowcs-Williams Hawking solver to propagate the acoustic field to the farfield. Farfield data is then recorded at locations corresponding to a microphone array, and this data is processed using the Beamform Interactive analysis software.

Demonstrations of each of these pieces were presented above, and work is ongoing to finish the complete analysis for the NREL 10 meter wind turbine test case. The identified shortcomings of the current results largely involve the limitations of the CFD solution.

The case is currently being rerun using the recommended AMR settings. Limited computational resources, however, require that we permit only a single level of refinement. With increased computational resources, two or three levels of refinement might be possible, which would greatly enhance the ability of the solver to propagate the unsteady 219ertical flow in the rotor wakes. More available computer resources would also allow the resolution of the near-body computational meshes to be improved, with a corresponding improvement to the predicted acoustic near-field. Due to the nature of the synthetic array technique, an improved CFD solution leads directly to an improved prediction of farfield noise and noise source location.

H. Performance of Wind Turbines in Rainy Conditions

Notations used in this section are listed as follows.

C_{b2}	Constant in Spalart-Allmaras turbulence model
d_p	particle diameter
D_ω	cross-diffusion term
F_D	drag force on particle
$\widetilde{G_k}$	generation of turbulence kinetic energy
G_v	production of turbulent viscosity
G_ω	generation of ω
g_x	gravitational acceleration
k	turbulence kinetic energy
m_p	parcel mass
p	static pressure
Re	relative Reynolds number
S_{α_q}	source term to phase q
u	free stream velocity
u_i	air velocity
u_p	particle velocity
$\bar{v}$	air velocity
V	volume of the impinging cell
y^+	non-dimensional wall distance
Y_v	destruction of turbulent viscosity
Y_k	dissipation of k
Y_ω	dissipation of ω
α_q	volume fraction of phase q
Γ_k	effective diffusivity of k
Γ_ω	effective diffusivity of ω
Δt	time interval of continuous phase solver
μ	air viscosity
υ	molecular kinematic viscosity
ρ	air density
ρ_P	particle density
ρ_q	density of phase q
$\sigma_{\bar{v}}$	Constant in Spalart-Allmaras turbulence model
$\bar{\bar{\tau}}$	stress tensor
ω	specific dissipation rate

Global climate change, increasing concentration of greenhouse gases in the atmosphere, and depletion of fossil fuel reserves have significantly increased demand for alternative energy. Wind energy is one of the most promising alternative energy sources due to its relatively lower cost, water consumption, and environmental effects.

Performance of a typical wind turbine is continuously influenced by the surrounding environmental conditions. Performance losses due to the sand-laden winds and dust accumulation, in arid regions, or insect debris build-up on the blades of the wind turbine, in tropical regions, have been reported by many researchers. Corten and Veldkamp [**59**] reported near 25% power losses on wind farms in California due to the accumulated insect debris on the leading edge of the wind turbine blades; while a performance loss of 50% has been reported due to the dust accumulation and increased roughness of the blades surface [**60**].

Moreover, other meteorological phenomena such as air moisture, rains, and, in the cloud regions, ice formation on the blades, could influence the performance of the wind turbine due to the impact on the geometry of the blades, increasing load on the blades, or vibrations caused by ice shedding [**61**], [**62**], [**63**], [**64**], [**65**], [**66**].

Investigating the effect of these phenomena is necessary to improve the design and performance of the wind turbines. Although there are a handful of studies on the performance of the airfoils under icing conditions, both in aviation and wind turbine applications, the same studies under heavy rain conditions were limited to the aviation applications [**67**], [**68**], [**69**], [**70**].

In work conducted by Valentine and Decker [**68**], the performance of the NACA64-210 airfoil under rain conditions was studied using the Lagrangian method. They had estimated a performance loss due to the decreasing boundary layer momentum absorbed by splashed back droplets, which shows only a fraction of the airfoil performance loss due to rain. Other researchers had estimated the impact of water film formation resulting in up to 83% degradation of the airfoil performance [**69**]. Therefore, study of the performance of the wind turbine under heavy rain conditions seems necessary as turbine efficiency is a critical component of the overall economic justification for a potential wind farm.

Moreover, wind turbine design and corresponding economic projections depend on accurate aerodynamic airfoil data and advanced design tools including extensive experimental data for lift, drag and moment coefficients, and computational fluid dynamics (CFD) analysis [**71**].

The objective of this study is to develop a numerical model for assessing and analyzing the performance of a horizontal-axis wind-turbine (HAWT) in the presence of rain droplets under heavy rain conditions using computational fluid dynamics (CFD) for multiphase flow systems [**72**].

H1. Approach

The CFD was chosen to obtain a comprehensive tool for design, scale-up, and performance evaluation of wind turbines, and also to overcome the lack of experimental data on the performance of wind turbines in rainy conditions. A set of benchmarking CFD simulations was performed, both in two and three dimensions. The simulation results were compared with the available experimental data for single phase flow in the literature to refine our CFD model. Then, the single-phase simulation results were used as a baseline to calculate the impact of rain on the performance of the wind turbine.

To summarize our approach, we can categorize the performed simulations into the following case studies:

Case 1: Simulation of single-phase flow around a 2-D airfoil

Initially, a single-phase CFD simulation was performed for a S809 airfoil which is a 21% thick, laminar-flow airfoil designed specifically for HAWT applications by the U.S. National Renewable Energy Laboratory (NREL) [**73**]. The S809 airfoil profile is shown in Figure 239. The blade sections were analyzed at different angles of attack using a two-dimensional CFD model and the results were compared with the available wind tunnel experimental data obtained using a low-turbulence wind tunnel at the Delft University of Technology. The results of these tests are reported by Somers [**73**]. Our main goal here was to test the available turbulence models in the commercial CFD code, ANSYS Fluent 13.0, and choose the most appropriate turbulence model for our simulations. We are also aware of some approximations of the standard turbulence models in predicting laminar to turbulence transition and flow separation at higher angles of attack; however, the improvement of turbulence models will be the subject of future research.

Case 2: Simulation of 3-D wind turbine using a single-phase flow model

A set of single phase three dimensional simulations based on the aerodynamic experiments of the U.S. National Renewable Energy Laboratory (NREL-Phase II) was performed to predict the power output of the wind turbine at different wind velocities. Figure 240 shows the test configuration of the simulated NREL-Phase II with an untwisted blade turbine. At this step, the validity of our model in prediction of the wind turbine performance in a rotating 3-D model has been verified.

Case 3: Simulation of two phase flow around a 2-D airfoil

In this case, the aforementioned 2-D model in case 1 was used as a base for our 2-D multiphase simulation to capture the water layer formation over the airfoil in presence of rain droplets. To model this phenomenon a novel approach by coupling a Lagrangian Discrete Phase Model (DPM) and an Eulerian Volume of Fluid Model (VOF) has been utilized. The effect of the formed water film was investigated on the aerodynamic performance of the airfoil.

Case 4: Simulation of 3-D wind turbine using a multi-phase flow model

This case is the subject of our future work and is not presented here.

Details and results of our simulations will be presented in the next sections followed by a summary and the scope of future work.

A commercial Computational Fluid Dynamics (CFD) code, ANSYS FLUENT 13.0, was selected to conduct our numerical simulation studies. ANSYS FLUENT is a CFD software package used to simulate fluid flow problems. It uses the finite-volume method to solve the governing equations, as presented in the Table 1, for a fluid flow on a discretized domain (mesh). Geometry and mesh generation were done using ICEM software, which is the pre-processor bundled with FLUENT. A two-dimensional mesh for case 1 and case 3 was built based on a unit length S809 airfoil using a C-type unstructured grid with a refined boundary layer region.

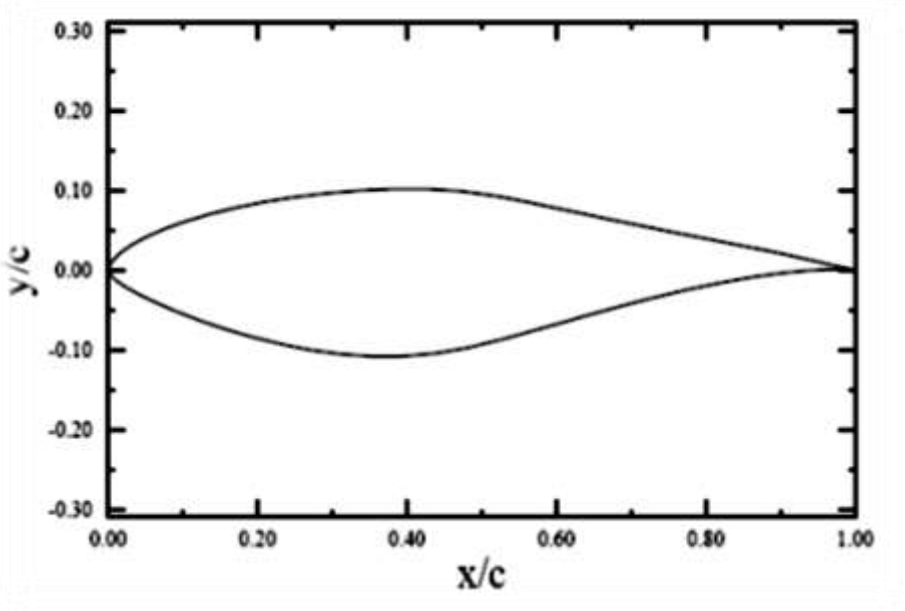

Figure 239: S809 airfoil profile

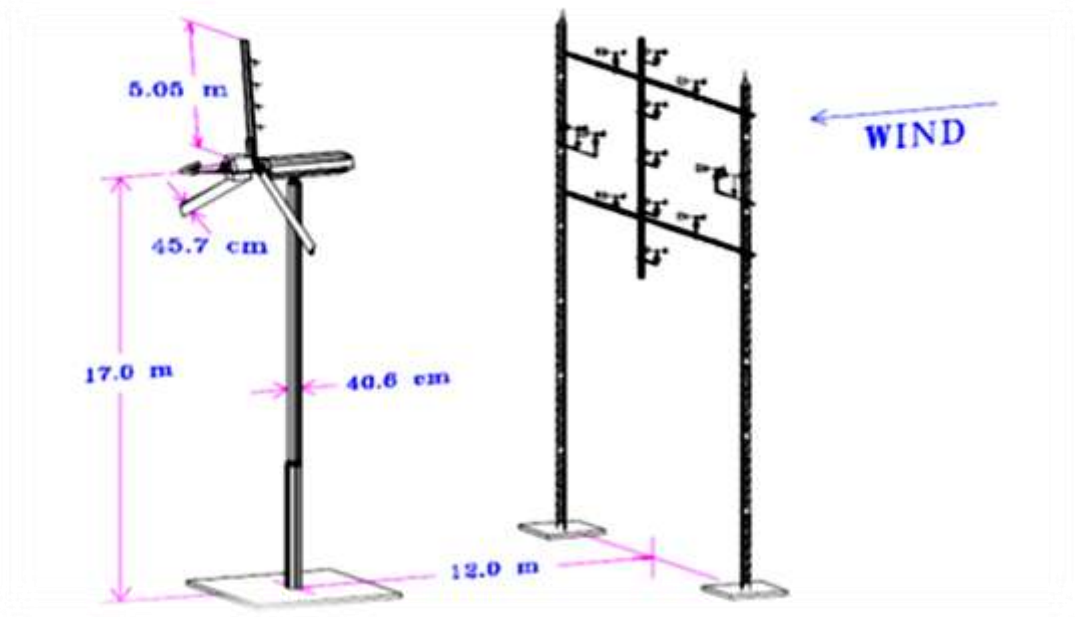

Figure 240: NREL: Phase II (untwisted blade) test configuration

We used approximately 180,000 cells in the domain and the boundary layer was refined so that the required cell thickness for resolving the turbulence flow near the wall was provided (i.e. $y^+ <1$). The computational domain is extended 10 chord lengths from the leading edge and 13 chord lengths from the trailing edge of the airfoil. All the simulations were performed at a Reynolds number of 2×10^6. The mesh for the two-dimensional domain and the refined boundary layer around the airfoil are shown in the Figure 241 and Figure 242, respectively.

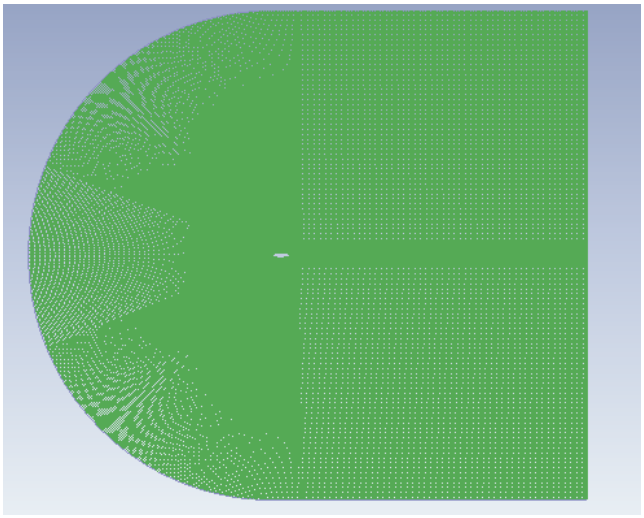

Figure 241: 2-D mesh for calculation

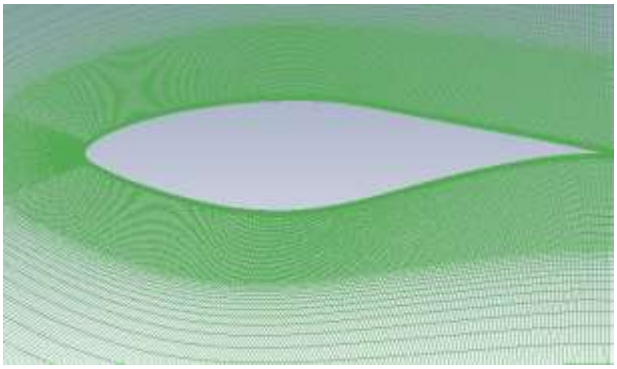

Figure 242: Refined boundary layer

The simulations for case 3 were performed based on the aerodynamic experiments of the U.S. National Renewable Energy Laboratory (NREL-Phase II). Due to periodic configuration, only one third of the domain and the 3-blade turbine (Figure 243) were considered for the calculations to reduce the computational cost.

A spherical domain measuring 40 m in diameter was adopted for our simulation as shown in Figure 244. A tetra mesh with 0.48 million cells was generated as shown in Figure 245. A rotational reference frame was employed and the rotational speed was set to be 72 rpm in order to be in line with NREL's field experiments. In all the cases, grid resolution ensures the grid independent solution.

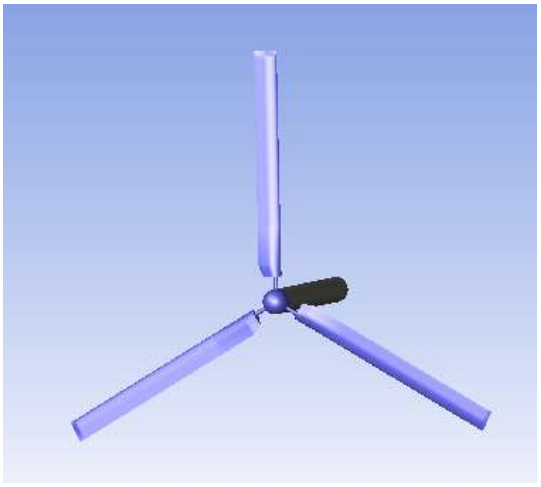

Figure 243: 3-D model of the turbine

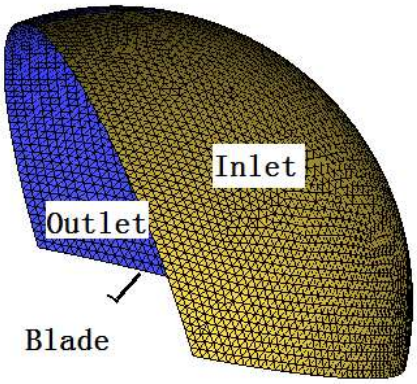

Figure 244: 3-D computational domain

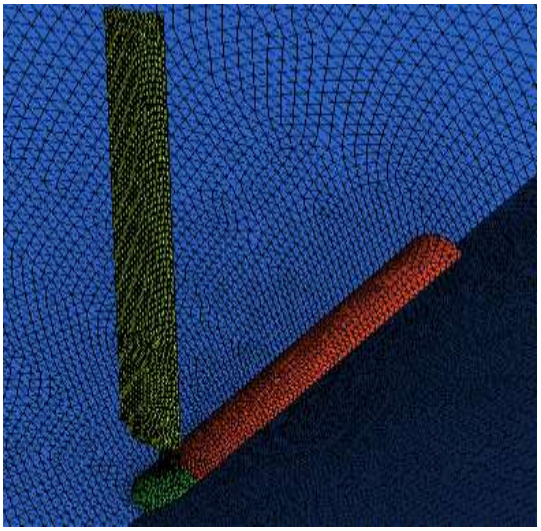

Figure 245: 3-D mesh

Table 16: Summary of Governing Equations

A. Single Phase Conservation Equations

Conservation of Mass

$$\frac{\partial \rho}{\partial t} + \nabla \cdot (\rho \bar{v}) = 0$$

Conservation of Momentum

$$\frac{\partial}{\partial t}(\rho \bar{v}) + \nabla \cdot (\rho \bar{v} \bar{v}) = -\nabla p + \nabla \cdot (\bar{\bar{\tau}})$$

$$\bar{\bar{\tau}} = \mu[(\nabla \bar{v} + \nabla \bar{v}^T)]$$

B. Turbulent Models

Spalart-Allmaras Model

$$\frac{\partial}{\partial t}(\rho \tilde{v}) + \frac{\partial}{\partial x_i}(\rho \tilde{v} u_i) = G_v + \frac{1}{\sigma_{\tilde{v}}}\left[\frac{\partial}{\partial x_j}\left\{(\mu + \rho \tilde{v})\frac{\partial \tilde{v}}{\partial x_j}\right\} + C_{b2}\rho\left(\frac{\partial \tilde{v}}{\partial x_j}\right)^2\right] - Y_v$$

SST k-ω Model

$$\frac{\partial}{\partial t}(\rho k) + \frac{\partial}{\partial x_i}(\rho k u_i) = \frac{\partial}{\partial x_j}\left(\Gamma_k \frac{\partial k}{\partial x_j}\right) + \widetilde{G_k} - Y_k$$

$$\frac{\partial}{\partial t}(\rho \omega) + \frac{\partial}{\partial x_i}(\rho \omega u_i) = \frac{\partial}{\partial x_j}\left(\Gamma_\omega \frac{\partial \omega}{\partial x_j}\right) + G_\omega - Y_\omega + D_\omega$$

C. Discrete Phase Model (DPM) Governing Equations

Particle Force Balance

$$\frac{du_p}{dt} = F_D(u - u_p) + \frac{g_x(\rho_P - \rho)}{\rho_P}$$

$$F_D = \frac{18\mu C_d\, Re}{\rho_P d_p^2\, 24}, \qquad Re = \frac{\rho d_p |u_p - u|}{\mu}$$

D. Volume of Fluid (VOF) Conservation Equations

Continuity Equation

$$\frac{\partial}{\partial t}(\alpha_q \rho_q) + \nabla \cdot (\alpha_q \rho_q \bar{v}_q) = S_{\alpha_q}$$

Momentum Equation based on shared-filed approximation

$$\frac{\partial}{\partial t}(\rho\bar{v}) + \nabla\cdot(\rho\bar{v}\bar{v}) = -\nabla p + \nabla\cdot[\mu(\nabla\bar{v} + \nabla\bar{v}^T)] + \rho\bar{g}$$

Source Term for coupling DPM and VOF

$$S_\alpha = \frac{m_p}{V\Delta t}$$

To simulate flow around the airfoil, we are dealing with a wall-bounded turbulent flow which is affected by the presence of a no-slip boundary condition at the airfoil surface. The numerical treatment of the near-wall flow directly impacts the fidelity of numerical solutions due to the large gradients of solution variables. Therefore, resolving the flow in the near-wall region is necessary in our simulation. Among the available turbulent models in ANSYS Fluent 13.0, the *k-ε* models, the RSM, and the LES model are primarily valid for turbulent core flows (i.e., the flow in the regions somewhat far from walls). The Spalart-Allmaras and *k-ω* models were designed to be applied throughout the boundary layer, provided that the near-wall mesh resolution is sufficient. In this study, we solved Navier-Stocks equations along with two different turbulence models, the Spalart-Allmaras and *SST k-ω* models.

The Spalart-Allmaras model is a one-equation model that solves for the kinematic eddy viscosity. It was developed for aerodynamic flows with a low-Reynolds-number requiring a fine mesh for the viscosity affected region of boundary layer (y^+ <1). The transport equation for $\bar{v}$ is

$$\frac{\partial}{\partial t}(\rho\bar{v}) + \frac{\partial}{\partial x_i}(\rho\bar{v}u_i) = G_v + \frac{1}{\sigma_{\bar{v}}}\left[\frac{\partial}{\partial x_j}\left\{(\mu + \rho\bar{v})\frac{\partial\bar{v}}{\partial x_j}\right\} + C_{b2}\rho\left(\frac{\partial\bar{v}}{\partial x_j}\right)^2\right] - Y_v \quad \textbf{(75)}$$

Where G_v is the production of turbulent viscosity, Y_v is the destruction of turbulent viscosity that occurs in the near-wall region due to wall blocking and viscous damping. $\sigma_{\bar{v}}$ and C_{b2} are the constants and v is the molecular kinematic viscosity.

The shear-stress transport (SST) *k-ω* model was developed to blend the accuracy and robustness of *k-ω* model in the near-wall region with the free-stream independence of the *k-ε* model in the far field. To convert the *k-ε* model to the *k-ω* model in the near wall region, standard *k-ω* model and *k-ε* models are both multiplied by a blending function and added together. The blending function is designed to activate the *k-ω* model in the near-wall region and activates *k-ε* model away from the surface.

The transport equations are given

$$\frac{\partial}{\partial t}(\rho k) + \frac{\partial}{\partial x_i}(\rho k u_i) = \frac{\partial}{\partial x_j}\left(\Gamma_k\frac{\partial k}{\partial x_j}\right) + \widetilde{G_k} - Y_k \quad \textbf{(76)}$$

$$\frac{\partial}{\partial t}(\rho\omega) + \frac{\partial}{\partial x_i}(\rho\omega u_i) = \frac{\partial}{\partial x_j}\left(\Gamma_\omega\frac{\partial\omega}{\partial x_j}\right) + G_\omega - Y_\omega + D_\omega \quad \textbf{(77)}$$

The term $\widetilde{G_k}$ represents the generation of turbulence kinetic energy due to mean velocity gradients. G_ω is the generation of ω, while Γ_k and Γ_ω represent the effective diffusivity of *k* and ω. Y_k and Y_ω are the dissipation of *k* and ω respectively and D_ω is the cross-diffusion term.

More details about these two models could be found in the literature [**74**], [**75**], and [**76**].

In this study, we utilized a coupled Lagrangian-Eulerian approach to model the water layer formation on the airfoil due to the rain. A Lagrangian discrete phase model was used for tracking the rain droplets and a Eulerian approach was employed for tracking the interface and water film accumulation. *SST k-ω* turbulence model was used for the turbulence since it gives more accurate results for wind turbine simulations based on our simulation results of part 1 and also the work of Pape and Lecanu [**77**].

Droplet trajectories are calculated by the parcel approach. Each parcel represents several physical droplets with the same diameter being convected by a common velocity. The injection condition was based on Dunham's study [**67**]. Once the parcel is injected into the domain, a Lagrangian force balance for that is solved and the trajectory of that parcel is updated at each time step. For simplicity, it is assumed that all the parcels have the same initial velocity and diameter. A rain fall rate of 1800 mm/h and a Reynolds number of 2×10^6 was used for all the simulations. The droplet diameter was set to 6mm based on the droplet size distribution reported by Markowitz et al. [**78**].

The key assumption in our simulations is the transformation of the rain droplets into the liquid elements of water film. We assumed that once a parcel impinges on a wall or pre-formed water film, it acts as a mass source for the film and will add to the mass of the film. Then, the volume fraction and momentum balance of the film are calculated using a Eulerian Volume of Fluid model with the Geo-Reconstruct scheme. The Geo-Reconstruct scheme is able to resolve the sharp interface between the water layer and air flow. However, the required time step is relatively small. For this reason a variable time step method was employed to change the time step size while keeping the courant number in a reasonable range. The calculation is based on a pressure-based solver using the implicit body force treatment to account for the effect of gravity. The same approach has been used by Arienti et al. [**79**] to model fuel atomization process in combustion devices.

The computational mesh is the same as the mesh we used for the single-phase simulations. A very fine layer was built along the airfoil surface in order to capture the thin film formation on the airfoil. In addition, an 8 m^2 injection surface was defined 3m above the airfoil.

The governing equations for the multiphase flow around the airfoil are based on part D of Table 16. The force balance equation for the parcels in discrete phase model is

$$\frac{du_p}{dt} = F_D\left(u - u_p\right) + \frac{g_x(\rho_P - \rho)}{\rho_P} \quad \textbf{(78)}$$

where $F_D\left(u - u_p\right)$ is the drag force per unit particle mass and

$$F_D = \frac{18\mu C_d\, Re}{\rho_P d_p^2\, 24} \quad \textbf{(79)}$$

u is the fluid phase velocity, u_p is the parcel velocity, μ is the fluid viscosity, ρ is the fluid density, $\rho_P$is the particle density and d_p is the particle diameter.

The equations for the Volume of Fluid model are the Continuity equation and Navier-Stokes equations based on the shared-field approximation:

$$\frac{\partial}{\partial t}\left(\alpha_q \rho_q\right) + \nabla \cdot \left(\alpha_q \rho_q \bar{v}_q\right) = S_{\alpha_q} \quad \textbf{(80)}$$

$$\frac{\partial}{\partial t}(\rho \bar{v}) + \nabla \cdot (\rho \bar{v} \bar{v}) = -\nabla p + \nabla \cdot [\mu(\nabla \bar{v} + \nabla \bar{v}^T)] + \rho \bar{g} \quad \textbf{(81)}$$

$$S_\alpha = \frac{m_p}{V \Delta t} \quad \textbf{(82)}$$

α_q is the volume fraction of phase q, ρ_q is the density of phase q, $\bar{v}_q$ is the velocity and S_{α_q} is the source term due to particle impingement. Where m_p is the mass of the particle, V is the volume of impinging cell and Δt is the time step size of continuous phase solver. ρ and μ are the density and viscosity of mixture and are changing with the volume fraction.

H2. Results and Discussion

Case 1: Simulation of single-phase flow around a 2-D airfoil

In this section, the results of the 2-D benchmarking simulation of Case 1 are presented. The comparison between the calculated Lift and Drag coefficients is considered, as the main measures of the aerodynamics performance of the airfoil. The comparison between the calculated lift and drag coefficients using the two turbulence models with the wind tunnel experiments of the Delft University of Technology is presented in Figure 246 and Figure 247.

As shown in Figure 246, at angles of attack higher than 14.24, the airfoil experienced a degradation of performance due to a decrease in lift coefficient. The *SST k-ω* model outperformed the Spalart-Allmaras model by predicting this degradation. However, this model is over predicting the lift coefficient at higher angles of attack. This is in line with the results of a previous study by Pape and Lecano concluding that the *SST k-ω* model is more suitable for wind turbine simulations [**77**]. In addition, we could not get a converged solution with the Spalart-Allmaras model at angles of attack higher than 14.24.

Figure 247 shows that the Spalart-Allmaras and *SST k-ω* models both are in a good agreement with the experiments in the calculation of the drag coefficient; however, both models under predict the drag at angles of attack greater than 9.22 degree.

Figure 248 shows the velocity contour around the airfoil under different angle of attacks calculated with the *SST k-ω* model. By increasing the angle of attack, the stagnation point goes downward and boundary layer separation starts at an angle of attack of 9.22 degree. As the angle of attack increases, the separation point moves toward the leading edge.

In summary, both the calculated lift and drag coefficients using our CFD model are in a reasonable agreement with the experiments up to an angle of attack of 9.22, while the flow is attached. At higher angles of attack when the boundary layer separation begins, the model over predicts the lift and under predicts the drag, possibly due to under predicting boundary layer separation.

Based on the above-mentioned results, the *SST k-ω* model was chosen as the turbulence model for further simulations.

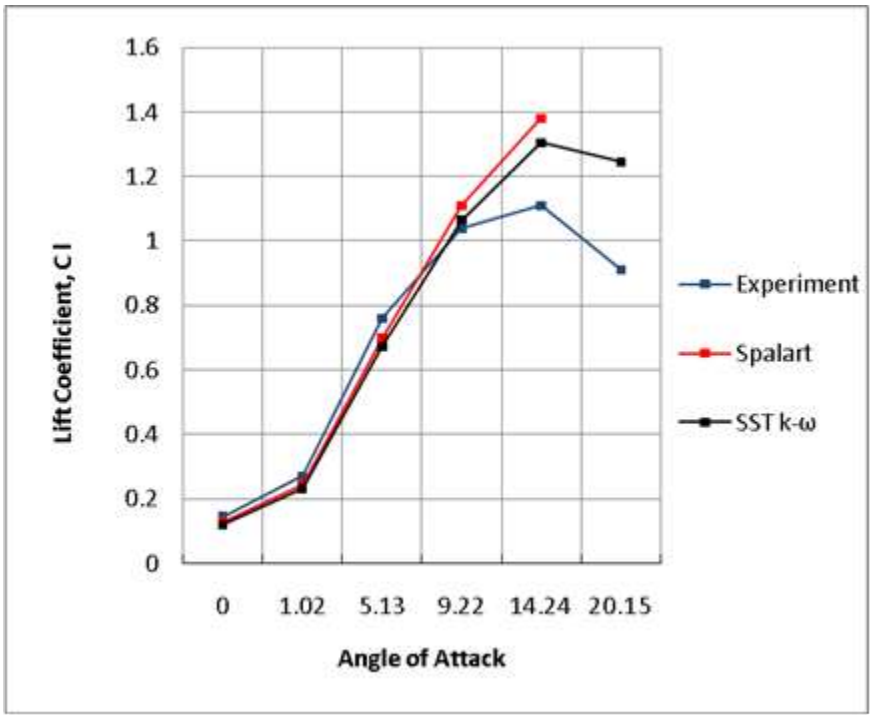

Figure 246: S809 Lift coefficients at different AoA

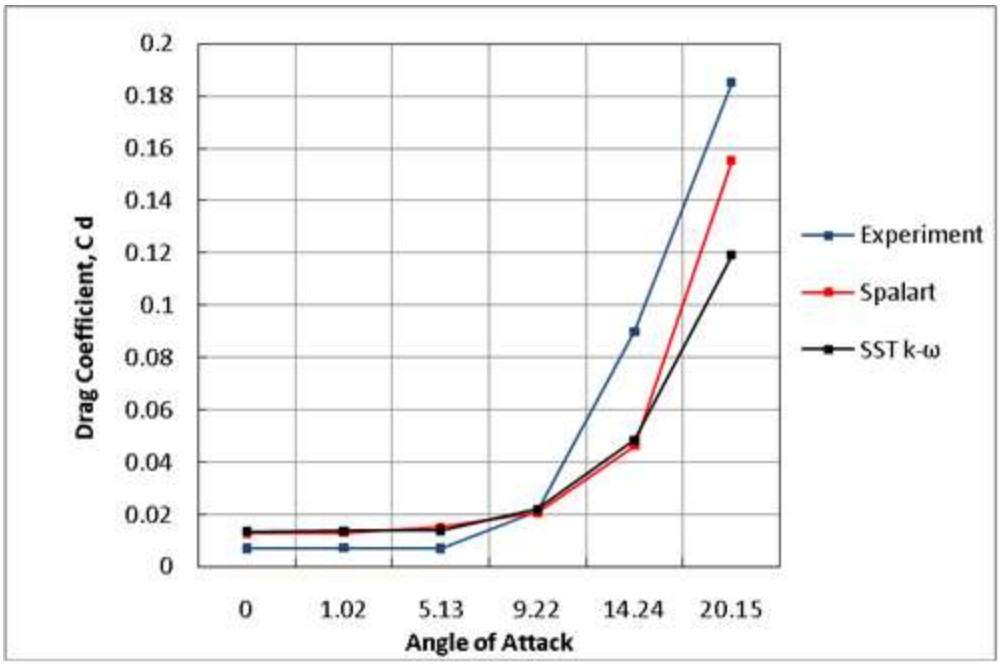

Figure 247: S809 Drag coefficients at different AoA

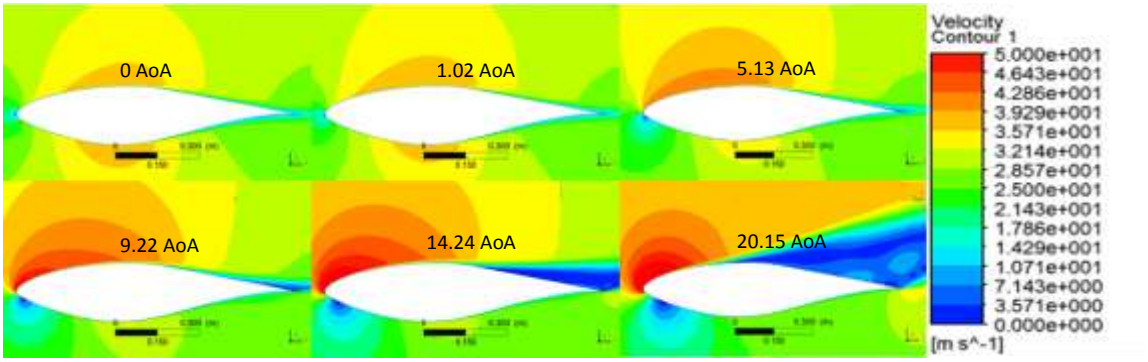

Figure 248: Velocity contour near the airfoil

Case 2: Simulation of 3-D wind turbine using a single phase flow model

In our 3-D simulations of Case 2, the torque of the turbine had been monitored during the simulations at different wind speed. Constant rotational speed is maintained during the operation of wind turbine to provide a steady power output. The shaft power could be related to the torque simply by

$$Total\ Shaft\ Power(kW) = \frac{Torque(N \cdot m) \times 2\pi \times rotational\ speed(rpm)}{60000} \times 3 \qquad (83)$$

The comparison between calculated shaft power and experimental data of the NREL-phase II field experiments for different wind speeds is presented in Figure 249. For wind velocity lower than 17 m/s, the simulation results show a very good agreement with the experimental data. For the higher wind velocities, the power output is slightly under predicted using our CFD model which could be due to the not fully resolved turbulence flow at higher wind velocities.

Case 3: Simulation of two phase flow around a 2-D airfoil

In our model, two processes are being considered during the formation of water film:

1. Accumulation of the water on the airfoil due to the rain
2. Stripping off of the film due to the wind shear stress

When the accumulation and stripping off processes on the surface of an airfoil balance each other, the system will reach a quasi-steady state and a thin layer of water film could be observed on the airfoil surface.

Figure 250 shows the accumulation of water on the trailing edge of the airfoil. At an angle of attack of zero, the formation of a bump by the film on the upper surface near the trailing edge is captured by the simulation. As the angle of attack increases, the "bump" moves toward the leading edge and less water is accumulated on the upper surface of the airfoil. We can define a "detach" point where water film detached from the upper face of the airfoil. As shown in Figure 250, the detach point moves towards leading edge with increasing angle of attack. These results are in qualitative agreement with the behavior of splashed water droplets distribution presented in Valentine and Decker's study [**68**].

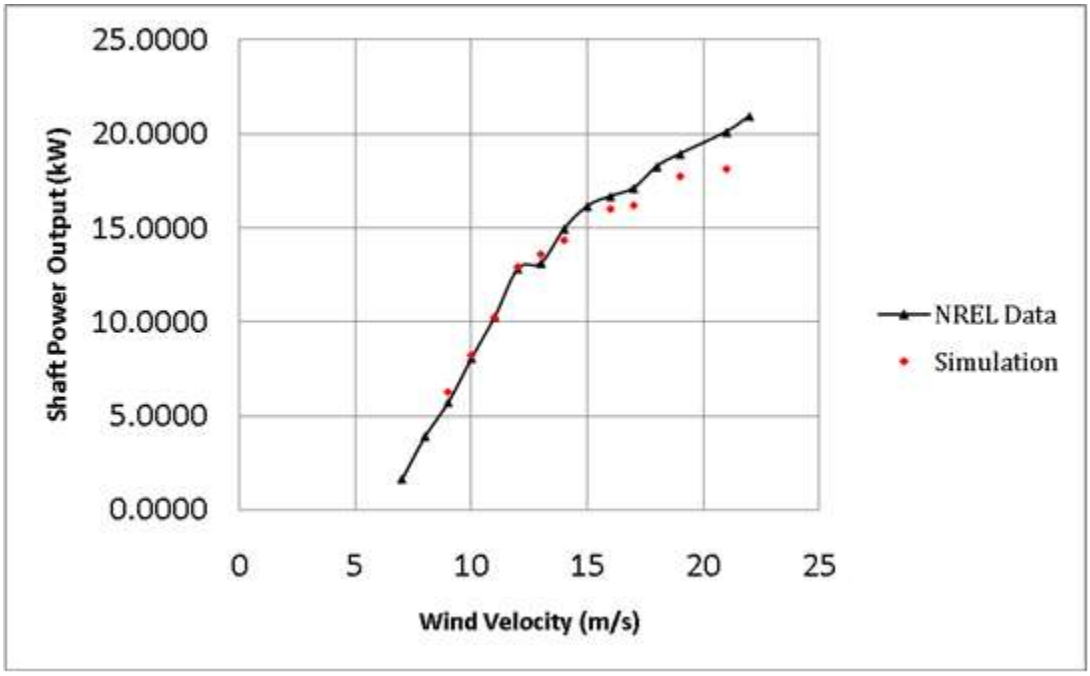

Figure 249: Power output vs. wind speed

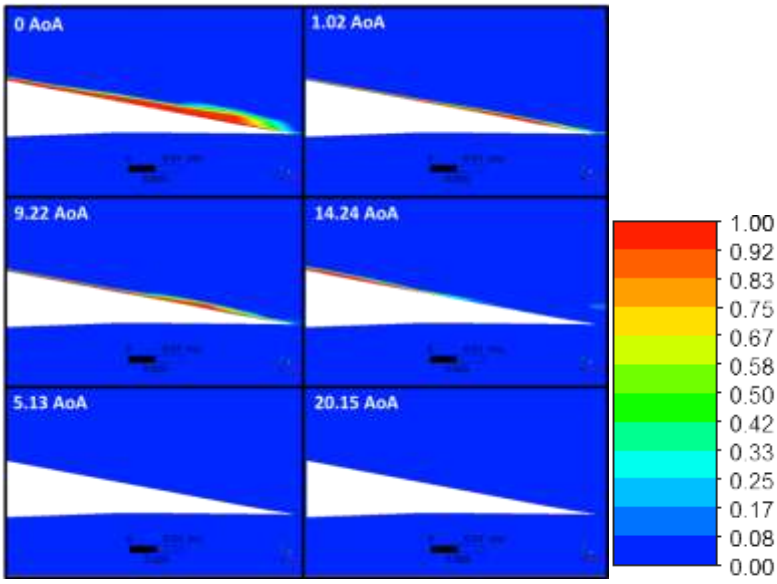

Figure 250: Contours of the water volume fraction on the trailing edge of the airfoil for different angles of attack shows accumulation of water on the airfoil

The accumulation of water on the leading edge is not significant due to the high shear stress that moves the film toward either trailing edge or off the blade. Since we applied a transient simulation and shape of water film changes with time, the lift and drag coefficients fluctuate in a small range. The time averaged values of lift and drag coefficients has been used for performance analysis of the airfoil. Water film formation due to rain affects airfoil performance coefficients (see Table 17 and

Table 18 and Figure 251 and Figure 252).

The simulation showed the lift coefficient decreases up to 34% due to the film formation, while the drag coefficient increases up to 40 percent for 5 different angles of attack. On average, the airfoil experienced a 12% loss in lift and a 30% increase in drag. Maximum lift coefficient loss appears at a 0 degree angle of attack and the degradation in lift decreases as the angle of attack increases. This is due to less water accumulation on the upper surface of the airfoil as shown in Figure 250.

Table 19 and Figure 253 show the Lift-to-Drag ratio as a measure of the airfoil performance for different angles of attack. The results show a significant degradation of airfoil performance due to the film formation with a maximum value of 48% and an average of 31%. The captured water film by our simulations is homogeneous and no wavy shape of the film has been captured. Our simulation results are in line with the behavior of an airfoil with wettable surface in rainy condition reported by Hansman and Barsotti [**70**]. They also studied the impact on performance of the airfoils with different surface materials and found that the airfoil with non-wettable materials experiences the most severe degradation in performance due to the surface tension effect.

Comparisons between the calculated pressure coefficient distribution with rain and without rain are presented in Figure 254. The difference in pressure coefficient distribution on the airfoil surfaces

indicates the appearance of a water layer. The water accumulation on the upper surface causes an increase in the pressure on the upper surface and leads to the degradation in the lift coefficient.

Table 17: Degradation of Lift Coefficient due to the Rain at Different Angles of Attack

Angle of Attack	No Rain	Rain	Absolute Difference	Percentage Difference
0	0.12022	0.07889	-0.04133	-34.38%
1.02	0.23237	0.181171	-0.0512	-22.03%
5.13	0.67224	0.611387	-0.06085	-9.05%
9.22	1.0655	1.045239	-0.02026	-1.90%
14.24	1.3044	1.295126	-0.00927	-0.71%
20.15	1.2452	1.198291	-0.04691	-3.77%

Table 18: Increase of Drag Coefficient due to the Rain at Different Angles of Attack

Angle of Attack	No Rain	Rain	Absolute Difference	Percentage Difference
0	0.01347	0.016918	0.00345	25.60%
1.02	0.013688	0.017408	0.00372	27.18%
5.13	0.013874	0.019667	0.00579	41.75%
9.22	0.021966	0.031529	0.00956	43.54%
14.24	0.048426	0.054785	0.00636	13.13%
20.15	0.11915	0.149746	0.0306	25.68%

Table 19: Lift-to-Drag Ratio

Angle of Attack	No Rain	Rain	Difference
0	8.925019	4.663081	-47.75%
1.02	16.97618	10.40734	-38.69%
5.13	48.45322	31.08695	-35.84%
9.22	48.50678	33.15167	-31.66%
14.24	26.93594	23.64016	-12.24%
20.15	10.45069	8.002157	-23.43%

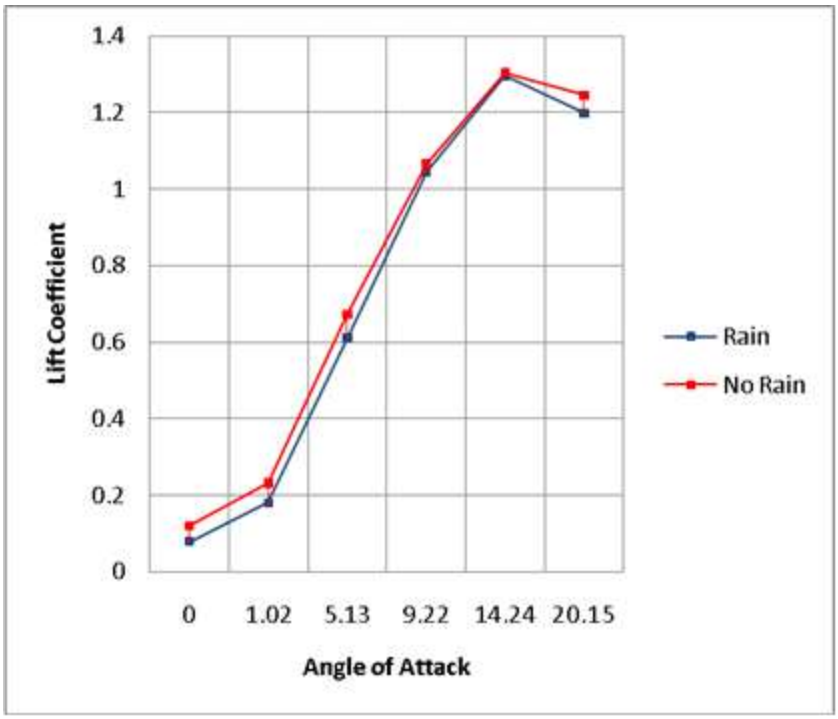

Figure 251: Comparison of lift coefficients at different angles of attack with and without rain

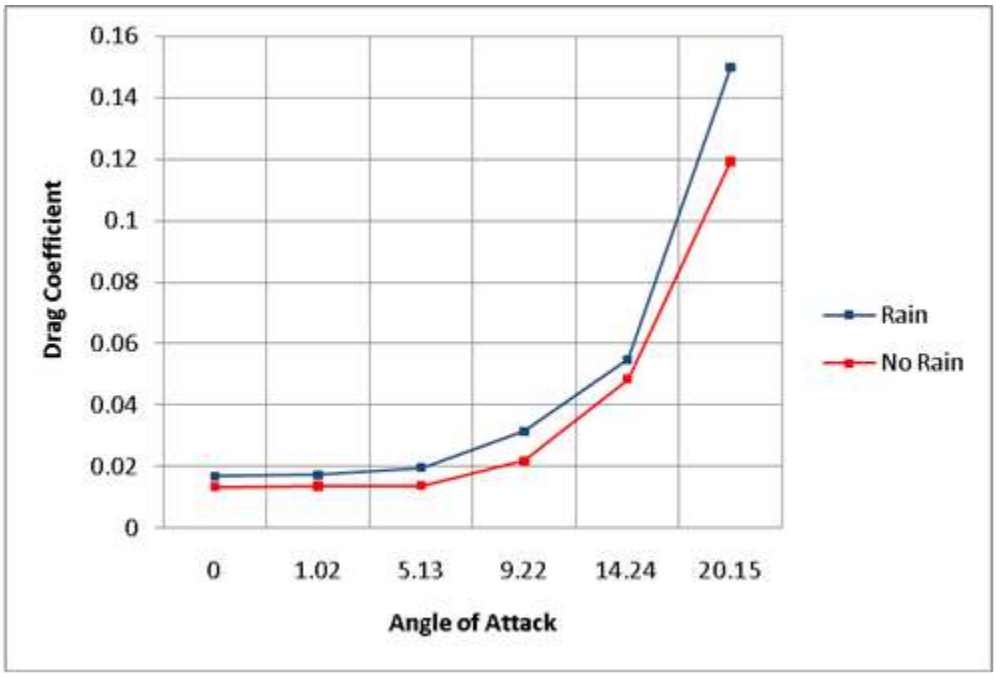

Figure 252: Comparison of drag coefficients at different angles of attack with and without rain

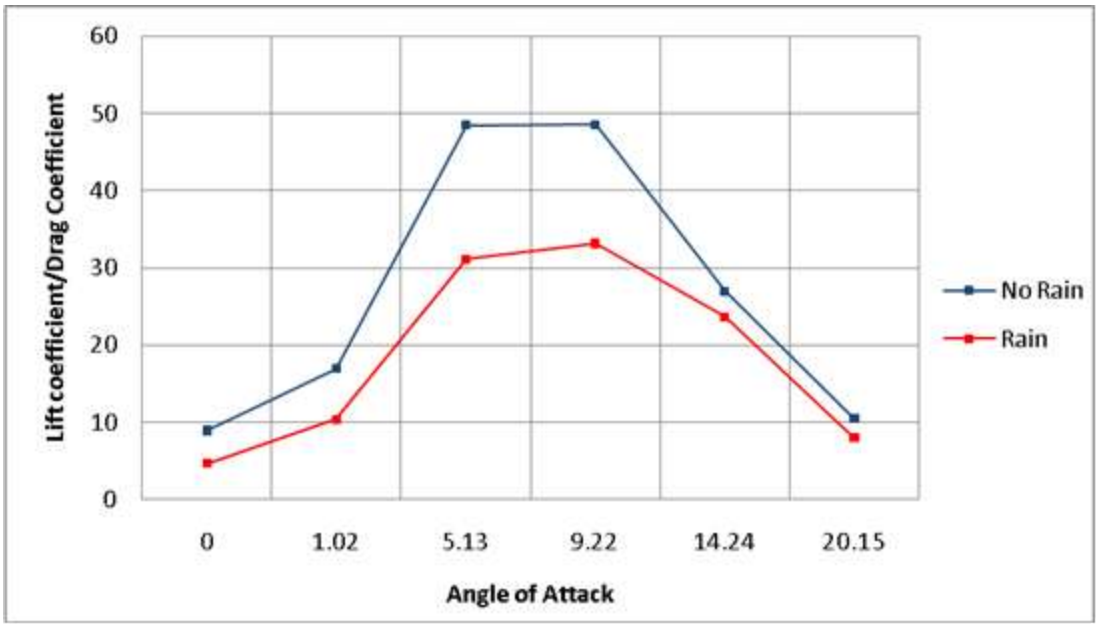

Figure 253: Lift-to-drag ratio at different angles of attack with and without rain

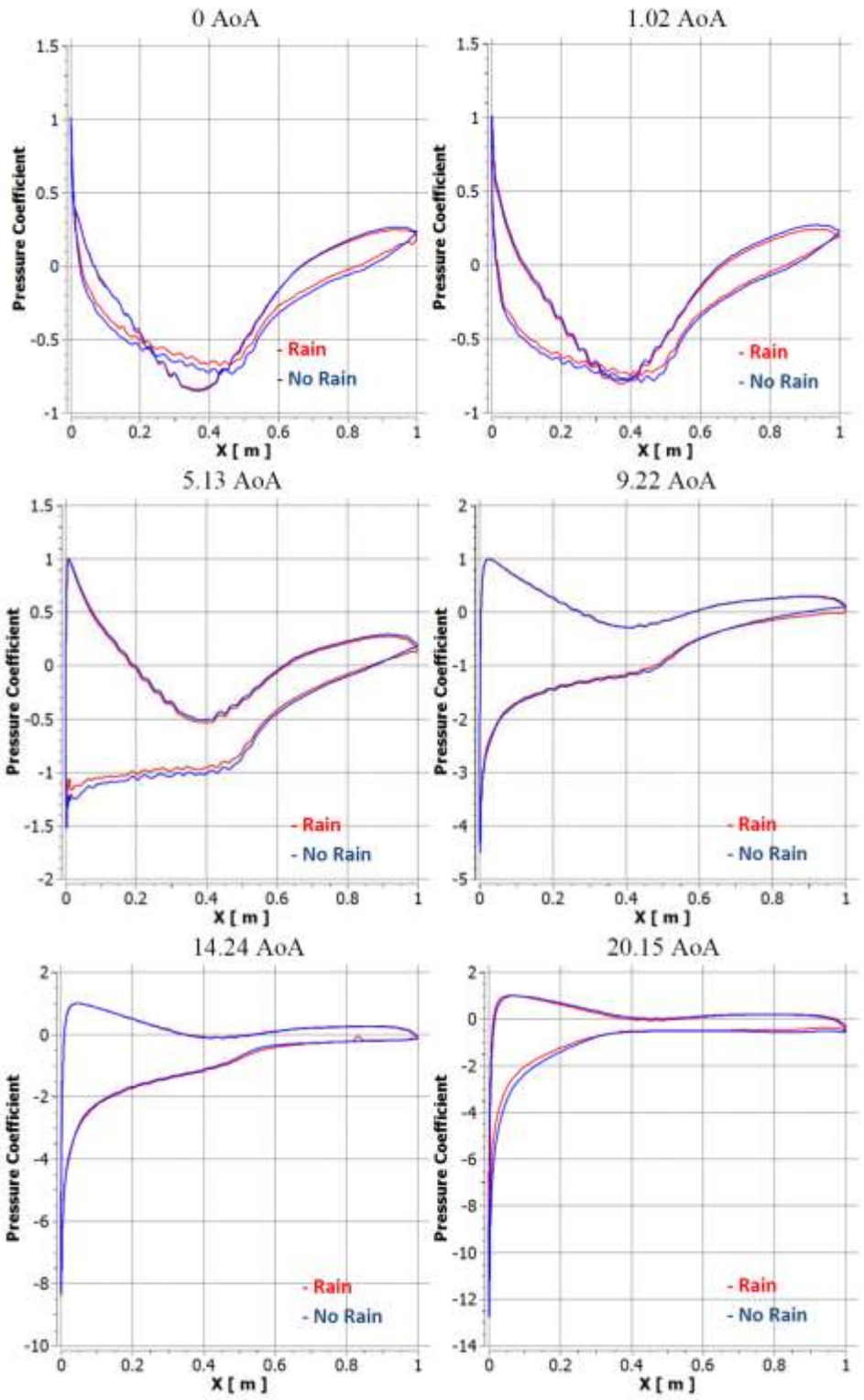

Figure 254: Comparison between pressure coefficient distribution on the airfoil at different angles of attack with and without rain

H3. Summary and Conclusion

We used the CFD approach to assess and predict the performance of a horizontal-axis-wind-turbine (HAWT). Initially a set of single-phase benchmarking CFD simulations was performed in 2-D and 3-D and the results were compared with the available experimental data in the literature to refine our CFD model. Then, the single phase simulation results were used as a baseline to calculate the impact of rain on the performance of the wind turbine.

To capture the water film formation over the airfoil, a new coupled Lagrangian-Eulerian approach was employed. By capturing the shape and position of the accumulated water film, we estimated the performance loss caused by the formation of the water film. The results of this study could help designers to minimize the impact of rain on the new generation of wind turbines.

Our future work is geared toward adding the effect of splash back of droplets in our model and considering the effect of surface tension on the water film formation. In addition, we are going to apply our Lagrangian-Eulerian model in a three-dimensional case and calculate the performance of the horizontal-axis-wind-turbine in a heavy rain condition.

3.2.2 Wind Energy Integration

A. Analysis of 2030 Large-Scale Wind Energy Integration in the U.S. Eastern Interconnection

A simulation of the 2030 load forecast in the Eastern Interconnection suggests that large-scale wind energy integration will have a major impact on the hourly commitment and dispatch of gas and coal units, especially at off-peak load hours. While fuel price alterations will have major impacts on the system production cost, load variation will have a larger impact and potential carbon costs will have the greatest impact.

Wind energy is an important component of the future energy portfolio throughout the world. In the United States, wind energy is expected to provide 20% of the electricity by 2030 [**1**], [**80**], [**81**]. However, the electricity market would require a detail simulation of the adequacy of energy portfolio before integrating the large-scale wind energy into the existing power systems.

The Eastern Interconnection is the largest interconnection in the world with more than 5,000 generating units and about 70,000 branches. The National Renewable Energy Laboratory initiated a study in 2008 to examine the impact of 20-30% wind energy penetration in the Eastern Interconnection [**82**]. The western wind and solar integration study in 2007 examined the operational impact of 35% renewable energy penetration in the Western Interconnection [**83**]. The impact of wind integration on power system operations is analyzed further in [**84**], [**85**].

An hourly unit commitment and economic dispatch model for analyzing large-scale power system operations was represented in [**86**]. A follow-up optimization-based SCUC model [**87**], [**88**], [**89**] was presented in [**90**] which took into account the intermittency and volatility of wind power generation and transmission network constraints.

In this section, we focus on studying the large-scale security-constrained wind energy integration in the Eastern Interconnection in 2030. The wind energy sites are analyzed and the impact of large-scale wind integration on existing generation resources and production costs are studied. Fuel price sensitivity, wind energy production sensitivity, load growth sensitivity, carbon cost sensitivity, and load management strategies are considered and analyzed in this chapter for the large-scale wind energy integration.

The rest of this section is organized as follows. Section A1 describes the proposed methodology, assumption and relevant evaluation metrics. Section A2 presents the wind energy integration study results for the Eastern Interconnections. The conclusions drawn from the study is provided in Section A3.

A1. Methodology for Wind Energy Integration

At Illinois Institute of Technology (IIT), we had developed over the years an efficient decision tool called POMS [**91**] for the day-ahead scheduling of large scale power systems. The expansion of POMS, which is referred to as WINS (Wind INtegration Simulator), is considered in this study to support the collaborative planning, analysis, and implementation of the large-scale wind energy integrations in the United States. The WINS architecture is depicted in Figure 255.

WINS applies unit commitment to simulate large-scale wind energy integrations in the hourly power system operation. The application of WINS in this chapter analyzes the impact of large-scale wind energy integration in the year 2030 on production costs, unit commitment, and dispatch of generation resources in the Eastern Interconnection. For the purpose of this energy adequacy study, we do not consider transmission constraints in this chapter. We use wind data given in [**82**]. A brief description of the wind data is given in [**92**]. The wind uncertainty is simulated by sensitivity analyses applied to the wind energy integration Scenarios.

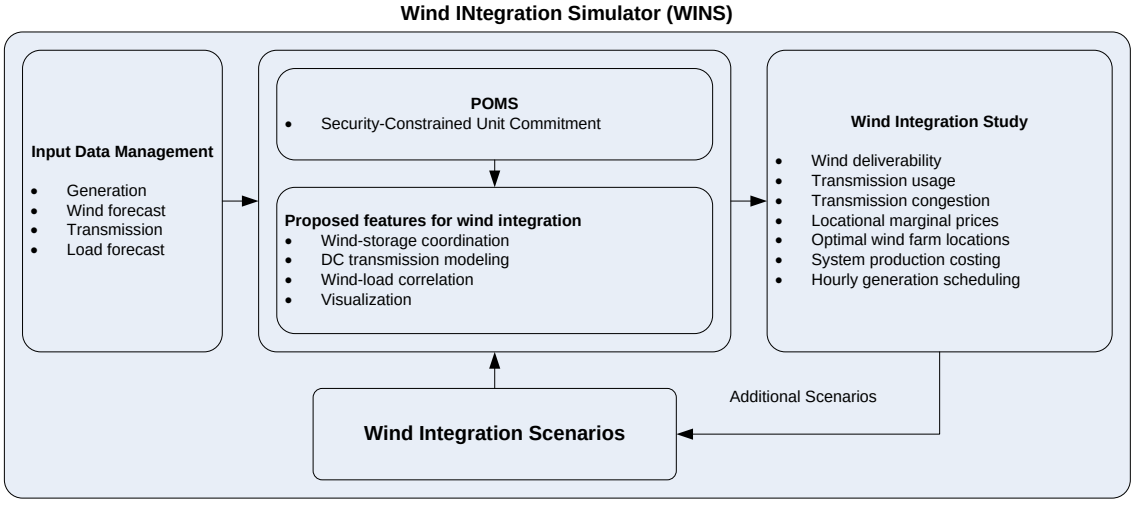

Figure 255: Framework of WINS

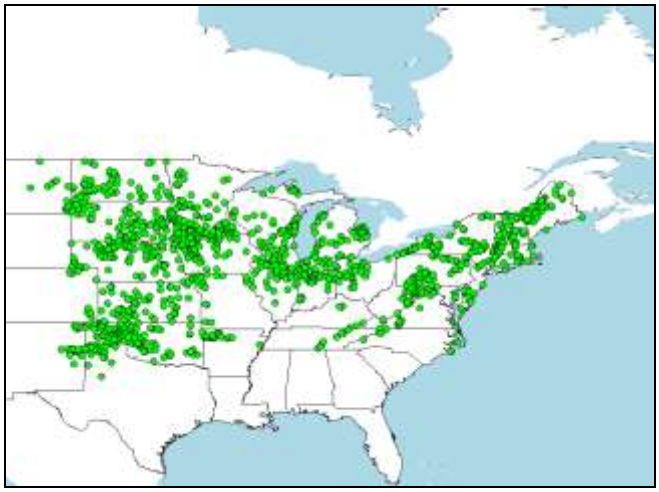

Figure 256: Potential Wind Sites in the Eastern Interconnection

Input Data

It is estimated that approximately 225GW of wind power generation is required to supply the 20%, and 330GW is required to supply the 30% of the total energy by 2024 in the Eastern Interconnection [**82**]. In this chapter, we utilize the land-based time series wind simulation results [**82**]. The potential land-based wind sites in the Eastern Interconnection are shown in Figure 256 for about 580GW of wind power generation capacity. The figure shows that there are potential wind sites with rich wind resources in the central parts of the United States.

In this study, we consider a 1.28% annual load growth rate which is based on the MTEP 2008 data. The hourly load distribution shown in Figure 257 is based on the MISO's hourly load profile in 2007 [**93**]. In Figure 257, peak load hours appear in July and August. The power flow solution is used for calculating the hourly load distribution at each bus.

Fuel prices are assumed to increase at an annual rate of 4% for oil and gas, 2% for coal, and 3% for nuclear fuel based on the fuel price given in 2008 [**93**].

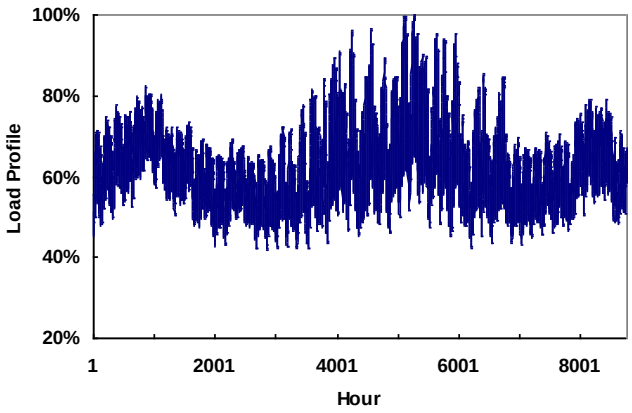

Figure 257: Annual Hourly Load Profile

Evaluation Metrics

The evaluation criteria and metrics used in the simulations are defined as follows.

Wind Energy Availability. The available wind energy is treated as dispatchable in WINS simulations. Here,

$$P_A = \sum_{t=1}^{T} \sum_{i=1}^{NG} p_i^{\max} w_{it} \quad \textbf{(84)}$$

where *T* represents the number of hours in a period (e.g., one year), *NG* represents the number of wind generators/farms, $p_i^{\max}$ is the nominal capacity of wind generator/farm *i*, w_{it} represents the wind power profile *i* at time *t*, P_A represents the system wind availability in the given study period.

We assume the available wind energy is much less than the total system load in the Eastern Interconnection. Therefore, the total available wind energy is to be dispatched without any curtailment.

Percentage of Wind Energy Contribution. This metric is to evaluate the percentage of wind energy contribution to the total energy utilized for supplying the load in the power system.

$$= \frac{Wind\ \ Ener\quad gy}{Total\ \ Ene\quad rgy} * 100\ \ \% \quad \textbf{(85)}$$

A2. Numerical Results

In this section, we utilize WINS to simulate the wind integration in the Eastern Interconnection of the United States based on the methodology presented in Section A1.

Level of Wind Integration

We simulate the hourly power system operation using WINS for a given wind power capacity factor (CF). Four scenarios are studied as follows.

- Scenario 1: No wind integration
- Scenario 2: Wind energy integration with a minimum 40% CF
- Scenario 3: Wind energy integration with a minimum 30% CF
- Scenario 4: Integration of all potential wind energy sites

Scenario 1: No wind integration. This is the base case in which the hourly loads will be served by fossil fuel and hydro units. Figure 258 shows the hourly production cost which is $217.5 billion per year with an average production cost of $45.64/MWh. The production cost will not change linearly with the hourly load fluctuations. Hydro units will have zero costs and be scheduled first to serve hourly loads or reserves; then cheaper units such as nuclear, coal, and large oil will be committed as loads pick up, and finally expensive units such as gas and oil will be committed to supply hourly loads. A higher production cost will occur at annual peak hours of 5000-5500 (i.e., July and August.) The production cost at peak

hours (6AM-10PM) will be $177.8 billion and the production cost at off-peak hours (11PM-5AM) will be $39.7 billion. The average production costs at peak/off-peak hours are $50.2/MWh and $32.5/MWh. The average production cost at peak load hours is higher when expensive generators are committed and dispatched.

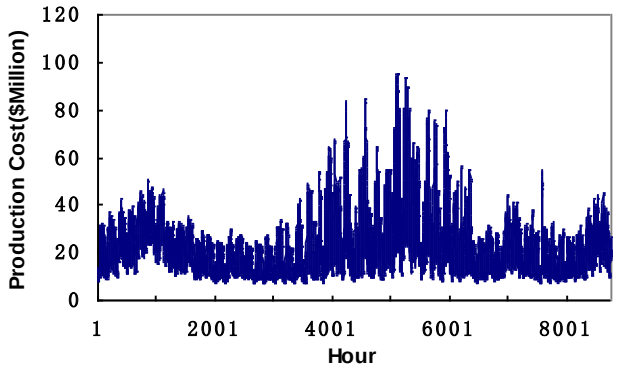

Figure 258: Hourly Production Cost without Wind Integration

Scenario 2: Integration of Wind Energy Sites with a minimum 40% CF. There are 399 of such potential wind energy sites with a total wind generation capacity of 230.5GW. The largest annual CF is 49%. Figure 259 shows the 399 potential wind energy sites in the Eastern Interconnection in which wind energy resources are mainly located remotely in the central region of the United States. The total available wind energy with a minimum 40% CF in that region is 845.2TWh.

The 2030 energy forecast in the Eastern Interconnection is 4,783.2TWh which indicates that the potential wind energy is about 17.67% of the total energy portfolio. We assume the wind energy has zero fuel cost and transmission congestion is not considered. So the entire available wind energy will be dispatched to satisfy the hourly load.

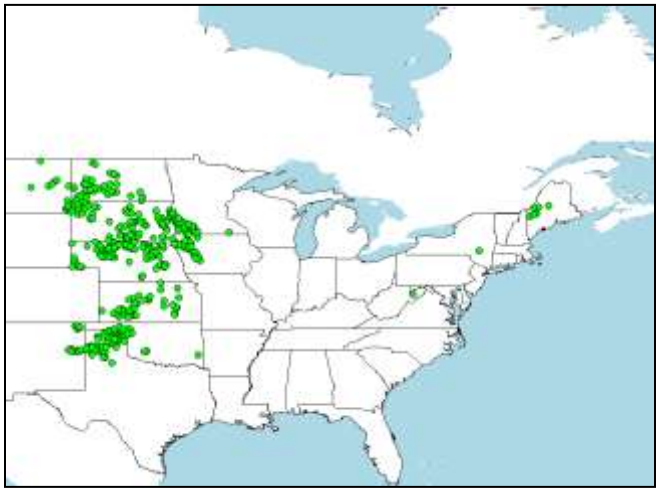

Figure 259: Potential Wind Sites with CF ≥ 40%

Figure 260 shows the monthly wind energy in 2030. The wind energy resources are mostly available in spring or winner; however, peak loads occur in summer. January has the highest level of available wind

energy of 86.4TWh which amounts to 21.11% of the total energy. March has the highest percentage for wind energy contribution (21.53%) because the load is lower than that of January. The available wind energy is scarce in August while the highest level of load occurs in this month. So August represents the month with the least available wind energy and the percentage of wind energy contribution (i.e., 57.5TWh and 12.2%) to the total energy portfolio.

Figure 261 shows the wind energy contribution at peak and off-peak hours. The figure shows that the wind is usually rich at night as compared with that in the day time especially in the summer. The hourly average wind energy at peak/off-peak hours are 2.27TWh and 2.69TWh in August, and the percentages of wind energy contribution are 10.88% and 16.22% respectively.

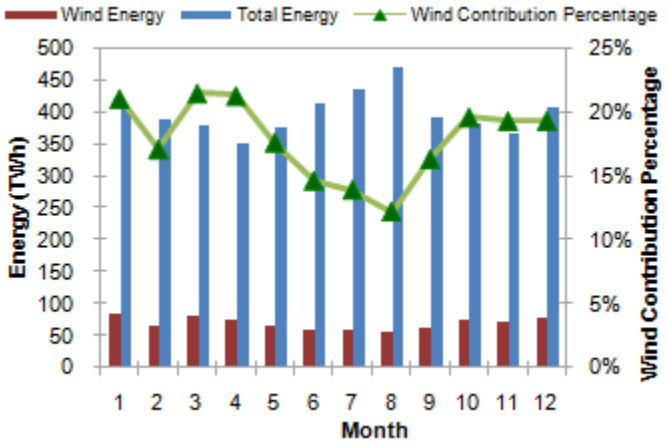

Figure 260: Monthly Wind Energy and its Contribution to Total Energy in Scenario 2

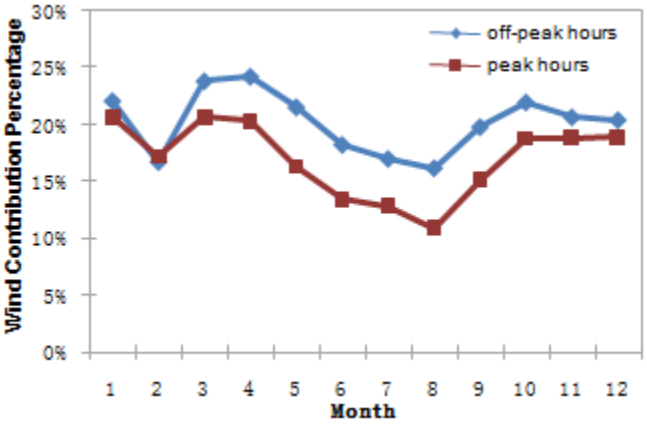

Figure 261: Wind Energy Contribution at Peak/Off-Peak Hours in Scenario 2

Figure 262 shows the hourly production cost. Compared to Figure 258, the production cost is lower when the large-scale wind energy is integrated. The annual production cost is $130.4 billion, which is about $87.1 billion less than that in Scenario 1. The annual average production cost decreases from $45.64/MWh to $27.25/MWh when the wind energy is integrated. Here, the production costs at peak/off-peak hours are $107.1 billion and $23.2 billion, and the average production cost at peak/off-

peak hours are 30.1$/MWh and 18.9$/MWh respectively. The average production cost is lower in this Scenario at peak/off-peak hours.

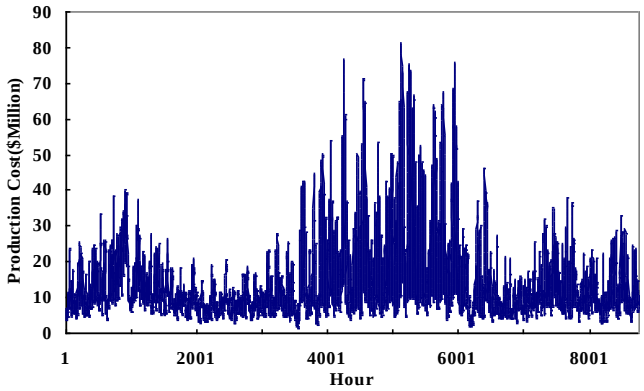

Figure 262: Hourly Production Cost in Scenario 2

Scenario 3: Integration of Wind Sites with a Minimum 30% CF. In this case, 972 wind sites are introduced in Figure 263 with a total capacity of 481.5GW. Compared to Figure 259, additional wind energy sites located in Wisconsin, Illinois, Indiana, and other sites are considered in this Scenario.

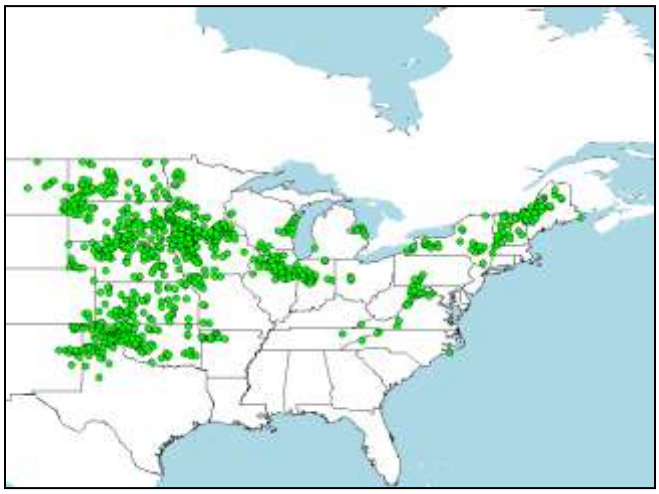

Figure 263: Potential Wind Sites with CF ≥ 30%

Figure 264 shows the annual wind energy contribution is 1,596TW which amounts to 33.37% percentage of the energy portfolio. Figure 265 shows the monthly wind energy contribution at peak/off-peak hours. Compared to the simulation results in Scenario 2, 573 additional potential wind energy sites with a 251GW of capacity are added here with a lower CF between 30% and 40%. In this case, the added wind capacity is 108.9% (i.e., 481.5GW VS 230.5GW) while the wind energy contribution increases about 88.85% (i.e., 33.37% VS 17.67%).

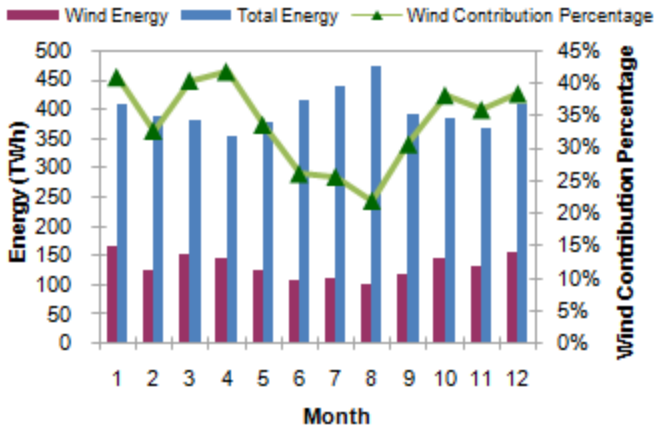

Figure 264: Monthly Wind Energy and its Contribution to Total Energy in Scenario 3

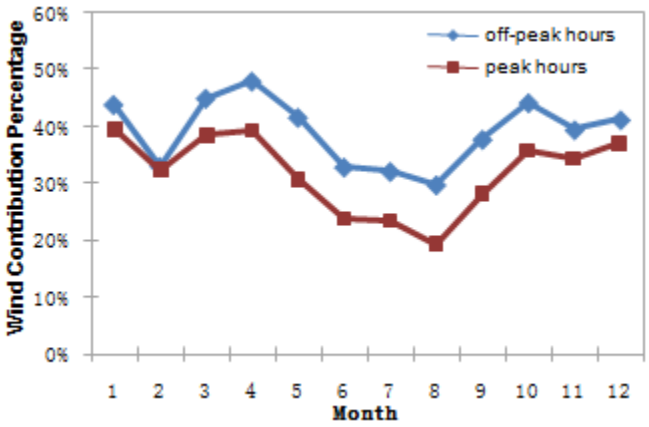

Figure 265: Wind Contribution at Peak/Off-Peak Hours in Scenario 3

The production cost in Figure 266 is $86.8 billion with an average hourly production cost of 18.14$/MWh. The average production costs at peak/off-peak hours are 20.33$/MWh and 11.33$/MWh, respectively.

Scenario 4: Integration of All Potential Wind Sites. There are 1,326 wind energy sites in the Eastern Interconnection with a total capacity of 580 GW. Figure 267 shows the monthly wind energy production and wind energy contribution. The annual wind energy production is about 1,816TWh and the annual percentage of wind energy contribution is about 38%. In this case, the minimum wind energy contribution will be more than 20% of the system load.

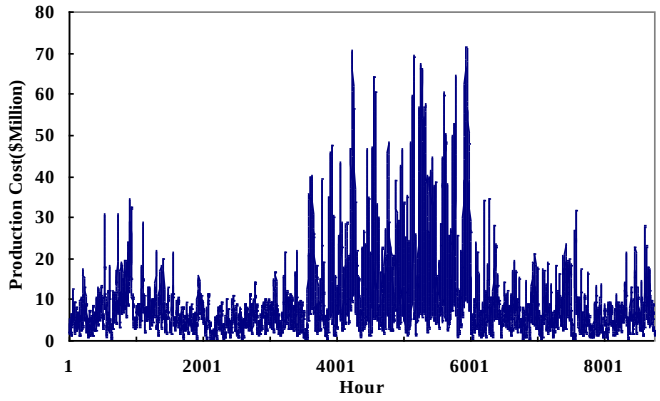

Figure 266: Hourly Production Cost in Scenario 3

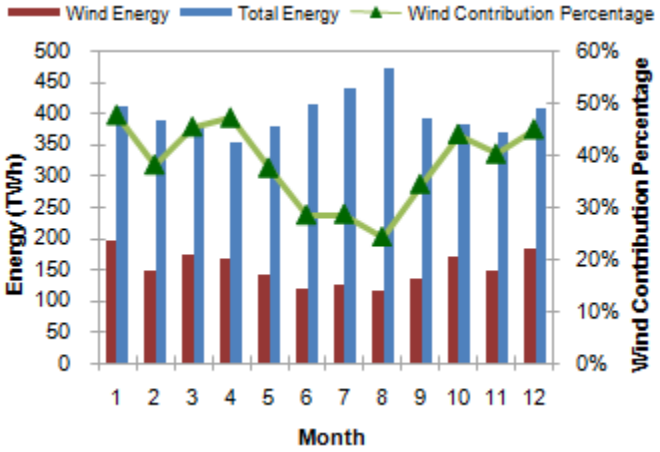

Figure 267: Monthly Wind Energy and its Contribution to Total Energy in Scenario 4

Figure 268 shows the percentage of wind energy contribution at peak/off-peak hours. Here, the wind energy contribution to the total energy at peak hours in August is 21.33%, which is also the lowest period for the wind energy production. The wind energy in this period is 75.83TWh as compared to 38.67TWh in Scenario 2 and 68.52TWh in Scenario 3. The annual production cost is $77 billion. Figure 269 shows the hourly production cost with an average production cost of $16.1/MWh, and peak/off-peak average production costs of $18.19/MWh and $10.04/MWh respectively. Compared to the simulation results in Scenarios 1-3, the production costs has dropped here as more wind energy sites are added. Figure 270 shows the wind energy contribution in all four Scenarios. Here, the gas unit production has decreased as more wind energy is considered. Also, the energy supplied by coal units is lower which is replaced by the integrated wind energy units. Figure 271-Figure 273 show the energy supplied by gas, coal and wind units in four Scenarios. These figures show that wind energy will replace some of the fossil energy especially at off-peak hours in the Eastern Interconnection.

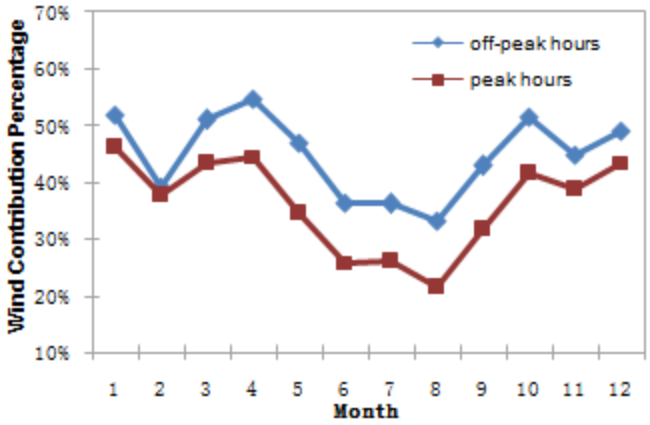

Figure 268: Wind Energy Contribution at Peak/Off-Peak Hours in Scenario 4

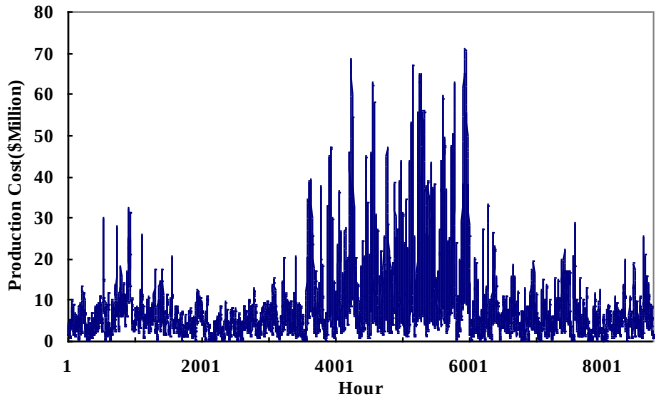

Figure 269: Hourly Production Cost in Scenario 4

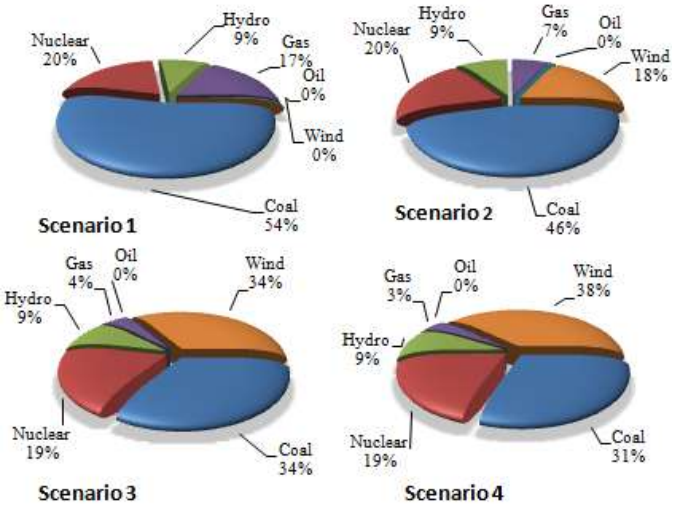

Figure 270: Energy Portfolio in Wind Integration Scenarios

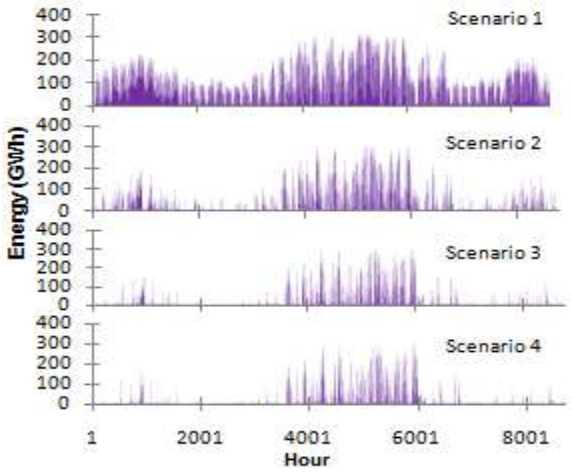

Figure 271: Hourly Energy Provided by Gas Units in Wind Integration Scenarios

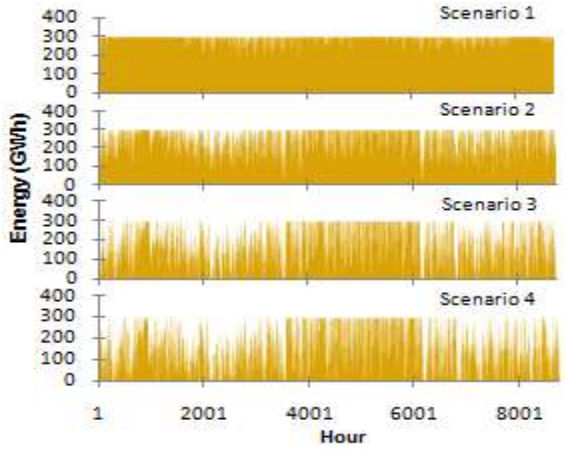

Figure 272: Hourly Energy Provided by Coal Units in Wind Integration Scenarios

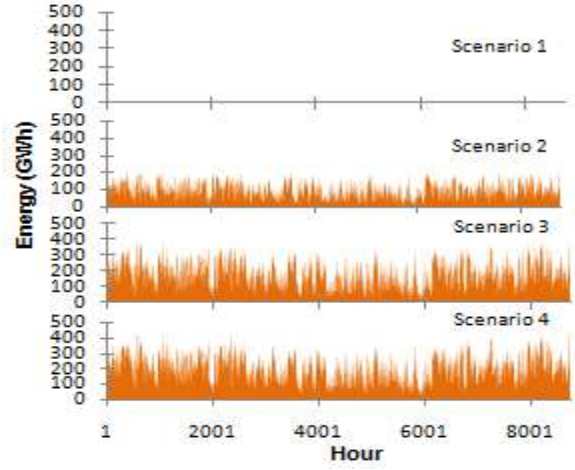

Figure 273: Hourly Wind Energy in Wind Integration Scenarios

Figure 274 show the annual commitment results of existing power plants in four Scenarios, in which red dots represents the power plants in which at least one unit is committed for a minimum of one hour per year. Also, blue dots show the plants which will be off throughout the year as more wind energy is integrated in the Eastern Interconnection.

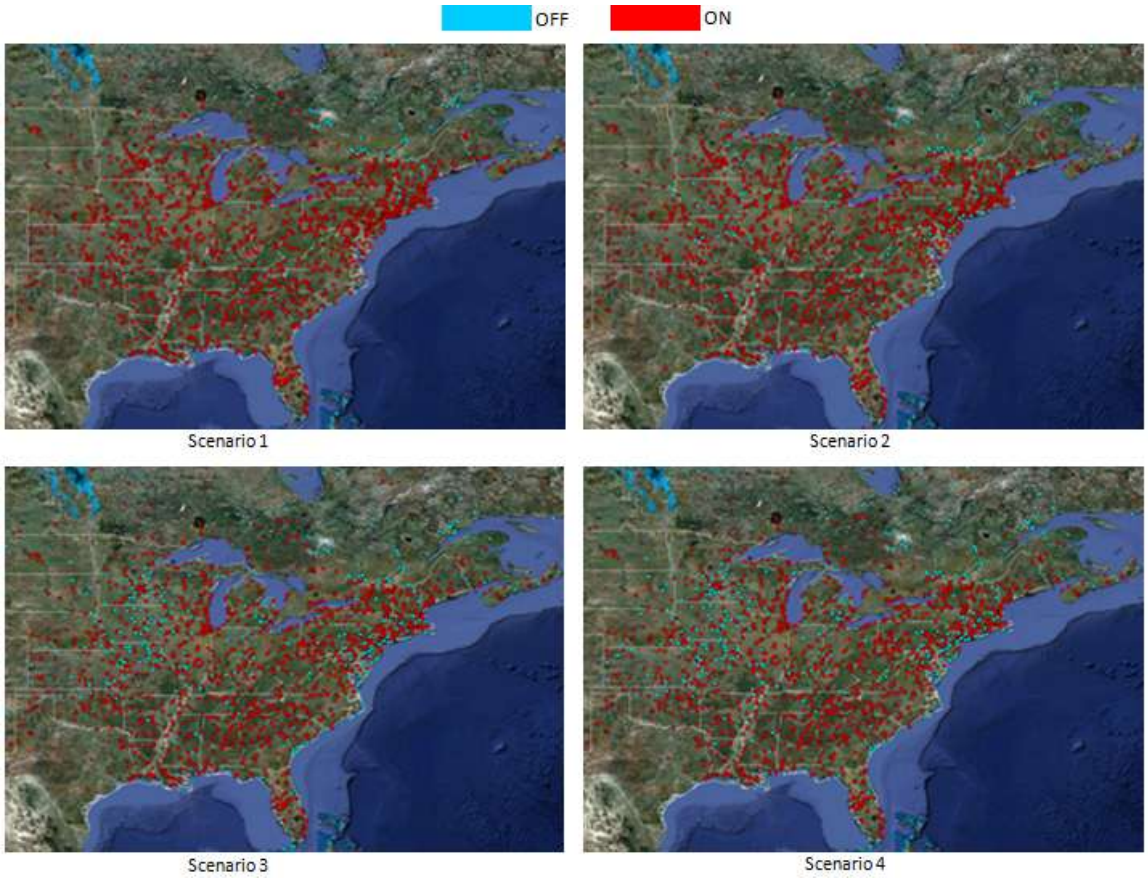

Figure 274: Unit Commitment Result in Wind Integration Scenarios

Sensitivity Analysis

There are several uncertain factors in the Eastern Interconnection, including fuel price, hourly wind speed, hourly loads, and carbon costs, which could have major impacts on the large-scale wind energy integration and the energy portfolio. It is perceived that the accurate forecast for some of these factors might not be readily available. In this section, we apply sensitivity analyses, based on the simulation results for Scenario 2 to study the impact of fluctuations in such factors on the wind energy integration and the annual energy portfolio in the Eastern Interconnection. The simulation results for Scenario 2 are considered as the base case in this Section.

Fuel Price Sensitivity

We apply the sensitivity analysis to the WINS simulation results for 2030, given for Scenario 2, in which the potential wind energy sites with a minimum CF of 40% and a total energy contribution of 17.67% (which is close to the expected 20% wind contribution in 2030) were considered. The following four scenarios would consider the impact of fuel price forecast.

- Scenario 5: Actual fuel price would be 20% lower than the forecast
- Scenario 6: Actual fuel price would be 10% lower than the forecast
- Scenario 7: Actual fuel price would be 10% higher than the forecast
- Scenario 8: Actual fuel price would be 20% higher than the forecast

As expected, the fuel price escalation has no impact on the wind energy dispatch since the wind energy has a zero price and will always be dispatched. The production cost in Figure 275 will increase as fuel price increases. The increase in fuel price at peak hours will have a more pronounced impact on the production cost as more expensive units are committed.

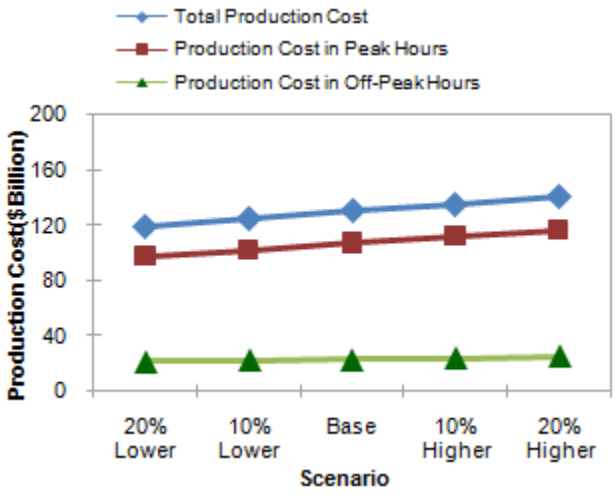

Figure 275: Production Cost in Fuel Cost Scenarios

Wind Energy Output Sensitivity Analysis

We apply the sensitivity analysis to the 2030 simulation results for Scenario 2. Four scenarios are studied as follows.

- Scenario 9: Actual wind energy production is 20% lower than the forecast
- Scenario 10: Actual wind energy production is 10% lower than the forecast
- Scenario 11: Actual wind energy production is 10% higher than the forecast
- Scenario 12: Actual wind energy production is 20% higher than the forecast

Figure 276 shows that the wind energy contribution to the total energy production is about 20% when the actual wind energy is 10% percent higher than that in the base case. Figure 277 shows that the total production cost decreases with the added wind energy production. Again, the production cost is more sensitive to the wind energy production at peak hours.

Figure 278 shows the energy portfolios in all four Scenarios. The energy produced by gas and coal units will decrease as the wind energy production is higher. Similar to that in Figure 276, the wind energy contribution is increased from 14% to 22%. The unit commitment and hourly generation dispatch show a similar pattern as that for Scenario 2.

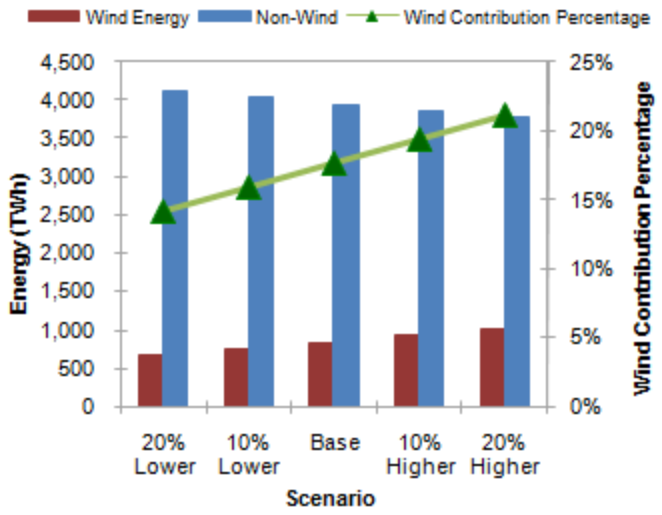

Figure 276: Wind/Non-Wind Energy for Wind Energy Scenarios

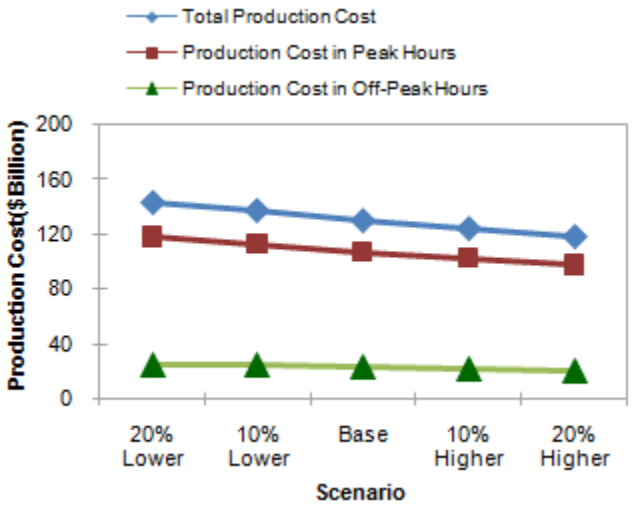

Figure 277: Production Cost for Wind Energy Scenarios

Load Sensitivity Analysis

In this section, we study the impact of load forecast errors on the WINS base case simulation results for Scenario 2. We do the sensitivity analysis based the load forecast in 2030. Four scenarios are studied as follows.

- Scenario 13: Actual load is 20% lower than the forecast
- Scenario 14: Actual load is 10% lower than the forecast
- Scenario 15: Actual load is 10% higher than the forecast
- Scenario 16: Actual load is 20% higher than the forecast

The wind energy contribution, depicted in Figure 279, shows a 19.62% contribution to the total energy production in Scenario 14 when the actual load is 10% lower than the forecast. The wind energy

contribution will decline as the actual load escalates because the additional load will be served by other types of units.

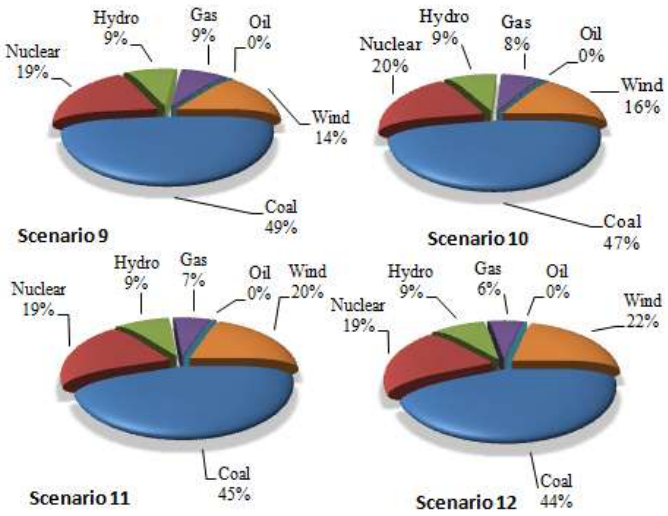

Figure 278: Energy Portfolio in Wind Energy Scenarios

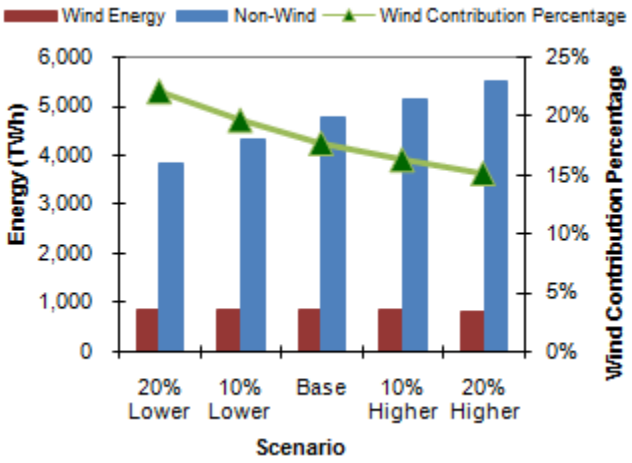

Figure 279: Wind/Non-Wind Energy in Load Scenarios

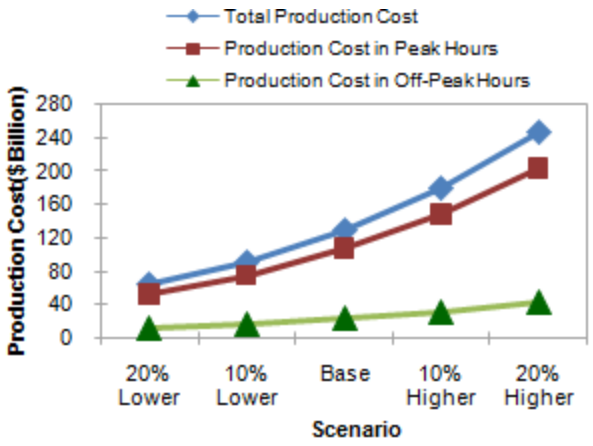

Figure 280: Production Cost in Load Scenarios

The production costs in Figure 280 show that the system load will have the largest impact on production costs. Here, the production cost increases a lot between Scenarios 13 and 16. The production cost at peak hours is more sensitive to load variations.

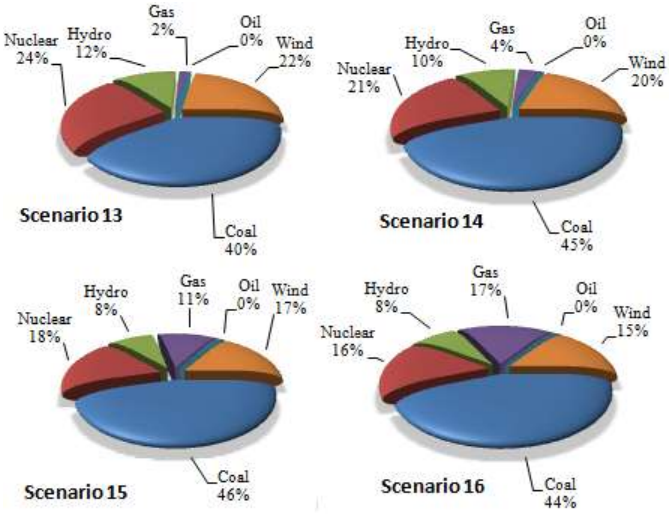

Figure 281: Energy Portfolio in Load Scenarios

Figure 281 shows the energy contribution in the given four Scenarios. The nuclear, hydro, and wind unit with their inexpensive fuel will supply much of the hourly load. However, their contributions will decline as the system load increases. Compared with the base case of Scenario 2, the energy contributions by gas and coal units, especially those supplied by gas units, will decrease as we reduce the system load. Furthermore, the contribution of gas units to the energy portfolio will increase from 7% in the base case (for Scenario 2) to 11% in Scenario 15 and 17% in Scenario 16 as we increase the system load, which means that the additional load is mainly supplied by gas units.

Figure 282 and Figure 283 show the hourly energy supplied by gas and coal units. In Figure 282, the energy supplied by gas units has increased as compared to that in Scenarios 13-14 especially at peak hours. In Scenario 13, gas units are mainly committed and dispatched at peak hours.

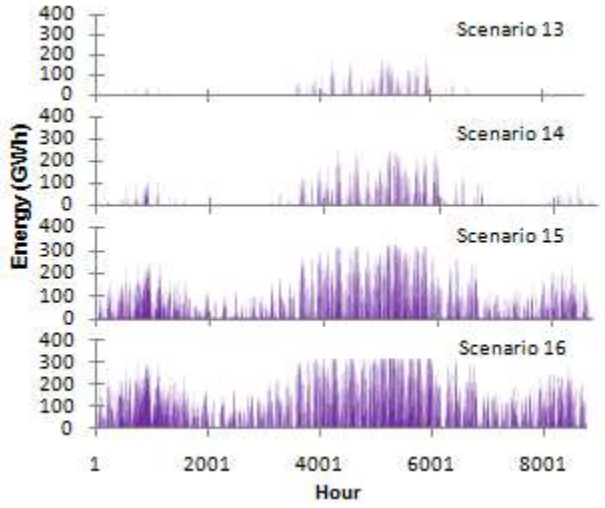

Figure 282: Hourly Energy Provided by Gas Units in Load Scenarios

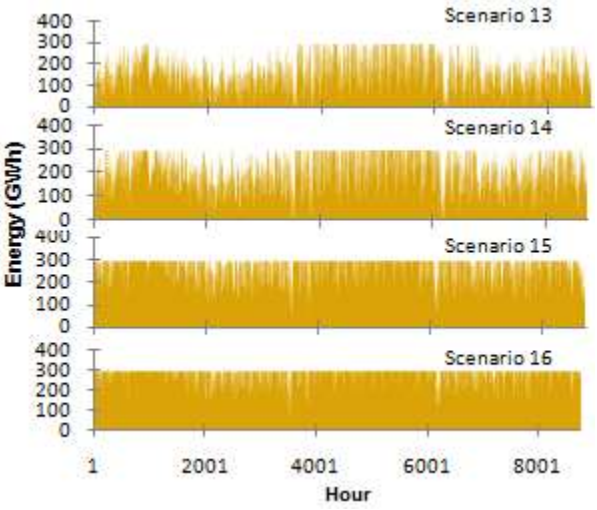

Figure 283: Hourly Energy Provided by Coal Units in Load Scenarios

Figure 284 shows that the load variation would have the largest impact on the commitment and the dispatch of generating units as compared to the fluctuation in fuel price or wind energy production. The commitment based on Scenarios 13-14 shows that many of the existing units will never be committed as hourly loads are lowered. On the other hand, almost all existing units will be committed when the hourly loads are higher than the forecast in Scenarios 15-16. The results indicate that the load management could introduce large incentives for improving the system operation bottlenecks and decreasing the operation costs.

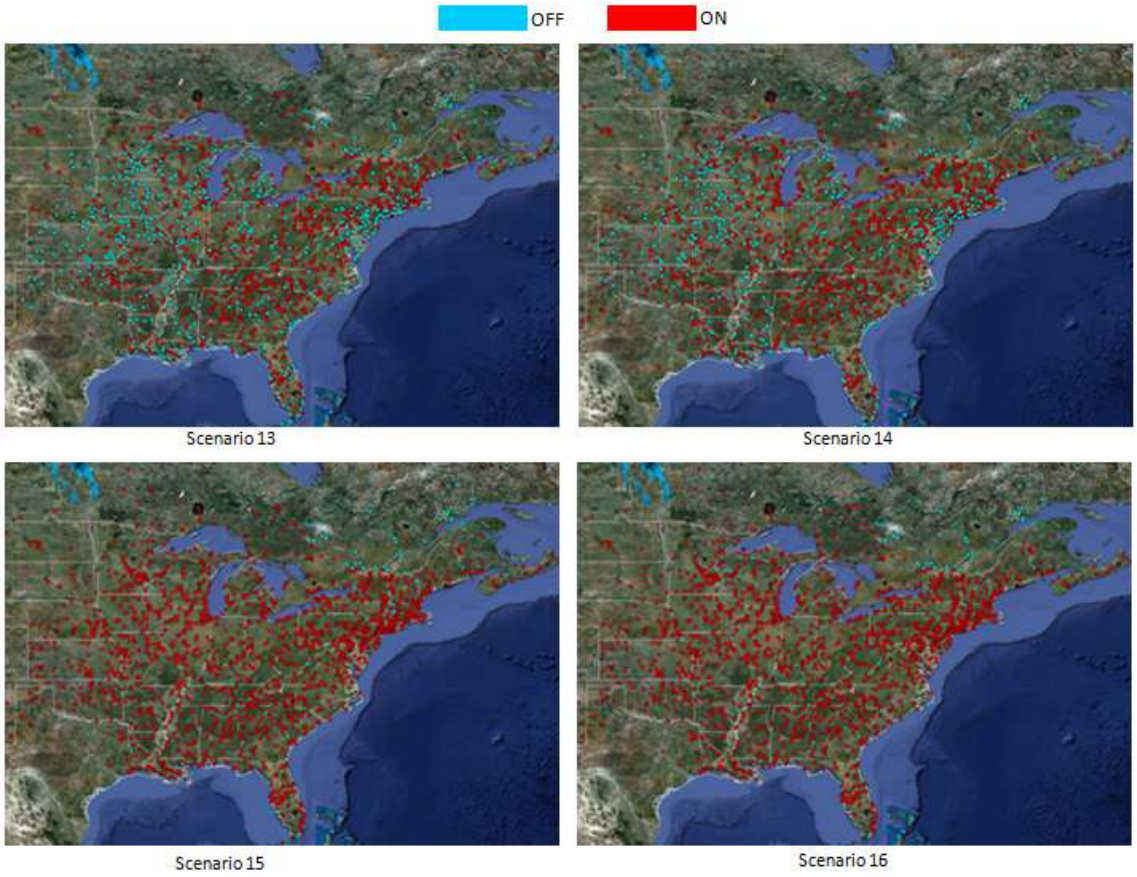

Figure 284: Unit Commitment Result in Load Scenarios

Carbon Cost Sensitivity Analysis

Higher carbon cost can be used as an incentive for promoting the development of clean, efficient or environmentally friendly power generation portfolios [**94**]. The carbon cost data given in [**94**] is considered here as the low carbon cost scenario. The high carbon cost scenario would consider a carbon cost that is doubled. In this section, we consider wind energy sites with CF ≥ 40% and CF ≥ 30% for analyzing the following four scenarios.

- Scenario 17: Low carbon cost with a minimum 40% CF for wind energy sites
- Scenario 18: High carbon cost with a minimum 40% CF wind energy sites
- Scenario 19: Low carbon cost with a minimum 30% CF wind energy sites
- Scenario 20: High carbon cost with a minimum 30% CF wind energy sites

The variations in carbon cost will not change the wind energy contribution to the energy portfolio. The production costs for all four Scenarios are $406.8 billion, $638 billion, $285.7 billion, and $448 billion. Therefore, the total production costs with higher carbon cost would be much higher. For example, the average production cost at peak/off-peak load hours are $89.5/MWh and $71.7/MWh in Scenario 17, and $140/MWh and $113.5/MWh in Scenario 18.

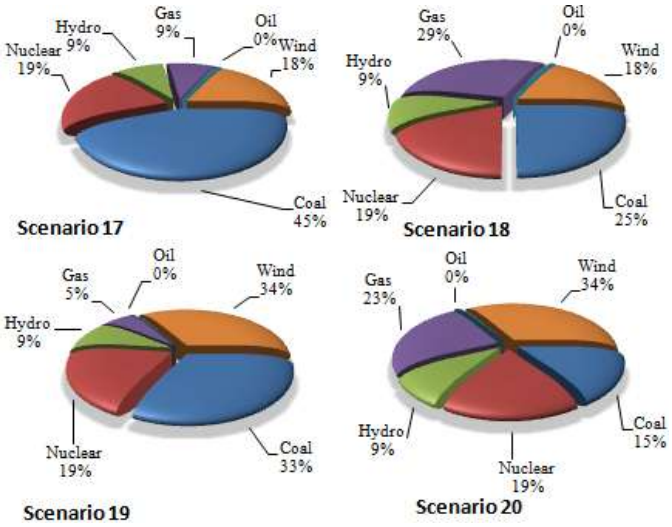

Figure 285: Hourly Energy Portfolio in Carbon Cost Scenarios

Figure 285 shows the energy portfolios in carbon cost Scenarios in which the high carbon cost will have a major impact on the energy supplied by gas and coal units. Since coal prices are lower than gas prices, the energy supplied by coal units does not change much in the low carbon cost Scenarios. The energy supplied by gas units increases from 9% in low carbon cost scenario (Scenario 17) to 29% in high carbon cost scenario (Scenario 18) while that of coal decreases from 45% to 25%. Similar results are obtained when we consider wind units with a minimum 30% CF.

Figure 286 and Figure 287 show the hourly energy supplied by gas and coal units, which is consistent with that of Figure 285. Here, gas units would be committed and dispatched in most hours with high carbon costs.

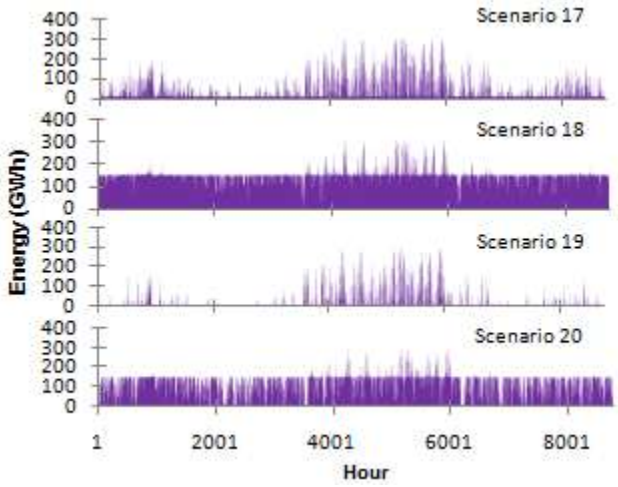

Figure 286: Hourly Energy Provided by Gas Units in Carbon Cost Scenarios

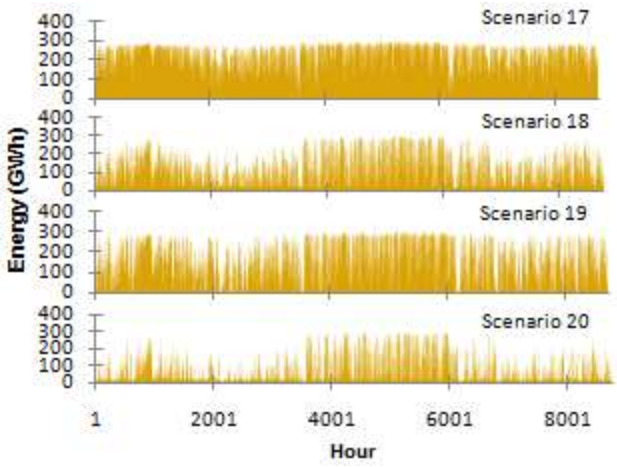

Figure 287: Hourly Energy Provided by Coal Units in Carbon Cost Scenarios

Load Management by Introducing Load Shedding

As presented for Load Sensitivity Analysis, the hourly load variations would have a major impact on the WINS simulation results. In this section, we consider load shedding as an option to manage the system operation more efficiently at peak hours. For instance, if the hourly load is higher than 80% of annual peak load, we would set it at 80%. Three scenarios are considered as follows.

- Scenario 21: No wind energy is considered when the load shedding is applied
- Scenario 22: Wind energy with a minimum CF of 40% is considered when the load shedding is applied
- Scenario 23: Wind energy with a minimum CF of 30% is considered when the load shedding is applied

Figure 288 shows the energy production portfolios for the three load shedding Scenarios.

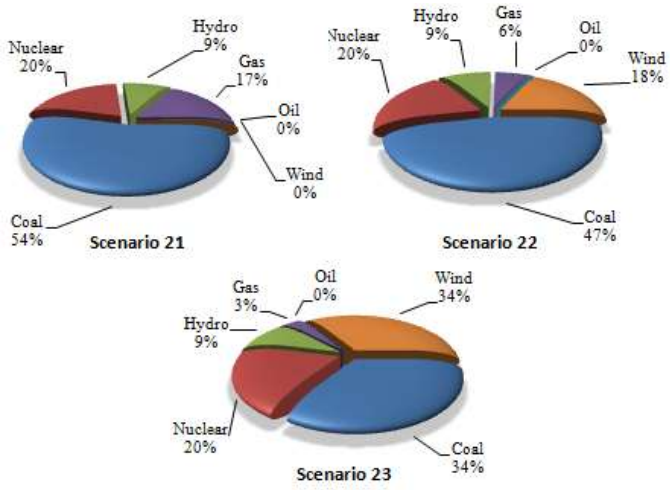

Figure 288: Energy Portfolio in Load Shedding Scenarios

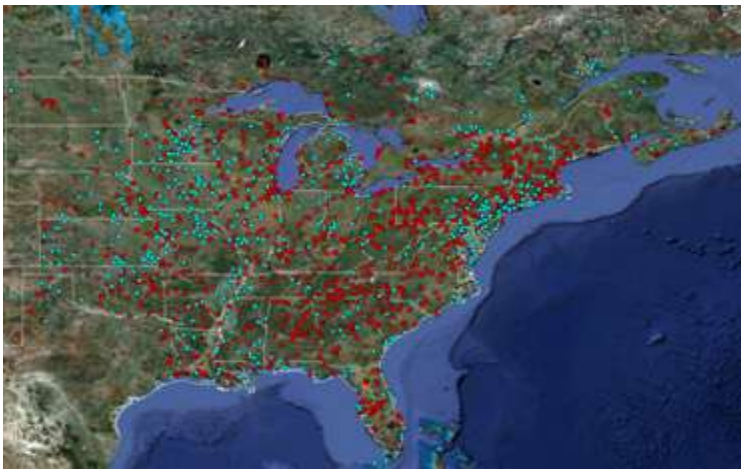

Figure 289: Unit Commitment Result in Scenario 21

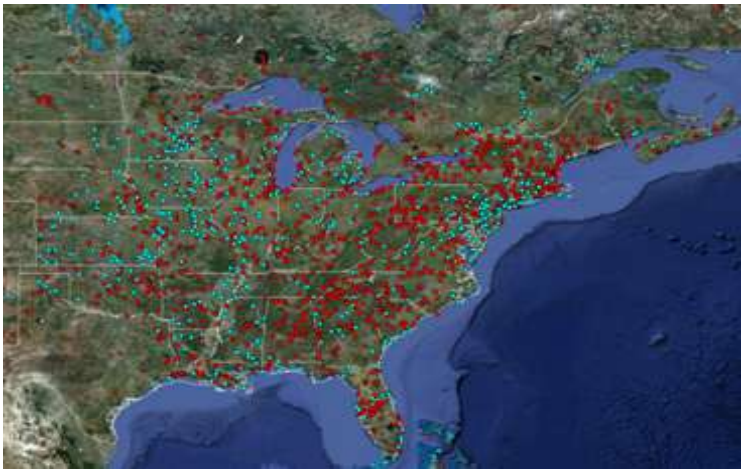

Figure 290: Unit Commitment Result in Scenario 22

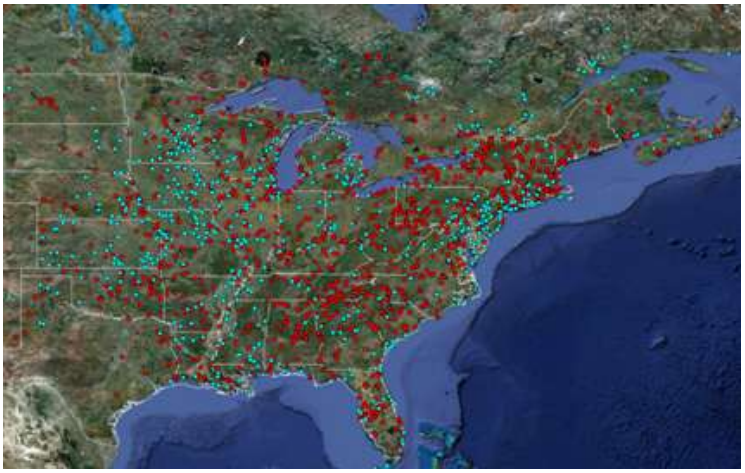

Figure 291: Unit Commitment Result in Scenario 23

Figure 289-Figure 291 show that the load shedding will alter the unit commitment as compared to those in Figure 274. Here, more gas units are turned off at peak hours when load shedding is applied. Here, there are about 1,200 gas units which would never be committed again when load shedding is considered as compared to those of the Scenarios 1, 2, and 3. These results are similar to those for load variation analysis given in Scenarios 13 and 14.

Figure 292 shows the hourly energy supplied by gas units in which the gas unit dispatch is lower because of the load shedding at peak hours. Load shedding has almost no impact on the hourly dispatch of coal units, as coal units are committed to serve the base load.

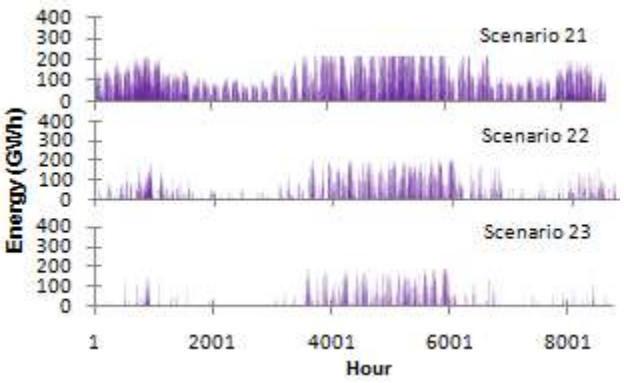

Figure 292: Hourly Energy Provided by Gas Units in Load Shedding Scenarios

A3. Conclusions

In this section, a comprehensive large-scale wind energy integration analysis is considered which is based on the 2030 load forecast in the Eastern Interconnection of the United States. Here, transmission constraints are not considered when studying the wind energy portfolios. The wind energy integration is studied based on the capacity factors of potential wind sites. Wind energy contributions to peak/off-peak annual production costs are studied based on the WINS simulation results. The sensitivity of fuel costs, wind energy production, hourly loads, carbon costs, and load management are analyzed in the wind energy integration Scenarios. The wind energy integration simulation results and their sensitivities are summarized in Table 20. Here, the contribution of wind energy to the 5 Scenarios is about 20% or higher.

Table 20: Summary of Simulation Results in All Scenarios

Scenario	Wind Capacity (GW)	Wind Generation (TWh)	Wind Contribution Percentage (%)	Production Cost ($ Billion)	Average Production Cost ($/MWh)
1	0	0	0	217.5	45.64
2	230.5	845.2	17.67	130.4	27.25
3	481.5	1,596	**33.37**	86.8	18.14
4	580	1,816	**38**	77	16.10
5	230.5	845.2	17.67	118.9	24.87
6	230.5	845.2	17.67	124.7	26.06
7	230.5	845.2	17.67	135.7	28.36
8	230.5	845.2	17.67	141.7	29.63
9	230.5	676.1	14.14	143.7	30.03
10	230.5	760.6	15.9	136.8	28.59
11	230.5	929.7	19.44	130.4	25.99
12	230.5	1014	**21.20**	124.3	24.80
13	230.5	845.2	**22.07**	64	16.73
14	230.5	845.2	19.62	91.6	21.27
15	230.5	845.2	16.29	178.5	34.65
16	230.5	845.2	15.12	245.9	44.54
17	230.5	845.2	17.67	406.8	84.97
18	230.5	845.2	17.67	638	133.3
19	481.5	1,596	17.67	285.7	69.68
20	481.5	1,596	17.67	448	93.59
21	0	0	0	208.7	44
22	230.5	845.2	17.81	123	25.9
23	481.5	1,596	**33.53**	80.6	16.97

B. Large-scale Analysis of 2018 Wind Energy Integration in the U.S. Eastern Interconnection

This section presents the hourly simulation results for the year 2018 with the large-scale wind energy integration in the Eastern Interconnection of the United States. A simulator referred to as WINS (Wind INtegration Simulator) is developed for this annual study. The wind energy integrations in the year 2018 are simulated using the hourly security-constrained unit commitment (SCUC) in WINS. The generation portfolio for supplying the hourly load in 2018 is developed with/without transmission network constraints. The sensitivities to the 2018 wind energy integration are carried out for fuel price, wind energy availability, load growth, carbon cost, and hourly load management strategies. The hourly production cost, generation credit, load payment, levelized congestion cost, LMPs, and wind energy contribution, are calculated and analyzed.

The U.S. Eastern Interconnection is the largest interconnection in the world with more than 5,000 generating units and about 45,000 transmission lines. The National Renewable Energy Laboratory (NREL) performed a study in 2008 to examine the impact of 20-30% wind energy integration in the Eastern Interconnection [**82**]. The western wind and solar integration study in 2007 examined the operational impact of 35% renewable energy penetration [**83**]. The impact of wind energy integration on power system operations is analyzed further in [**84**], [**85**]. An hourly unit commitment and economic dispatch model for analyzing large-scale power system operations was represented in [**86**]. A follow-up optimization-based security-constrained unit commitment (SCUC) model [**87**], [**89**] was presented in [**90**] which took into account the intermittency of wind power generation and transmission network constraints. A comprehensive adequacy analysis of energy production portfolio for 2030 was presented in [**95**]. The adequacy study in [**95**] did not consider transmission constraints as locations for the 2030 wind generation unit installations were not provided.

In this section, we focus on studying the 2018 large-scale wind energy integration in the Eastern Interconnection. The impact of large-scale wind energy integration on existing generation resources, production costs, LMPs, generation credits, load payments, transmission utilization, and wind energy deliverability are studied. The sensitivity of wind integration to fuel price, wind energy availability, load growth, carbon cost, and load management strategies is analyzed in this paper.

The rest of the section is organized as follows. Section B1 describes the proposed methodology, assumption and relevant evaluation metrics. Section B2 presents the wind energy integration study results for the Eastern Interconnections. The conclusions drawn from the study are provided in Section B3.

B1. Methodology for Wind Energy Integration

POMS (Power Market Simulator) is an efficient decision tool for the day-ahead scheduling of large-scale power systems which has been utilized in transmission congestion analysis for the Eastern Interconnection in [**91**]. WINS (Wind Integration Simulator) is the expansion of POMS in order to support the collaborative planning and implementation of the large-scale wind energy integration in the United States [**95**]. WINS applies SCUC to simulate the large-scale wind energy integration in the hourly power system operation. The application of WINS in this paper will analyze the impact of 2018 large-scale wind energy integration in the Eastern Interconnection.

Input Data

The generation and transmission data used in this study are based on the 2018 planning data in MTEP 08 (MISO Transmission Expansion Planning) [**93**]. We consider a 1.28% annual load growth which is based on the MTEP 08 assumptions. The hourly load distribution shown in Figure 293 is based on the MISO's hourly load profile in 2007.

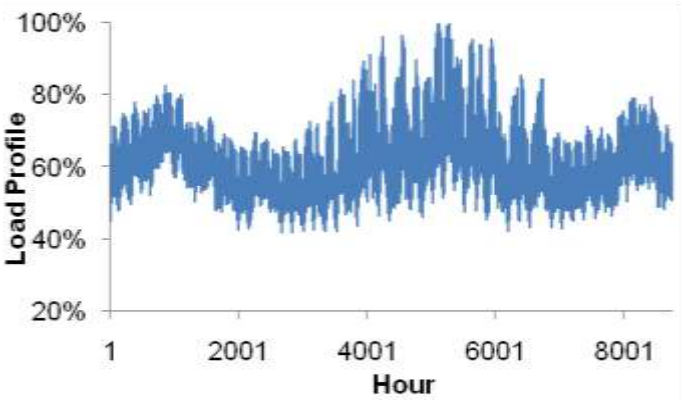

Figure 293: Annual Hourly Load Profile

In Figure 293, peak loads appear in July and August. The power flow solution is used for calculating the hourly bus load distribution. The wind unit data for the 2018 WINS simulation are based on MTEP assumptions for 2018 and the hourly wind profiles are provided by the land-based time series wind simulation results [**82**]. The hourly wind profiles based on geographical locations are considered for wind generation units. Fuel prices are assumed to increase at an annual rate of 4% for oil and gas, 2% for coal, and 3% for nuclear fuel based on the fuel price given in 2008 [**93**].

Evaluation Metrics

The evaluation criteria and metrics used in this study are defined as follows.

Wind Energy Availability

The available wind energy is treated as dispatchable in WINS simulations. Here,

$$P_A = \sum_{t=1}^{T} \sum_{i=1}^{NW} p_i^{\max} w_{it} \quad \textbf{(86)}$$

where *T* represents the number of hours in a period (e.g., one year), *NW* represents the number of wind generators/farms, $p_i^{\max}$ is the nominal capacity of wind generator/farm *i*, w_{it} represents the wind power generation profile for generator/ farm *i* at time *t*, P_A represents the available wind energy for dispatch that is subject to transmission constraints.

Percentage of Wind Energy Contribution

This metric will evaluate the percentage of the wind energy contribution to the total energy for supplying the load in the power system.

$$= \frac{Wind\ Ener\quad gy}{Total\ Ene\quad rgy} * 100\ \% \quad \textbf{(87)}$$

Production Cost

$$\text{Production Cost} = \sum_{t=1}^{T} \sum_{i=1}^{NG} F_i(P_{i,t}) \quad \textbf{(88)}$$

where *NG* is the number of generators, $P_{i,t}$ is the dispatch of generator *i* at period *t*, $F_i(.)$ is the production cost function of generator *i*.

Generation Credit

$$\text{Generation Credit} = \sum_{t=1}^{T} \sum_{i=1}^{NG} LMP_{i,t} * P_{i,t} \quad \textbf{(89)}$$

where $LMP_{i,t}$ is the LMP at generator bus *i* at period *t*.

Load Payment

$$\text{Load Payment} = \sum_{t=1}^{T} \sum_{j=1}^{ND} LMP_{j,t} * D_{j,t} \quad \textbf{(90)}$$

where *ND* is the number of load buses; $LMP_{j,t}$ represents the LMP of load bus *j* at period *t*; $D_{j,t}$ represents the load at bus *j* at period *t*.

Transmission Utilization

$$= \frac{\sum_{t=1}^{T} |flow_{i,t}|}{T * Cap_i} * 100\ \% \quad \textbf{(91)}$$

where $flow_{i,t}$ is the power flow on line *i* at period *t*; Cap_i is the capacity of line *i*. The transmission utilization could also be calculated based on voltage level of transmission line.

Levelized Congestion Cost

This metric represents the levelized congestion cost.

$$= \frac{(\text{Load Payment} - \text{Generation Credit})}{\text{Load Payment}} * 100\ \% \quad \textbf{(92)}$$

Transmitted Energy

$$= \sum_{i=1}^{NL} \sum_{t=1}^{T} |flow_{i,t}| \quad \textbf{(93)}$$

where *NL* represents the number of transmission lines. The transmitted energy is calculated for transmission lines grouped by voltage level (i.e., 230kV, 345kV, 500kV, and 765kV).

Levelized Energy Flow

$$= \frac{\sum_{i=1}^{NL} \sum_{t=1}^{T} | \, flow_{i,t} \, |}{T * NL} \quad (94)$$

It is the averaged value of transmitted energy at a given voltage level.

B2. Numerical Results

In this section, we utilize WINS to simulate the 2018 wind integration in the Eastern Interconnection of the United States based on the methodology presented in Section B1.

Wind Integration Reference Cases

We simulate the hourly power system operation using WINS. Four scenarios are studied as follows.

- Scenario 1: All wind unit generation and transmission constraints are excluded in 2018
- Scenario 2: All wind unit generation is excluded in 2018 while transmission constraints are considered
- Scenario 3: The 2018 wind unit integration is considered while all transmission constraints are excluded
- Scenario 4: The 2018 wind unit integration and transmission constraints are considered

These four scenarios are discussed here.

Scenario 1: All wind unit generation and transmission constraints are excluded in 2018. This is the reference case in which the hourly loads will be served by fossil fuel and hydro units without considering any wind energy or transmission constraint in 2018. Figure 294 shows the hourly production cost which is $92.25 billion per year with an average production cost of $22.4/MWh. The production cost will not change linearly with hourly load fluctuations. Hydro units will have zero costs and be scheduled first to serve hourly loads or reserves; then cheaper units such as nuclear, coal, and large oil will be committed, and finally expensive units such as gas and oil will be committed to supply hourly loads. A higher production cost will occur at annual peak hours of 5,000–5,500 (i.e., July and August of 2018). The total production cost at peak hours (6 AM–10 PM) is $74.04 billion and that at off-peak hours (11 PM–5 AM) is $18.21 billion. The average production costs at peak/off-peak hours are $24.2/MWh and $17.3/MWh. The average production cost at peak load hours is higher when expensive generators are committed and dispatched.

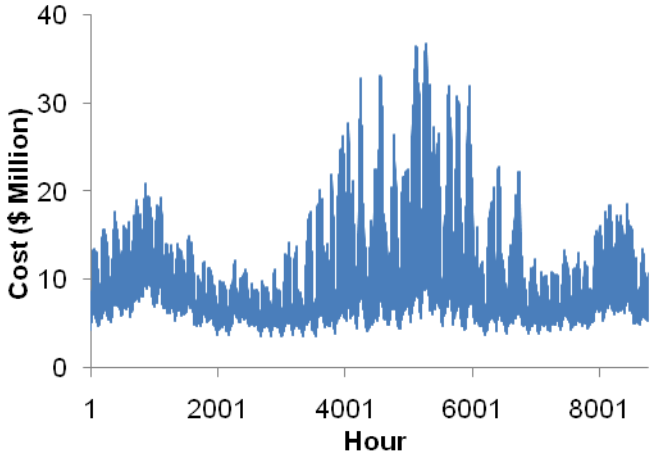

Figure 294: The 2018 Hourly Production Cost in Scenario 1

Scenario 2: All wind unit generation is excluded in 2018 while transmission constraints are considered. Figure 295 shows the hourly production cost. Compared to Figure 294, the production cost is higher when transmission constraints are taken into account. The annual production cost is $106.1 billion with an average production cost of $25.93/MWh. The production costs at peak and off-peak hours are $84.1 billion and $24.04 billion respectively. The average production costs at peak and off-peak hours are $27.49/MWh and $20.98/MWh respectively. Compared with Scenario 1, the production cost will increase by 15.06% when considering transmission constraints. The annual average LMPs based on the 2018 WINS simulation are shown in Figure 296. The annual average LMP in this scenario is $61.77/MWh. Without any wind energy integration, LMPs are lower in the northwest and a small area in New England, and are higher in the New York region.

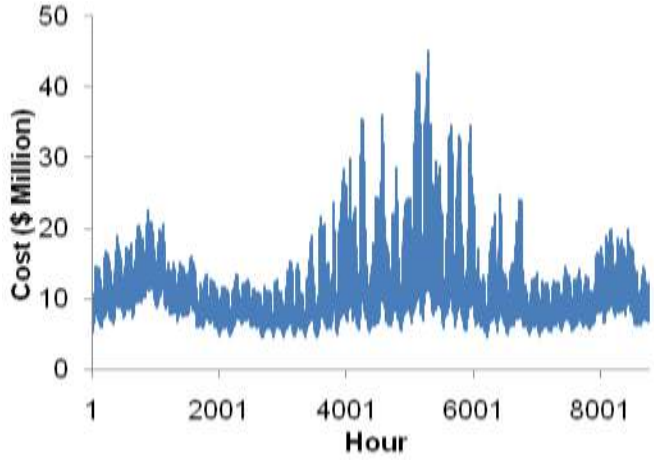

Figure 295: The 2018 Hourly Production Cost in Scenario 2

Figure 297 shows the monthly generation credit, load payment and production cost in Scenario 2. All three curves show a pattern similar to that of load profile in Figure 293. The incremental difference between the two curves shows the congestion cost. The annual generation credit, load payment and levelized congestion cost in 2018 are $254.2 billion, $270.7 billion, and 6.1% respectively.

Scenario 3: The 2018 wind unit integration is considered while all transmission constraints are excluded. Figure 298 shows the hourly production cost in Scenario 3. The annual production cost is $77.95 billion with an average production cost of $18.96/MWh. The production cost at peak and off-peak hours are $62.67 and $15.27 billion, respectively. Figure 298, the average production costs at peak and off-peak hours are $20.48/MWh and $14.54/MWh. Compared to Scenario 1, the production cost is 15.5% lower after taking into account the wind energy integration because wind energy is treated as zero fuel cost generation resource. Figure 299 shows the monthly wind energy in 2018 without considering transmission constraints. The wind energy resources are mostly available in spring and winter; however, peak loads occur in summer. January has the highest level of available wind energy of 27.8 TWh, which amounts to 7.9%, of the total energy. The wind energy is scarce in August when the highest level of annual load occurs. The available wind energy in August and the wind energy contribution (dispatch) to the total energy production portfolio are 16.8 TWh and 4.1% respectively. The annual wind energy contribution to the energy production portfolio is 6.5%.

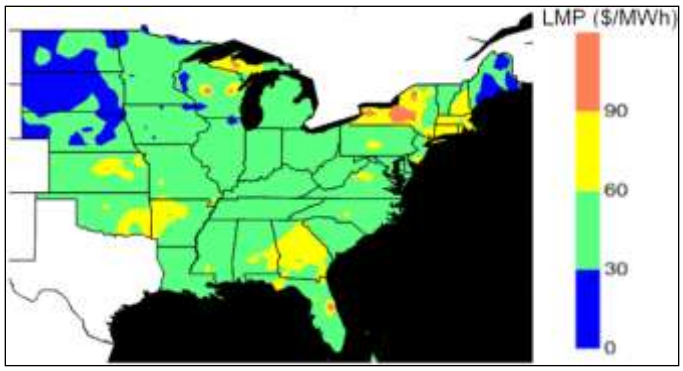

Figure 296: The 2018 Annual Average LMPs in Scenario 2

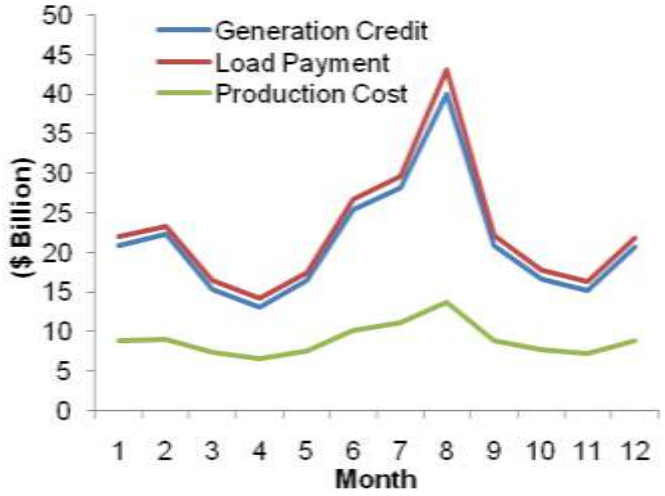

Figure 297: Monthly Generation Credit, Load Payment and Production Cost in Scenario 2

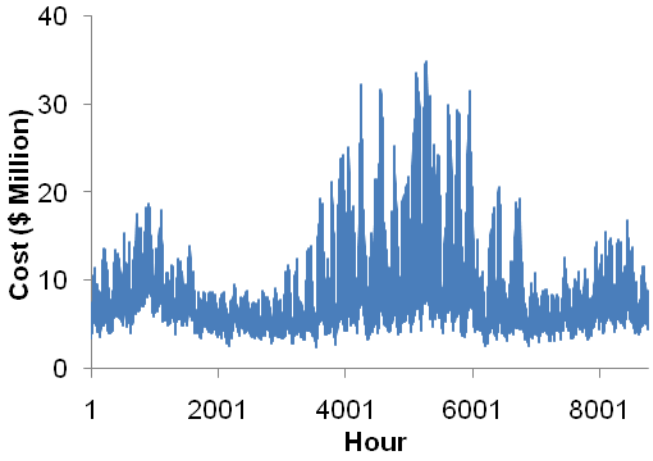

Figure 298: The 2018 Hourly Production Cost in Scenario 3

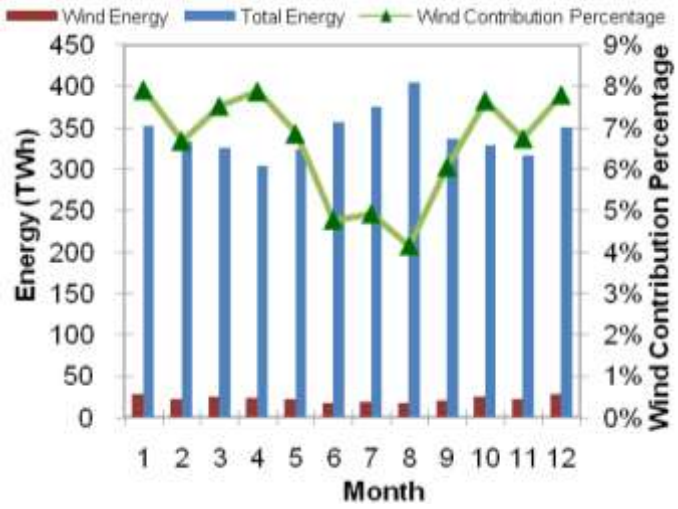

Figure 299: Monthly Available Wind Energy and its Contribution in Scenario 3

Scenario 4: The 2018 wind unit integration and transmission constraints are considered. Figure 300 shows the hourly production cost in which the annual production cost amounts to $99.39 billion with an average production cost of $24.18/MWh. The production costs at peak and off-peak hours are $78.76 billion and $20.63 billion respectively. The average production costs at peak and off- peak hours are $25.74/MWh and $19.63/MWh. Compared to Scenario 3, the production cost is 27.5% higher with the consideration of transmission constraints because transmission constraints would limit the flow from cheap and largely concentrated generation resources to load centers. Compared with the results in Scenario 2, the production cost is 6.8% lower when the wind energy is included. The production cost shows a higher sensitivity to the additional transmission constraints than to higher levels of wind energy integration.

Figure 301 shows the monthly wind energy in 2018 considering transmission constraints. December has the highest level of dispatched wind energy of 20.4 TWh, which amounts to 5.8% of the total energy supply. August represents the month with the least dispatched wind energy again (i.e., 13TWh and

3.2%). The annual wind energy contribution is 4.8%. Hence, about 26.1% of the available wind energy is curtailed due to transmission constraints.

Figure 302 represents the monthly available and dispatched wind energy in Scenario 4. Transmission constraints would limit the wind energy delivery to 73.88%. Here, 69.8TWh of wind energy is curtailed due to transmission congestion. The highest wind energy curtailment which is 7.46TWh occurs in January 2018. Figure 303 shows the monthly generation credit, load payment and production cost in Scenario 4. The annual generation credit, load payment and levelized congestion cost are $232.9 billion, $253.1 billion, and 7.97% respectively. All three indicators in Figure 303 exhibit a pattern similar to that in Figure 297.

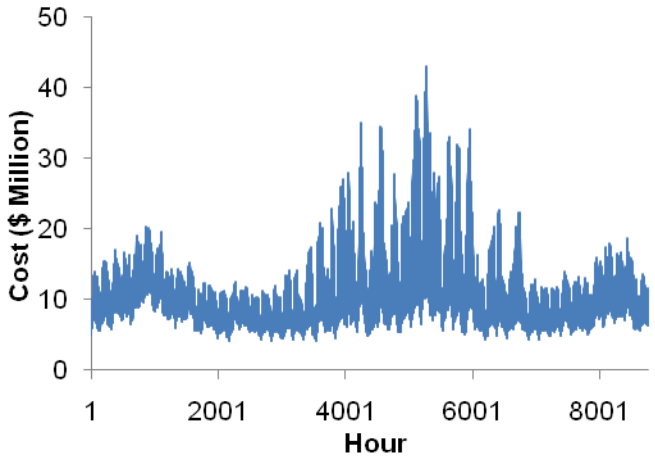

Figure 300: The 2018 Hourly Production Cost in Scenario 4

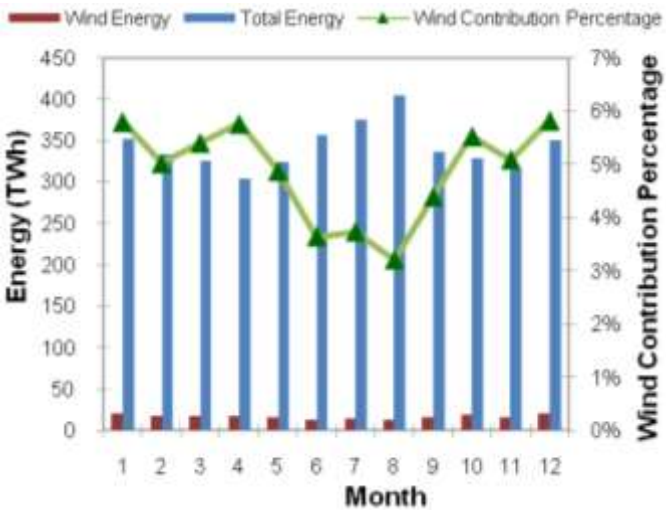

Figure 301: Monthly Wind Energy and its Contribution in Scenario 4

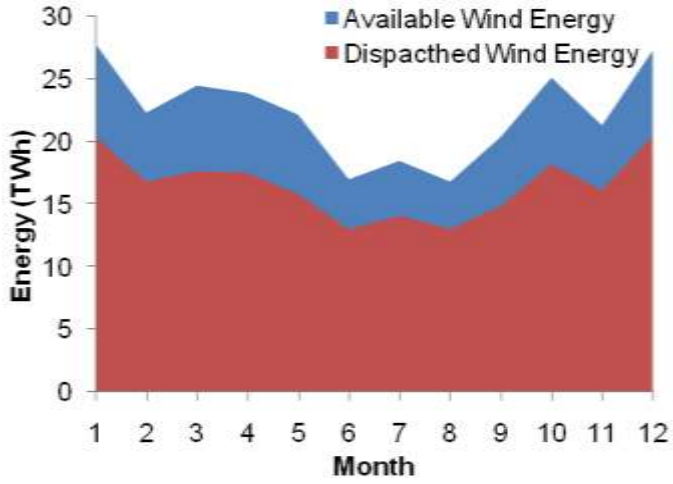

Figure 302: The 2018 Monthly Available and Dispatched Wind Energy

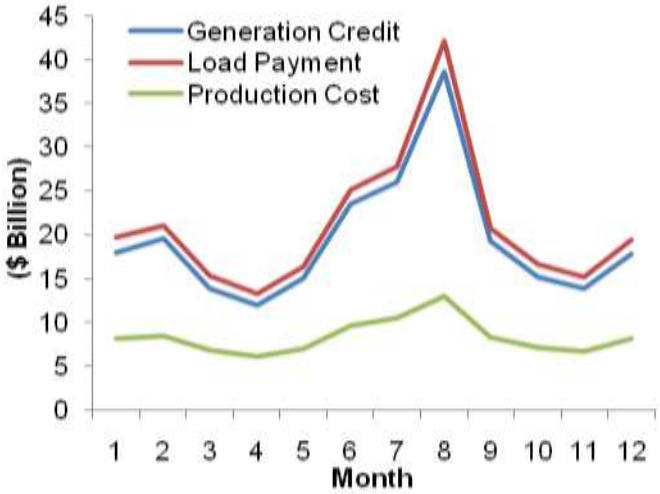

Figure 303: Monthly Generation Credit, Load Payment and Production Cost in Scenario 4

Compared to Scenario 2, generation credit and load payment quantities are reduced in this scenario when the wind energy is integrated; however, the levelized congestion cost increases from 6.1% to 7.97% which indicates that the wind integration will cause more congestion if there is no transmission expansion planning considered at the same time.

The annual average LMPs in Scenario 4 are shown in Figure 304. With the wind energy integration, LMPs in the northwest region drop which is due to rich wind energy resources in that region. The LMPs in New York, New England, and Florida are higher which demonstrate transmission congestion in those regions. The annual average LMP is $54.49/MWh which is lower than that in Scenario 2. Figure 304 shows a higher regional price increment than that in Figure 296 which is consistent with the higher levelized congestion cost in Scenario 4.

Figure 305 shows the energy production portfolio in all four Scenarios. Here, the gas unit production would increase as transmission constraints are considered. The energy supplied by coal units is

decreased, when transmission constraints are taken into account, which is replaced by the energy supplied by gas or wind generation units. Figure 306-Figure 308 show the energy supplied by gas, coal and wind units in four scenarios. With transmission constraints in place, more gas units are commitment and dispatched, less coal units are dispatched, and wind energy is partly curtailed. These figures show that wind energy will partly replace the fossil energy production especially at off-peak hours when the wind energy is mostly available in the Eastern Interconnection.

Figure 309 depicts the transmission utilization (see (6)) in 2018 at various voltage levels with and without the wind energy integration. The 500kV transmission system shows the highest utilization level at both scenarios. The transmission utilization at 765kV level is lower than those at other voltage levels (i.e., 230kV, 345kV and 500kV). In Figure 309, the 765 kV transmission utilization with the wind energy integration is lower than that of other voltages which indicates that the wind energy is transmitted mostly at 500kV, 345kV, and 230kV transmission levels.

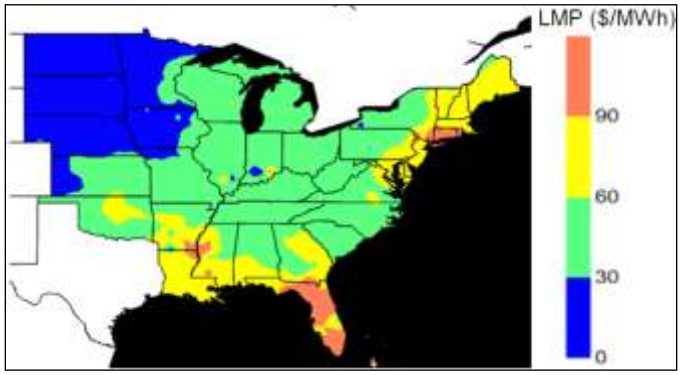

Figure 304: Annual Average LMPs in Scenario 4

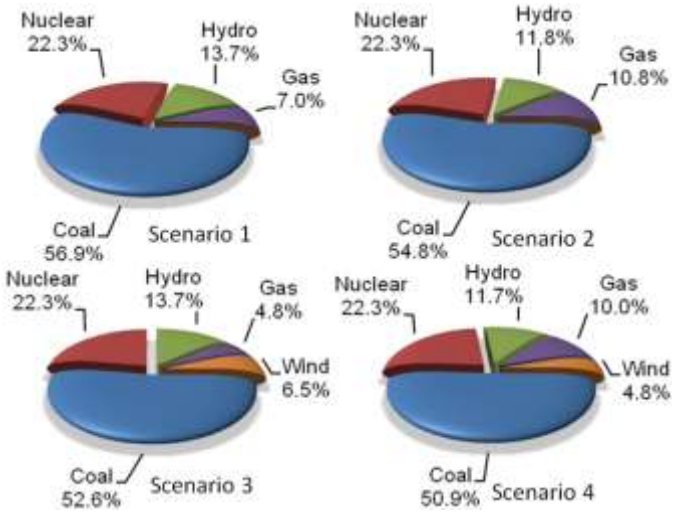

Figure 305: Energy Production Portfolios in Scenarios 1-4

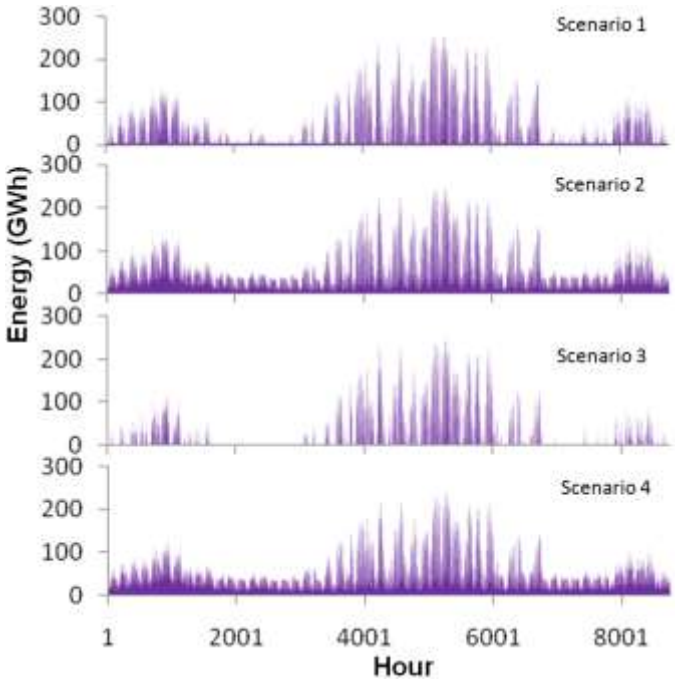

Figure 306: Hourly Energy Provided by Gas Units in Scenarios 1-4

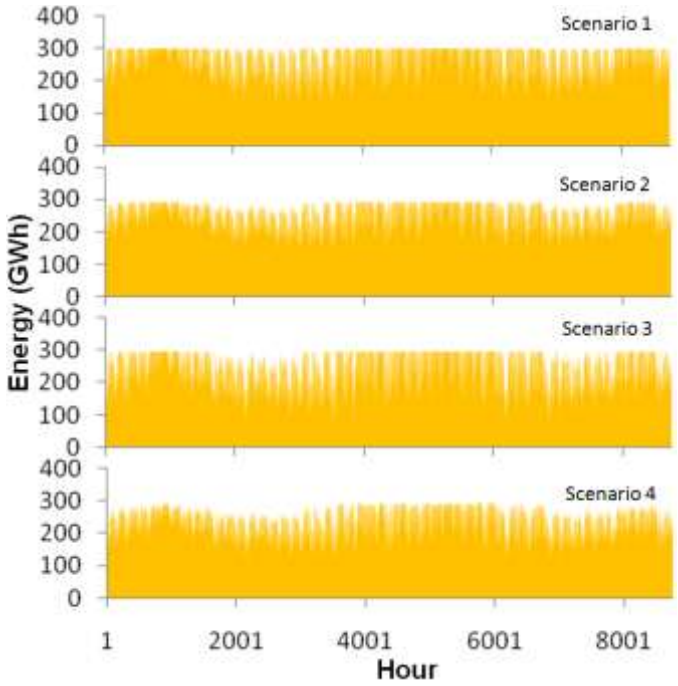

Figure 307: Hourly Energy Provided by Coal Units in Scenarios 1-4

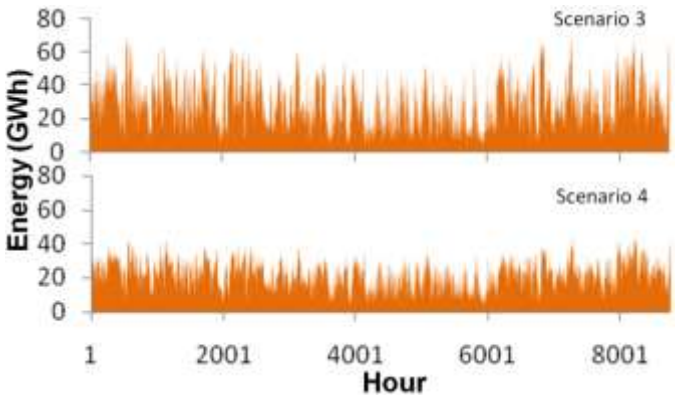

Figure 308: Hourly Wind Energy in Scenarios 2 and 4

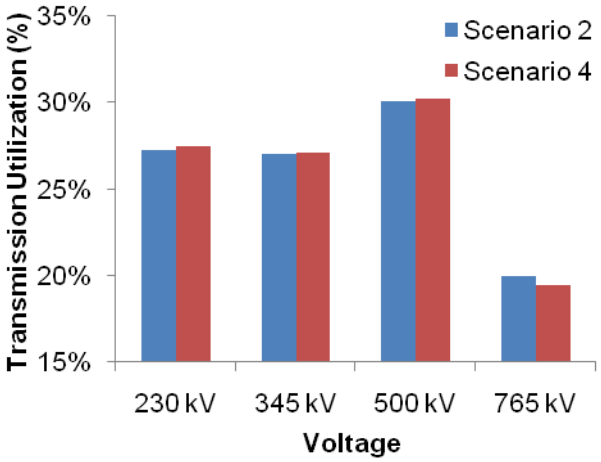

Figure 309: Transmission Utilization with/without Wind Energy Integration

Figure 310 shows the sum of hourly transmitted energy in 2018. The 230kV transmission lines will transmit the most energy in the Eastern Interconnection. As shown in Figure 310, the 765kV transmission lines will only transmit a small portion of the total energy because there are fewer of such lines in the Eastern Interconnection. Figure 311 shows the levelized energy flow over a year in 2018. The largest levelized energy flow would be on 765kV transmission lines which is due to the higher capacity offered by such lines. In Figure 311, the levelized energy flow at the 500kV level is close to that in 765kV and higher than that in lower voltage levels (230kV, 345kV).

Figure 312 shows the annual commitment of existing power plants in 2018 in which red dots represent power plants in which at least one unit is committed for a minimum of one hour per year. Also, blue dots show the plants which will be off throughout the year as more wind energy is integrated in the Eastern Interconnection.

Sensitivity Analysis

There are several uncertain parameters in large-scale power systems including fuel price, wind speed, hourly load, and carbon tax, which could have major impacts on the large-scale wind energy integration. These parameters may not be accurately forecasted for 2018. So, we apply sensitivity analyses to the

WINS simulation results given for Scenario 4 to study the impact of variations in such parameters on the wind energy integration. The WINS simulation results for Scenario 4 are treated as the base case.

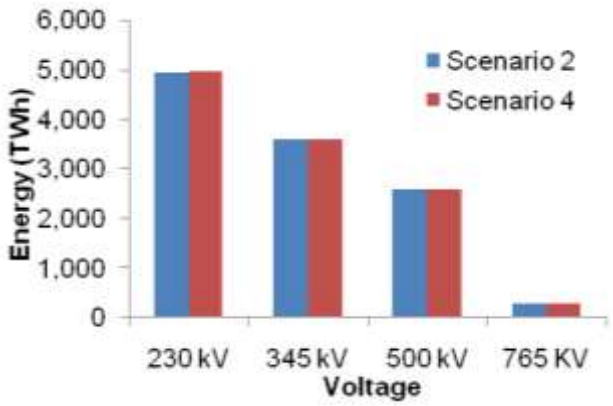

Figure 310: Transmitted Energy in 2018 with/without Wind Integration

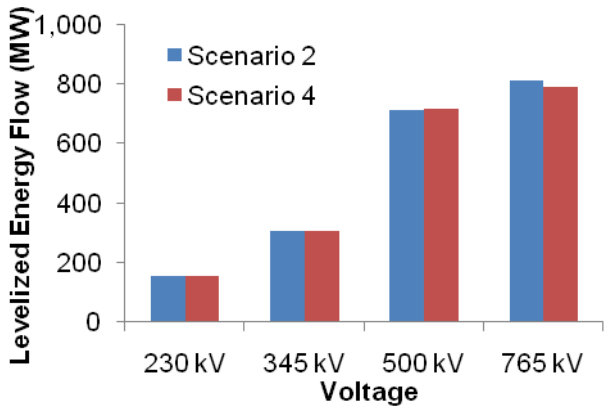

Figure 311: Levelized Energy Flow in 2018 with/without Wind Integration

Fuel Price Sensitivity

We apply the sensitivity analysis based on the WINS simulation results for Scenario 4. The wind energy integration was considered in transmission-constrained Eastern Interconnection. Generally, oil and gas prices are more volatile, while nuclear and coal prices are more settled. The following four scenarios are considered for analyzing the sensitivity of the WINS results to the fuel price volatility:

- Scenario 5: Oil and gas prices are 20% lower than the forecast
- Scenario 6: Oil and gas prices are 10% lower than the forecast
- Scenario 7: Oil and gas prices are 10% higher than the forecast
- Scenario 8: Oil and gas prices are 20% higher than the forecast

Figure 313 shows the production cost, generation credit, load payments and annual average LMP of four fuel price scenarios which are compared with the base case scenario results. The difference between load payments and generation credits represents the congestion cost in the Eastern Interconnection.

The production cost, generation credit, load payments, and LMPs in all scenarios will increase as fuel price goes up.

Figure 314 shows the levelized congestion cost and wind energy contribution in the four scenarios. In Figure 314, higher oil and gas prices would cause more transmission congestion which would limit the flow from cheaper and concentrated generation resources to load centers. In this case, the wind energy contribution will be slightly lower when fuel prices are higher. The reason is that more of large coal units will be used in such cases which could cause additional congestion for utilizing wind energy units. The fuel price volatility would have no impact on wind energy dispatch if transmission constraints are not taken into account [**95**].

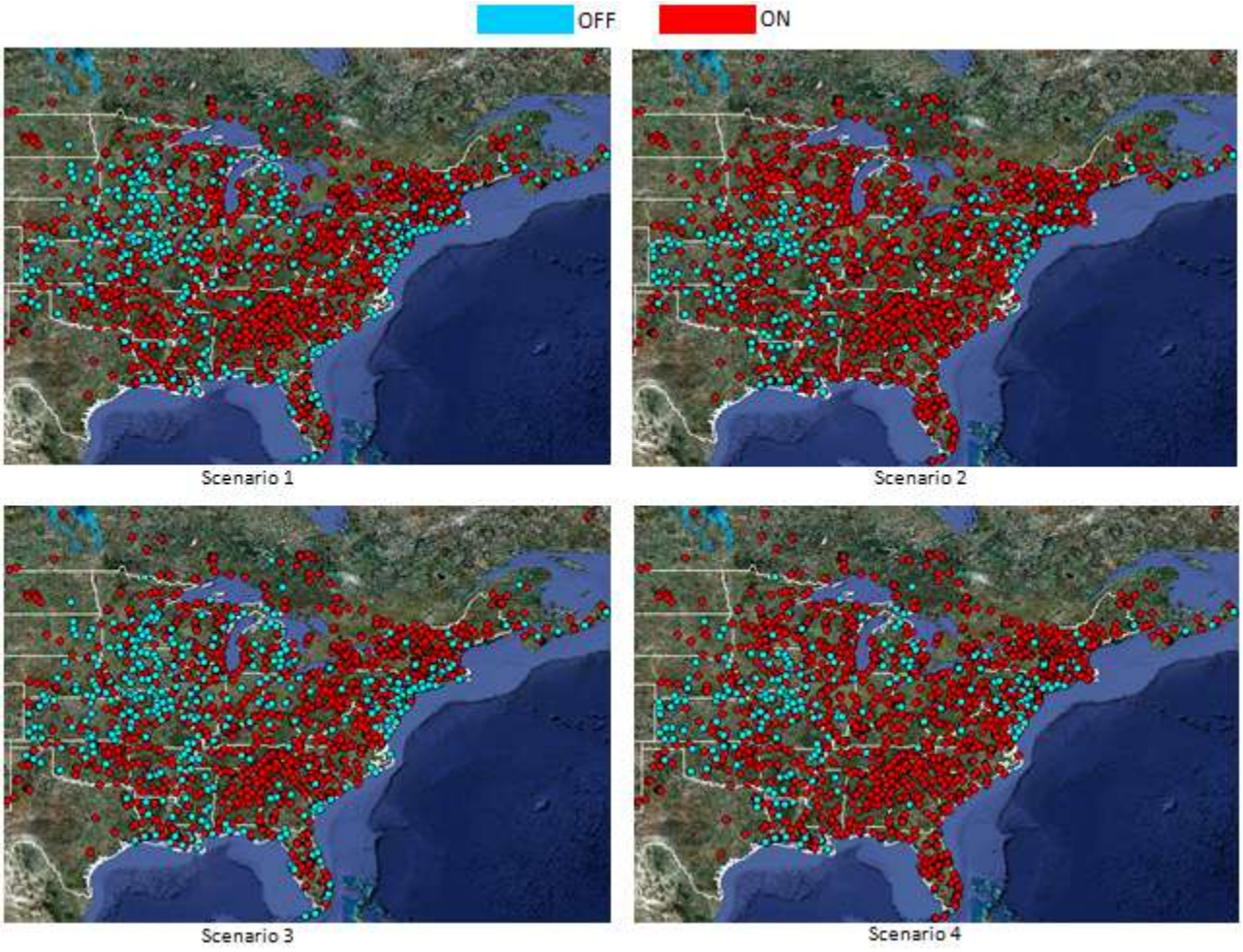

Figure 312: Annual Unit Commitment in Scenarios 1-4

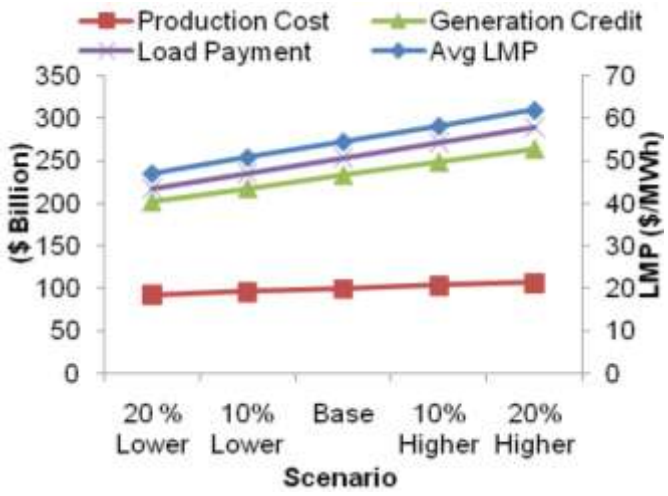

Figure 313: Economic Metrics in Fuel Price Scenarios

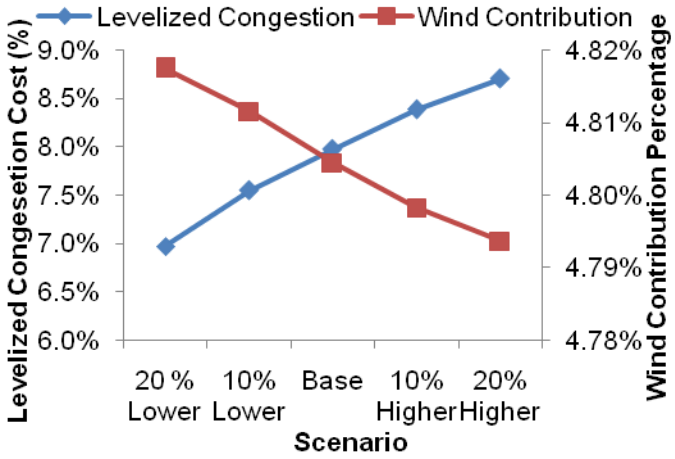

Figure 314: Levelized Congestion Cost and Wind Energy Contribution in Fuel Price Scenarios

Wind Energy Contribution Sensitivity Analysis

We implement the sensitivity analysis based the 2018 WINS simulation results for Scenario 4. Four scenarios are considered as follows.

- Scenario 9: Available wind energy is 20% lower
- Scenario 10: Available wind energy is 10% lower
- Scenario 11: Available wind energy is 10% higher
- Scenario 12: Available wind energy is 20% higher

Figure 315 shows the 2018 production cost, generation credit, load payments, and annual average LMP in the four wind production scenarios. As expected, the economic metrics will be more favorable as more wind energy is dispatched. Figure 316 shows the levelized congestion cost and wind energy contribution in the four wind energy production scenarios. Wind energy is assumed as a zero fuel cost resource, so the transmission system will try to deliver all the available wind energy to load centers.

Hence, higher wind energy production scenarios could cause additional transmission congestion. Figure 316 shows a higher wind energy contribution to the energy production portfolio and higher congestion in the Eastern Interconnection as more wind energy is made available.

Figure 317 shows the energy production portfolio in four wind energy production scenarios. The energy produced by gas and coal units will decrease as additional wind energy is made available.

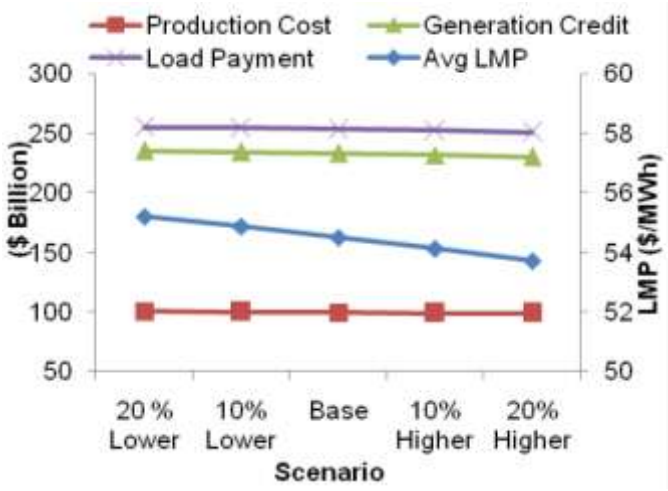

Figure 315: Economic Metrics for Available Wind Energy Scenarios

Load Variations Sensitivity Analysis

In this section, we carry out the load forecast sensitivity analysis based the 2018 load forecast. The WINS simulation results for Scenario 4 are treated as base case. Four load sensitivity scenarios are studied as follows.

- Scenario 13: Total load is 5% lower than the forecast
- Scenario 14: Total load is 3% lower than the forecast
- Scenario 15: Total load is 3% higher than the forecast
- Scenario 16: Total load is 5% higher than the forecast

Figure 318 shows the production cost, generation credit, load payment, and annual average LMP in the four load sensitivity scenarios which are compared with the base case scenario. In Figure 318, as compared with Figure 313 and Figure 315, the system load variations will have a larger impact on production costs, generation credit, load payment, and LMPs. Also, generation credit and load payment demonstrate a higher sensitivity than the production cost to load variations. Similar to the results in [**95**], Figure 319 shows that the system load variations will have the highest impact among the listed parameters on the commitment and dispatch of generating units. The unit commitment results based on Scenarios 13-14 shows that many generation units may never be committed again in 2018 as hourly loads drop.

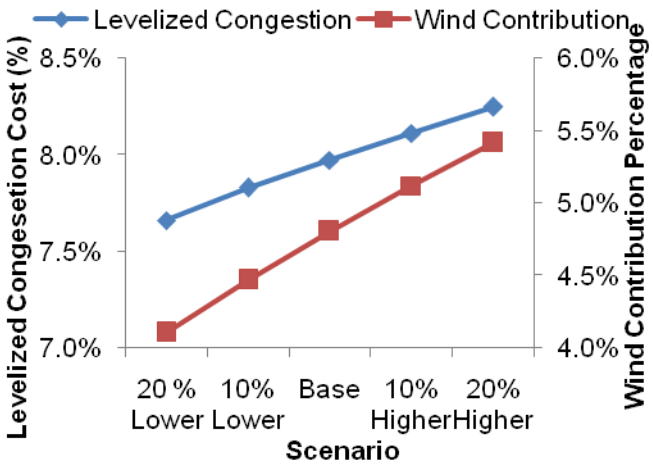

Figure 316: Levelized Congestion Cost and Wind Contribution in Wind Energy Scenarios

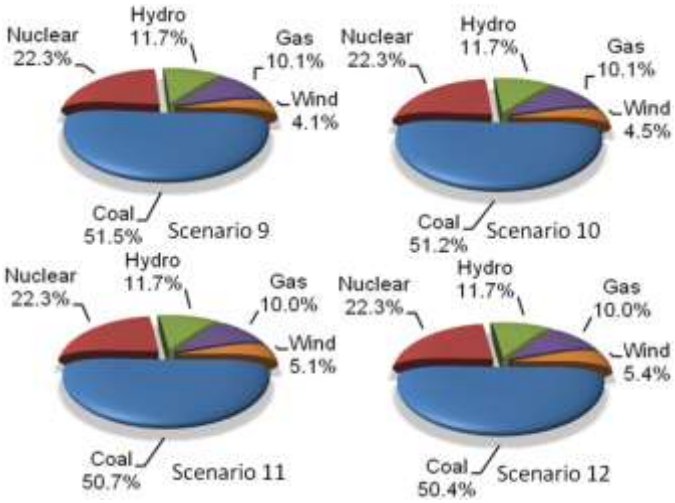

Figure 317: Energy Production Portfolios in Wind Energy Production Scenarios

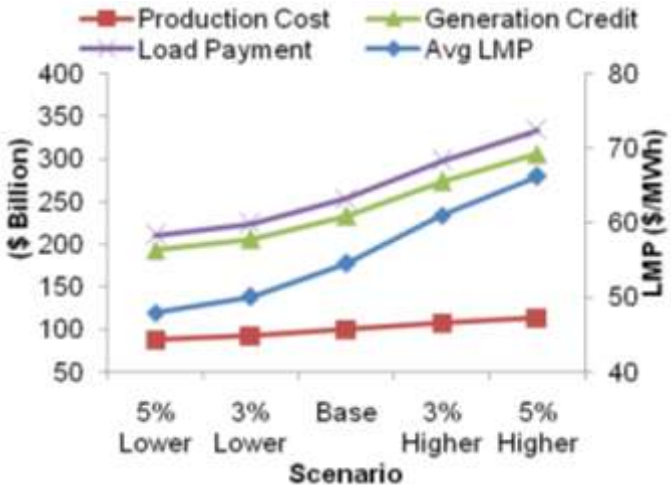

Figure 318: Economic Metrics in Load Scenarios

On the other hand, additional units are committed when the system load is higher. The results indicate that the hourly load management and demand response could introduce major alternatives for improving the system operation bottlenecks and enhancing the economic metrics of power systems in the Eastern Interconnection.

Figure 320 shows the levelized congestion cost and wind energy contribution in four load scenarios. The wind energy contribution will decrease as the system load increases because the additional load is served mainly by fossil generation units. The congestion cost for the four load scenarios are $17.47 billion, $18.05 billion, $24.20 billion and $28.03 billion respectively, which will increase with higher system loads. However, the levelized congestion cost in Figure 320 demonstrates a mixed result which is not increasing monotonically with the bus load level. The reason is that both generation credits and load payments are used to calculate the levelized congestion cost (7). However, generation credits and load payments which are determined by bus LMPs do not change uniformly with the bus load increments.

Figure 321 shows the energy contribution portfolio in the four load sensitivity scenarios. The cheaper nuclear, hydro, and wind generation units will supply much of the hourly load. However, their contributions will decline as load increases. Compared with the base case of Scenario 4, the energy contribution portfolio by gas and coal units, especially those supplied by gas units, will decrease as we lower the system load.

Furthermore, the contribution of gas units to the energy production portfolio will increase from 10% in the base case (Scenario 4) to 11.1% in Scenario 15 and 11.8% in Scenario 16 as we increase the system load. This observation shows that the additional load is mainly supplied by gas units.

Carbon Cost Sensitivity Analysis

Additional carbon cost can be used as an incentive for promoting the development of clean, efficient, and environmentally-friendly generation resource [**96**]. Two Scenarios are studied in this section as follows.

- Scenario 17: Low Carbon cost at $30/ton
- Scenario 18: High Carbon cost at $60/ton

Figure 322 shows the production cost, generation credit and load payment in carbon cost scenarios. All three economic parameters will be much higher than those in the base case when carbon costs are applied. Figure 323 shows the levelized congestion cost, wind energy contribution and annual average LMP for the base scenario and two carbon cost scenarios. It is observed that the higher carbon cost will reduce the levelized congestion cost because higher carbon costs could reduce fuel price increments between cheap generation resources (coal) and expensive generation resources (gas). The annual average LMP could increase a lot when the carbon cost is higher. Figure 324 shows the energy production portfolios in carbon cost scenarios in which the high carbon cost will have a major impact on the energy supplied by gas and coal units. Since coal prices are lower than gas prices, the energy supplied by coal units does not change much in the low carbon cost scenarios.

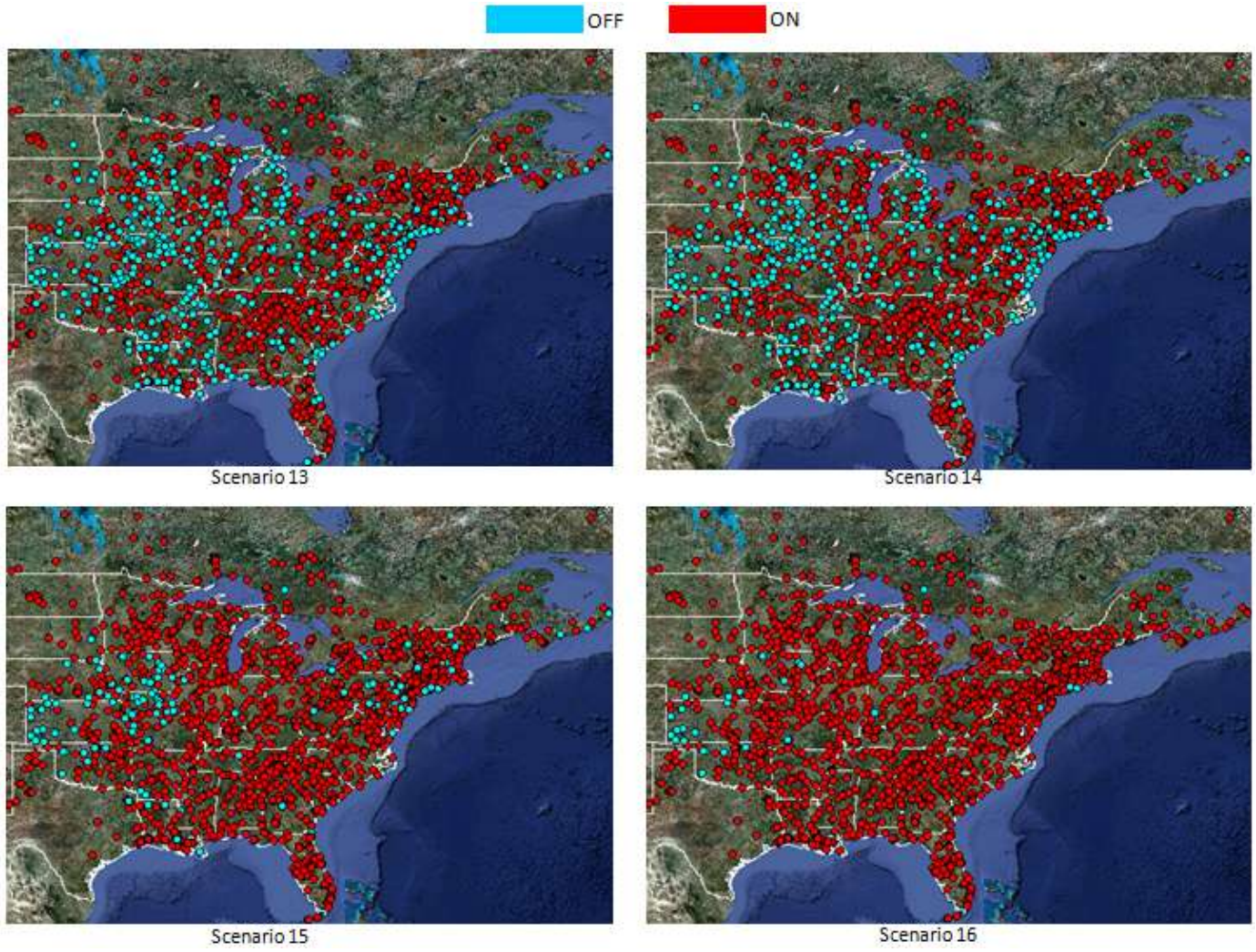

Figure 319: Annual Unit Commitment in Load Variation Scenarios

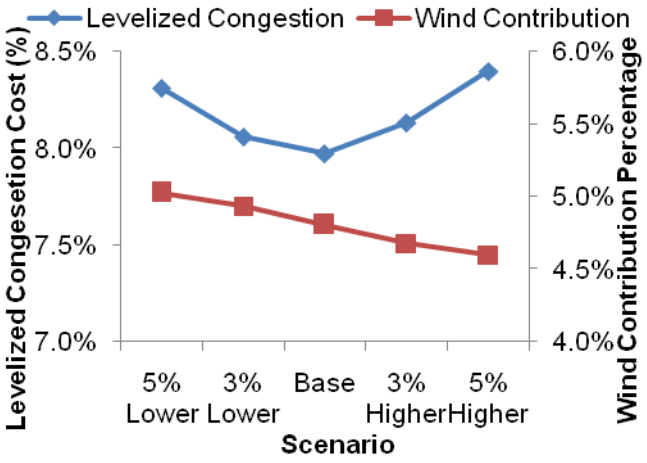

Figure 320: Levelized Congestion Cost and Wind Contribution in Load Scenarios

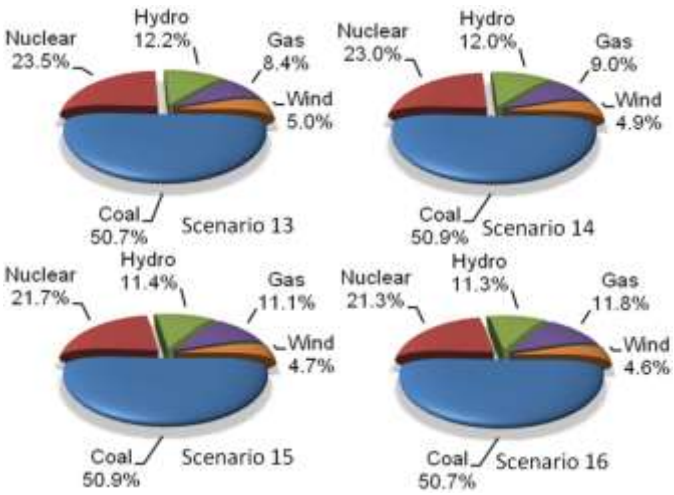

Figure 321: Energy Production Portfolios in Load Scenarios

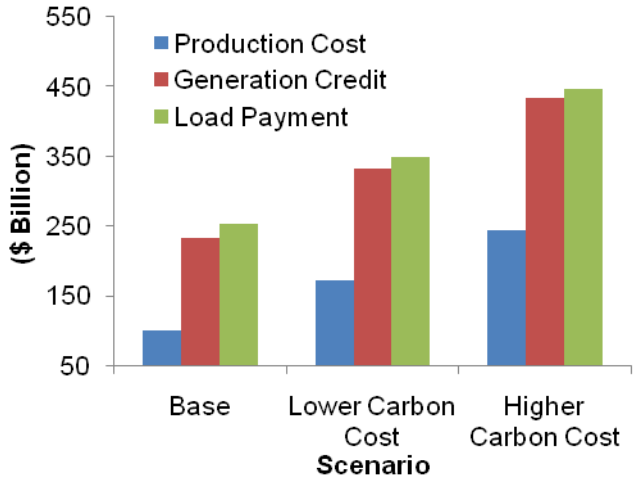

Figure 322: Economic Factors in Carbon Cost Scenarios

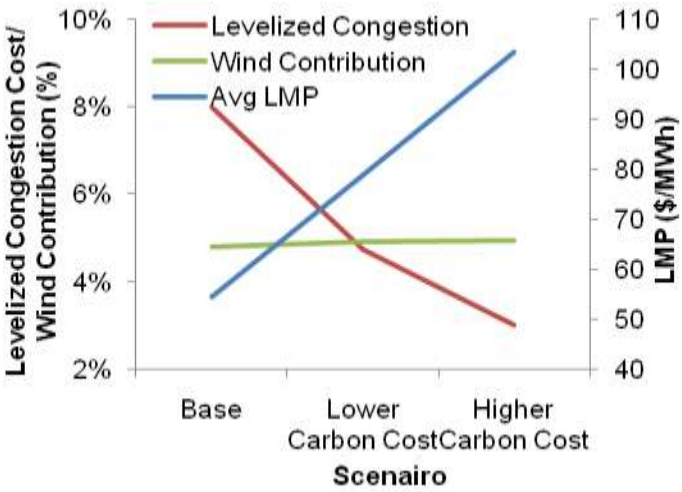

Figure 323: Levelized Congestion Cost, Wind Contribution, and LMP in Carbon Cost Scenarios

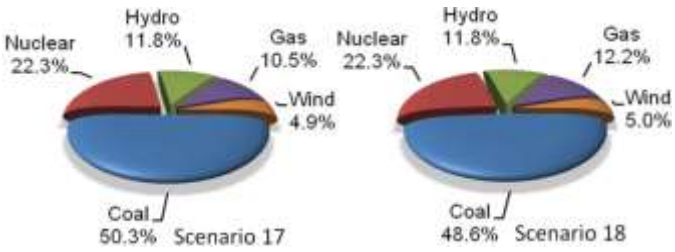

Figure 324: Energy Production Portfolios in Carbon Cost Scenarios

The energy supplied by gas units increases from 10.5% in Scenario 17 to 12.2% in Scenario 18 while that of coal decreases from 50.3% to 48.6%. Additional wind energy will be dispatched when the high carbon cost mitigates the transmission congestion. The wind energy contribution will be higher when the carbon cost increases. In this case, the wind energy contribution will increase from 4.8% in the base case (Scenario 4), to 4.9% in the low carbon cost scenario (Scenario 17) and 5.0% in the high carbon cost scenario (Scenario 18).

Load Management in 2018

As presented in section on load sensitivity analysis, the hourly load variations will have a major impact on the WINS simulation results. In this section, we consider load shedding at peak hours, i.e., if the hourly load at peak hour is higher than 80% of the annual peak load. In essence, the hourly load will be subject to demand response and set at 80% of annual peak load. One scenario is studied as follows.

- Scenario 19: Wind energy integration with possible load shedding

Figure 325 shows the production cost, generation credit and load payment for the base case and the load shedding scenario. All three economic factors will be lower with the load shedding implementation. Load shedding will almost have no impact on the hourly dispatch of coal units as coal units are committed to serve the base load.

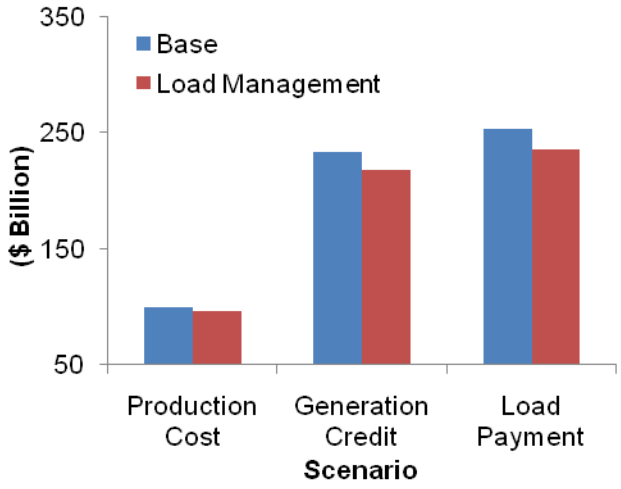

Figure 325: Economic Factors in Load Shedding Scenario

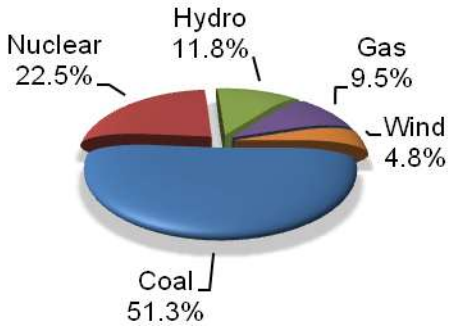

Figure 326: Energy Production Portfolios in Load Shedding Scenario

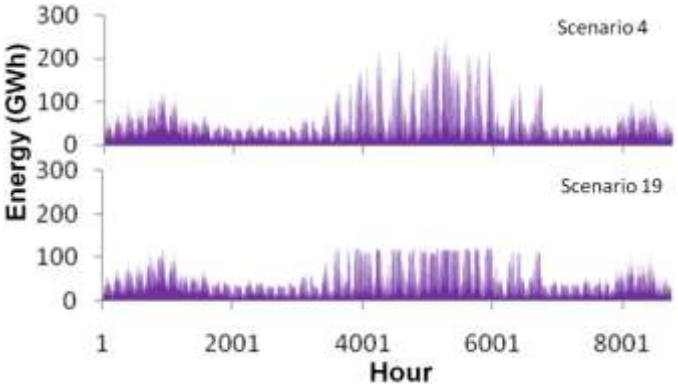

Figure 327: Energy Provided by Load Shedding Scenario

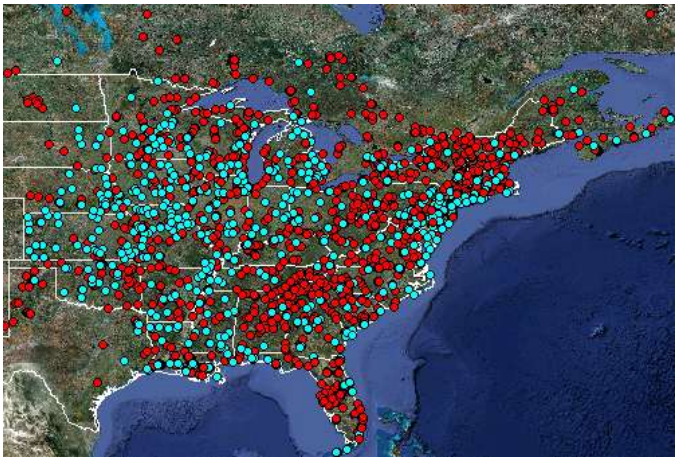

Figure 328: Annual Unit Commitment in Scenario 19

Figure 326 shows the energy production portfolios for the load shedding scenario. Figure 327 shows the hourly energy supplied by gas units in which the gas unit dispatch is lower due to load shedding at peak load hours. Figure 328 shows that the load shedding will alter the unit commitment as compared to that

of Scenario 4 shown in Figure 312. Here, additional gas units (1,700) are turned off at peak hours when the load shedding is applied.

B3. Conclusions

In this section, a comprehensive large-scale wind energy integration analysis is implemented based on the 2018 load forecast in the Eastern Interconnection of the United States. The wind energy integration with/without transmission constraints are studied and analyzed. The sensitivity of fuel price, wind energy production, load, carbon cost, and load shedding are implemented to study the impact of volatility of major parameters on the WINS simulation results. 19 Scenarios are studied and analyzed. The main observations based on the simulations are listed as follows:

- Production cost is more sensitive to transmission constraints than to wind energy integration.
- The location of wind energy integration could have an impact on the wind energy dispatch in the hourly generation portfolio.
- The addition of wind generation units at certain locations in the Eastern Interconnection may cause additional transmission congestion.
- In 2018, the replacement of coal units by wind energy at certain locations could mitigate transmission congestion.
- Wind energy is often available and can replace fossil energy at off-peak load hours. During certain seasons when wind is unavailable, wind energy supply could be replaced by fossil energy.
- In 2018, wind energy is transmitted mostly at 500kV, 345kV, and 230kV transmission levels while the 765kV transmission is utilized less by wind generation units.
- Higher costs for gas and oil will result in additional transmission congestion as power systems try to use cheaper coal units located centrally in fewer geographical spots. Such limited utilizations of centrally located resources may also limit the available dispatch of wind generating units.
- Higher levels of wind energy integration could result in higher levelzied congestion costs when wind generation units, located at few geographical spots, try to supply a significant level of load.
- Carbon cost demonstrates the highest impact on the 2018 simulation results. Higher carbon costs will be instrumental in mitigating the regional transmission congestion in the Eastern Interconnection.
- Load forecast uncertainty will have a larger impact on the 2018 simulation results as compared to fluctuations in fuel prices or possible levels of wind energy integration.
- The levelized congestion cost may not increase monotonically with higher levels of bus loads.
- Peak load shaving will have a major impact on the commitment and dispatch of gas units because peak loads are mostly supplied by such units

The WINS simulation results shows that lowering the hourly volatility of load profile by introducing smart grid, additional distribution automation for the utilization of demand response, and the large-scale integration of wind energy and storage could lower the transmission congestion and improve the economics and the optimal operation of power systems in the Eastern Interconnection of the United States.

C. *Integration of Non-dispatchable Resources in Electricity Markets*

The electricity market structure, involving generally a pool, a futures market and a bilateral trading floor, was designed before the large integration of non-dispatchable sources, particularly wind power. There is a need to address the suitability of the current electricity market structure for producers relying on non-dispatchable energy sources. Considering the intrinsic variability and uncertainty of the production level of non-dispatchable sources, appropriate changes in the current market structure are needed to adapt such structure to an increasingly non-dispatchable generation mix. To efficiently integrate non-dispatchable production, the questions below regarding market design and organization need to be answered:

- Which is the most appropriate time framework to clear short-term electricity markets? Is it a day-ahead horizon as today, or a shorter one?
- Should the algorithms to clear such markets be deterministic or stochastic? How should prices be derived?
- How much reserves should be scheduled to cope with the variable and uncertain nature of renewable non-dispatchable producers? Who should pay for such reserves?
- How the transmission infrastructure should be expanded and operated to avoid bottlenecks that hider the integration of renewable non-dispatchable resources?

The features of wind-dominated systems are listed as follows.

- Wind and demand correlation: Negative correlation (no good)
- Wind power dispersion: Geographical dispersion beneficial (production smoothing)
- Transmission network dependency: Network bottlenecks lead to wind spillage
- Increasing uncertainty: Need of volatility protection
- Wind zero fuel cost: Hydro + wind + nuclear may lead to zero or negative prices

The required improvements of wind-dominated systems include

- Encourage demand-side management: Load control from the demand side.
- Incorporate new loads: Controllable loads (plug-in cars)
- Promote electricity storage: Pumped-storage and others (compressed air)
- Achieve flexible thermal generation: Load-following units.
- Carry out wind technology upgrading: More flexible and controllable wind turbines
- Ensure optimal use & expansion of networks: Avoiding bottlenecks is a must
- Update tools for ISOs: Tools adapted to uncertain wind power behavior
- Redesign ancillary services: Reserve, regulation, voltage control, etc.
- Improve market-clearing tools
- Improve the market design

Specific issues are

- A non-dispatchable producer needs to establish an effective offering strategy in the pool.

- The market operator should use a stochastic clearing mechanism.
- The market operator needs to set up an efficient balancing market to cover production deviations.
- The regulator may need to restructure the markets within the pool.
- The ISO should determine the amount of reserve & its cost.

The specific market problems for wind producer regarding how to offer include

- How to represent the uncertainty pertaining to prices and wind production?
- Where to sell? In the day-ahead market, or rather in the adjustment markets?
- How to build hourly offer curves?
- Is it convenient to control the financial risk on a daily basis?

The specific market problems for market operator regarding the balancing market include

- How should the balancing market be organized?
- In which manner should deviations be penalized?
- How should deviations helping to offset the net system imbalance be considered?
- Which is the behavior of deviation prices?

The specific market problems for market operator regarding pool auctions include

- Is it appropriate to simultaneously clear energy and reserve markets?
- Is it economically reasonable to establish a deterministic reserve level?
- Is it feasible and socially acceptable to implement a probabilistic reserve level?
- How should prices for energy and reserve be derived?
- How to deal with non-convex prices?

The specific market problems for regulator adjustment markets include

- How many adjustment markets should be available?
- Is the day-ahead market still needed?
- Should the trade in adjustment markets be capped?

The specific market problems for ISOs regarding reserve determination and valuation include

- At which level of nondispatchable penetration are additional reserves needed?
- How the reserve level/cost increases as the nondispatchable power increases?
- How the variability level of the nondispatchable sources affects the reserve level/cost?
- Who should pay for the additional reserves needed as a result of integrating nondispatchable producers?

The implications for modeling include

- A redesign of the different markets in the pool might be needed as the level of wind power increases.
- Stochastic market clearing algorithms involving energy and reserve are needed.
- The stochastic nature of reserve and energy prices should be properly modeled.
- Locational issues need to be properly taken into account, because network bottlenecks may seriously hamper the advantages of wind power.
- Reserve determination and valuation are crucial for an efficient and fair cost allocation.

D. Integration of Wind Unit with Microgrid

This section discusses the data gathering and software integration of an 8kW Viryd Wind Turbine installed on the main campus. The primary purpose for installing this wind turbine was to increase public awareness of renewable energy technologies and thus the primary objective of this effort was to gather data from the wind turbine and make real time data viewable on campus, something that is not typically available for Viryd Wind Turbine Installations. A secondary objective in this work was to model and predict wind turbine output and compare the predictions to actual wind turbine data. This predictive modeling will be important as wind turbine penetration increases. IIT's existing microgrid provides a unique opportunity to see how local wind turbine generation might affect the microgrid.

D1. Background

Viryd typically supplies wind turbines with a data logger that accumulates real time data in a log file and transmits the data when the accumulator is full to one of Viryd's data servers. Viryd then uses this data for their purposes such as performance models and determining the condition of the wind turbine. This project required a modified approach so that real time data could be viewed on campus. This approach will be discussed in latter sections but it is important to note that the real time data view will be accomplished through IIT's microgrid master controller.

IIT's microgrid master controller, also called the Intelligent Perfect Power System Controller (IPPSC) is intended to coordinate the energy systems on the campus. An overview of the IPPSC is shown in Figure 329. The specific energy systems at IIT include existing onsite generation consisting of two 4MW gas turbines, several diesel and natural gas backup generators, renewable Solar PV generation, an intelligent electric distribution system consisting of intelligent sectionalized loops, building control systems which typically control lighting and HVAC systems within the buildings and a building metering system which measures the electric loads of the buildings. The primary scope of the IPPSC's control is:

- Campus and Building Load Prediction
- Turbine, Engine Generator and Solar PV Output Prediction
- Load management and coordination for Island Mode and Demand Response events
- Generation dispatching based on potential threats and dynamic market pricing
- Threat detection such as lightning detection or voltage sags

Modifications made to the IPPSC, as a result of this research effort, will have to allow for real time wind turbine data to be collected and stored for viewing through the IPPSC GUI interface. In order to meet the secondary objective of the project, the wind turbine modeling would theoretically account for the combined variability of both Solar PV and Wind, and will have to allow operation when the campus is in

island mode and is operating solely on the installed campus generation. Though the impact of both Wind and Solar PV resources installed at IIT will likely be relatively small compared to the campus's total load, an effort will be made to account for scenarios with a much larger portion of wind resources.

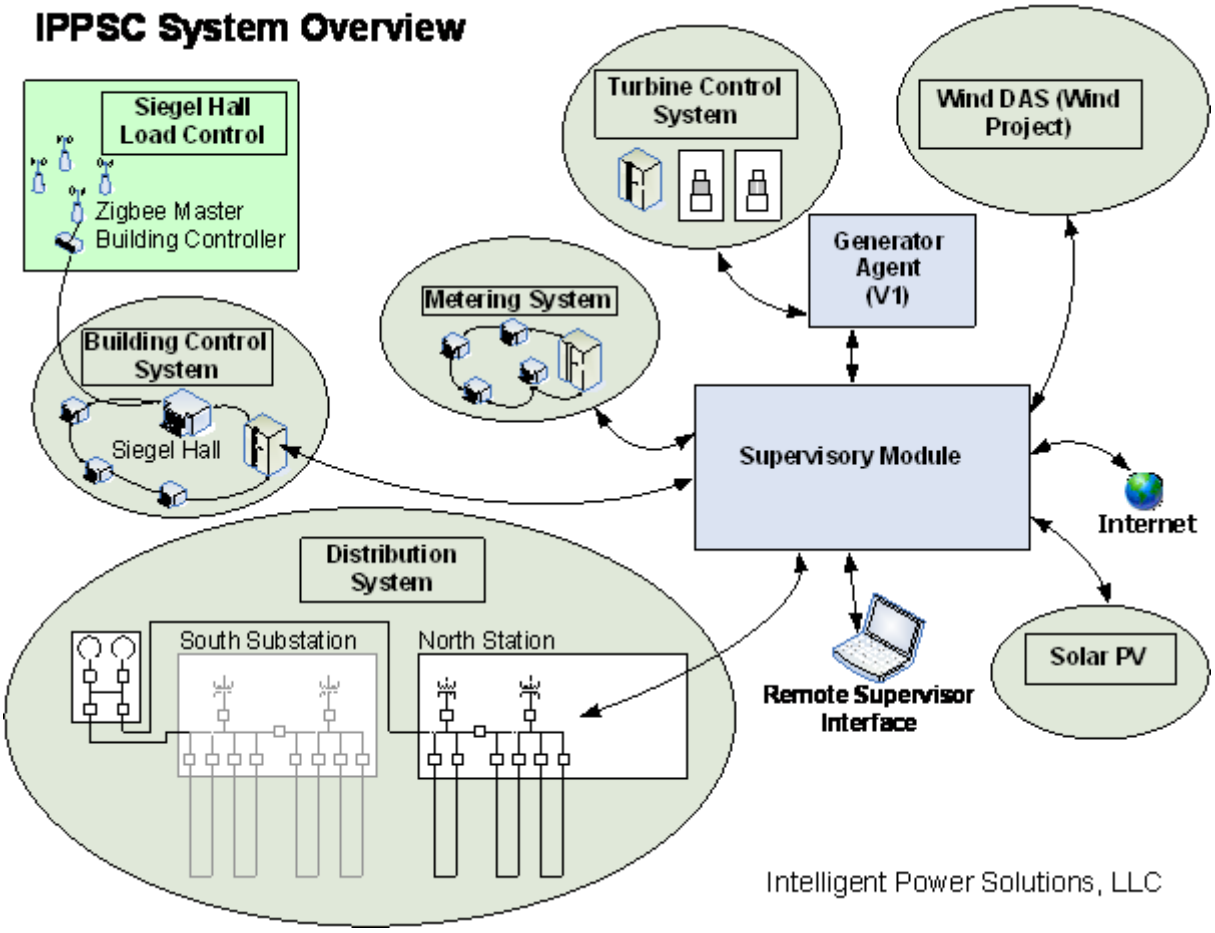

Figure 329: Overview of IPPSC

D2. Approach

As mentioned, the Viryd data logger is typically setup to log data and periodically post it to its data servers for future analysis and typically do not supply a real time data interface. As such Viryd modified the programming in their data logger to push real time data out to the IPPSC in addition to pushing logged data out to their own servers. A sketch showing the two communication schemes is shown in Figure 330.

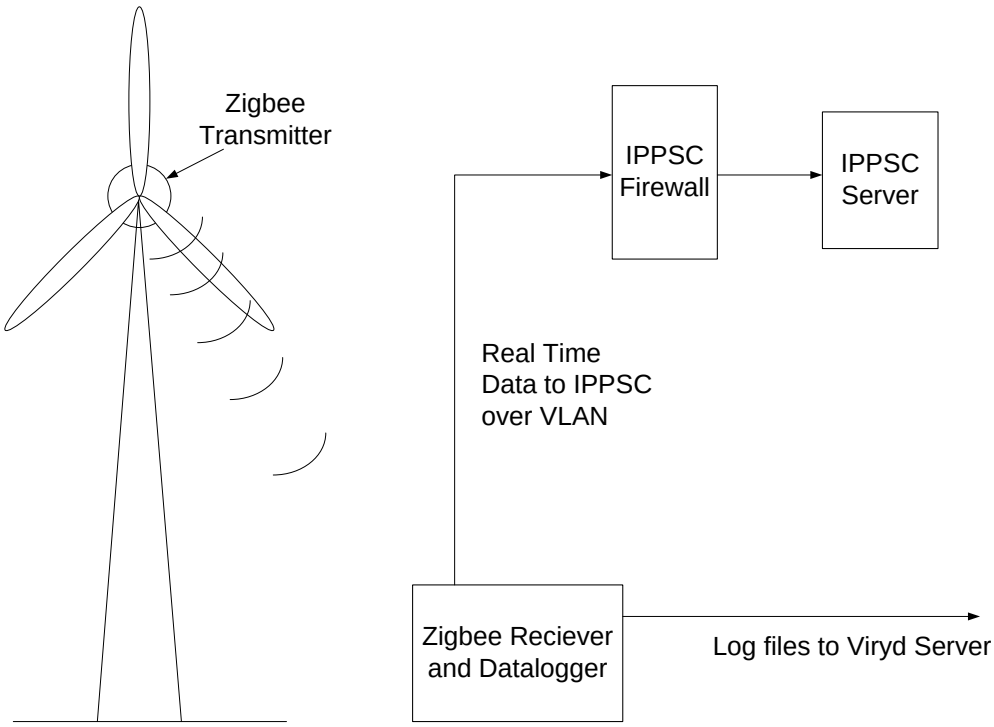

Figure 330: Viryd Data Logger Communications

Several studies have been made regarding the integration of utility scale wind project in to the grid. To a lesser extent, wind integration studies have been conducted on small scale wind projects. In the course of this effort, the project team attempted to glean as much as possible from studies regarding utility scale integration but took note of exceptions that might apply to small scale projects with microgrids. The project team proposed software changes to the IPPSC based on the results of this literature research and is working to implement these changes before the end of the related contract.

D3. Findings from Wind Integration Studies

Wind integration studies reveal several issues that were categorized into 4 areas:

- Large Variation in Wind Generator Output
- High Wind Generator Ramp Rates
- Power Factor
- Prediction Wind Generator Output

Brief descriptions of some of the main issues are given below. Some of the issues reviewed were considered less relevant to a microgrid and some of the issues are more critical.

Large Variation in Wind Output

Obviously, there can be large variations in wind output as wind output is primarily based on wind speed. Wind speed can vary significantly on gusty days and it can be more constant on other days. Wind speed variability is also dependent on the wind direction because local effects. In addition to output variation due to wind speed, wind output does not always correlate with wind speed due to more localized

effects such as wakes from buildings, trees and terrain. Wind output can also depend on a lesser extent on barometric pressure, air temperature and wind direction. These effects can be taken into account when possible.

Because of the variations in wind output, wind energy resources are not typically viewed as a good capacity resource. Instead they are viewed as an alternative source of energy that can be used to offset fossil fuels. Several wind integration studies have indicated that systems with large wind generation require higher spinning reserve requirement than systems without wind generation and therefore to some extent incur higher cost due to the higher reserve requirement and the higher maintenance costs of maintaining these reserves that are subject to higher output variations.

One study suggested that wind output variations are smoothed out in large wind farms as not every unit gets the same gust of wind at the same time. This would indicate that the worst case is installation of a single wind generator or just a few wind generators that don't benefit of smoothing.

High Wind Generator Ramp Rates

In addition to large output variations, wind generators can have high ramp rates meaning the rate at which the output changes is large. Wind generation is subject to large output changes in a short amount of time. Most generators, be it a coal plant, gas turbine, or hydroelectric dam have ramp rates defined by the nature of the equipment, due to mainly inertia and control lag, so their ramp rates are much better known. As it turns out on a utility scale, a hydroelectric dam has one of the highest ramp rates and is one of the few generation resources that can match the ramp rates of wind generation. High wind generation ramp rates create additional problems for the grid. Normally, the generation on the grid has to match the variation in loads caused by consumers. This type of generator is known as a load follower. Grids with wind generation require the load followers to match the variations in both load and wind energy.

There are two reasons for high wind ramp rates. One is that the speed of the wind can change rapidly, especially if the wind turbine is in an eddy cause by an obstruction from a mountain, tree or building. The steadiness of the wind often depends on the wind direction due to the lack of or presence of an obstruction in the wind direction. The other reason for high ramp rates is that the power of the wind, that is the theoretical power that can be captured by a wind turbine, is a cubic function of the wind speed. To illustrate this effect, if the wind speed changes from 10 meter per second to 5 meters per second, the wind power will drop to 1/8 of the power output at 10 meters per second. Additionally, the wind speed needs to only drop from 10 meters per second to 8 meters per second (20%) to reduce the wind power in half.

One way to reduce the impact of high wind generator ramp rates is to use energy storage such as flywheels and batteries, to provide energy when the wind generator is reducing output quickly, and to store energy when the wind generator is ramping up output quickly. Energy storage can also smooth out wind generator output variation but this will require much larger energy storage devices. The energy storage requirements required for reducing the wind energy ramp rates require energy storage

over much shorter time periods than what would be required for smoothing wind output variations over an entire day.

Power Factor and Voltages

Most wind generators use induction generators which required reactive voltage support from the grid. Newer induction generators reduce this requirement but still require power factor adjustment on the utility and transmission operator side of the grid and can consume valuable grid resources. Wind turbines with DC generators and inverters do not have this problem.

Prediction of Wind Generator Output

Prediction wind generator output has additional issues. As mentioned, power does not always correlate with wind speed. For instance if a model of a wind turbine's output is made assuming a uniform velocity flow field (constant velocity through the axis of the wind turbine) through the wind turbine, then "dirty" air will reduce the wind turbine's performance. Some factors that can cause deviations from a uniform flow field assumption are upward or downward components of wind direction that can be caused by the site or convection and wakes from nearby objects or wind turbines. Predicting the wind turbine, or wind farms output requires that a good model of wind output be made for each site and possibly each wind generator if they are dispersed throughout the campus. A good model will should account for the factors mentioned above. Another source of error is the fact that actual wind speed and direction do not always match predicted wind speed and direction. Large wind farms subscribe to sophisticated wind prediction services that can update predictions in shortened time intervals. This offering may not be practical for a microgrid depending on the price of such services. Additionally, results from these services are not perfect. Because of the cubic relationship between wind speed and wind power mentioned above, a seemingly small error in wind speed can lead to fairly large errors in wind output predictions.

Wind farms also use wind predictions to predict the ramp rates of wind generators. Since ramp rates can be dependent on local conditions prediction models should be site specific.

ISOs tend to use three time frames for wind predictions. A long term time frame might be from 48 to 168 hours ahead. A medium term forecast might be from 6 to 48 hours ahead and short term forecast might be from 5 to 10 minutes ahead to 6 hours ahead. The California ISO also required that meteorological data and wind turbine output data be transmitted to them every 4 seconds.

Other Issues

Transmission and distribution constraints should be considered for wind farms. The system operator needs to make sure that the transmission and distribution circuits have enough margin to handle load variations, and generator output variations on the circuits carrying power from the wind farm. For the same reasons, circuits on the microgrid should also be monitored to ensure that the local cables have enough margin to handle generator and load variations.

Another concern is that the issues associated with wind generation may be compounded when the system, circuit, or microgrid also have solar energy resources that can cause additional variations in generation output.

D4. Recommendations for Local Wind Integration in to Microgrids

When integrating local wind generation into a microgrid, the microgrid master controller should be able to mitigate all of the issues mention above. The functional requirements are given below.

Large Variation in Wind Generator Output. When the campus or microgrid is connected to the grid, variation in electrical output can be mitigated by the utility supply. This is not an option available to wind farms. Typical utility interconnection agreements require that a certain amount of power shall always be imported to the site to make sure that the onsite generation never back feeds the grid. In the case of IIT, the utility should factor wind variability into the interconnection agreement particularly if the rated output is significant relative to the campus's load. IIT will find out what the specific requirements are when they apply for an interconnect agreement but the microgrid master controller really does not need to account for this while in grid parallel mode. However, when the campus is in island mode, the load following capabilities of the campus generators will have to account for the additional variability. This should be factored into the reserve power requirement for the generators and be a considered in the microgrid master controller when reserve power requirements are calculated in real time.

High Wind Generator Ramp Rates. As with load variations, high ramp rates can be mitigated by the utility when the campus is operating parallel to the grid. When operating in island mode, the campus generation will have to account for the high ramp rates of the wind turbine. IIT's campus generation consists of two 4 MW gas turbines. Currently IIT is not planning a large scale deployment of wind on campus but, if a large scale deployment of wind were to be considered at IIT, the ramp rate specification of these turbines should be compared to the expect ramp rates of the wind turbine. In the event that IIT's gas turbine and wind turbine ramp rates are determined to not be compatible, additional measures would have to be taken. For an example, an energy storage system designed to reduce the ramp rates of a particular wind turbine would have to have a control system closely tied and integrated with the wind turbine and its controls. So the other option, if the ramp rates are found to not be compatible, would be to curtail the wind turbine when the campus is in island mode. The latter would be the least expensive option.

Power Factor. A small wind turbine should not cause much of an issue when the campus is in grid parallel or island mode. However, if the campus were to add a high percentage of wind turbines generation compared to the campus load, special provisions may be required. Depending on local utility rules, the campus may be required to add equipment for adjusting the power factor. It may be more effective to use a wind turbine with an inverter. When the campus is in island mode, the amount of wind resources that can be used in this mode would depend on the amount of wind generation installed, the power factor of the wind generation, the power factor characteristics of the campus loads, and the power factor capabilities of the campus's gas turbines.

Prediction Wind Generator Output. When the campus is operating parallel to the grid, the wind output predictions are not necessarily critical. As part of the research though, the project team was interested in working on models to predict wind output and ramp rates for the campus. The microgrid master controller, which is still in development, will have the capability to model the campus loads based on meteorological conditions and campus schedules. This modeling capability can be adapted to model the wind generation output as well as ramp rates. In island mode, wind generation output predictions become more critical as the percentage of wind generation versus campus load increases. The modeling capability already mentioned should help in this case.

A list of suggested features put together for a microgrid master controller designed to handle a large portion of wind generation on campus. Further analysis and experimentation would have to be performed to define what a large portion is, but for now it is estimated that it is somewhere near 20 to 30% of the campus load. Due to the limited scope and funding for this part of the project, these features will not necessarily be implemented into the IPPSC. Based on the research described above, the microgrid master controller should ideally:

- Have the capability to make adjustments to the campus's reserve power requirements when wind generation is added to the system when the campus is in island mode. These adjustments could be manual or automatically calculated based on the size of the wind generation resources and models of the wind generation resource output and ramp rates.
- Have the capability to curtail wind generation when the campus is in island mode and the wind generation ramp rates are not compatible with the rest of the campus. This feature would require that master controller can send control signals to the wind turbine to curtail its output. To do so, the turbine controls would have to be modified to allow for remote control. Alternatively, the campus could use energy storage to help manage the ramp rate issues associated with the wind turbine. In this case, the energy storage controls would have to be closely coupled with wind turbine models to help determine the optimal charge state of the energy storage system. Dump resistors may also be required as a way to dissipate excess energy.
- Should be able to model and a make short term predictions of wind generation output and ramp rate predictions based on meteorological conditions measured at the site.
- Should be able to model and a make long term predictions of wind generation output and ramp rate predictions based on NOAA weather predictions available over the internet.
- Should be able to make campus load ramp rate predictions based on campus meteorological predictions.
- Should be able to monitor real time wind generation output and distribution circuit power flows on the campus to ensure that circuits do not become overloaded. The controller should have the ability to curtail wind if necessary. This is more critical for higher levels on wind energy installations on campus.

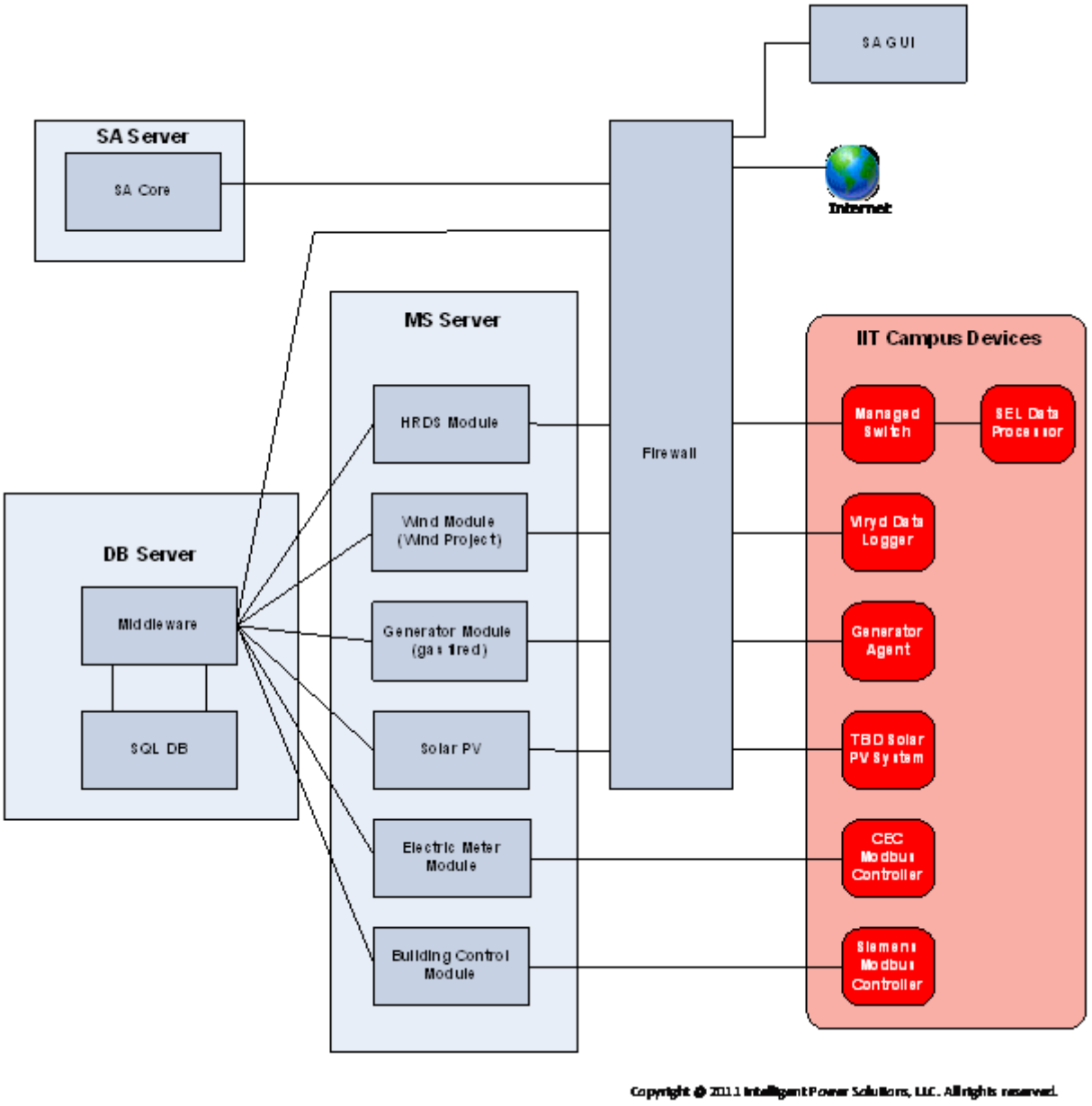

Figure 331: IPPSC Servers and Software Modules

D5. IPPSC Implementation and Integration

A more in depth description for the IPPSC software is shown in Figure 331. The IPPSC software resides on 3 different servers that operate behind the IPPSC firewall. The software is distributed on the servers for load management and for redundancy. If one of the servers goes down, the functions will be distributed between the two remaining servers. The database server will host a MS SQL database and middleware used to store and retrieve data from the database. The middleware uses a web services interface for transferring XML data to and from the database. The SA core, which is the Supervisor Agent (SA) core, operates on its own server. The SA core is the brains of the IPPSC and is responsible for the decision making and modeling making for the IPPSC. Currently the GUI (graphic user interface) for

the IPPSC, also called the SA GUI, communicates directly with the SA Core. In future revisions, the SA GUI will interact only with the middleware on the database server.

The MS server hosts several different modules that communicate with various devices at IIT. Specific to this project, the Wind Turbine Module collects data from the Viryd data logger and then sends it to the middleware by transferring XML data. The Wind Turbine Module transfer both real time data every few seconds and 15 minute averaged data every fifteen minutes. The real time data is used primarily for viewing the real time status of the wind turbine and the 15 minute data is used for data modeling of longer periods of time.

In order to integrate the wind turbine data into the IPPSC, it is necessary to modify the software specification, test the software modifications, and make sure that the campus network could handle the data communications from the wind turbine data logger to the Wind Turbine Module shown in Figure 331.

The project team procured and configured a firewall to setup a VLAN for securely transferring data to the IPPSC. This sounds like a simple effort, but the work had to be coordinated with several departments with IIT's OTS.

The Wind Turbine Module was written to receive data from the Viryd data logger. Viryd helped out in this effort by supplying a subroutine, written in Labview, to listen for data communications from the Viryd data logger and to parse it out into separate parameters. Functions were added around Viryd's data listener to accumulate the data into 15 minute averages and to convert it to and XML format readable by the IPPSC's middleware. An example of the wind turbine XML data is shown in the appendix. The Wind Turbine Module was written in Labview.

Example of the Wind Turbine Module XML that will be sent every 5 seconds

```
<Wind_Turbine_Data>
  <Current_Wind_Turbine_Data>
    <Index>0</Index>
    <Time_Stamp_String>09/28/11 02:21:06 PM</Time_Stamp_String>
    <Power_Output>1.5906138892429</Power_Output>
    <Power_Factor>0.88845417557357</Power_Factor>
    <Wind_Speed>13.414981866903</Wind_Speed>
    <Wind_Direction>259.6584167354</Wind_Direction>
    <Wind_Temperature>67.866002551997</Wind_Temperature>
    <State_Index>3</State_Index>
    <Fault_Number>5</Fault_Number>
    <Data_Okay>true</Data_Okay>
  </Current_Wind_Turbine_Data>
</Wind_Turbine_Data>
```

Example of the Wind Turbine Module XML that will be sent every 15 minutes

```
<Wind_Turbine_Data>
 <Current_Wind_Turbine_Data>
  <Index>0</Index>
  <Time_Stamp_String>09/28/11 02:12:03 PM</Time_Stamp_String>
  <Power_Output>5.8518867140121</Power_Output>
  <Power_Factor>1.0829881900052</Power_Factor>
  <Wind_Speed>77.284238904113</Wind_Speed>
  <Wind_Direction>370.96102237804</Wind_Direction>
  <Wind_Temperature>69.974370191443</Wind_Temperature>
  <State_Index>5</State_Index>
  <Fault_Number>2</Fault_Number>
  <Data_Okay>true</Data_Okay>
 </Current_Wind_Turbine_Data>
 <_15_Min__Wind_Turbine_Data>
  <Index>0</Index>
  <Time_Stamp_String>09/28/11 02:12:03 PM</Time_Stamp_String>
  <Power_Output>5.9756798295702</Power_Output>
  <Power_Factor>1.156556307218</Power_Factor>
  <Wind_Speed>68.331191820848</Wind_Speed>
  <Wind_Direction>433.21311222641</Wind_Direction>
  <Wind_Temperature>87.259401237249</Wind_Temperature>
  <State_Index>4</State_Index>
  <Fault_Number>2</Fault_Number>
  <Data_Okay>true</Data_Okay>
 </_15_Min__Wind_Turbine_Data>
</Wind_Turbine_Data>
```

In addition to developing the Wind Turbine Module, the IPPSC middleware was modified to accept the XML data from the Wind Turbine Module and write it to the database. New procedures in the middleware were also written to retrieve real time and 15 minute average wind turbine data from the database. IPPSC's middleware was written in C# which provides an easy interface into Microsoft's .NET functions in Windows.

The stored procedures in the database that retrieves actual and forecasted data from the National Weather Service were modified. These procedures request data from NWS web servers and store the data in the IPPSC database. The procedures are scheduled to run in the database scheduler. The stored procedures and the database were modified to gather data and forecasts for humidity, wind speed, and wind direction. These are in addition to the temperature, cloud cover, and parametric pressure data that was already programmed to be collected. The stored procedures were also improved to eliminate

sporadic errors found when communicating with the NWS web services, which would periodically report back random errors when data was requested.

A new GUI screen was developed to display the wind turbine data and relevant weather predictions on the same page. A screen shot of this display is shown in Figure 332. The GUI was written in Labview.

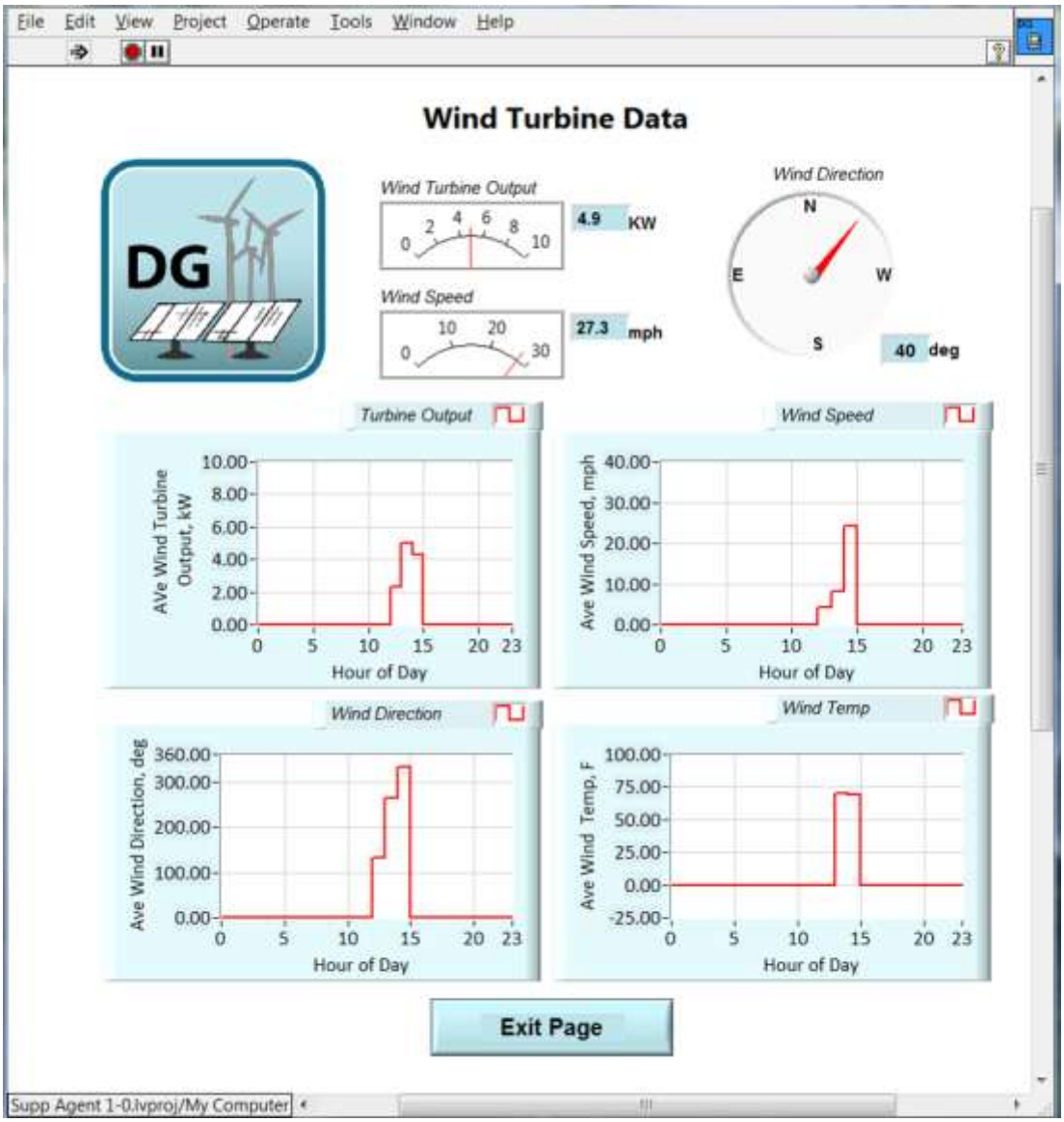

Figure 332: Screen Shot of IPPSC Wind Turbine Page

D6. Conclusions and Recommendations

A review of wind integration studies revealed several issues to consider in integrating wind energy resources in to IIT's microgrid. Since IIT to date has added only an 8 kW wind turbine on campus, these issue are not really severe enough to worry about. However, if the campus were to add a much higher percentage of the wind power, for example 20 to 30% relative to the campus's load, these issues should

be considered. The point of this research is to study these effects on a small wind turbine and to project how to handle these issues in a larger deployment of wind on campus.

In the interest of evaluating concerns with a large deployment of wind within the campus's microgrid, four categories of issues that might be of concern were identified:

- Large Variation in Wind Generator Output
- High Wind Generator Ramp Rates
- Power Factor
- Prediction Wind Generator Output

Microgrid master controller requirements were specified to help mitigate these issues, though some of the issues, such as power factor have more to do the details of the installation rather than the microgrid controls. The microgrid master controller requirements for wind integration are summarized below and pertain mostly when the campus is operating in island mode. When the campus is operating parallel to the grid, the utility supply will mitigate these issues for the campus and these issues will likely be passed on to the utility. The utility interconnection agreement for the wind turbines will likely address the issues in this case. The summarized list of microgrid master control requirements are:

- Make short term on long term predictions of wind output and ramp rates.
- Make adjustments to the campus reserve power requirements when operating in island mode.
- Be able to curtail wind power when wind intermittency and ramp rates as required to ensure the campus's power reliability and safety.
- Monitor distribution circuit power flows and curtail wind power if necessary to reduce over loading.

Non-controller issues that should be considered are:

- Though not necessary for installing the planed 8kW wind turbine on campus, in an larger scale deployment of wind on campus, the turbine ramp rate requirements should be evaluated against the expected ramp rates for the wind turbines to determine how much installed wind generation might start to cause ramp rate related issues on campus.

3.3 Wind Energy Education and Outreach

3.3.1 Wind Energy Training Facility Development

To fulfill our project tasks on workforce training and education, the project team erected a permanent facility at IIT for Workforce Training and Education on Sustainable Energy and Smart Grid. IIT secured funds from the State of Illinois to renovate the 16,000 sqft of space for establishing the proposed facility. This project provided funds to furnish the facility with the state-of-the-art equipment to offer a world-class training and education on sustainable energy at IIT. The proposed facility will provide training on sustainable energy to various sectors including power industry employees, union workers, high school teachers, the public, and students through instructor-led and internet-based training courses. The floor plan of the training facility is shown in Figure 333.

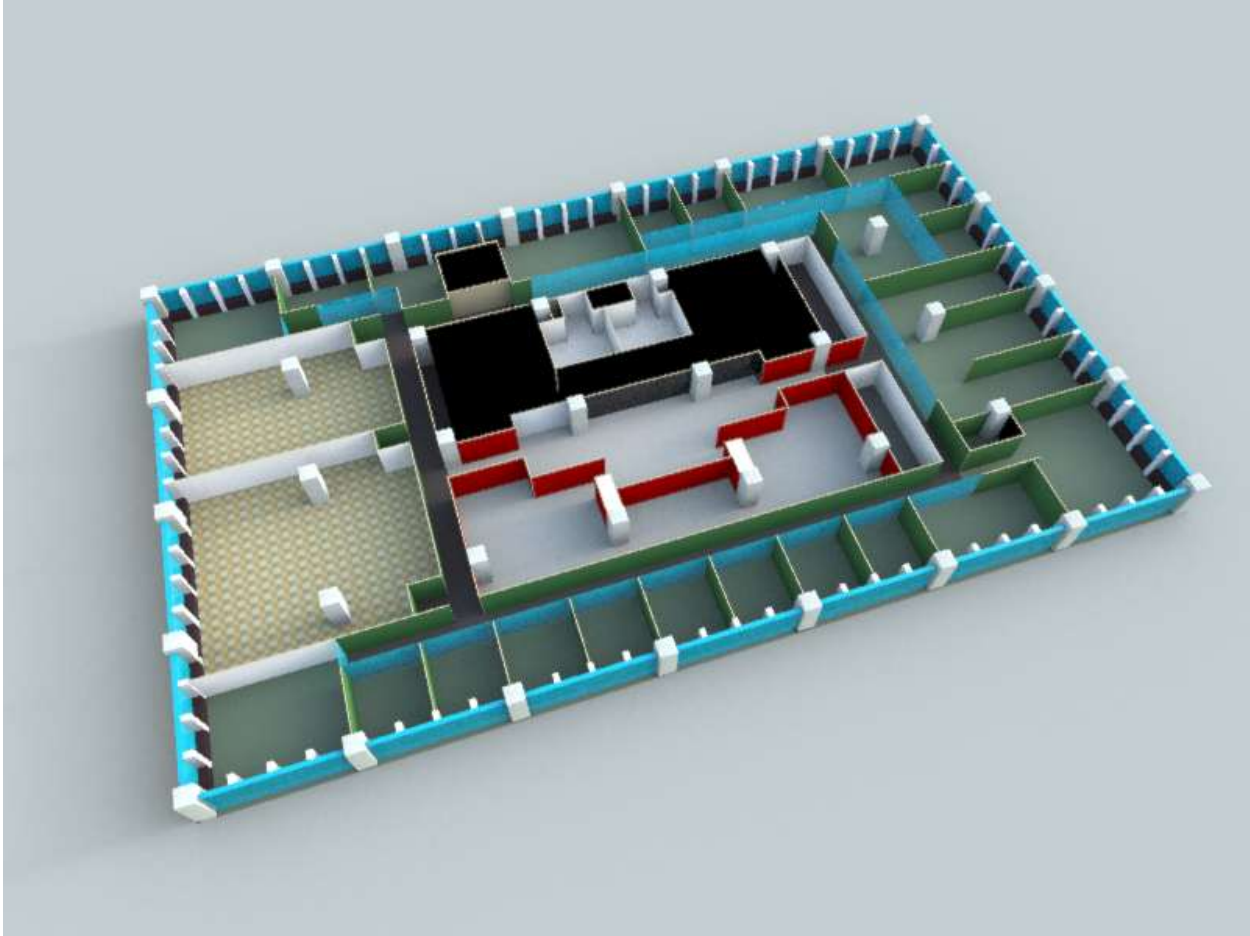

Figure 333: Floor plan of the training facility

A. Robert W. Galvin Center for Electricity Innovation

In 2010, Illinois Institute of Technology launched the Robert W. Galvin Center for Electricity Innovation, whose mission is to pursue groundbreaking work in the generation, transmission, distribution, management and consumption of electricity. The Galvin Center brings together faculty, students, researchers, industry, government, innovators, and entrepreneurs to collaborate to improve the reliability, security and efficiency of the electric grid and overcome obstacles to the national adoption and implementation of the Smart Grid. The center brings together researchers, industry, government, and innovators to "plug-in" to IIT's smart microgrid, research laboratories and technology park, creating a hub – or sandbox – for new innovations in advanced grid technology. IIT and the Galvin Center have become leaders of the Smart Grid technological revolution by building the first ever fully-functional Perfect Power system, a smart grid demonstration project, on IIT's Main Campus in Chicago.

- Pioneering Perfect Power – IIT and the Galvin Center have become leaders of the Smart Grid technological revolution by building the first ever fully-functional Perfect Power system, a smart grid demonstration project, on IIT's Main Campus in Chicago. The project eliminates blackouts, allows for "islanding" of the campus from the broader grid, integration of renewable energy and battery storage, and introduction of advanced smart buildings technology for energy efficiency. The Galvin

Center leadership is working with entities across the world to replicate and scale the microgrid model for communities, military bases, corporate parks, sports facilities, and other universities.

- IIT "Living Laboratory" for clean tech – IIT and the Galvin Center have transformed the IIT campus into a "Living Laboratory" for energy projects. This approach integrates advanced new technology demonstrations in visible locations with hands-on research and education opportunities for students and faculty. The technologies demonstrated as part of this approach include: building automation and control, master controller systems, rooftop solar, a wind turbine, electric vehicle charging stations, and large-scale batter storage.

- Smart Grid Workforce Training – The Galvin Center recently completed construction of a state-of-the-art facility to house its Smart Grid Education and Workforce Training Center. The 16,000-square-foot center contains offices, exhibition rooms, classrooms and student workrooms, acting as a living lab for Smart Grid and microgrid technology and education. The Center is engaging thousands of workers and students to accelerating the adoption of energy efficiency, renewable energy, and smart grid technologies across the world.

- IIT Wind Consortium – In 2009, the Galvin Center leadership was awarded a $9 million grant from the U.S. Department of Energy to establish a University-Industry Consortium for wind energy research and education. The Galvin Center leadership was also awarded $750,000 from DOE to study wind integration into the U.S. grid. The Consortium has engaged 50 companies and 8 universities in the U.S. and around the world in technological advances related to the next generation of wind energy manufacturing.

- Illinois Smart Grid Regional Innovation Cluster – IIT is leading the development of an innovation platform for Smart Grid technology that was awarded $1.5 million from the Small Business Administration. The Center is providing technical and business support to speed new Smart Grid technologies on the path to commercialization in Illinois.

- Global Smart Grid Technology Partnership – In 2011, the Galvin Center launched the Illinois-Korea Smart Grid R&D Collaboration, a joint international collaboration to accelerate the technological development of smart grid in Chicago. The Korea industries have awarded the Galvin Center a $2.5 million project for the installation of phasor measurement units (PMUs) at the IIT's microgrid. This partnership is intended to stimulate new interactions among stakeholders in Chicago and Korea and bring additional manufacturing jobs to Illinois.

The Galvin Center has led more than $40 million in projects with funding from the government and private sectors for research and development in microgrids, smart grid technology, and sustainable energy. All of these projects have been completed on-time and within budget. IIT has designated the campus as a "Living Laboratory" for smart grid, microgrid, and other energy technologies, training facility staff and other personnel on the operation, maintenance and repair of these and new technologies. This innovative partnership between facility managers and a research unit is one of the first of its kind in the U.S.

State-of-the-Art Facility. In January 2012, the Galvin Center completed and moved into a new, state-of-the-art facility designed to house its Smart Grid, microgrid and energy research, demonstration and education activities. Located on the 16th floor of the IIT Tower, the 16,000-square-foot center contains offices, exhibition rooms, classrooms and student workrooms, acting as a hands-on experience center for Smart Grid, microgrid and energy technology and education. The $3 million project was funded by the State of Illinois, U.S. Department of Energy and IIT.

Figure 334: State-of-the-art facility at the Galvin Center

Perfect Power System. In 2011, the Galvin Center completed the world's first Perfect Power System on its main campus in Chicago. Inspired by the leadership of Bob Galvin, the center's premier project is the development of the nation's first Perfect Power microgrid at IIT. When fully completed in the next year, the $14 million project has equipped IIT's microgrid with a new high-reliability distribution system for enhancing reliability, the ability to integrate new sustainable energy sources (roof-top solar panels, wind generation units, flow batteries and charging stations for electric vehicles), and smart building automation technology (building controllers, Zigbee sensors, controllable loads) for energy efficiency and demand response. The high-reliability distribution system was completed in 2011, allowing IIT to eliminate blackouts.

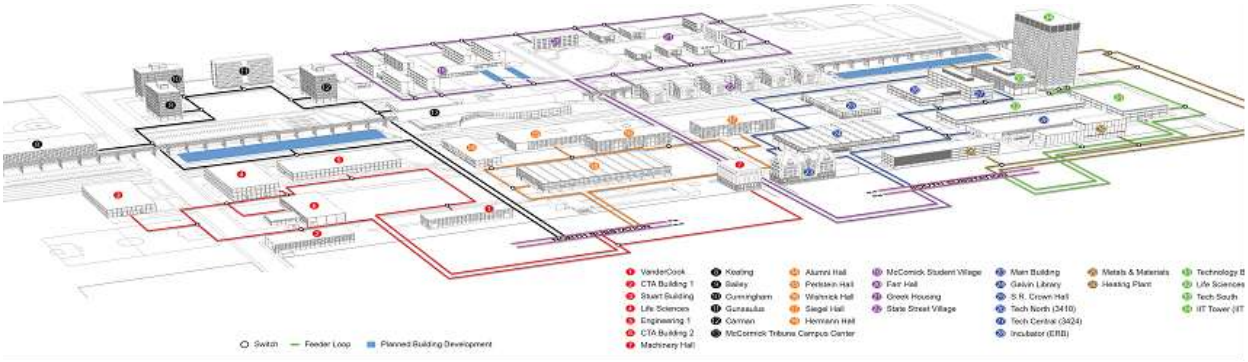

Figure 335: IIT Perfect Power System overview

Electric Vehicle Charging Stations. In 2012, the Galvin Center completed the installation of 7 Electric Vehicle charging stations on its main campus in Chicago. The installation includes 6 "Level 2" charging stations for 5-hour EV charging, and one of the first DC Quick Charge EV charging stations in the country, which can charge a vehicle in 20-30 minutes. The $120,000 project was funded by the U.S. Department of Energy and private partners.

Figure 336: IIT Electric Vehicle Charging Stations

Rooftop Solar. In 2012, the Galvin Center completed the installation of a 60 kW of rooftop solar on two campus buildings: Siegel Hall and Stuart Building. The $440,000 project was funded by the U.S. Department of Energy, the State of Illinois and private partners.

Figure 337: IIT Rooftop Solar Installation

Large-Scale Battery Storage. In 2012, the Galvin Center completed the installation of a next-generation smart grid-capable large-scale battery project on IIT's microgrid testbed for demonstration and evaluation. Produced by the ZBB Corporation, the 500 kWh zinc-bromide flow battery will be the first-of-its-kind in the U.S., demonstrating the ability of microgrid systems to island, coordinate peak load management and peak shaving, and provide backup power. The $1,000,000 project was funded by the U.S. Department of Energy, with cost-share provided by ZBB Corporation.

Figure 338: IIT Large-scale Battery Storage

B. WINS: Wind Integration Simulator

Wind Integration Simulator (WINS) is a decision tool that can facilitate the analyses for the integration of 20% or more wind energy. The development of WINS is funded by the U.S. Department of Energy and completed at Illinois Institute of Technology (IIT). WINS explores innovative solutions for continuing reliable operation of existing grid with the most economic integration of additional wind energy. WINS offers scheduling of wind power across interties and adopting new transmission for wind integration. WINS represents advanced features for the modeling and simulation of energy storage, DC transmission lines, hourly wind availability and system reserves, transmission utilization and congestion studies, optimal production costing and nodal price calculations, and advanced visualization techniques for representing the hourly results and facilitates operator training for wind integration. WINS represents a major expansion of a very efficient decision tool called Power Market Simulator (POMS), which was developed by IIT and has been used extensively for power system studies for decades. POMS offers outstanding features for power market simulation which will be embedded into WINS. WINS focuses on augmenting the existing power utility capabilities to support collaborative planning, analysis, and implementation of wind integration. In particular, WINS provides the following superiorities:

- An integrated framework is included in WINS for the comprehensive modeling of DC transmission configurations, including mono-pole, bi-pole, tri-pole, back-to-back, and multi-terminal connection, as well as AC/DC converter models including current source converters (CSC) and voltage source converters (VSC).
- An existing shortcoming of traditional decision tools for wind integration is the limited availability of user interface, i.e., decision results are often text-based demonstrations. WINS includes a powerful visualization tool and user interface capability for transmission analyses, planning, and assessment,

which will be of great interest to power market participants, power system planners and operators, and state and federal regulatory entities.

- WINS can handle extended transmission models for wind integration studies. WINS models include limitations on transmission flow as well as bus voltage for analyzing power system states. The existing decision tools often consider transmission flow constraints (dc power flow) alone which could result in the over-utilization of existing resources when analyzing wind integration.

The input WINS data include (1) generation data (unit type, capacity, availability; cost information; unit operating constraints such as max/min capacities, ramping up/down rates, min on/off times, maximum number of start-ups); (2) wind data (8760 hourly profile); (3) transmission data (network topology, line parameters, control transformers, normal/contingency limits for line flows and bus voltages); and (4) load data (hourly load and distribution, demand bids and load shedding cost and data).

WINS simulates the actual market operations which is based on the security-constrained unit commitment (SCUC) with full AC transmission and voltage constraints considered. The computational engine of WINS is written in Microsoft Visual C++, and the Graphical User Interface (GUI) is written in Microsoft Visual C# and ASP.NET. The database is based on ORACLE and can be extended to include other database formats as well. Microsoft Excel is used for the downloading reports.

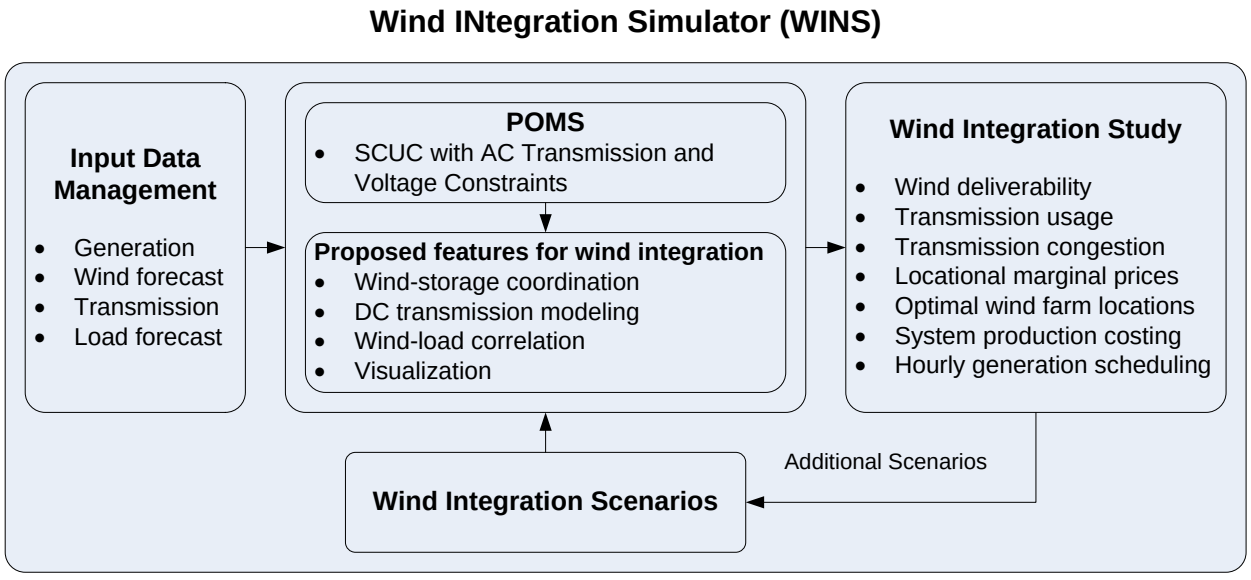

Figure 339: Architecture for the Design and the Implementation of WINS

C. Situation Awareness at Control Center: e-terravision

e-terravision is a system that was jointly developed by Alstom Grid with major utilities, a situation awareness expert, and in partnership with Microsoft for the use of the latest graphics technology. This system addresses the need for enhanced situation awareness in control centers. e-terravision is a relatively new product suite whose main purpose is to supplement control rooms with higher-level

decision support capability using visualizations for improving situation awareness. E-terravision complements Energy Management System (EMS) and Market Management System (MMS) user interfaces.

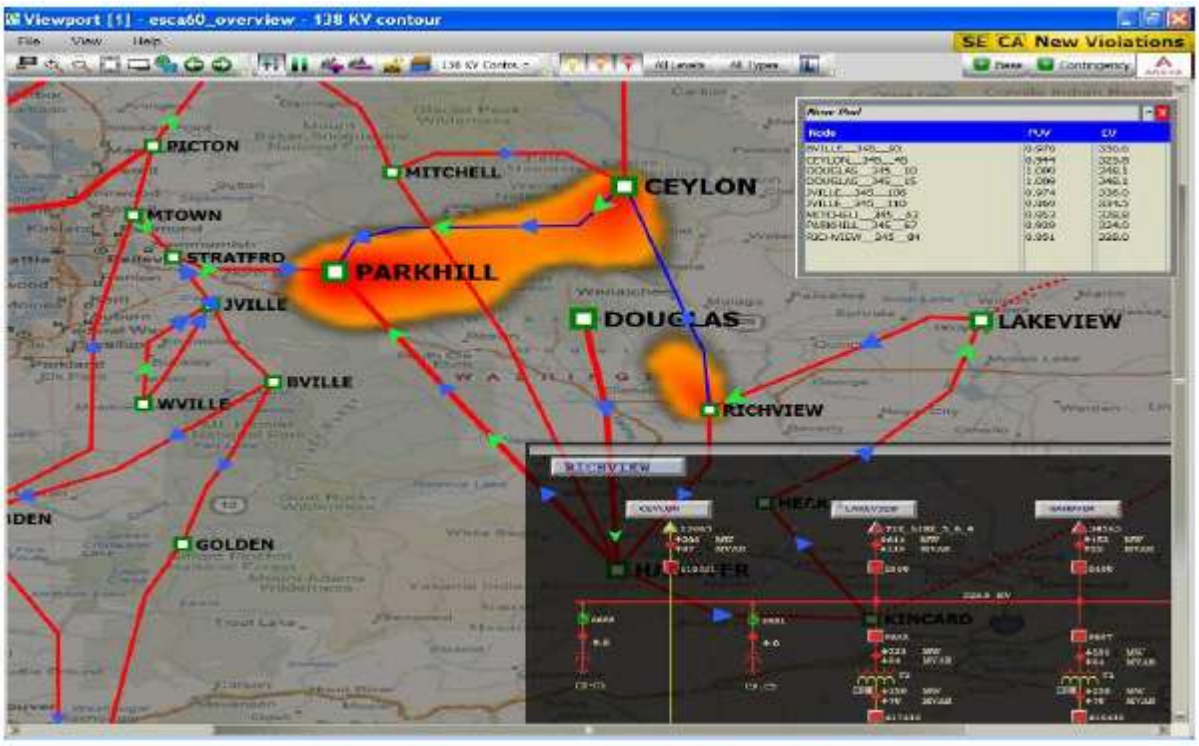

Figure 340: Enhanced Situation Awareness in Control Centers

The goals for e-terravision are to implement a control center "situation awareness" framework and tools to:

- Mitigate operational risks
- Present wide-area and "big picture" views of the system
- Assist in ensuring system reliability
- Increase the productivity of control center resources

With e-terravision, control room, operators can:

- Monitor the transmission network with large overviews,
- Assess the grid's reliability using advanced visualization,
- Perform predictive analysis, and
- Prioritize corrective actions.

3.3.2 Wind Energy Course Development

A. Engage Undergraduates in Wind Energy Research

A1. Interprofessional Projects at Illinois Institute of Technology

The Interprofessional Project (IPRO) course at IIT is a general education requirement. Specifically, all undergraduates must participate in at least two interprofessional project experiences to receive their respective Bachelor's degree. The IPRO program is described at http://ipro.iit.edu/about: "The IPRO program joins together students from various academic disciplines to work as a team to tackle a real-world problem. Students from architecture, engineering, and humanities may create low-cost shelter solutions, or chemistry, business, and law students may develop best practices in CO2-reducing technologies. Such experiential learning reinforces traditional education methods, providing students a richer academic experience. Each IPRO course is organized as a team of 5-15 students from sophomore to graduate level. All projects are designed with goals that can be completed in one semester. However, many projects continue over multiple semesters and years, with continuing areas of investigation. No two semesters are ever alike." "Teamwork, innovation, and complex problem-solving skills make successful professionals—and reflect the overall performance of their organizations. Since 1995, the IPRO team project course at IIT has been teaching students how to excel in the workplace by providing them the practical tools that can make a difference in their professional and personal lives."

A2. Integration of Plug-in Hybrid Electric Vehicles and Renewable Energy Systems

The purpose of the research project is to investigate the economic effects of the integration of wind power generation systems and PHEVs. For wind generations it is important to investigate factors that impact the generation of wind, like location of the wind farm, speeds of wind in the specific location, type of turbine and its characteristics. In the case of PHEVs a significant research on driving habits, type of battery and its life will be pursued. The final goal of the research is to determine the effectiveness of the method on lowering the operational cost by analyzing various cases which introduce the use of PHEVs into the power generation system. The results obtained from the research will serve targeted markets including, but not limited to, automotive industry, wind power generation industry, and utility companies. The advancement of alternative energy technology will also benefit the environment.

Organization and Approach

The problem of creating a basic model for the purpose of studying the effects of the integration of PHEVs and wind energy is split into four parts; wind energy, PHEVs, power generation costs, and creation of an objective function to minimize the operational cost of the model. These four parts are split up between the members of the group, who are responsible for researching their topic and reporting back to the team.

The first three parts require finding the necessary data regarding the topic. Analysis of how the data is to be used in the objective function, namely as a cost function or power curve, is determined. This determination requires deciding which variables are pertinent to the topic.

Conclusions for the initial three parts of the approach are used in the formulation of the objective function. The objective function is subsequently utilized to determine the effectiveness and feasibility of integration of PHEVs with wind energy.

Wind is one of the most important renewable energies used to generate electric energy. Wind energy is clean, renewable, and a potentially cost efficient method for energy production. The American Wind Energy Association AWEA notes that "wind power is one of the fastest growing methods of electricity generation in the United States. Approximately 40 % of all new generation capacity contributing to the power grid in the United States was from wind power projects in the recent years." [**97**] The U.S. Department of Energy's goal is to have 20% wind power generation by 2030 [**1**].

The downside of wind energy is that wind is typically intermittent. When wind is present, the laws of thermodynamics state that it is not possible to translate all the kinetic energy in wind into the same amount of electrical energy. Moreover, the implementation of more wind power to the grid will create storage problems. Wind will inevitably be available when electricity demand is low. Ideally, there would be a method or apparatus for storing the wind energy for use when electricity demand is low. PHEVs are a potential solution to the electrical energy storage problem.

When studying wind generation, it is important to take into account different variables such as, the speed of wind in a determined place, turbine location, and turbine characteristics. For the project's investigated system the above stated variables have been analyzed. The analysis of the problem has allowed for assumptions regarding some of the variables as constants to permit the simulation of a scenario to determine the feasibility of wind energy. The variables analyzed are described below.

A wind map is a useful tool to locate the areas of the United States where the winds are the highest. This map bases its determination of particular areas on the wind's annual average speed and power. For the study of this particular research project, an urban area of Chicago, Illinois is the focus of the group research interest for the simulation. Figure 341 shows the map of wind speeds at 80 meters above the ground level for Illinois [**98**]. Chicago is indicated as the spot where the turbines are going to be sitting.

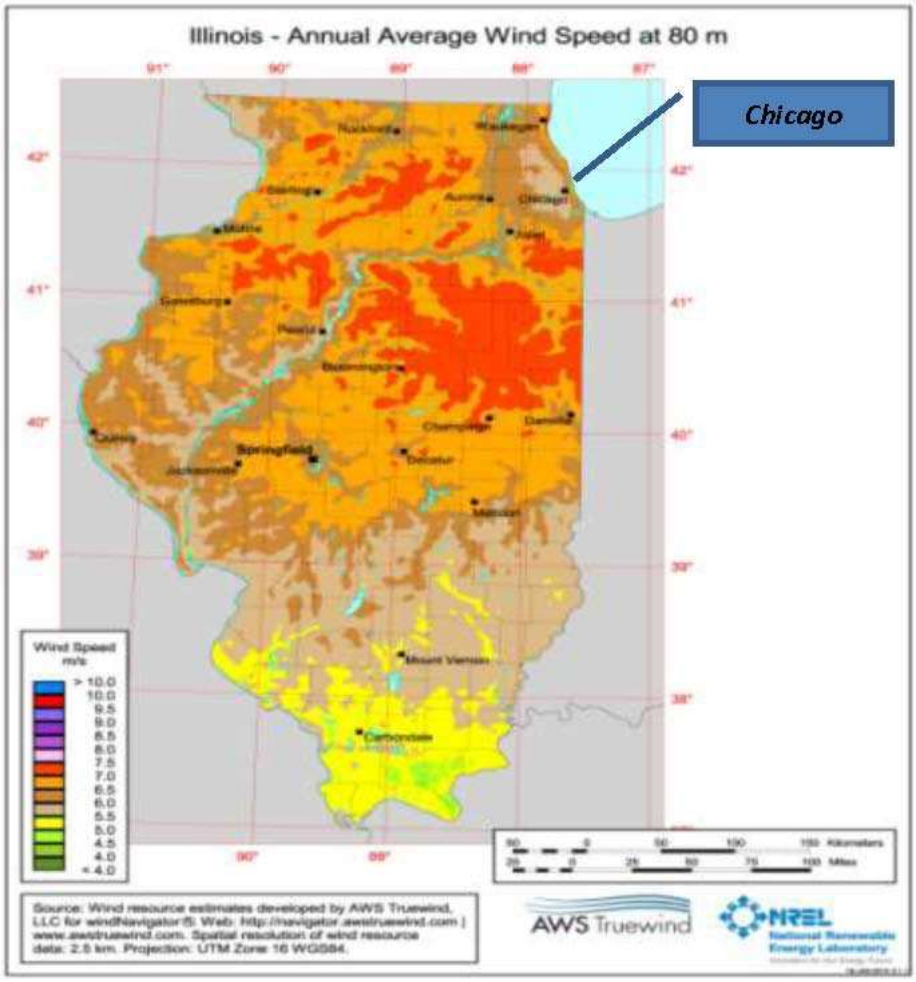

Figure 341: Wind map supplied by the U.S. Department of Energy

Having determined the location of a wind turbine, it is now possible to determine the friction coefficient and the roughness length which enables calculation of wind speed. The friction coefficient is a quantity that is used to quantify the resistance that an object imparts on wind flow. Obtaining the values of friction coefficient will allow for calculation of the wind speed at ground level. These values are taken into account when forecasting wind speeds. Since friction coefficient is already included in the forecast calculated data, it is not necessary for the research to obtain the friction coefficient value at this point. The research uses a 24 hour wind forecast to determine the wind speed per hour. The data will be considered for the months in which the winds are at their yearly average speeds. This speed forecast gives the speeds at ground level in the Chicago urban area. Table 21 shows the wind speed forecasted values.

Table 21: 24 hour forecasted wind speeds.

Time	Wind Speed [mph]	Wind Speed at Ground Level [m/s]
12am	8	3.576
1am	8	3.576
2am	8	3.576
3am	8	3.576
4am	8	3.576
5am	9	4.023
6am	9	4.023
7am	9	4.023
8am	9	4.023
9am	9	4.023
10am	8	3.576
11am	8	3.576
12pm	8	3.576
1pm	8	3.576
2pm	8	3.576
3pm	10	4.47
4pm	10	4.47
5pm	10	4.47
6pm	10	4.47
7pm	11	4.917
8pm	11	4.917
9pm	11	4.917
10pm	8	3.576
11pm	8	3.576
Average	*8.917*	*3.986*

The roughness length (z) [meters] depends on the terrain where the wind turbines are located. Roughness length is used to find hourly wind speed 80 meters above ground level. The values of roughness length are tabulated according to terrain conditions and roughness class. The terrain conditions are the characteristics of the various places where the turbines can be located. The roughness class is the rating of the terrain in ascending form. A value of zero is assigned to less rough terrain such as a water surface. A value of four is assigned the roughest terrain such as a dense urban area or forest. For the case of urban districts and farm lands with many windbreaks (obstacles) the roughness length is equal to 0.4 meters.

The equation to calculate the wind at a height above the ground level is shown below.

$$v = v_{ref} \frac{\ln \frac{z}{z_0}}{\ln \frac{z_{ref}}{z_0}} \quad (95)$$

Where,
v is wind speed at height z above ground level;
z is height above ground level for the desired velocity (v);
z0 is roughness length in the current wind direction;
zref is the height where the exact wind speed, vref, is known.

Table 22 shows the values of wind speed at 80 meters above ground level.

The Vestas V90 wind turbine is selected for research analysis. The performance, mechanical, and physical characteristics are listed in Table 23.

The maximum power that wind can produce in a determined area depends on blade size of the turbine and density of air. Note that the values of maximum power do not take into account the losses incurred from transformation of kinetic energy to electrical energy.

The following equation shows the maximum wind power equation.

$$P_{total} = \frac{1}{2} \cdot \rho \cdot R^2 \cdot \pi \cdot v_b^3 \quad (96)$$

Where,

ρ is the air density;
R is the radius of the blades;
vb are the wind speeds after and before passing through the turbine.

Wind turbines cannot absorb all the wind available in a certain location. Equation 3 calculates the turbine's captured power.

$$P_{total} = \frac{1}{2} \cdot \rho \cdot c_p \cdot R^2 \cdot \pi \cdot v_b^3 \quad (97)$$

Where cp is the power coefficient.

The power coefficient is the ratio of the electrical output power of the wind turbine to the total (potential) wind power. The values of the power coefficient depend on the type of turbine and are usually provided by turbine manufactures. For this specific case the power coefficient is 0.44.

The turbine does not output more than is specified by the generator. Therefore, 1.8 MW is the maximum power that the turbine used for this case of study can provide. In order not to surpass this value most turbines have mechanisms which prevents excessive angular velocity thereby preventing

mechanical failure of the turbine. One mechanism used is the pitch control which rotates around the turbines longitudinal axis of the blades to control the amount of wind energy captured.

The maximum power output for the simulation is set to 75 MW. 42 Vestas V90 turbines are required to produce 75 MW

$$\frac{75\ MW}{1.8\ \frac{MW}{turbine}} = 42\ turbines$$

Table 24 shows the maximum power, the captured power and the power produced by 42 turbines in a 24 hour window. Figure 342 shows the Power Output curve for 42 turbines outputting a maximum of 75 MW.

A PHEV is a vehicle that uses both an internal combustion engine and an electric motor, which utilizes an externally or internally charged battery. The distance the battery can solely drive the car is referred to as the All Electric Range (AER). The type of car that is focused on in this project is termed PHEV40, which has an AER of forty (40) miles. Another type of PHEV is the PHEV20, which can drive the car solely on the battery for approximately twenty (20) miles. The PHEV40 will be used for the reasons listed below.

- There are statistics from the University of Michigan Transportation Research Institute (UMTRI) that show the average distance traveled per day for Americans is about 40 miles with a standard deviation of about 10 miles.
- The current price for low-weight lithium ion batteries for use in PHEVs is relatively high: $400-700/kWh [**97**]. Therefore, the maximum battery pack size is limited, but this may change in the future as technology reduces battery cost.
    - Low weight batteries are preferred because the weight of the car has a great impact on the energy efficiency, and therefore, AER range of the vehicle.

A measure of the battery is its State of Charge (SOC), which is the percentage that the battery is charged. A battery cycle is defined as fully charging and discharging a battery, from its manufactured minimum SOC to maximum SOC. Batteries that go through too many cycles too often will have a reduced capacity and battery life. In order to increase the battery life, the usable SOC of the battery is limited to only half of its capacity. The model used in analysis is the Chevrolet Volt. Some specifications for the Chevrolet Volt are listed below [**99**]:

- Total battery size of 16 kWh
- SOC range of 0.3 to 0.85
- Battery energy range of 4.8 kWh to 13.6 kWh, which reflects the SOC range

Table 22: 24 hour wind speed values at 80 meters above ground level.

Time	Wind Speed [mph]	Wind Speed at Ground Level [m/s]	V @ 80 m above ground [m/s]
12am	8	3.576	8.058
1am	8	3.576	8.058
2am	8	3.576	8.058
3am	8	3.576	8.058
4am	8	3.576	8.058
5am	9	4.023	9.066
6am	9	4.023	9.066
7am	9	4.023	9.066
8am	9	4.023	9.066
9am	9	4.023	9.066
10am	8	3.576	8.058
11am	8	3.576	8.058
12pm	8	3.576	8.058
1pm	8	3.576	8.058
2pm	8	3.576	8.058
3pm	10	4.47	10.073
4pm	10	4.47	10.073
5pm	10	4.47	10.073
6pm	10	4.47	10.073
7pm	11	4.917	11.08
8pm	11	4.917	11.08
9pm	11	4.917	11.08
10pm	8	3.576	8.058
11pm	8	3.576	8.058
Average	*8.917*	*3.986*	*8.982*

Table 23: Vestas V90 wind turbine characteristics.

Model	Capacity [MW]	Blade Length [m]	Hub Height [m]	Total Height [m]	Area Swept by blades [m^2]	RPM Range	Maximum Blade Tip Speed [m/s]	Rated Wind Speed [m/s]
Vestas V90	1.8	45	80	125	6,362	8.8-14.9	70	11

Table 24: Maximum power, captured power, and produced power by 42 turbines.

Time	Wind Speed [mph]	Wind Speed at Ground Level [m/s]	V @ 80 m above ground [m/s]	P [MW]	Pcaptured [MW]	P output [MW]	nominal P @ 42 turbines [MW]	Pcaptured @ 42 turbines [MW]
12am	8	3.576	8.058	2.041	0.898	0.898	85.712	37.713
1am	8	3.576	8.058	2.041	0.898	0.898	85.712	37.713
2am	8	3.576	8.058	2.041	0.898	0.898	85.712	37.713
3am	8	3.576	8.058	2.041	0.898	0.898	85.712	37.713
4am	8	3.576	8.058	2.041	0.898	898	85.712	37.713
5am	9	4.023	9.066	2.906	1.279	1.279	122.039	53.697
6am	9	4.023	9.066	2.906	1.279	1.279	122.039	53.697
7am	9	4.023	9.066	2.906	1.279	1.279	122.039	53.697
8am	9	4.023	9.066	2.906	1.279	1.279	122.039	53.697
9am	9	4.023	9.066	2.906	1.279	1.279	122.039	53.697
10am	8	3.576	8.058	2.041	0.898	0.898	85.712	37.713
11am	8	3.576	8.058	2.041	0.898	0.898	85.712	37.713
12pm	8	3.576	8.058	2.041	0.898	0.898	85.712	37.713
1pm	8	3.576	8.058	2.041	0.898	0.898	85.712	37.713
2pm	8	3.576	8.058	2.041	0.898	0.898	85.712	37.713
3pm	10	4.47	10.073	3.986	1.754	1.754	167.406	73.659
4pm	10	4.47	10.073	3.986	1.754	1.754	167.406	73.659
5pm	10	4.47	10.073	3.986	1.754	1.754	167.406	73.659
6pm	10	4.47	10.073	3.986	1.754	1.754	167.406	73.659
7pm	11	4.917	11.08	5.305	2.334	1.8	222.818	75.6
8pm	11	4.917	11.08	5.305	2.334	1.8	222.818	75.6
9pm	11	4.917	11.08	5.305	2.334	1.8	222.818	75.6
10pm	8	3.576	8.058	2.041	0.898	0.898	85.712	37.713
11pm	8	3.576	8.058	2.041	0.898	0.898	85.712	37.713
Average	*8.917*	*3.986*	*8.982*	*2.953*	*1.299*	*1.233*	*124.034*	*51.77*

The large size of the PHEVs battery allows it to be used as an energy storage system; when not in use, the PHEV can be used to feed energy back into the power grid. This interaction of the vehicle with the power grid called Vehicle to grid (V2G) technology. V2G used during peak grid demand hours can reduce the cost of the grid operations but will also increase the cycling rate of the battery, reducing its capacity and life. The Chevrolet Volt is able to charge at two speeds; fast and slow. Fast charging occurs at 240V and takes 3 hours to charge the battery from minimum SOC to maximum SOC. Slow charging

occurs at 120V and takes 8 hours to charge the battery. Slow charging is the charging rate assumed for analysis simulations.

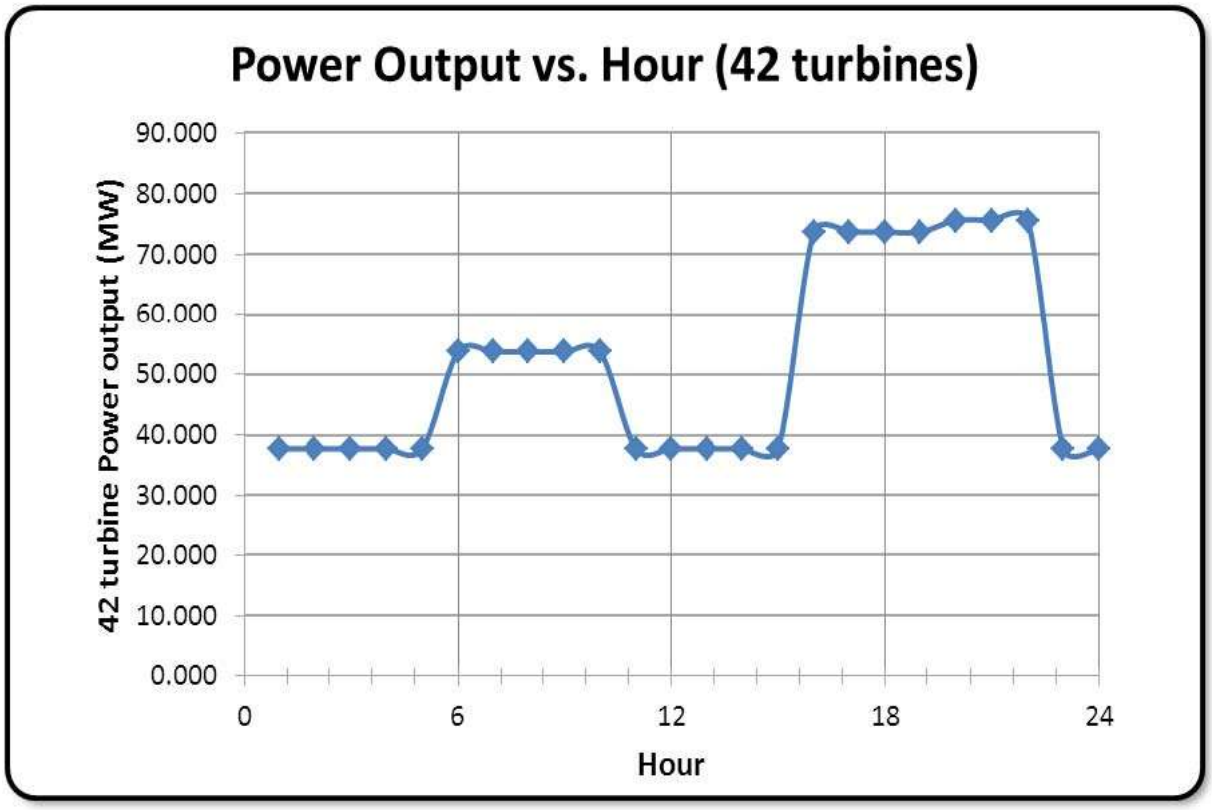

Figure 342: Power output vs. Hour for 42 turbines.

In order to derive an objective function with which to optimize the operational cost of the integrated PHEV and wind energy system, it is necessary to come up with several scenarios describing PHEV charging times and times that the PHEV would utilize V2G. The scenarios are created assuming the fleet of PHEVs leave home charging stations and travel to work between the hours of 8:00 am and 10:00 am and return home between the hours of 5:00 pm and 7:00 pm. The scenarios are varied by assuming certain percentages of the fleet would have differing states of charge and are discharging or charging during different parts of the day. From these scenarios an hourly load curve is generated for the PHEVs. Using the PHEV's load curve, the objective function is used to simulate the associated operational costs.

The power system optimal operational cost is the least amount of cost used to create electrical power to satisfy the load demand in a specific time. The power system operational cost is different from one generator to the other generator based on the type and the efficiency of energy convergence.

To compare and find the best optimal operational cost, objective function is used. The objective function is a function that enables to find the optimum value (either largest or smallest) by comparing all possible situations. However, the objective function is only effective on a linear function.

In this case the objective function is used to find the minimum operational cost spent by operating 3 conventional generators and 42 wind generators (wind farm). It is assumed that there is no operational cost for wind generators because they are the renewable resources. The cost functions of each generators is given in a polynomial way; $fG1 = c + b*X + a*X^2$ (the cost function for the 1st generator). In our case the coefficients of cost function, a, b, and c, are given but it can be obtained by analyzing the cost vs. time graph. The coefficients of cost function for generators are shown in Table 25.

Table 25: The coefficients of cost function for generators

Unit	a [$/MW^2]	b [$/MW]	c [$/h]	P_{min} [MW]	P_{max} [MW]
G1	0.099	6.589	211.4	100	320
G2	0.203	7.629	217.4	10	160
G3	0.494	10.07	102.8	10	100
Wind	0	0	0	37.7	75.6

Table 26: Linearized cost functions for generators

Dispatch	Gen1	Gen2	Gen3
P1(MW)	100	10	10
F1($)	1860.3	313.99	252.9
P2(MW)	120	30	30
F2($)	2427.68	628.97	849.5
P3(MW)	140	50	50
F3($)	3074.26	1106.35	1841.3
P4(MW)	160	70	70
F4($)	3800.04	1746.13	3228.3
P5(MW)	180	90	90
F5($)	4605.02	2548.31	5010.5
P6(MW)	200	110	110
F6($)	5489.2	3512.89	7187.9
P7(MW)	220	130	
F7($)	6452.58	4639.87	
P8(MW)	240	150	
F8($)	7495.16	5929.25	
P9(MW)	260	170	
F9($)	8616.94	7381.03	
P10(MW)	280		
F10($)	9817.92		
P11(MW)	300		
F11($)	11098.1		

P12(MW)	320		
F12($)	12457.48		

Table 27: Slopes of the linearized cost functions for generators

Segment	Gen1	Gen2	Gen3
1	28.369	15.749	29.83
2	32.329	23.869	49.59
3	36.289	31.989	69.35
4	40.249	40.109	89.11
5	44.209	48.229	108.87
6	48.169	56.349	
7	52.129	64.469	
8	56.089	72.589	
9	60.049		
10	64.009		
11	67.969		

At first, the power capacity should be divided as a certain value and the cost should be measured by each segments. In our case, we divided each segments by 20 MW power generations. We assumed all the generators are operating (never shutting down) so each generators are analyzed from the minimum power generations. The wind generators are not analyzed because of the assumption that there is no operational cost. The data is shown on Table 26.

Secondly, using the data from the Table 26, it is possible to calculate the gradient on each segment Table 27. At last, linear cost function is obtained. For example, the cost function for the 1st generator can be re-written as fG1 = 1860.3 + 28.369*X1,1 + 32.329*X1,2 + 36.289*X1,3 + 40.249*X1,4 + 44.209*X1,5 + 48.169*X1,6 + 52.129*X1,7 + 56.089*X1,8 + 60.049*X1,9 + 64.009*X1,10 + 67.969*X1,11. The code to find the minimum operational cost is attached on the appendix.

Analysis and Findings

The four cases that utilize PHEVs are labeled as Scenario 1, Scenario 2, Scenario 3, and Scenario 4. These scenarios were developed as a way to test the operational cost on the grid due to the introduction of PHEVs. The factors that affect the operational cost include the time of charging of the PHEVs and the time of V2G of the PHEVs. These PHEVs move around the six-bus system as fleets, with a total fleet size of ten thousand (10,000) units. We have designated bus 6 as the homes of the owners of the PHEVs and bus 4 as the workplace of the owners of the PHEVs. All cars stay at home at night, go to work in the afternoon, and come back home in the evening.

Throughout the research we analyzed 6 different scenarios to find the effectiveness of integrating wind energy and PHEV to the current system. All the scenarios are analyzed in a 6-bus system shown in Figure 343. The 6-bus system is the most commonly used system to simulate the real world. As you can see from the diagram below, we have 2 load bus, 2 generator bus, 1 wind generator & load bus, 1 generator & load bus. PHEV moves from one bus to the other bus. We assumed that there is no fault in the system, there is no transmission line loss, and there is no operational cost for wind power generation.

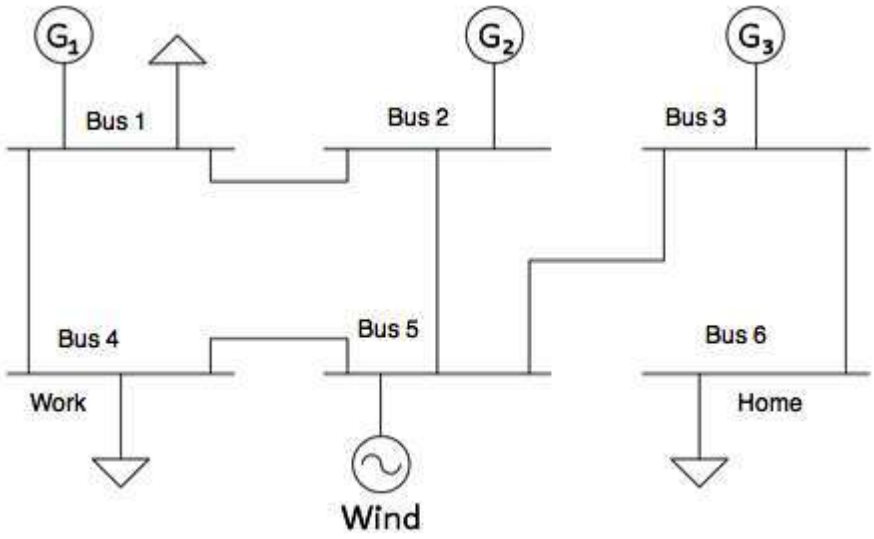

Figure 343: One-line Diagram of the 6-bus System

In this analysis, we are going to analyze the result in two ways. At first, we are going to observe how peak hour changes as wind energy and PHEV are integrated. Secondly, we are going to observe the total operational cost and find the best scenario based on it. The first scenario is the 6 bus system that doesn't have any wind energy. We are investigating the following scenarios:

Scenario 1: No wind
Scenario 2: Only wind
Scenario 3: PHEVs, no V2G, and night G2V (grid-to-vehicle)
Scenario 4: PHEVs, day time V2G, and night G2V
Scenario 5: PHEVs, evening V2G, and night G2V
Scenario 6: PHEVs, afternoon G2V, evening V2G, and night G2V

The peak demand is between 8:00pm to 10:00pm. The average load demand in an hour at this area is 261MW. As we said, we are going to observe how this peak demand changes as wind energy and PHEVs are integrated. Besides, we can also observe the patterns of power generation in 24 hours. For example from 2:00am to7:00am, 1st generator supplies 120MW, 2nd generator supplies 50MW, 3rd generator supplies from 22 MW to 26MW depending on the time.

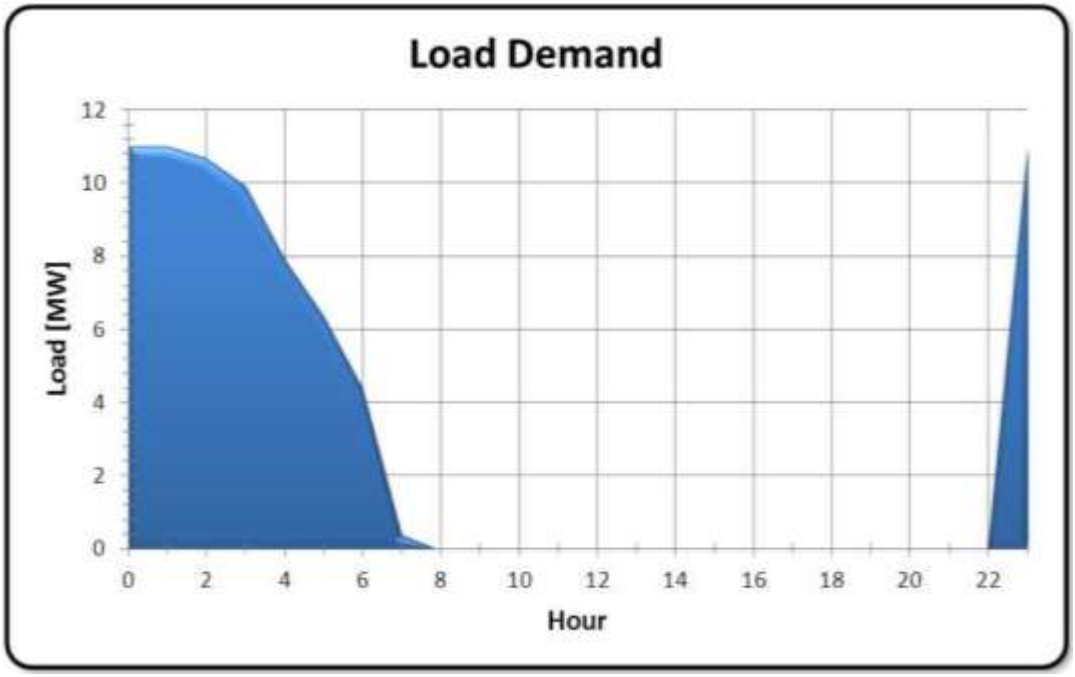

Figure 344: Scenario 3 PHEV Load Demand

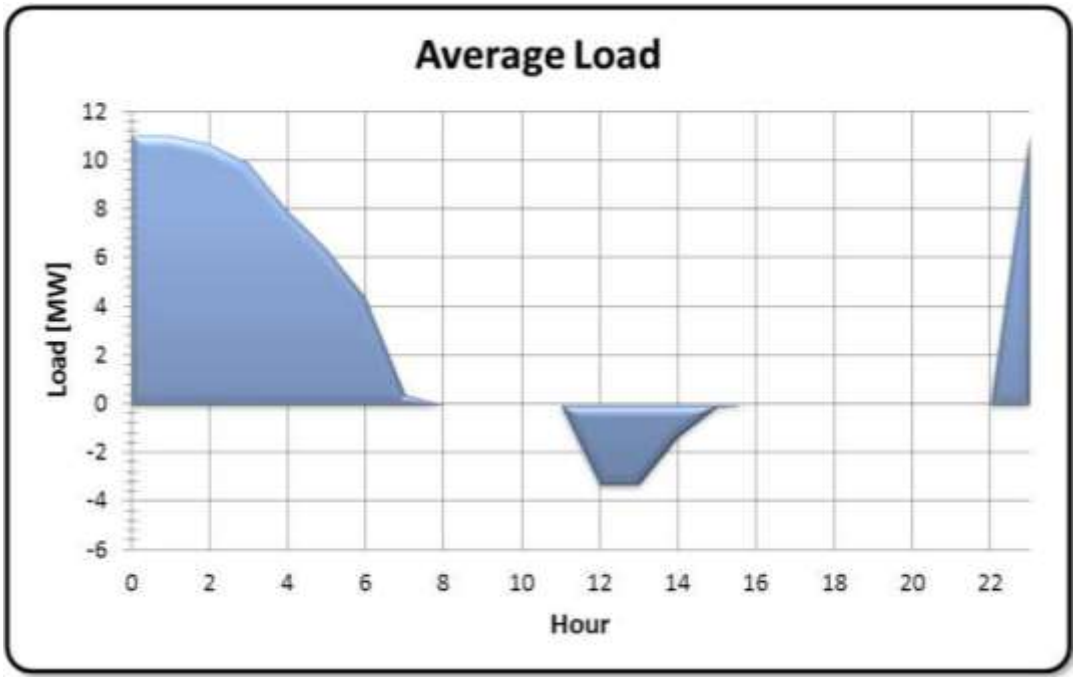

Figure 345: Scenario 4 PHEV Load Demand

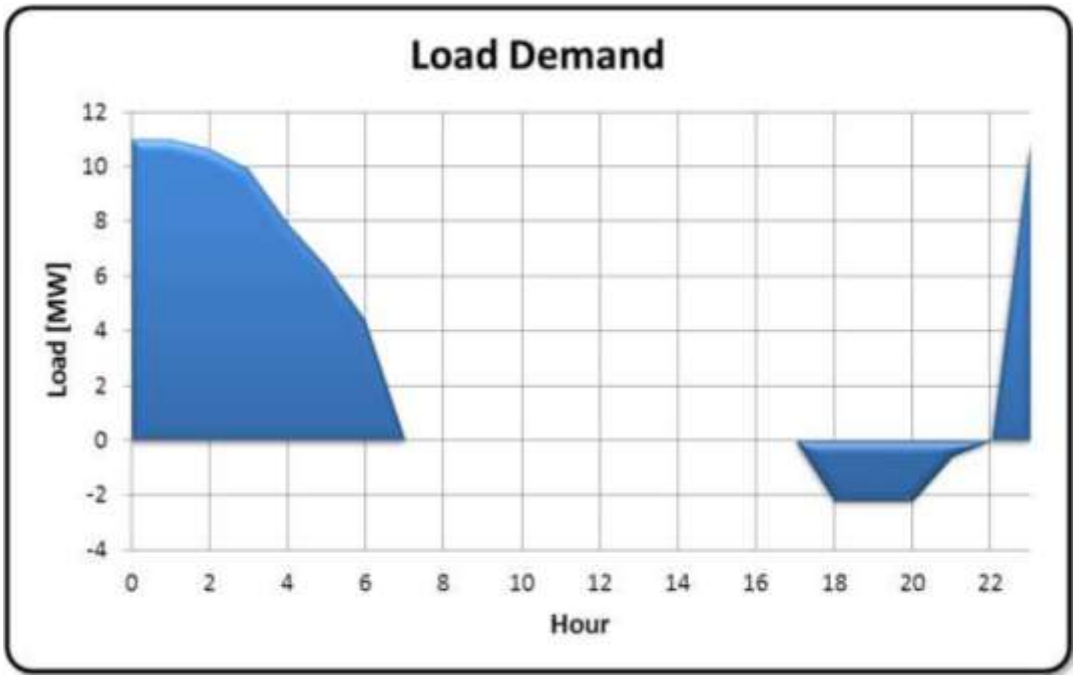

Figure 346: Scenario 5 PHEV Load Demand

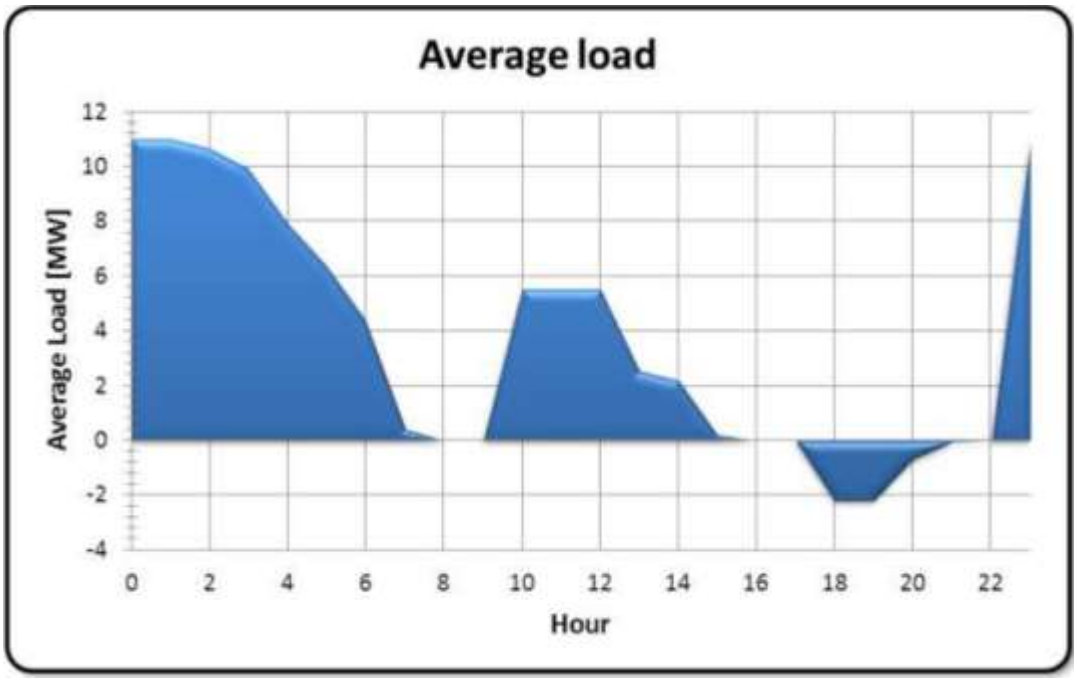

Figure 347: Scenario 6 PHEV Load Demand

It is shown that the cheapest way to generate 1MW after the 1st generator reaches 120MWand 2nd generator reaches 50 MW would be the generation from the 3rd generator. However, once the 3rd

generator reaches 30 MW generation and the 1st generator reaches 120 MW, the 2nd generator creates more power to satisfy the load demand (8:00am to 10:00am). In this analysis, we are going to focus on only the first part which is analyzing the peak demand.

The second scenario is the 6 bus system that does have only wind energy. The peak demand supplied by conventional units, which is between 8:00pm to 10:00pm, is delayed to 10:00pm to 1:00am because wind farm is added (The peak demand defines the amount greater than 140MW). The average load demand in an hour at this area is 154.6MW. In other word, adding wind energy relieves the stress to supply the power from the conventional units. From now on, the peak demand and the average load demand imply the values subtracting the amount supplied by wind energy. Besides, there is one more peak demand between 10:00am to 3:00 pm. The average load demand in an hour at this area is 151.2MW. The peak demand is reduced about 90MW which is 34.5% of the peak demand from the first scenario.

The third scenario has the same as peak demand as the second scenario. The first peak demand is between 10:00pm to 1:00am. The average load demand in an hour at this area is 161.9MW. The average load demand should be higher than the second scenario because we are starting to do G2V at night time. The second peak demand is between 10:00am to 3:00pm. The average load demand in an hour at this area is 151.2MW.

The first peak demand for the fourth scenario is between 10:00pm to 1:00am. The average load demand in an hour at this area is 161.9MW. The second peak demand is between 10:00am to 3:00pm. The average load demand in an hour at this area is 149.6MW. The reason for the decrease is because there is an afternoon V2G.

The first peak demand for the fifth scenario is between 10:00pm to 1:00am. The average load demand in an hour at this area is 161.9MW. The second peak demand is between 10:00am to 3:00pm. The average load demand in an hour at this area is 151.2MW. In this scenario, there is an evening V2G instead of afternoon V2G. Therefore, the average load demand is higher than the one from the fourth scenario.

The first peak demand sixth scenario is between 10:00pm to 1:00am. The average load demand in an hour at this area is 161.9MW. The second peak demand is between 10:00am to 3:00pm. The average load demand is 155.4MW. The reason for the increase is the afternoon V2G around 10:00am to 3:00pm.

In other word, by adding wind energy and PHEV, the peak demand have not been changed but it released the stress of the conventional units by 38.0% (comparing the first peak demand between scenario1 and scenario4).

Secondly, we are going to compare the total operational cost in each scenario and find the best scenario based on it. As you can see from Figure 348, the optimal operational cost dropped significantly when we added wind generation. No operational or installation cost for wind generation is assumed. In other words, wind generation acts like a free source so theoretically adding wind generation should reduce the operational cost. In the analyzed case, the total operational cost diminished by $37,590.35 which is

30.8% of the power generation without wind generation. The total power generation without wind and PHEV for one day is estimated to be 5308 MW. However, wind generation creates 1242.5 MW for one day which is 23.4% of total generation. Therefore, introducing 23.4% of wind generation reduced 30.8% of total operational cost.

As you can see from the Figure 349, the best scenario is the fourth scenario because it shows the least operational cost. The fourth scenario utilizes charging at night time (11pm ~ 7 am) and discharging at day time (12 pm ~ 3 pm). The total operational cost at this time is estimated as $85,953.03. The least efficient way of charging and discharging PHEVs is the fourth scenario. The sixth scenario utilizes charging at night time (11pm ~ 7am) and also day time (10 am ~ 3pm) and discharge during the late afternoon (6pm ~ 9pm). The total operation cost in this case is estimated as $86,681.53 which is $728.50 more expensive than the worst case. While this is a small difference between two cases, if the system is expanded to, a 150 bus system, there would be a significant difference between the two scenarios.

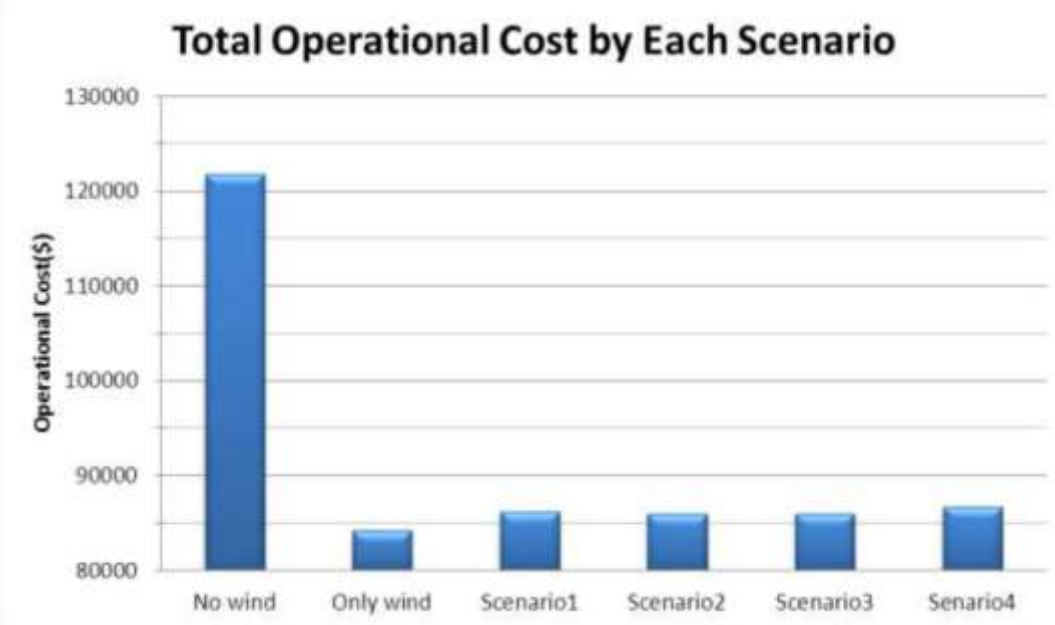

Figure 348: Total operational cost.

The fourth scenario utilizes charging at night time (11pm ~ 7 am) and discharging at day time (12 pm ~ 3 pm). The total operational cost at this time is estimated as $85,953.03. The least efficient way of charging and discharging PHEVs is the fourth scenario. The sixth scenario utilizes charging at night time (11pm ~ 7am) and also day time (10 am ~ 3pm) and discharge during the late afternoon (6pm ~ 9pm). The total operation cost in this case is estimated as $86,681.53 which is $728.50 more expensive than the worst case. While this is a small difference between two cases, if the system is expanded to, a 150 bus system, there would be a significant difference between the two scenarios.

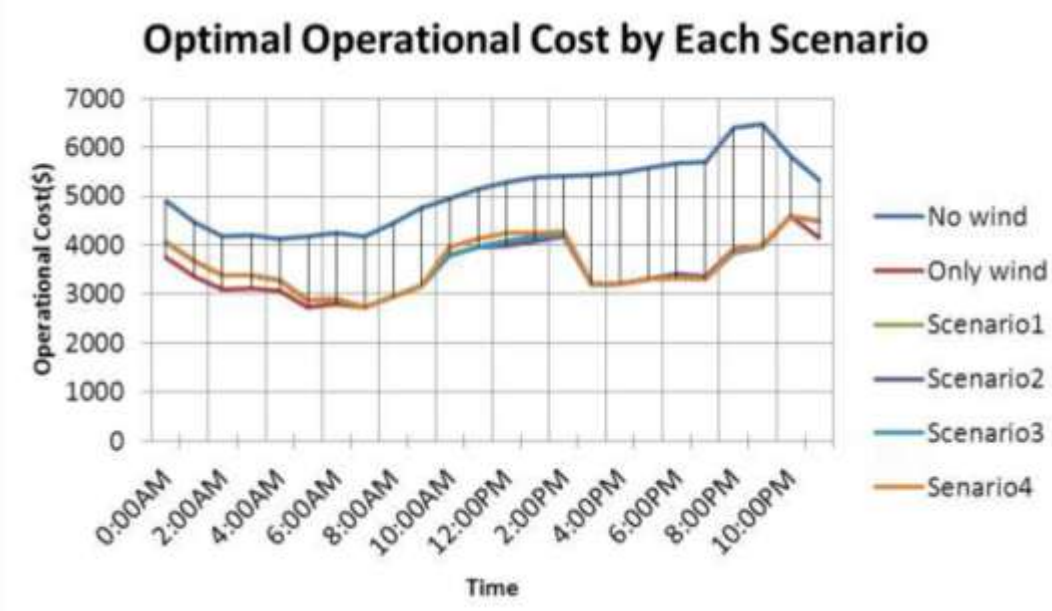

Figure 349: Optimal operational cost.

Conclusions and Recommendations

This IPRO team has researched the factors affecting the integration of renewable energy systems and PHEVs in the future. Wind power is expected to provide a 20% generation of all energy produced in the US and the introduction of PHEVs into the market will increase demand for electric power. Wind power was found to reduce the operational cost of the grid considerably, due to wind power's negligible operational cost relative to other power generation methods. There is the potential for reducing the operational cost of the grid by PHEVs being charged at night and utilizing the V2G feature during peak power demand on the grid. Our case simulations showed that the second scenario provided the optimal operational cost with respect to the charging times of the PHEVs. This scenario has the PHEVs utilizing charging at night time (11pm ~ 7 am) and V2G discharging at day time (12 pm ~ 3 pm), Our simulation may be improved in the future by including and/or simulating the following features:

- Simulation of more than 6 buses
- Operational cost of the PHEV batteries due to V2G (cycling)
- More scenarios of PHEV charging situations
- The feasibility of using PHEVs as an electric storage system to mitigate the natural inconsistencies of wind generated power can be investigated.

Our analysis was sufficient to provide us with answers to the question of how to integrate renewable energy systems and PHEVs.

A3. Modeling of Building Integrated Wind Turbine Modules

One of the tasks of this DOE project was to "Engage Undergraduate Students in Wind Energy Research". IPRO 323 was developed in response to this task and is currently in its second semester with plans for continuing on into next year. The overall goal for the students enrolled in IPRO 323 is to develop a

methodology for designing and developing building-integrated wind turbine modules so that more urban environments will see wind power as a viable alternate energy source. The project plan that the students' enrolled in the course developed was to investigate designing a surface shape integrated onto the roof and/or facades of buildings to increase the power output of building mounted wind turbines. This goal of course requires the understanding of the fluid dynamics/aerodynamics of wind turbines and also the architectural, social, public, safety and environmental issues associated with integrating wind turbines into urban environments. Therefore the IPRO course will benefit from the experience and knowledge of students enrolled in various academic majors at IIT. Several undergraduate disciplines have representation on the team: Architecture, Mechanical Engineering, Aerospace Engineering, Materials Science and Engineering, Electrical Engineering and Architectural Engineering. This diverse mix of students working on one project provides a unique and interesting learning environment not typical of conventional undergraduate education.

Organization and Approach

Each semester the IPRO team was divided into several subdivisions in order to achieve the IPRO 323 goals. These subdivisions included research and development, wind tunnel testing, computational fluid dynamics, and architectural analysis. The research and development team investigated the best methods for conducting the research and analysis with specific emphasis on the development of the prototype and testing components. The wind tunnel team was responsible for conducting the experiments, as well as analyzing the data. The computational fluid dynamics team was in charge of working with the experimental team to help guide the testing parameters and analysis of the data. The architectural analysis team was responsible for determining whether the theoretical power output measurements were viable for an urban high-rise building as well as determining how the finished product would be integrated into the structure taking into account the social, public and safety issues.

The research team read through a number of articles in order to determine the best experimentation method. The discussion of testing an actual model scale wind turbine versus a simulated (i.e., actuator disc) wind turbine resulted in the conclusion that because of the time and cost limitations for IPRO 323, creating a real turbine and calculating the actual power output of the turbine would not be practical. It was decided that for the first semester or two the goal would be focused on the building shape rather than the wind turbine design. Therefore, the class decided to adopt an idea that other investigators have used which is to use a porous plate (actuator disc) to simulate a wind turbine. Aubrun, et al. [**100**] tested a 3-blade wind turbine by using a porous disc to investigate the wind turbine wake characteristics. The idea behind this 'mock turbine' is that it acts as a drag source and creates a pressure drop across the porous plate similar to the pressure drop across an actual spinning turbine.

The fluid mechanics/aerodynamics describing the behavior of wind turbines was researched with emphasis on the main mechanisms responsible for optimized power output. Articles describing the well accepted Betz' limit [**101**], proved very useful in the selection of the porous plate. It was decided that the students would simulate an "ideal wind turbine" from an aerodynamics point of view (as in the Betz' limit) by suitably choosing the porosity of the porous plate to provide the same pressure drop across the plate as one would see with an "ideal wind turbine".

After the porosity was determined, the students' focused on shaping the surface that the "wind turbine" would be placed upon in addition to determining what type of data would be acquired in the wind tunnel. The goal being: by shaping the surface (both upstream and/or downstream) of the wind turbine an increase in power output could be achieved. They determined that the most important measurements to take would be of the velocity and static pressures at several locations upstream and downstream of the porous plate in addition to several height locations off the surface. Measurements of velocity and pressure would allow the data analysis to be done to determine the effects of the surface shape on the theoretical power output of the wind turbine module.

Several hurdles had to be overcome by the students to get to the stage of taking any data. The experiments were designed and fabricated from scratch which included determining what equipment was necessary, how to use the equipment and fabrication of model support structures. Several pieces of instrumentation also required calibration in addition to the writing and testing of data acquisition software. The Computational Fluid Dynamics team used FLUENT to numerically analyze the fluid flow in the wind tunnel/porous plate configuration. This was seen as a complement to the experimental work with the goal being that the students would get the FLUENT code set up with the appropriate turbulence model along with appropriate boundary and initial conditions. With that in place the investigation of the optimum shape could proceed at a faster pace since changing the shape in the computational code and testing it would be faster than fabricating and testing several shapes in the wind tunnel. This would help narrow down the range of shapes to be tested in the wind tunnel.

The architectural analysis team had two major responsibilities involving the end product of this semester's IPRO. The first was to design a structure integrating the wind turbine in such a way that the final design would be aesthetically pleasing and it was also important for the architects to consider the material used to create the surface design, noise and safety implications among other factors. The interactions from turbine to turbine for designs incorporating several on one building must also be taken into account. With these in mind, they were able to design several three-dimensional renderings of possible ways the wind turbine modules could be incorporated in typical urban buildings.

The second goal of the architectural analysis team was to gather information in regards to energy and power consumption of average high-rise office buildings, and to relate these to the power output of the wind turbine module designed by the engineers. They were compared to the theoretical power output calculated from the experimental data in order to determine whether the proposed turbine design would be viable.

Results from Students Work

For the first several weeks the students' in the wind tunnel team as well as the research and development team secured, learned to use and calibrated the necessary instrumentation, software and equipment:

- DigiTec Temperature Sensor, Model: 5810, S/N: 65360672
- Validyne, Model: DP45-34, S/N: 43444. Demodulator, Model: CD15, S/N: 109352
- Engineering Corp Pressure Transducer, Model: DP103-10, S/N: 67548 10310N1S4D

- Keithley Autoranging Multimeter
- Pertec Peripheral Corp. Traverse System Motors, Model: PSX01 PWR.SUP, S/N: 2552
- National Instruments DAQ: 16-Input 16-bit, Model: USB 6221, S/N: E88779
- Dwyer Microtector Manometer, Model: 23-206
- M.V. Morkovin Wind Tunnel at Illinois Institute of Technology
- Pitot Tubes
    - Labview 8
    - Matlab 7.4.0 (R2007a)
    - Microsoft Excel

The porous (perforated) plate was the first component to be tested since the goal was to simulate an ideal wind turbine. In order to achieve the pressure drop associated with an ideal turbine the porosity of the plate needed to be tailored for that condition. Velocity measurements were taken at various streamwise (horizontal) and vertical locations behind the plate. Based on the Betz' limit [**101**] for an ideal wind turbine it is well known how the velocity and static pressure distributions should develop downstream of an ideal turbine.

Description of Betz' Limit

A wind turbine's ideal efficiency can be derived using Betz' Law. By analyzing the fluid dynamics through an "actuator disc" the limit for power output can be obtained using conservation of mass and momentum and Bernoulli's equation.

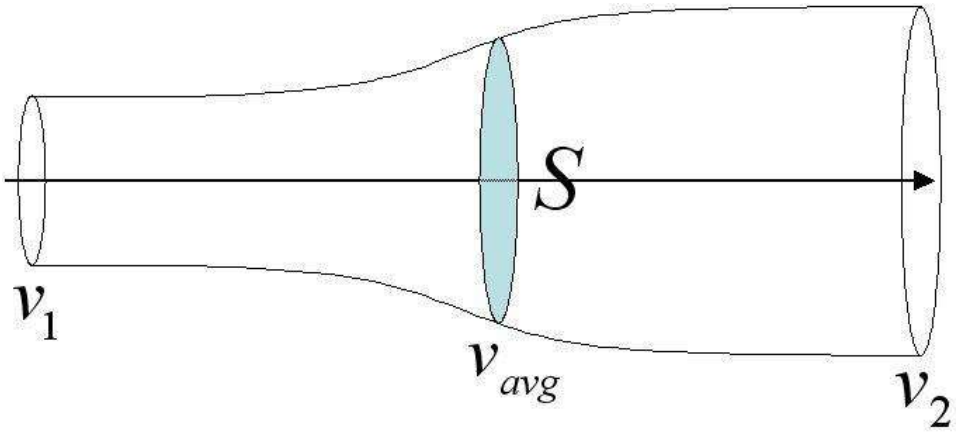

Figure 350: Schematic representation of flow through an actuator disc.

Bernoulli's equation can be applied to two points along a streamline for incompressible, steady and frictionless flow. For this case we can apply Bernoulli's equation from point 1 which is far upstream of the turbine where the velocity and pressure are V_1 and P_1 respectively, to a point just upstream of the disc where the velocity is some V_{avg} and the pressure is P_A. We can again apply Bernoulli's equation from a point just downstream of the disc where the velocity and pressure are V_{avg} and P_B respectively, to

a point far downstream of the turbine where the velocity and pressure are V_2 and P_2 respectively. This analysis will result in giving us the pressure drop across the turbine which can then be related to the power output as:

$$Power = (P_A - P_B)A_t V_{avg} \quad \textbf{(98)}$$

where A_t is the area of the rotor, P_A is the pressure just before the rotor, P_B is the pressure just after the rotor, and V_{avg} is the average velocity at the rotor. From conservation of mass,

$$A_1 V_1 = A_t V_{avg} = A_2 V_2. \quad \textbf{(99)}$$

Using conservation of momentum and noting that $P_1 = P_2$, the force on the fluid caused by the rotor can be calculated as:

$$F = \dot{m}\Delta V = \rho A V(V_1 - V_2) = (P_A - P_B)A_t \quad \textbf{(100)}$$

Using Bernoulli's equation for the fluid flow before and after the rotor yields equations 4a and 4b respectively,

$$P_1 + \frac{1}{2}\rho V_1^2 = P_A + \frac{1}{2}\rho v_{avg}^2 \quad \textbf{(101)}$$

$$P_2 + \frac{1}{2}\rho V_2^2 = P_B + \frac{1}{2}\rho v_{avg}^2 \quad \textbf{(102)}$$

Combining equations (99) through (102) provides,

$$P_A - P_B = \frac{1}{2}\rho(v_1^2 - v_2^2) = \frac{\dot{m}}{A_t}(v_1 - v_2) = \rho v_{avg}(v_1 - v_2) \quad \textbf{(103)}$$

Therefore, it can be shown that the average velocity at the rotor is simply the arithmetic mean of the velocity far upstream and far downstream of the rotor.

$$V_{avg} = \frac{1}{2}(V_1 + V_2) \quad \textbf{(104)}$$

Finally, the efficiency can be given from the following equation:

$$\eta = \frac{Power}{\frac{1}{2}\rho A_t v_1^3} \quad \textbf{(105)}$$

Plotting the velocity ratio versus efficiency, results in :

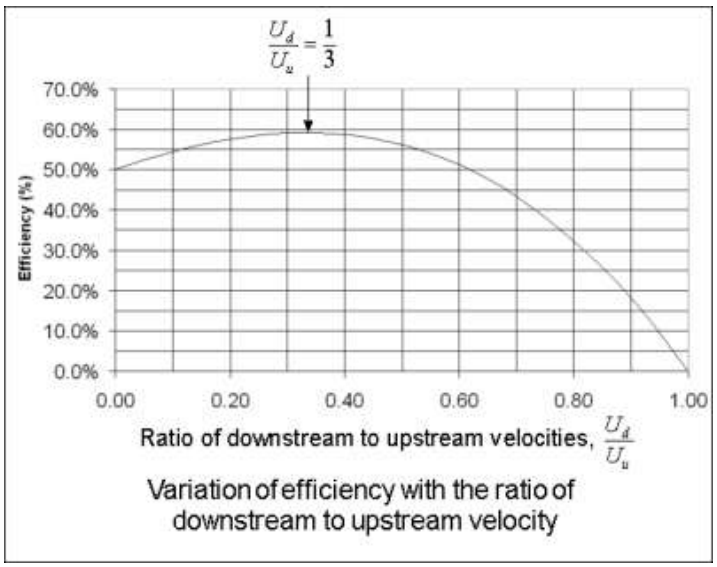

Figure 351: Plot of velocity ratios versus efficiency

(from http://www.wind-power-program.com/betz.htm)

It is apparent from this plot that the highest efficiency occurs when the lowest downstream velocity is a third of the free stream velocity before the rotor (V_1). This efficiency is calculated to be 59.3%.

Determining Plate Porosity

The next step for the wind tunnel team was to determine the porosity of the porous plate needed to simulate an ideal wind turbine. That is, what porosity will result in a $V_m/V_1 = 1/3$ where V_m is the minimum downstream velocity which will be determined from wind tunnel tests? For a too porous of a plate the pressure drop would be too small ($V_m/V_1 > 1/3$) and would simulate a very inefficient turbine and conversely if the porous plate were too dense the pressure drop would be very large ($V_m/V_1 < 1/3$) and indicative of a wind turbine exceeding the Betz' limit. Therefore, the porosity of the plate was adjusted until the experimental measurements indicated that we had achieved the desired velocity and static pressure distributions close to those predicted with the Betz' theory. These results would then be compared with those for the cases where the surface shape was modified. Figure 352 is a photograph of the porous plate mounted in the test section of the wind tunnel. The direction of flow is from right to left and two Pitot-static tubes can be seen just downstream of the porous pate. The Pitot-static tubes provide for both pressure measurements and velocity measurements in the wind tunnel. The traverse mechanism is also seen in the photograph and for the results shown in Figure 353, one of the Pitot-static tubes was secured to the traverse mechanism in order to move the Pitot-static probe to various x and y locations with respect to the porous plate. The x direction is defined as the streamwise location with respect to the plate whereas the y location is the wall-normal (vertical) distance as measured from the wind tunnel floor. In Figure 353 the minimum value for the velocity is seen to occur around y ≈ .86 which indicates the centerline of the porous plate. The flow velocity increases away from the centerline and for large enough y locations the velocity would be approximately that of the free stream value. The

velocity is also a function of distance from the porous plate and is consistent with those from earlier investigations, see Castro [**102**].

Figure 352: Photograph depicting porous plate set-up in wind tunnel

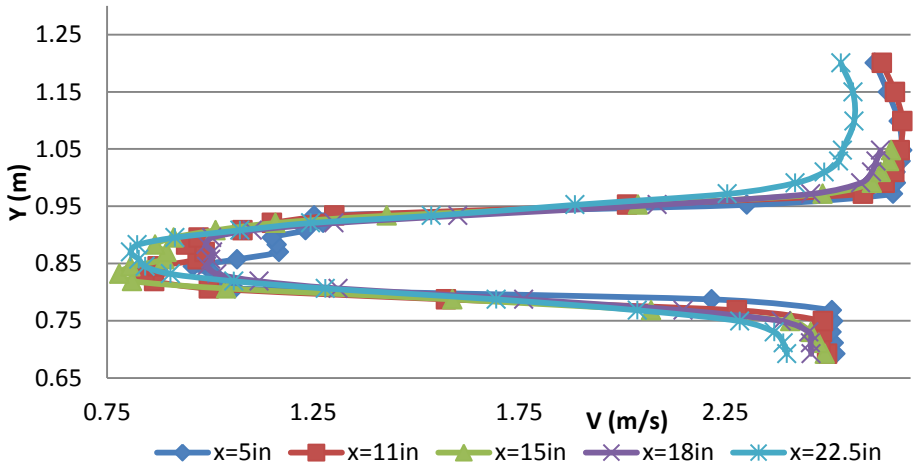

Figure 353: Velocity profiles downstream of a porous plate for several streamwise and vertical locations.

These velocity profiles were acquired for several mesh porosities and for several streamwise locations. V_m is determined for each porosity by looking for the minimum value of the velocity on the centerline (y

≈ .86) as a function of streamwise location. The plot shown in Figure 354 is the value of the velocity on the centerline normalized with the far upstream velocity for a porous plate with a 62.3% porosity. This porosity was shown to provide the closest results to the Betz' limit for the range of plates investigated; namely, by plotting the velocity on the centerline (y ≈ 0.86m) normalized by the approach wind speed, U_o, as a function of x/c, where c is the chord length (height) of the porous plate, the lowest velocity reached downstream of the mesh is in the 1/3 range. The students' results compare well with previous published work done in the 70's on flow downstream of perforated plates by Castro [**102**].

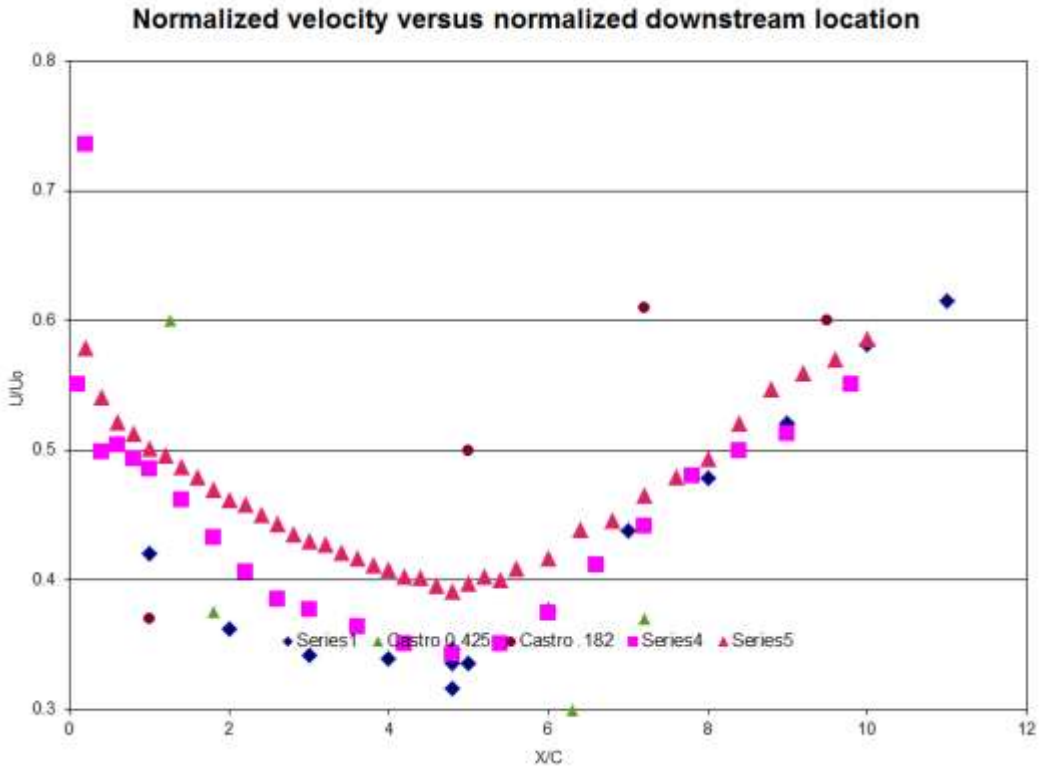

Figure 354: Normalized Velocity as a function of normalized streamwise distance for a 62.3% porous plate.

Surface Shape Modification

After the porosity was determined, the attention was directed on shaping the surface that the "wind turbine" would be placed upon with the goal being that by shaping the surface (both upstream and/or downstream) of the wind turbine an increase in power output could be achieved. For this experiment on the "ideal wind turbine" this change in power output would be measured by a change in static pressure across the turbine: $Power = \Delta P V_{avg} A_t$ where V_{avg} is the flow speed, A_t is the plate surface area and $\Delta P = (P_A - P_B)$. Figure 355 is a photograph of the first modified surface shape to be tested with the porous plate installed in the wind tunnel. The first shape tested was simply a Gaussian shape. It can be seen in Figure 355 that there is a Pitot-static tube on each side of the perforated plate facing the oncoming airflow. The actual fabricated shape can be seen, as well as the final perforated plate with the

correct size and porosity. Data were taken with the mesh at 1 inch above the centerline of the shape and at various locations downstream of the shape centerline. Those locations were 0 inches, 0.75 inches, 1 inch, and 5 inches as shown schematically in Figure 356.

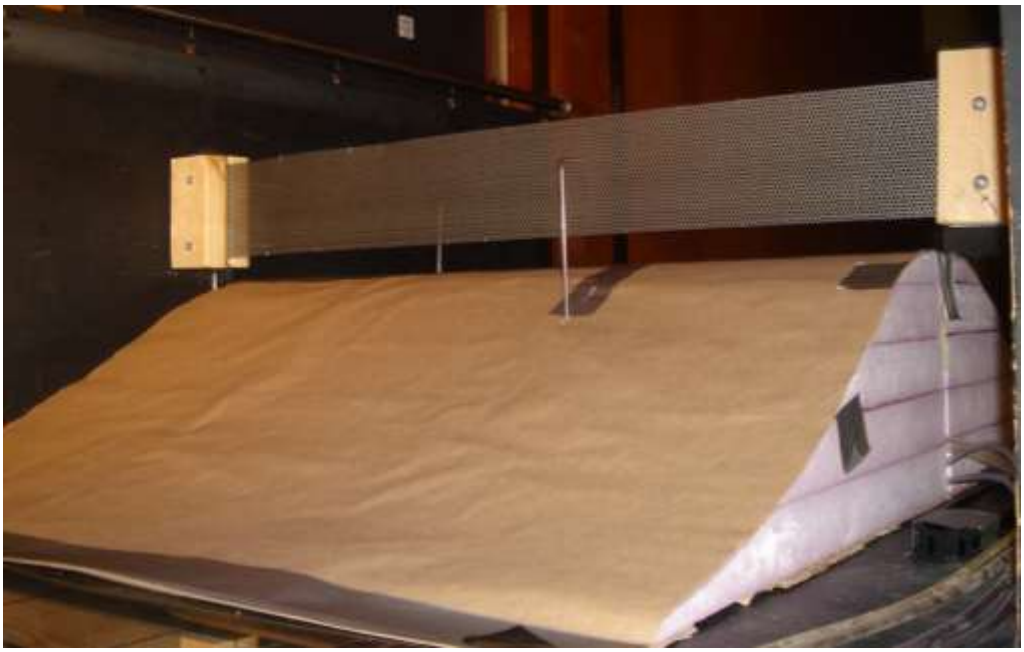

Figure 355: Photograph of Porous plate and surface shape in wind tunnel.

The ΔP was measured and the theoretical power was calculated for different flow speeds in the wind tunnel the various plate locations shown in Figure 356. The results are given below in Figure 357 where the power output is compared against the condition with a flat surface (no shape). The architectural analysis team was responsible for investigating power consumption levels in urban environments, determining how surface integrated wind modules could be integrated into architectural structures all while taking into account the social, public and safety issues. In addition rough cost estimates for implementing these structures into buildings was also performed by this group. Urban environments currently use over 66% of the world's energy. In the US, buildings represent 50% of the total national energy consumption and 77% of electricity use. It is also important to mention that 30% of energy production and 67.5% of all electrical energy is lost with current infrastructure, deeming them inefficient and wasteful [5].

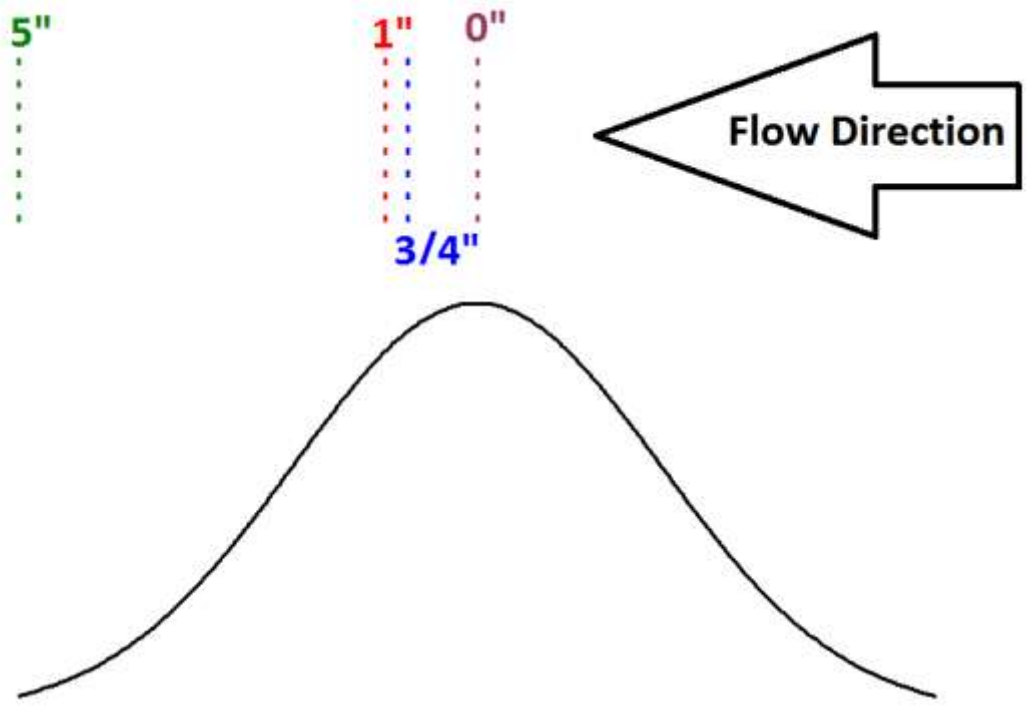

Figure 356: Schematic illustrating several porous plate testing locations.

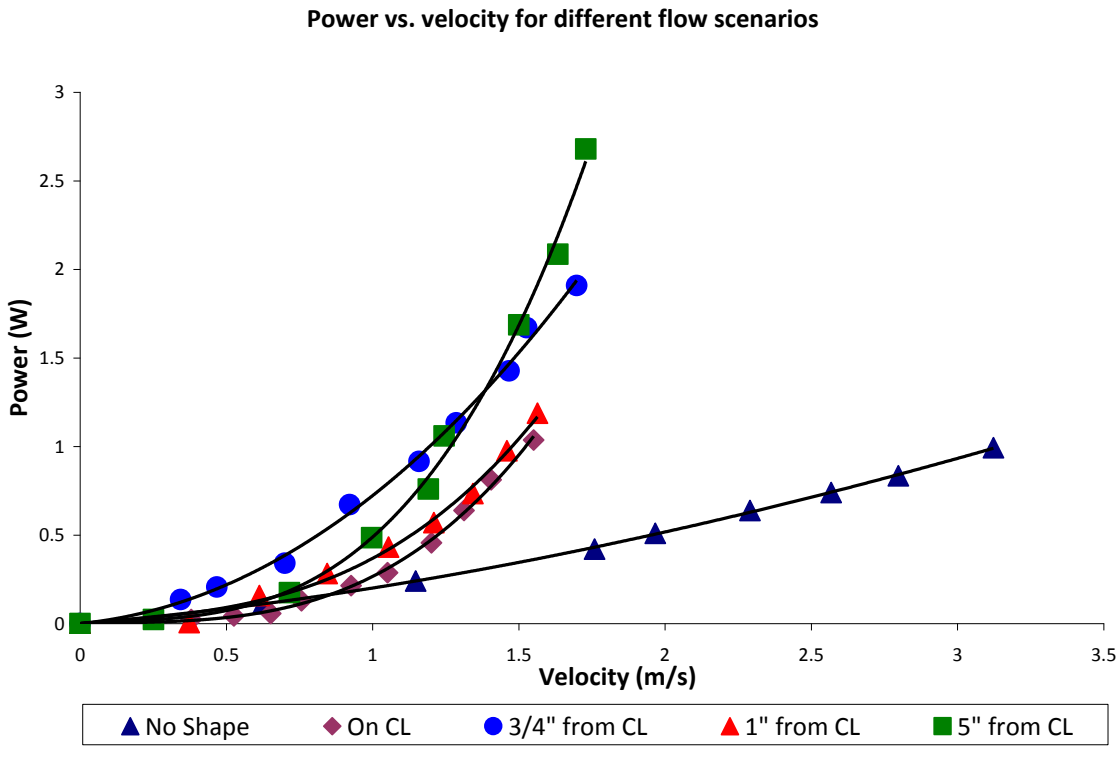

Figure 357: Power output for various wind speeds and mesh locations.

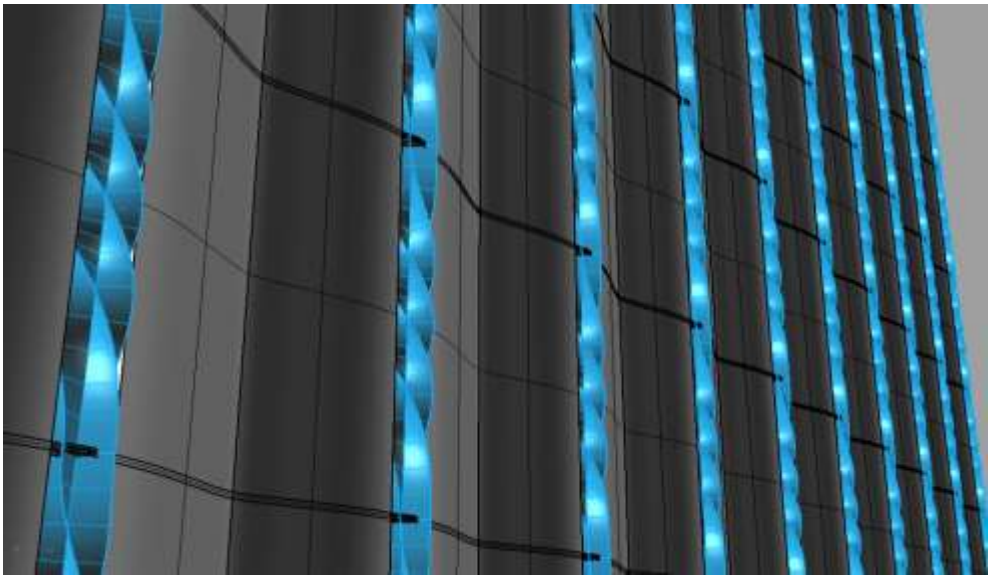

Figure 358: Surface Design with helical turbines located at the center of each shape.

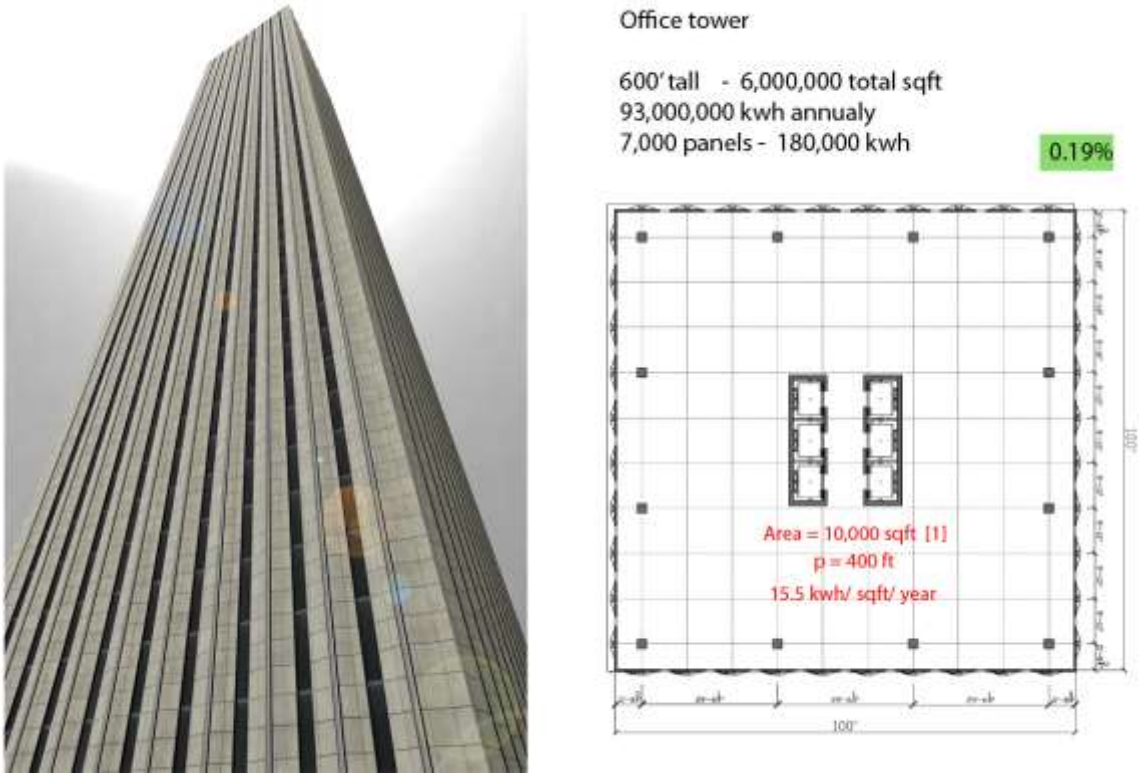

Figure 359: Example of a high-rise building with the surface design implemented vertically along the sides of the building

Figure 360: Example of shorter buildings with the surface shape designed to cover the roof.

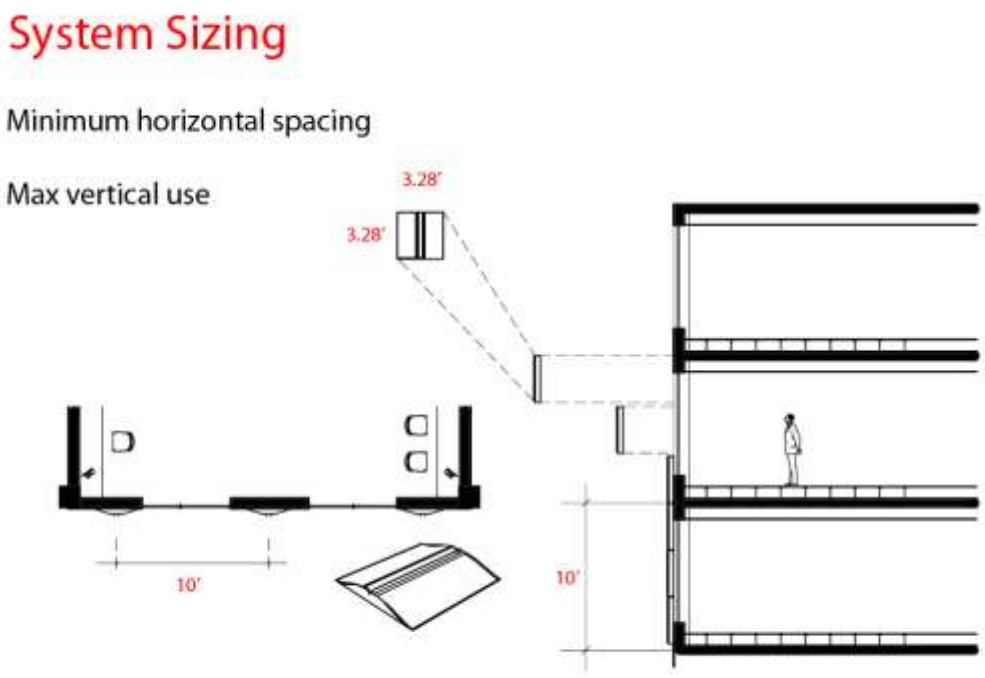

Figure 361: A schematic of a building with the wind turbine surface design integrated onto the side.

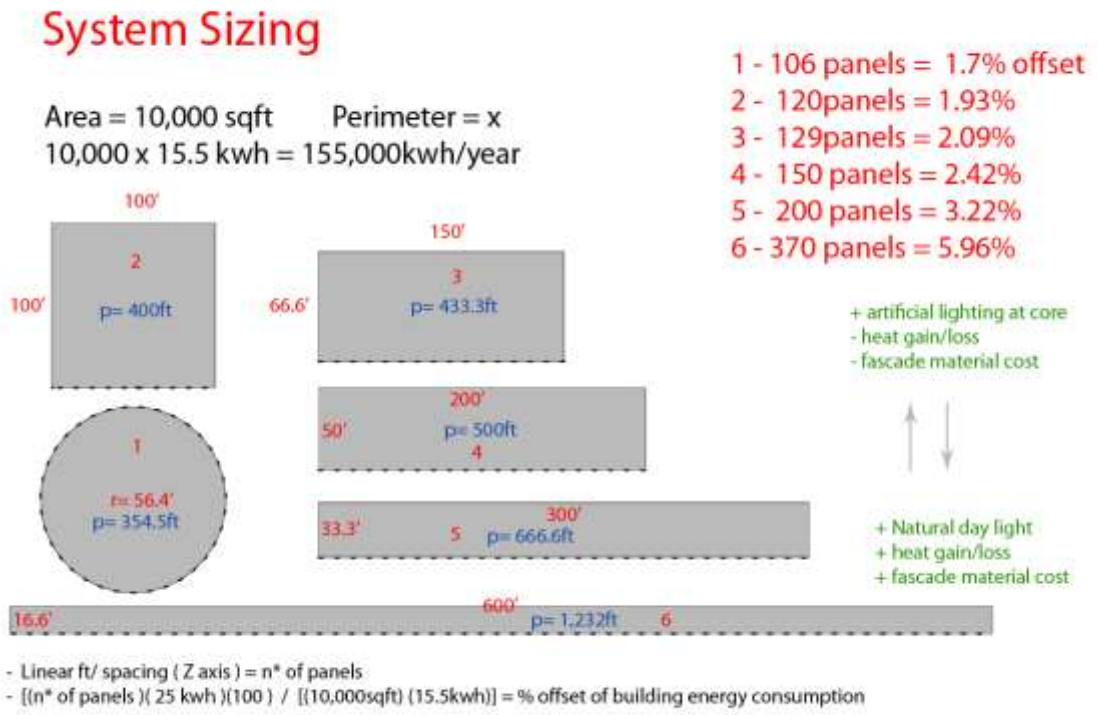

Figure 362: An example of buildings with the same area and different perimeters.

Studies indicate that urbanization causes an increase in CO_2 emissions as countries shift from using CO_2-neutral energy sources to CO_2-intensive energy sources in urban areas [6]. In addition to this, projections indicate that cities are likely to increase their share in global energy consumption to 73% by 2030 and 87% in the U.S. alone [**103**]. Some three-dimensional architectural renderings were created to visualize the surface of a building with surface integrated wind turbines and are shown below. An analysis of the surface area of building sides, sizing and spacing was done to determine the most efficient architectural set-up for the wind turbine modules. The Power consumption of typical urban buildings was researched, which was important in the architectural analysis to assess the percentage of power a series of surface mount wind turbines would produce for a typical urban building.

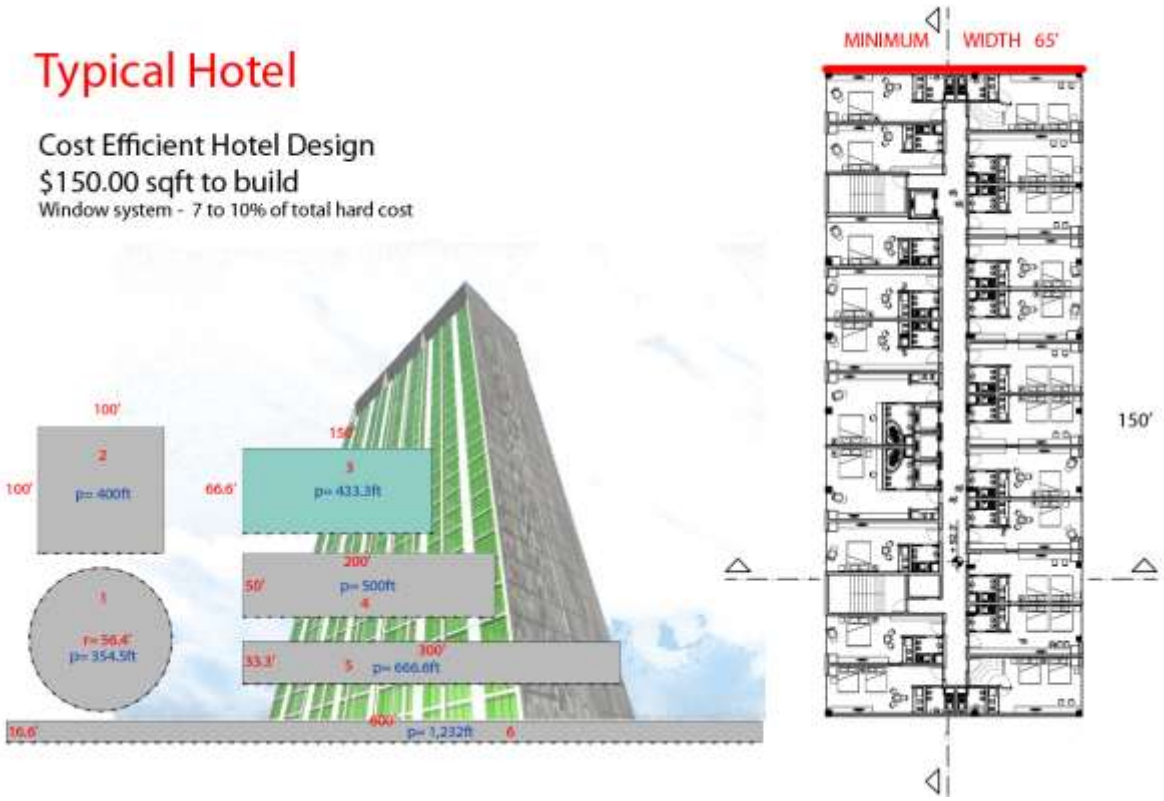

Figure 363: Analysis of hotel design and building perimeter.

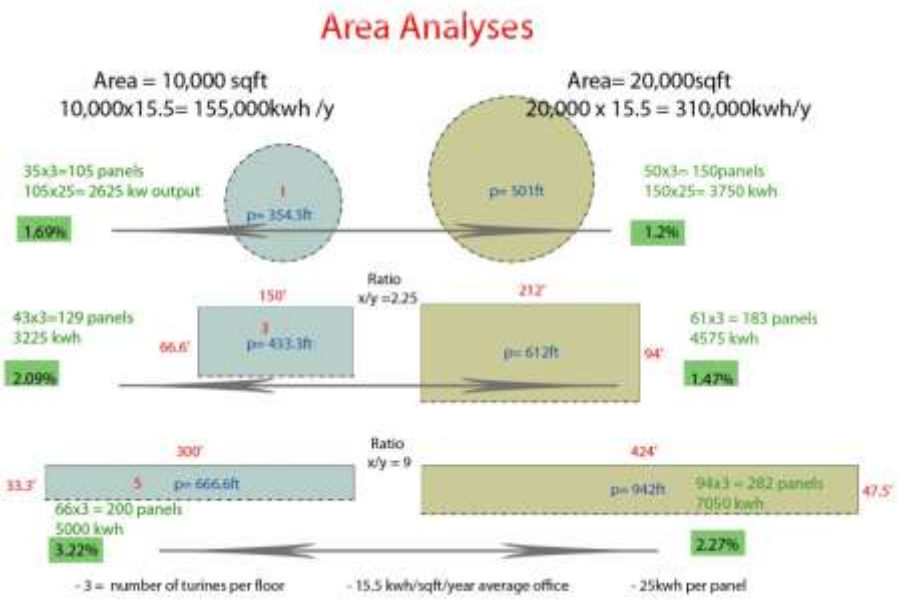

Figure 364: Analysis of power consumption for different sized buildings.

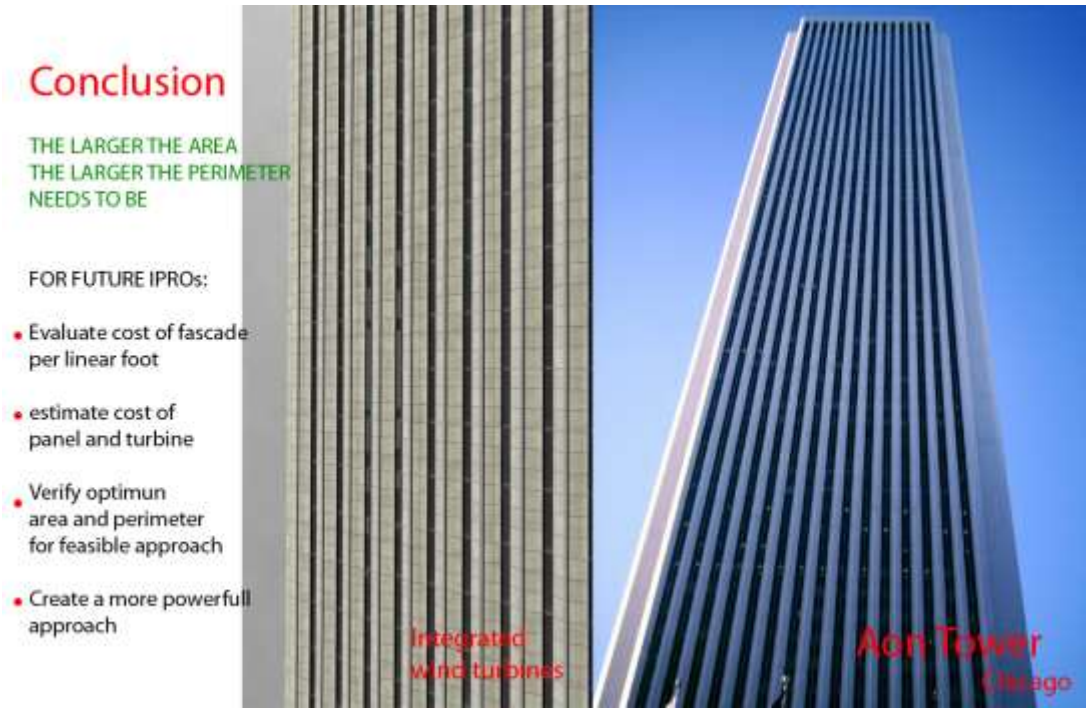

Figure 365: Recommendations for future architectural research in IPRO 323.

Another aspect the architectural research team had to consider was the power output at different wind speeds, and the average wind speeds in Chicago at different building heights. Calculations were made using the data gathered for the current surface design prototype and an ideal wind turbine, assuming that the ideal Betz' limit of 59.3% of the wind power was extracted and used by the turbines, and that the air density is 1.225 kg/m^3. The area used for the calculations was 0.137 m^2, which was the area of the perforated plate tested. The calculated values are as follows:

Table 28: Annual power output for increasing wind speeds typical of urban environments.

Wind Speed (m/s)	Wind Speed (mi/hr)	Annual Power (kW-hr/m^2)	Annual Power (kW-hr)
5	11.2	398	54.53
10	22.4	3182	435.9
15	33.6	10,740	1471

Another major task for the architecture team was to come up with estimations of how much it would cost to implement these structures onto urban buildings. After some research, estimated prices for fabricating one surface mount structure with a wind turbine are as follows:

- Tubular aluminum frame
  - Approx. 45' of ¾" sq. tubing $50
  - Welded $15
- Molded plastic upper $5

- Turbine body
  - Solid paddle $10
  - Solid savonious $20
  - Membrane paddle/savonious $30
- Magnetic generator $100
- Transformer $70
- Total $300

This cost estimates the price of only one component being implemented on a building; however, to produce useful energy, many of these structures must be implemented on the same building just as many horizontal axis wind turbines are installed in fields of wind farms.

Conclusion and Future Work

During the Spring 2011 semester, the students worked mainly on developing the methodology, setting up the experiments and investigating various aspects of incorporating wind energy into urban architectural structures. The data gathered showed promising results, in that there is a significant change in the pressure drop across an "ideal wind turbine" when the surface shape is modified.

During the Fall 2011 semester the students needed to move their experimental setup to a different wind tunnel test section which consumed approximately 3-4 weeks. For the remaining weeks, the main goal for the wind tunnel team is to test various surface shapes to determine which surface shape would optimize power output. The architectural team is further investigating various possibilities for incorporating these wind models into an urban environment and also is discussing with IIT facilities the possibility of placing an actual wind turbine model on the roof of IITRI.

With renewable energy becoming an increasingly desirable source, wind power is among the most sought after technologies at present. The development of wind turbines in rural areas has been steadily increasing in the past decades, but the overall goal of IPRO 323 is to develop a way to integrate efficient wind turbines into an urban environment where energy is most heavily consumed. With the help of engineers, architects, and industrialists, wind energy in large cities will become a common technology.

A4. Capstone Senior Design Project at Southern Illinois University

This course is designed to teach senior level students about team approach to engineering projects. The students are expected to understand and analyze RFPs (Request for Proposals), identify tasks, develop team organization, and assignment of tasks. In addition as part of their work, they are required to have a work plan and time schedule. The projects must have: feasibility analysis, team approach in engineering projects, understanding and analyzing a request for proposals, identification of tasks, assignment of tasks and team organization, work plan and time scheduling, feasibility analysis and cost-benefit analysis, ethics and professionalism issues related to engineering projects in general and to the specific project assigned, team coordination and documentation of team member efforts, documentation of team communications and the team decision making processes, development, presentation and defense of the final proposal for the assigned project.

Each semester, a number of projects are posted and students are asked to pick one and submit a proposal for their choice of project. The following description of project was posted as an RFP for senior level students.

Create a Z-scale model of a 3-phase power generation and distribution system. This model will have the following areas: residential, commercial, industrial, coal-fired generation, and wind generation. This will be a dynamic model where the user can specify the real and reactive power demand from the residential, commercial, and industrial loads as analog inputs, the wind input from a fan, and the state of various power factor correcting capacitor banks. The system will respond by showing the real and reactive power generated by the coal fired power plant and the wind farm required to supply the specified loads. Additionally the model will report the current on each distribution line and the voltage at each end of each distribution line. The inputs from the user will be analog and the currents, voltages, and powers will be displayed as analog values. The values will be determined by a microprocessor using equations that describe the load flow of the power system.

The finished project will require:

- A set of power equations that describe the behavior of the system
- A set of appropriate limits for each input for each of the various loads
- A fan to use to simulate the wind and turn the wind turbine(s)
- An animated Z-scale model that shows light and/or action for the user selected demand for each load type
- A suitable way for the user to input the desired demands
- A suitable way to display the voltages and currents associated with the load flow on the lines
- A suitable way to display the power produced by the wind farm and the coal-fired plant
- A carrying case to transport the system

The objective of this project is to simulate a 3-phase power generation and distribution system to incorporate wind energy as a supplemental source. The system will be a portable Z-scale model on a scale of 1:220. This single-phase model will be used to demonstrate 3-phase power to an audience at conferences or high schools. This model will have the following areas: residential, commercial, industrial, coal-fired generation, and wind generation. This will be a dynamic model where the user can specify the real and reactive power demand from the residential, commercial, and industrial loads. The wind speed will utilize a controlled fan, and the power factor will be corrected by capacitor banks automatically by an SVC. The system will respond by showing the real and reactive power generated by the coal fired power plant and the wind farm required to supply the specified loads. Additionally the model will report the line current, power flows, bus voltage and power, and display their values. These values will be calculated by a microprocessor using power equations.

Description:

The power system display will be 2’ x 4’ in dimensions. The system for this project is composed of three main parts: power sources, control station, and the power loads. The system will be a five-bus system

utilizing relays and breakers. Figure 366 is the diagram of the control system. Figure 367 is a diagram of power system.

Power Sources: There are two types of power sources: the coal-fired generation station and the wind generation station. The coal-fired generation will be the main source of power for the town. Under windy conditions, the windmill will begin to produce power so that the coal plant's output will be decreased. A fan will be used to simulate high-wind and low-wind conditions. During low- or no- wind conditions, the town will run solely on power obtained from the coal plant. An inverter circuit will be connected to the windmill to invert the dc power to ac power. The system will function on 110V.

Control Station: The main component for the control station will be an Arduino microprocessor for switch control. Arduino is a tool for making computers that can sense and control more of the physical world than your desktop computer. It is a physical computing platform based on a simple microcontroller board, and a development environment for writing software for the board. It can be used to develop interactive objects, taking inputs from a variety of switches or sensors, and controlling a variety of lights, motors, and other physical outputs. The Arduino programming language is an implementation of Wiring, a similar physical computing platform, which is based on the Processing multimedia programming environment. There are many reasons why Arduino is preferable over other microcontroller devices:

- Inexpensive: Arduino boards are relatively inexpensive compared to other microcontroller platforms. The least expensive version of the Arduino module can be assembled by hand, and even the pre-assembled Arduino modules cost less than $50.
- Cross-platform: The Arduino software runs on Windows, Macintosh OSX, and Linux operating systems. Most microcontroller systems are limited to Windows.
- Simple programming environment: The Arduino programming environment is easy to use.
- Open source and extensible software and hardware: The Arduino software is published as open source tools and the language can be expanded through C++ libraries. Hence, people wanting to understand the technical details can make the leap from Arduino to the AVR C programming language on which it's based.

The user will utilize a laptop/tablet to input values and limits to the power system model and the outputs will be displayed on Matlab/Simulink graphical user interface (GUI). The power system simulation involves modeling power generation equipment, planning the integration of power plants onto the electric grid, and performing generator control system parameter estimation. MATLAB and Simulink will be used to perform critical power system simulation and optimization tasks such as simulating performance against grid code, ensuring production goals are met, and automating control system parameter estimation to meet regulatory requirements.

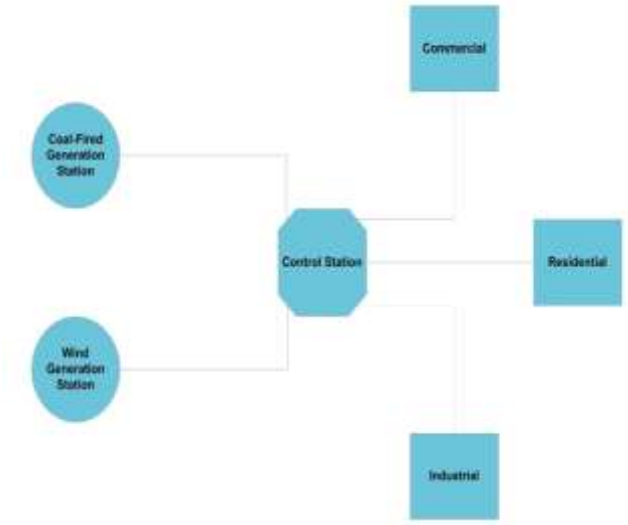

Figure 366: Control System Diagram

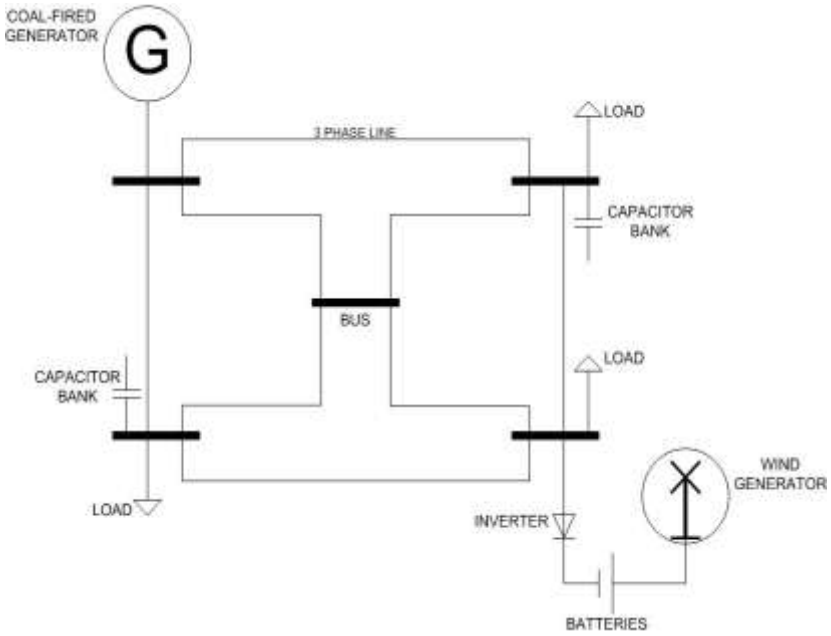

Figure 367: Power System Diagram

A Simulink Support Package for Arduino will be used to create an application that will run autonomously on the Arduino board. We will simulate and visualize our application on the host computer. This will allow us to communicate with Simulink on the host computer for testing, and read from and write to the Arduino's analog and digital I/O channels.

Power Loads: There will be three types of loads: residential, commercial, and manufacturing. The residential will operate on real power (large resistance and low induction). A capacitor bank will be used to increase the power factor. No substations or transformers will be used.

A5. Wind Energy Research Course at Southern Illinois University

This course which is delivered during the summer has been redesigned recently to introduce the concept of Clean Energy Resources. The course is not restricted to ECE students and has been very popular between all students from different disciplines. Upon completion of this course students are supposed to be able to:

- Understand the energy supply and demand patterns for the United States and the world. Calculate energy consumption based on historic data, and future consumption based on past and predicted growth rates. Know the time until the reserve is depleted.
- Understand the basic laws and the role of all clean resources of energy, such as, wind, solar, hydro, oceanic, tidal, fuel cell, waste, and clean coal technology.
- Appreciate the social and economic issues, including public acceptance and economics of all alternative energy sources. Appreciate the role of government regulations and world events on energy utilization.
- Research and investigate issues related to energy resources of a specific energy source.

A6. Add Wind Energy Component to Traditional Course at Southern Illinois University

Course description of ECE-456 Embedded Control and Mechatronics lectures: Introduction to mechatronic systems, systems modeling and simulation, sensors and actuators, real-time interfacing, DSPs and micro-controllers, analysis of sampled-data systems, z-transform, digital control design techniques, emulation method, direct method, industrial applications.

This course is delivered once a year, in spring semester. It has been recently redesigned to introduce model-based control design techniques for embedded mechatronic systems using microcontrollers and Mathworks toolboxes, and has been offered twice a year so far. The course is offered to ECE senior undergraduate and graduate students. However, it is also open to students with appropriate background from other disciplines.

In the redesigned course, a number of recorded webinars from Mathworks, on the subject of modeling and control of wind turbines, have been presented in the lectures to expose the students to wind energy as an alternative energy source and to explore the techniques for modeling and control of turbines for harvesting this energy. The webinars include:

- Modeling a Wind Turbine Using MathWorks Tools, 53:00 minutes
- Designing Pitch and Yaw Actuators for Wind Turbines, 36:00 minutes
- Determining Mechanical Loads for Wind Turbines, 34:00 minutes
- Designing Control Systems for Wind Turbines, 34:00 minutes

The integration of webinars in some of the class lecture has been received well by the students.

B. Develop Graduate Courses in Wind Energy

B1. Elements of Sustainable Energy at Illinois Institute of Technology

This course covers cross-disciplinary subjects on sustainable energy that relate to energy generation, transmission, distribution, and delivery as well as theories, technologies, design, policies, and integration of sustainable energy. Topics include wind energy, solar energy, biomass, hydro, nuclear energy, and ocean energy. Focus will be on the integration of sustainable energy into the electric power grid, the impact of sustainable energy on electricity market operation, and the environmental impact of sustainable energy. The syllabus of this course is as follows.

B2. Elements of Smart Grid at Illinois Institute of Technology

This course covers cross-disciplinary subjects on smart grid that relates to energy generation, transmission, distribution, and delivery as well as theories, technologies, design, policies, and implementation of smart grid. Topics include: smart sensing, communication, and control in energy systems; advanced metering infrastructure; energy management in buildings and home automation; smart grid applications to plug-in vehicles and low-carbon transportation alternatives; cyber and physical security systems; microgrids and distributed energy resources; demand response and real-time pricing; and intelligent and outage management systems. The syllabus of this course is as follows.

B3. Wind Energy Power Systems at Southern Illinois University

This course, which is in the area of wind energy (wind turbine control, wind power generation, smart grid, etc.), has been developed and is being offered as part of the ECE Department Curriculum at graduate level. The catalog description of the course is as follows: “The course introduces graduate students to advanced configurations of wind energy power systems with an in-depth treatment of their control and protection. Wind speed and power relations, basic design of wind energy power systems, synchronous and induction generators, power inverters, generator drives-control modes, interface with the power grid-system modeling, stability, control and protection.” The syllabus of this course is as follows.

ECE 580 – Elements of Sustainable Energy, Fall 2010

Class Meetings: 6:25-9:05 PM, Tuesday; Location: Wishnick Hall 115

Instructor: Zuyi Li, PHD; Office: Room 223, Siegel Hall; Phone: (312) 567-5259; E-mail: lizu@iit.edu

Office hours: 3-5PM, Tuesday, or by appointment.

Textbook: No textbook is required

References

- Gilbert Masters, Renewable and Efficient Electric Power Systems, Wiley, 2004.
- Leon Freris and David Infield, Renewable Energy in Power Systems, Wiley, 2008.
- U.S. Department of Energy, 20% Wind Energy by 2030, 2008.
- Selected papers from the IEEE and other journal publications and conference proceedings.

Grading

Homework: 50%

Exam: 20%

Research Paper: 30%

The exam is open-book and open-notes.

A: [85, 100]

B: [70, 85)

C: [60, 70)

E: [0, 60)

Course Schedules (subject to change)

Week 1	August 24	Introduction to Sustainable Energy
Week 2	August 31	Renewable Energy Technologies
Week 3	September 7	Variability of Renewable Energy
Week 4	September 14	Operational Issues of Renewable Energy (1)
Week 5	September 21	Operational Issues of Renewable Energy (2)
Week 6	September 28	Operational Issues of Renewable Energy (3)
Week 7	October 5	Planning Issues of Renewable Energy (1)
Week 8	October 12	Planning Issues of Renewable Energy (2)
Week 9	October 19	Planning Issues of Renewable Energy (3)
Week 10	October 26	**Exam**
Week 11	November 2	Other Issues Related to Sustainable Energy (1)
Week 12	November 9	Other Issues Related to Sustainable Energy (2)
Week 13	November 16	Other Issues Related to Sustainable Energy (3) Presentation of Research Paper (1)
Week 14	November 23	Presentation of Research Paper (2)
Week 15	November 30	Presentation of Research Paper (3)
Week 16	Final Exam Week	Research Paper Due

ECE 581 – Elements of Smart Grid, Fall 2010

Class: W-F 10:00- 11:15 am; Location: PH 131

Instructor: Professor Mohammad Shahidehpour, 222 SH, (312) 567-5737, ms@iit.edu

Office Hours: W and F 2-3 pm (or by appointment)

Grading: HW: 30%, Class participation: 10%, Midterm exam: 25%, Final: 35%

Homework Assignments: Students must review the power point slides before attending the lecture. I will distribute eight technical papers throughout the semester. Students are required to summarize each paper and write a review on the paper within two weeks. Midterm and final exams will include questions on class presentations and the technical papers. Exams will be open book.

Course Schedules

August 25 Mohammad Shahidehpour Professor, IIT
August 27 Steve Blume President, Applied Professional Training
September 1 Mohammad Shahidehpour Professor, IIT
September 3 Christian Herzog President, Software Technologies Group
September 8 John Kelly President, IPS Corporation
September 10 Al Stevens Director, S&C Electric Company
September 15 Ken Zduneck Professor, IIT
September 17 Tony Metke Distinguished Member of Technical Staff, Motorola
September 22 Kui Ren Professor, IIT
September 24 Jim Gagnard President, Smart Signal
September 29 Terry Schuster Director, Energy Connect
September 30 Mohammad Shahidehpour Wind Energy Conference
October 1 Mohammad Shahidehpour Perfect Power Presentation
October 6 Robert Holz Director, Smart Lab
October 8 Tom Hulsebosch West Monroe Partners
October 13 Alireza Khaligh Professor, IIT
October 15 Joshua Milberg Deputy Commissioner, City of Chicago
October 20 Ali Emadi Professor, IIT
October 22 Midterm Exam Midterm Exam
October 27 Paul McCoy President, TransElect
October 29 Tim Stojka CEO, Fast Heat
November 3 Yang Xu Professor, IIT
November 5 Terence Donnelly Senior VP, ComEd
November 10 Mohammad Shahidehpour Professor, IIT
November 12 Mark Pruitt Director, Illinois Power Agency
November 17 Kevin Dennis VP, ZBB Energy
November 19 Tom Overbye Professor, University of Illinois
December 1 Farrokh Rahimi VP, Open Access Technology International
December 3 Mohammad Shahidehpour Professor, IIT
Final Exam

ECE 5813 Wind Energy Power Systems, Spring 2011

Instructor: C.J. Hatziadoniu, Professor: ENGR-E221; (618) 453-7036; hatz@siu.edu.

Office Hours: TR 10:00-11:30.

Lectures: TR 03:35-04:50 at ENGR-A0210.

Objectives: To introduce graduate students to the principles of electric power generation from the wind and to present issues related to the planning, design and control and protection of a wind generation system.

Description: Planning of wind farms, mechanical component design, electrical component design, wind generator to network interface, control and protection of wind generators.

Text: Grid Integration of Wind Energy Conversion Systems, 2nd Edition, by Siegfried Heier, translation by Rachel Waddington, Willey and Sons. ISBN: 978-0-470-86899-7.

Reference: Wind and Solar Power Systems, by Mukund R. Patel, CRC Press, 1999, ISBN 0-8493-1605-7. IEEE and IET Transactions, Class notes.

Class work: Three design projects.

Grading: Letter grade assignment is done according to the rule, A>=90>B>=80>C>=70>D>=60>F.

Topic by Lecture (with the corresponding text/reference book chapters) based on 75-min lectures:

1. Wind energy power plants (Chapter 1/1, 2 lectures).
2. Wind energy planning and economics (Chapter 6/(2,4,15,16), 6 lectures);
3. Power extraction from wind and energy conversion, Wind turbines, basic mechanical system design (Chapter 2/5, 4 lectures).
4. Synchronous and induction generators (Chapter 3/6, 5 lectures).
5. Power electronic converters and drive systems (Chapter 4/(7,11), notes, 4 lectures).
6. Grid-connected generators-grid interface; control and protection (Chapter 4/13, 5 lectures);
7. Generator monitoring and supervisory control, interactions with the power grid (Chapter 5, 4 lectures).
8. Examples of practical systems and bench marks (2 lectures).

C. Develop Professional Training Courses in Wind Energy

A Short Course on Wind Energy Technology, Interconnection and Integration

Wind power is an abundant, widely distributed energy resource that has zero fuel cost, zero emissions and zero water use. Wind power is the fastest growing form of generation in the world today, growing worldwide at the rate of 22.5% more than in 2009. Today, there is over 40.2 GW of wind capacity installed in the US, and over 194.4 GW of total wind capacity installed worldwide. American wind power is a mainstream electricity generation source and has been responsible for 35 percent of all new electric generating capacity over the last four years-more than coal and nuclear combined. In U.S. 38 states now have utility-scale wind projects, and 14 states have now installed more than 1,000 MW of wind power.

Wind turbine technology evolved remarkably over the past 20 years. The newer turbines have increased output and reduced generation costs with tall towers and longer blades. The newer machines also has better availability factor than that of coal and nuclear plants. Wind energy is one of the lowest priced renewable energy technologies available today, costing between 4 and 6 cents per kilowatt-hour. Moreover, a decline in the prices of wind turbines was observed which was due to (1) improved turbine technology, as witnessed by the recent and continued growth in average hub heights and rotor diameters, and (2) favorable terms for turbine purchasers, including reduced turbine delivery lead times, lesser need for large frame-agreement orders, initial operations and maintenance (O&M) contract durations that have increased from an average of 2-5 to 5-10 years, improved warranty terms, and more-stringent performance guarantees.

Despite growing demand for wind energy, the present technology still present significant challenges. Wind's challenges are largely related to its variable nature which can change by the season, day, hour and minute. For electricity grid operators the variability of wind, sometimes too much wind is blowing and at others too little, makes it difficult to integrate wind into a grid that was not designed for fluctuations.

Wind technology behaves differently than the conventional generating technologies and therefore in order to properly study and evaluate the impact of wind on power systems it is essential to understand its characteristics. This short course will provide an introduction to the underlying technology of wind turbine generators and wind power plants, how they are modeled for power system analysis purposes for planning and operating studies, and an introduction to using actual models in simulation programs.

This course is intended to provide the necessary background for engineers and researchers by addressing various aspects of interconnecting wind power plants into electric power systems. The study course is designed to provide knowledge on the state-of-the-art of wind-technology and wind-integration related issues.

The study course will mainly discuss insights on dealing with high wind power penetration levels in North America networks. In addition, a brief summary on the European wind energy performance is also presented.

This course is targeted towards power systems engineering and management personnel from utilities, RTOs, ISOs, and ITCs as well as consultants, manufacturers and developers involved with the evaluation and planning of the interconnection and operation of new wind plants. The students and professors who are working in the field of wind energy and technology will also benefit from this study course.

The wind study course is divided in 11 sessions which will be covered in 3 days. The sessions will begin at 10.00 AM each day. The duration of each session will be 45 minutes. At the end of each day attendees will be given an opportunity to raise any topics for discussion. The Course Outline is as follows.

Day 1: Introduction to Wind Energy and Technology

10.00 AM to 10.45 AM	Session 1: Wind Energy Outlook in 2010 • Growth of wind energy, market barriers & technology development
10.50 AM to 11.15 AM	Coffee Break
11.15 AM to 12.00 PM	Session 2: Wind Turbine Technology and Control – Part 1 • Components of wind turbine, power generation from wind, & different types of turbines
12.00 PM to 2.00 PM	Lunch Break
2.00 PM to 2.45 PM	Session 3: Wind Turbine Technology and Control – Part 2 • Control sub-systems, mechanical speed control, and generator configuration/control
2.50 PM to 3.15 PM	Coffee Break
3.15 PM to 4.00 PM	Session 4: Wind Plant Design • Components of wind power plant
3.15 PM to 4.00 PM	Q&A Session/Discussion

Day 2: Modeling and Grid Interconnection

10.00 AM to 10.45 AM	Session 5: Modeling and Simulation • Modeling of wind turbines for power flow, dynamic and short circuit studies
10.50 AM to 11.15 AM	Coffee Break
11.15 AM to 12.00 PM	Session 6: Introduction to Grid Codes • Summary of North American and European grid codes
12.00 PM to 2.00 PM	Lunch Break
2.00 PM to 2.45 PM	Session 7: Interconnection Case Studies • Steady state, transient and dynamic studies
2.50 PM to 3.15 PM	Coffee Break
3.15 PM to 4.00 PM	Q&A Session/Discussion

Day 3: Wind Plant Integration

10.00 AM to 10.45 AM	Session 8: Power System Operation • AGC, EMS, SCADA, control performance metrics, ancillary service requirements, operations planning
10.50 AM to 11.15 AM	Coffee Break
11.15 AM to 12.00 PM	Session 9: Impact of Wind Energy on Power System Operation • Wind power characteristics & uncertainties, Wind forecasting methods, and tools
12.00 PM to 2.00 PM	Lunch Break
2.00 PM to 2.45 PM	Session 10: Wind Integration Case Studies • Cost of wind integration
2.50 PM to 3.15 PM	Coffee Break
3.15 PM to 4.00 PM	Session 11: Capacity Value and Ancillary Services • System adequacy, and methods for calculating capacity credit
4.00 PM to 4.30 PM	Q&A Session/Discussion

3.3.3 Wind Energy Outreach

A. First Consortium Conference, September 30, 2010

On September 30, 2010, IIT's Center for Electricity Innovation hosted the 2010 meeting of the Consortium members on IIT's main campus in Chicago. The schedule for the day is as follows:

8:00-8:30 am Registration and Introduction
8:30-10:45 Discussion on implementation of the DOE-funded Wind Consortium project
10:45-12:00 Tour of the DOE-funded projects at IIT
12:00-1:00 pm Lunch
1:00-3:00 Symposium on Future of Wind Power Event
3:00-4:00 Reception

MORNING SESSION

The morning session will include presentations by consortium members and discussions of ongoing tasks. The discussions will be followed up by a tour of the DOE-funded projects at IIT.

Presentations (8:30-10:15 am)

Mohammad Shahidehpour, IIT
Frank Bristol, Acciona
Jim Gagnard, SmartSignal
Alan Cain, Innovation Technology Applications, and Ganesh Raman, IIT
Greg Rouse and John Kelly, Intelligent Power Solutions
Alireza Khaligh, IIT
Richard Gowen, Dakota Power
Zuyi Li, IIT
John Birge, University of Chicago

Discussion (10:15-10:45 am)

All Consortium members

Tour of the IIT Projects (10:45-12:00 noon)

- Wind Turbine Installations. The wind energy consortium tasks include the installation of two 8-kW wind units at IIT for research and education. The first unit already installed in one of the laboratories at IIT will be demonstrated as part of the campus tour.
- Perfect Power Smart Microgrid. IIT has been working on a DOE-funded perfect power project since 2008. The project is converting IIT to a microgrid for enhancing reliability, sustainability, and efficiency of its electricity grid. A tabletop model of the campus buildings is developed and a demonstration of the perfect power concept will be presented to the consortium members and guests.

Lunch (12:00 noon-1:00 pm) at McCormick Tribune Campus Center

AFTERNOON SESSION

Symposium on Future of Wind Power (1:00-3:00 pm)

The symposium will bring industry and government leaders together to discuss breakthrough technologies, innovations, and implementation developments in the industry. The state of the Wind Energy industry in the United States is facing numerous challenges, from wildlife and zoning concerns to the deficiencies of our nation's electric transmission grid. Yet, the industry is also being presented with new opportunities, from the country's first offshore wind farms, to new smart grid technologies that allow better integration of intermittent power into the grid.

Symposium Speakers:

Brian Connor – U.S. Department of Energy
Sonny Garg – President, Exelon Power & Senior Vice President, Exelon Generation
Michael Polsky – President/CEO, Invenergy
Paul McCoy – President, Trans-Elect
Kurt Yeager – Former President, EPRI / Executive Director, Galvin Electricity Initiative
Joshua Milberg - First Deputy Commissioner, City of Chicago Department of Environment

Reception (3:00-4:00 pm)

B. Second Wind Consortium Conference, July 20, 2011

On July 20, 2011, IIT's Center for Electricity Innovation hosted the 2011 meeting of the Consortium members on IIT's main campus in Chicago. The schedule for the day is as follows:

7:45-8:00 am Continental Breakfast

Introduction and Welcome Remarks

8:00-8:10 Mohammad Shahidehpour, PI, DOE Wind Consortium Project
8:10-8:15 Brian Connor, U.S. Department of Energy
8:15-8:20 Dave Loomis, Chair, Illinois Wind Working Group Annual Conference

Wind Energy Integration in the Eastern Interconnection

8:20-8:30 Paul McCoy, McCoy Energy and AWC
8:30-8:40 Aidan Tuohy, EPRI
8:40-8:45 Zuyi Li, Electrical and Computer Engineering Department, IIT
8:45-8:55 Panel Discussion

Wind Energy Installation at IIT

8:55-9:05 Marty Price, Viryd
9:05-9:15 C.S. Choi, KERI / Alex Flueck, IIT
9:15-9:25 Greg Rouse, IPS
9:25-9:35 Panel Discussion
9:35-9:50 BREAK

Wind Energy Research and Development

9:50-10:00 Richard Gowen, Dakota Power
10:00-10:10 Jay Giri, Alstom
10:10-10:20 David Chiesa, S&C
10:20-10:30 Panel Discussion

Wind Energy Education and Workforce Development

10:30-10:40 Hamid Arastoopour, Chemical & Biological Engineering Department, IIT
10:40-10:50 Ganesh Raman, MMAE Department, IIT
10:50-11:00 Bob Zavadil, EnerNex
11:00-11:10 Alireza Khaligh, ECE Department, IIT / Dietmar Rempfer, MMAE Department, IIT
11:10-11:20 Panel Discussion

Wind Energy Installation at Grand Ridge

11:20-11:30 Dave Parta, Smart Signal
11:30-11:40 Steve Moffitt, GE
11:40-11:50 Bill Fetzer, Catch the Wind
11:50-12:00 Panel Discussion
12:00 Closing

12:15 pm Ribbon Cutting Event – 8kW Wind Unit at IIT

Hamid Arastoopour, WISER (Moderator)
Mohammad Shahidehpour, Robert Galvin Center for Electricity Innovation
Brian Connor, U.S. Department of Energy
Robert Galvin, Galvin Electricity Initiative
Marty Price, Viryd
Michael Polsky, Invenergy

Kurt Yeager, Galvin Electricity Initiative
Terry Frigo, IIT

2:30 pm Ribbon Cutting Event – 1.5MW IIT Wind Unit at Grand Ridge, Illinois
Andrew Barbeau, IIT (Moderator)
Mohammad Shahidehpour, Robert Galvin Center for Electricity Innovation
Gary Nowakowski, U.S. Department of Energy
Stacy Kacek, Smart Signal
Bill Fetzer, Catch the Wind
James Rafferty, Invenergy

5:30 pm Adjourn

C. Great Lakes Symposium on Smart Grid and the New Energy Economy 2011

The first Great Lakes Symposium on Smart Grid and the New Energy Economy was held on October 18-19, 2011 on IIT's main campus. The symposium was presented by the Midwestern Governors Association, Illinois Science & Technology Coalition, Illinois Institute of Technology, Galvin Electricity Initiative, Citizens Utility Board, Environmental Defense Fund, Clean Energy Trust, UL, S&C Electric Company, Northwestern University, Argonne National Laboratory, Sierra Club, and Illinois Manufacturing Extension Center. The symposium was sponsored by Commonwealth Edison, Eaton Corporation, General Electric, Silver Spring Networks, and the Joyce Foundation. The agenda of the symposium is as follows.

TUESDAY, OCTOBER 18, 2011

Master of Ceremonies: Dr. Mohammad Shahidehpour
Director of the Robert W. Galvin Center for Electricity Innovation, Illinois Institute of Technology

Welcome and Keynote — AUDITORIUM

8 – 8:50 a.m.	**Registration in Lobby/Gallery**
9 – 9:10 a.m.	**Welcome** **Hon. Rahm Emanuel, Mayor, City of Chicago**
9:10 – 10 a.m.	**Keynote: Smart Grid and the New Energy Economy** **Ellen Alberding**, President, Joyce Foundation **Scott Lang**, President and CEO, Silver Spring Networks **Luke Clemente**, General Manager of Metering & Sensing Systems, GE Energy's Digital Energy Services
10 – 10:15 a.m.	**Leveraging the Convening Power of the PUC** **Doug Scott**, Chairman, Illinois Commerce Commission

MORNING SESSION

	EXPO CENTER	AUDITORIUM
	Midwest Policy Summit	Consumer Track: Path to Perfect Power
10:30 a.m. – Noon	How Can Smart Grid Technologies Increase the Efficiency between Transmission and Distribution? • Moderator: Mark Brownstein, Chief Counsel of the Energy Program, Environmental Defense Fund • Philip Moeller, Commissioner, Federal Energy Regulatory Commission • Vladimir Koritarov, Deputy Director of the Center for Energy, Environmental and Economic Systems Analysis, Argonne National Laboratory • Chantal Hendrzak, Director of Applied Solutions, PJM • Paul Centolella, Commissioner, Public Utilities Commission of Ohio	Leading Practices for Ensuring Consumer Empowerment • Moderator: Brewster McCracken, Executive Director, Pecan Street Inc. • Eric Dresselhuys, Executive Vice President and Chief Marketing Officer, Silver Spring Networks • Dr. Kristin B. Zimmerman, Manager of Advanced Technology Infrastructure, General Motors Research and Development Center • Dr. Louay Eldada, Chief Science Officer, VP Global R&D, SunEdison

LUNCHEON EXECUTIVE PANEL: The Pursuit of Quality and Innovation — BALLROOM

Noon – 1:30 p.m.

Moderator: **Jim Buckman**, Quality Advisor, Galvin Electricity Initiative
Michael Niggli, President and CEO, San Diego Gas & Electric
Anne Pramaggiore, President and COO, ComEd
Teri Ivaniszyn, Senior Director of Corporate Excellence, Florida Power & Light

AFTERNOON SESSION

	EXPO CENTER	AUDITORIUM
	Innovation and Economic Opportunity Track	**Consumer Track: Path to Perfect Power**
1:30 – 3 p.m.	**Smart Grid and Energy Business Leadership Roundtable** • **Session Kick-Off: A Futurist Point of View:** Michael J. Meehan, Senior Principal Consultant, KEMA • **Integration of Renewable Resources/Energy Storage:** Jay Marhoefer, CEO, Intelligent Generation; Chris Walti, Power Originator, Acciona Energy • **Smart Buildings:** Chris Thomas, Policy Director, Citizens Utility Board; Peter Scarpelli, Vice President of Global Leader of Energy Services, CB Richard Ellis • **Electrified Transportation:** Paul H. Pebbles, Global Electrification Product Manager, OnStar®; Sam Ori, Director of Policy, The Electrification Coalition • **Home/Community Adoption:** Jonathan "JT" Thompson, Smart Appliance Utility Leader, GE Appliances – Home and Business Solutions; Rep. Daniel Biss, Illinois State Representative, 17th District	**Leading Practices for Grid Safety, Reliability and Power Quality** • Moderator: Mike Edmonds, Vice President of Strategic Solutions, S&C Electric Company • David Wade, EVP and COO, Electric Power Board of Chattanooga, Tenn. • Mark Curran, Director of Public Utilities – Electric, City of Naperville, Ill. • Greg Blake, Global Smart Grid Sales Director, GE Energy's Digital Energy Services • Terence Donnelly, Executive Vice President of Operations, ComEd
	Midwest Policy Summit	**Innovation and Economic Opportunity Track**
3:15 – 4:15 p.m.	**Articulating the Benefits of Smart Grid** • Suzanne Malec-McKenna, Former Commissioner, City of Chicago Department of Environment • David Kolata, Executive Director, Citizens Utility Board • Michael Gregerson, Energy Consultant, Great Plains Institute • Beth Soholt, Director, Wind on the Wires • Jacqueline Voiles, Director of Regulatory Affairs, Ameren Illinois • Wade Malcolm, Global Senior Director for Smart Grid Operations Technology, Accenture	**Innovative Marketplace Quick Pitch Competition** **JUDGES:** • Doug Dillie, Director of Smart Grid Solutions, Eaton Corporation • Mark Zhu, Investment Professional, DTE Energy Ventures • Paul H. Pebbles, Global Electrification Product Manager, OnStar® • Chris Walti, Power Originator, Acciona Energy • Kerri Breen, Principal, Arsenal Venture Partners • Rob Schultz, Senior Director, IllinoisVENTURES • Teresa Esser, General Partner, Capital Midwest Fund • Sam Hogg, Director of Venture Development, NextEnergy • Kirk Colburn, Managing Director, SURGE • Rep. Robyn Gabel, Illinois State Representative, 18th District • Steve Moffitt, Account Executive, GE
4:15 – 4:30 p.m.	**BREAK**	
4:30 – 5:30 p.m.	**Midwest Smart Grid Pilots: Realizing the Economic Value of Smart Grid** • Moderator: Matthew Summy, President, Illinois Science and Technology Coalition • Nic Stover, Regional Sales Director, Northwest, EnerNOC	

4:30 – 5:30 p.m. **Midwest Smart Grid Pilots: Realizing the Economic Value of Smart Grid** (Continued)

- Shaun Summerville, Marketing Program Manager, DTE Energy
- Dan Francis, Manager of gridSMART Policy, American Electric Power
- DeWayne Todd, Corporate Compliance and Regulatory Affairs, Warrick Primary Metals

NETWORKING RECEPTION: 5:30 – 7 p.m.

WEDNESDAY, OCTOBER 19, 2011

Keynote: Smart Grid and Climate Change

9 – 10 a.m. Michael Brune, Executive Director, Sierra Club

MORNING SESSION

	EXPO CENTER	AUDITORIUM	ARMOUR DINING ROOM
	Midwest Policy Summit	Consumer Track: Path to Perfect Power	Innovation and Economic Opportunity Track
10 – 11 a.m.	**Developing Good Smart Grid Policy** • Moderator: Lauren Navarro, Attorney, Environmental Defense Fund • Phyllis Reha, Vice Chair, Minnesota Public Utilities Commission	**Leading Practices for Integrating Clean and Efficient Power** • Moderator: John Kelly, Executive Director, Galvin Electricity Initiative • Sue Tierney, Managing Principle, Analysis Group • Mike Bull, Manager of Environmental Policy, Xcel Energy • Shawn Marshall, Executive Director, Lean Energy • Tom Barwin, Village Manager, Oak Park	**Growing the Smart Grid Regional Innovation Cluster Workshop** • Matthew Summy, President, Illinois Science and Technology Coalition • Dan Bowman, Principal, PricewaterhouseCoopers PRTM Management Consulting • Oliver Hazimeh, Principal, PricewaterhouseCoopers PRTM Management Consulting • Jared Racine, Senior Associate, PricewaterhouseCoopers PRTM Management Consulting
11 a.m. – Noon	**Developing Great Midwest Smart Grid Strategies** • Moderator: Miriam Horn, Director, Smart Grid Initiatives, Environmental Defense Fund • Ed Miller, Environment Program Manager, Joyce Foundation • Tom Catania, Vice President of Government Relations, Whirlpool • Ade Dosunmu, Senior Director of Strategic Markets, Comverge		

LUNCHEON: Midwest Energy Leadership Awards

Noon – 1:30 p.m. Luncheon and Awards Presentation

1:30 – 3 p.m. Tour of the Perfect Power Microgrid at Illinois Institute of Technology

D. Great Lakes Symposium on Smart Grid and the New Energy Economy 2012

On September 24-26, 2012, the Robert W. Galvin Center for Electricity Innovation will host the second annual Great Lakes Symposium on Smart Grid and the New Energy Economy, on the Illinois Institute of Technology's campus in Chicago. The Symposium will feature keynote and plenary sessions, technical presentations, and tutorials by international experts on smart grid applications. The Symposium is a one-of-a-kind event that breaks new ground in smart grid design and development and showcases smart grid best practices from around the country along with new technologies and ideas that are spurring innovation, growing state economies, reducing emissions and empowering consumers to conserve and save. Participants will have the opportunity to engage thought leaders on key policy questions, identify investment and job creation opportunities, and learn about projects already underway.

The symposium was technically sponsored by the Robert W. Galvin Center for Electricity Innovation and the IEEE Power and Energy Society. The symposium was financially sponsored by Commonwealth Edison, Environmental Defense Fund, Silver Spring Networks, Ameren Illinois, Eaton Corporation, Landis+Gyr, S&C Electric Company, the Joyce Foundation, OSIsoft, and General Electric. The agenda of the symposium is as follows.

MONDAY | SEPTEMBER 24, 2012

MONDAY MORNING

8:30 a.m. – Noon

SHORT COURSES

1. **Introduction to Smart Grids and Smart Grid Roadmaps**
   Room: Hermann Lounge
2. **How Today's Grid is Evolving for the 21st Century**
   Room: Hermann Hall – Trustee Dining Room
3. **Microgrids – Designing Their Role in Smart Grid**
   Room: Hermann Hall – 007

MONDAY | SEPTEMBER 24, 2012

MONDAY AFTERNOON

1:30 pm – 2:00 pm

4. Introduction and Welcome Remarks
Hermann Hall Ballroom

- Mohammad Shahidehpour, Chair, Great Lakes Symposium on Smart Grid and the New Energy Economy
- Noel Schulz, President, IEEE Power and Energy Society

2:00 pm – 3:00 pm

5. Plenary Session: Illinois Smart Grid Deployment
Hermann Hall Ballroom

- Chair: Wanda Reder, S&C Electric
- Anne Pramaggiore, President and CEO, ComEd
- Richard Mark, President and CEO, Ameren Illinois
- Scott Lang, President and CEO, Silver Spring Networks

3:00 pm – 3:30 pm

AFTERNOON BREAK
Expo Room

3:30 pm – 5:15 pm

6. Panel Session: Military Microgrids
Hermann Hall Ballroom

- Chair: Tom Podlesak, US Army
- Robert Lasseter, University of Wisconsin-Madison
- Tristan Glenwright, Boeing
- Tarek Abdalla, U.S. Army Engineer Research and Development Center
- Gary Wetzel, S&C Electric
- Doug Houseman, EnerNex

7. Panel Session: Electric Vehicles and Mobility in Energy Systems
McCormick Tribune Campus Center (MTCC) Auditorium

- Chair: Sharon Feigon, CEO, I-GO Cars
- Gary Rackliffe, ABB
- Abas Goodarzi, US Hybrid
- Mike McMahan, ComEd
- Ramteen Sioshansi, Ohio State University
- Michael Abba, Ameren

8. Panel Session: Smart Grid Cyber Security and Data Management
McCormick Tribune Campus Center (MTCC) Ballroom

- Chair: Erich Gunther, EnerNex
- Tony Metke, Motorola Solutions
- Joseph Giampapa, Carnegie Mellon University
- Alfonso Valdes, University of Illinois
- Michael Manske, West Monroe Partners

9. Panel Session: Transmission Planning Issues for Variable Energy Resources
Armour Dining Room

- Chair: Paul McCoy, McCoy Energy Consulting
- Marcelino Madrigal, World Bank
- Beth Soholt , Wind on the Wires
- John Moore, Sustainable FERC Project
- Julija Matevosyan, ERCOT
- Scott Deffenderfer, Ameren

10. Paper Session: Advanced Distribution Systems
Alumni Lounge

- Chair: Amin Khodaei, University of Houston
- *Electricity Fraud Detection by Incorporating PV System Using Support Vector Machines*
  Yonghe Guo and Chee-Wooi Ten, Michigan Technological University
- *An Analytical Approach for Reliability Evaluation of Aged Distribution Systems*
  Masood Parvania, Mahmud Fotuhi-Firuzabad, Sharif University of Technology
- *Online Management Framework for Distribution System with Wind Generation*
  Bhairavi Pandya and Chee-Wooi Ten, Michigan Technological University

5:30 pm – 7:00 pm

EVENING RECEPTION
Expo Room

TUESDAY | SEPTEMBER 25, 2012

TUESDAY MORNING

8:00 am – 8:30 am

BREAKFAST
Expo Room

8:30 am – 9:00 am

11. Keynote Speaker: Michael Polsky, President and CEO, Invenergy
Hermann Hall Ballroom

9:00 am – 10:00 am

12. Plenary Session: Offshore Wind at Great Lakes
Hermann Hall Ballroom

- Chair: The Honorable Robyn Gabel, Representative, 18th District, Evanston, Illinois
- Lorry Wagner, President of LEEDCo
- Jack Darin, Sierra Club
- Mary Ann Christopher, Esq., Law Office of Mary Ann Christopher

10:00 am – 10:30 a.m.

MORNING BREAK
Expo Room

10:30 am – 12:15 pm

13. Panel Session: Wind Turbine Operation and Control
McCormick Tribune Campus Center (MTCC) Auditorium

- Chair: Bill Fetzer, VP, BlueScout Technologies
- Don Doan, GE Intelligent Platforms (Smart Signal)
- Aidan Tuohy, EPRI
- Steve Moffitt, GE Energy

14. Panel Session: Power System Operations: EV Infrastructure and Smart Distributed Systems
Hermann Hall Ballroom

- Chair: Kate Tomford, Illinois Department of Commerce and Economic Opportunity
- Stephanie Cox, Ecotality
- Ted Bohn, Argonne National Laboratory
- Johan Enslin, University of North Carolina
- Paul Myrda, EPRI

15. Panel Session: Smart Homes, Electric Vehicles and Demand Response
Armour Dining Room

- Chair: Jianhui Wang, Argonne National Laboratory
- Vladimir Koritarov, Argonne National Laboratory
- Marty Cohen, Board Chairman, Illinois Science and Energy Innovation Fund
- John Finnigan, Environmental Defense Fund
- Prakash Thimmapuram, Argonne National Laboratory
- Zhi Zhou, Argonne National Laboratory

16. Panel Session: Solar Energy Integration
McCormick Tribune Campus Center (MTCC) Ballroom

- Chair: Mark Handy, KenJiva Energy Systems
- Jeff Smith, West Monroe Partners
- Madeleine Weil, SoCore Energy
- Tom Tansy, SunSpec Alliance

17. Paper Session: Impacts of PHEV on Transportation and Energy Systems
Alumni Lounge

- Chair: Kuilin Zhang, Argonne National Laboratory
- *An Information System for Electric Vehicle Charging Infrastructure Deployment*
  Diego Klabjan and Timothy Sweda, Northwestern University
- *An Analysis of Car and SUV Daytime Parking for Potential Charging of Plug-in Electric Vehicles*
  Yan Zhou, Argonne National Laboratory
- *Dynamics of PEV Driving and Charging Behavior under Intelligent Energy Management Systems*
  Kuilin Zhang, Argonne National Laboratory

TUESDAY | SEPTEMBER 25, 2012

TUESDAY AFTERNOON

12:15 pm – 1:30 pm

18. Luncheon Keynote Speaker

Expo Room

- Chair: Alex Flueck, Illinois Institute of Technology
- Presenter: Mani Venkata, Principal Scientist, Alstom

1:30 pm – 3:00 pm

19. Plenary Session: Great Lakes Forum on Regulatory Policy

Hermann Hall Auditorium

- Chair: Joshu Milberg, Willdan Energy
- Andre Porter, Ohio Public Utility Commission
- Eric Callisto, Wisconsin Public Utility Commission
- Ed Miller, Program Manager, Joyce Foundation

3:00 pm – 3:30 pm

AFTERNOON BREAK

Expo Room

3:30 pm – 5:15 pm

20. Panel Session: Microgrid Planning and Operation

Hermann Hall Auditorium

- Chair: Shay Bahramirad, S&C Electric
- Mani Venkata, Alstom
- Maryam Saeedifard, Purdue University
- Ernst Camm, S&C Electric
- Steve Pullins, Horizon Energy Group
- Mike Presutti, Agentis

21. Panel Session: Electric Vehicle Manufacturing in Great Lakes States

Armour Dining Room

- Chair: Steve Johanns, Eaton
- John Wirtz, Eaton Business Unit Manager
- Angela Strand, Chief Marketing Officer, Smith Electric
- Ron Prosser, CEO, Green Charge Networks and Chair, Smart Grid on the U.S.–China Clean Energy Forum
- John Shen, University of Central Florida

22. Panel Session: Smart Grid Workforce Training and Education

McCormick Tribune Campus Center (MTCC) Auditorium

- Chair: Bruce Hamilton, President, Adica and Smart Grid Network
- Gary Blank, Vice-President, IEEE-USA
- Marge Anderson, Executive Vice President, Energy Center of Wisconsin
- Julie Elzanati, Executive Director, Illinois Green Economy Network
- Matt Shields, Workforce Development Agency, State of Michigan

23. Panel Session: Geomagnetic Disturbances on the Power Grid

McCormick Tribune Campus Center (MTCC) Ballroom

- Chair: Tom Overbye, University of Illinois
- David Wojtczak, ATC
- Scott Dahman, PowerWorld Corporation
- Alan Engelmann, ComEd
- Tom Overbye, University of Illinois

24. Paper Session: Smart Grid: Policy, Regulation and Customer Engagement

Alumni Lounge

- Chair: Alex Tang, Clean Energy Trust
- *Regulation, Competition, and New Technology Adoption: Applying the Bell Doctrine to Retail Electricity Markets*

  Lynne Kiesling, Northwestern University
- *Customer Privacy & The Smart Grid: Where the Policy Debate Presently Stands & the Strategic Steps Utilities Should be Taking Today*

  Will McNamara, West Monroe Partners
- *Infinite-horizon Economic MPC for HVAC systems with Active Thermal Energy Storage*

  David Mendoza-Serrano and Donald Chmielewski, Illinois Institute of Technology
- *Communicating to Engage the Modern Customer in the New Energy Economy*

  David Tilson, West Monroe Partners

5:30 pm – 6:15 pm

NETWORKING RECEPTION

Gallery Lounge

6:15 pm – 8:00 pm

25. Dinner and Keynote Session

- Speaker: Alan Wendorf, Chairman, President, and CEO, Sargent and Lundy

WEDNESDAY | SEPTEMBER 26, 2012

WEDNESDAY MORNING

8:00 am – 8:30 am

BREAKFAST

Expo Room

8:30 am – 9:00 am

26. Keynote Speech

Hermann Hall Ballroom

- Chair: Peter Sauer, University of Illinois
- Presenter: Wanda Reder, Vice President, S&C

9:00 am – 10:00 am

27. Plenary Session: Recovery Act Demonstrations of Smart Grid Development

Hermann Hall Ballroom

- Chair: Joseph Paladino, U.S. Department of Energy
- Jim Hull, DTE
- Olga Geynisman, City of Naperville
- Barry Feldman, Indianapolis Power and Light

10:00 am – 10:30 a.m.

MORNING BREAK

Expo Room

10:30 am – 12:15 pm

28. Panel Session: Microgrid Storage

McCormick Tribune Campus Center (MTCC) Auditorium

- Chair: Troy Miller, S&C
- Tony Siebert, ZBB Energy Corporation
- James J. Greenberger, National Alliance for Advanced Technology Batteries
- Henry Louie, Seattle University
- Mitch Mabrey, Dow Kokam

29. Panel Session: Utilizing Smart Grid Test Beds in Illinois

McCormick Tribune Campus Center (MTCC) Ballroom

- Chair: Robert Greenlee, Illinois Science & Technology Coalition
- Joseph Clair, Illinois Institute of Technology
- Timothy Yardley, University of Illinois
- David Pope, Village of Oak Park
- Rod Hilburn, Ameren

30. Panel Session: Customer Engagement and Empowerment

Hermann Hall Ballroom

- Chair: Scott Binnings, Patton Boggs
- Michael Murray, Lucid Design Group
- Val Jensen, ComEd
- David Hodgson, UK Trade & Investment
- Tom Wieser, PaceControls

31. Panel Session: Storage for Power System Operation

Armour Dining Room

- Chair: Caisheng Wang, Wayne State University
- Daniel Lindenmeyer, Infineon
- Anurag K Srivastava, Washington State University
- Roland Kibler, NextEnergy
- Piyush Desai, Danfoss

32. Paper Session: Smart Grid Monitoring and Cyber Security

Alumni Lounge

- Chair: Zuyi Li, Illinois institute of Technology
- *Video Monitoring Solutions for Utilities – Using video to make a Grid Smarter*

  John McClean, Powerstream Inc.
  Anselm Viswasam, Systems with Intelligence, Inc.
- *How Electrical System Monitoring Improves Facility Efficiency, Reliability and Safety*

  Dave Loucks, Eaton Corporation, Greg Reed, University of Pittsburgh
- *Substation Cybersecurity Architectural Design*

  Pingal Sapkota and Chee-Wooi Ten, Michigan Technological University

WEDNESDAY | SEPTEMBER 26, 2012

WEDNESDAY AFTERNOON

12:15 pm – 1:30 pm

33. Luncheon Keynote Speaker
Expo Room
- Chair: Andrew Barbeau, Robert W. Galvin Center, Illinois Institute of Technology
- Presenter: Arlene Juracek, Director, Illinois Power Agency at State of Illinois

1:30 pm – 3:00 pm

34. Plenary Session: Shifting Smart Grid focus to Customer Driven Performance Outcomes
Hermann Hall Ballroom
- Chair: John Kelly, Perfect Power Institute
- Farokh Rahimi, OATI
- Austin Montgomery, Carnegie Mellon University
- Dave Roberts, OSIsoft
- Paul Alvarez, Wired Group

3:00 pm – 3:30 pm

AFTERNOON BREAK
Expo Room

3:30 pm – 5:15 pm

35. Panel Session: Smart Grid Innovation in Great Lakes Region
Hermann Hall Ballroom
- Chair: Karen Weigert, City of Chicago
- Jay Marhoefer, Intelligent Generation
- Scott Henneberry, Schneider Electric
- Dan Francis, American Electric Power
- Jett Tackbary, West Monroe Partners

36. Panel Session: Community Choice Aggregation: Progress and Promise
McCormick Tribune Campus Center (MTCC) Auditorium
- Chair: Mark Pruitt, Power Bureau
- Ghida Neukirch, Buffalo Grove Deputy Village Manager
- Maria Fields, Joule Assets
- David Kolata, Citizens Utility Board
- Kris Torvik, Wired Group

37. Panel Session: Smart Homes and Distributed Generation
McCormick Tribune Campus Center (MTCC) Ballroom
- Chair: Joyce Coffee, Edelman
- Colin Meehan, Environmental Defense Fund
- Paul Navratil, University of Texas
- Charles O'Donnell, Siemens
- George Thomas, Contemporary Controls

38. Panel Session: Future of Nuclear
Armour Dining Room
- Chair: Michael Corradini, American Nuclear Society
- Jack Grobe, Exelon Nuclear Partners
- Alexander Marion, Nuclear Energy Institute.
- Yoon Il Chang, Argonne National Laboratory
- Scott Bond, Ameren

39. Paper Session: Power System Planning
Alumni Lounge
- Chair: Lei Wu, Clarkson University
- *Probabilistic Production Cost Simulation and Reliability Evaluation of Composite Power System Including Renewable Generators*
  Jintaek Lim, Jinhwan Jang and Jaeseok Choi, Gyeongsang National University, South Korea
  Keonghee Cho, Korea Economic Research Institute (KERI), South Korea
  Junmin Cha, Daejin University, South Korea
- *A Hybrid Method for Long-Term Transmission Lines Expansion in Large-Scale Electric Grids*
  Mohammad Albaijat, University of California at Davis
  Kaveh Aflaki, Illinois Institute of Technology
- *Coordinated Expansion Planning of Generation and Transmission Systems Considering Outage Cost*
  Jintaek Lim, Jinhwan Jang and Jaeseok Choi, Gyeongsang National University, South Korea
  Donghoon Jeon, Korea Electric Power Corporation (KEPCO), South Korea